Inversion of Seismic Data for Layered Crustal Structure

Nicholas Rawlinson
B.Sc. Hons (1997)

Dissertation for the degree of Doctor of Philosophy

Department of Earth Sciences
Monash University
Clayton VIC 3800
Australia

December 2000

Contents

Summary **v**

Declaration **vii**

Acknowledgements **viii**

1 Introduction **1**

1.1 Mapping Earth Structure Using Seismic Waves 1

1.1.1 Defining Seismic Tomography 4

1.1.2 Seismic Structure from Controlled Sources 10

1.1.3 Mapping Local Structure Using Earthquakes 15

1.1.4 Regional and Global Studies Using Earthquakes 20

1.1.5 Summary 26

1.2 Outline of Research Project 26

1.2.1 Aims 28

1.2.2 Method and Software Development 29

1.2.3 2-D Teleseismic Analysis 31

1.2.4 3-D Wide-Angle Analysis 31

1.3 Structure of Thesis 33

2 Methods of Traveltime Inversion **35**

2.1 Representation of Structure 35

2.2 Traveltime Determination 44

2.2.1 Ray Tracing 45

2.2.2 Wavefront Tracking 52

2.2.3 Shortest Path Ray Tracing (SPR) 57

2.3 Solving the Inverse Step . . . 59
2.3.1 Backprojection . . . 59
2.3.2 Gradient Methods . . . 61
2.3.3 Global Optimisation . . . 73
2.4 Analysis of Solution Quality . . . 76

3 Inversion of Teleseismic Traveltime Residuals 80
3.1 Introduction . . . 80
3.2 Method . . . 82
3.3 Tests with Synthetic Data . . . 85
3.4 Application to Central Australia Dataset . . . 92
3.5 Discussion . . . 102
3.6 Summary . . . 105

4 3-D Wide-Angle Traveltime Inversion Method 107
4.1 Introduction . . . 107
4.2 Method . . . 110
4.2.1 Model Parameterisation . . . 110
4.2.2 Ray Tracing . . . 113
4.2.3 Inversion Scheme . . . 122
4.3 Synthetic Tests . . . 125
4.3.1 Inversion for 2-D Structure . . . 126
4.3.2 Inversion for 3-D Structure . . . 151
4.3.3 Subduction Zone Setting . . . 168
4.4 Summary . . . 176

5 Crustal Studies of Tasmania 179
5.1 Tectonic Evolution of Tasmania . . . 179
5.2 Previous Geophysical Work . . . 186
5.3 TASGO Wide-Angle Seismic Survey . . . 193
5.3.1 Aims of the TASGO Project . . . 193
5.3.2 Details of the TASGO Wide-Angle Survey . . . 196
5.3.3 Data Coverage and Quality . . . 198

6 Processing and Picking of TASGO Data 202

6.1 Introduction . . . 202
6.2 Trace Visualisation . . . 203
6.3 Filtering . . . 205
6.4 Stacking . . . 208
6.5 Static Correction . . . 211
6.6 Deconvolution . . . 216
6.7 Picking of TASGO Data . . . 223

7 Inversion of TASGO Data 232

7.1 Introduction . . . 232
7.2 Inversion for 1-D Structure . . . 233
7.3 Inversion for 2-D Structure . . . 240
7.4 Inversion for 3-D Structure . . . 247
7.4.1 Crustal Structure of NW Tasmania . . . 249
7.4.2 Moho Structure of Tasmania . . . 262
7.5 Comparison with Results from Other Deep Crustal Studies of Tasmania . . 277
7.6 Geological and Tectonic Implications . . . 289
7.7 Summary . . . 292

8 Conclusions 295

References 307

Appendices

A Linearisation 333

B Ray Tracing Equations 335

C Fréchet Derivatives 338

D Description of Inversion Program 341

E Static Correction for Water Depth 349

F Contents of Enclosed CD 352

Summary

In this study, tomographic inversion techniques are applied to seismic traveltime data in order to constrain layered crustal structure. Methods for teleseismic data and wide-angle data are separately considered. Inversion of teleseismic data conventionally uses a model parameterisation that describes a variable velocity field. An interesting and viable alternative to this approach is to represent structure using layers separated by variable depth interfaces. A 2-D interface inversion method is used to test this claim. Structure is represented by constant velocity layers separated by smooth interfaces and a shooting method of ray tracing is used for traveltime determination. A conjugate gradient method is used to iteratively improve the fit between observed and predicted traveltime residuals. Application of the method to data collected in central Australia produces a solution consistent with a previously published solution that used the same data but represents structure with a variable velocity parameterisation. These results demonstrate that variations in lateral structure represented by interface deflections can be resolved by teleseismic data.

A new method is presented for the determination of 3-D layered crustal structure by simultaneous inversion of seismic refraction and wide-angle reflection traveltimes. Crustal structure is represented by layers in which velocity varies linearly with depth, separated by smooth interfaces defined by a bicubic B-spline parameterisation. Lateral variations in structure are therefore represented by variations in interface depth only. For this choice of model parameterisation, ray paths consist of piecewise circular arc segments for which analytic expressions of trajectory and traveltime are calculated. A shooting method is employed to solve the two-point problem and a subspace inversion method is used to solve the inverse problem of minimising the traveltime misfit, subject to model regularisation.

Synthetic tests show that the method can simultaneously reconstruct interface geometry and layer velocity in the presence of realistic levels of noise. These tests also demonstrate that layer pinchouts can be effectively represented and resolved by the data, making the method suitable for use in complex tectonic environments like subduction zones. Estimates of *a posteriori* model covariance and resolution obtained from linear theory were found to be useful in analysing solution reliability despite the non-linear nature of the problem.

Application of the method to data collected as part of the 1995 TASGO project in

Tasmania produced a four-layer crustal model of NW Tasmania and a Moho map of the entire island. The average velocity of the crust is 6.2 km/s, the average P_n velocity is 8.0 km/s and the average depth of the Moho is approximately 31 km, though the Moho is unresolved beneath central Tasmania where ray path coverage is poor. This estimate of Moho depth is significant because previous studies have suggested a much thinner crust. The Rocky Cape Element in the NW was found to be composed of relatively thin crust, which thickens rapidly to the SE beneath the Arthur Lineament. A local thickening of the crust to 37 km just west of the Tamar River is consistent with the juxtaposition of the East and West Tasmania Terranes during the Tabberabberan Orogeny.

Declaration

I declare that this thesis contains no material that has been accepted for the award of any other degree or diploma at any university or other institution. I also declare that, to the best of my knowledge, this thesis contains no material previously published or written by another person, except where due reference is made in the text.

Nicholas Rawlinson

Acknowledgements

I would like to thank a number of people for their assistance during the completion of my PhD work. First and foremost, I would like to thank my supervisor Greg Houseman whose guidance and unfailing high standards were much valued. His meticulous review of the original version of this thesis has led to significant improvements.

I would also like to thank several people from AGSO (Australian Geological Survey Organisation) who provided me with the digitised TASGO dataset that forms the basis of much of this work. Clive Collins is especially thanked for his patience in dealing with my constant queries regarding data format, data availability, etc. Clive also made numerous suggestions about appropriate methods for processing and picking the data throughout the course of my PhD. Thanks also to Tanya Semenova for undertaking and successfully completing the daunting task of digitising the analogue data and converting the digital observatory data into a comprehensible format. I also appreciate the support of Barry Drummond, who was instrumental in making the wide-angle component of the TASGO survey happen, and who was a constant source of motivation during my attempts to interpret this challenging dataset.

Others who contributed significantly to the collection of the TASGO data include Tony Brown, Director of Mineral Resources, Tasmania, and Tim Barton, Ed Chudyk, Ray Bracewell and Tony Yeates from AGSO. The air gun shots were provided by the AGSO Marine personnel and the Master and Crew of the R/V *Rig Seismic*. I also acknowledge the Tasmanian Geological Survey and University of Tasmania personnel who assisted with the deployment of the portable seismic array. Professor R. Large of the University of Tasmania is thanked for access to the University of Tasmania seismic network data.

I wish to thank Herb McQueen and Kurt Lambeck for kindly providing the central Australian teleseismic dataset, on which Chapter 3 is based.

Thanks also to everyone in the Department of Earth Sciences, Monash University for providing a friendly and constructive work environment. In particular, I would like to thank Frank Graeber for his many suggestions and constructive criticism of my work. His knowledge of LaTeX, xfig, GMT and Unix were of great benefit to me. I would also like to thank Lynn Evans and Cameron Blackwood for their assistance in solving numerous software and hardware problems. I thank Julie Elders and Trudi Hoogenboom for proof reading the penultimate version of this thesis and making sure that I wasn't lonely in my

isolated office. I also thank Geoff Pike and Caroline Forbes for motivating me to work long hours towards the latter stages of writing up.

I would like to acknowledge the financial support provided to me by way of an Australian Postgraduate Award and the additional funds provided by the AGCRC (Australian Geodynamics Cooperative Research Centre).

Last but not least, I would like to thank my family and friends for their support and understanding over the last few years.

All figures in this thesis were produced by the author using the free software packages Geomview, GMT, PGPLOT and xfig unless referenced otherwise. Several figures were kindly provided by Tim Barton (Figures 7.39, 7.40, 7.41, 7.42 and 7.43) and Clive Collins (Figure 5.1) of AGSO, Herb McQueen of ANU (Figure 3.12b), and Frank Graeber, now of CTBTO (Figure 1.6a,b). This thesis was typeset using the free teTEXversion of LATEX 2_ε.

Chapter 1

Introduction

1.1 Mapping Earth Structure Using Seismic Waves

Although the origins of seismology as a science can be traced back to the mid 1700s with the work of John Michell (Davison, 1978), the use of seismic waves to map earth structure really only began in the late 1800s with the advent of the seismogram. A seismogram is a record of the time-dependent ground displacement of the earth due to the passage of seismic waves. There are three basic ingredients that contribute to the shape of a seismogram: the source signature, the elastic properties of the earth through which the wave propagates and the detection and recording characteristics of the seismic recorder. One additional ingredient that is ubiquitous to all seismograms is noise. If the term *signal* defines those events on the seismogram from which we wish to obtain information, then everything else is *noise* (causes include spurious sources, near surface effects, electrical components of receiver etc.). When seismic waves are used to map earth structure, a major task is to identify those parts of the seismogram that are due to the elastic response of the earth. It is then possible to use the seismic data to constrain models (mathematical representations) of earth structure. This thesis aims to use the traveltimes of seismic waves to constrain layered models of the earth's crust. More specifically, inversion schemes are developed and applied to controlled source wide-angle data collected in Tasmania and data from distant earthquakes (teleseismic data) collected in central Australia. Since the subject of this thesis falls within the broad category of mapping earth structure using seismic waves, in this chapter I first give a brief overview of the methods, data and results associated with this field of seismology.

When a seismometer detects and records seismic energy from an event such as a distant earthquake, the record is usually characterised by a number of distinct peaks which indicate the arrival of different phases. These phases represent different types of waves that propagate in an elastic medium (P-wave, S-wave, Love wave, Rayleigh wave) and the interactions of the source waveform with the material through which it propagates. Figure 1.1 shows an example of a distant earthquake record with several phases identified. Receivers placed at varying distances from a source will record phase arrivals at different times. If records are positioned side by side according to distance from the source, then coherent phases will form traveltime curves whose geometries are dependent on subsurface velocity structure. This type of display is widely used in seismology because it helps identify different phases and gives an insight into subsurface structure.

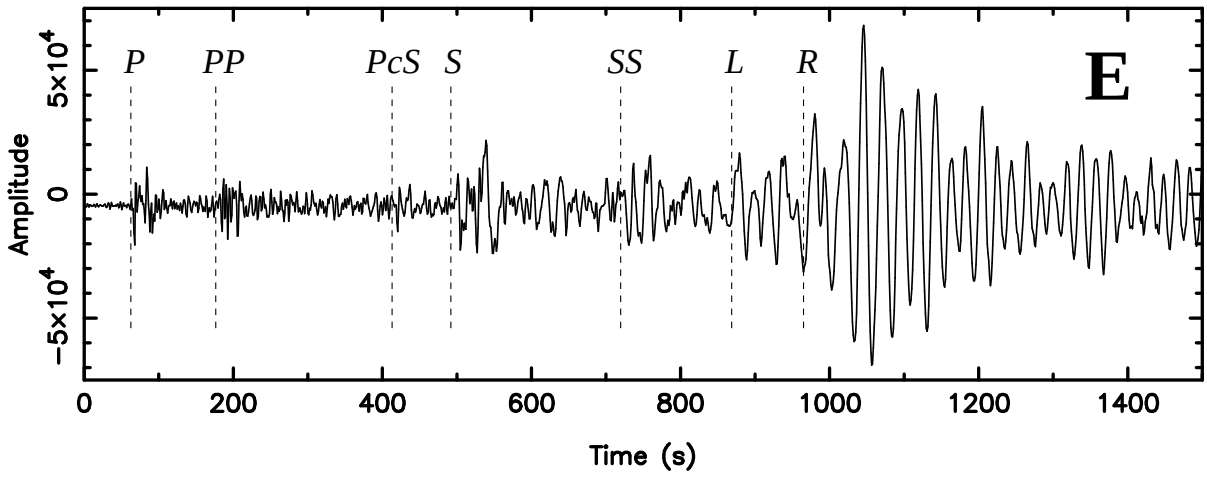

Figure 1.1: E-W component of a seismic waveform recorded in Shanghai, China from a magnitude 6.7 earthquake in the New Britain Region, PNG on 6th February 2000. Seven readily identifiable phases are picked. The angular distance between the earthquake source and receiver is 46°.

The origin of this approach can be traced back to John Milne (Davison, 1978) who, in 1902, constructed the first time-distance curves for a spherically symmetric earth model (see Figure 1.2) by averaging the arrival times of P, S and Love waves from a number of earthquakes. While these curves are primitive in terms of detail and accuracy with respect to their modern counterparts, they represent one of the most important advances in the history of seismology.

One of the first people to deduce earth structure from seismic records was Mohorovičić, a Serbian seismologist who, in 1909, observed two distinct first-arrival traveltime curves

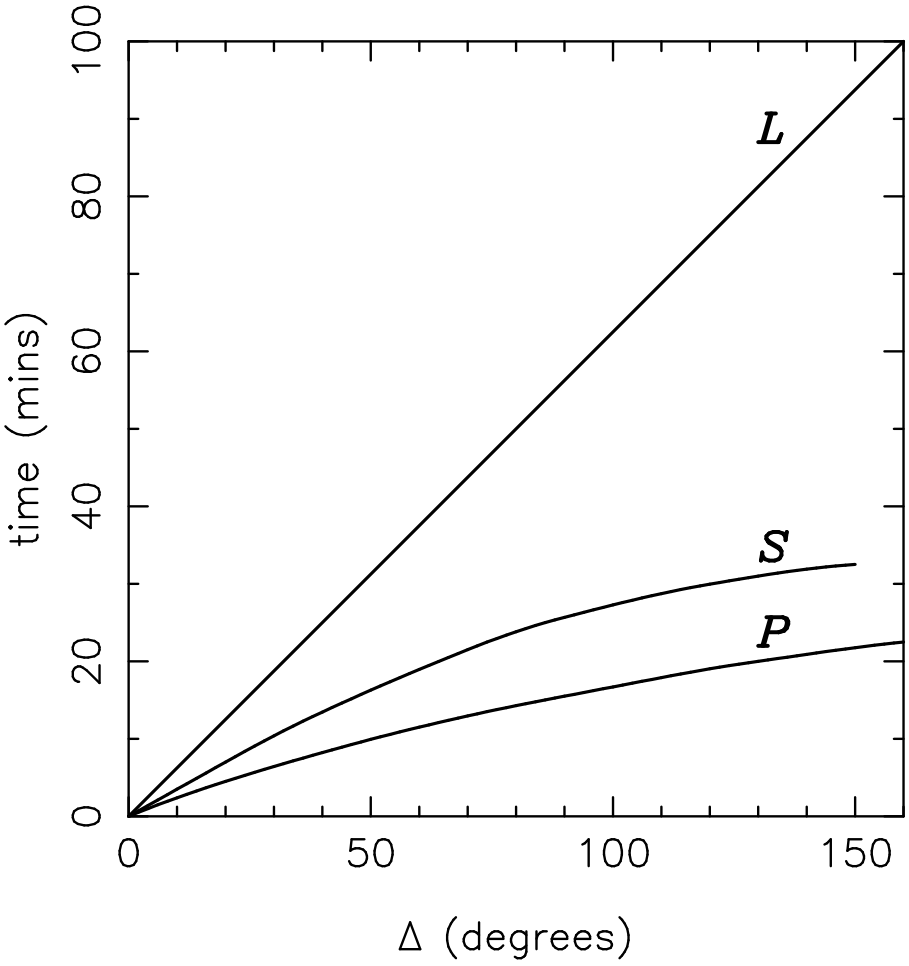

Figure 1.2: Time-distance curves for P, S and Love waves as determined by John Milne in 1902 (after Davison, 1978).

from a regional earthquake (Aki & Richards, 1980). He determined that one curve corresponded to a direct crustal phase and the other to a wave refracted by a discontinuity in elastic properties between crust and upper mantle. This world-wide discontinuity is now known as the Mohorovičić discontinuity or Moho. On a larger scale, the method of Herglotz and Wiechert (see, for example, Gubbins, 1992) was implemented in 1910 to construct a 1-D whole-earth model. The method uses the relationship between angular distance and ray parameter to determine velocity as a function of radius within the earth.

A major breakthrough in global seismology occurred in 1935 with the construction of the Jeffreys-Bullen (J-B) traveltime tables. These tables summarise global data for the arrival times of various phases through a spherically symmetric earth with vastly greater detail (a large variety of P, S and core phases are included) and accuracy than previous tabulations. The robustness of these tables and the underlying assumptions of spherical

symmetry are verified by the observation that travel-times for any given source-receiver pair are principally dependent on angular separation and source depth. Variations with source or receiver location are generally not more than several seconds in traveltimes measured in tens of minutes (Gubbins, 1992). Most of the discrepancies between model and observed traveltimes can be attributed to lateral variations in lithospheric structure. The J-B tables and their modern equivalents such as IASP91 (Kennett & Engdahl, 1991) are used extensively in earthquake location and analysis and in studies which use distant earthquakes to map earth structure (e.g. teleseismic tomography).

Today an abundance of methods exist for determining earth structure from seismic waves. Different components of the seismic record may be used, including traveltimes, amplitudes, waveform spectra, full waveforms or the entire wavefield. Source-receiver configurations also differ (e.g. Figure 1.4) - receiver arrays may be in-line or 3-D, sources may be close or distant to the receiver array, sources may be natural or artificial and the scale of the study may be from tens of meters to the whole earth. Finally, there are a multitude of ways of translating the data extracted from the seismogram into a representation of seismic structure. One of the most common methods for mapping seismic data into an image of subsurface structure is seismic tomography.

1.1.1 Defining Seismic Tomography

The word *tomography* literally means *slice picture* and was first used in medical imaging to describe the process of mapping the internal density distribution of the human body using x-rays (Lee & Pereyra, 1993). The term was later appropriated by the seismological community to describe a similar process involving the mapping of earth structure using seismic waves. In essence, tomography can be described as the reconstruction of an internal property of a medium from line integrals through the medium.

If we represent some elastic property of the subsurface (e.g. velocity) by a set of model parameters $\mathbf{m}$, then we can predict a set of data (e.g. traveltimes) $\mathbf{d}$ for a given source-receiver array by line integration through the model. The relationship we can define between data and model parameters - $\mathbf{d} = \mathbf{g}(\mathbf{m})$ - forms the basis of any tomographic method. For an observed dataset $\mathbf{d}_{obs}$ and an initial model $\mathbf{m}_0$, the difference $\mathbf{d}_{obs} - \mathbf{g}(\mathbf{m}_0)$ gives an indication of how well the current model satisfies the data. The inverse problem in tomography is then to manipulate $\mathbf{m}$ in order to minimise the difference between

observed and predicted data subject to any regularisation that may be imposed. The end result will be a mathematical representation of the true structure whose accuracy will depend on a number of factors including: i) how well the observed data is satisfied by the model predictions, ii) assumptions made in parameterising the model, iii) errors in observed data, iv) accuracy of method for determining model data $\mathbf{g}(\mathbf{m})$, and v) the extent to which the data constrains the model parameters. The tomographic method therefore depends implicitly on the general principles of inverse theory.

The steps required to produce a tomographic image from seismic data can thus be defined as follows:

1. **Model parameterisation:** The seismic structure of the region being mapped is defined in terms of a set of unknown model parameters. Tomographic methods generally require an initial estimate of model parameter values to be specified.

2. **Forward calculation:** A procedure is defined for the calculation of model data (e.g. traveltimes) given a set of values for the model parameters.

3. **Inversion:** Automated adjustment of the model parameter values with the object of better matching the model data to the observed data subject to any regularisation that may be imposed.

4. **Analysis of solution robustness:** May be based on estimates of covariance and resolution from linear theory or on the reconstruction of test models using synthetic datasets.

Steps 2 and 3 are performed iteratively if the non-linear nature of the problem is taken into account (i.e. the path taken by a seismic wave is dependent on the velocity structure of the medium through which it passes). In linear tomography, the forward step is performed only once based on the assumption that the paths taken by the seismic waves between sources and receivers are not significantly perturbed by the adjustments made to the model parameter values in the inverse step. For non-linear tomography, the forward and inverse steps are performed iteratively (adjusting the ray paths at each step) until, for example, the data is satisfied or the rate of data fit improvement per iteration satisfies a given tolerance. Studies that use linear tomography may deal with tens to hundreds of thousands of model parameters (e.g. Spakman, 1991; van der Hilst et al., 1997), making

an iterative approach computationally impractical, or have data geometries (such as teleseismic) that make a linear assumption more valid (e.g. Achauer 1994). Experiments that deal with the often complex structure of the crust and lithosphere, like local earthquake and wide-angle tomography, commonly use a non-linear approach (e.g. Graeber & Asch, 1999; Hole, 1992).

The way in which seismic structure is represented in a tomographic problem is of great importance, not only because it imposes limitations on the kinds of structure that may be imaged, but also because it influences the implementation of the forward and inverse steps of the solution process. Probably the most widely used type of seismic tomography is traveltime tomography, which attempts to reconstruct subsurface velocity distribution from the delays between source events and receiver arrivals. A common way of representing this velocity distribution is by a set of constant velocity (or slowness) blocks or velocity nodes joined by an interpolation function (e.g. Aki et al., 1977; Evans, 1982; Walck & Clayton, 1987; Humphreys & Clayton, 1990; Hole, 1992). Constant velocity blocks are simple to define and make the calculation of $\mathbf{g}(\mathbf{m})$ a relatively rapid task, but they introduce an unrealistic set of velocity discontinuities into the model. Parameterisation via interpolated velocity nodes avoids this problem by being at least C_1 continuous in velocity, but have the disadvantage that $\mathbf{g}(\mathbf{m})$ is generally more time-consuming to calculate.

The problem with both constant velocity blocks and interpolated velocity nodes is that neither representation allows discontinuous changes in velocity to be accurately reconstructed. In the earth, distinct geological features such as interfaces between layers, fault surfaces, unconformities and the boundaries of intrusive bodies cause seismic wave speed to change discontinuously, while gradual changes in density or composition within a layer or body may cause seismic wave speed to vary smoothly. Interpolated velocity nodes and constant velocity blocks address the latter property. A number of authors have included the representation of geological discontinuity by specifying one or more usually subhorizontal and laterally continuous interfaces with variable geometry (e.g. Chiu et al., 1986; Greenhalgh et al., 1989b; Lutter & Nowack, 1990; Hole, 1992; Rawlinson & Houseman, 1998). In such cases, the model parameters are generally defined by a set of interface node depths. If data coverage is adequate, then it is possible to invert for both continuous velocity variation and interface geometry (Zelt & Smith, 1992; Wang & Braile, 1996; Zelt, 1999).

The forward problem in seismic tomography is solved by integrating (e.g. for traveltime) along the ray path from source to receiver. If the velocity structure is complex, this path is not known *a priori*, and must be determined in order to correctly calculate the model data $\mathbf{g}(\mathbf{m})$. Ray-tracing methods (Julian & Gubbins, 1977; Červený, 1987; Sambridge & Kennett, 1990) are commonly used to solve the forward step of the tomographic problem. Wavefront tracking schemes based on the numerical solution of the eikonal equation are becoming increasingly popular (Vidale, 1990; Hole, 1992; Sethian & Popovici, 1999) as a means of rapidly determining first-arrival traveltimes. Network theory (Moser, 1991; Cheng & House, 1996), which involves finding the shortest time-path between source and receiver through a predefined network, is also gaining popularity as a method for finding first-arrival paths and traveltimes. In each of these schemes, locating multi-paths can present difficulties.

At the core of the inverse problem is the requirement that the model parameter values need to be adjusted to improve the fit between model data and observed data. A common way of dealing with this inverse problem is to formulate it as an optimisation problem in which one seeks to minimise a least-squares type objective function that consists of a data residual term and one or more regularisation terms. The regularisation terms are normally related to damping (Kennett et al., 1988), which helps prevent poorly constrained parts of the model (e.g. Figure 1.3) from assuming unrealistic values, and smoothing (Sambridge, 1990), which helps reduce the effects of short wavelength variations in the image associated with overparameterisation. Ultimately, regularisation reduces the non-uniqueness of the inverse problem. Gradient methods such as Gauss-Newton, steepest descent, conjugate gradient or subspace inversion (Tarantola, 1987; Kennett et al., 1988) are commonly used to minimise the objective function.

Another common approach to solving the inverse problem is backprojection (e.g. McMechan, 1983; McQueen & Lambeck, 1996), which iteratively maps traveltime anomalies into slowness perturbations along the ray paths until the data is satisfied. Two basic backprojection techniques are ART (Algebraic Reconstruction Technique) and SIRT (Simultaneous Iterative Reconstruction Technique); ART updates the model on a ray by ray basis while SIRT updates the model using the perturbations from all rays simultaneously.

A drawback of gradient and backprojection methods is that there is no guarantee of convergence to a global minimum solution, because they exploit information in model space only in the vicinity of the initial model. A different approach is to use random

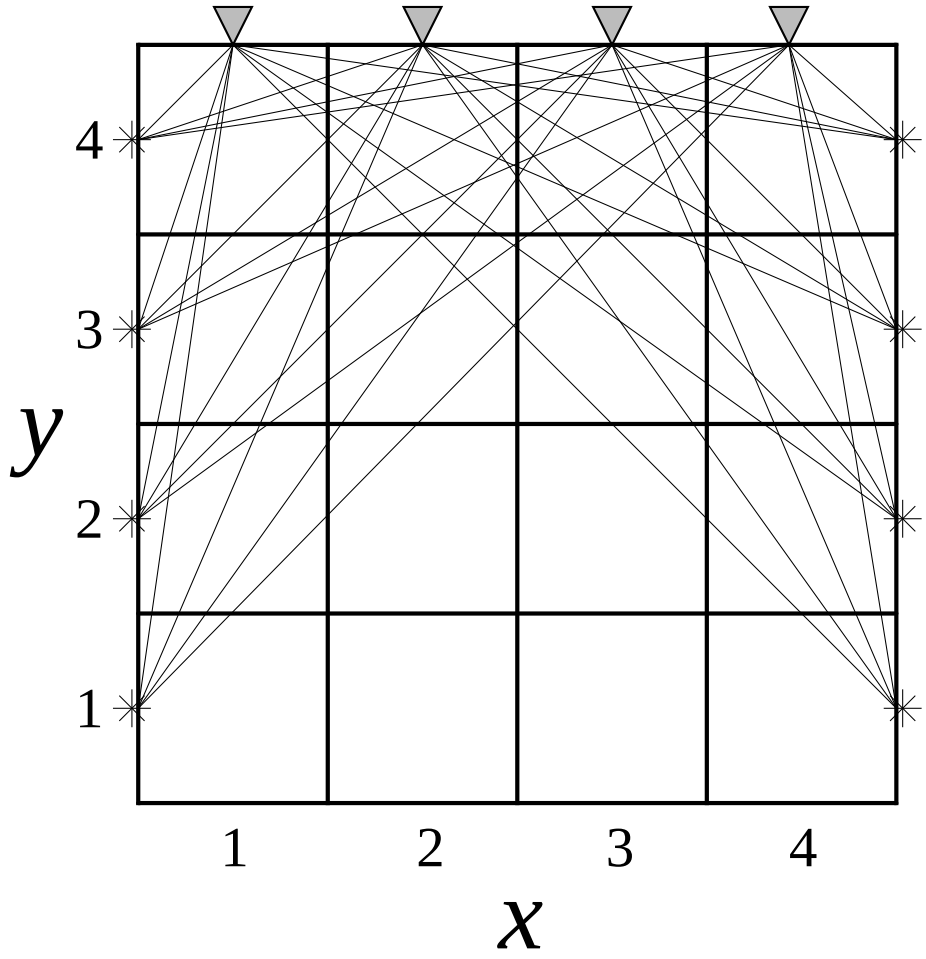

Figure 1.3: Schematic representation of a source-receiver array (sources denoted by asterisks, receivers by triangles) that bounds a model volume represented by a set of 16 blocks labelled using (x, y) coordinates. Blocks (2,1) and (3,1) are not constrained by the data, blocks (1,1), (2,2), (3,2) and (4,1) are relatively poorly constrained by the data while blocks like (2,4) and (3,4) are relatively well constrained by the data. For simplicity, the rays are traced assuming that the velocity of each cell is identical - this would not normally be the case.

processes to search model space and find better models. Monte Carlo, genetic algorithms and simulated annealing fall into this class of global optimisation techniques. These methods require a comparatively large number of forward steps and as a result, current applications are limited to fewer than 100 parameters (Sambridge & Drijkoningen, 1992; Drijkoningen & White, 1995; Boschetti et al., 1996).

Up to this point, it was indicated that the unknowns in the inverse problem consist exclusively of parameters that define the distribution of seismic velocity or interface depth. Other unknowns may also be included. For example, if earthquake sources are used, then source location and origin time are usually not known very accurately. Inclusion of these parameters into the inversion (Thurber, 1983) will help reduce their uncertainty,

although there will be a trade-off with solution uniqueness. Station corrections or delay times (Humphreys & Dueker, 1994) may also be included as unknowns in the inversion to account for near surface structure.

Due to its origins in radiology and early seismic imaging, the term tomography is generally only applied to methods that invert for a property (e.g. velocity) that varies with position in 2-D or 3-D. If only interface structure is inverted for (Hole, 1992; Rawlinson & Houseman, 1998), then the term tomography is generally not applied, even though the method conforms to the procedures described above. In this thesis I assume, however, that the term tomography may be appropriately applied to any method that generally follows the four steps listed above and results in 2-D or 3-D representations of subsurface structure.

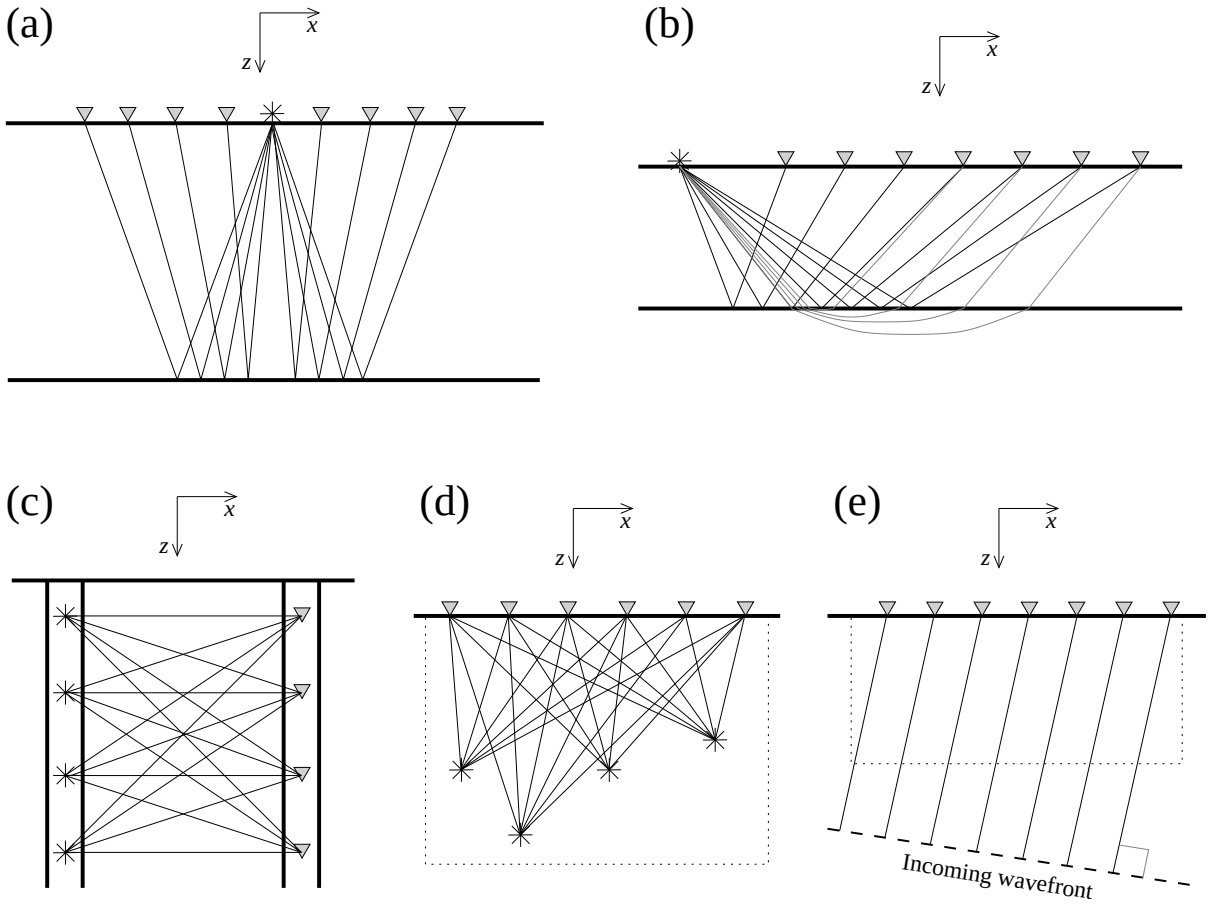

Figure 1.4: Schematic source-receiver geometries for various seismic surveys (sources are denoted by asterisks or stars, receivers by triangles or diamonds): (a) Normal incidence reflection array (common source), (b) wide-angle seismic survey. Thin black lines denote reflected rays, gray lines denote refracted rays. (c) Cross-hole array, (d) local earthquake survey - sources lie within modelled region (dotted line), (e) Teleseismic study - sources lie outside modelled region (dotted line).

1.1.2 Seismic Structure from Controlled Sources

The use of controlled or artificial sources (e.g. airgun shots, explosions, vibroseis) in seismic experiments has a number of benefits including precise identification of source location and origin time, control over data coverage and knowledge of source waveform. Reflection, refraction, wide-angle and cross-hole seismic studies fall within this category. However, compared to experiments that use earthquakes, surveys of this nature tend to be more expensive and cannot be used to probe deep structure unless powerful sources such as nuclear explosions are used. PNEs (Peaceful Nuclear Explosions) can be detected thousands of km away and have been recorded by long in-line receiver arrays (Priestley et al., 1994; Ryberg et al., 1996; Nielsen et al., 1999). Events recorded in this manner often probe the mantle to depths of 800 km or more and are usually interpreted using wide-angle seismic inversion techniques.

Normal incidence reflection analysis

Normal incidence reflection seismic surveys use in-line arrays of sources and receivers to image crustal structure on depth scales of tens of metres to tens of km. This seismic method is referred to as *normal incidence* because the aim is to map reflections from sub-horizontal interfaces using near-vertically propagating P-waves (see Figure 1.4a). Traces from adjacent sources or receivers are plotted next to each other on a horizontal distance versus two-way traveltime axis to produce a reflection section (e.g. Figure 1.5a). Variations in the earth's impulse response can be linked to variations in earth structure. To produce a usable reflection section such as Figure 1.5a from the raw data, significant processing is required (Yilmaz, 1987; Telford et al., 1990) to remove or reduce effects caused by the source wavetrain, multiples, normal moveout, near-surface complexities, diffraction and data noise. The entire seismic wavefield is used and is mapped directly to the model space. For this reason, reflection seismic sections are unequalled in terms of detail and resolution. The method is most effective when used to image discontinuous changes in seismic structure (i.e. reflectors). For example, Chávea-Pérez et al. (1998) imaged shallow faults (several km depth) in the southern Death Valley Basin, Goleby et al. (1988) imaged crustal scale faulting and basin structure in central Australia, and Stern & McBride (1998) imaged continental strike-slip zones using seismic reflection profiling. For its high resolution and effectiveness in the presence of layered structures, the normal incidence

reflection method is used extensively in the oil industry in the search for hydrocarbons.

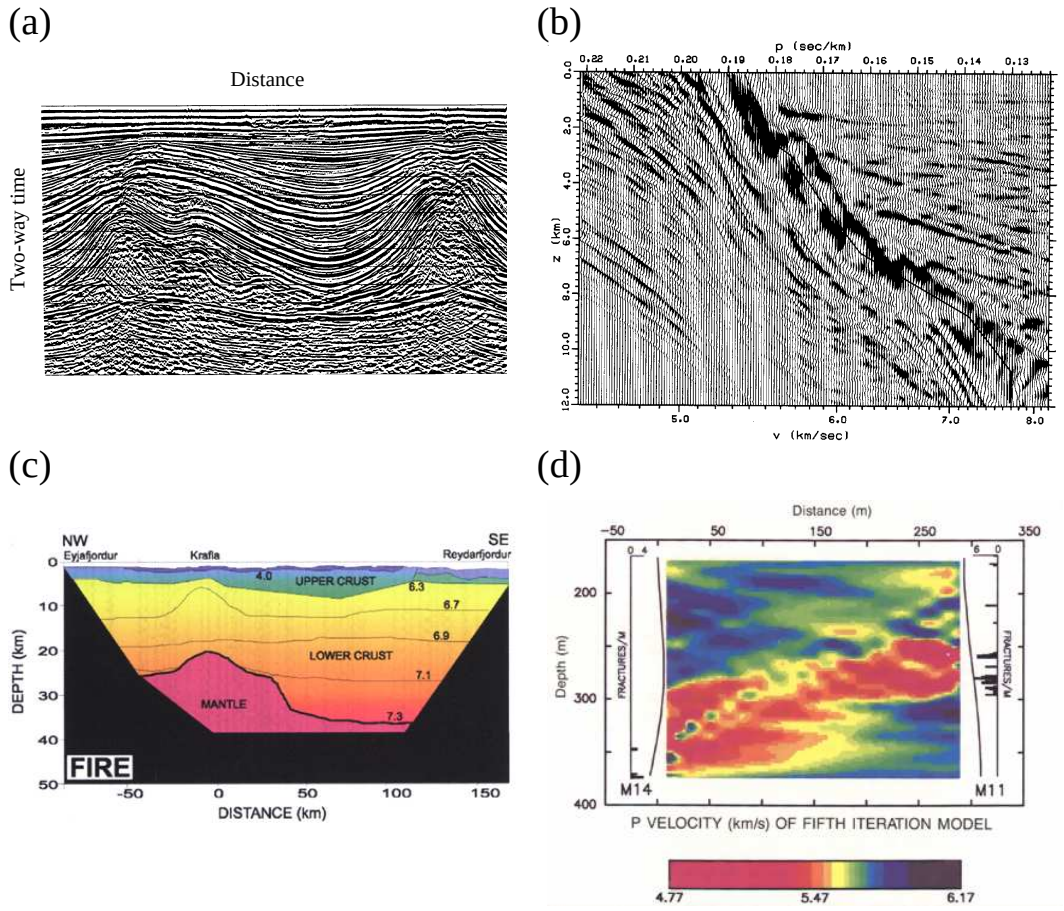

Figure 1.5: Mapping earth structure with artificial sources: (a) Normal incidence reflection section (from Yilmaz, 1987), (b) 1-D P velocity model of Mojave Desert upper crust produced by wavefield continuation (from McMechan et al., 1982), (c) P velocity and interface model of crust above Iceland mantle plume derived from wide-angle seismic data (from Darbyshire et al., 1998), (d) Cross-hole tomographic image; low velocity zones correspond to regions of heavy fracturing in the boreholes (from Bregman et al., 1989).

Reflection tomography

As shown in Figure 1.4a, the paths taken by the seismic energy in a seismic reflection experiment are not strictly vertical, as the shot is recorded by an array of receivers at varying offsets (usually small compared to the maximum depth of the recorded energy) from the source. The multiplicity of data permits stacking to boost signal-to-noise ratio and the variation of ray trajectories also makes it possible to explicitly image elastic properties using traveltimes and/or amplitudes in a process known as reflection tomography

(Bishop et al., 1985; Farra & Madariaga, 1988; Williamson, 1990; Blundell, 1993; Carroll & Beresford, 1996; Kosloff et al., 1996; Wang & Houseman, 1995). Structure is commonly represented by a series of sub-horizontal layers separated by continuous interfaces. For example, in the 2-D approach of Bishop et al. (1985), interfaces are defined by a discrete set of nodes interpolated by cubic spline functions. The velocity field is represented by a matrix of rectangular cells, each having a slowness value specified at its centre and a constant velocity gradient elsewhere in the cell. The forward problem of determining model traveltimes is accomplished using a shooting method of ray tracing. The inversion step uses a Gauss-Newton algorithm to adjust interface and velocity parameters to minimise the misfit between observed and model traveltimes. The ray tracing and inversion steps are performed iteratively until the match between the observed and model traveltimes satisfies a given tolerance. Similar approaches have been used by Farra & Madariaga (1988), Williamson (1990) and Kosloff et al. (1996), with the main differences being in the detail of the parameterisation, ray-tracing and inversion method. Chiu et al. (1986) extended the procedure to 3-D but assumed constant velocity layers. To a lesser extent, amplitudes have been used in reflection tomography to invert for interface geometry (Wang & Houseman, 1994) and velocity variation (Wang & Houseman, 1995). Using both amplitude and traveltime data to tomographically image seismic structure (Wang & Pratt, 1997) offers potentially better resolution than is possible with traveltime data alone.

Refraction and wide-angle interpretation

Refraction and wide-angle surveys both use arrays with large offsets between sources and receivers so that refraction and wide-angle reflection phases may be recorded (Figure 1.4b). Traces from adjacent receivers recorded from a single shot, or traces recorded by a single receiver from adjacent shots, may be plotted on a time versus offset plot to reveal the presence of coherent traveltime curves. Refraction interpretation, as its name suggests, only utilises the refraction component of the dataset. Traditionally, interpretation has been simple (Telford et al., 1990), with models consisting of constant velocity layers separated by horizontal or dipping planar interfaces (Mota, 1954). More sophisticated techniques such as the ABC method or Halés method (Sjögren, 1984) have been used to determine laterally varying structure. In the exploration industry, refraction studies are often performed together with reflection studies. Refraction arrivals better constrain

velocity than near-vertical reflection arrivals and velocity versus depth is required for normal-moveout correction. Reflection sections also benefit if static corrections, which remove the effects of near-surface variations in velocity, are applied.

Another means of deriving velocity-depth profiles, known as wavefield continuation (Clayton & McMechan, 1981; McMechan et al., 1982), uses the entire recorded wavefield in the interpretation procedure. The method involves two steps. First, the wavefield is mapped into the $\tau - p$ (intercept time - ray parameter) domain using a linear transformation known as a slant stack (Stoffa et al., 1981; Wang & Houseman, 1997). The second step involves transforming the data from the $\tau - p$ domain to the $p - z$ (slowness - depth) domain using downward continuation (Clayton & McMechan, 1981). In this step it is explicitly assumed that the velocity structure is laterally homogeneous. The second step is iterative because a velocity function needs to be specified to perform the transformation. The process is repeated until the input velocity function matches the downward continued wavefield. An example of a velocity model produced by downward continuation is shown in Figure 1.5b. The thin black line is the input velocity model at the final iteration.

The term *wide-angle data* normally implies the presence of both refraction and reflection information (e.g. Riahi & Lund, 1994; Zelt et al., 1996). The interpretation of wide-angle data is often done using a tomographic approach. In fact, the procedure is usually similar to that outlined for reflection tomography earlier, except that both refracted rays and reflected rays are used in the inversion. Traveltimes are again the key measurement of the recorded seismic wavefield that is normally used. These types of methods have also been separately applied to the refraction component of the data (Greenhalgh et al., 1990; Hole, 1992) and to the wide-angle reflection component of the data (Riahi et al., 1997). One of the most frequently used methods for the tomographic inversion of wide-angle traveltimes was developed by Zelt & Smith (1992). Their 2-D model is parameterised in terms of a layered irregular network of trapezoids. Velocity nodes are defined at each corner of the trapezoid and the upper and/or lower boundary of the trapezoid can be used to represent an interface. In this method, both refraction and wide-angle reflection traveltimes can be inverted for interface geometry and layer velocity. Asymptotic ray theory is used to determine ray paths and traveltimes, and damped least-squares inversion is used in the inversion step of the problem. Other authors to use this scheme include Kanasewich et al. (1994), Riahi & Lund (1994), Staples et al. (1997), Ye et al. (1997), Darbyshire et al. (1998), Kodaira et al. (1998), Morozov et al. (1998) and Navin

et al. (1998). Figure 1.5c shows a typical model constructed using this method.

Forward modelling is also commonly used in wide-angle data interpretation. In practice, it is similar to the tomographic approach except that the inversion step is performed manually by the user (i.e. one adjusts model parameter values by trial and error to improve the data fit). This approach tends to be more time consuming and does not allow for quantitative analysis of solution robustness. However, it does permit greater control over the model result and allows amplitudes to be used as an additional constraint, an aspect that has received only limited development in inversion methodology. Authors who have employed forward modelling of wide-angle data include Iwasaki et al. (1990), Grad et al. (1997), Recq et al. (1998) and Stadtlander et al. (1999).

Recently, interpretation of wide-angle seismic data has been carried out in 3-D using multiple in-line arrays of sources and large receiver arrays. Inversion methods for 3-D wide-angle data have been presented by a number of authors including Hole (1992), Hole et al. (1992), Riahi et al. (1997), Zelt & Barton (1998), Zelt et al. (1999) and Rawlinson (2000). Interpretation methods for such datasets have developed rapidly in recent years, although many still cannot deal with the level of structural detail commonly obtained from 2-D datasets (e.g. Kodaira et al., 1998).

Although reflection tomography and wide-angle tomography have been discussed separately, the underlying principles are in fact very similar. The main difference is in the source-receiver offset. Attempts have therefore been made to combine both these types of data in a single inversion. Using different parameterisations, Wang & Braile (1996) and McCaughey & Singh (1997) have inverted refraction, wide-angle reflection and normal-incidence reflection traveltimes for interface depth and layer velocity. They found that the use of all three data types helps greatly in reducing the non-uniqueness of the result. Recent developments in wavefield inversion (Pratt et al., 1996) also promise dramatically increased resolution over conventional traveltime inversion, but more development is required before these methods can be practically applied to image complex structures.

Crosshole tomography

Another class of seismic tomography that is frequently used in the exploration industry is cross-hole tomography. A basic source-receiver configuration (Figure 1.4c) for a crosshole experiment consists of two boreholes with sources down one and a receiver array down

the other. Crosshole seismic experiments may also include sources or receivers on the surface between the boreholes (McMechan, 1983). Typically, the scale of such studies is on the order of tens to hundreds of metres. The region between the boreholes may be mapped by inverting the first-arrival traveltimes for P-wave velocity structure (Ivansson, 1987). The velocity field is usually described by constant velocity cells (Goulty, 1993) or by a discrete set of velocity nodes with a specified interpolation function (Bregman et al., 1989).

It is commonly assumed that the ray paths between sources and receivers are straight lines (e.g. McMechan, 1983; Wong et al., 1983), which greatly simplifies the problem. However, if significant velocity heterogeneities are present, then a non-linear approach which recognises the dependence of the ray path on the velocity structure becomes necessary (Bregman et al., 1989; Zhou et al., 1992). Figure 1.5d shows a P-wave velocity field between two boreholes produced by non-linear inversion of first-arrival traveltimes. Mining applications for cross-hole tomography include mineral exploration (e.g. ore body location), coal exploration (imaging coal seams) and mining hazards such as coal outburst and water-filled old workings (Goulty, 1993). Cross-hole studies are also employed in civil engineering projects (McCann et al., 1986; Goulty, 1993) where the locations of fracture zones are of particular interest. In these types of studies, S-waves are also used extensively because they are strongly attenuated by water-filled fracture zones (Fehler & Pearson, 1984). Other investigations in the field of crosshole tomography have considered the effects of anisotropy (Carrion et al., 1992; Pratt et al., 1993) and have combined wave-equation imaging with traveltime inversion to better delineate discontinuous structure (Pratt & Goulty, 1991). Young (1989) applied diffraction tomography to crosshole data to image short wavelength structure that resulted in significant scattering of incident seismic energy.

1.1.3 Mapping Local Structure Using Earthquakes

The two principle types of studies involving the mapping of local structure from earthquake sources are local earthquake tomography and teleseismic tomography. Such surveys employ receiver arrays that span distances from tens to hundreds of km and target crustal to upper mantle depths.

Local earthquake tomography

One of the first papers to be published on seismic tomography was that of Aki & Lee (1976), who inverted first-arrival P-wave traveltimes from local earthquakes for velocity structure and hypocenter location in Bear Valley, California. The source-receiver geometry for this type of study is shown schematically in Figure 1.4d - the earthquake sources lie beneath the receiver array within the model volume. The hypocenter coordinates, which are not accurately known, must be included in the inversion. Although Figure 1.4d shows a 2-D experiment, most local earthquake studies are 3-D. Since the publication of the Aki & Lee (1976) paper, this branch of tomography has come into common usage and is now popularly known as Local Earthquake Tomography or LET (Thurber, 1993). The sophistication of the methodology has also increased. Aki & Lee (1976) used a linear inversion with a homogeneous initial model and a constant velocity block parameterisation. Thurber (1983) used an Approximate Ray Tracing (ART) method to facilitate an iterative non-linear inversion of P-wave traveltimes for continuously varying velocity structure and hypocenter location. More recently, authors have included S-wave data in their analyses to invert for V_P/V_S ratio also (Walck, 1988; Graeber & Asch, 1999). The V_P/V_S ratio is a better indicator of hydration levels than is V_P. Figure 1.6a shows a vertical cross-section through a V_P/V_S ratio model of the Southern Central Andes. The anomalously high V_P/V_S ratio above the subducting slab between 67° and 68° has been interpreted to be caused by a considerable amount of partial melt (Graeber & Asch, 1999).

An obvious drawback of LET is that it can only be used in regions of active seismicity, usually at or near plate boundaries. Studies have been carried out in many different regions including California (Aki & Lee, 1976; Thurber, 1983; Walck & Clayton, 1987; Eberhart-Phillips & Michael, 1993), Taiwan (Kao & Rau, 1999), Japan (Zhao et al., 1992), South America (Bosch, 1997; Graeber & Asch, 1999), South Australia (Greenhalgh et al., 1989a) and the Mediterranean (Luca et al., 1997; Papazachos & Nolet, 1997; Haslinger et al., 1999).

LET has been used to image the lithosphere and upper asthenosphere to depths of up to 200 km in subduction zone settings (Abers, 1994; Graeber & Asch, 1999). High resolution images of the crust have also been obtained using shallow earthquakes (Thurber, 1983; Chiarabba et al., 1997). In such cases, the results of LET can be usefully compared with wide-angle studies of the same region (Eberhart-Phillips, 1990). Advantages of LET

over wide-angle tomography include greater depth of penetration and the added structural information provided by the relocated hypocenters, e.g. the existence of double seismic zones (Hasegawa et al., 1978; Kawakatsu, 1985; Kao & Rau, 1999). On the other hand, the relocation of hypocenters adds to the non-uniqueness of the solution and phases other than first-arrival P and S are difficult to incorporate. For this reason, LET models rarely include interfaces, although Zhao et al. (1992) included interfaces in their LET model of NE Japan by using observed SP waves converted at the Moho and PS/SP waves converted at the upper boundary of the subducted Pacific Plate.

Teleseismic tomography

The significant difference between LET and teleseismic tomography is source location; in a teleseismic study, earthquakes are normally thousands of km away from the receiver array. The target region of the crust and upper mantle lies beneath the receiver array. A key assumption in teleseismic tomography is that lower mantle velocity heterogeneities are of small enough amplitude and/or long enough wavelength that the wavefront incident on the model region is of small curvature (Dueker et al., 1993). Therefore it is possible to trace the rays through a simple 1-D model of the earth until they strike the target volume. Figure 1.4e shows a schematic diagram of a wavefront from a distant earthquake incident on a teleseismic receiver array. As in LET, teleseismic tomography is usually carried out in 3-D.

Normally teleseismic tomography is based on the relative traveltime residuals of first-arriving P-waves. The model parameterisation is similar to that used in LET: constant velocity blocks or nodes with continuous velocity interpolation. A seminal paper by Aki et al. (1977) used teleseismic data recorded at the Norsar array to invert for velocity anomalies to a depth of 126 km. Their model was parameterised in terms of constant slowness blocks and the initial model consisted of a structure with laterally invariant slowness. The final solution was produced by linear inversion. The assumption of linearity is more accurate in teleseismic tomography than in LET or wide-angle inversion. This occurs because the ray paths tend to be near-vertical as they transmit through the model volume and hence are less deviated by the dominant variations in velocity which invariably are a function of depth. Consequently, many teleseismic tomography images, even those published recently, are the result of linear inversions (Humphreys & Clayton, 1990; Glahn

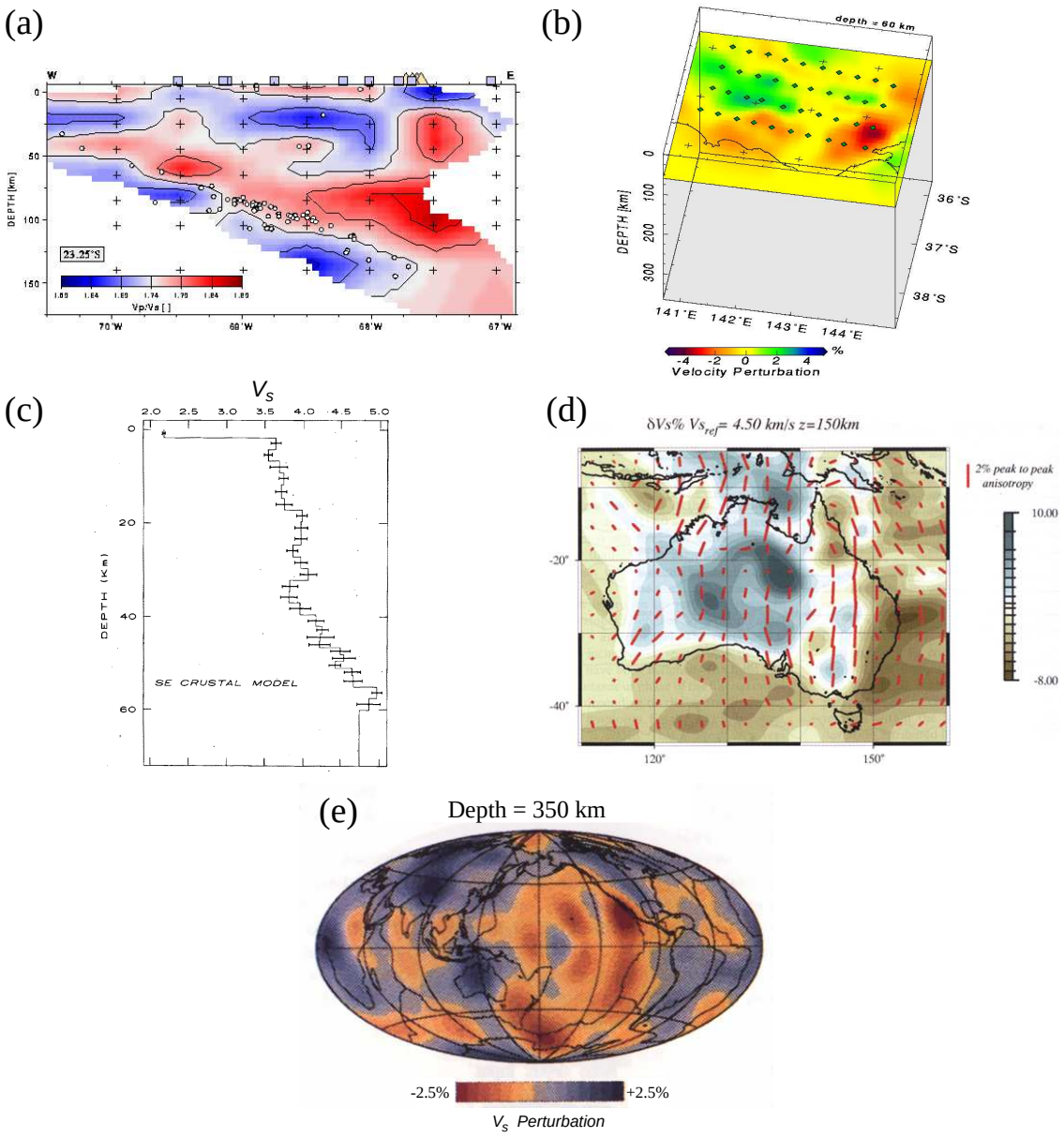

Figure 1.6: Mapping earth structure using earthquakes: (a) Cross-section of a 3-D V_p/V_s model of southern central Andes from local earthquake data. Crosses indicate velocity nodes and circles represent hypocenter locations (from Graeber & Asch, 1999), (b) Teleseismic tomography image of NW Victoria (from ?), (c) S-velocity model beneath Cumberland Plateau, Tennessee derived by teleseismic receiver function analysis (from Owens et al., 1984), (d) Shear-wave velocity and SV anisotropy variations in Australia derived by inversion of surface waveforms (from Debayle, 1999), (e) Global model of S velocity perturbations developed from inversion of body and Love SH waveform data (from Li & Romanowicz, 1996).

& Granet, 1993; Seber et al., 1996; Saltzer & Humphreys, 1997). Figure 1.6b illustrates a 2-D horizontal cross-section of a tomographic image of the Lachlan Fold Belt, SE Australia based on a linear inversion of teleseismic data. If the traveltime residuals are suggestive

of significant lateral structure, then an iterative non-linear approach may be required (Weiland et al., 1995; McQueen & Lambeck, 1996; Rawlinson & Houseman, 1998; Steck et al., 1998).

The main difficulties in teleseismic tomography arise because of the irregular and unpredictable nature of earthquakes. Because earthquakes tend to occur at plate boundaries, it is common to have a very uneven distribution (in terms of azimuth and inclination) of ray paths through the target volume. Relative traveltime residuals provide good constraints on lateral variations in velocity relative to an *a priori* lateral average. Vertical variations in the velocity field of the solution model are less well constrained and therefore must be interpreted with caution (Lévêque & Masson, 1999).

The depth extent of teleseismic investigations may range from crustal (e.g. Lambeck et al., 1988; Rawlinson & Houseman, 1998) to many hundreds of km (e.g. Humphreys & Clayton, 1990). The horizontal extent of the receiver array and the source distribution determines the depth to which features may be resolved. The vertical dimension of the model volume is often chosen on this basis, but it is always possible that structure outside the solution region causes some of the variation in traveltime (e.g. Benz et al., 1992). Variations to the standard teleseismic tomography approach include inversion for interface structure (Davis, 1991; Rawlinson & Houseman, 1998), inversion using S-wave arrival times (Ritsema et al., 1998) and joint inversion of traveltimes and amplitudes for velocity perturbation (Neele et al., 1993).

Receiver function analysis

Receiver function analysis of teleseismic data (Owens et al., 1984; Langston, 1989) is used to obtain a representation of S-wave velocity versus depth beneath individual seismic stations (e.g. Figure 1.6c). The method assumes that the teleseismic P arrivals generate reflections and transmissions of mode-converted SV waves at interfaces beneath the recorder (Sheehan et al., 1995). The converted modes are assumed to be much weaker on the vertical component than on the radial component. Thus, the vertical component of the seismogram can be considered to be an estimate of the P source function incident at the base of the crust plus P reverberations, and can be deconvolved from the radial component to isolate the P to S conversions. Typically the first 20-30 seconds of data (Ammon et al., 1990) from the onset of the first arrival are analysed. The earth

model is represented by a series of fixed thickness, constant velocity layers (Owens et al., 1984; Ammon et al., 1990) and the time delays of the arrivals on the deconvolved horizontal component time series may be directly interpreted as the S-wave traveltime from horizontal interfaces.

Ray paths from teleseismic events propagate through the crust at near vertical inclination, so it is common to interpret models produced by receiver function analysis as local samples of the vertical velocity structure. Lateral variations in structure may then be inferred from an array of recorders. Using this approach, Baker et al. (1996) and Sheehan et al. (1995) infer Moho topography beneath the Colorado Rockies and Piñon Flat, California respectively. Clitheroe et al. (2000) employ receiver function analysis to investigate the crustal thickness of Australia using data from 65 broadband recorders. Jones & Phinney (1998) determine lateral variations in crustal structure from an in-line array of recorders but use migration to compensate for the variations in inclination and azimuth of the ray paths. Data from a single recorder can be used to examine lateral variation by separately examining events from different azimuth and inclination sectors (Kanao, 1997).

1.1.4 Regional and Global Studies Using Earthquakes

Global and regional networks of seismic stations allow the whole earth, or large portions of it, to be investigated in a single study. The WWSSN (World Wide Standard Seismograph Network) was the first global seismic array. It commenced operation around 1961 using analogue recorders. The contemporary equivalent of the WWSSN is the digital Global Seismograph Network (GSN) which runs approximately 128 permanent seismic recording stations. Body waves, surface waves and normal modes are all employed to constrain structure in this type of study.

Regional mapping using body waves

Regional scale seismic studies use receiver arrays with horizontal dimensions on the order of 1,000s of km. Mapping structure on this scale requires the curvature of the earth to be taken into account which generally means using a spherical parameterisation to describe the model (Wang et al., 1998). Apart from this, the methods of analysis are similar to those described earlier for local studies. For example, Bowman & Kennett

(1993) apply refraction-style interpretation to first-arrival P and S traveltimes of regional earthquakes in Australia to determine 1-D P and S velocity structure to a depth of 500 km. Spakman (1991) inverts the traveltimes of regional earthquakes for P-wave velocity heterogeneities in the upper mantle of central Europe, the Mediterranean and Asia Minor, imaging velocity structure to a depth of $\sim$700 km. The method used by Spakman (1991) has similarities with LET and teleseismic tomography in that event mislocation and station delay time corrections are inverted for, and the linear inversion uses delay times calculated from a spherical 1-D earth model to constrain the velocity perturbations, which are defined by constant slowness cells.

Widiyantoro & van der Hilst (1997) use a similar approach to invert for the P-wave velocity structure of the mantle beneath Indonesia using data generated and recorded in the model region. A global dataset was also used to construct a low resolution global model of mantle P-wave velocity structure in addition to the higher resolution regional model for Indonesia. Both were inverted for simultaneously in order to help minimise the mapping of distant aspherical mantle structure into the study region. Regional inversions using body wave data tend to be large. For example, Widiyantoro & van der Hilst (1997) used more than six million traveltimes and solved for almost 110,000 unknowns.

Global tomography using body waves

In global seismic tomography using body waves, earth structure is generally parameterised in terms of constant velocity cells in spherical coordinates (e,g, Clayton, 1983; Inoue et al., 1990; van der Hilst et al., 1997). Like regional body-wave tomography, the number of cells tends to be very large. For example, Inoue et al. (1990) use 32,768 cells of surface dimension $5.625^\circ \times 5.625^\circ$ and variable depth division. A disadvantage of this approach is that cell size and shape vary with latitude and depth, though the model parameterisation may use cells whose longitude range increases with latitude (Morelli, 1993). Nolet & Moser (1993) use the novel approach of embedding the spherical earth in a Cartesian grid of nodes, which allows an even distribution of parameters and an increase in ray tracing efficiency. The initial model can be translated from the spherical system to the Cartesian system quite easily, but the drawback is that discontinuities such as the core-mantle boundary and Moho are harder to represent.

The main difficulty with global body wave tomography is the uneven distribution of

sources and receivers. Sources tend to be restricted to plate boundaries while receivers are almost always land based. The latter restriction means that shallow mantle structure beneath the oceans is hard to resolve. Regular cell parameterisation may therefore result in significant numbers of unconstrained parameters. Variable gridding can be used to compensate for this problem. Sambridge & Gudmundsson (1998) propose an irregular cell parameterisation based on Delaunay triangulation (or tetrahedralisation for 3-D) and Voronoi polyhedra, and Wang et al. (1998) use a cubic B-spline basis on a triangular grid of knots which supports variable spacing.

Instead of representing structure in terms of local basis functions, global basis functions may be used. These are particularly popular for whole earth studies, with the most common representation being a truncated spherical harmonic expansion (Dziewonski et al., 1977; Dziewonski & Woodhouse, 1987; Li & Romanowicz, 1996). Advantages of this approach include fewer parameters to describe a model of similar smoothness to an equivalent block model, and direct comparison with other geophysical variables such as gravity and magnetic field intensity, which are also presented using spherical harmonics (Inoue et al., 1990). However, if parts of the earth are poorly constrained by the data, then any biases that are introduced will effect the entire model if global basis functions are used. Zhang & Lay (1996) tested both block model and spherical harmonic parameterisation and found that, while spherical harmonic expansion gave superior recovery of long wavelength structure, heavy damping was required to suppress artifacts if high-order harmonics ($l > 22$) were used. Inoue et al. (1990) invert P-wave traveltimes for the velocity structure of the whole mantle using a spherical block model; van der Hilst et al. (1997) invert both pP and P traveltimes for mantle structure represented by 300,000 blocks and found evidence for whole mantle circulation. Morelli (1993) inverted PcP and PkP traveltimes for the geometry of the core-mantle boundary using a spherical harmonic representation and Dziewonski & Woodhouse (1987) describe several studies that use $PKIKP$ traveltimes to determine the structure of the core and core-mantle boundary. Inversion of body waveforms have also been carried out. Kohler (1997) inverted over 5000 waveforms for the P and S velocity structure of the mantle and outer core (P velocity only). Spheroidal modes with periods between 33 and 100 s were used to model the body wave portion of seismograms recorded from global earthquakes. As in other forms of earthquake tomography, it is common practice to include station correction terms (Morelli, 1993) and source mislocation parameters in global inversions when

traveltimes are involved (Inoue et al., 1990).

Regional mapping using surface waves

Surface waves have also been widely used in tomographic mapping of the earth. These waves travel more slowly than body waves and propagate across the free surface. The two principle types of surface waves, Rayleigh waves comprising P and SV motion and Love waves comprising SH motion, are both dispersive. Surface wave phase velocities are sensitive to vertical variations in velocity, but because they propagate horizontally are only capable of low resolution in the horizontal directions. Surface wave data has been particularly important in mapping beneath the oceans (Nolet, 1987); oceanic upper mantle is rarely probed by body wave tomography since few seismic recorders are placed in an ocean setting. In providing good vertical resolution of velocity structure, surface waves are complimentary to body waves whose near vertical incidence (Nolet, 1987) restricts vertical resolution but enhances horizontal resolution.

Surface waves are important for the analysis of earth structure because of their dispersion characteristics. Dispersion is caused by variations, principally with depth, of the elastic moduli (shear and adiabatic bulk) and density, resulting in waves of different frequency travelling at different velocities. As an example of the many regional surface wave studies that have been completed, Cotton & Avouc (1994) studied the crust and upper mantle structure of the Tien Shan. They obtained group velocity dispersion curves (plots of group velocity versus period) for fundamental mode Rayleigh waves from earthquakes and nuclear explosions in central Asia that were recorded in France. Variations between the dispersion curves from different source regions are used to infer changes in lateral structure in the Tien Shan described by variations in the depth dependence of shear wave velocity. Ritzwoller & Levshin (1998) constructed group velocity maps of Eurasia from 20 s - 200 s period Rayleigh Waves and 20 s -125 s period Love waves. These maps are constructed from the dispersion curves of ∼9,000 different paths and contain the signatures of geological features including continental roots, subducting slabs, continental flood basalts and sedimentary basins.

Analysis of surface wave dispersion data is usually based on a 1-D model of earth's seismic structure. Methods used to analyse surface wave data for 3-D variations of shear wave speed (see Figure 1.6d) typically involve two steps (Kennett, 1998). First, the surface

wave portion of each source-receiver waveform is inverted for a 1-D model that represents the path average of shear wave speed along great circle source-receiver paths. Second, a linear inversion is performed to construct a 3-D velocity model that is consistent with the set of 1-D path-averaged models. This method was used by Zielhuis & van der Hilst (1996) to map the upper mantle shear velocity beneath eastern Australia using data from the SKIPPY array. The assumption of great-circle propagation, the shortcomings of ray theory and the use of the path-average approximation as a basis for a 3-D velocity model limit the accuracy and resolving power of surface wave inversions.

Global tomography using surface waves

Surface wave studies on a global scale have revealed significant information on the earth's mantle structure. As with regional scale investigations, the dispersion characteristics of surface waves can be used to infer structure. Trampert & Woodhouse (1995) analyse fundamental-mode Rayleigh and Love waveforms to obtain global phase velocity maps in the period range 40 - 150 s. Relative phase-velocity perturbations are represented by a spherical harmonic expansion. Zhang & Lay (1996) perform a similar study with Love and Rayleigh waves of period 85 - 250 s except that the data used are phase velocity measurements rather than waveforms. They found that the shorter period phase velocity maps contain the clear signatures of continental shields, mid-ocean ridges and tectonically active areas. For similar periods, the Love and Rayleigh phase velocity maps of Trampert & Woodhouse (1995) and Zhang & Lay (1996) are well correlated.

Global tomographic studies that invert surface waveforms almost exclusively represent structure by using spherical harmonic expansions (Dziewonski & Woodhouse, 1987; Romanowicz, 1995). Inversions are performed under the path averaged approximation (i.e. that the recorded seismogram is assumed to be dependent only on the horizontally averaged structure along the source-receiver great-circle path). Surface waves are primarily sensitive to shear wave velocities, so global surface wave inversions produce maps of S-wave velocity variation (Dziewonski & Woodhouse, 1987). Figure 1.6e shows an example of a shear wave velocity model of the earth's upper mantle derived from surface wave inversion. Even at this depth (350 km), shear velocity still tends to be faster under continents than oceans.

Another approach that has been used in global surface-wave tomography is based on

spectral analysis of normal modes (Dziewonski & Woodhouse, 1987; Snieder, 1993). On an amplitude vs. frequency plot, normal modes appear as pronounced peaks, since constructive interference of surface wave trains occurs at precise frequency values. Attenuation in the earth leads to a broadening of these spectral peaks. Splitting of the spectral peaks is caused by the earth's ellipticity, lateral heterogeneity and Coriolis force (Snieder, 1993). The splitting caused by lateral heterogeneity can be isolated and used to determine the harmonic component of S-wave velocity structure.

Anisotropy in tomographic velocity models

Anisotropy within the earth causes the phase speed of seismic waves to vary with their direction of propagation. Distinguishing between variations in velocity and variations in anisotropy is a significant challenge in extracting anisotropic information from seismic data. The problem may be simplified if anisotropy is assumed to be a function of azimuth only. For example, Hearn (1996) applies anisotropic P_n tomography to regional earthquake data collected in the western United States. In this approach, ray paths are assumed to propagate along a planar Moho separating crust and mantle. The Moho plane is divided into a 2-D grid of cells and the inversion adjusts cell velocity, cell anisotropy (defined by two anisotropic coefficients for each cell) and station and event delay times in order to satisfy the set of traveltime residuals. Hearn (1996) found that fast directions of P_n anisotropy parallel the subduction direction of the Juan de Fuca Plate beneath the northwest Pacific coast.

Surface waves can also be used to determine azimuthal variations in anisotropy. Montagner & Jobert (1988) applied "vectorial tomography", which allows the simultaneous determination of lateral heterogeneities and azimuthal anisotropy, to a dataset of Rayleigh and Love wave dispersion velocities in the Indian Ocean. Results showed that within the lithosphere, maximum horizontal velocity is in the direction of contemporary plate motion, but beneath the lithosphere, this correlation vanishes, suggesting a complex convection pattern. Debayle (1999) used the method of Cara & Lévêque (1987) and Lévêque et al. (1999) to determine lateral variations in SV velocity and SV azimuthal anisotropy in the Australian upper mantle using SKIPPY data. Figure 1.6d shows a horizontal cross-section of the solution model produced by Debayle (1999). The vectors of fast SV velocity anisotropy are generally in the direction of contemporary plate motion and the velocity

perturbations appear to distinguish between younger crust in the east and older crust in the west. On a global scale, anisotropy from surface waves has been constrained using tomography by a number of authors (e.g. Montagner & Tanimoto, 1991; Nakanishi, 1993).

1.1.5 Summary

The aim of this brief overview was to outline some of the more important survey and data interpretation methods used to determine earth structure from seismic waves. The different approaches may be classified in terms of source-receiver geometry, scale, data type and techniques used to relate observed data to model structure (Table 1.1). The data may also be used together e.g. by combining local earthquake and teleseismic data (Sato et al., 1996; Zhao et al., 1996), local earthquake and artificial source data (Parsons & Zoback, 1997) or traveltimes and amplitudes (e.g. Wang & Houseman, 1997). With global studies, it is common practice to combine several data types in a single inversion. Li & Romanowicz (1996) invert the SH waveforms of both body waves and Love waves for mantle shear velocity and Su & Dziewonski (1997) invert surface waveforms and body waveforms and traveltimes for P and S wave velocity structure of the mantle. In both cases, spherical harmonic expansions are used to represent lateral velocity perturbations while Legendre polynomials are used to describe radial variations.

Another major branch of seismology is concerned with the location and identification of the source mechanism of earthquakes (e.g. Dziewonski et al., 1981; Quintanar et al., 1999). While source parameter determination can reveal important information on earth structure and tectonic activity, it has not been considered in this overview, which instead considers the relationship between earth structure and the propagation characteristics of seismic waves.

1.2 Outline of Research Project

It is clear from Section 1.1 that there are many different ways of imaging earth structure using seismic waves. In this thesis, I develop and apply methods that invert seismic traveltimes for layered crustal structure. The availability of two data sets helped to inspire this work: i) a previously published dataset consisting of teleseismic traveltime anomalies recorded by an in-line array of seismometers across the northern margin of the

Approach	**Data type**	**Source-receiver configuration**	**Scale**	**Model scope**	**Representation of structure**
Normal incidence reflection seismic analysis	Complete wavefield	In-line, normal incidence Artificial source	Crustal: depths of 100^sm to 10^skm	2-D	Structure inferred from plotting traces on dist. vs. TWT section
Reflection tomography	Reflection traveltimes or amplitudes	In-line, near normal incidence Artificial Source	Crustal: depths of 100^sm to 10^skm	2-D	Continuous interfaces and layer velocity nodes or blocks
Refraction interpretation	First-arrival traveltimes	In-line, wide aperture Artificial source	Crustal: depths of 100^sm to 10^skm	1-D or 2-D	Continuous interfaces and layer velocity nodes or blocks
Wide-angle forward modelling or inversion	Refraction and reflection traveltimes or amplitudes	Wide aperture in-line or broadside Artificial source	Crustal or Lithospheric: depths of km to 10^skm	2-D or 3-D	Continuous interfaces and layer velocity nodes or blocks
Wavefield continuation	Complete wavefield	Same as wide-angle	Same as wide-angle	1-D	Transform wavefield to $v(z)$ domain via $\tau - \rho$ domain
Crosshole tomography	First-arrival traveltimes	Sources and receivers down adjacent boreholes	Shallow crust: depths of $10^s - 100^s$ of m	2-D	Velocity nodes or blocks
Local earthquake tomography (LET)	First-arrival P and S traveltimes or amplitudes	Receiver array above model volume which contains earthquake sources	Crust or: upper mantle depths up to 200 km	3-D	Velocity, V_P/V_S or Q nodes or blocks plus hypocenter relocation
Teleseismic tomography	First-arrival traveltimes	Local receiver array and distant earthquake sources	Upper mantle: depths of $10^s - 100^s$ of km	3-D	Velocity nodes or blocks
Receiver function analysis	Waveform of teleseismic P arrival	Same as teleseismic tomography	Lithospheric: depths up to 100 km	1-D	Constant S velocity layers
Surface wave analysis	Surface waveforms or phase velocity	Receiver with distant source	Mid-upper mantle: depths to 100^s of km	1-D	Constant S velocity layers
Regional body wave tomography	Traveltimes of first-arrival P and S	Regional array Sources inside or outside array	Mid-upper mantle: depths to 100^s of km	3-D	Velocity nodes or blocks
Regional surface wave tomography	Surface waveforms	Regional array Sources outside array	Upper mantle: depths of several 100 km	3-D	Velocity nodes or blocks
Global body wave tomography	Traveltimes of global phases	Global network of receivers Earthquake sources	Whole earth	3-D	Velocity blocks/nodes or spherical harmonic parametrization
Global surface wave tomography	Long-period surface waveforms	Global network of receivers Earthquake sources	Mid-upper mantle: depths to 100^s of km	3-D	Velocity blocks/nodes or spherical harmonic parametrization
Global inversion using normal modes	Normal mode frequency spectra	Gobal network of receivers Earthquake sources	Mid-upper mantle: depths to 100^s of km	3-D	Velocity or local frequency shift parametrization

Table 1.1: Commonly used approaches for mapping earth structure using seismic waves.

Musgrave Block, central Australia (McQueen & Lambeck, 1996), and ii) an unpublished 3-D wide-angle seismic dataset recorded in Tasmania in 1995 as part of the TASGO project (Chudyk et al., 1995). The PhD project that I have undertaken may be summarised by the following aims.

1.2.1 Aims

- To invert teleseismic traveltime residuals for layered crustal structure using a dataset collected in central Australia. The method (Rawlinson, 1996a) is 2-D and uses traveltime residuals to constrain multiple interface geometry.

- To compare these 2-D results with results from other studies that use the same data but different methods, most notably the standard tomographic approach that inverts for variable velocity distribution rather than interface structure.

- To develop practical methods and software for the inversion of 3-D wide-angle seismic traveltimes for layered crustal structure. In particular, the method must deal with sparse data and/or data with variable coverage and be able to simultaneously invert both reflection and refraction traveltimes for layer velocity and interface geometry. Complex layer geometries such as pinchouts must be permitted.

- To assess the characteristics of the 3-D method by using synthetic tests based on reconstructing known structures from traveltime information.

- To develop a suite of software tools for the processing, visualisation and interactive picking of wide-angle seismic data. Processing steps include bandpass filtering, stacking, static correction and deconvolution.

- To construct a 3-D layered model of the Tasmanian crust by picking refraction and wide-angle reflection traveltimes from the TASGO dataset, and using the 3-D inversion program to invert these traveltimes for interface geometry and layer velocity.

- To assess the quality of the inversion solutions and extract the maximum possible geological information from the results.

1.2.2 Method and Software Development

The method used for the inversion of the central Australian teleseismic traveltime residuals was first presented by Rawlinson (1996a). A subsequent publication (Rawlinson & Houseman, 1998) describes the method together with some synthetic tests and real data inversions. Hence, I will not describe in detail the inversion method. In brief though, a tomographic approach is used. The model parameterisation describes a 2-D stratified velocity structure with constant velocity layering. Interfaces are described by piecewise cubic spline functions. The forward problem of determining ray paths and traveltimes between incident wavefronts below the structure and receivers located on the earth's surface is solved by an efficient and robust shooting method. A conjugate gradient method is employed to solve the inverse problem of minimising a least-squares type objective function based on the difference between observed and calculated traveltimes. Teleseismic data do not accurately constrain average vertical structure, so *a priori* information in the form of layer velocities and average layer thicknesses is required. These techniques were developed in FORTRAN77 code which is documented in Rawlinson (1996a). The code is also included on the CD attached to this thesis (see Appendix F).

The inversion of wide-angle traveltimes for 3-D crustal structure required the development of new analysis methods. Seismic refraction and wide-angle reflection traveltimes are simultaneously inverted for crustal structure represented by layers in which velocity varies linearly with depth, separated by smooth interfaces with a bicubic B-spline parameterisation. Lateral variations in structure are therefore represented by variations in interface depth. This choice of model parameterisation means that ray paths consist of piecewise circular arc segments for which analytic expressions of trajectory and traveltime are calculated. The two-point problem of finding the first-arrival ray path and traveltime of a specified phase between a given source and receiver is solved using a shooting technique. A subspace inversion method is used to solve the non-linear inverse problem in which an objective function that consists of a data residual term and a regularisation term is minimised. Since the method represents structure in terms of interfaces, fewer parameters are required compared to an equivalent 3-D variable velocity inversion. The method is well suited to surveys that consist of many sources and relatively few receivers (or vice-versa), such as marine shot lines used in conjunction with land based receivers. Data coverage in this kind of survey is often sparse and, especially if near-offset ray paths

are unavailable, highly variable. Estimates of *a posteriori* model covariance and resolution obtained from linear theory are used to analyse solution reliability. The inversion methodology is developed in a mixture of FORTRAN77 and C code which is included on the attached CD (see Appendix F). A 2-D version of the program was also developed in order to assist in the formulation and testing of the 3-D inversion code.

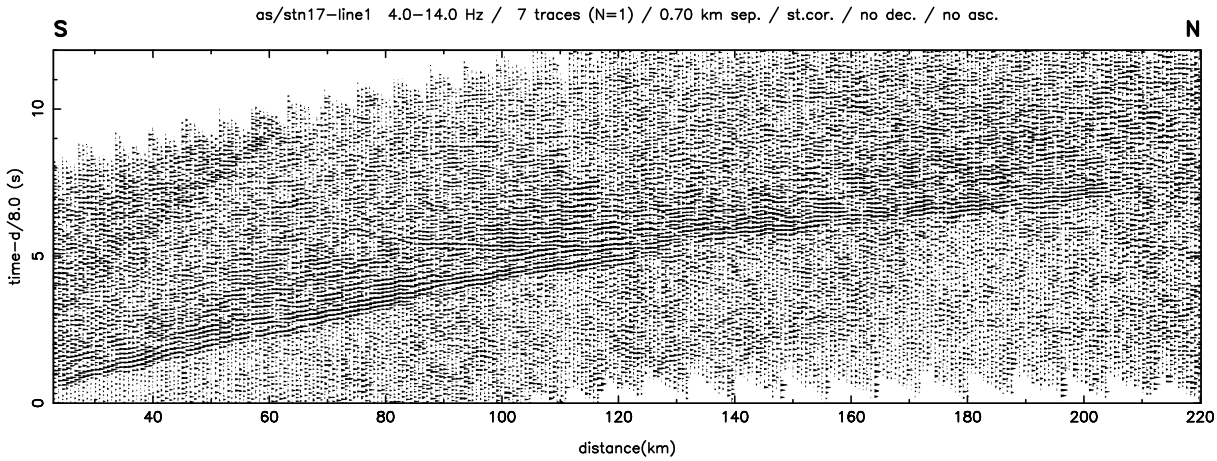

Figure 1.7: Example of output from data processing, visualisation and picking program. Vertical axis is reduced time and data is from line 1 recorded at station 17 (see Figure 1.9).

Synthetic tests are an essential part of any presentation that involves the introduction of new inversion methodology. A synthetic dataset is created by ray tracing through a specified model structure and recording source-receiver traveltimes. Inversion of these traveltimes with an initial model estimate produces a solution model which may be compared with the original model. The performance of the method in the presence of data noise, over/under-parameterisation and poor initial model estimates can also be examined along with the reliability of estimates of *a posteriori* model covariance and resolution.

The software tools constructed for the processing, visualisation and picking of the TASGO wide-angle traveltimes were unified in a single FORTRAN77 program, which is included on the attached CD (see Appendix F). The standard way of displaying this data is to plot traces from adjacent shots to a single receiver on a time vs. offset graph (Figure 1.7). On these *refraction profiles*, coherent phases appear as relatively continuous *traveltime curves*. Identification of these curves makes the picking of individual arrivals from different phases more reliable and straightforward. The purpose of the processing step is to improve the signal-to-noise ratio and trace-to-trace coherency of the data to aid the picking process.

The two principal processing techniques that are applied are bandpass filtering and stacking. Bandpass filtering removes unwanted low and high frequency components of the traces. Stacking operates under the assumption that noise is random; when adjacent traces are summed together, the noise is diminished and the signal is reinforced. Other processing techniques include static corrections, which are designed to boost coherency between adjacent traces prior to stacking and predictive deconvolution, which helps to remove the effects of the source wavetrain and reverberation. N^{th}-root stacking, which exhibits a dynamic noise reduction and sharpens wavelets, is also investigated and notch filtering is used to remove unwanted noise spikes. The software includes an interactive component that allows the rapid pick-and-click of identifiable phases.

1.2.3 2-D Teleseismic Analysis

In the application of the teleseismic inversion method, the central Australian teleseismic dataset from McQueen & Lambeck (1996) is utilised. It consists of events recorded at 26 sites on a north-south line from Lake Amadeus to near the southern margin of the Musgrave Block (Figure 1.8). When a strictly 2-D inversion method is applied to data generated from earthquake sources, only a small percentage of sources are likely to lie on the great circle that passes through the receiver array. In this case, only three of the available source regions have back-azimuths that differ by less than 10° from the receiver line azimuth. The closest source region is Mindanao (between 31° and 37° angular distance) for which incoming P-waves will have curvature small enough to make a plane-wave approximation acceptable. Mean-removed teleseismic traveltime residuals vary between ± 0.4 s, indicating the presence of significant lateral structure. The initial model used in the inversion process is based on an Amadeus Basin refraction profile (Collins, 1988) and the investigation of western and central Australian crustal structure by Bowman & Kennett (1993). Comparisons are made between the solutions produced by this method and results of more standard tomographic methods used by McQueen & Lambeck (1996) and the forward modelling of Lambeck & Burgess (1992).

1.2.4 3-D Wide-Angle Analysis

The TASGO wide-angle dataset (Chudyk et al., 1995) to which the inversion method presented in this thesis is applied, was recorded in 1995 under the auspices of AGSO (Aus-

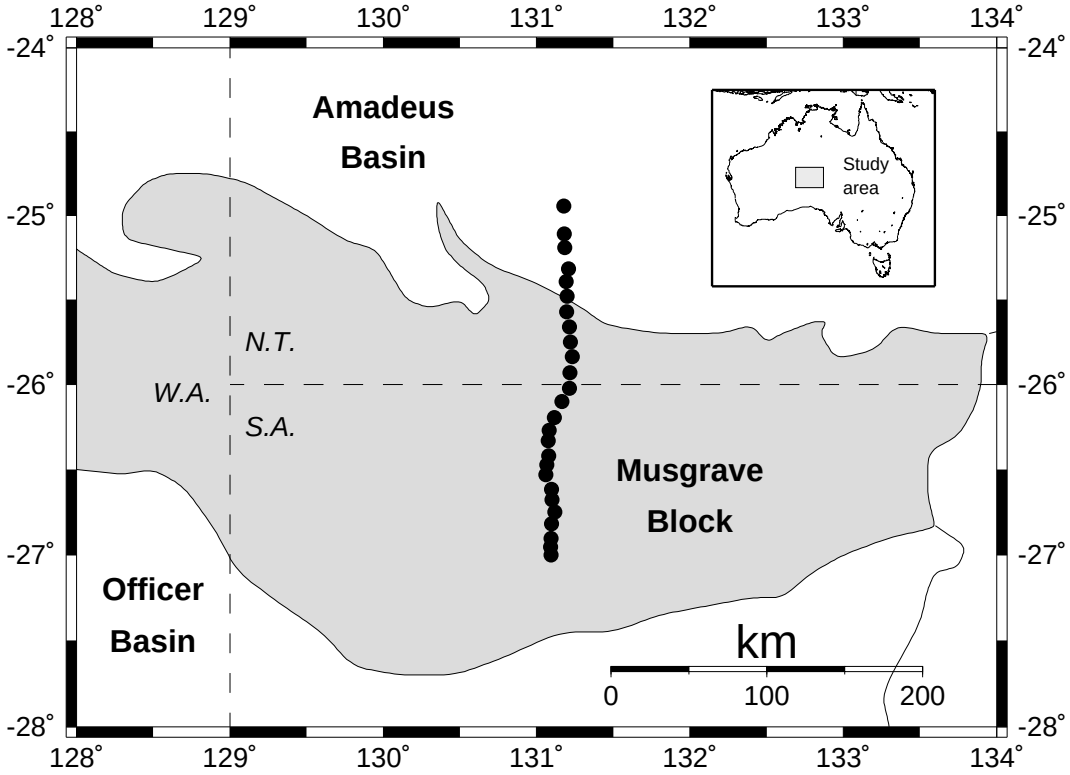

Figure 1.8: Array of 26 recorders (solid circles) deployed in central Australia to record teleseismic events.

tralian Geological Survey Organisation) and the Tasmanian Geological Survey. AGSO's research vessel *Rig Seismic* performed a circumnavigation of Tasmania during which it fired approximately 36,000 airgun shots with an average shot spacing of 50 m. A network of 38 portable analogue recorders and six digital observatory stations distributed throughout Tasmania recorded the seismic energy. Figure 1.9 shows the source-receiver configuration of the survey. With over 1,500,000 potential source-receiver combinations, the TASGO wide-angle dataset is quite substantial in size. However, the significant number of stations with recording problems and the low signal-to-noise ratio of data recorded from west coast shots means that a well-resolved inversion model of the whole Tasmanian crust cannot be obtained. The procedure for constraining Tasmania's crustal structure began by inverting data from single receiver/shot line combinations for 1-D structure. As well as providing preliminary results, these 1-D models were also used to construct initial models for inversions that permit lateral variations in structure. Using several sources in line with shot line 5, a 2-D inversion model along the western north coast was then constructed. All of the picked data from NW Tasmania were subsequently inverted for 3-D multi-layered crustal structure. This data subset was chosen because most of the us-

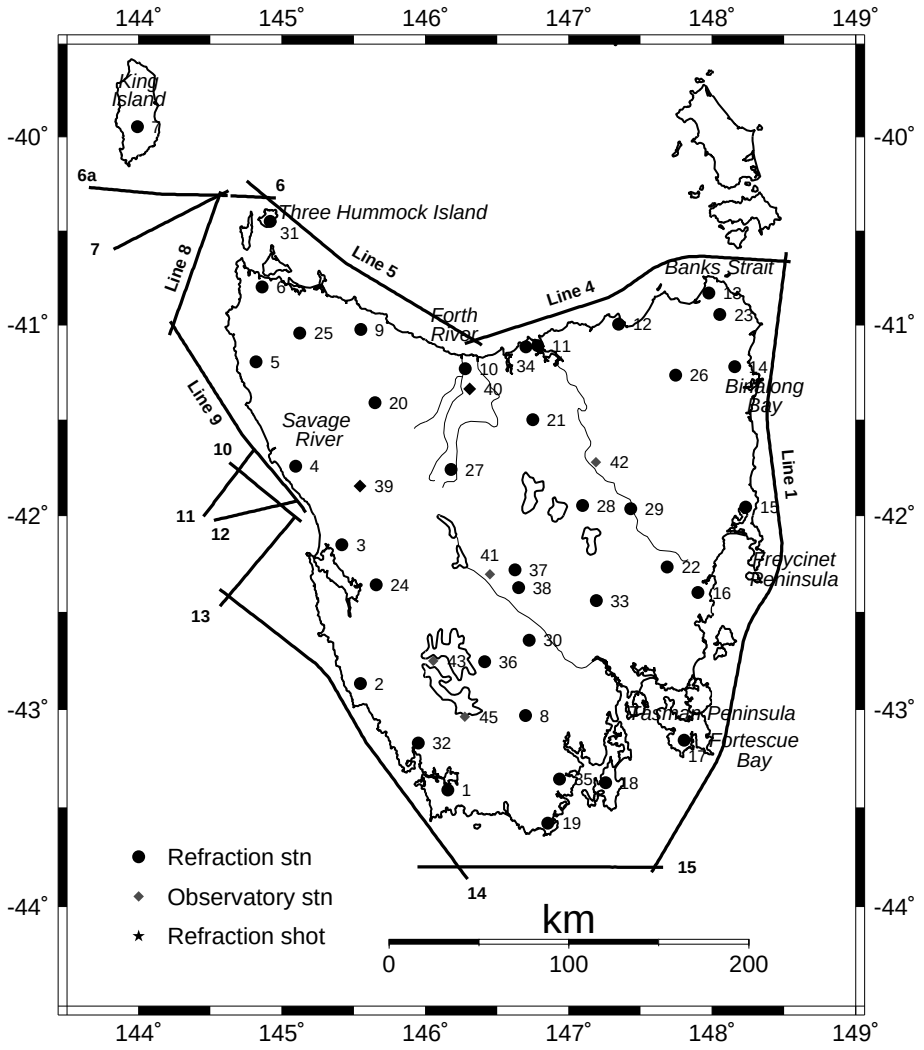

Figure 1.9: Network of 44 recorders distributed throughout Tasmania to record seismic energy from marine shot lines (thick lines).

able data recorded by the TASGO wide-angle survey was from NW Tasmania. Elsewhere, data coverage tends to be sparse, with the highest concentrations occurring near the coast and the lowest concentrations occurring towards the centre of the island. Since reflections from the Moho are by far the most common arrival type identifiable on the TASGO wide-angle records, the final inversion result that is presented constrains the structure of the Moho beneath Tasmania using all available P_mP and P_n arrivals.

1.3 Structure of Thesis

Chapter 2 describes in some detail the methodology that is commonly used in traveltime inversion, with particular emphasis on wide-angle and teleseismic applications. Model

parameterisation, methods of traveltime determination, inversion techniques and methods for analysing solution robustness are considered. Chapter 3 briefly describes the teleseismic inversion method of Rawlinson (1996a) before applying it to synthetic data and to the central Australian dataset. Comparisons with solutions obtained by using the same data but different methods and model parameterisations are also presented. The inversion method for determining 3-D layered crustal structure from wide-angle seismic traveltimes is presented in Chapter 4, along with the results from a number of synthetic tests. The synthetic tests analyse the effectiveness of the method in the presence of data noise, different source-receiver configurations, damping and poor initial model estimates. In addition, the effects of over, under and irregular parameterisations are tested and reconstructions involving layer pinchouts are carried out. Finally, a synthetic test is performed to investigate the usefulness of the method in a complex 3-D subduction zone setting.

Chapter 5 gives a brief description of Tasmania's tectonic evolution, and previous geophysical work in Tasmania that focused on mapping deep crustal structure, before describing the TASGO wide-angle survey and analysing data coverage and quality. Chapter 6 describes the processing and picking procedures used to obtain the set of traveltimes for inversion. A number of picked wide-angle sections are illustrated at the end of this chapter.

The inversion of the 1995 TASGO wide-angle dataset for the crustal structure of Tasmania is presented in Chapter 7. The robustness of the solution models are examined and the geological and tectonic significance of the results are discussed. The inversion results are compared with interpretations of the normal incidence reflection data that were collected concurrently with the wide-angle data. The final chapter (Chapter 8) contains general conclusions and includes a summary of the significant outcomes of the research project.

Computer programs used in this study for the inversion of traveltime data for layered crustal structure are contained in a CD that is attached to the back cover of this thesis. An MPEG movie of the NW Tasmania solution model described in Section 7.4.1 is also on this CD. The contents of this CD are described in more detail in Appendix F.

Chapter 2

Methods of Traveltime Inversion

In this chapter, I review some of the more common inversion methods for determining subsurface structure from seismic traveltimes. Since this thesis develops and implements inversion methods for teleseismic and wide-angle data, discussion will centre around the techniques that have been used in this area of research. Most methods of traveltime inversion are tomographic in nature, and so abide by the four steps outlined in Section 1.1.1 (Model parameterisation, forward step, inverse step, analysis of solution robustness). The following description of common traveltime inversion methods is divided according to these steps.

2.1 Representation of Structure

The traveltime of a seismic wave between source and receiver is solely dependent on the velocity structure of the medium through which the wave propagates. Therefore, subsurface structure in a seismic traveltime inversion is represented by variations in P or S wave velocity (or slowness). As mentioned in Section 1.1.1, velocity variations may be defined by a set of interfaces whose geometry is varied to satisfy the data, a set of constant velocity blocks or nodes with a specified interpolation function, or a combination of velocity and interface parameters. The most appropriate choice will depend on the *a priori* information (e.g. known faults or other interfaces), whether or not the data indicates the presence of interfaces (e.g. reflections, mode conversions), whether data coverage is adequate to resolve the trade-off between interface position and velocity, and finally, the capabilities of the inversion routine.

Constant velocity blocks (Figure 2.1a) are simple to define and allow rays to be traced in a straightforward manner. When they are used in an inversion, the intention is often to try to recover smooth variations in velocity. Although this parameterisation is not optimal for such a purpose, if a large number of blocks are used and smoothing is applied, then an acceptable approximation to a continuously varying velocity field is possible. Another potential problem of constant velocity blocks is that the artificial discontinuities in velocity may cause ray shadow zones and triplications. In teleseismic tomography, constant velocity blocks have been used by many authors including Aki et al. (1977), Oncescu et al. (1984), Humphreys & Clayton (1988), Humphreys & Clayton (1990), Benz et al. (1992), Achauer (1994) and Saltzer & Humphreys (1997). In wide-angle traveltime inversions, the use of constant velocity blocks is not as common. Zhu & Ebel (1994) and Hildebrand et al. (1989) use constant velocity blocks in the inversion of 3-D refraction traveltimes while Williamson (1990) and Blundell (1993) use them in an inversion of reflection traveltimes.

An alternative to describing a velocity field in terms of constant velocity blocks is to define a set of discrete velocity nodes on a grid (see Figure 2.1b) together with a specified interpolation function. One of the first authors to use this approach was Thurber (1983) in the context of local earthquake tomography. To describe the velocity at any point (x, y, z) within a rectangular grid of nodes, he used a trilinear interpolation function:

$$v(x,y,z) = \sum_{i=1}^{2}\sum_{j=1}^{2}\sum_{k=1}^{2} V(x_i, y_j, z_k)\left(1 - \left|\frac{x - x_i}{x_2 - x_1}\right|\right)\left(1 - \left|\frac{y - y_j}{y_2 - y_1}\right|\right)\left(1 - \left|\frac{z - z_k}{z_2 - z_1}\right|\right) \tag{2.1}$$

where $V(x_i, y_j, z_k)$ are the velocity values at the eight grid points surrounding (x, y, z). The use of Equation 2.1 ensures that the velocity field will be continuous throughout the model volume, although the velocity gradient will be discontinuous from cell to cell. Zhao et al. (1994) and Steck et al. (1998) have used this parameterisation in teleseismic tomography, although Zhao et al. (1994) uses a modified form of Equation 2.1 for spherical coordinates.

Higher order interpolation functions must be used if the velocity field is to have continuous first and second derivatives, which are required for some ray tracing methods (Thomson & Gubbins, 1982). Cubic spline interpolation results in continuous first and second derivatives and has been used by a number of authors. Thomson & Gubbins (1982), in a NORSAR teleseismic study, use the following cubic spline function to describe the

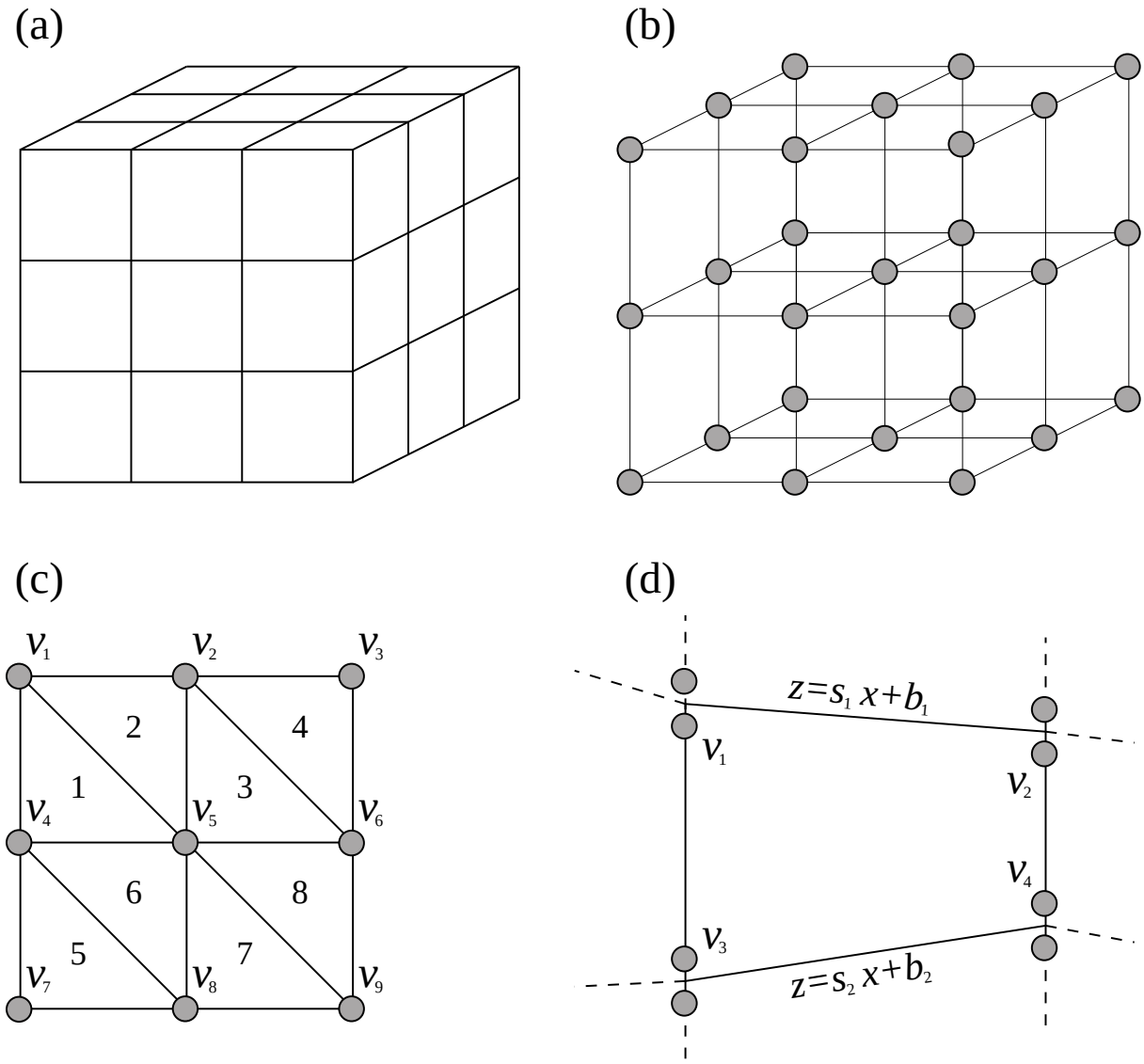

Figure 2.1: Different types of velocity parameterisation: (a) constant velocity blocks, (b) a grid of velocity nodes, (c) triangulated velocity grid designed for constant velocity gradient cells (after White, 1989), (d) velocity defined by a trapezoidal block (after Zelt & Smith, 1992). The four corner vertices labelled v_1 to v_4 define the velocity within the block. If adjacent nodes in vertically adjacent blocks are the same, velocity will be vertically continuous. If not, then a sub-horizontal interface will be defined.

slowness field within a 3-D spherically symmetric grid of nodes:

$$s(r,\theta,\phi) = \sum_{i,j,k=1}^{4} S_{ijk} C_i(R) C_j(\Theta) C_k(\Phi) \tag{2.2}$$

where S_{ijk} are the slowness values at the nodes of the $4 \times 4 \times 4$ grid surrounding the point (r,θ,ϕ). $C_i(R)$, $C_j(\Theta)$ and $C_k(\Phi)$ (see Thomson & Gubbins, 1982) are known as the cardinal splines and R, Θ and Φ are the local coordinates of r, θ and ϕ. Nodal values do not necessarily equal the interpolated spline functions at the node points. Sambridge

(1990) uses a similar parameterisation in Cartesian coordinates to describe a 3-D model constrained by traveltimes from a regional earthquake network.

Cubic B-splines are similar to the cardinal splines described above in that they are locally supported and do not necessarily pass through the node values. Conventional cubic spline interpolation forces the spline to pass through node values and is not locally supported. Undesirable effects of non-local support include poorly resolved portions of the model having a global influence and unrealistic velocity fluctuations between nodes (Shalev, 1993). In 2-D wide-angle traveltime tomography, cubic spline interpolation has been employed by Lutter et al. (1990) while Farra & Madariaga (1988) and McCaughey & Singh (1997) have used cubic B-spline bases.

An interpolation method which features inherent flexibility is splines under tension. Here, a tension factor is used to control the mode of interpolation, which, in the case of Neele et al. (1993), can vary between near trilinear interpolation and cubic spline interpolation. The scheme features continuous first and second derivatives. Usually, one will choose a tension factor that results in a smooth model but minimises unrealistic oscillations and maximises local control. Neele et al. (1993); VanDecar et al. (1995) and Ritsema et al. (1998) all use this approach in the inversion of teleseismic traveltimes.

A method of parameterisation that goes some way towards bridging the gap between a block approach and a grid approach is one which uses cells with a constant velocity gradient. White (1989) describes a method of 2-D refraction tomography in which a rectangular grid of nodes is used to define triangular regions of constant velocity gradient (see Figure 2.1c). The velocity within each cell is given by:

$$v(x, y) = v_o + (x - x_o)\nabla_x v + (z - z_o)\nabla_z v \tag{2.3}$$

where v_o, $\nabla_x v$ and $\nabla_z v$ are determined using the velocities at the vertices of the triangle (e.g. $v_o = 1$, $\nabla_x v = (v_2 - v_1)/\Delta x$, $\nabla_z v = (v_5 - v_2)/\Delta z$ in cell 1 of Figure 2.1c). The attributes of this method are that velocity varies continuously throughout the medium and rays can be traced analytically within each cell. However, the velocity gradient is discontinuous at each cell boundary which, in conjunction with their triangular shape, can result in difficulties in finding the source-receiver ray path. Similar methods were used by Chapman & Drummond (1982) and by Bishop et al. (1985). Another interpolation function which can be used with the triangular cell geometry and also allows analytic ray tracing is the constant gradient of quadratic slowness $1/v^2$ (Červený, 1987). The

extension of these procedures to 3-D involves the use of tetrahedral cells, with the linear interpolation functions described in terms of the velocity nodes at the four apexes of the tetrahedron. It is important to note that these methods of parameterisation are used primarily because they facilitate analytic ray tracing and secondly because they provide an adequate approximation to actual subsurface velocity distribution, which is inevitably more complex.

The use of irregular blocks or grid nodes to describe velocity distribution is not very common in traveltime tomography. However, irregular shaped elements can be adapted to suit variations in subsurface data coverage. The frequently used 2-D wide-angle inversion method of Zelt & Smith (1992), briefly alluded to in Section 1.1.2, uses such a method. The velocity field is discretised into a series of trapezoidal blocks, with four corner vertices used to specify the velocity within the block. Figure 2.1d shows the design of the trapezoid. The velocity within the trapezoid is given by (Zelt & Smith, 1992):

$$v(x,z) = \frac{c_1 x + c_2 x^2 + c_3 z + c_4 xz + c_5}{c_6 x + c_7} \tag{2.4}$$

where c_i are linear combinations of the corner velocities (see Zelt & Smith, 1992). Discontinuities are permitted in the velocity field through the inclusion of pairs of nodes on sub-horizontal boundaries (see Figure 2.1d). If these nodal values are equal, the velocity field is continuous. The inherent flexibility of this technique means that a velocity structure with with or without layering can be represented. If layers are present, then it is possible for the velocity within the layers to vary arbitrarily. Pinchouts and isolated bodies can be represented by using three-sided blocks. Finally, the size and shape of the trapezoids can be varied to suit the resolving power of the dataset.

Rather than use a block or grid-based parameterisation, one could use a scheme in which velocity is discretised in the wavenumber domain rather than the spatial domain. Spectral parameterisations that use some form of truncated Fourier series fall into this category. In their inversion of reflection amplitudes and traveltimes, Wang & Pratt (1997) describe a 2-D slowness distribution using the Fourier series:

$$\begin{aligned} s(\mathbf{r}) &= a_{00} + \sum_{m=1}^{N} [a_{m0}\cos(\mathbf{k}.\mathbf{r}) + b_{m0}\sin(\mathbf{k}.\mathbf{r})] \\ &\quad + \sum_{m=-N}^{N}\sum_{n=1}^{N} [a_{mn}\cos(\mathbf{k}.\mathbf{r}) + b_{mn}\sin(\mathbf{k}.\mathbf{r})] \end{aligned} \tag{2.5}$$

where $\mathbf{r} = x\mathbf{i} + z\mathbf{j}$ and $\mathbf{k} = m\pi k_0\mathbf{i} + n\pi k_0\mathbf{j}$ are the position and wavenumber vector respectively, and a_{mn} and b_{mn} are the amplitude coefficients of the $(m,n)^{th}$ harmonic

term, which become the unknowns in the inversion step. The advantage of this type of parameterisation is that it defines a velocity field which is infinitely differentiable and whose smoothness can be controlled through the choice of the number of harmonic terms N that are used. Equation 2.5 defines a non-local parameterisation, however, so poorly resolved portions of a solution model may have a detrimental effect on other regions of the model. Spectral parameterisations have been used in wide-angle traveltime inversion by Hildebrand et al. (1989) and Wiggins et al. (1996) to study crustal structure beneath deep oceans.

Velocity discontinuities are most commonly included in velocity models when the subsurface is represented by sub horizontal layers (see Figure 2.2). In 2-D and 3-D traveltime inversion, the use of layered parameterisations has almost exclusively been the domain of reflection and refraction tomography. Reflection sections only image reflectors and refraction sections usually contain obvious later-arriving traveltime curves associated with velocity discontinuities. The issues related to choosing an appropriate interface parameterisation are similar to those for choosing an appropriate velocity parameterisation - representation of the geological structure and suitability for use in the forward and inverse solution steps.

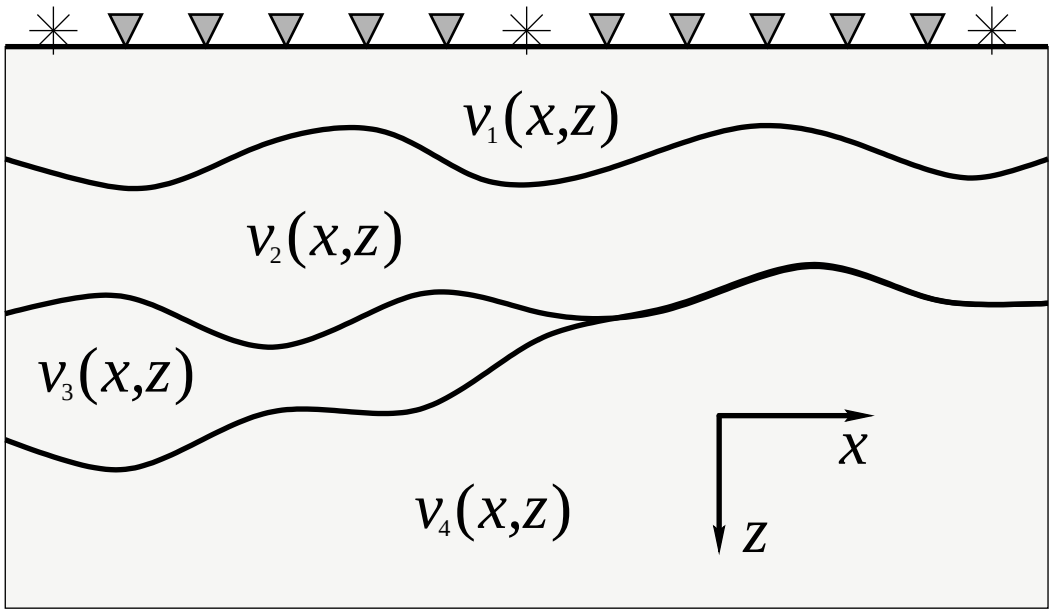

Figure 2.2: Schematic representation of the kind of layered velocity structure that can be imaged in reflection and wide-angle traveltime inversion. The velocity functions $v_i(x, z)$ describe the velocity variation within a layer.

In 2-D, piecewise linear segments (see Figure 2.3a) are probably the simplest means of representing interface geometry. The wide-angle method of Zelt & Smith (1992) and the reflection method of Williamson (1990) employ this type of interface parameterisation. One obvious problem with using piecewise linear segments is that the gradient of the interface is discontinuous at the joins between segments. Such discontinuity may not be geologically realistic and create artificial shadow zones because incident rays with very similar paths may depart from the interface along very different paths if they intersect the interface on either side of a point of gradient discontinuity. Zelt & Smith (1992) avoid this problem by using an averaging filter to smooth the interface so that the departing ray has a trajectory consistent with the smooth interface, but the point of projection is still given by the intersection point of the incident ray with the piecewise linear interface.

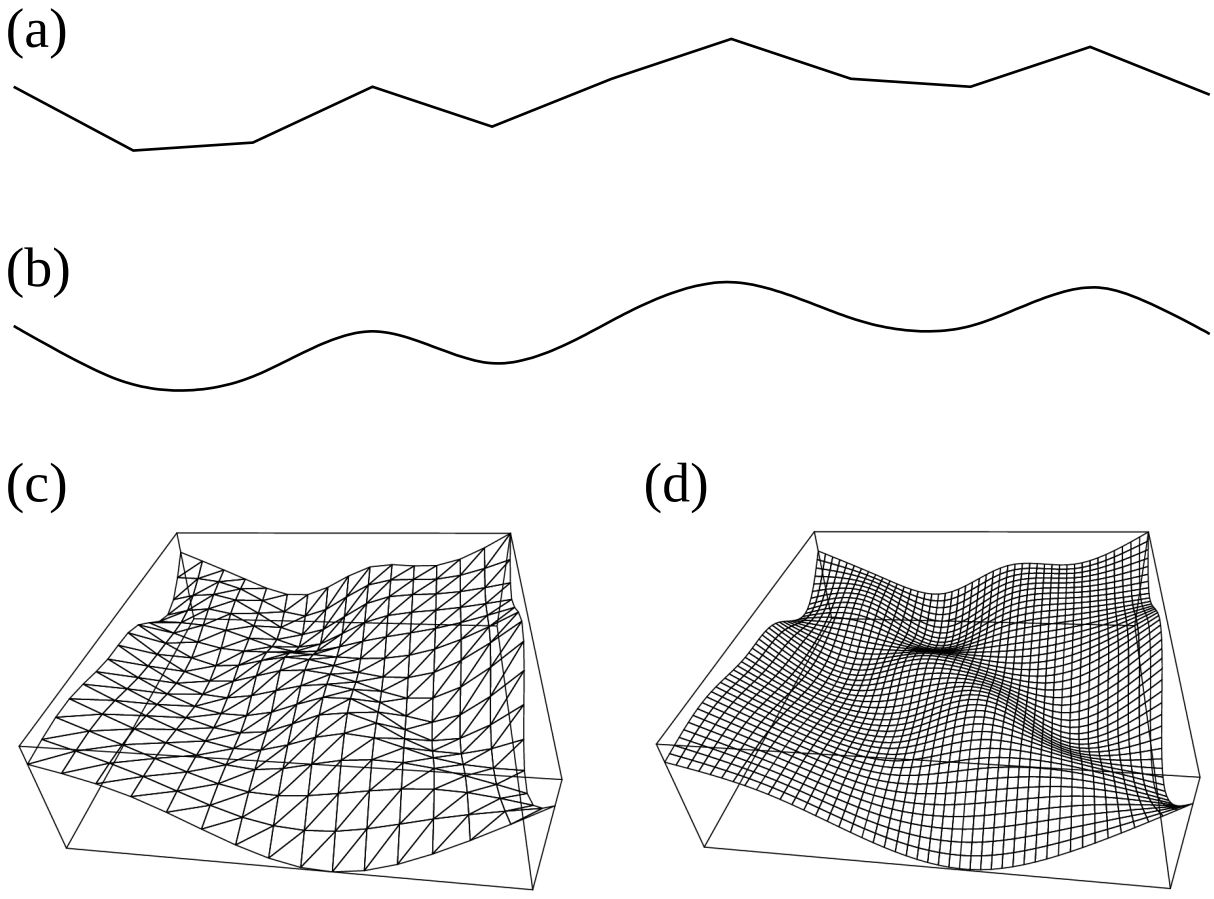

Figure 2.3: Types of interface parameterisation for 2-D (a-b) and 3-D (c-d) models. (a) Piecewise linear interpolation, (b) piecewise cubic B-spline interpolation, (c) surface defined by mosaic of triangular patches, (d) surface defined by mosaic of bicubic B-spline patches - note that the surface is visualised here by orthogonal sets of lines.

The logical extension of piecewise linear segments to a 3-D model with interface surfaces is to use piecewise triangular area segments (see Figure 2.3c). Sambridge (1990) has used this approach in the inversion of regional earthquake and quarry blast traveltimes. Guiziou et al. (1996) also used a triangulated interface structure in the tomographic inversion of reflection traveltimes in order to work with geological models created by GOCAD. One advantage of triangulation is that multi-valued surfaces are easily described.

Analogous to defining velocity on a grid of nodes, an interface may be described by a grid of depth nodes with a specified interpolation function (piecewise linear segments can be viewed as a special case of this). Piecewise cubic spline functions with C_2 continuity (see Figure 2.3b) are commonly used in wide-angle inversions. Conventional cubic splines have been used in a number of 2-D schemes including those by White (1989) and Lutter & Nowack (1990). Inversion methods based on the SEIS83 ray-tracing package of Červený (e.g. Červený & Firbas, 1984), which can trace reflected and refracted rays through layered media, also use cubic splines to describe interface geometry. Cubic B-splines, which feature local control of interface geometry, have been used by Farra & Madariaga (1988) and McCaughey & Singh (1997). In 3-D, the use of smooth interfaces (see Figure 2.3d) is less common, mainly because methods for the inversion of 3-D layered structures are less wide spread. The ray tracing method of Gjøystdal et al. (1984) parameterises interfaces in terms of bicubic splines; the reflection tomography method of Chiu et al. (1986) describes interfaces using n^{th} order polynomials (in practice, they use $n \leq 3$); Hole et al. (1992) fit adjustments to a set of depth nodes using a Laplacian surface when inverting broadside refraction traveltimes. In the latter case, the interpolation function $\Delta z(x, y)$ must satisfy:

$$\nabla^2[\Delta z(x, y)] = 0 \tag{2.6}$$

everywhere except at the node points. An advantage of a Laplacian surface is that it will extrapolate smoothly toward an average value outside the region sampled by the data (Hole et al., 1992). Riahi & Juhlin (1994) apply a similar method to reflection traveltimes. Like velocity, interfaces are also amenable to spectral parameterisation. Wang & Houseman (1994) describe interfaces using a truncated Fourier series where the number of harmonic terms controls the allowable flexibility of the interface. The problems associated with the use of a global parameterisation outlined above for velocity also apply to interface structure.

Fault surfaces are another common feature of earth structure that may need to be

represented in a model. Explicit representation of faults is not common in seismic methods. Faults are often near-vertical and cause discontinuities in the interfaces and velocity fields of subhorizontal layers offset by the fault. Ray-tracing through such a medium may be difficult and the inverse problem would likely be highly non-linear. Lambeck et al. (1988) and Lambeck & Burgess (1992) computed teleseismic traveltime residuals for a 2-D model in which constant velocity layers bounded by piecewise linear interfaces are not required to be laterally continuous across the model, thus allowing faults to be defined. Inversion of traveltime residuals was not attempted in either study, however. Wide-angle inversion methods that allow for complex lateral structure (e.g. Zelt & Smith, 1992) are usually not designed to represent faults. Laterally discontinuous structures like those found at subduction zones (Zelt, 1999) can be represented because interfaces tend to have a shallow dip and layer dislocation is not usually needed. Wang & Braile (1996), using a method based on that of Zelt & Smith (1992), represent faults implicitly by sharp near-vertical jumps in sub-horizontal interface structure in adjacent interfaces. However, these structures were constrained manually during the inversion process.

When interfaces are used in conjunction with layer velocities specified by blocks or a grid of nodes, then it is usually necessary to extrapolate the velocity field of each layer beyond the surrounding interfaces. These velocity parameters are redundant unless changes in interface geometry made by the inversion step causes the relevant nodes to lie within the layer. The velocity within each layer is usually defined to be independent of velocities in other layers, so any spatial overlap of velocity nodes from adjacent layers is of no consequence. In a 3-D wide-angle inversion study, Zelt et al. (1999) describe velocity structure using a continuous velocity parameterisation but include "floating" reflectors. These floating reflectors allow reflections to be used to constrain interface structure and velocity but simplify traveltime determination by associating the reflectors with sharp gradients in velocity rather than with velocity discontinuities.

As mentioned earlier, the use of interfaces in teleseismic traveltime tomography is rare. Zhao et al. (1994) employ fixed interfaces described either by a power series or piecewise linear interpolation in their simultaneous inversion of local, regional and teleseismic traveltimes for velocity variation. Davis (1991) uses backprojection to invert teleseismic traveltime residuals for the structure of the lithosphere-asthenosphere boundary in East Africa, defining interface geometry in terms of a polynomial expansion. Kohler & Davis (1997) use a similar procedure to determine 2-D crustal thickness variations in California

from teleseismic traveltime residuals.

2.2 Traveltime Determination

The aim of the forward step of the inverse problem is to determine the theoretical traveltimes of seismic waves between a given set of sources and receivers that lie within or on the surface of a specified velocity structure. When more than one ray path exists between a given source and receiver, the path with minimum traveltime is the one usually required because first-arrivals are always easier to identify on a seismogram. Often, other quantities such as Fréchet derivatives are calculated together with traveltime, but these parameters and their methods of computation are described in the next section in the context of the relevant inversion method.

The traveltime of a seismic wave between source S and receiver R is given by the integral:

$$t = \int_S^R \frac{1}{v(\mathbf{x})} \mathrm{d}l \tag{2.7}$$

where $\mathrm{d}l$ is differential path length, $\mathbf{x}$ is the position vector and v is velocity. The difficulty in performing this integration is that the path taken by the wave depends on the velocity structure, and the path needs to be known in order to evaluate the integral in Equation 2.7. For an elastic medium, the propagation of seismic wavefronts can be described by the eikonal equation:

$$(\nabla_{\mathbf{x}} T)^2 = \frac{1}{[v(\mathbf{x})]^2} \tag{2.8}$$

where T is traveltime. This description of wave propagation is subject to the so-called high frequency assumption: the wavelength of a seismic wave should be much less than the length scale of the velocity variations of the medium through which it passes. If traveltime is described by the equation $T = T(\mathbf{x})$ and time is held constant, then $T_A = T(\mathbf{x})$ is an implicit equation for the wavefront at time T_A (Aki & Richards, 1980). If T_A is increased to, say, T_B, then the equation $T_B = T(\mathbf{x})$ will describe the new geometry and position of the wavefront at a time $T_B - T_A$ later. If instead a point of constant phase on the wave is described as $\mathbf{x} = \mathbf{x}(T)$ then, rather than implicitly describing a wavefront (i.e. a surface), we explicitly describe a ray path (i.e. a curve). Ray paths are by definition everywhere normal to wavefronts. The equation that governs the geometry of ray paths can be derived from the eikonal equation by considering how a small change in time $\mathrm{d}t$

effects a point $\mathbf{x}$ on a wavefront (see Aki & Richards, 1980). The resultant *ray equation*:

$$\frac{\mathrm{d}}{\mathrm{d}l}\left(\frac{1}{v(\mathbf{x})}\frac{\mathrm{d}\mathbf{x}}{\mathrm{d}l}\right) = \nabla\left(\frac{1}{v(\mathbf{x})}\right) \tag{2.9}$$

can be used to describe ray path geometry for any given velocity field $v(\mathbf{x})$. A consequence of Equation 2.9 is Fermat's principle - that of all the paths that join two points A and B in a velocity medium, the true ray path(s) will be stationary in time. In other words, the path along which the integral in Equation 2.7 is performed is one which extremizes t.

In traveltime inversion, the traditional means of determining source-receiver traveltimes is ray tracing. More recently, wavefront tracking via finite difference solutions of the eikonal equation have been employed. Another method that has seen recent application is network/graph theory, which makes direct use of Fermat's principle. Each of these methods of traveltime determination is described below.

2.2.1 Ray Tracing

The problem of finding a ray path between a source and receiver is a boundary value problem. There are two basic solution methods: shooting and bending.

Shooting method

Shooting methods of ray tracing rely on formulating the ray equation (Equation 2.9) as an initial value problem, where a complete ray path can be determined provided the source coordinates and initial ray direction are supplied. The boundary value problem is then solved by shooting rays through the medium from the source and using information from the computed paths to update the initial ray trajectories so that they more accurately target the receivers (see Figure 2.4). Rays may also be shot from receivers towards the sources as the principle of reciprocity applies in ray tracing.

The ease with which the initial value problem can be solved depends on how the velocity distribution is parameterised. For constant velocity (or slowness) block models, the path within a block is simply a straight line with traveltime varying linearly with distance. At cell boundaries, new trajectories are calculated using Snell's Law:

$$\frac{\sin\theta_1}{v_1} = \frac{\sin\theta_2}{v_2} \tag{2.10}$$

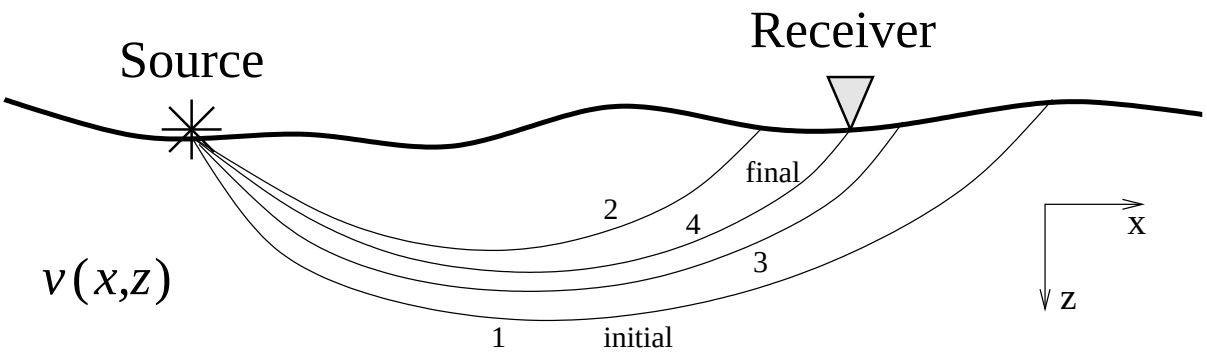

Figure 2.4: Principle of the shooting method. The initial projection angle of ray 1 is iteratively adjusted until the final ray (4) passes sufficiently close to the receiver.

where θ_1 and θ_2 are the angles of incident and refracted rays relative to the normal vector to the interface, and v_1 and v_2 are the velocities of the media containing the incident and refracted rays respectively.

Analytic ray tracing is also possible for media with a constant velocity gradient. Telford et al. (1976) derive parametric equations for ray path geometry and traveltime when velocity varies linearly with depth z:

$$\left.\begin{aligned} x &= \frac{1}{pk}(\cos i - \cos i_o) \\ z &= \frac{1}{pk}(\sin i - \sin i_o) \\ t &= \frac{1}{k}\ln\left(\frac{\tan\frac{i}{2}}{\tan\frac{i_o}{2}}\right) \end{aligned}\right\} \tag{2.11}$$

where i is the inclination of the ray, i_o is the initial inclination, k is the velocity gradient and p is ray parameter. When the velocity gradient is arbitrarily orientated, such as when a grid of constant velocity gradient triangles or tetrahedra are used (see Section 2.1), then these expressions are modified by rotation of the coordinate system (White, 1989). Simple analytic solutions are also possible when there is a constant gradient of quadratic slowness (see Červený, 1987).

Only a few simple velocity functions allow for analytic solutions of the initial value problem. For the case of an arbitrary differentiable velocity function $v(\mathbf{x})$, numerical solution of an initial value formulation of the ray equation is required. For example, Zelt & Smith (1992), as part of their 2-D wide-angle traveltime inversion method, solve two pairs of first-order differential equations:

$$\frac{\mathrm{d}z}{\mathrm{d}x} = \cot\theta \qquad\qquad \frac{\mathrm{d}\theta}{\mathrm{d}x} = \frac{v_z - v_x\cot\theta}{v} \tag{2.12}$$

or

$$\frac{\mathrm{d}x}{\mathrm{d}z} = \tan\theta \qquad\qquad \frac{\mathrm{d}\theta}{\mathrm{d}z} = \frac{v_z \tan\theta - v_x}{v} \tag{2.13}$$

with initial conditions provided by source location (x_o, z_o) and ray take-off angle θ_o. θ is the angle of incidence (relative to the z-axis), $v_z = \partial v/\partial z$ and $v_x = \partial v/\partial x$. Equation 2.12 is used for near horizontal rays and Equation 2.13 is used for near vertical rays. Both systems of equations are solved using a Runge-Kutta method with error control. Traveltime is determined by numerical integration of Equation 2.7 using the trapezoidal rule. Sambridge & Kennett (1990) use the following set of equations to solve the initial value problem in 3-D:

$$\left.\begin{aligned}
\frac{\partial x}{\partial t} &= v \sin i \cos j \\
\frac{\partial y}{\partial t} &= v \sin i \sin j \\
\frac{\partial z}{\partial t} &= v \cos i \\
\frac{\partial i}{\partial t} &= -\cos i \left(\frac{\partial v}{\partial x} \cos j + \frac{\partial v}{\partial y} \sin j \right) + \frac{\partial v}{\partial z} \sin i \\
\frac{\partial j}{\partial t} &= \frac{1}{\sin i} \left(\frac{\partial v}{\partial x} \sin j - \frac{\partial v}{\partial y} \cos j \right)
\end{aligned}\right\} \tag{2.14}$$

where i and j represent the incidence angle and azimuth respectively of the ray. They also use a Runge-Kutta method to solve the system with the ray traveltime t as the integration variable. The accuracy of the ray path and associated traveltime determined via numerical ray tracing depend on the accuracy of the solution scheme (4^{th} order accurate in this case) and the length of the integration step.

When interfaces are included in a discontinuous velocity model, the reflection and transmission laws for a ray path at an interface can be described in terms of Snell's Law (Equation 2.10), the requirement that the angle of reflection equals the angle of incidence, and the requirement that the reflected/transmitted ray must lie in the same plane as the incident ray and the vector normal to the interface at the intersection point. Formulating these constraints into a procedure for determining the new ray direction is relatively straightforward once the ray-interface intersection point is located. When numerical ray tracing is used, the step length of the numerical integration may be iteratively varied in order to obtain a point on the ray path sufficiently close to the interface (e.g. Sambridge & Kennett, 1990).

Solution of the initial value problem is the first step in finding a ray path from source to receiver. The next and generally more difficult step is to solve the two-point boundary value problem. Julian & Gubbins (1977) suggest two iterative methods of solution. The first of these is Newton's method which can be written for the 3-D problem:

$$\begin{bmatrix} \dfrac{\partial h}{\partial i_o} & \dfrac{\partial h}{\partial j_o} \\ \dfrac{\partial g}{\partial i_o} & \dfrac{\partial g}{\partial j_o} \end{bmatrix}_n \begin{bmatrix} i_o^{n+1} - i_o^n \\ j_o^{n+1} - j_o^n \end{bmatrix} = \begin{bmatrix} H - h(i_o^n, j_o^n) \\ G - g(i_o^n, j_o^n) \end{bmatrix} \tag{2.15}$$

where (h, g) are the calculated horizontal coordinates of the ray endpoint, (H, G) are the desired coordinates and (i_o, j_o) are respectively the inclination and azimuth of the ray at the source. Solution of this system gives the updated projection coordinates (i_o^{n+1}, j_o^{n+1}), and the process is iterated until an appropriate tolerance criterion is met. The difficulty with this scheme is the accurate determination of the partial derivative matrix. The second method is that of false position, which involves fitting a plane to the $h(i_o, j_o)$ and $g(i_o, j_o)$ of three known rays. The improved estimate (i_o^{n+1}, j_o^{n+1}) corresponds to where (H, G) lies on the plane. The method of false position is quicker at each iteration than Newton's method but converges more slowly. Sambridge & Kennett (1990) use Equation 2.15 to solve the two point problem and determine accurate values for the partial derivatives by solving, in conjunction with the initial value problem, two systems of first-order differential equations that describe the geometrical spreading of the wavefront. A perturbation is applied to the initial ray projection angle if the ray gets trapped in a local minimum. In an application of the method (Sambridge, 1990), the initial trajectory of the first-guess ray path is provided by solving the 2-point problem for a laterally averaged version of the model.

The method used by Sambridge (1990) to calculate the partial derivatives in Equation 2.15 is a specific application of paraxial ray approximation (Červený & Pšenčik, 1983; Červený et al., 1984; Červený, 1987; Farra & Madariaga, 1988), a method that is commonly used to solve the two-point problem in reflection and refraction ray tracing. The method is based on using a ray-centred coordinate system, where a particular ray Ω is taken to define one of the three coordinate axes. The wavefield in the vicinity of the central ray can be determined from quantities that are integrated along the central ray using dynamic ray tracing. Geometric spreading and wavefront curvature parameters along the initial ray Ω can be used to rapidly locate the two-point ray path from an initial ray that is not too far from the target (see Červený et al., 1984).

In 2-D problems, a shooting approach is often used because the source-receiver array lies on a single vertical plane, making the shooting of a single fan of rays an effective way of obtaining nearby rays to all targets. Zelt & Smith (1992) use a bisection method to find rays that bound each required phase (e.g. a set of rays that all reflect back to the surface from a particular interface). The boundary value problem is solved by shooting a fan of rays into each defined region and linearly interpolating the required quantities between the two closest rays that bracket a receiver. Blundell (1993) uses a similar approach of shooting a fan of rays from the source to find 2-D reflection arrivals. The two-point problem is then solved using a secant algorithm or a bisection algorithm with a pair of rays that bracket the receiver. Similar methods were used by Cassell (1982) and Langan et al. (1985). Other applications of shooting methods in 2-D reflection and/or refraction traveltime inversion include those by Farra & Madariaga (1988), White (1989), Lutter et al. (1990), Williamson (1990), Zelt & Smith (1992) and McCaughey & Singh (1997). Examples of its use in 3-D reflection and/or refraction traveltime inversions are harder to find although several 3-D tomographic studies that combined refraction and local earthquake data (Benz & Smith, 1984; Ankeny et al., 1986; Sambridge, 1990) and some teleseismic tomography studies (Neele et al., 1993; VanDecar et al., 1995) have used shooting methods of ray tracing.

Bending method

The bending method of ray tracing operates by adjusting the geometry of an initial arbitrary path that joins the source and receiver (Figure 2.5) until it becomes a true ray path (i.e. it satisfies Fermat's principle). The bending method proposed by Julian & Gubbins (1977) is designed for a continuous 3-D velocity medium and locates a two-point ray path by solving a system of first-order differential equations. If the ray path is described parametrically as $\mathbf{x} = \mathbf{x}(q)$ where the choice for q can be made later, then Equation 2.7 can be written:

$$t = \int_{q_S}^{q_R} sF \mathrm{d}q \tag{2.16}$$

where s is slowness and:

$$F = \frac{\mathrm{d}l}{\mathrm{d}q} = \sqrt{\dot{x}^2 + \dot{y}^2 + \dot{z}^2} \tag{2.17}$$

with the differentials $\dot{x}$, $\dot{y}$ and $\dot{z}$ being taken with respect to q. The calculus of variations can be employed to describe the path which extremizes t. The Euler-Lagrange equations

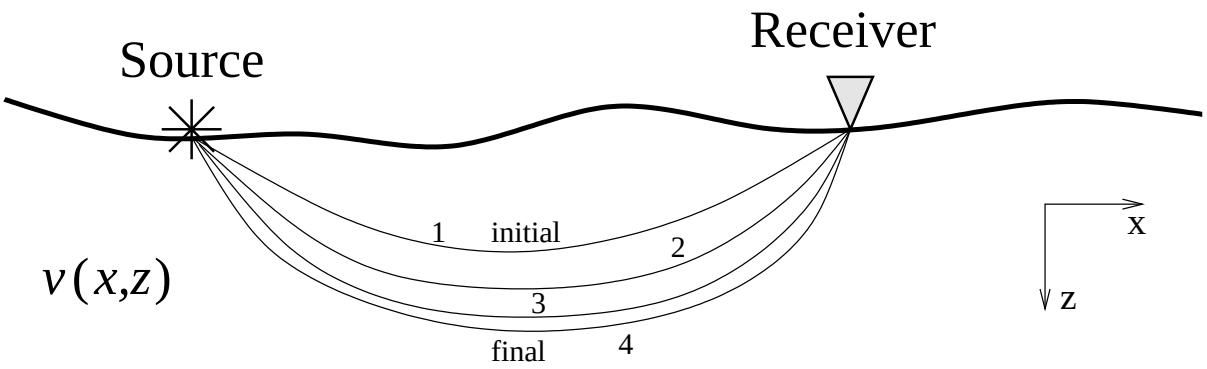

Figure 2.5: Principle of the bending method. The geometry of the initial path (ray 1) is adjusted until it satisfies Fermat's principle (ray 4).

can be written (Julian & Gubbins, 1977):

$$\left.\begin{aligned} \frac{\mathrm{d}}{\mathrm{d}q}\frac{\partial}{\partial \dot{x}}(sF) &= \frac{\partial}{\partial x}(sF) \\ \frac{\mathrm{d}}{\mathrm{d}q}\frac{\partial}{\partial \dot{y}}(sF) &= \frac{\partial}{\partial y}(sF) \\ \frac{\partial F}{\partial q} &= 0 \end{aligned}\right\} \tag{2.18}$$

where $q = l/L$: L is the total length of the source-receiver ray path and $0 \leq l \leq L$. This choice for q results in a single-valued representation of the ray. The boundary conditions are then $\mathbf{x}(0) = \mathbf{x}_S$ and $\mathbf{x}(1) = \mathbf{x}_R$ where $\mathbf{x}_S$ and $\mathbf{x}_R$ are the source and receiver coordinates respectively. These equations are non-linear and cannot be solved directly. If some initial path $\mathbf{x}^0(q)$ is chosen that passes through S and R, then an improved estimate may be given by:

$$\mathbf{x}^1(q) = \mathbf{x}^0(q) + \boldsymbol{\xi}^0(q) \tag{2.19}$$

where $\boldsymbol{\xi}^0(q)$ represents a perturbation to the initial path. If Equation 2.19 is substituted into Equation 2.18, then the resulting equations for $\boldsymbol{\xi}^0$ can be linearised and solved (see Julian & Gubbins, 1977), thus giving the improved estimate $\mathbf{x}^1$. This process can be repeated until the solutions converge.

Pereyra et al. (1980) use a similar approach to locate two-point paths in arbitrary continuous media. They also extend their method to allow for the presence of interfaces. For a medium with an arbitrary number of interfaces that separate regions of smooth velocity variation, the bending problem can be treated by considering a separate system of nonlinear differential equations in each smooth region. It is then possible to use the known discontinuity condition at each interface that is traversed by the ray to couple the

separate systems. The disadvantage here is that the order in which the interfaces are traversed needs to be known for the problem to be solved.

Um & Thurber (1987) develop a pseudo-bending technique for solving the two-point problem in continuous 3-D media. Their method is based on a perturbation scheme in which the integration step size is progressively halved. The initial guess path is defined by three points which are linearly interpolated. The centre point is then iteratively perturbed using a geometric interpretation of the ray equation until the traveltime extremum converges within a specified limit, at which point the ray equation will be approximately satisfied. The number of path segments is then doubled and the three-point perturbation scheme is repeated working from both endpoints to the middle (a total of three times for this step). The number of segments is doubled again and the procedure is repeated iteratively (see Figure 2.6), until the change in traveltime between successive iterations satisfies some convergence criterion.

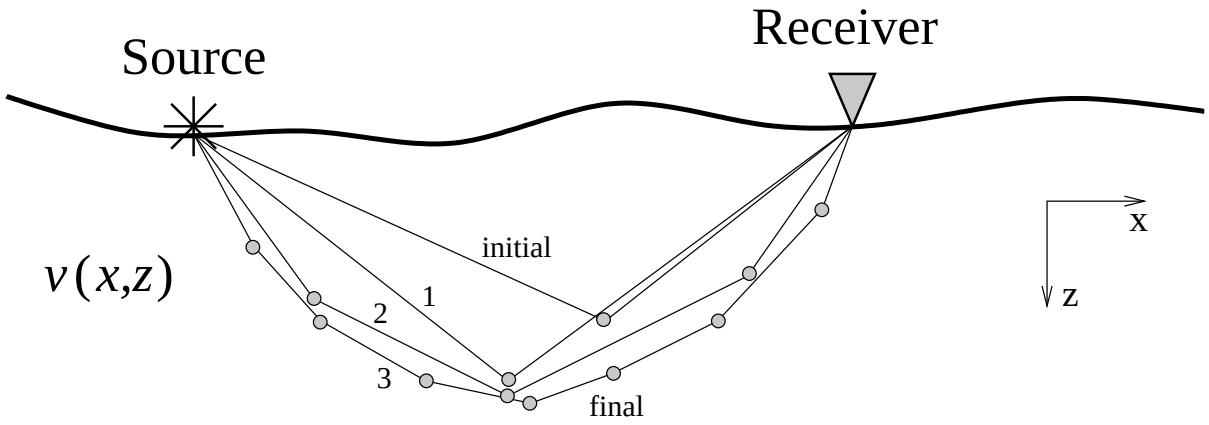

Figure 2.6: Principle of the pseudo-bending method of Um & Thurber (1987). An initial guess ray defined by three points is provided. The centre point is perturbed to best satisfy the ray equation. Then the number of segments is doubled and the process is repeated. This figure schematically represents three such iterations.

Compared to earlier bending methods, the pseudo-bending technique is much faster (Um & Thurber, 1987). Zhao et al. (1992) modify this technique to cope with interfaces as follows. Consider two points A and B close to but on either side of an interface. Straight lines connect A and B separately to a point C on the interface. The correct ray-interface intersection point is obtained by adjusting the point C using a bisection method until Snell's Law is satisfied.

Prothero et al. (1988) develop a 3-D bending method based on the simplex method of

function minimisation. The first stage of the method is to locate the minimum-time circular path between source and receiver using an exhaustive search method. Perturbations to this path, described by a sum of sine wave harmonics, are then made using the simplex method which searches for the amplitude coefficients that produce the path of least time. The method is more robust than the pseudo-bending method of Um & Thurber (1987) but is significantly slower (Prothero et al., 1988).

Bending methods of ray tracing have been used by a number of authors in studies that invert teleseismic data (Thomson & Gubbins, 1982; Zhao et al., 1994, 1996; Steck et al., 1998), but not by many in the inversion of reflection or refraction data. Chiu et al. (1986) use a bending method in the inversion of 3-D reflection traveltimes and Zhao et al. (1997) use the pseudo-bending method in the inversion of refraction traveltimes for 2-D crustal structure. In comparing their bending and shooting methods, Julian & Gubbins (1977) found that bending is computationally faster than shooting by a factor of 10 or more in media with continuous velocity variations. When discontinuities are present, however, the formulation of the bending problem becomes much more complex. In general, for smooth velocity structures that do not cause complex ray geometries, bending methods are more efficient, but when interfaces or strong velocity gradients are present, shooting methods tend to be more robust and therefore preferable (Červený, 1987; Sambridge & Kennett, 1990).

2.2.2 Wavefront Tracking

Rather than tracing rays from point to point through a medium to determine source-receiver traveltimes, an alternative is to track the propagation path of the entire wavefront. The traveltime from the source to all points in the medium is found using this approach. The most common means of wavefront tracking employs finite-difference solutions of the eikonal equation.

Vidale (1988) proposed a finite difference scheme that involved progressively integrating the traveltimes along an expanding square in 2-D. The eikonal equation (Equation 2.8) in 2-D is:

$$\left(\frac{\partial T}{\partial x}\right)^2 + \left(\frac{\partial T}{\partial z}\right)^2 = [s(x,z)]^2 \tag{2.20}$$

where $s(x,z)$ is slowness and $T(x,z)$ is the first arrival time for a seismic wave propagating from a point source. Vidale's method is formulated for a structure defined by a square

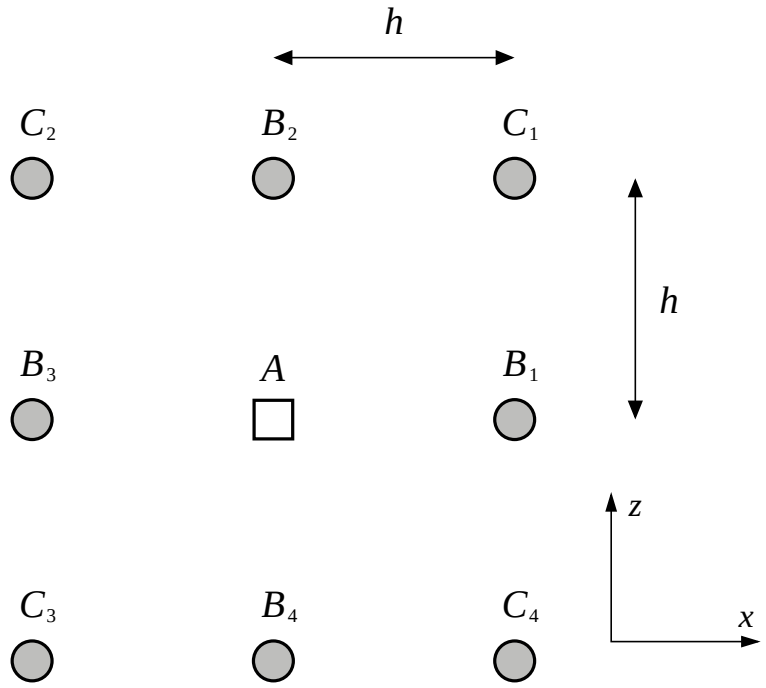

Figure 2.7: Method used by Vidale (1988) to find first-arrival traveltime field for a continuous velocity medium. See text for details.

grid of velocity nodes. Consider the grid points surrounding some local source point A in Figure 2.7. If the traveltime to point A is T_0 then the traveltime to the points B_i are given by:

$$T_{B_i} = T_0 + \frac{h}{2}(s_{B_i} + s_A) \tag{2.21}$$

where h is the node separation and s_{B_i} and s_A are the slowness at the nodes B_i and A respectively. The next step is to find the traveltime to the corner points T_{C_i}. If the top right hand group of nodes in Figure 2.7 with known traveltimes to $A(T_0)$, $B_1(T_1)$ and $B_2(T_2)$ are considered, then the traveltime to the point $C_1(T_3)$ can be determined from the eikonal equation. The two differential terms in Equation 2.20 can be approximated with finite differences:

$$\left.\begin{aligned} \frac{\partial T}{\partial x} &= \frac{1}{2h}(T_1 + T_3 - T_0 - T_2) \\ \frac{\partial T}{\partial z} &= \frac{1}{2h}(T_2 + T_3 - T_0 - T_1) \end{aligned}\right\} \tag{2.22}$$

which, when substituted into Equation 2.20, gives:

$$T_3 = T_0 + \sqrt{2(h\bar{s})^2 - (T_2 - T_1)^2} \tag{2.23}$$

where $\bar{s}$ is the average slowness of all four points under consideration. This formulation gives the traveltime to C_1 in a plane wave approximation.

The resulting scheme can be used to calculate the traveltimes to all the C_i. The traveltimes to the next set of grid points can then be determined as the scheme progresses by solving along squares of increasing size around the source point (see Figure 2.8). Solving for the traveltime to node points along a new square cannot be done in an arbitrary order; a scheme (e.g. Vidale, 1988) is required to determine the order of solution that will result in the least traveltime to each new node. Only these times will be valid seismic traveltimes. Vidale (1988) also gives another formulation that assumes locally circular wavefronts. The locally circular wavefront approximation is most accurate for strongly curved wavefronts and the locally plane wavefront approximation is most accurate for wavefronts with low curvature. Vidale (1990) extends the method to 3-D.

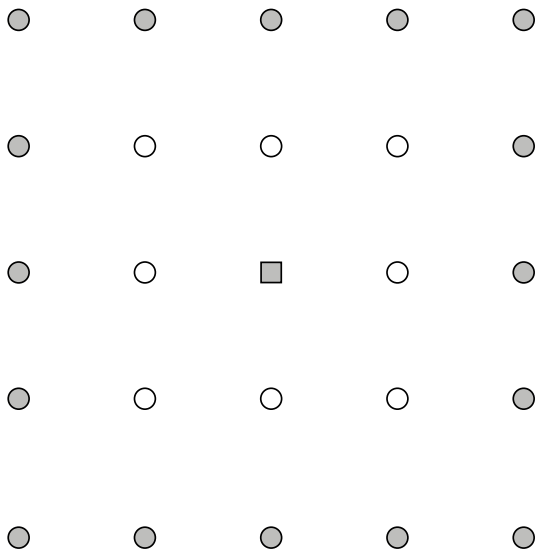

Figure 2.8: The expanding square method for determining the traveltime field. Traveltimes to the filled circles are determined from the open circles. The filled square is the source.

The problem with using an expanding square to progressively determine the traveltime field is that its geometry does not, in general, resemble the shape of the first-arrival wavefront. Consequently, the computed traveltimes may not represent first-arrivals, especially if the structure contains large velocity contrasts. Figure 2.9 illustrates a schematic example in which the traveltime from A to B is determined for path 1 by the expanding square method, but path 2 has the least traveltime by virtue of the high velocity zone. Qin et al. (1992) propose a scheme that calculates the traveltime field using an expanding wavefront method. They use the same propagator equations (Equations 2.21 and 2.23) and start by calculating the traveltimes to the eight grid points (in 2-D) about the source. Thereafter,

the point of global minimum traveltime along the perimeter of the points processed so far is used as the next source to locally expand the solution region. Using this approach, the traveltime field is determined using an expanding geometry that closely resembles the true shape of the wavefront and the possibility of computing arrivals other than first-arrivals is minimised. Where steep velocity gradients or discontinuities are encountered, however, problems can still occur as only outward propagating rays are considered.

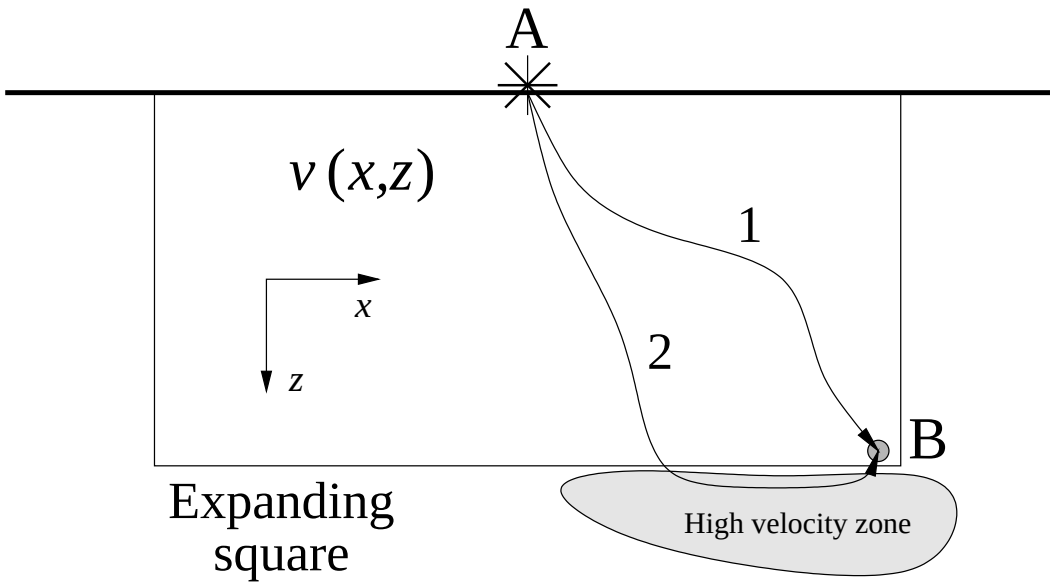

Figure 2.9: Schematic illustration showing how the expanding square method can fail. The traveltime along path 1 is determined by the expanding square but path 2 has a shorter traveltime due to the high velocity zone.

Cao & Greenhalgh (1994) also solve the eikonal equation using a finite difference scheme and a solution region defined by an expanding wavefront. They consider two different model discretisation schemes; one in which each node is placed at the centre of a cell (i.e. same as the Vidale (1988) scheme), and one in which the nodes are placed at the corner of a cell with uniform slowness. They found that the corner node discretisation provided superior solutions. Sethian & Popovici (1999) present a scheme for solving the 3-D eikonal equation based on the fast marching method (a type of upwind difference scheme) and an expanding wavefront. They claim it to be stable and the fastest of all consistent schemes for computing first-arrivals.

The presence of discontinuities such as interfaces between layers can be simulated by assigning the appropriate velocity values to the grid points that lie on either side of the interface. This means that the correct first-arrival times can be determined without

separately parameterised interfaces forming a part of the model for the forward step. However, if reflection traveltimes are sought, the method is modified. Riahi & Juhlin (1994) and Hole & Zelt (1995) both develop schemes for calculating reflection traveltimes using modifications of the Vidale (1990) method. Ray paths can be found with all finite difference methods by simply tracing backwards from the receiver through the computed traveltime field in the direction of $\nabla_{\mathbf{x}} T$ where T is the first-arrival at a given point.

A number of authors have developed schemes that draw on the basic idea of Vidale (1988); van Trier & Symes (1991) determine traveltimes on a regular grid using an upwind finite-difference method which solves a hyperbolic conservation law that describes changes in the gradient components of the traveltime field. Podvin & Lecomte (1991) employ a method that uses Huygen's principle in the finite difference approximation; Faria & Stoffa (1994) propose a scheme that explicitly uses Fermat's Principle to determine first-arrivals on a gridded traveltime field. These three methods are more suited to solution by massively parallel or vector computation than the methods of Vidale (1988) and Qin et al. (1992).

Finite difference grid methods are generally much quicker (Vidale, 1988; Sethian & Popovici, 1999) than the ray tracing methods described in Section 2.2.1. They are designed to calculate first-arrival traveltimes, they find diffraction paths in shadow zones, and they can often work in regions of complex velocity (Sethian & Popovici, 1999). Ray methods do not necessarily find the first-arrival path and often fail in shadow zones. The grid-based methods can also determine the arrivals of head-waves and diffractions that cannot be found by conventional geometric ray tracing.

Finite-difference schemes do have their disadvantages, one of the principle being algorithm stability (Sethian & Popovici, 1999). They also only locate first-arrivals, unless explicit conditions, such as reflections from an interface, are specified. While this is desirable in many cases, later arrivals can be of interest, such as in the generation of synthetic seismograms. Vinje et al. (1993) present a wavefront tracking method based on constructing a new wavefront by ray tracing from an old one. The method is robust, accurate and can find multiple arrivals. It can also be used to determine amplitude, something finite-difference methods are not good at doing. Lambaré et al. (1996) propose a method for determining multivalued traveltime and amplitude maps using a similar method of wavefront construction. Another disadvantage of grid methods is that the medium needs to be densely sampled by velocity nodes in order to achieve accurate traveltimes, with conse-

quent demands on processing power and memory. While these problems can be overcome, it is probably one reason why grid methods are not commonly used in the inversion of teleseismic traveltimes.

By contrast, finite difference solutions of the eikonal equation have been used frequently in the forward step of wide-angle traveltime inversions, especially in 3-D. Hole (1992) presents a method for the inversion of first-arrival traveltimes for 3-D velocity variation using a finite-difference approach. Hole et al. (1992) use a similar forward scheme in the inversion for interface structure using broadside refractions from the Queen Charlotte Basin, Canada. Also using finite-difference techniques, Riahi et al. (1997) invert wide-angle reflections for Moho structure beneath the Gulf of Bothnia and Zelt et al. (1996) invert both reflection and refraction traveltimes for velocity and interface structure beneath the southwestern Canadian Cordillera. Other studies to use finite difference solutions of the eikonal equation in 3-D wide-angle traveltime inversions include Zelt & Barton (1998) and Zelt et al. (1999). Parsons et al. (1996) use a finite difference approach in the inversion of wide-angle traveltimes for the 2-D crustal structure of the Colorado Plateau.

2.2.3 Shortest Path Ray Tracing (SPR)

The shortest path or network method uses Fermat's principle directly to find the path of the first-arrival ray between source and receiver. To do this, a grid of nodes is specified within the velocity medium and a network or graph is formed by connecting neighbouring nodes with traveltime path segments. The first-arrival ray path between source and receiver will then correspond to the path through the network which has the least traveltime.

In a seminal paper by Nakanishi & Yamaguchi (1986), the velocity field is defined by a set of constant velocity blocks with network nodes placed on the interface between the blocks. Connection paths between adjacent nodes do not cross any cell boundaries (see Figure 2.10a), so the traveltime t between two nodes is simply $t = ds$ where d is the distance between the two nodes and s is cell slowness. A similar approach is used by Fischer & Lees (1993). Moser (1991) uses a rectangular grid with the network nodes coinciding with the velocity nodes (see Figure 2.10b). The traveltime between two connected nodes is estimated by $t = d(s_1 + s_2)/2$ where s_1 and s_2 are the slowness at the

two nodes.

Once the network structure and method of traveltime determination between two nodes has been chosen, the next step is to use a shortest path algorithm to locate the ray path. Essentially, the problem is to locate the path of minimum traveltime from all the possible paths between source and receiver through the given network. An algorithm that is often used (after Moser, 1991) in network theory is that of Dijkstra (1959) for which computation time is proportional to the number of nodes squared.

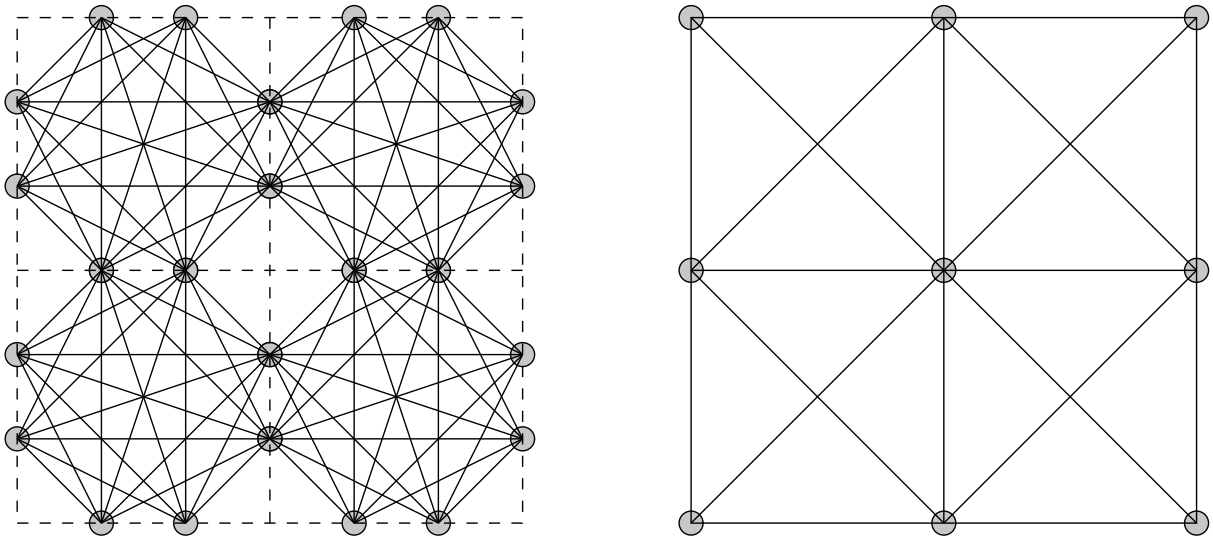

Figure 2.10: Two types of node arrangements for an SPR network (after Moser, 1991). Connectors are indicated by solid lines in both cases. (a) Network nodes along constant slowness cell boundaries (dotted). (b) Network nodes that coincide with velocity nodes.

Errors in SPR are due to the finite node spacing and angular distribution of node connectors (Moser, 1991). A coarse grid of nodes may poorly approximate the velocity variations while a limited range of angles between adjacent connectors may result in a poor approximation to the true path. Obviously, increasing the number of nodes and connectors will result in superior solutions but may come at a significant computational cost. Much work has been done to increase the computational speed of the shortest path algorithm, with particular attention given to the use of efficient sorting algorithms (Moser, 1991; Klimeš & Kvasnička, 1994; Cheng & House, 1996; Zhang & Toksöz, 1998).

SPR will by definition find the first-arrival traveltime between any given source and receiver. However, it is possible to impose constraints on the path so that other arrivals such as reflections or multiples can be determined. Moser (1991) demonstrates a method

for reflections which requires the shortest path to visit a specified set of nodes that lie on the interface.

In their original implementation of SPR, Nakanishi & Yamaguchi (1986) invert traveltimes from local earthquakes, while Zhang & Toksöz (1998) use it in the inversion of refraction traveltimes. SPR shows similar advantages to finite differences (see Section 2.2.2) relative to conventional ray tracing methods. It can find paths in shadow zones, can correctly locate diffraction paths and head waves and always finds first-arrivals. The main advantage SPR has over finite difference methods is robustness; it is capable of working in highly complex media. Cheng & House (1996) claim it to be the most robust numerical scheme for traveltime calculations, although it is generally not as fast as finite-difference methods.

2.3 Solving the Inverse Step

The inversion step, which involves the adjustment of the model parameters $\mathbf{m}$ to better satisfy the observed data $\mathbf{d}_{obs}$ through the known relationship $\mathbf{d} = \mathbf{g}(\mathbf{m})$, can be performed a number of ways. In the case of the data being traveltimes and the model parameters being velocity, the functional $\mathbf{g}$ is nonlinear because the trajectory of a ray path is dependent on the velocity structure of the medium through which it passes. Hence, inversion schemes should account for this nonlinearity unless it can be shown that its effects are not severe. The three approaches to solving the inversion step that will be considered below are backprojection, gradient methods and global optimisation techniques.

2.3.1 Backprojection

The traveltime of a seismic ray can be written as a path integral of slowness s:

$$t = \int_{L(s)} s(\mathbf{x}) \mathrm{d}l \tag{2.24}$$

where $L(s)$ is the path along which the integration is performed and $\mathbf{x}$ is the position vector. If $s(\mathbf{x}) = s_o(\mathbf{x}) + \delta s(\mathbf{x})$, then the modified path is $L_o + \delta L = L(s_o + \delta s)$ and the adjusted traveltime is:

$$t = \int_{L_o+\delta L} s_o(\mathbf{x}) \mathrm{d}l + \int_{L_o+\delta L} \delta s(\mathbf{x}) \mathrm{d}l \tag{2.25}$$

Fermat's principle can be invoked to replace $L_o + \delta L$ with L_o (see Appendix A) to give the traveltime perturbation accurate to first order:

$$\delta t = \int_{L_o} \delta s(\mathbf{x}) \mathrm{d}l + O(\delta s(\mathbf{x})^2) \tag{2.26}$$

Note that $\delta t = t - t_o$ where $t_o = \int_{L_o} s_o(\mathbf{x}) \mathrm{d}l$ is the path integral for the unperturbed medium. If a continuum is described by M constant slowness blocks, then the discrete form of Equation 2.26 for N rays can be written:

$$\mathbf{d} = \mathbf{G}\mathbf{m} \tag{2.27}$$

where $\mathbf{d}$ are the traveltime residuals, $\mathbf{m}$ the slowness perturbations and $\mathbf{G}$ an $N \times M$ matrix of ray lengths l_{ij} corresponding to the distance traversed by each ray in each m_i. Note that for the general case $\mathbf{m}$ (e.g. velocity nodes, interface depths etc.) in Equation 2.27, $\mathbf{G} = \partial \mathbf{g}/\partial \mathbf{m}$ where $\mathbf{g}(\mathbf{m})$ is the model prediction. Many of the elements of $\mathbf{G}$ will be zero since each ray path will usually only traverse a small subset of the M blocks. Backprojection methods are used to solve Equation 2.27 for the slowness perturbations $\mathbf{m}$ by iteratively mapping traveltime anomalies into slowness perturbations along the ray paths until the data are satisfied. Backprojection methods generally use constant slowness (or velocity) blocks in which case $\mathbf{G} = \partial \mathbf{g}/\partial \mathbf{m} = [l_{ij}]$. Two of the basic backprojection techniques for solving equations of the form of Equation 2.27 are ART and SIRT which both owe their origins to the CT (Computerised Tomography) methods used in medical imaging.

In ART (Algebraic Reconstruction Technique), the model is updated on a ray by ray basis. The residual d_n for the n^{th} ray path is distributed along the ray path by adjusting each component of $\mathbf{m}$ in proportion to the length of the corresponding $\{l_{nj}\}$:

$$m_j^{k+1} = m_j^k + \frac{t_n^{k+1} l_{nj}}{\sum_{m=1}^{M} l_{nm}^2} \tag{2.28}$$

where $t_n^{k+1} = d_n - t_n^k$ is the difference between the initial residual and the residual at the k^{th} iteration, m_j^k is the approximation to the j^{th} model parameter at the k^{th} iteration, $m_j^1 = 0$ and $t_n^1 = 0$. The residual along the $(n+1)^{th}$ ray is then determined for the updated $\mathbf{m}$ along its original path and is projected back down its path in the same manner as done for the n^{th} ray. A single iteration of the method consists of performing this backprojection for the N ray paths. The main problem with ART is that it suffers from poor convergence properties

(Blundell, 1993). It has been used by McMechan (1983) in cross-hole tomography and Nakanishi & Yamaguchi (1986) in local earthquake tomography.

SIRT (simultaneous Iterative Reconstruction Technique) addresses some of the convergence problems associated with ART by averaging the perturbations applied to each parameter from all the rays that are influenced by the parameter. Thus, the SIRT algorithm may be written (Blundell, 1993):

$$m_j^{k+1} = m_j^k + \frac{1}{R_j^k} \sum_{i=1}^{R_j^k} \left[\frac{t_n^{k+1} l_{nj}}{\sum_{m=1}^{M} l_{nm}^2} \right] \tag{2.29}$$

where R_j^k is the number of rays that the j^{th} model parameter influences for the k^{th} iteration. The SIRT method has been used in the inversion of teleseismic traveltime residuals by Dueker et al. (1993), Granet & Trampert (1989) and McQueen & Lambeck (1996). Blundell (1993) used SIRT (as well as other methods) in the inversion of reflection traveltimes for both velocity structure and interface depth.

Other authors who have used variants of the basic backprojection routines include Humphreys & Clayton (1990), Hole (1992) and Zelt & Barton (1998). Humphreys & Clayton (1990) use block subbinning, filtering and spatial averaging in the backprojected inversion of teleseismic traveltimes. Block subbinning is used to reduce the weight of rays that come from dominant directions, and thus reduces blurring of the image along these paths. Filtering is done using point spread functions to reduce blurring produced by backprojection, and spatial averaging is used to smooth the solution. Hole (1992) also uses smoothing in the backprojected inversion of wide-angle traveltimes. Zelt & Barton (1998), in their 3-D wide-angle seismic inversion method, implement several other modifications aimed at improving the convergence and accuracy of backprojection.

2.3.2 Gradient Methods

The inverse problem in seismic tomography can be formulated as an optimisation problem in which an objective function that consists of a data residual term and one or more regularisation terms is minimised. As before, let $\mathbf{d}$ denote a data vector of length N which is dependent on a model vector $\mathbf{m}$ of length M as $\mathbf{d} = \mathbf{g}(\mathbf{m})$. For an initial estimate $\mathbf{m}_0$ of the model parameters, comparing $\mathbf{d} = \mathbf{g}(\mathbf{m}_0)$ with the observed traveltimes $\mathbf{d}_{obs}$ gives an indication of the accuracy of the model. The misfit can be quantified by constructing

an objective function $S(\mathbf{m})$ that is to be minimised.

An essential component of the objective function is a term $\Psi(\mathbf{m})$ which measures the difference between the observed and predicted data. If it is assumed that the error in the relationship $\mathbf{d}_{obs} \approx \mathbf{g}(\mathbf{m}_{true})$ is Gaussian, then a least squares or L_2 measure of this difference is applicable:

$$\Psi(\mathbf{m}) = \|\mathbf{g}(\mathbf{m}) - \mathbf{d}_{obs}\|^2 \tag{2.30}$$

If uncertainty estimates have been made for the observed data, then more accurate data is given a greater weight in the objective function by writing $\Psi(\mathbf{m})$ as:

$$\Psi(\mathbf{m}) = (\mathbf{g}(\mathbf{m}) - \mathbf{d}_{obs})^T \mathbf{C}_d^{-1} (\mathbf{g}(\mathbf{m}) - \mathbf{d}_{obs}) \tag{2.31}$$

where $\mathbf{C}_d$ is a data covariance matrix. If the errors are assumed to be uncorrelated, then $\mathbf{C}_d = [\delta_{ij}(\sigma_d^j)^2]$ where σ_d^j is the uncertainty of the j^{th} traveltime.

A common problem with tomographic inversion is that not all model parameters will be well constrained by the data alone (i.e. the problem may be underdetermined). A regularisation term $\Phi(\mathbf{m})$ is often included in the objective function to provide additional constraints on the model parameters, thereby reducing the non-uniqueness of the solution. The regularisation term is typically defined by:

$$\Phi(\mathbf{m}) = (\mathbf{m} - \mathbf{m}_0)^T \mathbf{C}_m^{-1} (\mathbf{m} - \mathbf{m}_0) \tag{2.32}$$

where $\mathbf{C}_m$ is an *a priori* model covariance matrix. If uncertainties in the initial model are assumed to be uncorrelated, then $\mathbf{C}_m = [\delta_{ij}(\sigma_m^j)^2]$ where σ_m^j is the uncertainty associated with the j^{th} model parameter of the initial model. The effect of this term is to favour solution models $\mathbf{m}$ that are near a reference model $\mathbf{m}_0$.

Another approach to regularisation is the minimum structure solution (Sambridge, 1990) which attempts to find an acceptable trade-off between satisfying the data and finding a model with the minimum amount of structural variation. One way of including this requirement in the objective function is to use the term (Blundell, 1993):

$$\Omega(\mathbf{m}) = \mathbf{m}^T \mathbf{D}_n^T \mathbf{D}_n \mathbf{m} \tag{2.33}$$

where $\mathbf{D}_n\mathbf{m}$ is a finite difference estimate of the n^{th} spatial derivative. When $n = 1$, the aim is to minimise gradients and when $n = 2$, the aim is to minimise curvature (i.e. smoothing). Using the L_2 terms described above in Equations 2.31 - 2.33, the objective function $S(\mathbf{m})$ can be written in full as:

$$S(\mathbf{m}) = \Psi(\mathbf{m}) + \epsilon\Phi(\mathbf{m}) + \eta\Omega(\mathbf{m}) \tag{2.34}$$

where ϵ is referred to as the *damping factor* and η as the *smoothing factor* (when $n = 2$ in Equation 2.33). These factors govern the trade-off between how well the solution $\mathbf{m}_{est}$ will satisfy the data, how closely $\mathbf{m}_{est}$ is to $\mathbf{m}_0$, and the smoothness of $\mathbf{m}_{est}$.

In the following description of methods for minimising an objective function, I will use the form of $S(\mathbf{m})$ in which the smoothing factor η is zero:

$$S(\mathbf{m}) = (\mathbf{g}(\mathbf{m}) - \mathbf{d}_{obs})^T \mathbf{C}_d^{-1} (\mathbf{g}(\mathbf{m}) - \mathbf{d}_{obs}) + \epsilon (\mathbf{m} - \mathbf{m}_0)^T \mathbf{C}_m^{-1} (\mathbf{m} - \mathbf{m}_0) \tag{2.35}$$

This is the most commonly used form of objective function and is the one that I use for inverting wide-angle traveltimes (see Chapter 4). Amendments required to incorporate a smoothing term are straightforward.

Gradient-based inversion methods use a knowledge of the derivatives of $S(\mathbf{m})$ at a specified point in model space. A basic assumption that is shared by all practical gradient methods is that $S(\mathbf{m})$ is sufficiently smooth to validate a locally quadratic approximation about some current model:

$$S(\mathbf{m} + \delta\mathbf{m}) \approx S(\mathbf{m}) + \hat{\boldsymbol{\gamma}} \delta\mathbf{m} + \tfrac{1}{2} \delta\mathbf{m}^T \hat{\mathbf{H}} \delta\mathbf{m} \tag{2.36}$$

where $\delta\mathbf{m}$ is a perturbation to the current model and $\hat{\boldsymbol{\gamma}} = \partial S / \partial \mathbf{m}$ and $\hat{\mathbf{H}} = \partial^2 S / \partial \mathbf{m}^2$ are the gradient vector and Hessian matrix respectively. Evaluating these partial derivatives (e.g. Tarantola, 1987) gives:

$$\hat{\boldsymbol{\gamma}} = \mathbf{G}^T \mathbf{C}_d^{-1} [\mathbf{g}(\mathbf{m}) - \mathbf{d}_{obs}] + \epsilon \mathbf{C}_m^{-1} (\mathbf{m} - \mathbf{m}_0) \tag{2.37}$$

$$\hat{\mathbf{H}} = \mathbf{G}^T \mathbf{C}_d^{-1} \mathbf{G} + \nabla_{\mathbf{m}} \mathbf{G}^T \mathbf{C}_d^{-1} [\mathbf{g}(\mathbf{m}) - \mathbf{d}_{obs}] + \epsilon \mathbf{C}_m^{-1} \tag{2.38}$$

where $\mathbf{G} = \partial \mathbf{g} / \partial \mathbf{m}$ is the Fréchet matrix of partial derivatives calculated during the solution of the forward problem. For the case of constant slowness blocks, $\mathbf{G} = [l_{ij}]$ where l_{ij} is the ray segment length of the i^{th} ray in the j^{th} block. Usually, the second derivative term in $\hat{\mathbf{H}}$ is neglected since it is time consuming to evaluate, and its effect is small if $\mathbf{g}(\mathbf{m}) - \mathbf{d}_{obs}$ is small or if the forward problem is quasi-linear ($\nabla_{\mathbf{m}} \mathbf{G} \approx 0$). Both $\hat{\boldsymbol{\gamma}}$ and $\hat{\mathbf{H}}$ do not lie in model space, but in the dual of model space (Tarantola, 1987). If $\boldsymbol{\gamma}$ is the steepest ascent vector in model space then $\boldsymbol{\gamma} = \mathbf{C}_m \hat{\boldsymbol{\gamma}}$ and $\mathbf{H}$, the curvature operator in model space, is $\mathbf{H} = \mathbf{C}_m \hat{\mathbf{H}}$.

Since $\mathbf{g}$ is generally non-linear, the minimisation of Equation 2.35 requires an iterative approach:

$$\mathbf{m}_{n+1} = \mathbf{m}_n + \delta\mathbf{m}_n \tag{2.39}$$

where $\mathbf{m_0}$ is the initial model. The objective function is minimised for the current ray path estimate at each step to produce $\mathbf{m}_{n+1}$, after which new ray paths are computed for the next iteration. The iterations cease either when the observed traveltimes are satisfied or when the change in $S(\mathbf{m})$ with iteration gets sufficiently small. The following gradient-based inversion methods are used to determine $\delta\mathbf{m}_n$.

Gauss-Newton method and damped-least squares

The Gauss-Newton method locates the updated point $\mathbf{m}_{n+1}$ by locating the minimum of the tangent paraboloid to $S(\mathbf{m})$ at $\mathbf{m}_n$. At the minimum of S, the gradient will vanish, so $\mathbf{m}$ is required such that:

$$\mathbf{F}(\mathbf{m}) = \mathbf{G}^T\mathbf{C}_d^{-1}(\mathbf{g}(\mathbf{m}) - \mathbf{d}_{obs}) + \epsilon\mathbf{C}_m^{-1}(\mathbf{m} - \mathbf{m}_0) = 0 \tag{2.40}$$

where $\mathbf{F}(\mathbf{m}) = \hat{\boldsymbol{\gamma}}$. If we are at some point $\mathbf{m}_n$, then a more accurate estimate $\mathbf{m}_{n+1}$ can be obtained using a Taylor series expansion of Equation 2.40 and ignoring second order terms:

$$F_i(m_{n+1}^1, \ldots, m_{n+1}^M) = F_i(m_n^1, \ldots, m_n^M) + \sum_{j=1}^{M}(m_{n+1}^j - m_n^j)\left.\frac{\partial F_i}{\partial m^j}\right|_{\mathbf{m}_n} = 0 \tag{2.41}$$

which may be rewritten as:

$$\mathbf{m}_{n+1} = \mathbf{m}_n - \left[\frac{\partial\mathbf{F}}{\partial\mathbf{m}}\right]_n^{-1}[\mathbf{F}_n] = \mathbf{m}_n - \left[\frac{\partial^2 S}{\partial\mathbf{m}^2}\right]_n^{-1}\left[\frac{\partial S}{\partial\mathbf{m}}\right]_n \tag{2.42}$$

where $(\partial S/\partial\mathbf{m})_n$ is the gradient vector and $(\partial^2 S/\partial\mathbf{m}^2)_n$ is the Hessian matrix. Substituting Equation 2.37 and Equation 2.38 into Equation 2.42 gives the Gauss-Newton solution:

$$\begin{aligned}\delta\mathbf{m}_n &= -[\mathbf{G}_n^T\mathbf{C}_d^{-1}\mathbf{G}_n + \nabla_{\mathbf{m}}\mathbf{G}_n^T\mathbf{C}_d^{-1}(\mathbf{g}(\mathbf{m}_n) - \mathbf{d}_{obs}) + \epsilon\mathbf{C}_m^{-1}]^{-1} \\ &\quad \times[\mathbf{G}_n^T\mathbf{C}_d^{-1}[\mathbf{g}(\mathbf{m}_n) - \mathbf{d}_{obs}] + \epsilon\mathbf{C}_m^{-1}(\mathbf{m}_n - \mathbf{m}_0)]\end{aligned} \tag{2.43}$$

As mentioned earlier, the second derivative term in the Hessian matrix is usually ignored, which gives the quasi-Newton solution:

$$\delta\mathbf{m}_n = -[\mathbf{G}_n^T\mathbf{C}_d^{-1}\mathbf{G}_n + \epsilon\mathbf{C}_m^{-1}]^{-1}[\mathbf{G}_n^T\mathbf{C}_d^{-1}[\mathbf{g}(\mathbf{m}_n) - \mathbf{d}_{obs}] + \epsilon\mathbf{C}_m^{-1}(\mathbf{m}_n - \mathbf{m}_0)] \tag{2.44}$$

Straightforward implementation of this method requires an $M \times M$ matrix equation to be solved. If the number of model parameters is large, the solution will be computationally expensive, and if data coverage is poor, the problem may well be ill-conditioned.

Assuming that the relationship $\mathbf{d} = \mathbf{g}(\mathbf{m})$ is linearisable then (c.f. Equation 2.27):

$$\mathbf{d}_{obs} \approx \mathbf{g}(\mathbf{m}_0) + \mathbf{G}(\mathbf{m} - \mathbf{m}_0) \tag{2.45}$$

or $\delta\mathbf{d} = \mathbf{G}\delta\mathbf{m}$ with $\delta\mathbf{d} = \mathbf{d}_{obs} - \mathbf{g}(\mathbf{m}_0)$ and $\delta\mathbf{m} = \mathbf{m} - \mathbf{m}_0$ (i.e. Equation 2.27 with $\mathbf{G} = \partial\mathbf{g}/\partial\mathbf{m}$). If Equation 2.45 is exactly linear, then the Newton and quasi-Newton solutions are the same because the second derivative terms in the Hessian matrix are zero. Because a one-step solution is possible in the linear case, the objective function may be simplified:

$$S(\mathbf{m}) = (\mathbf{G}\delta\mathbf{m} - \delta\mathbf{d})^T\mathbf{C}_d^{-1}(\mathbf{G}\delta\mathbf{m} - \delta\mathbf{d}) + \epsilon\delta\mathbf{m}^T\mathbf{C}_m^{-1}\delta\mathbf{m} \tag{2.46}$$

in which case the functional (c.f. Equation 2.40) is:

$$\mathbf{F}(\mathbf{m}) = \mathbf{G}^T\mathbf{C}_d^{-1}(\mathbf{G}\delta\mathbf{m} - \delta\mathbf{d}) + \epsilon\mathbf{C}_m^{-1}\delta\mathbf{m} = 0 \tag{2.47}$$

and the solution can be written as:

$$\delta\mathbf{m} = [\mathbf{G}^T\mathbf{C}_d^{-1}\mathbf{G} + \epsilon\mathbf{C}_m^{-1}]^{-1}\mathbf{G}^T\mathbf{C}_d^{-1}\delta\mathbf{d} \tag{2.48}$$

which is known as the *damped least-squares* (DLS) solution to the inverse problem or the *stochastic inverse* (Aki et al., 1977).

For the non-linear problem, the DLS solution (Equation 2.48) differs from the quasi-Newton solution (Equation 2.44) only in its use of the regularisation term. In the latter, the term $\mathbf{m}_0$ usually represents the initial or starting model and the effect of the regularisation is to favour a solution near the initial model (how "near" will depend on the value of ϵ). If, however, $\mathbf{m}_0 = \mathbf{m}_{prior}$, where $\mathbf{m}_{prior}$ is the solution at the previous iteration, then the quasi-Newton solution reduces to the DLS solution, and the effect of the regularisation is to favour a solution near the solution from the previous iteration. The DLS solution (Equation 2.48), along with its variants, is the technique most commonly used to solve the inverse step in seismic tomography.

Studies that have used the DLS solution to the inverse problem in teleseismic tomography include those by Aki et al. (1977), Zhao et al. (1994), Weiland et al. (1995), Wiggins et al. (1996) and Steck et al. (1998). Authors who have used DLS solutions to invert wide-angle traveltimes include Kanasewich & Chiu (1985), Chiu et al. (1986), Farra & Madariaga (1988), White (1989), Lutter & Nowack (1990), Lutter et al. (1990), Zelt & Smith (1992), Lutter et al. (1994), Kosloff et al. (1996), Wang & Braile (1996),

McCaughey & Singh (1997) and Zelt & Barton (1998). The basic DLS solution (Equation 2.48) is sometimes modified to allow for additional terms in the objective function. For example, Wang & Braile (1996) modify Equation 2.48 by including a smoothing term.

The most computationally expensive part of the Newton or DLS solution is to solve a matrix equation of order M. If the number of parameters is small, then the solution may be found using methods like LU decomposition (Press et al., 1992) or Cholesky decomposition (Tarantola, 1987). For models defined by large numbers of parameters, direct solution methods are cumbersome and iterative techniques are more practical. One such method is the conjugate gradient method of Hestenes & Stiefel (1952), which is able to take advantage of the sparse nature of linear systems commonly associated with seismic tomography problems (Scales, 1987). Conjugate gradients and LSQR, a variant of the conjugate gradient algorithm, are probably the most commonly used methods for solving linear systems of the form of Equation 2.48 with a large number (e.g. 1000's - 100,000's) of unknowns (Nolet, 1985; Scales, 1987; VanDecar & Snieder, 1994).

Steepest descent

The method of steepest descent is probably the simplest gradient-based method for iterative minimisation of an objective function. It is based on the idea that the objective function S may be minimised by successive searches along local directions of steepest descent. If $\boldsymbol{\gamma}_n$ is the direction of steepest ascent in model space at a point $\mathbf{m}_n$, the model correction is given by:

$$\delta\mathbf{m}_n = -\mu_n\boldsymbol{\gamma}_n \tag{2.49}$$

where the scalar μ_n is a positive real number whose value locates the minimum in the direction specified by $\boldsymbol{\gamma}_n$. The parameter μ_n can be found by line minimisation as follows. By assuming that $\mathbf{g}(\mathbf{m})$ is locally linear, so that $\mathbf{g}(\mathbf{m}_{n+1}) = \mathbf{g}(\mathbf{m}_n)+\mathbf{G}_n(\mathbf{m}_{n+1}-\mathbf{m}_n)$, then $S(\mathbf{m})$ is quadratic so $\partial S(\mathbf{m})/\partial\mu_n = 0$ will give the value of μ_n. Substituting Equation 2.49 into Equation 2.36 gives:

$$S(\mathbf{m}_n - \mu_n\boldsymbol{\gamma}_n) = S(\mathbf{m}_n) - \mu_n\hat{\boldsymbol{\gamma}}_n^T\boldsymbol{\gamma}_n + \tfrac{1}{2}\mu_n^2\boldsymbol{\gamma}_n^T\hat{\mathbf{H}}_n\boldsymbol{\gamma}_n \tag{2.50}$$

The partial derivative of Equation 2.50 is:

$$\frac{\partial S(\mathbf{m}_n - \mu_n\boldsymbol{\gamma}_n)}{\partial\mu_n} = -\hat{\boldsymbol{\gamma}}_n^T\boldsymbol{\gamma}_n + \mu_n\boldsymbol{\gamma}_n^T\hat{\mathbf{H}}_n\boldsymbol{\gamma}_n = 0 \tag{2.51}$$

which can be rearranged to give:

$$\mu_n = \frac{\hat{\boldsymbol{\gamma}}_n^T \boldsymbol{\gamma}_n}{\boldsymbol{\gamma}_n^T \hat{\mathbf{H}}_n \boldsymbol{\gamma}_n} \tag{2.52}$$

An iterative line search could also be implemented to determine μ_n, but this may require numerous calculations of the forward step. The efficiency of the steepest descent method depends on the character of $S(\mathbf{m})$, but usually it is slow because the local direction of steepest descent may differ greatly from the direction in which the minimum is to be found. Figure 2.11 schematically illustrates how the steepest descent method may be inefficient. Blundell (1993) investigates the properties of the steepest descent method in the context of inverting reflection traveltimes for velocity and interface depth but the method has not been widely used in seismic tomography.

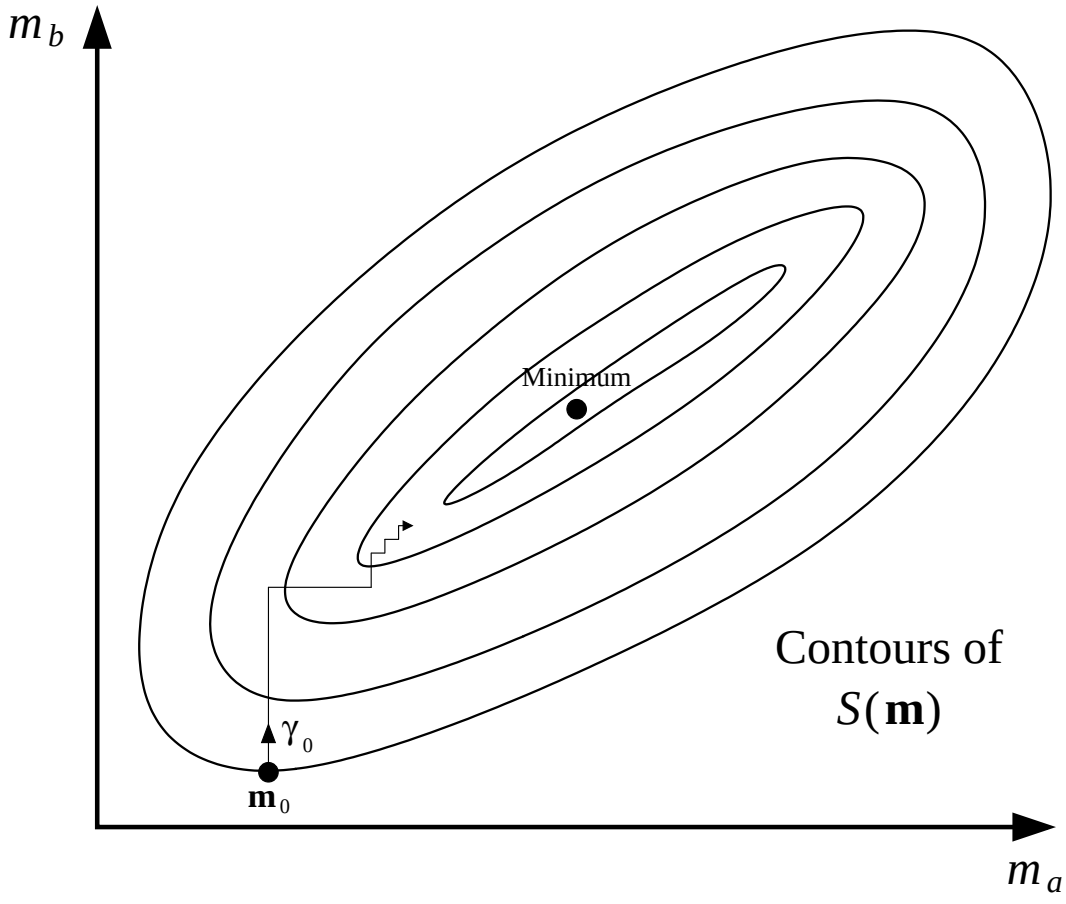

Figure 2.11: Illustration of the method of steepest descent in 2-D model space. The method can be inefficient in locating the solution if the local direction of steepest descent is oblique to the direction in which the minimum is to be found.

Conjugate gradients

Hestenes & Stiefel (1952) first suggested the idea of conjugate gradient methods in regard to solving systems of linear equations. Fletcher & Reeves (1964) subsequently applied it to unconstrained optimisation. At each iteration, the conjugate gradient method uses a new search direction that is conjugate to all the previous ones (assuming $S(\mathbf{m})$ is quadratic). In other words, the n^{th} iteration of the conjugate gradient method locates the minimum in an n-dimensional subspace spanned by the current steepest descent vector and the $n-1$ previous search directions. The algorithm may be defined by (see Tarantola, 1987):

$$\boldsymbol{\phi}_n = \boldsymbol{\gamma}_n + \alpha_n \boldsymbol{\phi}_{n-1} \tag{2.53}$$

$$\delta \mathbf{m}_n = -\mu_n \boldsymbol{\phi}_n \tag{2.54}$$

where $\{\boldsymbol{\phi}_n\}$ is a set of conjugate directions and $\boldsymbol{\phi}_0 = \boldsymbol{\gamma}_0$. The scalar μ_n can be determined by Equation 2.52 (using $\boldsymbol{\phi}_n$ in place of $\boldsymbol{\gamma}_n$) and α_n is defined so that the new search direction is conjugate to the previous search directions (see Press et al., 1992):

$$\alpha_n = \frac{\boldsymbol{\gamma}_n^T \hat{\boldsymbol{\gamma}}_n}{\boldsymbol{\gamma}_{n-1}^T \hat{\boldsymbol{\gamma}}_{n-1}} \tag{2.55}$$

or

$$\alpha_n = \frac{\boldsymbol{\gamma}_n^T \hat{\boldsymbol{\gamma}}_n - \boldsymbol{\gamma}_n^T \hat{\boldsymbol{\gamma}}_{n-1}}{\boldsymbol{\gamma}_{n-1}^T \hat{\boldsymbol{\gamma}}_{n-1}} \tag{2.56}$$

Equation 2.55 is the Fletcher-Reeves variant and Equation 2.56 is the Polak-Ribiere variant. This second formulation sometimes gives superior results when $S(\mathbf{m})$ is non-quadratic (Tarantola, 1987). In the context of seismic inversion, the conjugate gradient method has been used by Rawlinson & Houseman (1998) in teleseismic traveltime tomography and by Blundell (1993) in the inversion of reflection traveltimes.

The principle advantage that both the steepest descent and conjugate gradient method have over the Newton and DLS methods is that a large system of potentially ill-conditioned linear equations does not need to be solved. Consequently, these methods are much more rapid at the inverse step. However, since they only minimise in one dimension at each iteration, they tend to converge more slowly. If the procedure for solving the forward step is fast compared to solving the $M \times M$ matrix equation, then steepest descent or conjugate gradients may be preferable. However, if the forward step is slow compared to solving the matrix inverse, then a Newton or DLS approach may be quicker.

Subspace method

Both the steepest descent method and conjugate gradient method are examples of 1-D subspace methods in that they perform a line minimisation at each iteration. In general, however, subspace methods may be constructed in which the minimisation is carried out simultaneously along several search directions that together span a subspace of the model space. The basic theory for the general subspace inversion method is presented here; more details can be found in Kennett et al. (1988), Sambridge (1990) and Williamson (1990).

At each iteration, the subspace method restricts the minimisation of the quadratic approximation of $S(\mathbf{m})$ to an n-dimensional subspace of model space, so that the perturbation $\delta\mathbf{m}$ (ignoring the iteration subscript n in $\delta\mathbf{m}_n$ for convenience) occurs in the space spanned by a set of n M-dimensional basis vectors $\{\mathbf{a}^j\}$:

$$\delta\mathbf{m} = \sum_{j=1}^{n} \mu_j \mathbf{a}^j = \mathbf{A}\boldsymbol{\mu} \tag{2.57}$$

where $\mathbf{A} = [\mathbf{a}^j]$ is the $M \times n$ projection matrix. The component μ_j determines the length of the corresponding vector $\mathbf{a}^j$ that minimises the quadratic form of $S(\mathbf{m})$ in the space spanned by $\mathbf{a}^j$. Hence, $\boldsymbol{\mu}$ is found by substituting Equation 2.57 into Equation 2.36, which gives in summation form:

$$S(\mathbf{m}+\delta\mathbf{m}) = S(\mathbf{m}) + \sum_{j=1}^{n} \mu_j \hat{\boldsymbol{\gamma}}^T \mathbf{a}^j + \tfrac{1}{2} \sum_{j=1}^{n}\sum_{k=1}^{n} \mu_j \mu_k [\mathbf{a}^k]^T \hat{\mathbf{H}} [\mathbf{a}^j] \tag{2.58}$$

and locating the minimum of S with respect to $\boldsymbol{\mu}$:

$$\frac{\partial S(\mathbf{m})}{\partial \mu_q} = \hat{\boldsymbol{\gamma}}^T \mathbf{a}^q + \sum_{k=1}^{n} \mu_k [\mathbf{a}^k]^T \hat{\mathbf{H}} [\mathbf{a}^j] = 0 \tag{2.59}$$

for $q = 1, \ldots, n$. Rearranging Equation 2.59 for $\boldsymbol{\mu}$ gives:

$$\boldsymbol{\mu} = -[\mathbf{A}^T \hat{\mathbf{H}} \mathbf{A}]^{-1} \mathbf{A}^T \hat{\boldsymbol{\gamma}} \tag{2.60}$$

and since $\delta\mathbf{m} = \mathbf{A}\boldsymbol{\mu}$, the solution, taking $\hat{\mathbf{H}} = \mathbf{G}^T \mathbf{C}_d^{-1} \mathbf{G} + \epsilon \mathbf{C}_m^{-1}$, is:

$$\delta\mathbf{m} = -\mathbf{A}[\mathbf{A}^T (\mathbf{G}^T \mathbf{C}_d^{-1} \mathbf{G} + \epsilon \mathbf{C}_m^{-1}) \mathbf{A}]^{-1} \mathbf{A}^T \hat{\boldsymbol{\gamma}} \tag{2.61}$$

which can be used iteratively in the manner specified by Equation 2.39. The quantities $\mathbf{A}$, $\hat{\boldsymbol{\gamma}}$ and $\mathbf{G}$ are re-evaluated between successive iterations. Most implementations of the subspace method construct the basis vectors $\{\mathbf{a}^j\}$ in terms of the steepest ascent vector

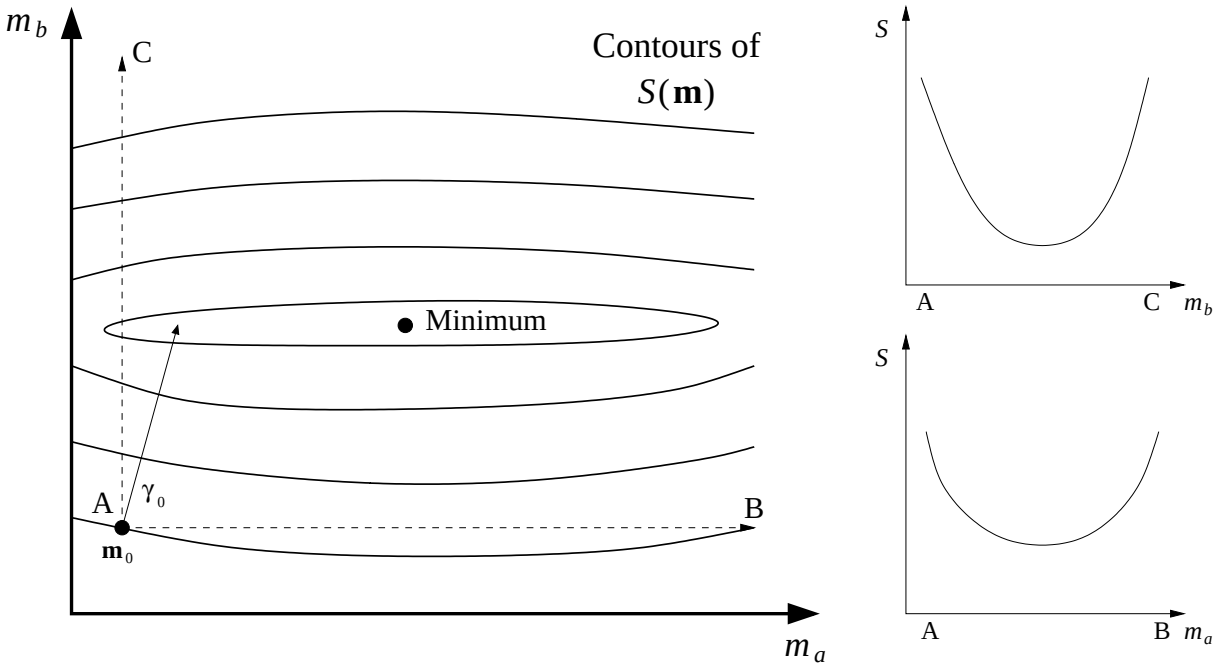

Figure 2.12: A contour plot of $S(\mathbf{m})$ which is a function of two parameters of different physical dimensions. $S(\mathbf{m})$ is much more sensitive to m_b than m_a, and a gradient method like steepest descents will converge slowly. Searching in directions specified by basis vectors (dotted lines) that only lie in space defined by a single parameter class eliminates these problems, since $S(\mathbf{m})$ is a function of only one parameter class in each of these directions.

in model space $\boldsymbol{\gamma}$ and its rates of change (e.g. Kennett et al., 1988; Sambridge, 1990; Williamson, 1990; Blundell, 1993).

The subspace method has several desirable characteristics. First, the determination of $\delta\mathbf{m}$ only requires the solution of a relatively small $n \times n$ system of linear equations - Williamson (1990) uses $n = 6$ and Blundell (1993) uses $n \leq 8$. Second, it offers a natural way of dealing with multiple parameter classes. If the basis vectors $\{\mathbf{a}^j\}$ are chosen such that each vector only lies in the space spanned by a particular parameter class, then the minimisation will account for the different sensitivities of $S(\mathbf{m})$ with respect to the different parameter classes in a balanced way (see Figure 2.12). Other gradient methods in which parameters of different physical dimensions are mixed can exhibit slow convergence and a strong dependence on relative scaling of the different parameter types (Kennett et al., 1988).

Subspace methods have been applied to the inversion of reflection traveltimes for velocity and interface structure (Williamson, 1990; Blundell, 1993), to the inversion of local earthquake and artificial source traveltimes for velocity, interface structure and hypocenter location (Sambridge, 1990) and to the inversion of reflection amplitude data for interface

structure (Wang & Houseman, 1994) and velocity (Wang & Houseman, 1995).

Fréchet matrix

All gradient methods require the calculation of the Fréchet matrix $\mathbf{G} = \partial\mathbf{g}/\partial\mathbf{m}$, which describes the rate of change of every traveltime with respect to every model parameter. This calculation is usually done during the forward step of the tomographic problem. The two basic parameter types that are normally encountered in traveltime inversion, especially of wide-angle data, are velocity (or slowness) and interface depth. First-order accurate expressions for the Fréchet derivatives can be derived quite simply for both cases.

Equation 2.26 describes the linearised relationship between traveltime residual and slowness perturbation. The equivalent expression (see Appendix A) for velocity $v(\mathbf{x})$ is:

$$\delta t = -\int_{L(v_o)} \frac{\delta v}{v_o^2} \mathrm{d}l \tag{2.62}$$

where δv is the velocity perturbation and v_o is the reference velocity field. If the velocity field is defined by a grid of velocity nodes, then the first-order accurate Fréchet derivatives are given by:

$$\frac{\partial t}{\partial v_n} = -\int_{L(v_o)} v_o^{-2} \frac{\partial v}{\partial v_n} \mathrm{d}l \tag{2.63}$$

where v_n is the velocity of a particular node and $\partial v/\partial v_n$ is the change of velocity along the ray with respect to a change in v_n. This expression is usually straightforward to calculate if the velocity interpolation function $v = f(v_n)$ has a simple form (e.g. cubic B-splines). Fréchet derivatives have been calculated using Equation 2.63 (or its equivalent for slowness) by most authors who use gradient methods and models parameterised by a grid of velocity nodes (e.g. White, 1989; Lutter et al., 1990; Sambridge, 1990).

First-order accurate analytic expressions can also be obtained for the Fréchet derivatives when the model parameters describe interface depth. The basic approach is to partition the problem:

$$\frac{\partial t}{\partial z_n} = \frac{\mathrm{d}t}{\mathrm{d}h_{int}} \frac{\mathrm{d}h_{int}}{\mathrm{d}z_{int}} \frac{\partial z_{int}}{\partial z_n} \tag{2.64}$$

where z_n is the depth coordinate of the interface node, h_{int} is displacement normal to the interface at the point of intersection by the ray and z_{int} is the depth coordinate of the intersection point. The two total derivatives in Equation 2.64 can be worked out analytically to first-order accuracy by assuming a locally linear wavefront and interface. (e.g. Bishop et al., 1985; Nowack & Lyslo, 1989; White, 1989; Sambridge, 1990; Zelt &

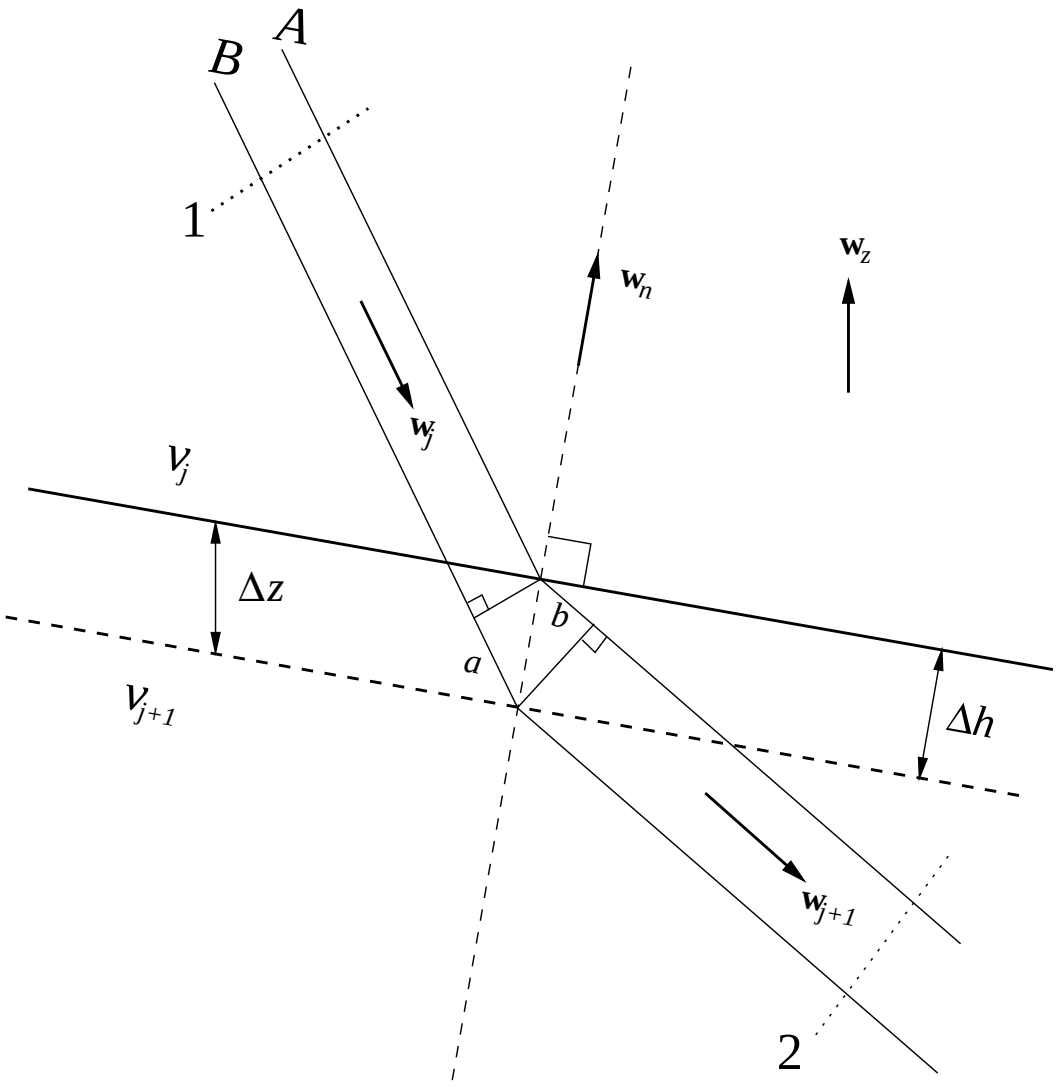

Figure 2.13: Plane wave incident on a perturbed planar interface for first-order approximation of interface Fréchet derivatives. $\mathbf{w}_j$ is a unit vector parallel to rays A and B in layer j and $\mathbf{w}_{j+1}$ is a unit vector parallel to rays A and B in layer $j+1$. $\mathbf{w}_n$ is the unit normal vector to the interface at the intersection point and $\mathbf{w}_z = [0, 0, 1]$.

Smith, 1992; Blundell, 1993; Riahi & Juhlin, 1994). Consider Figure 2.13 which shows a plane wave impinging on a planar interface that is perturbed by a distance Δh. Rays A and B show the path taken by the wave before and after the perturbation. It is easy to see that the difference in traveltime Δt between rays A and B from position 1 to position 2 is:

$$\Delta t = \frac{a}{v_j} - \frac{b}{v_{j+1}} \tag{2.65}$$

and since $a = -\mathbf{w}_j \cdot \mathbf{w}_n \Delta h$ and $b = -\mathbf{w}_{j+1} \cdot \mathbf{w}_n \Delta h$ (all vectors are unit vectors), substitution

into Equation 2.65 gives:

$$\Delta t = \left[\frac{\mathbf{w}_{j+1} \cdot \mathbf{w}_n}{v_{j+1}} - \frac{\mathbf{w}_j \cdot \mathbf{w}_n}{v_j} \right] \Delta h \tag{2.66}$$

and the partial derivative approximation is:

$$\frac{\partial t}{\partial h_{int}} \approx \frac{\mathbf{w}_{j+1} \cdot \mathbf{w}_n}{v_{j+1}} - \frac{\mathbf{w}_j \cdot \mathbf{w}_n}{v_j} \tag{2.67}$$

The second term in Equation 2.64 can be derived from the fact that $\mathbf{w}_n \cdot \mathbf{w}_z = -\Delta h / \Delta z$ so the partial derivative is:

$$\frac{\partial h_{int}}{\partial z_{int}} \approx -\mathbf{w}_n \cdot \mathbf{w}_z \tag{2.68}$$

Substitution of both partial derivatives into Equation 2.64 gives:

$$\frac{\partial t}{\partial z_n} \approx \left[\frac{\mathbf{w}_j \cdot \mathbf{w}_n}{v_j} - \frac{\mathbf{w}_{j+1} \cdot \mathbf{w}_n}{v_{j+1}} \right] [\mathbf{w}_n \cdot \mathbf{w}_z] \frac{\partial z_{int}}{\partial z_n} \tag{2.69}$$

Note that Equation 2.69 will work for any ray direction provided $\mathbf{w}_j$ always points towards the interface and $\mathbf{w}_{j+1}$ always points away from the interface, irrespective of whether the ray is upgoing or downgoing. For reflections, $\mathbf{w}_{j+1} \cdot \mathbf{w}_n = -\mathbf{w}_j \cdot \mathbf{w}_n$ and $v_{j+1} = v_j$. The term $\partial z_{int} / \partial z_n$ depends on the form of the interface depth interpolation function $z = f(z_n)$.

2.3.3 Global Optimisation

The inversion methods described in Section 2.3.1 and Section 2.3.2 are local in that they exploit information in regions of model space near an initial model estimate and thus avoid an extensive search of model space. Consequently, they cannot guarantee convergence to a global minimum solution. Local methods are prone to entrapment in local minima, especially if the subsurface velocity structure is complex and the starting model is not close to the true model. Figure 2.14 illustrates these problems.

Recent interest in the use of global optimisation techniques for solving geophysical inverse problems has been generated to a large degree by rapid advancements in computer power. Several types of global optimisation that have been applied to seismic inversion use random processes to search model space and find better models. These methods include Monte Carlo, genetic algorithms and simulated annealing.

The Monte Carlo approach, defined as a purely random search of model space, is the simplest of these global methods. The misfit function is evaluated at a set of points in

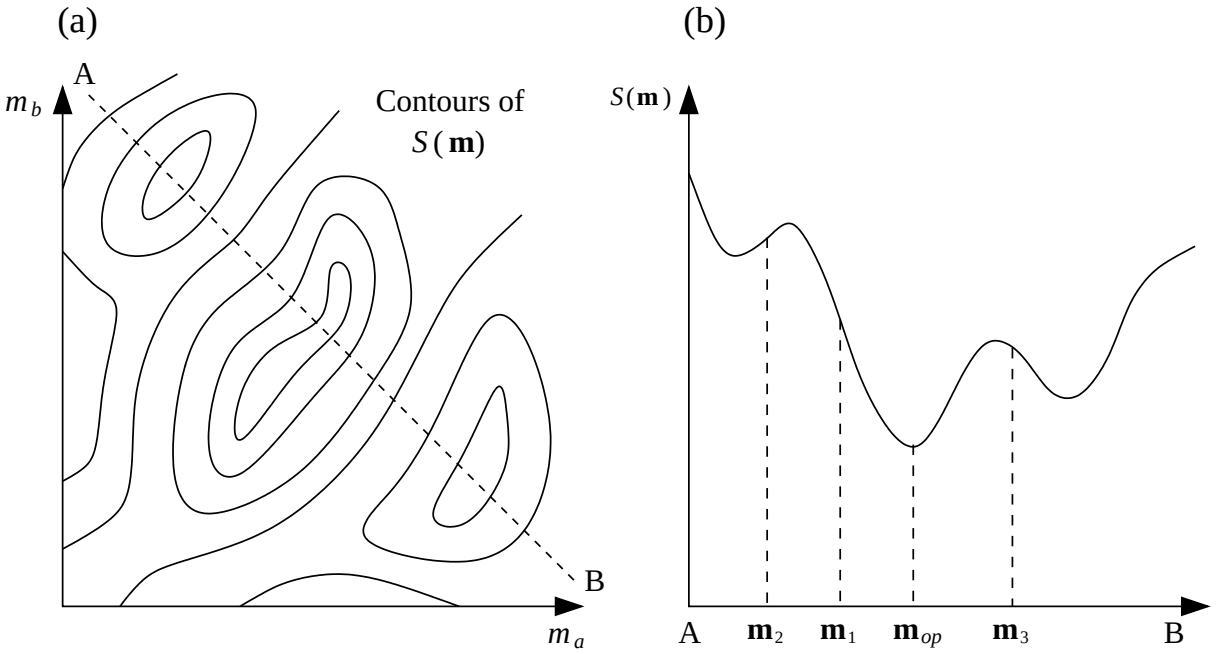

Figure 2.14: (a) Contours of $S(\mathbf{m})$ for a two parameter model. (b) Cross section through (a). Local methods are likely to locate the global optimum solution $\mathbf{m}_{op}$ if initial model $\mathbf{m}_1$ is used, but are more likely to find local minima if initial models $\mathbf{m}_2$ or $\mathbf{m}_3$ are used.

model space that are randomly chosen. The preferred solution is the model with minimum misfit. The selection of points in model space has no dependence on previous points. If model space is not very large, say $M = 80$, and each m_i is discretised to assume only 10 possible values, the number of different models is 10^{80}. Of course, the Monte Carlo approach will not test every model, but it is likely to spend significant amounts of computation time exploring unfavourable regions of model space. Computation requirements will therefore become prohibitive if large numbers of model parameters are involved (Sambridge & Drijkoningen, 1992). Consequently, a basic Monte Carlo approach is not suited to most seismic traveltime inversion problems.

Genetic algorithms use an analogue to biological evolution to develop new models from an initial pool of randomly picked models. The process of producing a new set of models from a pre-existing set involves four basic steps, summarised in the flowchart of Figure 2.15. The first step is to solve the forward problem (i.e. determine traveltimes) for the set of input models. The next step, selection and reproduction, assigns a measure of fitness to each model in the pool based on the magnitude of the misfit function at the corresponding point in model space. Then a rule for selecting which models are to be used to create the next generation must be chosen. Two common choices for the selection

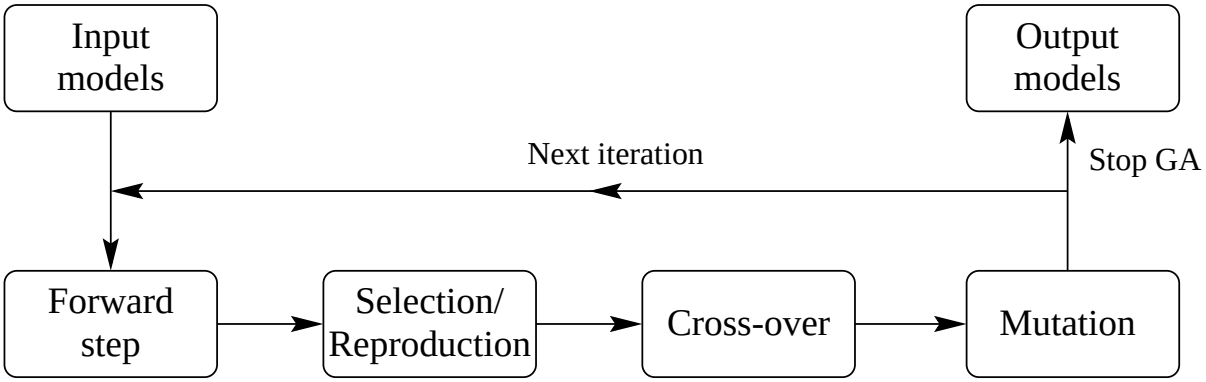

Figure 2.15: Flow chart for genetic algorithm solution of the inversion problem. Each step is carried out on a population of models and the process is terminated when the maximum fitness parameter of the population exceeds a given threshold.

operator are linear normalisation selection and parent selection (Boschetti et al., 1996). Linear normalisation selection ranks each model according to its fitness and then allows each model to generate a number of offspring proportional to its rank position. Parent selection causes pairs of models to be mated randomly so that each couple creates two offspring in the cross-over stage. The cross-over step creates a pool of offspring, each of which is a "mix" of its two parents. Sambridge & Drijkoningen (1992) represent models by binary strings and perform the cross-over by simply cutting and transposing two segments at a randomly chosen point along the two strings.

Mutation involves randomly changing some parameter values (or bits if a binary string representation is used) in selected models. This ensures that some "freshness" remains in the model pool, although the mutation rate should be kept low (Boschetti et al., 1996, use a mutation rate of 1%) so that "good" models are not corrupted. The basic principle behind genetic algorithms is that models with a high fitness index will pass their characteristics to subsequent generations, while those aspects of the cycle that introduce random changes to the population permit new parts of the model space to be tested.

Simulated annealing is based on an analogy with physical annealing in thermodynamic systems to guide variations to the model parameters. The process of annealing in metallurgy involves the slow cooling of metal, which allows the atoms to order themselves into stable, structurally strong, low energy configurations. In the analogue process, some starting model is represented by a collection of atoms (parameters) in equilibrium at a given temperature T. At each iteration, an atom is displaced (a parameter is varied) and the resultant change in the energy of the system ΔE (change in the objective function)

is computed. If $\Delta E \leq 0$ the displacement is accepted and the new model is used as the starting point of the next iteration. If $\Delta E > 0$, then acceptance is probabilistic. Kirkpatrick et al. (1983) use the probability $P(\Delta E) = \exp(-\Delta E/K_B T)$ where T is analogous to temperature in controlling the probability of a randomly selected move and the constant K_B is analogous to Boltzmann's constant. By repeating this step many times, the model evolves with the variation of parameters simulating the thermal motion of atoms held at a temperature T. The simulated annealing process consists of "melting" the system at a high T, then progressively lowering T until the system reaches an equilibrium state (it "freezes"). At each T, the simulation is iterated until a steady state is reached before moving to the next temperature level. A detailed explanation of this method can be found in Kirkpatrick et al. (1983).

Global optimisation using stochastic methods is a rapidly developing field of science. However, current applications to seismic traveltime inversion problems have been limited due to computational expense. Genetic algorithms have been used in the 1-D inversion of marine refraction waveforms (Sambridge & Drijkoningen, 1992; Drijkoningen & White, 1995) and the 2-D inversion of refraction traveltimes (Boschetti et al., 1996). The latter paper inverted for 45 model parameters, which is a relatively large number for a global optimisation. While this number of parameters is insufficient to adequately parameterise many seismic datasets, it is possible to use such a coarse model as a starting point for subsequent refinement using local optimisation techniques. The idea behind this two-stage inversion is that the globally optimised coarse model will be near enough the global minimum to allow the local method to locate the global solution. Boschetti et al. (1996) use genetic algorithms in this context. Global optimisation techniques can find global minimum solutions to highly nonlinear inverse problems, but the computational expense when large numbers of parameters are involved currently limits their use in seismic data inversion.

2.4 Analysis of Solution Quality

The process of producing a solution to an inverse problem using the above methods is not complete until some estimate of solution robustness or quality is made. Simply producing a solution that minimises an objective function (i.e. best satisfies the data and *a priori* constraints) without knowledge of resolution or non-uniqueness is a recipe

for erroneous interpretation of the solution. Two methods are commonly used to assess solution robustness in traveltime tomography. The first method assumes local linearity to estimate model covariance and resolution; the second tests resolution by reconstructing a synthetic model using the same source-receiver geometry as the real experiment.

For an objective function of the form of Equation 2.35, the maximum likelihood solution is given by the $\mathbf{m}$ that satisfies Equation 2.40, which is written here as:

$$\epsilon \mathbf{C}_m^{-1}(\mathbf{m} - \mathbf{m}_0) = -\mathbf{G}^T \mathbf{C}_d^{-1}(\mathbf{g}(\mathbf{m}) - \mathbf{d}_{obs}) \tag{2.70}$$

Adding $\mathbf{G}^T \mathbf{C}_d^{-1} \mathbf{G}(\mathbf{m} - \mathbf{m}_0)$ to both sides gives:

$$\mathbf{m} - \mathbf{m}_o = [\mathbf{G}^T \mathbf{C}_d^{-1} \mathbf{G} + \epsilon \mathbf{C}_m^{-1}]^{-1} \mathbf{G}^T \mathbf{C}_d^{-1} [\mathbf{g}(\mathbf{m}) - \mathbf{d}_{obs} - \mathbf{G}(\mathbf{m} - \mathbf{m}_o)] \tag{2.71}$$

which is an implicit equation for $\mathbf{m}$. Following Tarantola (1987), let $\mathbf{m}_{true}$ represent the true model, which is unknown. The observed data is related to $\mathbf{m}_{true}$ by:

$$\mathbf{d}_{obs} = \mathbf{g}(\mathbf{m}_{true}) + \boldsymbol{\zeta} \tag{2.72}$$

where $\boldsymbol{\zeta}$ represents observational and model representation errors. The resolution operator $\mathbf{r}$ defines the relationship between the calculated solution $\mathbf{m}$ and the true solution:

$$\mathbf{m} = \mathbf{r}(\mathbf{m}_{true}) \tag{2.73}$$

If $\mathbf{r}$ is linear, then $\mathbf{m} = \mathbf{r}(\mathbf{m}_0) + \mathbf{R}(\mathbf{m}_{true} - \mathbf{m}_0)$, where $\mathbf{R} = \partial \mathbf{r} / \partial \mathbf{m}$ and $\mathbf{m}_0 = \mathbf{r}(\mathbf{m}_0)$ so that:

$$\mathbf{m} - \mathbf{m}_0 = \mathbf{R}(\mathbf{m}_{true} - \mathbf{m}_0) \tag{2.74}$$

If we assume that $\boldsymbol{\zeta} = \{0\}$ in Equation 2.72 and let $\mathbf{m} = \mathbf{m}_{true}$ on the RHS of Equation 2.71, then Equation 2.74 can be written in the form of Equation 2.71 with the resolution matrix $\mathbf{R}$ given by:

$$\mathbf{R} = [\mathbf{G}^T \mathbf{C}_d^{-1} \mathbf{G} + \epsilon \mathbf{C}_m^{-1}]^{-1} \mathbf{G}^T \mathbf{C}_d^{-1} \mathbf{G} \tag{2.75}$$

The diagonal elements of R range between zero and one. If $\mathbf{R} = \mathbf{I}$, then, according to Equation 2.74, $\mathbf{m} = \mathbf{m}_{true}$ and the solution model is perfectly resolved. If $\mathbf{R} \neq \mathbf{I}$, then the model parameter estimates represent weighted averages of the true model parameters.

The matrix $\mathbf{C}_m$ describes *a priori* model covariance, with the square root of the diagonal entries indicating the uncertainty associated with the initial model parameter values. The constraints supplied by the data will result in changes to these uncertainties. The

posteriori covariance matrix $\mathbf{C}_M$ describes the error in the solution parameters and is related to the resolution matrix by (Tarantola, 1987):

$$\mathbf{R} = \mathbf{I} - \mathbf{C}_M \mathbf{C}_m^{-1} \tag{2.76}$$

Substituting Equation 2.75 for $\mathbf{R}$ and solving for $\mathbf{C}_M$ gives:

$$\mathbf{C}_M = \epsilon[\mathbf{G}^T \mathbf{C}_d^{-1} \mathbf{G} + \epsilon \mathbf{C}_m^{-1}]^{-1} \tag{2.77}$$

The diagonal elements of $\mathbf{C}_M$ indicate the posterior uncertainty associated with each model parameter. The Fréchet matrix $\mathbf{G}$ in Equations 2.75 and 2.77 is calculated at the solution point. Off-diagonal elements of the posterior covariance matrix are hard to interpret directly, but may be considered in terms of correlations (Tarantola, 1987):

$$\rho^{ij} = \frac{C_M^{ij}}{(C_M^{ii})^{\frac{1}{2}} (C_M^{jj})^{\frac{1}{2}}} \tag{2.78}$$

where $-1 \leq \rho^{ij} \leq 1$ and $i, j = 1, \ldots, M$. A strong correlation on uncertainties means that the two parameters have not been independently resolved by the dataset.

The principle difficulties with $\mathbf{R}$ and $\mathbf{C}_M$ are (i) that they are derived from linear theory and are less meaningful as the non-linearity of the problem increases, (ii) errors in model representation are not taken into account, and (iii) they require the inversion of an $M \times M$ matrix, $\mathbf{G}^T \mathbf{C}_d^{-1} \mathbf{G} + \epsilon \mathbf{C}_m^{-1}$, which may be impractical for large numbers of parameters. Nevertheless, they have been used in many teleseismic traveltime studies (e.g. Aki et al., 1977; Benz et al., 1992; Steck et al., 1998) and wide-angle traveltime inversions (e.g. White, 1989; Hole, 1992; Zelt & Smith, 1992; Riahi & Lund, 1994; Wang & Braile, 1996). Zelt & Smith (1992) and Wang & Braile (1996) both recommend using the linearised resolution estimates in a relative rather than an absolute sense. McCaughey & Singh (1997) and Zhang & Toksöz (1998) also consider correlations (Equation 2.78) as part of their interpretation of solution quality.

Parameterisations that describe continuous velocity fields often opt for resolution tests that attempt to reconstruct a synthetic model using the same source-receiver geometry as the real experiment. The rationale behind this approach is that if a known structure with similar length scales to the solution model can be recovered using the same (for linearised solutions) or similar (for non-linear solutions) ray paths, then the solution model should be reliable. The quality criterion is the similarity between the recovered

model and the synthetic model. The so-called "checkerboard test", in which the synthetic model is divided into alternating regions of high and low velocity with a length scale equal to the smallest wavelength structure recovered in the solution model, is a common test model. Regions in which the checkerboard pattern is recovered clearly are those regions in which structure in the solution model can be considered to be well resolved. Lévêque et al. (1993) demonstrate that such an approach is not necessarily as reliable as it might seem. It is possible for the small scale structure of the checkerboard test to be well retrieved while larger-scale structure is poorly retrieved. Furthermore, if the non-linearity of the problem is accounted for, the ray paths through the synthetic model may have significantly different geometries to those through the solution model. In these situations, testing a number of different synthetic models is advisable, especially if the solution model is complex.

Teleseismic traveltime tomography studies that used checkerboard resolution tests include those by Glahn & Granet (1993), Achauer (1994) and Seber et al. (1996). Ritsema et al. (1998) used several different synthetic models rather than checkerboards and analysed the accuracy of their recovery. This kind of analysis is not commonly used in wide-angle studies, although recently, Zelt (1998) and Zelt et al. (1999) implemented checkerboard tests for analysing the resolution of velocity and interface structure derived from wide-angle traveltime inversion.

Chapter 3

Inversion of Teleseismic Traveltime Residuals for Interface Structure in Central Australia

3.1 Introduction

Most methods of teleseismic traveltime inversion assume a continuous velocity distribution, represented either by constant velocity or slowness blocks, or velocity nodes joined by an interpolation function (e.g. Aki et al., 1977; Evans, 1982; Humphreys & Clayton, 1990; Achauer, 1994, etc.). As pointed out in Chapter 2, the disadvantage of this approach is that discontinuous changes in velocity cannot be accurately reconstructed. While the inclusion of interfaces in velocity models is common practice for studies that invert reflection or wide-angle traveltimes (e.g. Bishop et al., 1985; Chiu et al., 1986; White, 1989; Williamson, 1990; Hole et al., 1992; Zelt & Smith, 1992; Blundell, 1993; Zelt et al., 1999), it is not very common in teleseismic traveltime inversion. There are two principal reasons for this practice. First, teleseismic data do not contain obvious indicators of an interface, such as the "reflectors" seen in normal-incidence seismic sections, or the later arriving, large amplitude reflection curves evident in refraction sections. Interfaces may cause mode conversions in teleseismic arrivals, but these are not always easy to detect, particularly if the analysis relies on single component data. Thus, if interfaces are to be included in a teleseismic traveltime inversion, some *a priori* knowledge of interface structure is required. Potentially, if three-component data are recorded, receiver function

analysis (see Section 1.1.3), which interprets mode-converted teleseismic arrivals, could be used to identify major velocity interfaces. Second, methods that invert for both interface structure and continuous velocity variation must be able to address the trade-off between velocity and interface position. The trade-off is maximised when the traveltime variation can be modelled equally well by velocity or interface perturbations (Blundell, 1993). It has been shown (Wang & Braile, 1996) that simultaneously inverting reflection and refraction data helps significantly to reduce solution non-uniqueness. In teleseismic tomography, however, only the transmitted rays are usually available, so the prospect of producing a unique velocity plus interface solution is low. Consequently, the few teleseismic studies that have included interfaces in their representation of structure, have either not inverted for interface structure (Zhao et al., 1994), or have only inverted for interface structure and not velocity (Davis, 1991; Kohler, 1997). Davis (1991) and Kohler & Davis (1997) only inverted for a single interface representing the Moho in their analyses.

In this chapter, the novel method of Rawlinson (1996b) is applied to a previously published dataset consisting of teleseismic traveltime anomalies recorded by an in-line array of seismometers across the northern margin of the Musgrave Block in central Australia. Prior to this study, the method had not been applied to observed data. The model parameterisation is based on a 2-D velocity structure consisting of homogeneous and isotropic layers of variable thickness. Layer interfaces are described by a set of nodes interpolated by cubic splines, with the vertical coordinates of the nodes constituting the unknown parameters that are to be determined by the inversion. Layer velocities are assumed to be known *a priori*. The forward problem of determining traveltimes from an incident wavefront located below the crust to a set of receivers on the earth's surface is solved by an efficient and robust shooting method. A conjugate gradient method is used to solve the inverse problem. The solution requires the minimisation of a least-squares type objective function based on the difference between model and observed traveltime residuals.

Following a brief description of the method, the results of several tests with synthetic data for a multiple interface model are presented. The precision of the reconstruction in the presence of accurate data and *a priori* information on the mean vertical structure is demonstrated, and robustness with respect to noise and inaccurate vertical structure is also investigated. These synthetic tests provide invaluable knowledge on how the method might be expected to work with real data. Finally, the method is applied to a dataset

collected in central Australia and the solution model is interpreted. Solution robustness is analysed by attempting to reconstruct a known structure using a synthetic dataset that has the same source-receiver geometry as the observed data. Comparisons are also made between the Central Australian solution obtained here and previously published solutions that used the same data but different methods, most notably the standard tomographic approach used by McQueen & Lambeck (1996) in which the solution is described in terms of variable velocity distribution rather than interface structure. The aim here is to show that the subsurface structural information contained in the teleseismic traveltime residuals can be interpreted in terms of interface geometry, and that interface parameterisation represents a valid alternative to velocity parameterisation, neither method being complete, but each having advantages for specific datasets.

3.2 Method

The parameterisation used here describes a 2-D velocity structure with constant velocity layers of variable thickness. Each layer interface is described by a set of splined node points whose vertical coordinates constitute the unknown parameters to be estimated. The interface between adjacent nodes is interpolated by cubic splines, which are described for n nodes by:

$$f_i(x) = a_i(x - x_i)^3 + b_i(x - x_i)^2 + c_i(x - x_i) + d_i \tag{3.1}$$

where $i = 1, \ldots, n-1$ and $f_i(x)$ interpolates between (x_i, z_i) and (x_{i+1}, z_{i+1}). The spline coefficients $\{a_i, b_i, c_i, d_i\}$ are defined such that the cubic functions interpolate the nodes, are C_2 continuous at the nodes, and are points of inflection at the endpoints $(x_1, f_1(x_1))$ and $(x_n, f_{n-1}(x_n))$. The smoothly varying nature of cubic splines means that virtually any smooth interface can be represented. Features such as faults or chevron folds, however, can only be approximated. In addition, the use of Equation 3.1 means that each interface is assumed to be single-valued in the independent variable x (the horizontal coordinate), so that intrusive bodies and recumbent folds are again only approximated.

Given a model structure, the forward problem is to determine the ray paths and traveltimes from a teleseismic wavefront (assumed planar) initially located beneath the structure to a set of receivers located on the surface. A shooting method is used to trace rays from selected points on the wavefront until they strike the receiver plane. Since layers are constant velocity, the ray path consists of piecewise linear segments. The point

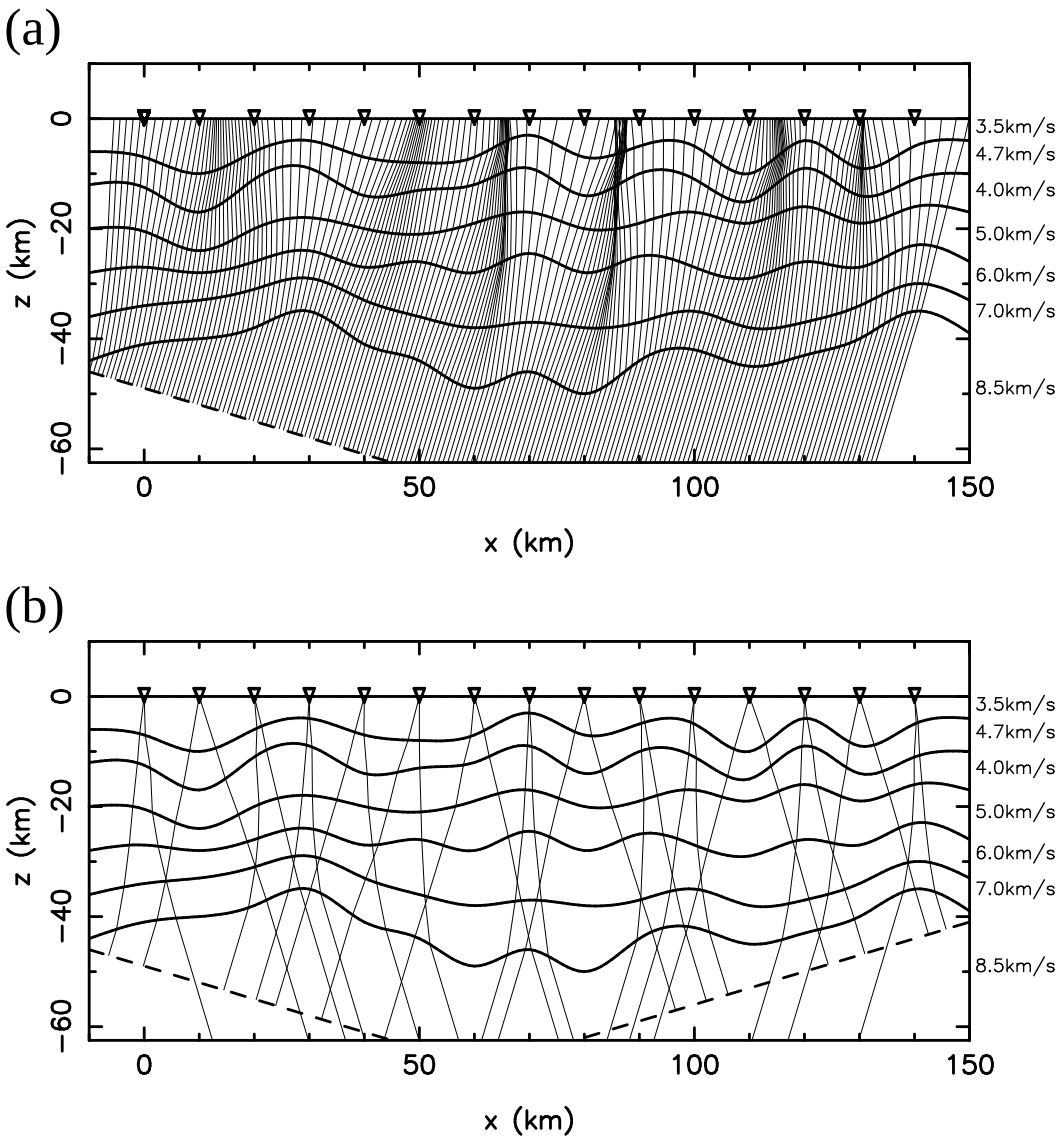

Figure 3.1: (a) An even spread of 204 rays shot from an incident planar wavefront with gradient -0.3 through a seven layer structure. The symbol ∇ represents a station location on the surface, while thick solid lines denote interfaces and thin solid lines denote ray paths. The incident wavefront is represented by the dashed line. (b) First-arrival rays to each station from two incident wavefronts impinging on the structure shown in (a). The wavefronts have gradients of -0.3 (the initial shoot shown in (a)) and +0.3.

of intersection of a ray and interface is thus given by solving a cubic equation, which is done using the Newton-Raphson method. The initial guess is provided by the point at which the ray intersects a linear segment joining the appropriate pair of interface nodes. Once the intersection point is determined, Snell's Law is used to determine the new trajectory of the ray. The boundary value problem is solved by shooting an evenly sampled spread of rays from the wavefront (see Figure 3.1a) and then choosing an initial

guess ray by linearly interpolating between two rays that bracket a receiver. An iterative correction strategy that accounts for the effects of interface curvature on ray trajectory using a geometric relationship (see Rawlinson, 1996b) is then applied to accurately locate the two-point ray. If more than one pair of rays bracket a receiver, the two-point path is located for each case and the one with minimum traveltime is selected. Figure 3.1b shows the first-arrival rays to each station from two incident wavefronts with gradients ± 0.3 (the gradient w of the wavefront is related to the incidence angle of the rays in the half-space by $w = \tan i$) through the same structure shown in Figure 3.1a. Each ray hits the surface within 5 mm of the target station and none of the rays require more than four iterations to achieve this accuracy. Note the effect that interface geometry has on ray coverage, with the first-arrival paths being focused or defocused by the curvature of the interfaces.

The inverse problem is treated as an optimisation problem in which an objective function is defined and minimised to produce a solution. The form of the objective function used here gives a measure of how well the predictions of the model agree with the observed data:

$$S(\mathbf{m}) = (\mathbf{g}(\mathbf{m}) - \mathbf{d}_{obs})^T \mathbf{C}_d^{-1} (\mathbf{g}(\mathbf{m}) - \mathbf{d}_{obs}) \tag{3.2}$$

where $\mathbf{m}$ is the set of node depths to one or more interfaces. Equation 3.2 is the same as Equation 2.34 with no damping or smoothing ($\epsilon = \eta = 0$). Since cubic splines are C_2 continuous at every point, a smoothing term is not considered necessary provided the interface node separation is optimal for the data set used. Damping has the effect of attracting the solution to regions of model space near an *a priori* model. Although it does not appear explicitly in the objective function (Equation 3.2), the initial model estimate does assume a significant role in the model reconstruction. In the synthetic tests (next section), I show that teleseismic traveltime residuals, adjusted for source-time uncertainty by subtracting the mean, do not constrain average vertical structure. Consequently, the average vertical structure of the solution model is effectively determined by the initial model estimate.

The Polak-Ribiere conjugate gradient method is used to perform the function minimisation. A description of the method is given in Section 2.3.2, but two modifications to this standard approach have been implemented. First, instead of assuming that the objective function is quadratic in each conjugate direction (Equation 2.52 locates the line minimum

in this case), a line search is implemented. Thus, the true local minimum is found in each of the conjugate directions. Second, the gradient vector $\hat{\boldsymbol{\gamma}} = \partial S/\partial \mathbf{m}$ is found without evaluating the Fréchet matrix $\mathbf{G}$. Instead, a finite difference formulation is used, in which each m_i is perturbed by an amount Δm_i and the objective function re-evaluated to give $S(\mathbf{m})_{\Delta m_i}$. Then the gradient vector is approximated by:

$$\frac{\partial S(\mathbf{m})}{\partial m_i} \approx \frac{S(\mathbf{m})_{\Delta m_i} - S(\mathbf{m})}{\Delta m_i} \tag{3.3}$$

A small value for Δm_i (typically between 3-5 m) can be used due to the high precision of the ray-tracing routine. This method is favoured over the analytic approximations of the Fréchet matrix (see Section 2.3.2) because tests showed that it results in superior solutions when interfaces with strong curvature are present. Both these modifications mean that the ray tracing routine must be used many times at each iteration of the conjugate gradient method. However, the ray tracing routine is fast enough that the additional computational burden is not significant. Further details of the method can be found in Rawlinson (1996b) and Rawlinson & Houseman (1998).

3.3 Tests with Synthetic Data

The aim of these synthetic tests is to examine how accurately the interface inversion algorithm can solve for a known structure. To do this, a set of rays is traced through a given model to obtain traveltimes (the synthetic data) and these times are then used in conjunction with a starting model to reconstruct the original interface geometry. Tests using synthetic data also provide invaluable insight into how sensitive the method is to data noise and an inaccurate mean (i.e. horizontally averaged) vertical structure.

The model chosen for the synthetic tests consists of a three-layered structure as shown in Figure 3.2a. Both interfaces are parameterised by 18 equally spaced nodes and the velocity discontinuity across each interface is 1.5 km/s. Although not obvious in this figure, a topographic relief not exceeding 1 km in amplitude has been incorporated in the model. Synthetic data are generated by ray tracing from three incident wavefronts (with gradients of 0.5, 0.0 -0.5) to the receivers on the surface. Receiver separations vary between 8 and 10 km across the 130 km line, which contains 16 stations. Ray traveltimes from the three wavefronts are plotted in Figure 3.2b-d, reduced to highlight the variations in traveltimes caused by changes in lateral structure. The reduced traveltimes are defined

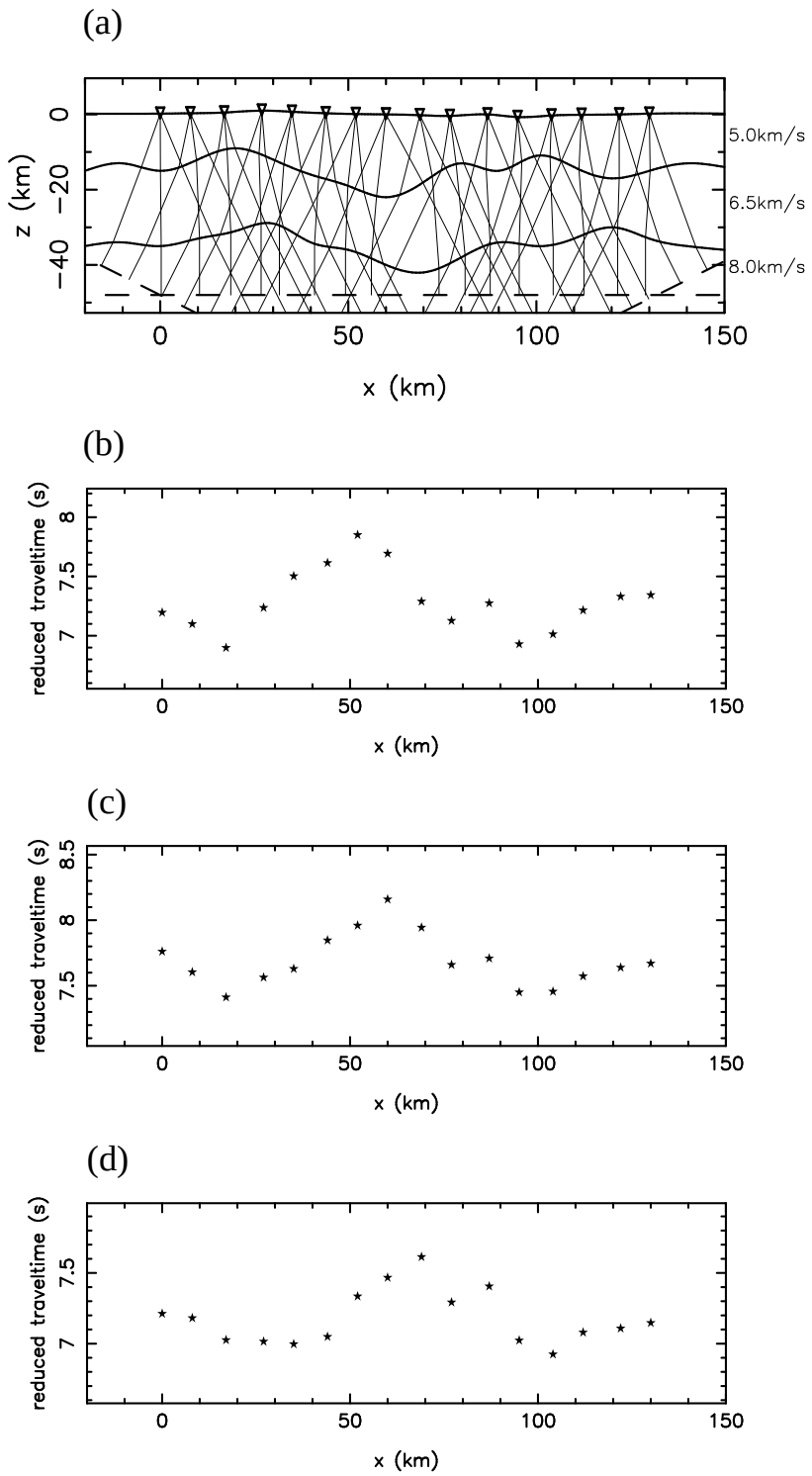

Figure 3.2: The three layer model used in the synthetic tests is shown in (a), along with the incident wavefronts (dashed lines) and ray paths (thin solid lines). Interfaces are denoted by thick solid lines. The reduced traveltimes for the waves with gradients 0.5, 0.0 and -0.5 are shown in (b), (c) and (d) respectively. The minor surface topography does not significantly affect the appearance of the reduced traveltime plots.

by $\hat{t} = t - d/v_x$, where t is the actual traveltime of the ray from the wavefront to the surface, d is the horizontal distance from a reference station, and $v_x = v \sin i$ is the horizontal component of velocity of the wave in the half space. For waves with gradient 0.5 and -0.5, the reference stations are at $x = 130$ and 0 km respectively; the wave with gradient 0.0 has $\hat{t} = t$ for all rays. The surface topography is only responsible for a minor component of the variations in reduced traveltimes that are computed here.

The starting model for the inversion has a 1-D structure (except for the surface topography) consistent with what could be determined from a refraction survey of the region. In the first test, the horizontal positions of the nodes along each interface and the velocity of each layer are the same as those used in the model from which the synthetic data are obtained. The depth to each interface in the starting model is equal to the average depth of the corresponding interface in the test model. Noise is not added to the data for this test so all the diagonal elements of C_d are set to 1.

The results of the inversion are shown in Figure 3.3a-c. After 40 iterations, the objective function (Figure 3.3a) has dropped to less than 0.0001% of its original value, at which point the RMS data residual (the RMS difference between observed and model traveltimes) is less than 0.063 ms. To track the behaviour of the model through the inversion process, a model misfit function $E(\mathbf{m})$ is calculated at each iteration; this misfit function is defined to be the RMS distance between corresponding node points in the test model and the reconstructed model:

$$E(\mathbf{m}) = \left[\frac{(\mathbf{m}_{true} - \mathbf{m})^T (\mathbf{m}_{true} - \mathbf{m})}{M} \right]^{\frac{1}{2}} \tag{3.4}$$

where the M-dimensional vectors $\mathbf{m}_{true}$ and $\mathbf{m}$ are the set of interface depth parameters of the test model and the reconstructed model respectively. In the current example, the model misfit function (Figure 3.3b) shows that the most significant reductions occur over the first few iterations, and the algorithm produces only trivial improvements after about 10 iterations. The initial misfit is approximately 3 km and the final misfit is about 0.3 km. A comparison between the reconstructed model and the synthetic model (Figure 3.3c) shows that the structure is recovered almost exactly. Only at the endpoints, where the boundary nodes are not well constrained by the rays (see Figure 3.2a), are the two models perceptibly different. Lack of information about the interfaces in these regions explains why the model misfit function is not much closer to zero at the final iteration. The monotonic behaviour of the model misfit function illustrates the stability of the inversion

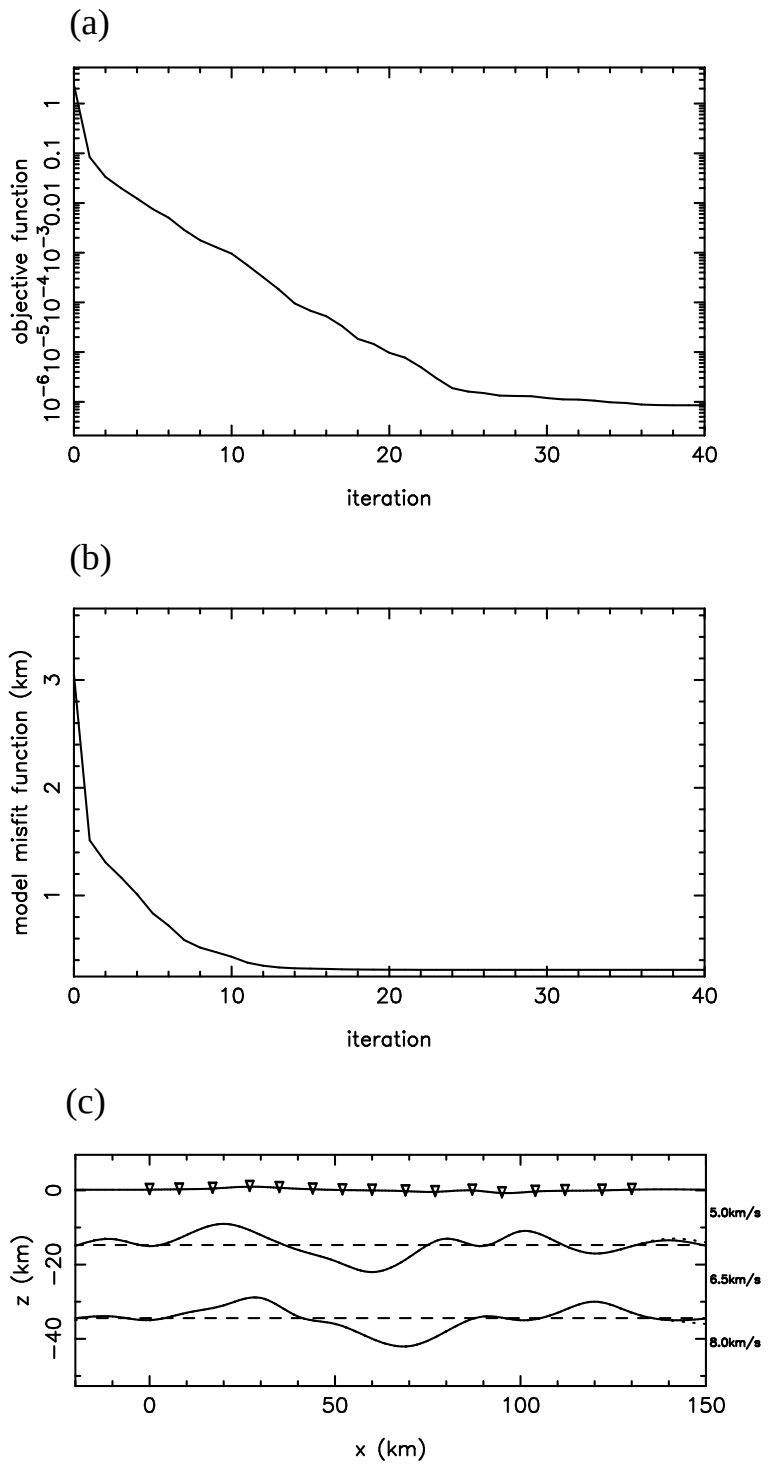

Figure 3.3: Ideal case inversion results. (a) Objective function versus iteration number, (b) model misfit function versus iteration number, and (c) comparison of final model interface structure (solid lines) with synthetic model interface structure (dotted lines). The starting model for the inversion is shown by the dashed lines.

algorithm.

The above test shows that, given accurate data and *a priori* information on the mean

vertical structure, the interface inversion algorithm is capable of producing accurate results. Before applying the method to real data, however, a number of other synthetic tests should be carried out. First, the problem of event-time uncertainties needs to be addressed since earthquakes are uncontrolled events. A common way of dealing with event-time uncertainty (e.g. Humphreys & Clayton, 1990) is to remove the mean from each residual set (each event producing a set of residuals) under the assumption that the mean vertical structure of the initial model is correct. Traveltime residuals are defined here by the difference between the synthetic traveltimes and the corresponding traveltimes through the initial model. Setting the mean residual to zero means that the iterative inversion process should not change the mean vertical structure introduced in the initial model. In all the following examples, the mean has been removed from each of the three sets of traveltime residuals.

An intrinsic property of real data is that they contain noise, so the robustness of the inversion with respect to noisy data needs to be tested. In the next example, Gaussian noise is added to the synthetic traveltime data set of Figure 3.2b-d. A standard deviation for each source-receiver pair is chosen and Gaussian noise is generated so that the error added to each traveltime is normally distributed with that standard deviation (the $\{\sigma_j\}, j = 1, \ldots, N$ in this example vary between 0.02 and 0.08 s). When inverting the noisy data, these standard deviations are used in the data covariance matrix (whose ij^{th} entry is $[C_d]_{ij} = \delta_{ij}\sigma_j^2$) contained in the objective function (see Equation 3.2). Figure 3.4 shows results from this inversion using the same starting model as the Figure 3.3 example. One obvious feature of the model misfit function (Figure 3.4b) is that, after an initial period of decrease, it gradually begins to increase again from about iteration 7. Beyond this point, the algorithm generates structure that is consistent with the noise but is not part of the true model. Correspondingly, the objective function continues to decrease monotonically, albeit slowly, throughout the remaining inversion process. Evidently, the best model occurs at iteration 7, but in the absence of a model misfit function, some other criterion is required to indicate when this model has been achieved. One strategy is to terminate the iterative procedure once the residuals of the model estimate are of a similar magnitude to the standard deviation of the data noise. An alternative is to base the cut-off point on the shape of the objective function versus iteration number curve (Figure 3.4a). A feature of Figure 3.4a is that the curve flattens out after the optimum model has been achieved. Tests involving several different synthetic models indicate that the

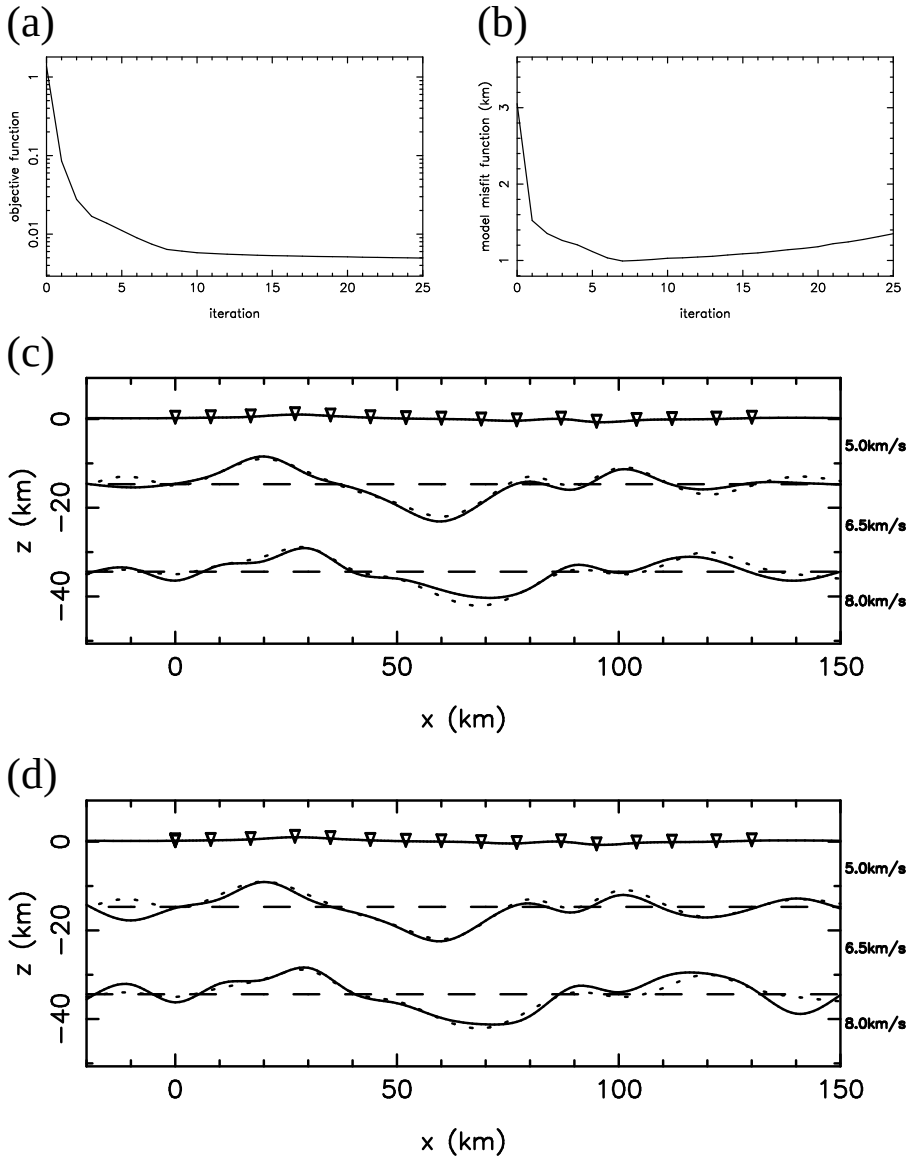

Figure 3.4: Inversion results for noisy data. (a) Objective function versus iteration number, (b) model misfit function versus iteration number, (c) comparison of model (at iteration 7) interface structure (solid lines) with synthetic model interface structure (dotted lines), and (d) comparison of model (at iteration 25) interface structure (solid lines) with synthetic model interface structure (dotted lines). In both (c) and (d), the starting model is indicated by the dashed lines.

best place to cease the iterative process occurs when the objective function has a value approximately 33% greater than its plateau value. This criterion combined with the one based on the RMS traveltime residuals provide a reasonable estimate of the model misfit minimum. Further investigation of methods aimed at a more accurate location of the minimum is not warranted since the model misfit function increases only gradually once the optimum model is achieved. Also, as Figure 3.4c-d shows, the reconstructed models

after 7 and 25 iterations both recover the basic structure of the test model. The unconstrained adjustment near the endpoints of the interfaces, where ray coverage is sparse, is the primary cause of the poorer model fit at iteration 25.

In addition to data noise, other factors that contribute to the error in the final model include choosing interface depths in the initial model that are not near the mean depth of the corresponding true interface, and choosing incorrect layer velocities. These two factors represent different aspects of uncertainty in defining the mean vertical structure. Figure 3.5a demonstrates the result of inversion when the two horizontal interfaces in the starting model are each in error by 4 km (-4 km for the top interface and +4 km for the bottom interface). While the correct mean vertical positions of the interfaces are not recovered by the inversion, their lateral structure is accurately represented. The inversion is unable to retrieve the mean vertical structure even if no event-time errors are present and the traveltime residuals are absolute, because a vertical shift of one interface can be traded off against a vertical shift in another. The solution of this inverse problem is not unique with respect to average vertical structure because of the near-vertical incidence of the ray paths.

Figure 3.5b demonstrates the effect of inverting when the velocities in the top two layers are 0.2 km/s too slow and the velocity in the bottom layer is 0.1 km/s too slow. The correct interface geometry is approximately recovered after seven iterations. If no source-time errors are present in the data and absolute traveltime residuals are inverted, then the result is similar to Figure 3.5b but with a positive vertical shift of each interface, which compensates for the errors in layer velocity.

The examples shown in Figure 3.5 illustrate several points. First, this type of data does not constrain mean vertical structure; the mean vertical structure in the solution is simply inherited from the starting model used in the inversion if the residuals are first demeaned. Second, in order for the interface inversion method to recover lateral structure, an initial model with a highly accurate mean vertical structure is not necessary. Finally, accounting for event-time errors by mean residual removal does not result in the loss of important information from the reconstructed model.

The horizontal node separation chosen for the reconstructed model plays an important role in regularising the inverse problem because it controls the minimum allowable wavelength of the interface features. The results of several synthetic tests indicate that the optimum node separation in the presence of a good angular coverage of rays (such as

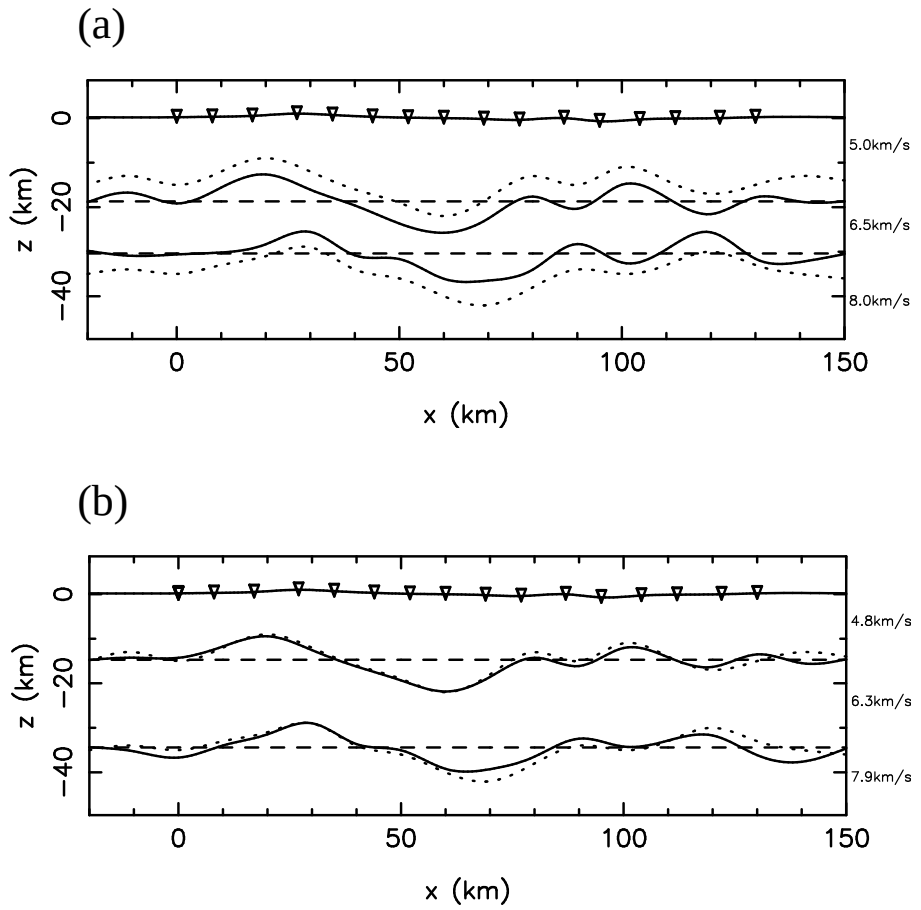

Figure 3.5: Inversion results with poor velocity or initial depth estimation. Final model interfaces are denoted by solid lines, synthetic model interfaces are denoted by dotted lines, and starting models are denoted by dashed lines. (a) Solution (at iteration 10) with poor initial depth estimates, and (b) solution (at iteration 7) with inaccurate velocity estimates.

in Figure 3.2a) is approximately equal to the station separation; smaller node separations tend to lead to the generation of spurious structure.

3.4 Application to Central Australia Dataset

On a crustal scale, the geology of central Australia consists of a number of intracratonic sedimentary basins separated by uplifted blocks of basement (Plumb, 1979). From north to south, there is the Arunta Block, which hosts the much smaller Ngalia Basin, the Amadeus Basin, the Musgrave Block and the Officer Basin; the area that these structures occupy is approximately 750 km by 750 km. Geological evidence (Wells et al., 1970; Plumb, 1979) suggests that exposed crust varies in age from Proterozoic (for the uplifted basements) to Carboniferous (for the sedimentary basins). A model for the evolution of

this region has been proposed by Lambeck (1983), who describes the formation of the structures in terms of horizontal compressive forces acting on inhomogeneous viscoelastic lithosphere. The deformation caused by compression is increased by erosion of the uplifted areas and sediments being deposited in the downwarps to form the basins. Thrust faulting is predicted to occur as a result of cumulative bending stresses. More recently, Lindsay & Korsch (1991) used sequence stratigraphy to identify three major stages of tectonic development. The first two stages consisted of distinct periods of extension commencing at about 900 and 580 Ma, while the final stage involved a major compressional event beginning at approximately 450 Ma. The compressional event is primarily responsible for the present-day structure of the basin margins.

Teleseismic traveltime residuals from several surveys have previously been used to constrain the crustal structure of central Australia (Lambeck & Penney, 1984; Lambeck et al., 1988; Lambeck & Burgess, 1992; McQueen & Lambeck, 1996). In this application of the inversion method just described, data from the Musgrave Line (see McQueen & Lambeck, 1996) is used. Figure 3.6 shows the receiver array for the Musgrave Line which has been superimposed on an elevation map of the region. Several significant fault lines and block boundaries are also included. The dataset consists of teleseismic events recorded by 26 stations positioned along a north-south line from Lake Amadeus in the Amadeus Basin to near the southern margin of the Musgrave Block.

The methods used to pre-process the Musgrave Line data into the form used by McQueen & Lambeck (1996) are described in detail by Lambeck & Penney (1984) and Lambeck et al. (1988). A brief description is included here for completeness. Observed traveltimes t_{ij}^0 from each event (j) to each receiver (i) are found by comparing arrival times with the monthly listings of the US Geological Survey, National Earthquake Information Service (NEIS). Theoretical traveltimes t_{ij}^c are determined from the Herrin et al. (1968) traveltime model. Hence, a differential traveltime anomaly is defined by:

$$\Delta t_{ij} = t_{ij}^0 - t_{ij}^c - \frac{1}{m}\sum_{i=1}^{m}(t_{ij}^0 - t_{ij}^c) \tag{3.5}$$

for a set of m receivers. The last term in Equation 3.5 subtracts the mean residual for each event because source-time uncertainties are unconstrained, as outlined in Section 3.3. The next step is to determine an average station anomaly for events that originate in a given source region. For a set of events from each source region, the anomalies are

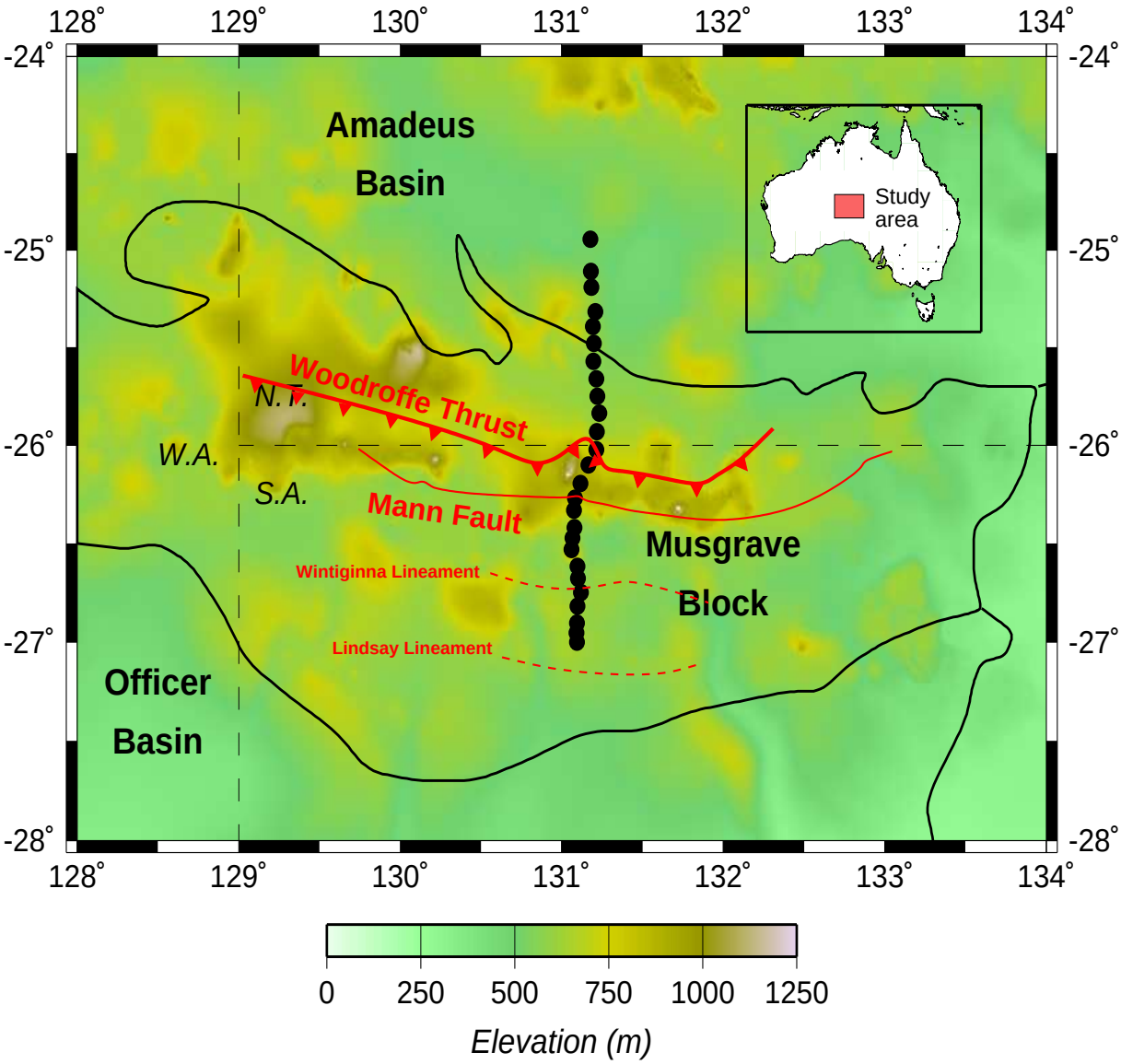

Figure 3.6: Map of central Australia showing receiver array (black dots) superimposed on contours of surface topography. Significant structural features evident in the surface geology are shown by solid red lines; dashed red lines indicate major magnetic lineaments.

written as:

$$\Delta t_{ij} = a_j + t_i + \epsilon_{i,j} \tag{3.6}$$

where $j = 1, \ldots, n$ now ranges over all the rays from a particular source region. In Equation 3.6, $\epsilon_{i,j}$ is the measurement error, a_j is the event correction and t_i is the station anomaly. The nm equations (Equation 3.6) are solved for the $n + m$ unknowns $\{a_j\}$ and $\{t_i\}$ by a least-squares minimisation of the error. From the solution of Equation 3.6, a set of n error values are produced for each source region-receiver pair. In the inversion of the Musgrave Line data, the ith diagonal element of the data covariance matrix is set equal to

the variance of the n error values for station i, so that stations whose traveltime anomaly is more precisely defined have a greater influence on the objective function. Table 3.1 shows the number of events, azimuth range and distance range for each source region.

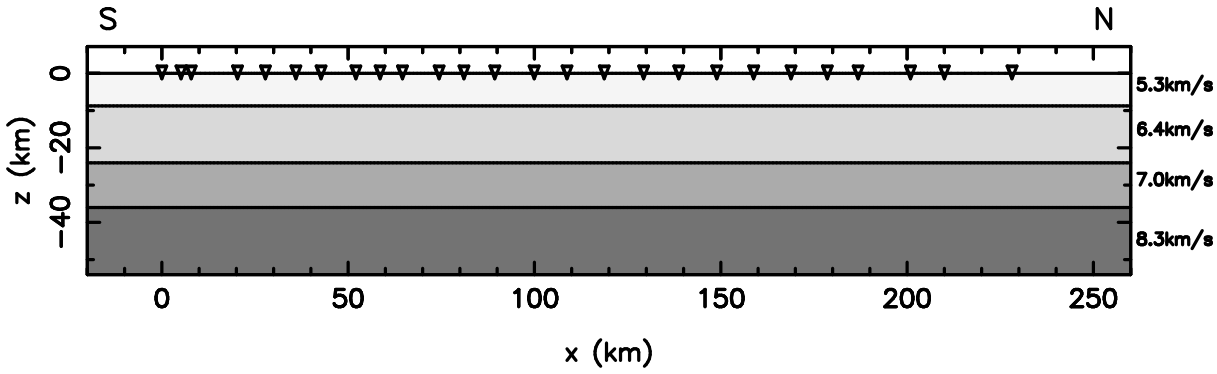

Figure 3.7: The starting model for the inversion of Musgrave Block data. Velocities in each layer are 0.3 km/s faster than those given by Collins (1988), based on the Amadeus Basin deep reflection seismic data.

The azimuth of the receiver array is about 5° (see Figure 3.6), but not all sources lie on this great circle path. Using out-of-plane sources in a problem treated strictly in 2-D may result in artifacts appearing in the solution. The back-azimuths of three source regions, Japan, South Sandwich Islands and Kuril, all lie within 10° of the receiver array azimuth, so the errors in the traveltime anomalies, caused by projecting the incident wavefronts into the plane of the section, are small. These data are used in the inversion without further correction.

The receiver array that forms the Musgrave Line traverses about 70 km of the Amadeus Basin and 150 km of the Musgrave Block. Hence, the initial model used in the inversion should recognise characteristics of both the uplifted block and the sedimentary basin. While no deep reflection/refraction model has been published for the Musgrave Block, a deep reflection model (PBW01) for the Amadeus Basin can be found in Collins (1988). PBW01 shows an 8.75 km thick layer of sediment overlying middle and lower crustal layers of higher velocity. The initial model (Figure 3.7) chosen for the inversion is based on PBW01, but the average crustal velocities have been increased by 0.3 km/s in acknowledgement of the higher velocities that are likely to be present in the Musgrave Block. This change means that the average crustal velocity of the initial model is very similar to that found by Bowman & Kennett (1993) for the western and central Australian crusts using local and regional earthquake traveltimes. By using the structure shown in Figure 3.7 as

the initial model, I assume that velocity variations in the upper mantle are not required to explain the observed traveltime residuals.

Source region	Distance range (°)	Azimuth range (°)	No. of events
Japan	53-65	358-12	10
S. Sandwich Is.	92-97	191-194	5
Kuril	69-79	10-17	3
Mindanao	31-37	348-353	4
SE Indian Rise	28-33	211-222	2
New Zealand	40-44	115-119	2
Fiji	43-52	89-98	13
Kermadec	44-46	105-109	3

Table 3.1: Parameters associated with events from source regions recorded by the Musgrave Line stations for the dataset described by McQueen & Lambeck (1996). The regions used in this study are Japan, South Sandwich Islands, Kuril, Mindanao and South East Indian Rise. An average station anomaly is determined for events that occur in a particular source region.

A total of 87 nodes are used to parameterise the three interfaces of the inversion model, and the horizontal separation between adjacent nodes is 10 km in all cases. This distance is comparable to the station separation. The data do not justify the use of more interface parameters and the use of fewer nodes will compromise the ability of the method to resolve detailed structure. Figure 3.8 shows the model structure and ray paths after nine iterations of the inversion procedure, in which the data from all three source regions were inverted simultaneously. At this point, the objective function has decreased to less than 5% of its original value, corresponding to an RMS data misfit reduction of 78%. With further iterations, the objective function versus iteration curve began to achieve a plateau value. Stopping the iterative process after nine iterations is consistent with the convergence criterion described in the previous section. The improvements in data misfit are illustrated in the plots of the observed and model traveltime anomalies (Figure 3.9) for each source region. Ray coverage through the final model (Figure 3.8a) gives a qualitative indication of how well the model parameters are resolved by the data.

The model parameterisation used here cannot explicitly describe a fault, but if crustal scale faulting is assumed to be present, it will be represented within the model in a

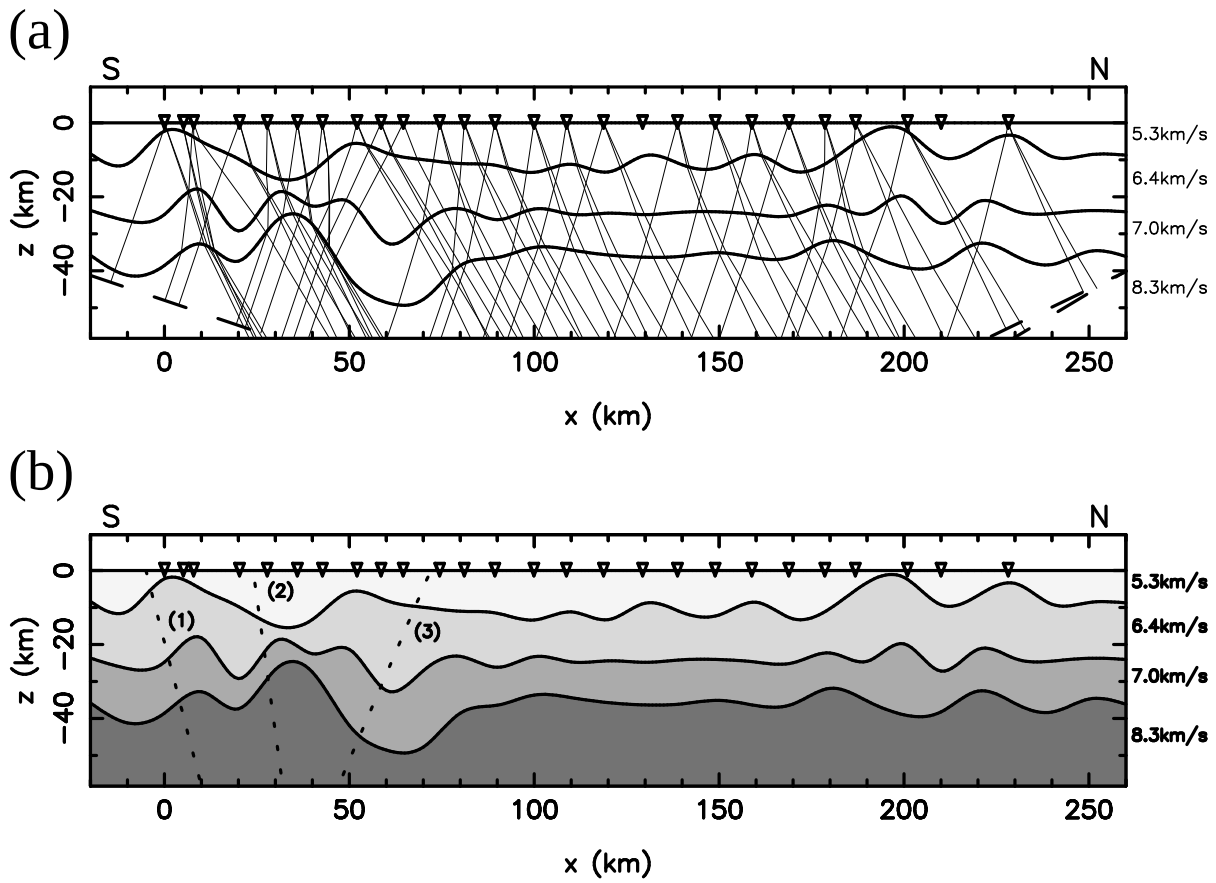

Figure 3.8: Inversion results for the Musgrave Line after nine iterations using data from three source regions: South Sandwich Islands, Kuril and Japan. (a) Ray coverage through the final model and (b) Final model with interpreted faults (dashed lines) corresponding to (1) Lindsay Lineament, (2) Wintiginna Lineament and (3) Mann Fault (see Figure 3.6).

smoothed form (i.e. locally steep interface gradients). The importance of crustal-scale faulting in this region has previously been emphasised in the interpretation of Lambeck & Burgess (1992). On Figure 3.8b, three inferred "fault structures" are superimposed. The *a priori* information used to help place these faults consists of the locations of known fault features on the surface (Figure 3.6) and their direction of dip. Consistent with the *a priori* information, the interpreted fault structures cut through the interfaces where the interface gradients are steepest. While the steep interface gradients between $x = 0$ and $x = 70$ km are consistent with the presence of several faults, this model gives no evidence of major crustal faulting in the region $90 \leq x \leq 170$ km.

Interpreted faults 1 and 2 (Figure 3.8b) correspond to the Lindsay and Wintiginna Lineaments respectively (see Figure 3.6), which are major magnetic lineaments (Lambeck & Burgess, 1992). From this solution, they both have a northerly dip of about 80°.

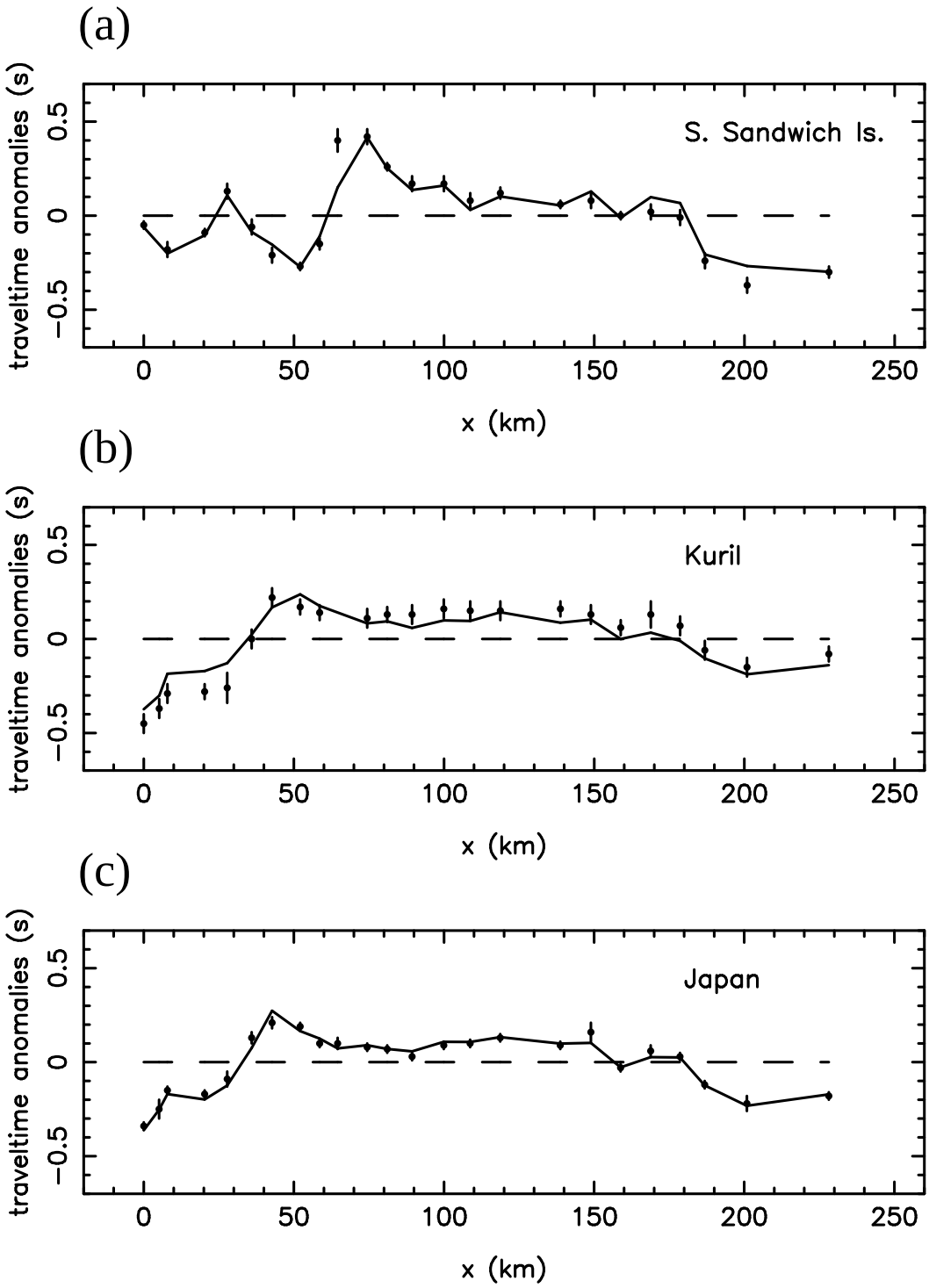

Figure 3.9: Comparisons between the traveltime anomalies of the starting model (dashed line), final model (solid line) after nine iterations (see Figure 3.8) and observed values from McQueen & Lambeck (1996) (dots with error bars) are given for each of the three source regions: (a) South Sandwich Islands, (b) Kuril, and (c) Japan.

Interpreted fault 3, with a southerly dip of about 70°, corresponds to the Mann Fault

(see Figure 3.6), a major thrust fault which, along with its eastern continuation the Ferdinand Fault, forms a large structure that extends across almost the entire width of the block (Lambeck & Burgess, 1992). Looking at Figure 3.8b, there is evident uncertainty associated with the positioning of the fault surfaces and estimation of the dip angles. For example, interpreted fault 3 could be horizontally translated some ±10 km or varied in dip by about ±10° and still cross-cut the same interface deflections. Nevertheless, given the limitations imposed by the inherent resolution of the seismic data and the restrictions of this simple parameterisation, the results are quite encouraging.

Two issues regarding the robustness of the solution shown in Figure 3.8 need to be addressed. First, only three incoming wavefronts have been used to constrain the model, and, of these, two have an angular separation of only 5°. By including data from other sources, model parameters will be better constrained. However, as the sources become further out of plane, the 2-D ray tracing scheme becomes less accurate. Figure 3.10 shows the result of including data from the Mindanao and South East Indian Rise source regions in the inversion. These sources are approximately 14° and 31° out of plane respectively. Figure 3.10a shows the ray coverage through the final model, which is greatly increased from that of Figure 3.8a. Figure 3.10b shows the final model with the same fault structure interpretation as given in Figure 3.8b. The most noticeable change in the model is a slight reduction in the amplitude of the interface deflections. Otherwise, there is little difference and the structural interpretation remains the same. The RMS data misfit reduction is about 62% in this case compared to 78% for Figure 3.8b, a decrease that reflects the apparent inconsistencies inherent in using out-of-plane sources in a 2-D algorithm.

Second, it was noted earlier that the Amadeus Basin deep reflection model (PBW01) is probably not a good representation of the velocity characteristics of the Musgrave Block. For instance, much of the exposed Musgrave Block consists of granulite grade facies that have a higher velocity than sedimentary rock. Although the average crustal velocity of the starting model used here was increased accordingly, it remains approximately 0.3 km/s less than that used by Lambeck & Burgess (1992) in their forward modelling of the same data. However, as demonstrated with the synthetic tests, teleseismic data do not constrain mean vertical structure. Tests with the velocity of the starting model increased by 0.3 km/s showed only minor changes in the amplitude of the interface deflections, with the top interface nearly intersecting the surface at some points and the undulations in the bottom interface increasing slightly. The increased amplitude of interface topography

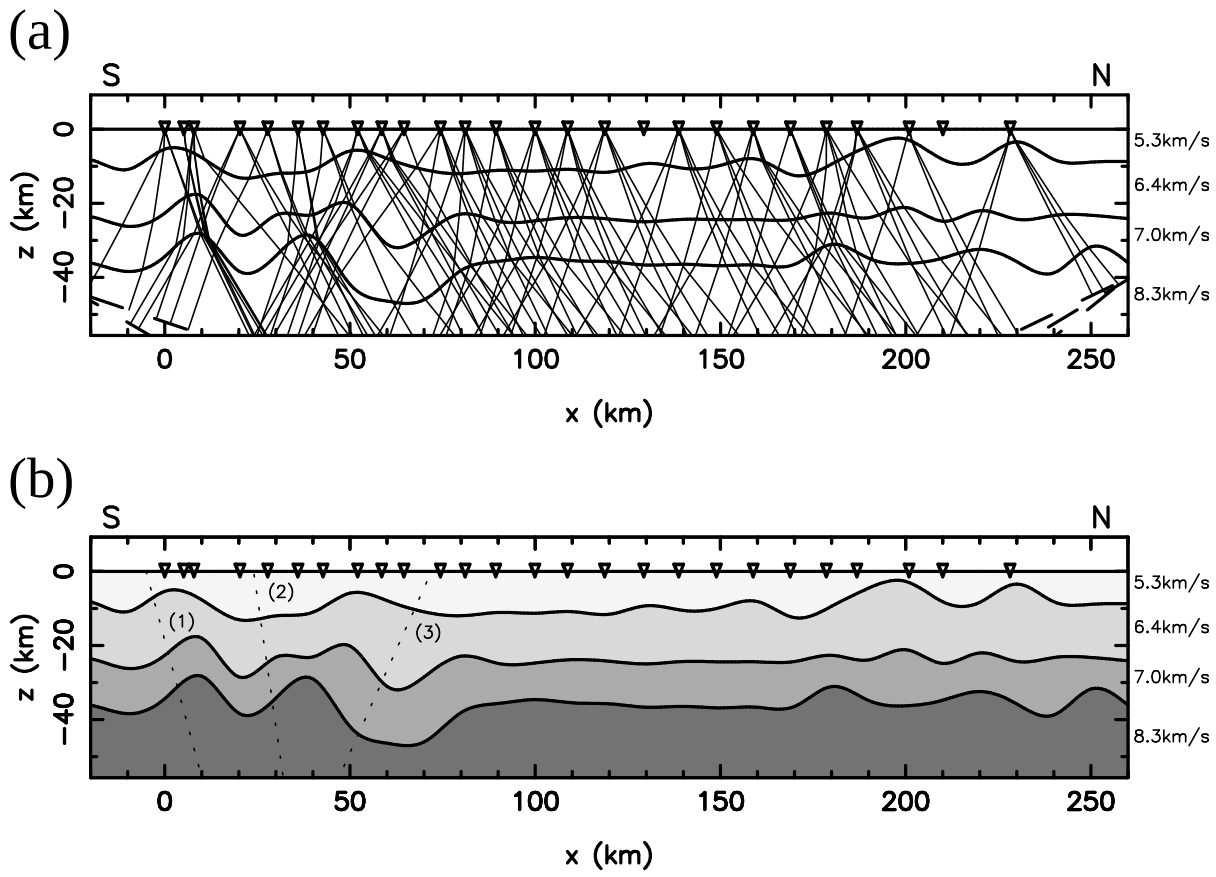

Figure 3.10: Inversion results for the Musgrave Line after six iterations using data (McQueen & Lambeck, 1996) from five source regions (south Sandwich Islands, Kuril, Mindanao and South East Indian Rise). (a) Ray coverage through final model, and (b) final model with the same interpreted faults (dashed lines) as the three source solution model shown in Figure 3.8.

is to be expected in this test since more variation in interface geometry is required to compensate for a decreased velocity ratio across an interface. The important point is that the basic horizontal variations in structure are relatively insensitive to the mean vertical structure assumed in the model. Similarly, increasing the depths of the interfaces by between 4 and 7 km does not result in any marked changes in interface geometry.

The robustness of the final solution (Figure 3.10) can be examined more closely. One option is to use linear estimates of *a posteriori* model covariance and correlation (Section 2.4), but they are defined in terms of the Fréchet matrix $\mathbf{G}$, which is not calculated by the inversion method used. Besides, the non-linear nature of the inversion and the complex structure present in the solution model may result in poor estimates of these quantities even if $\mathbf{G}$ was available. Instead, I choose to use the other approach outlined in Section 2.4, which attempts to reconstruct a known structure using a synthetic dataset based on

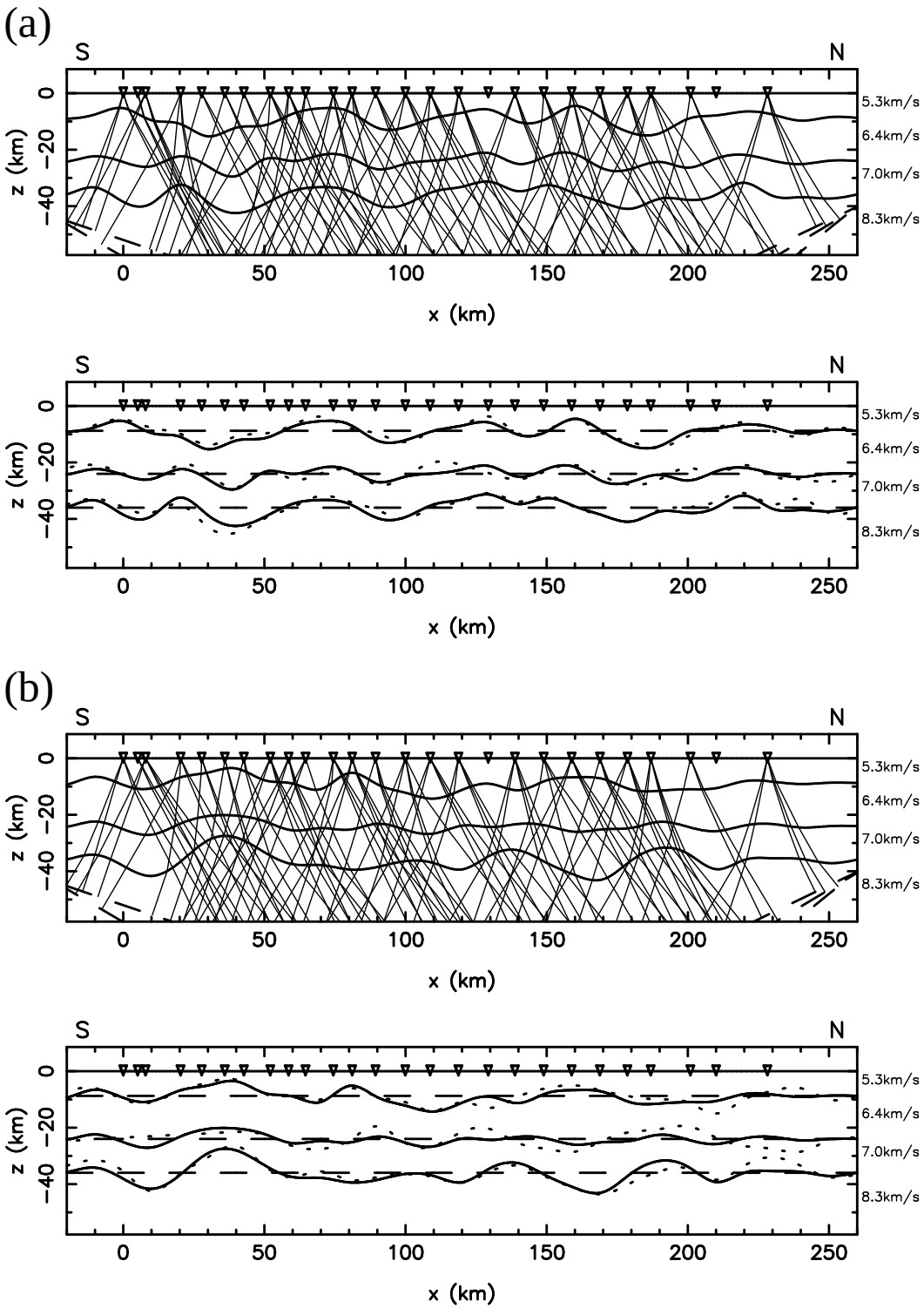

Figure 3.11: Two synthetic tests designed to analyse the robustness of the solution given in Figure 3.10. Ray diagrams show paths through the recovered structure. Dashed lines show the initial model, dotted lines the true model and solid lines the reconstruction. The synthetic models in (a) and (b) were chosen to be quite different in order to illustrate the effect of different ray path geometries on the reconstruction.

the same source-receiver geometry as the real dataset. Figure 3.11 shows the results of two such experiments in which the synthetic datasets are corrupted by Gaussian noise with a 40 ms standard deviation, consistent with the picking accuracy of the Musgrave Line dataset. The RMS data misfit reduction is about 80% for both inversion solutions, and the test structures are generally well recovered, except in regions of poor ray coverage such as $210 \leq x \leq 260$ km. The bottom and top interfaces tend to be more accurately recovered than the middle interface, especially in Figure 3.11b. Smearing effects can be seen to some extent in the middle interface. In particular, there are regions where the middle interface mimics the geometry of the lower interface in places where the structure of the two interfaces actually differ (e.g. $180 \leq x \leq 220$ km in Figure 3.11a and $-20 \leq x \leq 30$ in Figure 3.11b).

3.5 Discussion

So far, it has been shown that the interface inversion method presented in this chapter is capable of explaining observed traveltime residuals in terms of interface depth variation rather than continuous velocity variation, as is usually the case for teleseismic traveltime inversion. With synthetic data, the target structure was known, so it was straight forward to see whether the inversion result was accurate or not. Although resolution estimates from synthetic reconstructions based on identical source-receiver geometries can contribute valuable information on solution robustness, there is usually no independent check when real data is used. Since the observed dataset used here has been analysed previously, it is possible to compare our solution model with those determined by other authors using the same data but different methods. Figure 3.12 shows a comparison between three models produced by different analyses of the same dataset, with Figure 3.12c being the solution determined in the previous section.

Lambeck & Burgess (1992) applied forward modelling to the Musgrave Line dataset to determine crustal structure that is consistent with the data. Their model (Figure 3.12a) is defined by relatively few linear interface segments and contains upper crust, lower crust, mantle and a sediment layer, all with fixed velocities. The modelling process they use: (i) allows for laterally discontinuous interfaces and under/overthrusting of crust, (ii) traces rays through the 2-D structure in three dimensions and allows for diffractions, and (iii) attempts to fit the model to data from all available source regions (Table 3.1). The most

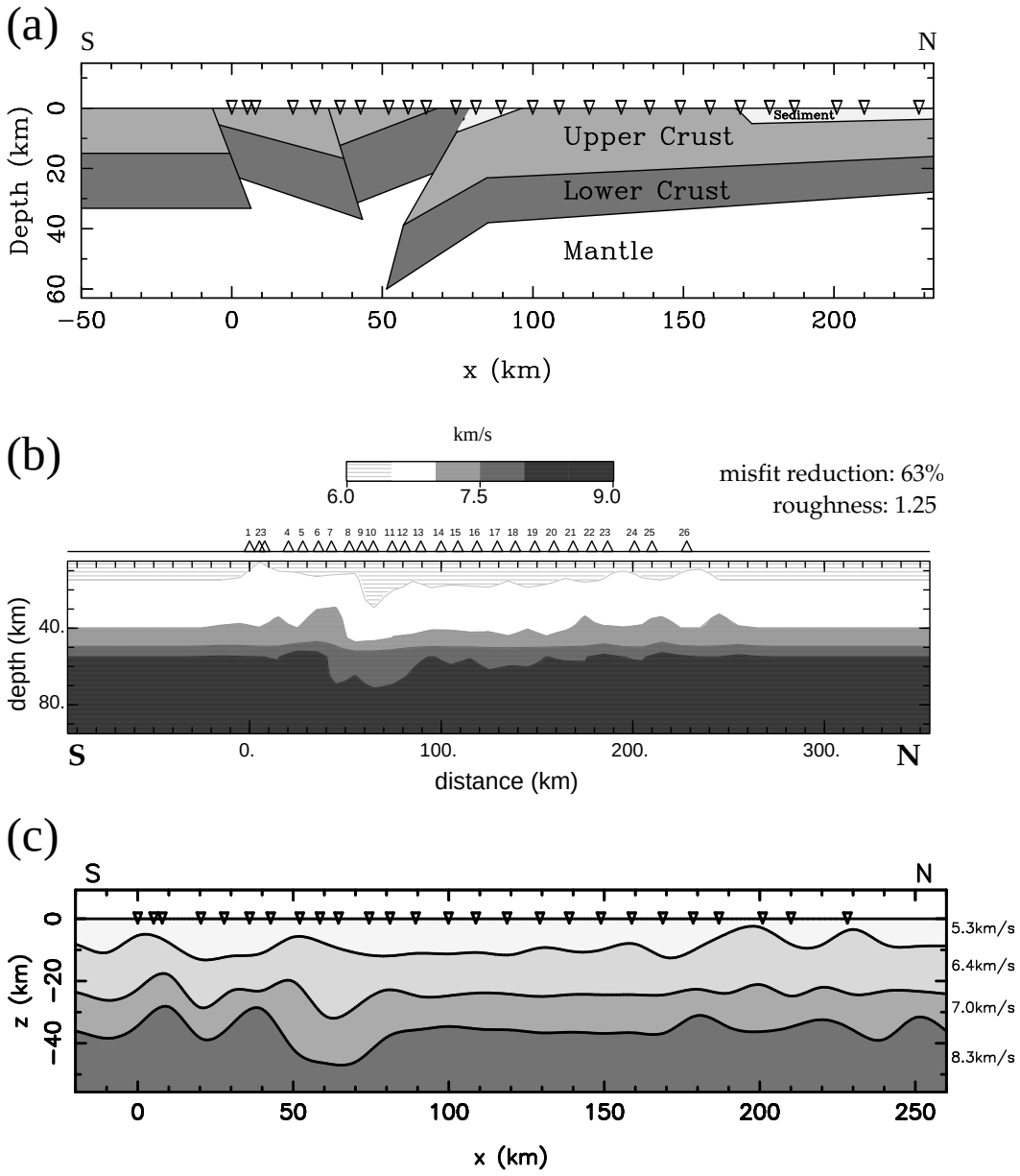

Figure 3.12: Three models derived from the Musgrave Line dataset using different methods. (a) Crustal structure obtained by forward modelling (after Lambeck & Burgess, 1992), (b) contours of velocity for the model obtained by inversion for slowness (from McQueen & Lambeck, 1996), and (c) solution derived in this thesis by inversion for interface structure (same as Figure 3.10b). Note the differences in scale between (a), (b) and (c).

significant feature of their model is a steep southerly dipping thrust fault, corresponding to the Mann Fault, that results in a wedge of crust penetrating deeply (20-30 km) into the mantle. The secondary features of the model are two steep (even steeper than the main fault) northerly dipping faults corresponding to the Lindsay and Wintiginna Lineaments. Comparing Figure 3.12a and Figure 3.12c, the strong lateral variation in the distance

range $0 \leq x \leq 80$ km of Figure 3.12c is consistent with a smoothed approximation to the fault structures of Figure 3.12a.

McQueen & Lambeck (1996) applied inverse modelling techniques to the same dataset to image the crustal structure. The inversion in this case is for slowness rather than interface structure, with the model parameterised using a regular grid of constant-slowness blocks. The slowness model produced by their inversion strongly indicates the presence of a southerly dipping fault in the approximate location of the Mann Fault. When this slowness is superimposed onto a continuous 1-D background velocity model, a velocity section is produced (see Figure 3.12b). A direct comparison between this and Figure 3.12c is not straightforward because McQueen & Lambeck's solution: (i) allows lateral structure to occur as deep as 90 km, (ii) uses a different background model for the mean vertical structure, (iii) traces rays through the 2-D structure in three dimensions, and (iv) has lateral structure indicated by isovelocity contours. However, the two solutions, one based on interface inversion, the other based on velocity inversion, are quite similar in terms of lateral structure, with both models indicating a large low-velocity trough beneath the Mann Fault, with significant structure to the south but relatively minor structure to the north ($x > 90$ km). Both inversions also suggest zones of higher velocity beneath stations 1-3 and station 26; these features correspond to known positive gravity lineaments. In addition, note that the RMS data misfit reductions are almost identical for the two models: 63% for Figure 3.12b and 62% for Figure 3.12c. The similarity of the two interpretations demonstrates that inversion for velocity and inversion for interface structure are alternative but equally valid ways of treating the data.

The robustness of the interface inversion solution (Figure 3.12c) was examined in the previous section using a synthetic reconstruction approach. The two models that were used (Figure 3.11a and b) differ significantly in their interface geometries and, as a result, the ray paths also differ significantly. The fact that both reconstructions, which use the same source-receiver geometry as the Musgrave Line data, are quite accurate with different ray path geometries implies that the interface inversion solution (Figure 3.12c) is robust.

Another factor that should be considered with regard to the inversion method is the likely presence of lateral variations in velocity within a layer. In a solution model, these will manifest as errors in interface position. Figure 3.12 shows, however, that the structure can be adequately represented either by variation of velocity or by deflection of interfaces.

These two possibilities clearly represent the end members of a spectrum of possible models which include components of both velocity variation and interface deflection. Using either a velocity only or an interface only model means that the actual structure will be approximated in the solution. If a velocity model is used, interface structure will be mapped into velocity variation. Conversely, if an interface model is used, velocity variation will be mapped into interface structure. For example, in interpreting a velocity model, regions of high velocity could be caused by upward displacement of an interface separating low velocity over high; in interpreting an interface model, interfaces displaced upwards could be caused by locally high velocities in the layer above the interface. The results from the two different inversions of the Musgrave Line data show that teleseismic data generally does not contain sufficient information to discriminate between alternative models that fall within this spectrum.

3.6 Summary

Inversion for interface geometry using teleseismic traveltime residuals represents an interesting and viable alternative to the usual approach of inverting for velocity structure. A relatively simple 2-D interface inversion method, which assumes constant velocity layers separated by smooth interfaces, has been used to test this claim. A shooting method was used to solve the forward problem of traveltime determination and a conjugate gradient method was used to solve the inverse problem of minimising the traveltime residuals. Synthetic tests showed that accurate results could be produced in the presence of realistic noise levels, and that lateral structure was recoverable even if layer velocities and initial interface positions were poorly chosen. The application of the method to data collected in central Australia produced a solution that is consistent with previously published solutions that used the same data but different analysis methods. The comparison illustrates in particular the general equivalence of the two alternative methods of representing structure within near-surface earth models: (i) by using a discretised, continuously variable velocity field, and (ii) by using constant velocity layers separated by variable depth interfaces. The solution produced by interface inversion is shown to be robust by performing two synthetic tests using known models and the same source-receiver geometry as the Musgrave Line dataset; quite accurate reconstructions are achieved in both cases. Using teleseismic data to constrain interface geometry has much potential in regions of com-

plex lithospheric structure. More conventional methods of resolving interface structure, such as inversion of wide-angle data, would have great difficulty in imaging the complex interface structures determined by inversion of the Musgrave Line teleseismic dataset.

Chapter 4

Method for the Inversion of Wide-Angle Traveltimes for 3-D Layered Crustal Structure

4.1 Introduction

In recent times, wide-angle seismic data (which includes both reflection and refraction information) has been used extensively to map the earth's crustal structure, generally using traveltimes rather than other components of seismic waves such as amplitudes or waveforms. Interpretation methods for this type of data are often based on the principles of tomographic reconstruction. As described in Chapter 2, the procedure typically involves a forward step of calculating theoretical data values by line integration through a structure defined by a set of model parameters, and an inverse step which manipulates these parameter values to improve the fit between theoretical and observed data. In this chapter, an original tomographic inversion method is described and tested with synthetic wide-angle seismic traveltime data.

To date, most wide-angle seismic traveltime tomography has been 2-D and has included inversion for velocity parameters, interface parameters or both, using refraction and/or reflection traveltimes. Lutter et al. (1990) invert refraction traveltimes for velocity, White (1989) inverts refraction traveltimes for interface depth and velocity, Carroll & Beresford (1996) invert reflection traveltimes for velocity, Lutter & Nowack (1990) invert reflection traveltimes for interface depth, and Bishop et al. (1985), Farra & Madariaga (1988) and

Williamson (1990) use different approaches to invert reflection traveltimes for velocity and interface depth. Zelt & Smith (1992) use both refraction and reflection traveltimes to constrain velocity and depth parameters. Methods that invert for both velocity and depth parameters can have difficulty in producing well-constrained solutions due to the possibility of trade-offs between the two parameter types. Simultaneously using both refraction and reflection information can help to reduce the non-uniqueness of the result (Wang & Braile, 1996).

The 3-D wide-angle tomography problem has not been as widely investigated as its 2-D counterpart, mainly due to the increased cost and time required to collect the data and the added complexities at each step of the reconstruction process. However, it deserves consideration when the assumption of 2-D structure is not valid or when an in-line array of sources and receivers is not possible. 3-D wide-angle inversion methods and applications have been documented by several authors; Hole (1992) and Zelt & Barton (1998) invert first arrivals for velocity, Hole et al. (1992) invert first arrivals for interface geometry, Riahi et al. (1997) invert wide-angle reflection traveltimes for interface geometry, and Chiu et al. (1986) invert reflection traveltimes for both interface geometry and layer velocity (assumed constant). Inversion for both laterally varying velocity and interface geometry using wide-angle data has been performed by Zelt et al. (1996), although they used a layer stripping approach and did not simultaneously invert refraction and reflection traveltimes. More recently, Zelt et al. (1999) simultaneously invert reflection and refraction data for both laterally varying velocity and interface structure.

In general, the potential for non-uniqueness in 3-D inversions is greater than in 2-D inversions, since the data/model parameter ratio is often lower, and uniform sampling of the subsurface by the data is much more difficult to achieve. For these reasons, Zelt & Zelt (1998) conclude that, unless a dense grid of shots and receivers is used, it is hard to justify a fully 3-D experiment over a network of 2-D profiles, even if 3-D inhomogeneities are present. However, the nature of the survey region and/or logistical restrictions may leave a 3-D survey as the only practicable option. For example, surveys that involve only marine shots and land-based receivers may provide much more information if ray paths cover a range of azimuths.

This chapter introduces a method for the determination of 3-D crustal structure from wide-angle seismic traveltimes using the principles of tomographic reconstruction. The method is applied to models consisting of one or more layers overlying a half-space sep-

arated by smooth interfaces. The velocity within each layer varies linearly with depth. Each interface is described by a mosaic of bicubic B-spline surface patches which have the property of being C_2 continuous across suture. Both the velocity parameters and interface depths are varied in the reconstruction process. Ray paths within layers consist of circular arc segments whose trajectory and traveltime are computed from analytic expressions. The two-point problem of determining the source-receiver ray paths of specific phases is solved using a shooting method, which uses simple geometric considerations to iteratively adjust the ray projection vector at the source so that the emerging ray more accurately targets the receiver. If multiple two-point paths are found for a single phase, the path with minimum traveltime is used in the inversion. The inverse problem requires the adjustment of model parameter values (velocities and layer depths) to minimise an objective function that contains a data residual term and a regularisation term. A subspace inversion method that only requires the solution of a relatively small system of linear equations and naturally deals with different parameter classes is used. All refraction and reflection data are used in a simultaneous inversion for all model parameters. The seismic tomography problem is inherently non-linear, so the forward and inverse steps are performed iteratively.

Apart from the obvious difference in source location between teleseismic data and wide-angle data, the method presented here differs from the method presented in Chapter 3 in a number of ways. (i) It is 3-D so that interfaces are represented by surfaces rather than curves, (ii) B-splines are used to describe interfaces; these are more flexible than natural splines as they are not forced to pass through node points, can be multi-valued and are locally controlled, (iii) velocity is assumed to vary linearly with depth rather than being constant, (iv) velocity parameters are also inverted for; wide-angle data can constrain velocity and depth parameters but teleseismic data only constrains lateral variations in structure, and (v) a subspace method is used to perform the inversion because it deals with multiple parameter classes more effectively than the conjugate gradient method. It is, however, the intention of both methods to interpret observed traveltimes in terms of layered crustal/lithospheric structure.

Following the description of the wide-angle method, a number of synthetic tests are carried out to assess the effectiveness of the method. Several of these tests are performed using a 2-D version of the algorithm, which is effectively identical to the 3-D method except for the difference in spatial dimensions. The 2-D method is used in the synthetic

tests because it is easier to visualise rays and interfaces in 2-D and allows some of the basic characteristics of the method to be demonstrated more efficiently. The synthetic tests analyse the effectiveness of the method in the presence of data noise, different source-receiver configurations, damping and poor initial model estimates. I also investigate the effects of over, under and non-uniform parameterisation, the ability of the method to resolve complex structures such as layer pinchouts and its usefulness in a complex 3-D situation inspired by subduction zone models. Model resolution and *a priori* model covariance are calculated for several of the synthetic inversions assuming a locally linear relationship between the data and model parameters at the solution point. The aim here is to determine whether these quantities may be used to assess the quality of the solution for this class of non-linear inverse problem.

4.2 Method

4.2.1 Model Parameterisation

In choosing a suitable model parameterisation, the criteria included (i) ability to represent geologically realistic structure, (ii) satisfying the data using a minimal number of model parameters, (iii) ability to generate refraction and reflection arrivals, (iv) compatibility with methods used to solve the forward and inverse steps, and (v) flexibility to allow for non-uniform node spacing (related to ii). To these ends, the model parameterisation I employ is for a 3-D layered velocity structure described as follows.

The model is defined by a set of p layers (with the bottom layer being a half-space) separated by $p-1$ smooth continuous interfaces. Within a layer, velocity v varies linearly with depth:

$$v(z) = v_0 - kz \tag{4.1}$$

where z is the vertical coordinate (up is positive), $v_0 = v(0)$ and k is the velocity gradient. Each interface is described by a mosaic of uniform bicubic B-spline surface patches in parametric form. Given a set of control vertices $\mathbf{p}_{i,j} = (x_{i,j}, y_{i,j}, z_{i,j})$ where $i = 1, \ldots, m$ and $j = 1, \ldots, n$, the B-spline for the ij^{th} surface patch ($i = 2, \ldots, m-2; j = 2, \ldots, n-2$) is:

$$\mathbf{B}_{i,j}(u, v) = \sum_{k=-1}^{2} \sum_{l=-1}^{2} b_k(u) b_l(v) \mathbf{p}_{i+k,j+l} \tag{4.2}$$

so that any point on a surface patch is a function of two independent parameters u ($0 \leq u \leq 1$) and v ($0 \leq v \leq 1$). The weighting factors $\{b_i\}$ are the uniform cubic B-spline basis functions which are defined as follows (Bartels et al., 1987):

$$\left.\begin{aligned} b_{-1}(u) &= \tfrac{1}{6}(1-u)^3 \\ b_0(u) &= \tfrac{1}{6}(4-6u^2+3u^3) \\ b_1(u) &= \tfrac{1}{6}(1+3u+3u^2-3u^3) \\ b_2(u) &= \tfrac{1}{6}u^3 \end{aligned}\right\} \tag{4.3}$$

A single surface patch and its control vertices are shown in Figure 4.1a. The spline formulation of Equation 4.2 means that the control vertices may lie on a grid with irregular spacing (e.g. Figure 4.1b) and, by virtue of its parametric form, the surface that is constructed need not be a single-valued function of depth (e.g. Figure 4.1c). Other useful properties of Equation 4.2 are that the control vertices do not necessarily lie on the surface, and that the surface is everywhere continuous in curvature.

Equation 4.2 defines $(m-3)(n-3)$ surface patches, so the surface is not defined in regions adjacent to the boundary nodes (see Figure 4.1d). The boundary patches are constructed by defining a set of perimeter phantom vertices for $i = 0$ and $m+1$ and $j = 0$ and $n+1$ using the condition that the second partial derivative (with respect to the parametric direction across the boundary) is zero at the endpoint of each boundary curve segment. Thus, the phantom vertices are defined by (Barsky, 1982):

$$\left.\begin{aligned} \mathbf{p}_{0,0} &= 4\mathbf{p}_{1,1} - 2\mathbf{p}_{1,2} - 2\mathbf{p}_{2,1} + \mathbf{p}_{2,2} \\ \mathbf{p}_{0,j} &= 2\mathbf{p}_{i,j} - \mathbf{p}_{2,j} \qquad j = 1,\ldots,n \\ \mathbf{p}_{0,n+1} &= 4\mathbf{p}_{1,n} - 2\mathbf{p}_{1,n-1} - 2\mathbf{p}_{2,n} + \mathbf{p}_{2,n-1} \\ \mathbf{p}_{i,n+1} &= 2\mathbf{p}_{i,n} - \mathbf{p}_{i,n-1} \qquad i = 1,\ldots,m \\ \mathbf{p}_{m+1,n+1} &= 4\mathbf{p}_{m,n} - 2\mathbf{p}_{m,n-1} - 2\mathbf{p}_{m-1,n} + \mathbf{p}_{m-1,n-1} \\ \mathbf{p}_{m+1,j} &= 2\mathbf{p}_{m,j} - \mathbf{p}_{m-1,j} \qquad j = 1,\ldots,n \\ \mathbf{p}_{m+1,0} &= 4\mathbf{p}_{m,1} - 2\mathbf{p}_{m,2} - 2\mathbf{p}_{m-1,1} + \mathbf{p}_{m-1,2} \\ \mathbf{p}_{i,0} &= 2\mathbf{p}_{i,1} - \mathbf{p}_{i,2} \qquad i = 1,\ldots,m \end{aligned}\right\} \tag{4.4}$$

and the entire surface is described by Equation 4.2 with $i = 1,\ldots,m-1; j = 1,\ldots,n-1$ patches. The phantom vertices are used only in the definition of the boundary patches and are *not* inverted for.

The model parameterisation method described above is quite general with respect to interface geometry, but velocity is assumed to be laterally homogeneous within a layer.

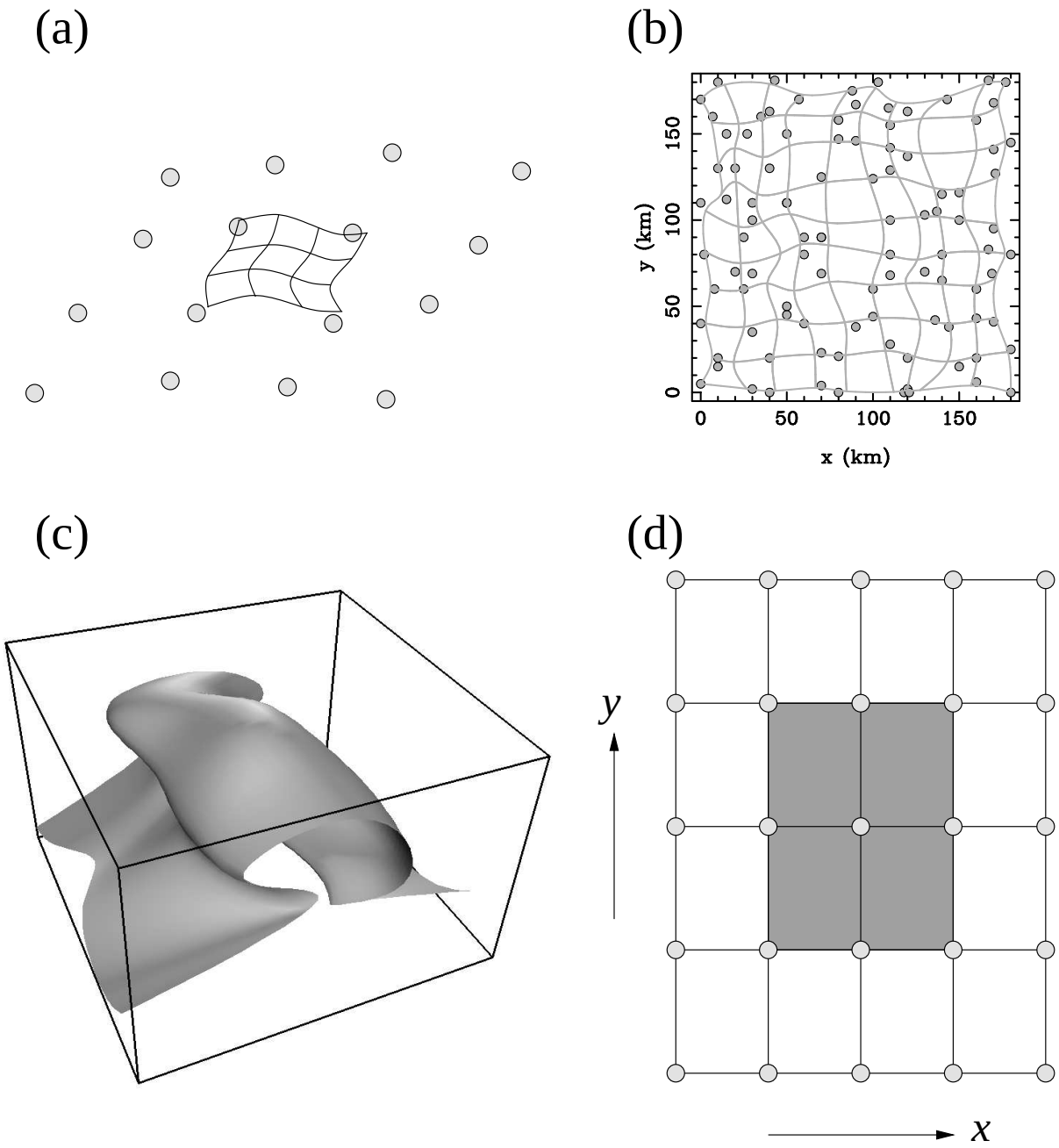

Figure 4.1: B-spline properties: (a) 16 control vertices (shaded circles) are required to define a single surface patch (solid lines), which need not interpolate any of the vertices. (b) View of a B-spline surface looking down the z-axis. Control vertices need not lie on a rectangular grid. Patch boundaries are indicated by grey lines. (c) Multi-valued B-spline surface defined by 100 control vertices. The advantage of a parametric description is that the surface may fold back on itself. (d) Plan view of a rectangular grid of 5×5 control vertices. With no boundary conditions specified, the surface is only defined by the grey region. The use of phantom vertices will allow the surface to be defined over 16 rectangles.

Not allowing lateral structure within a layer means that a class of geologically realistic models cannot be explored. However, gross lateral variations within a single layer may be

represented by the inclusion of additional internal interfaces which subdivide the layer. In practice, the method is sufficient if it can adequately satisfy the data with a geologically plausible structure.

4.2.2 Ray Tracing

Methods for finding source-receiver traveltimes in 3-D laterally varying structures (see Section 2.2) include ray tracing, numerical solution of the eikonal equation and network/graph theory. Wavefront tracking schemes based on the numerical solution of the eikonal equation are probably the most commonly used to solve the forward step of the 3-D wide-angle tomography problem. Here, traveltimes and ray paths are determined using ray tracing. The ray tracing method is well suited to our choice of model parameterisation because the ray path in each layer is defined by an analytic expression and the number of model parameters is not large compared with conventional velocity inversion techniques. Of the two principle forms of two-point ray tracing - shooting and bending, shooting is chosen because it tends to be more robust in complex media that contain velocity discontinuities (Sambridge, 1990). The initial value problem essentially has two parts: determining the path of a ray in a layer and finding the new trajectory of the ray after interaction with an interface.

If the wave speed in a continuous velocity medium is described by $v(x, y, z)$, then a ray path connecting two points A and B is one which extremizes the traveltime integral $t = \int_A^B 1/v(x, y, z)\mathrm{d}l$ where $\mathrm{d}l$ is differential path length. Using the Euler-Lagrange equation from the calculus of variations, the equation of the ray path which extremizes the traveltime integral when v is described by Equation 4.1 is given (see Appendix B for a derivation) in parametric form by:

$$\mathbf{x} = \frac{v(z_o)}{k}\left[\frac{a_o(c-c_o)}{1-{c_o}^2}, \frac{b_o(c-c_o)}{1-{c_o}^2}, 1-\sqrt{\frac{1-c^2}{1-{c_o}^2}}\right] + \mathbf{x}_o \tag{4.5}$$

where $\mathbf{x}_o$ is the origin of the ray segment, $[a, b, c]$ is a unit vector tangent to the ray path, and $[a_o, b_o, c_o]$ is a unit vector tangent to the ray path at $\mathbf{x}_o$. Equation 4.5 is the parametric equation of a circular arc in terms of the z-component of the unit direction vector c. It is equivalent to the expression given in Equation 2.11 for 2-D structure except that by using c instead of the inclination angle i (where $\cos i = c$), the use of transcendental functions is avoided. Any ray path from a source to a receiver in this model will consist of one or

more circular arc segments. The traveltime to a point on the current ray segment is given by:

$$t = \frac{1}{2k} \ln \left[\left(\frac{1+c}{1-c} \right) \left(\frac{1-c_o}{1+c_o} \right) \right] + t_o \tag{4.6}$$

where t_o is the traveltime from the source to $\mathbf{x}_o$.

The point of intersection between a ray and an interface can be found by equating (4.2) with (4.5) to give:

$$\left.\begin{aligned} f_1(u,v,c) &= \sum_{k=-1}^{2} \sum_{l=-1}^{2} b_k(u) b_l(v) x_{k,l} - \frac{a_o v(z_o)(c-c_o)}{k(1-c_o^2)} - x_o = 0 \\ f_2(u,v,c) &= \sum_{k=-1}^{2} \sum_{l=-1}^{2} b_k(u) b_l(v) y_{k,l} - \frac{b_o v(z_o)(c-c_o)}{k(1-c_o^2)} - y_o = 0 \\ f_3(u,v,c) &= \sum_{k=-1}^{2} \sum_{l=-1}^{2} b_k(u) b_l(v) z_{k,l} - \frac{v(z_o)}{k} \left(1 - \sqrt{\frac{1-c^2}{1-c_o^2}} \right) - z_o = 0 \end{aligned}\right\} \tag{4.7}$$

which is a system of three non-linear equations for three unknowns u, v and c. Note that the i and j subscripts have been dropped assuming that the relevant surface patch is identified. Equation 4.7 is solved using the generalised Newton method in which a solution estimate (u_i, v_i, c_i) is iteratively improved by:

$$\left.\begin{aligned} u_{i+1} &= u_i + \Delta u_i \\ v_{i+1} &= v_i + \Delta v_i \\ c_{i+1} &= c_i + \Delta c_i \end{aligned}\right\} \tag{4.8}$$

where

$$\begin{bmatrix} \frac{\partial f_1}{\partial u} & \frac{\partial f_1}{\partial v} & \frac{\partial f_1}{\partial c} \\ \frac{\partial f_2}{\partial u} & \frac{\partial f_2}{\partial v} & \frac{\partial f_2}{\partial c} \\ \frac{\partial f_3}{\partial u} & \frac{\partial f_3}{\partial v} & \frac{\partial f_3}{\partial c} \end{bmatrix}_i \begin{bmatrix} \Delta u_i \\ \Delta v_i \\ \Delta c_i \end{bmatrix} = \begin{bmatrix} -f_1(u_i, v_i, c_i) \\ -f_2(u_i, v_i, c_i) \\ -f_3(u_i, v_i, c_i) \end{bmatrix} \tag{4.9}$$

The iterative process is stopped when the distance between the end of the ray and the point on the interface is less than a specified value (5 cm in all of the following calculations). The initial guess (u_o, v_o, c_o) required by the Newton method is determined by approximating each surface patch with a mosaic of piecewise triangular plates and finding the point at which the ray intersects the relevant planar segment.

To approximate a surface patch with triangular segments, the patch is sampled on a rectangular grid in u and v to produce a set of $m_t \times n_t$ points $\{\mathbf{q}_{i,j}\}$ where typically

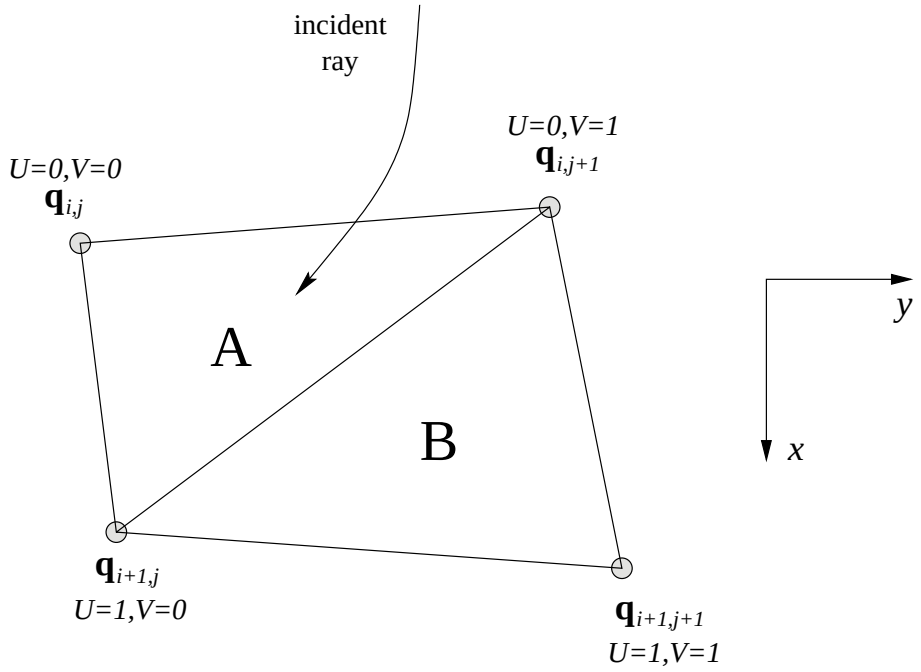

Figure 4.2: Two triangular plates defined from four samples of a B-spline patch as used for an initial estimate of the intersection point between a ray and surface patch.

$m_t = n_t = 3$. Each set of four nodes produces two triangular plates, as shown in Figure 4.2. Using U and V ($U, V \in [0, 1]$) as local coordinates of u and v on each triangular segment (see Figure 4.2), the parametric equations describing the patches can be formulated. For patch A:

$$\mathbf{x} = \mathbf{q}_{i,j} + (\mathbf{q}_{i+1,j} - \mathbf{q}_{i,j})U + (\mathbf{q}_{i,j+1} - \mathbf{q}_{i,j})V \tag{4.10}$$

and for patch B,

$$\mathbf{x} = \mathbf{q}_{i+1,j+1} + (\mathbf{q}_{i,j+1} - \mathbf{q}_{i+1,j+1})(1 - U) + (\mathbf{q}_{i+1,j} - \mathbf{q}_{i+1,j+1})(1 - V) \tag{4.11}$$

where patch A is defined by the region $U + V \leq 1$ and patch B by the region $U + V \geq 1$. Equating either (4.10) or (4.11) with (4.5) produces a system of three equations with three unknowns U, V and c. One of the equations will be nonlinear since the circular arc intersects the plane twice, but the system can easily be solved analytically; of the two possible solutions, the correct one minimises the traveltime. The initial guess required by Equation 4.9 will be then be given by $u_0 = u^q_{i,j} + U/(m_t - 1)$, $v_0 = v^q_{i,j} + V/(n_t - 1)$, $c_0 = c$, where $u^q_{i,j}$ and $v^q_{i,j}$ are the values of u and v at $\mathbf{q}_{i,j}$, the local origin point of triangle A (see Figure 4.2).

To determine the new direction of the ray after it intersects the interface, Snell's Law is used. At the point of intersection, let $\mathbf{w}_i$, $\mathbf{w}_r$ and $\mathbf{w}_t$ define the unit tangent vectors to

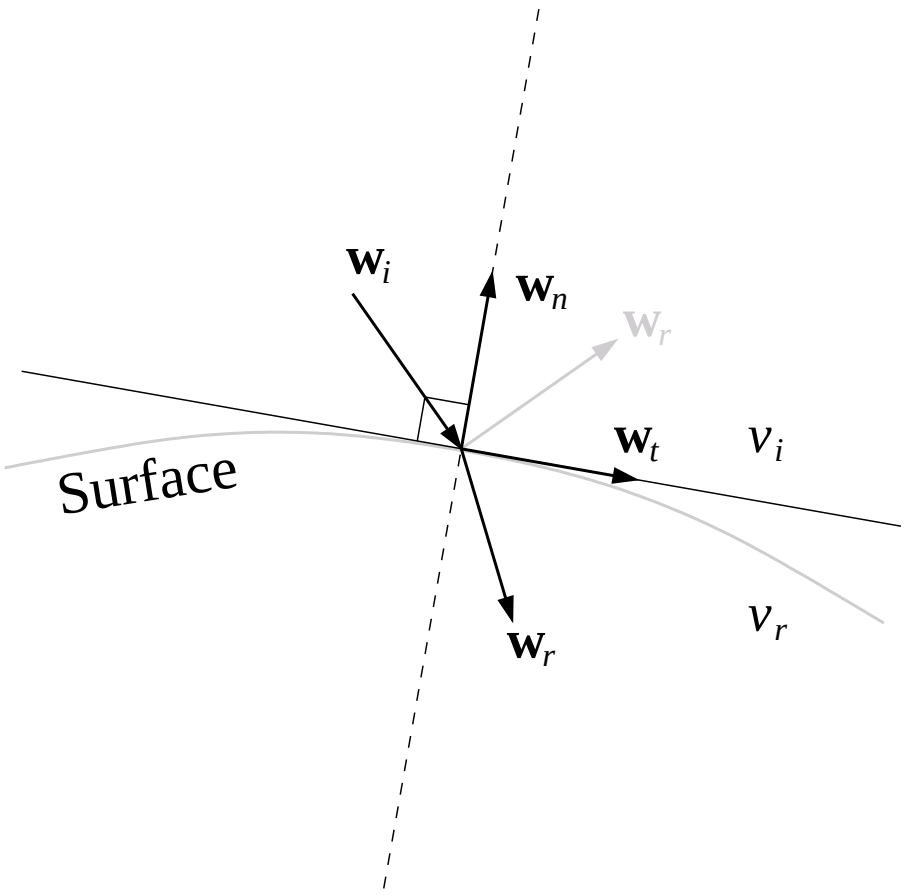

Figure 4.3: Definition of variables used in Equation 4.12 and 4.13.

the incident ray, refracted/reflected ray and tangent to the surface in the plane defined by $\mathbf{w}_i$ and $\mathbf{w}_n$ (see Figure 4.3). $\mathbf{w}_n$ is the unit normal vector to the surface at the point of intersection. Application of Snell's law and the fact that $\mathbf{w}_r$ is a unit vector and must lie in the same plane as $\mathbf{w}_i$ and $\mathbf{w}_t$ yields:

$$\left.\begin{aligned} &\frac{\mathbf{w}_r \cdot \mathbf{w}_t}{v_r} = \frac{\mathbf{w}_i \cdot \mathbf{w}_t}{v_i} \\ &|\mathbf{w}_r| = 1 \\ &(\mathbf{w}_i \times \mathbf{w}_t) \cdot \mathbf{w}_r = 0 \end{aligned}\right\} \tag{4.12}$$

which can be solved analytically for the three components of $\mathbf{w}_r$. Of the two possible solutions to Equation 4.12, the refracted ray is the one which maximises $\mathbf{w}_i \cdot \mathbf{w}_r$. Equation 4.12 can be used to find the change in direction of refracted or reflected ($v_r = v_i$) rays, although in the latter case, since less calculation is required to determine $\mathbf{w}_n$ than $\mathbf{w}_t$, the

following system can instead be solved:

$$\left.\begin{aligned} &\mathbf{w}_r \cdot \mathbf{w}_n = -\mathbf{w}_i \cdot \mathbf{w}_n \\ &|\mathbf{w}_r| = 1 \\ &(\mathbf{w}_i \times \mathbf{w}_n) \cdot \mathbf{w}_r = 0 \end{aligned}\right\} \tag{4.13}$$

where again the required solution is the one which maximises $\mathbf{w}_i \cdot \mathbf{w}_r$.

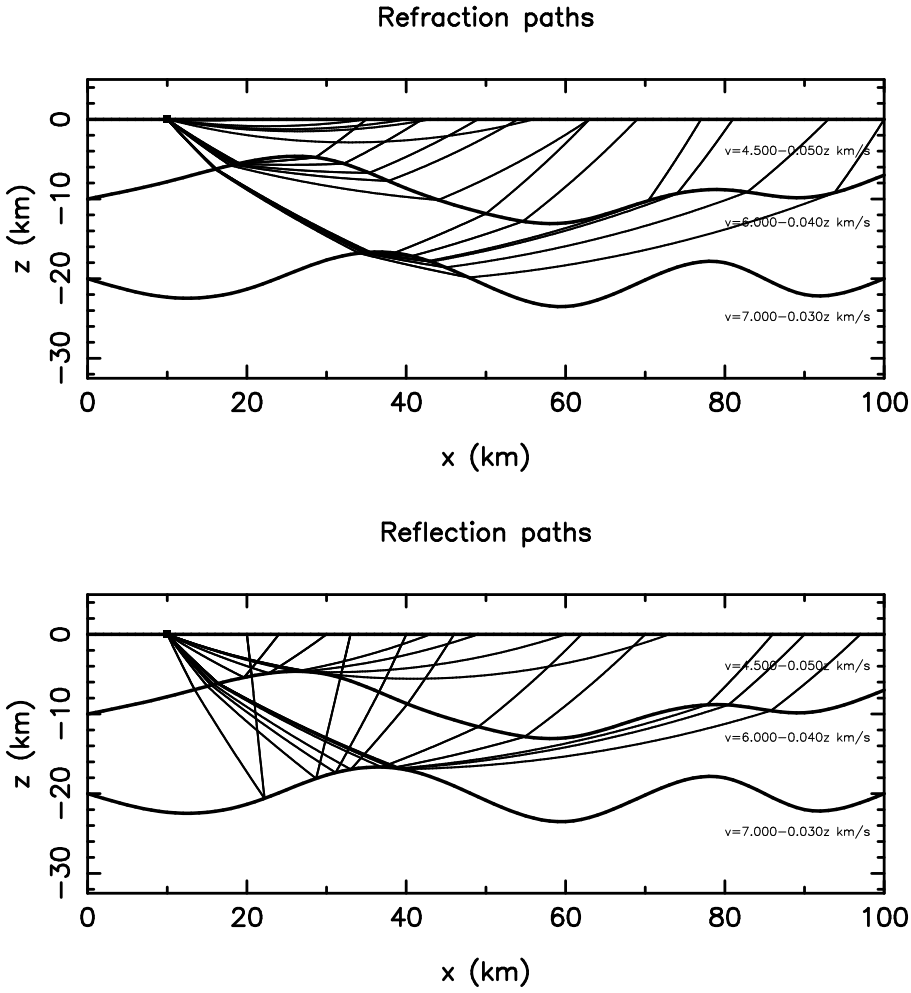

Figure 4.4: Example of solving the ray tracing initial value problem using the method outlined in the text for a number of randomly selected initial projection angles. There are three refraction phases and two reflection phases. Structure and paths are 2-D in this example.

Refracted and reflected rays may thus be traced through the layered models defined in Section 4.2.1 after defining a source point and an initial trajectory. The ray path is projected to the point where it hits an interface, upon which it is refracted or reflected, and then projected to the next interface. The cycle is repeated until the ray emerges from the model region. Figure 4.4 shows a spread of refracted and reflected rays traced from a

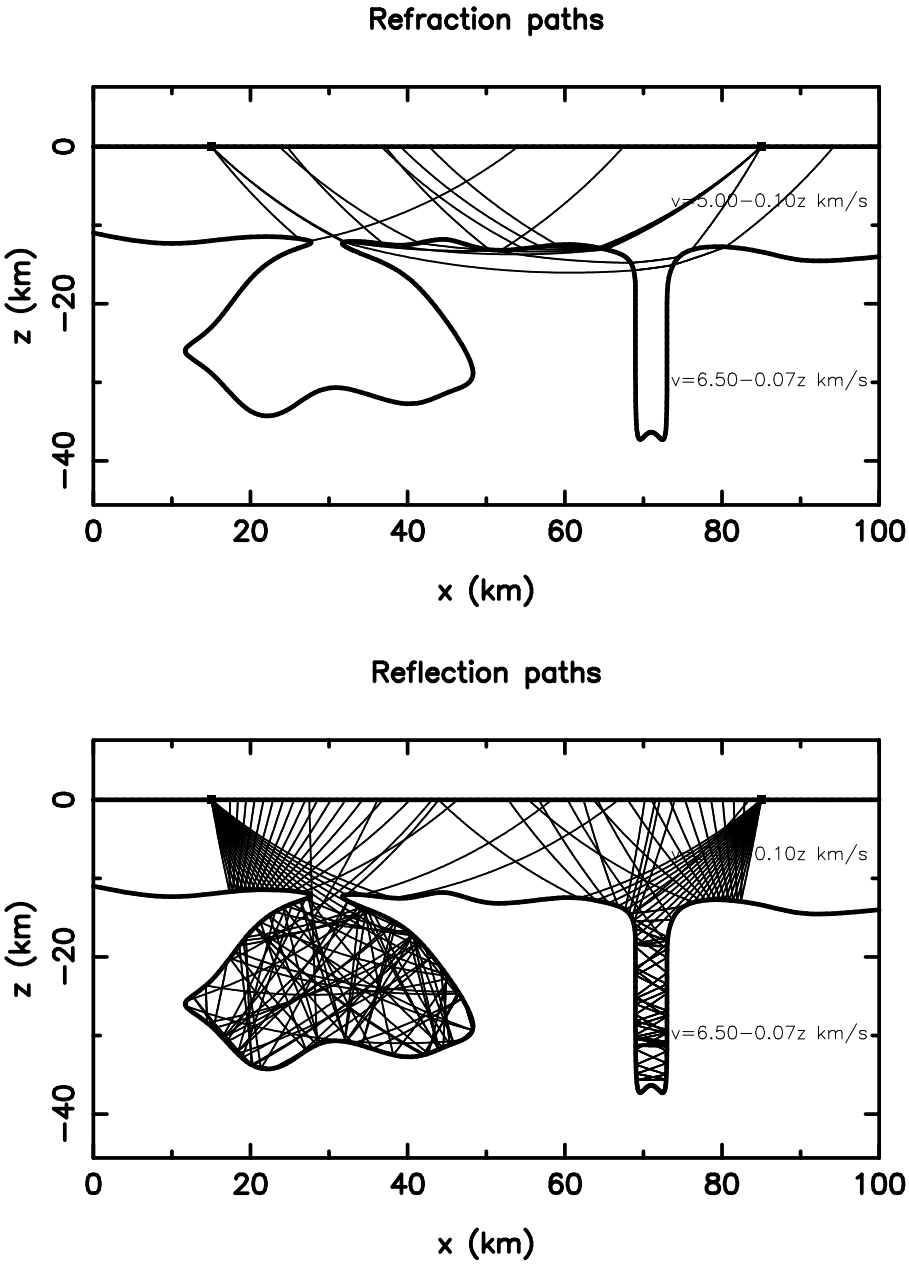

Figure 4.5: Refracted and reflected rays in the presence of an arbitrary multi-valued structure. This 2-D example illustrates the flexibility of the initial value ray tracing method. However, two-point paths are hard to locate and the identification of the multiple reflections on a seismogram would probably not be possible.

source to a receiver plane through a two-interface model. This method of solving the initial value problem is robust with respect to interface complexity, giving solutions even when an interface is a multi-valued function of depth, as illustrated in Figure 4.5. Reflecting rays get trapped within the inverted mushroom and the vertical column structures and must reflect many times before escaping.

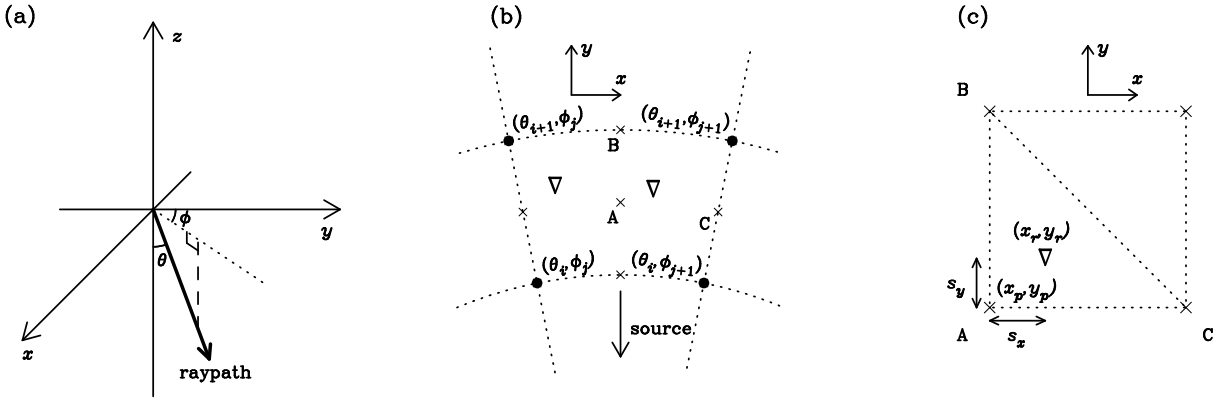

Figure 4.6: (a) Ray projection parameters: θ (inclination) and ϕ (azimuth). (b) If stations (triangles) fall within a region bracketed by four rays from step 2 (dots) at the surface, a more concentrated shoot (step 3) is used to target the region more closely (crosses). (c) For a station lying in the triangle formed by the end points of rays A, B and C, the projection vector of ray A is adjusted to target the point (x_r, y_r) using position derivatives calculated from all three rays (step 4). Ray terminals need not lie on a regular grid on the receiver plane for the method to work.

To find the correct two-point paths (i.e. the first arrivals of refracted or reflected phases at specified receivers) a four-step shooting method is employed that utilises the initial value method. The first step of the procedure involves shooting out a coarse spread of rays in constant increments of θ (typically $\sim 2^\circ$) and ϕ (typically $\sim 8^\circ$), the inclination and azimuth respectively of a ray at the source (see Figure 4.6a). The purpose of this step is to determine the ray projection angles at the source which bound each refraction and reflection phase type. Step 2 of the method involves shooting out a more concentrated spread of rays of each phase type into the regions defined by the previous step. The angular distance in θ and ϕ between projected rays is typically reduced by a factor of four or more from step 1. Step 3 shoots an even more concentrated spread of rays (usually decreasing the increments of θ and ϕ by a factor of two or three from step 2) into each region bracketed by four adjacent rays (see Figure 4.6b) from step 2 that contains one or more receivers. Step 4 is an iteration cycle that targets each receiver that falls inside a triangle whose vertices are the endpoints of three adjacent rays from step 3 (Figure 4.6c). Let $\mathbf{x}_r$ be the position of the receiver being targeted and $\mathbf{x}_p$ be the point where the nearest ray (θ_i, ϕ_i) intersects the receiver plane $z_p = z_r$. Also, let $s_x = x_p - x_r$ and $s_y = y_p - y_r$ (see Figure 4.6c). A more accurate estimate $(\theta_{i+1}, \phi_{i+1})$ of the initial ray trajectory is

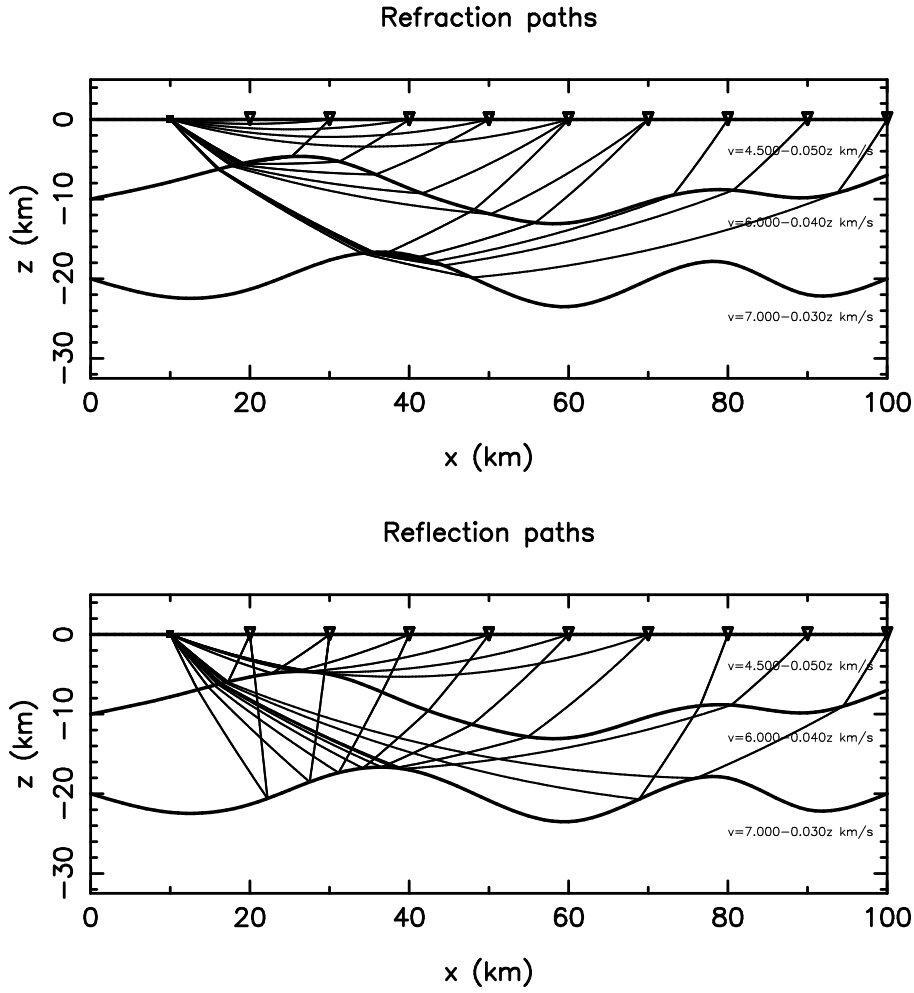

Figure 4.7: Source-receiver refraction and reflection ray paths found using the shooting method. Structure is identical to Figure 4.4 and rays are traced in 2-D.

then obtained by solving:

$$\begin{bmatrix} \frac{\partial s_x}{\partial \theta} & \frac{\partial s_x}{\partial \phi} \\ \frac{\partial s_y}{\partial \theta} & \frac{\partial s_y}{\partial \phi} \end{bmatrix} \begin{bmatrix} \theta_{i+1} - \theta_i \\ \phi_{i+1} - \phi_i \end{bmatrix} = \begin{bmatrix} -s_x(\theta_i, \phi_i) \\ -s_y(\theta_i, \phi_i) \end{bmatrix} \tag{4.14}$$

The new ray is then traced from the source and the procedure is repeated using the three rays closest to the receiver (the derivatives are re-evaluated at each iteration) until the ray strikes the receiver plane within a specified distance (50 m) of the receiver. The partial derivatives in Equation 4.14 are approximated by an explicit finite difference using the three closest rays. If a station falls inside more than one triangle, then triplication has occurred. A two-point ray is then found in each case and the one with minimum traveltime is selected.

A problem that can occur with step 1 of the shooting method above is that the region

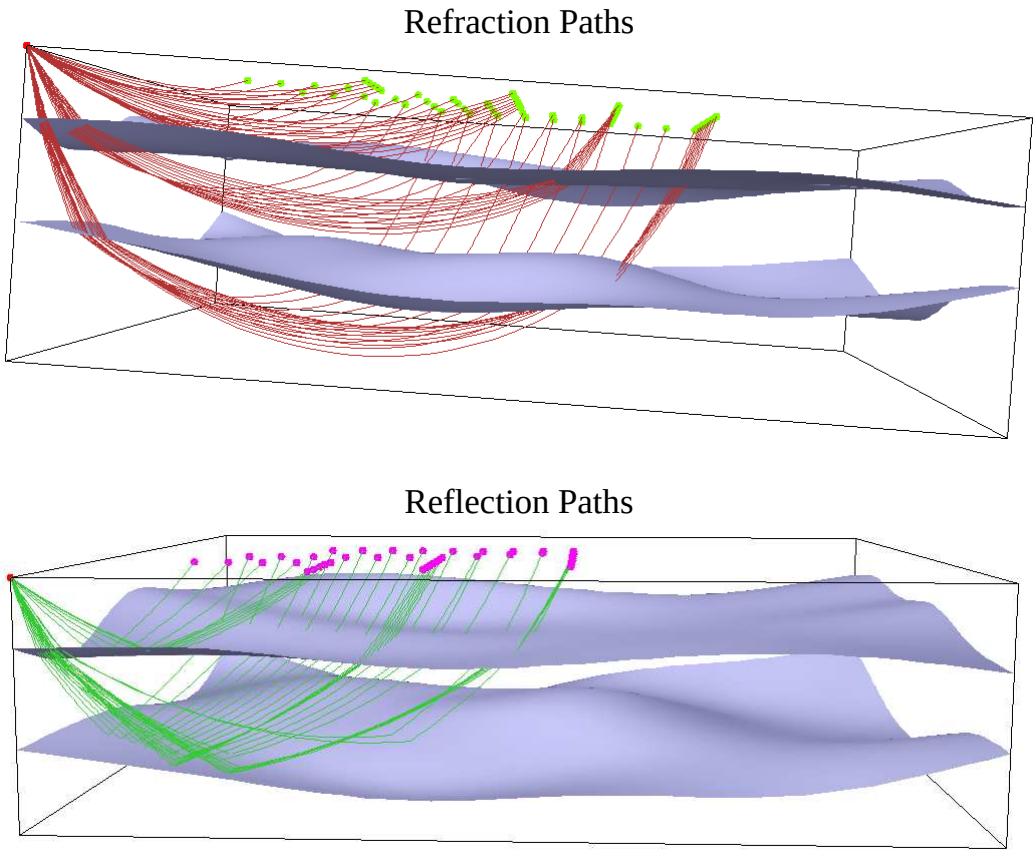

Figure 4.8: Refraction and reflection ray paths traced between a source and receiver array using the shooting method described. The 3-D structure consists of two interfaces.

which is defined for a particular phase may not include all possible paths. If the initial shoot is too coarse, near-critical refractions or very wide-angle reflections may not be located. To remedy this, a concentrated spread (in inclination) of rays is shot into the interval where these arrivals are likely to occur.

If a model consists of p layers, the first arrivals of up to p refraction phases and $p-1$ reflection phases can be located. A refraction phase is identified by the deepest layer it samples whilst a reflection phase is identified by the reflecting interface; multiples are ignored in both cases. Figure 4.7 shows the same structure as Figure 4.4 but now with refracted and reflected rays from the source to specified receiver locations traced using the above shooting method. The shooting method in 2-D is somewhat simpler than in 3-D because there are no variations in azimuth. Figure 4.8 shows two-point reflection and refraction paths through a 3-D structure.

The iterative method for determining the correct two-point ray relies on the use of smooth interfaces. If interfaces composed of piecewise planar segments were used for

example, the discontinuities in gradient between segments would undermine the basic assumption of Equation 4.14: that θ and ϕ vary smoothly with s_x and s_y.

4.2.3 Inversion Scheme

The aim of the inversion procedure is to minimise the misfit between observed and calculated traveltimes by adjusting the values of the model parameters, subject to regularisation constraints. In this case, there are three classes of model parameters that are adjusted: Velocities, velocity gradients and the depths of the interface vertices. If these parameters are described by the vector $\mathbf{m}$ of length M, and are related to the model data $\mathbf{d}$ (ray traveltimes) of length N as $\mathbf{d} = \mathbf{g}(\mathbf{m})$, then the misfit can be formalised as the objective function:

$$S(\mathbf{m}) = (\mathbf{g}(\mathbf{m}) - \mathbf{d}_{obs})^T \mathbf{C}_d^{-1} (\mathbf{g}(\mathbf{m}) - \mathbf{d}_{obs}) + \epsilon (\mathbf{m} - \mathbf{m}_0)^T \mathbf{C}_m^{-1} (\mathbf{m} - \mathbf{m}_0) \tag{4.15}$$

which is identical to the objective function described by Equation 2.35 in Section 2.3.2, where $\mathbf{d}_{obs}$ are the set of observed traveltimes, $\mathbf{C}_d$ is a data covariance matrix, $\mathbf{C}_m$ is an *a priori* model covariance matrix, and ϵ is a damping factor. A smoothing term is not incorporated into the objective function here since the parameterisation is naturally smooth and can be adjusted to suit the resolving power of the dataset.

The preferred method used to minimise S is the subspace inversion method described in Section 2.3.2. The conjugate gradient and steepest descent methods described in the same section are also investigated in order to measure the performance of the subspace method. At each iteration, the subspace algorithm requires the solution of (see Equation 2.61):

$$\delta\mathbf{m} = -\mathbf{A}[\mathbf{A}^T(\mathbf{G}^T\mathbf{C}_d^{-1}\mathbf{G} + \epsilon\mathbf{C}_m^{-1})\mathbf{A}]^{-1}\mathbf{A}^T\hat{\boldsymbol{\gamma}} \tag{4.16}$$

where $\hat{\boldsymbol{\gamma}} = \partial S/\partial\mathbf{m}$, $\mathbf{G} = \partial\mathbf{g}/\partial\mathbf{m}$ is the Fréchet matrix of partial derivatives and $\mathbf{A}$ is the $M \times n$ projection matrix (n is the subspace dimension). The Fréchet matrix is calculated during the solution of the forward problem. Appendix C describes the analytic techniques used to produce first-order accurate approximations of the Fréchet derivatives. An original approach is used to approximate the velocity and velocity gradient partial derivatives while the interface depth partial derivatives are determined using the method described in Section 2.3.2 (see Equation 2.69).

The projection matrix $\mathbf{A} = [\mathbf{a}^j]$, where $\{\mathbf{a}^j\}$ is the spanning set of basis vectors, needs to be chosen with consideration to the fact that the inverse problem can have up to three

parameter classes: interface depth, velocity and velocity gradient. A strong dependence on scaling and poor convergence are typically observed (Kennett et al., 1988) when gradient methods like steepest descent or conjugate gradients are applied to problems with different parameter types. By using a judicious choice of basis vectors, the subspace method can avoid such problems. Here, the $\{\mathbf{a}^j\}$ are constructed in terms of the steepest ascent vector in model space $\boldsymbol{\gamma} = \mathbf{C}_m\hat{\boldsymbol{\gamma}}$ at each iteration. Three separate search directions can be obtained by partitioning this vector on the basis of parameter class:

$$\boldsymbol{\gamma} = \mathbf{a}^1 + \mathbf{a}^2 + \mathbf{a}^3 = \begin{bmatrix} \boldsymbol{\gamma}^1 \\ 0 \\ 0 \end{bmatrix} + \begin{bmatrix} 0 \\ \boldsymbol{\gamma}^2 \\ 0 \end{bmatrix} + \begin{bmatrix} 0 \\ 0 \\ \boldsymbol{\gamma}^3 \end{bmatrix} \tag{4.17}$$

where $\mathbf{a}^1$, $\mathbf{a}^2$ and $\mathbf{a}^3$ represent ascent vectors that lie in the parameter space of interface depth, velocity and velocity gradient respectively. To increase the dimension of the subspace (in order to increase the rate of convergence), more basis vectors are obtained by determining the rate of change of the ascent vectors. A further nine basis vectors are obtained by pre-multiplying $\mathbf{a}^1$, $\mathbf{a}^2$ and $\mathbf{a}^3$ by the model space Hessian $\mathbf{H} = \mathbf{C}_m\hat{\mathbf{H}}$ and partitioning the three vectors that result, as is done in Equation 4.17. Additional basis vectors can be produced by repeating the process of pre-multiplication of the latest set of vectors by the partitioned model space Hessian. Once the required number of basis vectors is obtained, Gram-Schmidt orthogonalisation is applied to avoid interdependence:

$$\mathbf{a}^i_{orth} = \mathbf{a}^i - \sum_{j=1}^{i-1} \frac{\mathbf{a}^i \cdot \mathbf{a}^j}{\mathbf{a}^j \cdot \mathbf{a}^j}\mathbf{a}^j \tag{4.18}$$

for $i = 1, \ldots, n$. The basis vectors $\{\mathbf{a}^i_{orth}\}$ are normalised and used in Equation 4.16 via the projection matrix $\mathbf{A}$. Choosing an appropriate number of basis vectors requires finding an acceptable balance between computational effort and rate of convergence. In the application of the method, subspaces whose dimensions do not exceed 20 are used.

The complete inversion method is iterative and, starting from a suitable initial model, involves the alternating use of ray tracing (to determine model traveltimes and the Fréchet matrix) and subspace inversion (to calculate $\delta\mathbf{m}$). The iterations cease either when the observed traveltimes are satisfied by the model predictions or when the change in $S(\mathbf{m})$ with iteration gets sufficiently small. If picking errors are constant, then the data is satisfied when the RMS data misfit, defined by:

$$T_{RMS} = \sqrt{\frac{\sum_{i=1}^{N}(d^i_m - d^i_{obs})^2}{N}} \tag{4.19}$$

where $\{d_m^i\} = \mathbf{g}(\mathbf{m})$, falls below the RMS picking error. However, since picking errors need not be identical for all picks, the χ^2 misfit, which weights the residuals according to the size of their uncertainties, is used to analyse the data fit when uncertainty estimates are available. The χ^2 misfit is defined by:

$$\chi^2 = \frac{1}{N} \sum_{i=1}^{N} \left(\frac{d_m^i - d_{obs}^i}{\sigma_d^i} \right)^2 \tag{4.20}$$

where the $\{\sigma_d^j\}$ indicate traveltime uncertainty obtained from picking error estimates. The quantity $N\chi^2$ is thus equal to the data term of the objective function (Equation 4.15). The solution fits the data to the level of the noise when $\chi^2 = 1$.

Picked data must be assigned to a reflection or refraction phase from a particular layer or interface prior to the inversion. This may be difficult to do when the velocity contrast across an interface is small, but incorrect assignment may result in that portion of the data being poorly satisfied by the solution model, which suggests either an incorrect assignment or pick. Knowing which traveltime is associated with which phase is *a priori* information for the inversion, so if it is possible to identify different phases in the data, then this information should be used to help constrain the solution.

In order for an inversion to be carried out, the damping parameter ϵ, the data covariance matrix $\mathbf{C}_d$ and the *a priori* model covariance matrix $\mathbf{C}_m$ are also required. Uncorrelated errors are assumed, which implies that $\mathbf{C}_d = \{\delta_{ij}(\sigma_d^j)^2\}$ and $\mathbf{C}_m = \{\delta_{ij}(\sigma_m^j)^2\}$ where the $\{\sigma_m^j\}$ indicate the uncertainty of the initial model parameters. Determining $\{\sigma_m^j\}$ requires *a priori* information on the error associated with the initial estimate of each model parameter. If, for example, 1-D refraction interpretations were used to construct the initial model, $\{\sigma_m^j\}$ could be estimated by adjusting the interface and velocity parameters in the refraction interpretation to determine the range over which they will reasonably satisfy the data.

The relative values of σ_d^j control the weight of each traveltime datum in the inversion. Similarly, the relative values of σ_m^j control the freedom each model parameter has to deviate from its initial value. The choice of $\mathbf{C}_d$ and $\mathbf{C}_m$ also influence the relative magnitudes of the data residual term and the model term in Equation 4.15, thereby influencing the trade-off in the inversion between satisfying the observed data and matching the initial model estimate. Ultimately, however, this trade-off is controlled by the damping factor ϵ in the objective function (Equation 4.15). A value of ϵ is required that results in a model that adequately satisfies the data, only differs from the initial model where required by

the data, and is physically reasonable. The choice of ϵ is based on χ^2 misfit versus RMS model perturbation (ψ_{mo}) trade-off curves for a range of damping factors, as demonstrated in the synthetic tests that follow. The quantity ψ_{mo} is defined by:

$$\psi_{mo} = \sqrt{\frac{\sum_{i=1}^{M}(m^i - m_0^i)^2}{M}} \tag{4.21}$$

and is calculated separately for each parameter class so that separate trade-off curves are generated for interface depth, velocity and velocity gradient.

One other aspect of the inversion method that requires discussion is the treatment of layer pinchouts. A layer pinchout may be represented in the model by two distinct interfaces which are separate in one region of the model but elsewhere come together with an identical set of interface vertices. If a layer pinchout is expected to occur, then the two interfaces in question are required to have the same vertex distribution in the (x, y) domain. In adjusting the model parameters, the condition that no vertex in the upper interface can lie at a greater depth than the corresponding vertex in the lower interface is set. It follows from the B-spline definition (Equation 4.2) that the interfaces will not be able to cross over. If, in an inversion, two surface patches become coincident in space, then the ray tracing routine treats them as a single surface patch. Subsequent inversion iterations may separate them or they can be locked together for the remainder of the inversion process if desired.

Appendix D gives a brief synopsis of the FORTRAN77 program that was written to perform the inversion (see also Appendix F). Once a solution is found, solution quality is analysed using linear theory (see Section 2.4), in particular the *a posteriori* model covariance $\mathbf{C}_M$ (Equation 2.77), the model resolution $\mathbf{R}$ (Equation 2.76) and correlations ρ^{ij} (Equation 2.78), which are calculated at the solution point (a separate program performs this task). The compact parameterisation used by our model means that the matrix inversion required by Equation 2.77 can be solved without resorting to sophisticated iterative methods - LU decomposition was found to be sufficient.

4.3 Synthetic Tests

The aim of this section is to examine the performance of the inversion method with synthetic data by (i) specifying a synthetic (or "true") model and a source-receiver geometry, (ii) generating a synthetic dataset by ray tracing through the true model and recording

traveltimes of both refracted and reflected rays, (iii) inverting the synthetic data for interface depth and/or layer velocity starting with a given initial model, and (iv) evaluating the differences between the recovered model and the synthetic model. A number of tests are performed here, beginning with relatively simple 2-D models and gradually evolving to models with complex 3-D structure. Simple 2-D inversions are useful for demonstrating some of the basic characteristics of the method.

4.3.1 Inversion for 2-D Structure

The first synthetic structure (Model A, Figure 4.9) considered here contains two interfaces of relatively simple geometry. Each interface is defined by 14 evenly spaced nodes. The layer velocities v_0 (and velocity gradients k) are 4.5 (0.1), 5.0 (0.1) and 4.5 (0.2) km/s (s^{-1}) from top to bottom. A source-receiver array that consists of three sources and 25 evenly-spaced receivers is used to generate the data. Figure 4.9 shows both refracted and reflected ray paths and their associated traveltimes. These traveltimes constitute the synthetic data, which at this stage are free from added noise.

Figure 4.10 shows the result, after 15 iterations, of a 12-D subspace inversion of all the synthetic data for all 34 parameters. The initial interface model (dashed lines) is laterally invariant and was obtained by taking the average depth to each of the true model interfaces (dotted lines). The initial layer velocities (velocity gradients) are 4.2 (0.12), 5.3 (0.09) and 4.3 (0.22) km/s (s^{-1}) from top to bottom. Both the interface structure and velocities are reconstructed accurately, as seen in Figure 4.10 and Figure 4.11. The basis vectors that span the 12-D subspace consist of six interface, three velocity and three velocity gradient vectors. Since there are only three layers in the model, the basis vectors completely span velocity and velocity gradient space. Increasing the number of interface basis vectors only lead to superficial improvements; the 12-D reconstruction is very accurate.

The damping parameter ϵ was set to zero for this inversion and the diagonal entries of the data covariance matrix $\mathbf{C}_d$ were set to 1; the magnitude of this value is not important since no damping is applied. The ray coverage (see Figure 4.9) is dense and relatively even, so no parameters, except perhaps the nodes at the ends of the interfaces, are poorly constrained by the data. Figure 4.12 shows the behaviour of the RMS data misfit (Equation 4.19) during the iterative process. The monotonic nature of the curve indicates a stable inversion. χ^2 misfit is not used here because the data is essentially noise-free and

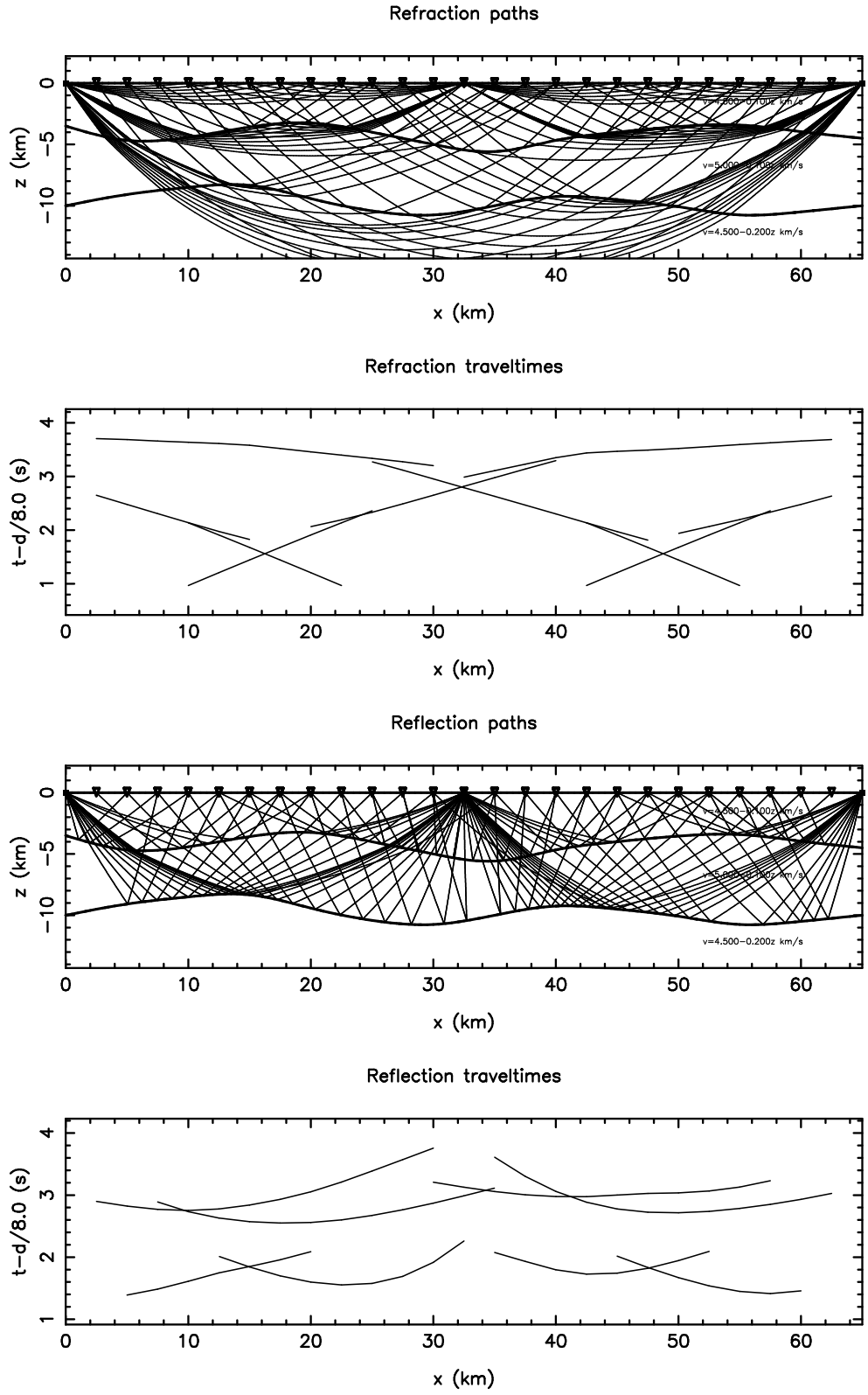

Figure 4.9: Simple two-interface model (Model A) used to generate synthetic data, which consists of the traveltimes of the reflected and refracted ray paths illustrated. Note that the traveltimes have been interpolated to show traveltime curves. Receivers are denoted by ∇ and sources by filled squares.

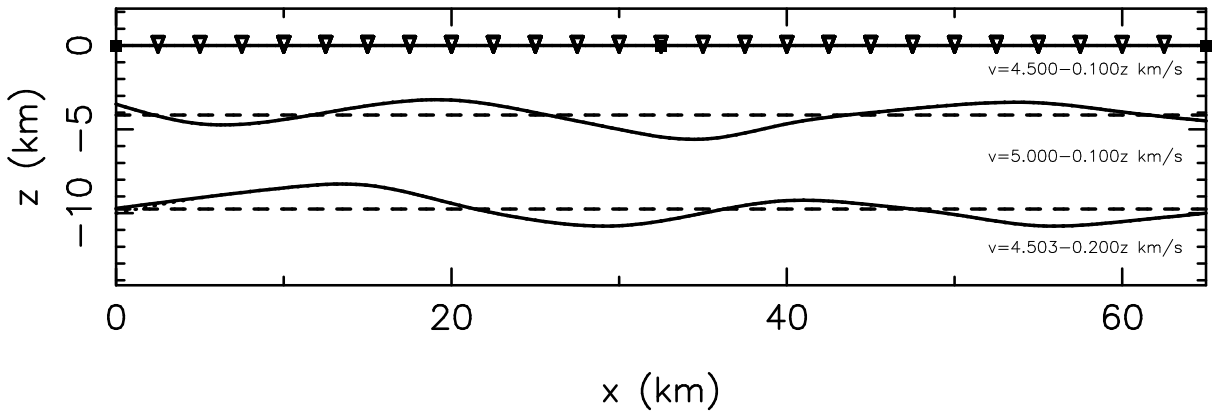

Figure 4.10: 12-D subspace inversion result for Model A after 15 iterations using both reflection and refraction traveltimes. All model parameters are inverted for. Starting interface structure is denoted by dashed lines, recovered interfaces by solid lines and true interface structure by dotted lines. The recovered model is virtually coincident with the true model. Recovered velocities are shown.

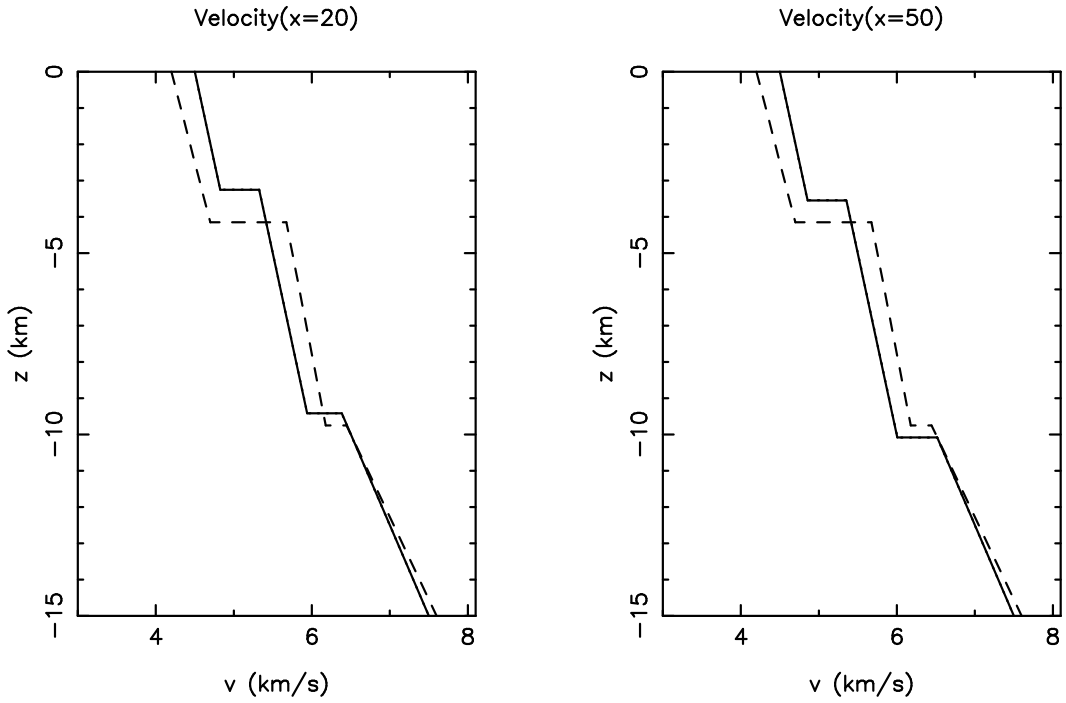

Figure 4.11: Velocity profiles through models shown in Figure 4.10 at $x = 20$ km and $x = 50$ km. The starting model is shown by dashed lines, recovered model by solid lines and true model (Model A) by dotted lines. The recovered model is virtually coincident with the true model.

χ^2 is defined (Equation 4.20) on the basis that non-zero noise level estimates are available. The only source of "noise" in the synthetic data comes from inaccuracies in the ray-tracing procedure (in this case, due primarily to the 50 m convergence criterion used in the shooting method), which is why the RMS misfit curve (Figure 4.12) doesn't level out closer to zero.

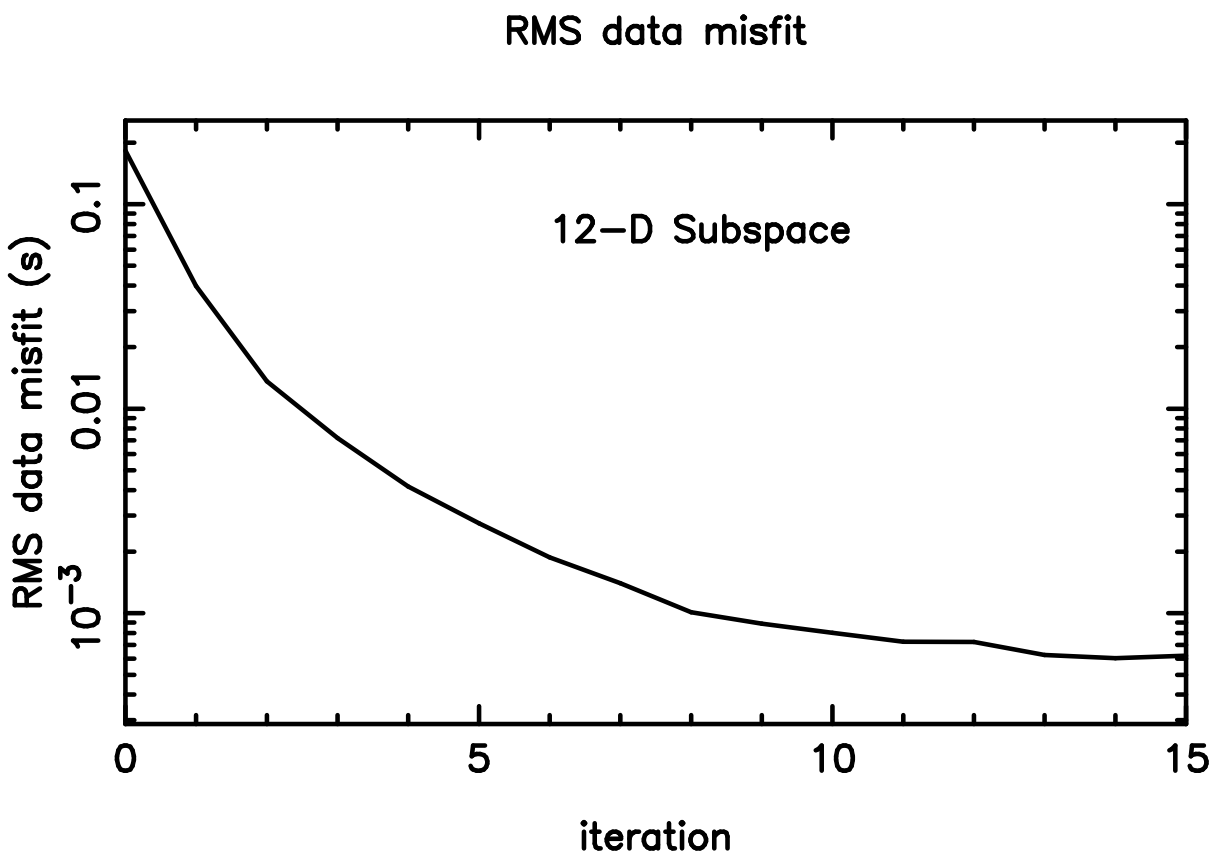

Figure 4.12: RMS data misfit versus iteration number for the inversion result shown in Figure 4.10.

The subspace inversion method represents the preferred method of inversion here, and the example above shows that it can be used to accurately reconstruct multi-parameter class models. Also shown for comparison are the results of inversions obtained using steepest descent (Figure 4.13) and conjugate gradient (Figure 4.14) methods (described in Section 2.3.2). For the steepest descent method, the interface (Figure 4.13a) and velocity (Figure 4.13b) reconstructions are both poor after 15 iterations and the behaviour of the misfit function (Figure 4.13c) is erratic and finishes at a much higher value than it starts with. The reason for the poor convergence is clear: the objective function is most sensitive to the layer velocity gradients. A small change in a velocity gradient will result in a much greater change in S than is produced by a similar change in velocity or interface depth. Thus, the direction of steepest descent will be nearly orthogonal to any vector that lies in velocity and interface model space. The steepest descent method tries unsuccessfully to satisfy the data in terms of variations in layer velocity gradients and the interface and layer velocity parameters are virtually unaffected by the inversion.

Figure 4.14 shows the result of inversion using the Polak-Ribiere variant of the con-

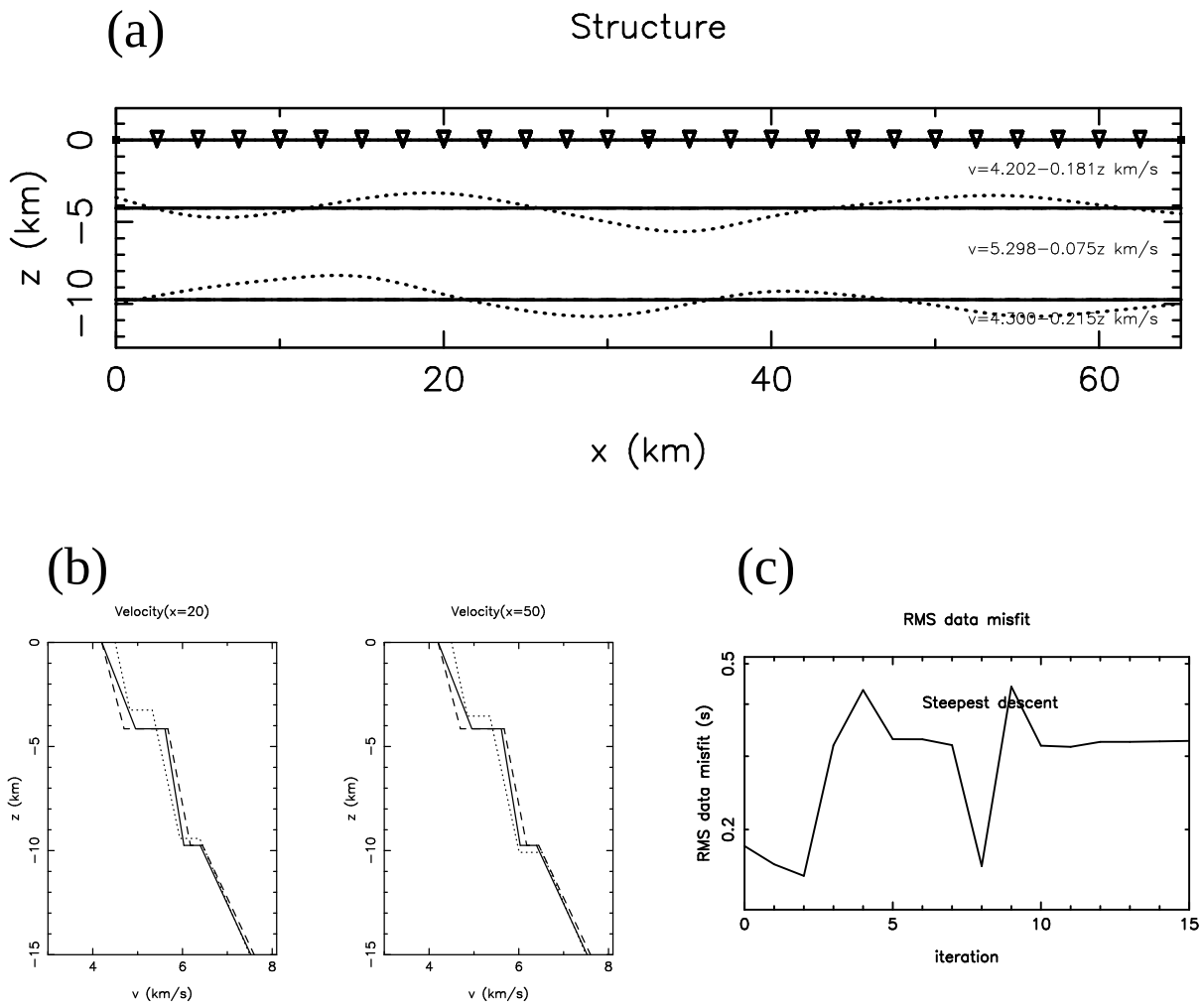

Figure 4.13: Inversion result (for Model A dataset) using steepest descent method. (a) Interface structure: initial model shown by dashed lines, recovered model by solid lines and true model by dotted lines. (b) Velocity structure: models denoted as in (a). (c) Misfit function versus iteration.

jugate gradient method applied to the same problem. The solution at iteration 15 is just as poor as the steepest descent solution (Figure 4.13). Like steepest descent, the conjugate gradient method also tries to satisfy the data by mainly varying velocity gradients. These examples show that the subspace method is preferable to both steepest descent and conjugate gradient methods for multiple parameter classes.

When only one parameter class is inverted for the steepest descent and conjugate gradient methods can be expected to work much more successfully. Figure 4.15 shows a comparison between steepest descent (Figure 4.15a), conjugate gradient (Figure 4.15b) and 4-D subspace (Figure 4.15c) inversions of the data for interface only; correct layer velocities are assumed. Five iterations are performed in each case. All methods produce relatively accurate interface reconstructions, but it is clear that the steepest descent

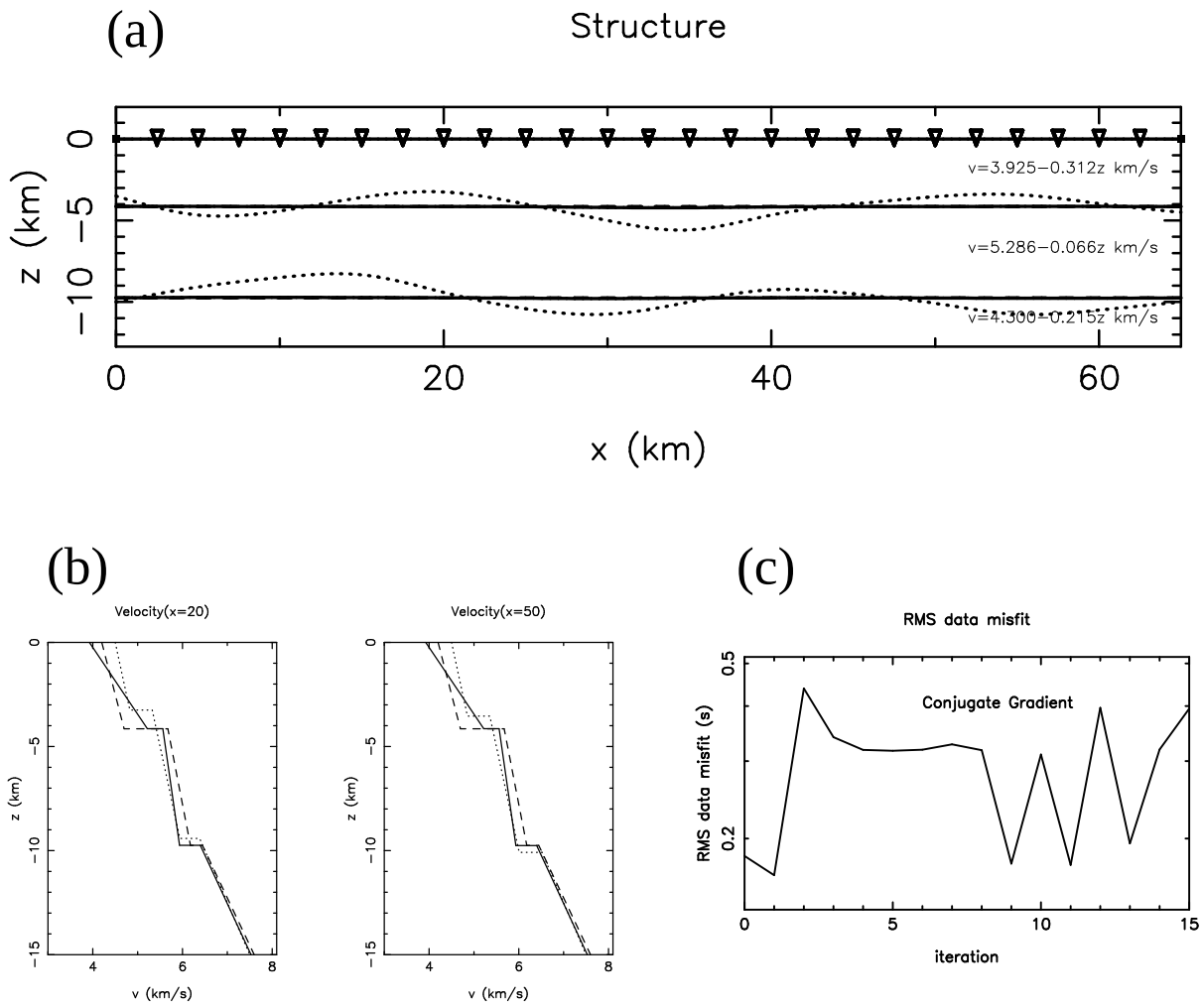

Figure 4.14: Inversion result (for Model A dataset) using conjugate gradient method. (a) Interface structure: initial model shown by dashed lines, recovered model by solid lines and true model by dotted lines. (b) Velocity structure: models denoted as in (a). (c) Misfit function versus iteration.

method produces the least accurate reconstruction and the 4-D subspace method produces the most accurate reconstruction after the same number of iterations. This result is reflected in the behaviour of the data misfit function (Figure 4.16) for each method; the 4-D subspace results in a significantly greater reduction than either the steepest descent or conjugate gradient method. With an appropriate number of basis vectors, the subspace method will generally exhibit faster convergence than either steepest descent or conjugate gradient methods. The subspace inversion method is therefore used in all subsequent inversions described in this thesis.

In a final test with Model A synthetic data, inversions are performed separately using only refraction and only reflection traveltimes. These tests indicate whether one data type may be more sensitive to a particular parameter class than the other. Using only

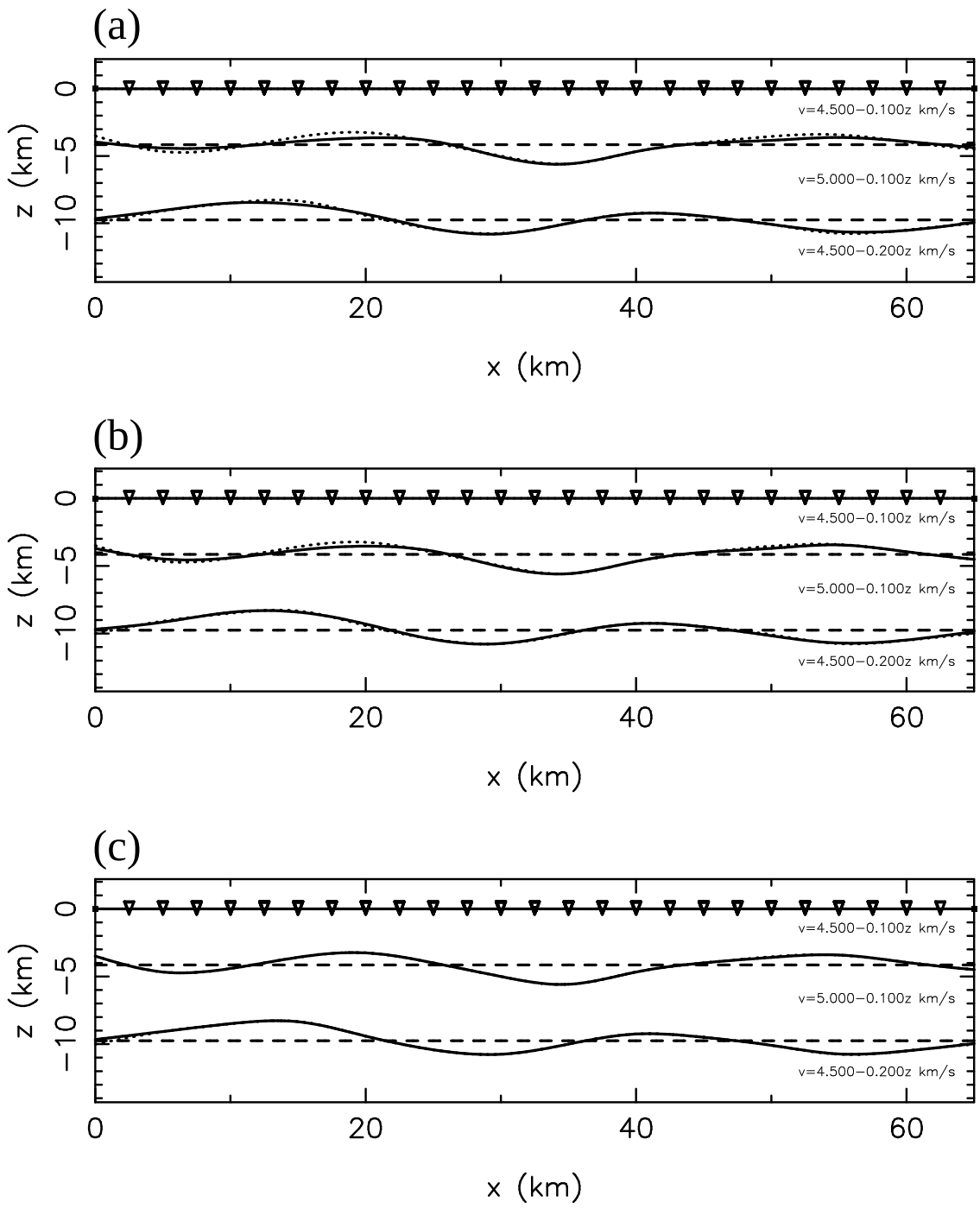

Figure 4.15: Inversion of Model A dataset for interface structure only. Initial model shown by dashed lines, recovered model by solid lines and true model by dotted lines. Five iterations of each method are used to achieve these solutions. (a) Steepest descent, (b) conjugate gradient, and (c) 4-D subspace.

the refracted arrivals (Figure 4.17), data misfit reduction is not monotonic (Figure 4.17c), nor is it as rapid as the combined inversion (Figure 4.12), but the interface (Figure 4.17a) and velocity variations (Figure 4.17b) are quite accurately reconstructed. Interface error

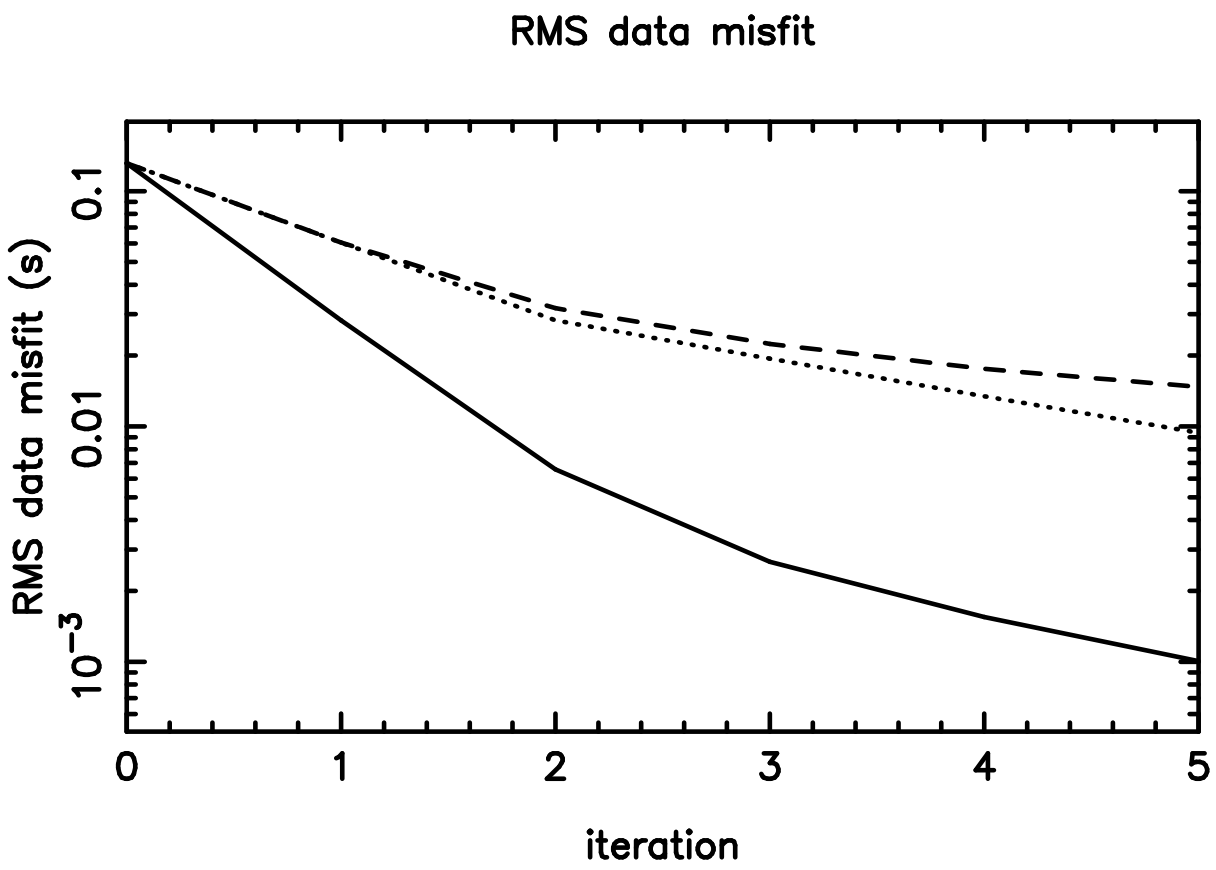

Figure 4.16: Data misfit versus iteration number for interface inversion (Figure 4.15) using steepest descent (dashed line), conjugate gradient (dotted line) and 4-D subspace (solid line).

is most evident in regions of poor ray coverage (see Figure 4.9).

Using only the reflection traveltimes (Figure 4.18), the interfaces are again accurately reconstructed, except for those parts of the interface that are not near reflection points (see Figure 4.9). While the velocity profile is reasonably well recovered (Figure 4.18b), there is some trade-off between velocity and velocity gradient parameters (a change in v_o can be compensated for by a change in k). Thus, while reflection traveltimes constrain interface structure well, they do not constrain velocities as well as refraction traveltimes.

Apart from demonstrating that the inversion method works successfully, the preceding tests illustrate various characteristics of the subspace, conjugate gradient and steepest descent methods. However, the synthetic dataset was in many ways ideal; it was essentially noise free, it evenly and densely sampled the model with both reflections and refractions, the model structure was simple and smooth, and the initial model structure was relatively accurate. These factors allowed damping to be ignored. In real applications, the data

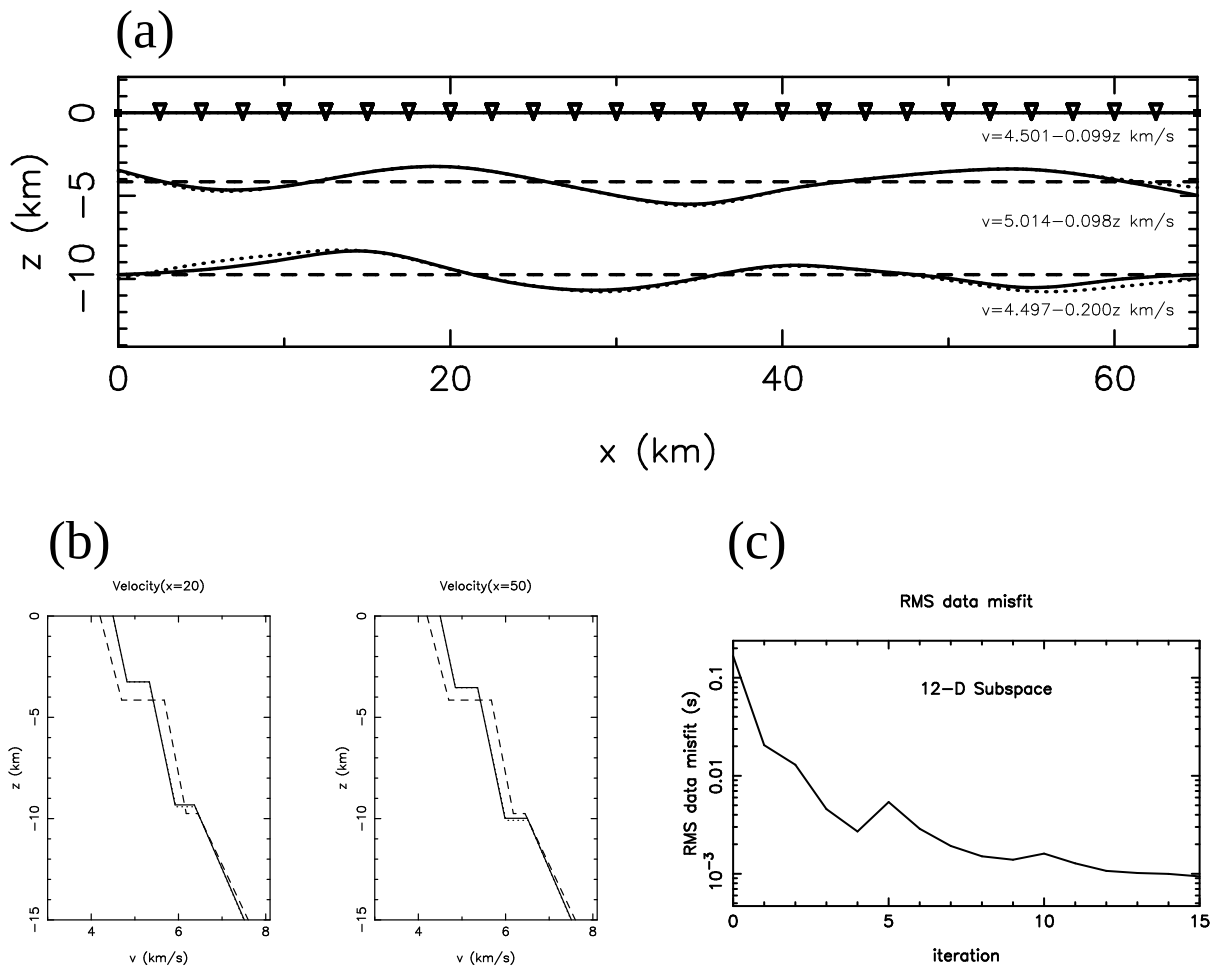

Figure 4.17: Inversion result (Model A) using 12-D subspace and refraction data only. (a) Interface structure: initial model shown by dashed lines, recovered model by solid lines and true model by dotted lines. (b) Velocity structure: models denoted as in (a). (c) Misfit function versus iteration.

contains noise, ray path coverage is likely to be uneven, and the initial model may poorly satisfy the data. The next set of examples will consider damping and how it can be used when model structure is more complex and data distribution is less even.

Figure 4.19 shows a new 3-layer structure (Model B) with refracted and reflected ray paths from a source-receiver configuration similar to that used in the above examples. The interface structure of Model B has a greater degree of lateral heterogeneity than that of Model A (Figure 4.9), which is reflected in the less homogeneous distribution of ray paths (Figure 4.19). Interface nodes are evenly distributed 10 km apart, so each interface is described by 16 nodes, and the model is defined by a total of 38 model parameters. The layer velocity v_0 (and velocity gradient k) are 4.5 (0.1), 5.0 (0.08) and 6.8 (0.05) km/s (s^{-1}) from top to bottom. The velocity gradients used in Figure 4.19 are generally less

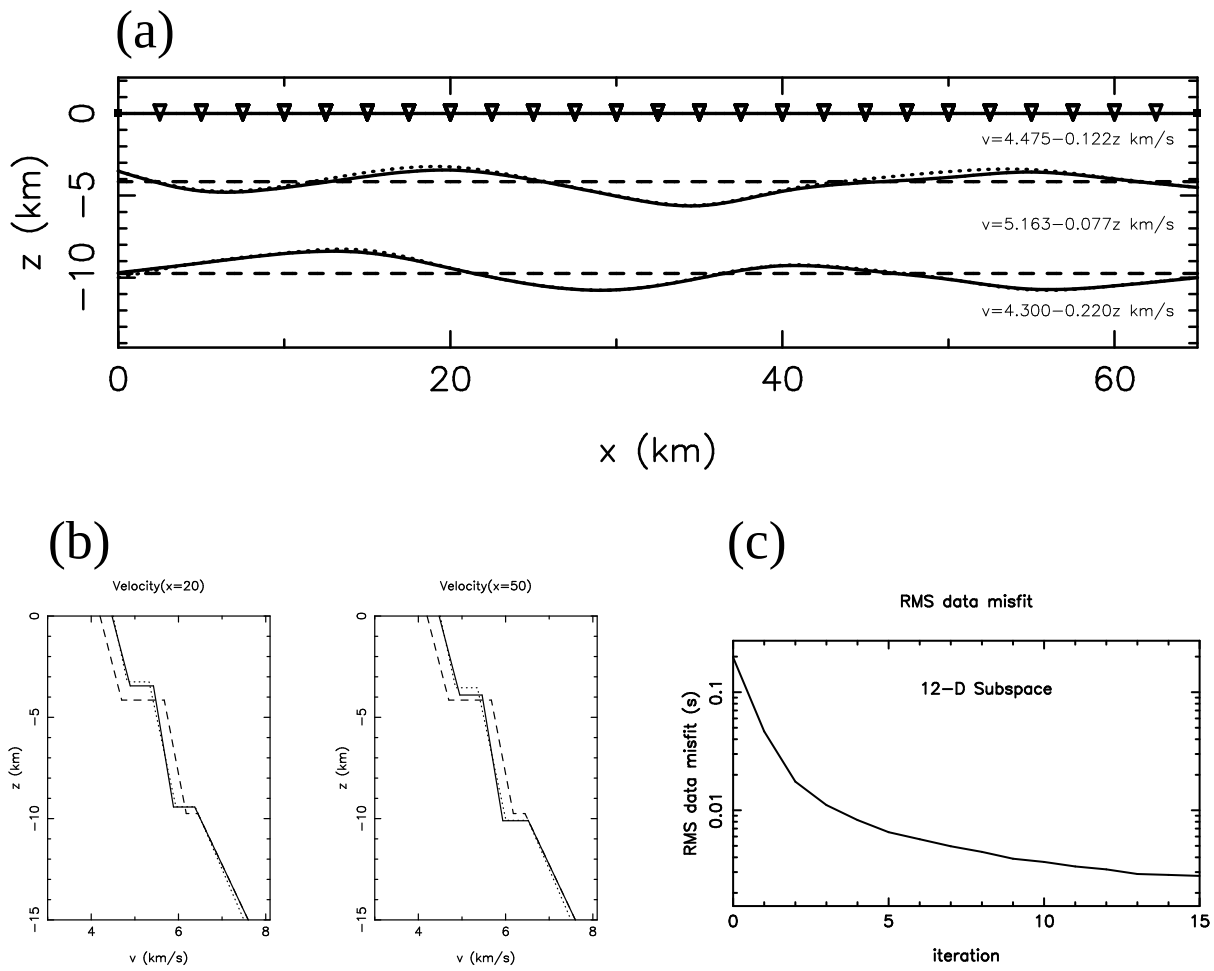

Figure 4.18: Inversion result (Model A) using 12-D subspace and reflection data only. (a) Interface structure: initial model shown by dashed lines, recovered model by solid lines and true model by dotted lines. (b) Velocity structure: models denoted as in (a). (c) Misfit function versus iteration.

than those used in Figure 4.9, and as a result, the rays show less curvature. The synthetic dataset consists of the traveltimes shown in Figure 4.19, this time corrupted by Gaussian noise with a standard deviation of 70 ms to simulate the noise content of real data. This value is used in the diagonal elements of the data covariance matrix $\mathbf{C}_d$, and also in the definition of the χ^2 misfit function (Equation 4.20), which is used from now on to measure data misfit.

In the initial inversion test using the Model B dataset, the damping factor was set to $\epsilon = 0$ and the starting model consists of horizontal interfaces with layer velocities (and layer velocity gradients) of 5.1 (0.08), 5.4 (0.10) and 6.4 (0.07) km/s (s^{-1}) from top to bottom. Figure 4.20 shows the result of a 12-D subspace inversion after 4 iterations (the top and bottom interfaces intersect after 5 iterations, which stops the ray-tracing

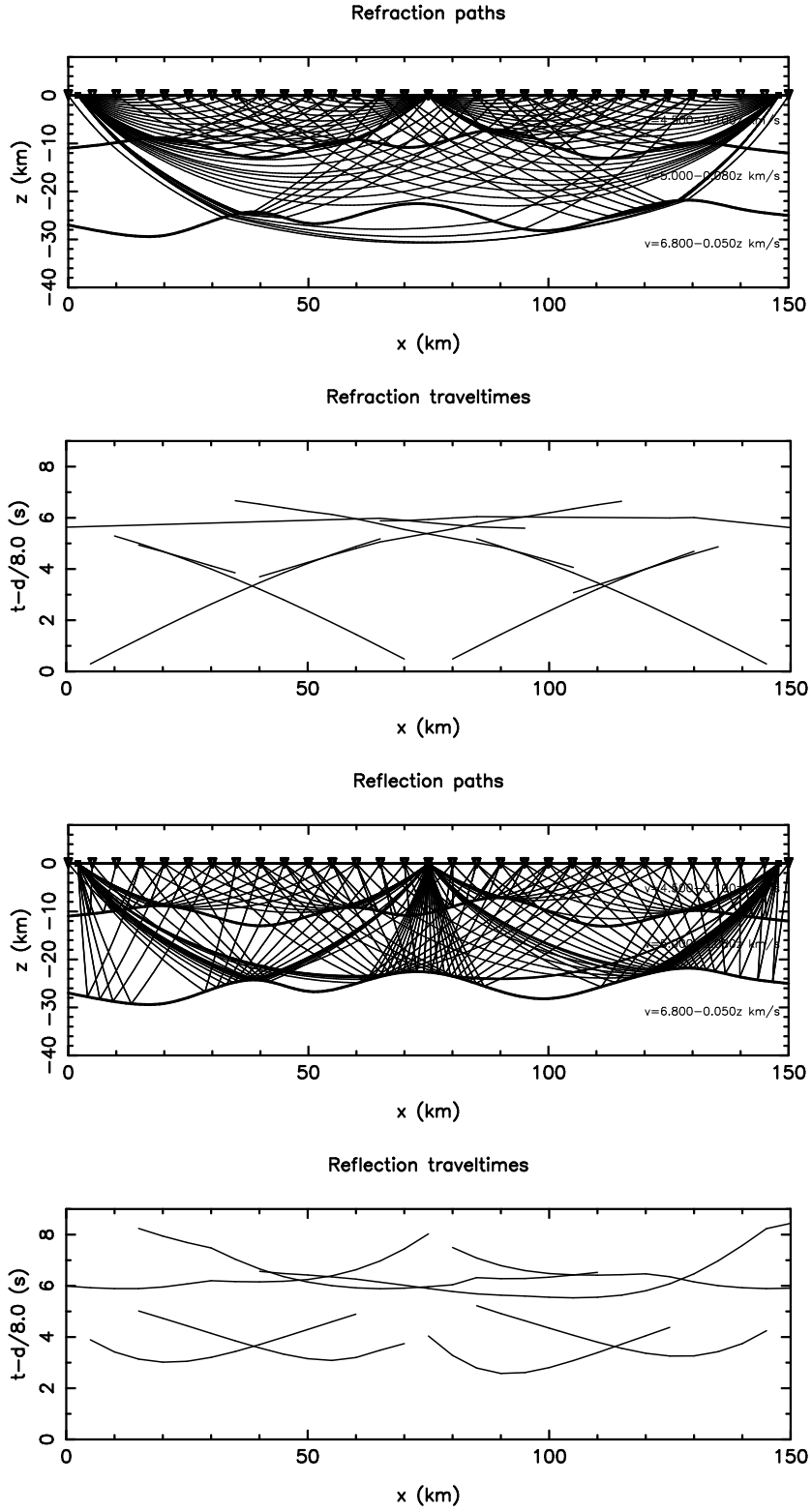

Figure 4.19: Model B defined by two interfaces as shown. Synthetic data consists of the traveltimes of the reflected and refracted ray paths illustrated. Note that the traveltimes have been interpolated to show traveltime curves. Receivers are denoted by ∇ and sources by small filled squares.

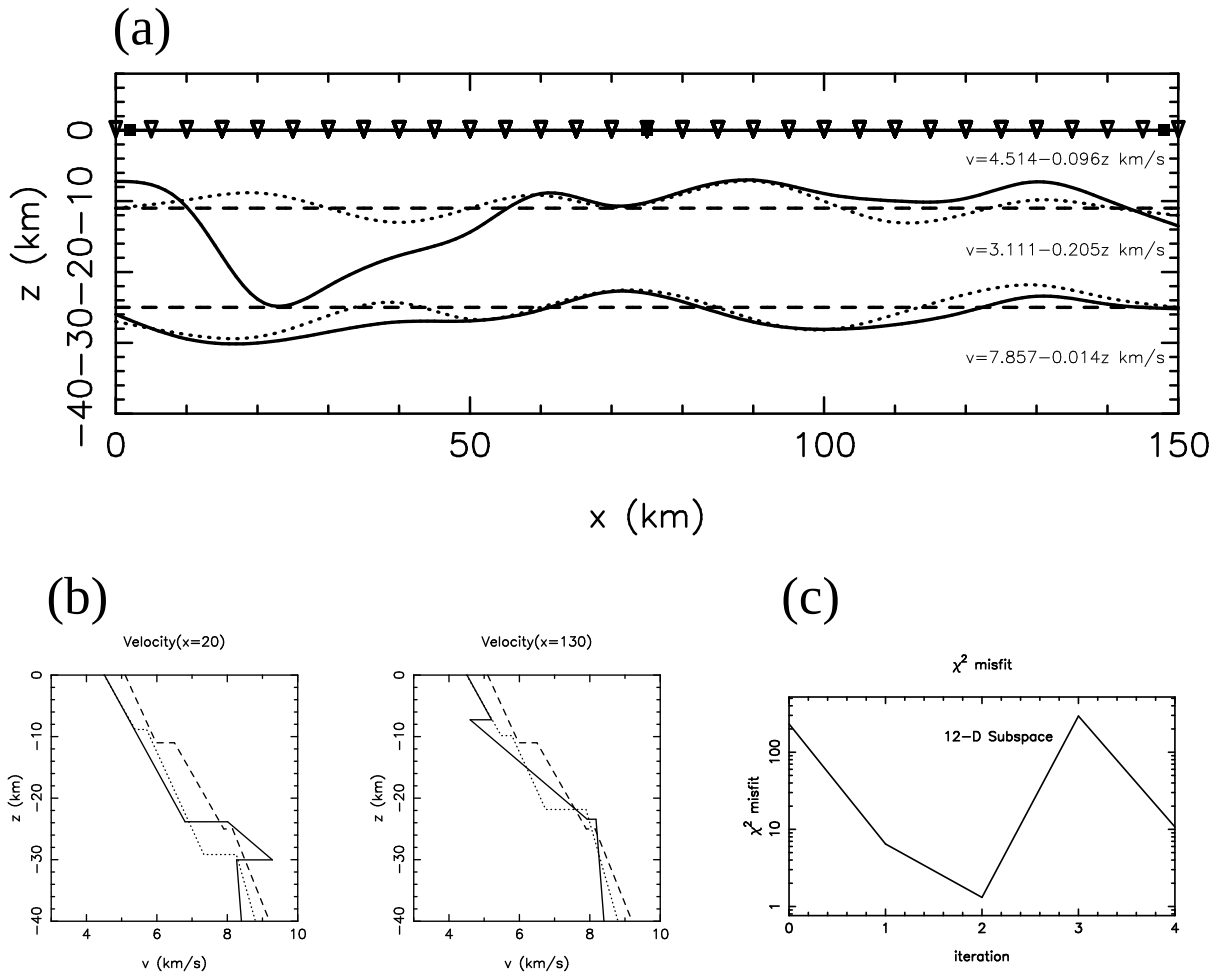

Figure 4.20: Inversion result using Model B data with 70 ms data noise and $\epsilon = 0$ after 4 iterations. (a) Interface structure: initial model shown by dashed lines, recovered model by solid lines and true model by dotted lines. (b) Velocity structure: models denoted as in (a). (c) χ^2 misfit function versus iteration.

routine). The initial model used in the inversion produces an RMS data misfit of 1.07 s, which is relatively large compared to the 183 ms RMS misfit produced by the initial model used for the Model A reconstructions. Although parts of the interface structure are well recovered, the sector $0 \leq x \leq 50$ km in the top interface is clearly not recovered (Figure 4.20a). In addition, apart from layer 1, the velocities of the solution model are less accurate than those of the starting model (Figure 4.20b). The behaviour of the χ^2 misfit function (Figure 4.20c), which suddenly increases at iteration 3, also suggests that the inversion has become unstable. Evidently, the problem is not adequately constrained by the data alone, and additional constraints are required.

Setting ϵ to a value greater than zero decreases the non-uniqueness of the solution

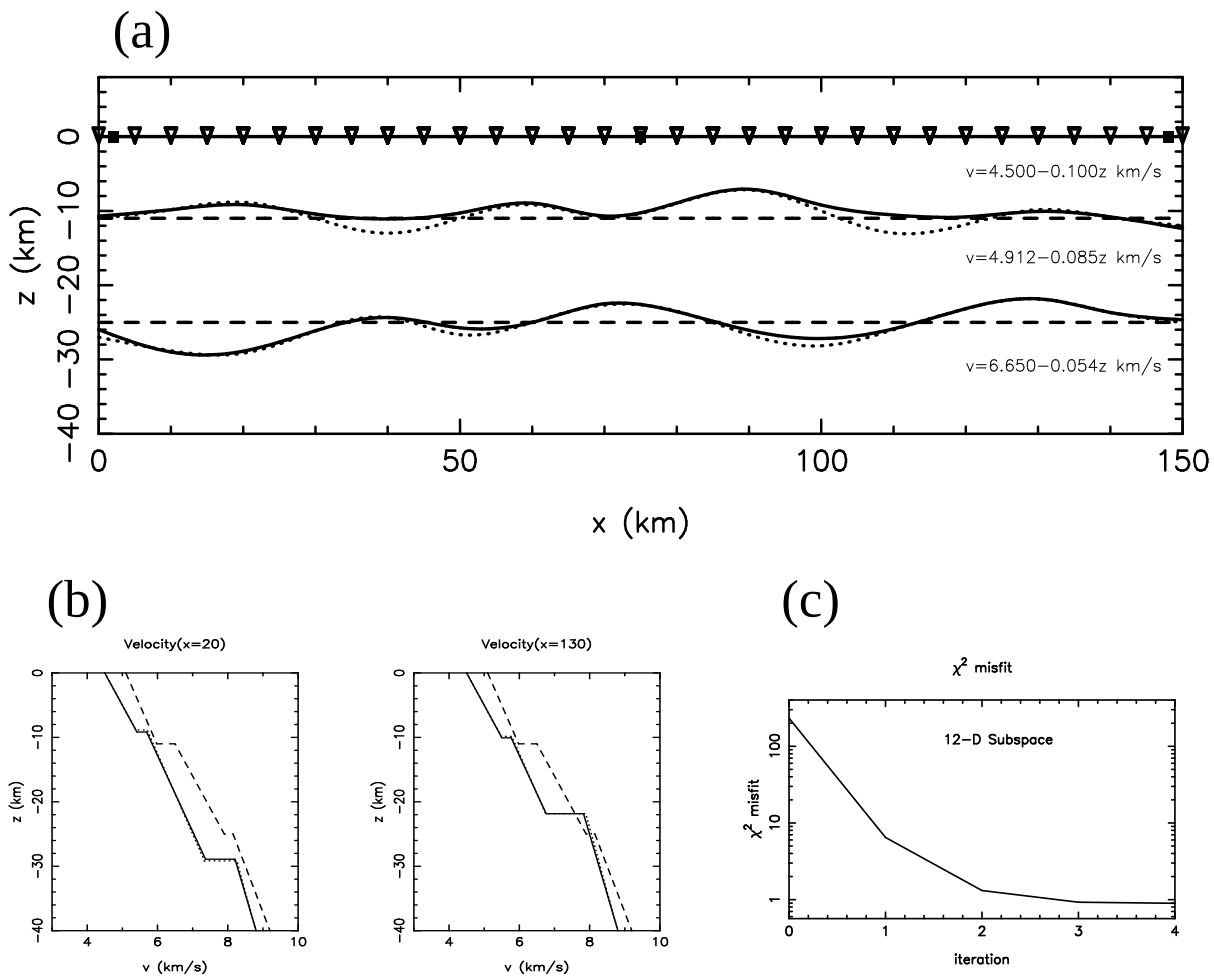

Figure 4.21: Inversion result using Model B data with 70 ms data noise and $\epsilon = 1$ after 4 iterations. (c.f. Figure 4.20). (a) Interface structure: initial model shown by dashed lines, recovered model by solid lines and true model by dotted lines. (b) Velocity structure: models denoted as in (a). (c) χ^2 misfit function versus iteration.

because it restricts the minimum of the objective function to regions of model space "near" the initial model. The value of ϵ governs the trade-off between how well the data is fit and how closely the recovered model resembles the initial model. The relative freedom of each model parameter is determined by the entries of the *a priori* model covariance matrix $\mathbf{C}_m$. In this case, the $\{\sigma_m^j\}$ are based on the standard deviations of the differences (calculated for each parameter) between the true and initial depths of each interface, the true and initial velocities and the true and initial velocity gradients. The values used are 2.0 km for the top interface, 2.5 km for the bottom interface, 0.53 km/s for the velocities and 0.02 s^{-1} for the velocity gradients.

The solution with $\epsilon = 1$ (Figure 4.21) is clearly superior to the solution shown in

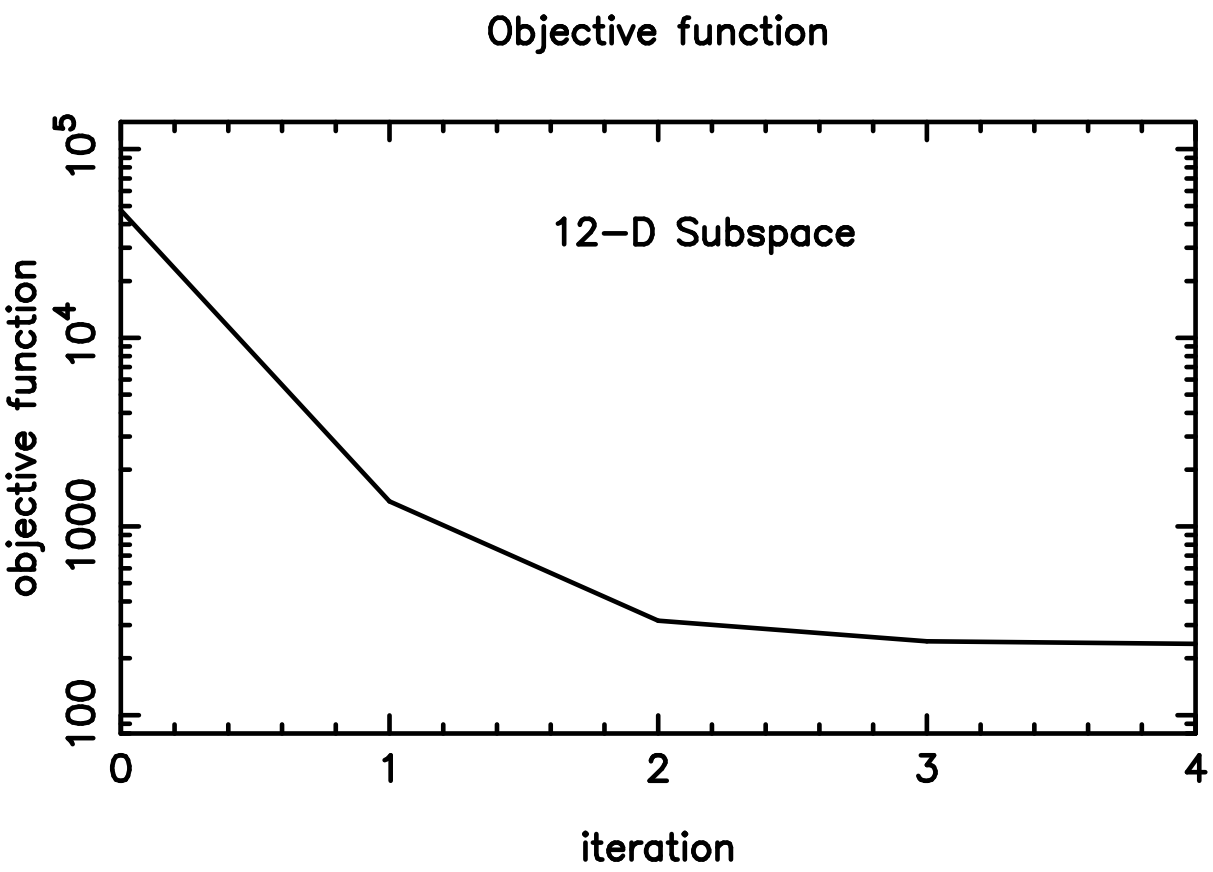

Figure 4.22: Objective function versus iteration for the inversion solution shown in Figure 4.21.

Figure 4.20 with $\epsilon = 0$. Interface structure is generally well recovered, except for those regions that are less well constrained by ray paths (see Figure 4.19). In particular, the top interface in the intervals $20 \leq x \leq 50$ km and $100 \leq x \leq 120$ km is not hit by reflected rays and is only hit by a few refracted rays. The velocity field in each layer is accurately recovered (Figure 4.21b) and the χ^2 misfit function (Figure 4.21c) reduces monotonically from its initial value of about 233 to below 1 after 4 iterations, indicating that the data is satisfied. The behaviour of the objective function for the inversion result of Figure 4.21 is shown in Figure 4.22. It is similar in shape to the χ^2 misfit function since the data residual term is the dominant term in the objective function.

The optimum value of ϵ is that which results in a solution that adequately satisfies the data while minimising the perturbation from the initial model. One way of locating this point is to plot χ^2 misfit versus RMS model perturbation (see Equations 4.20 and 4.21). Figure 4.23a shows the final misfit function values for inversions with ϵ ranging between 0 and 100 after 4-iteration inversions. For all three parameter classes, $\epsilon = 0$ results in a poor fit to the data and results in a solution model that is distant from the initial model. Using

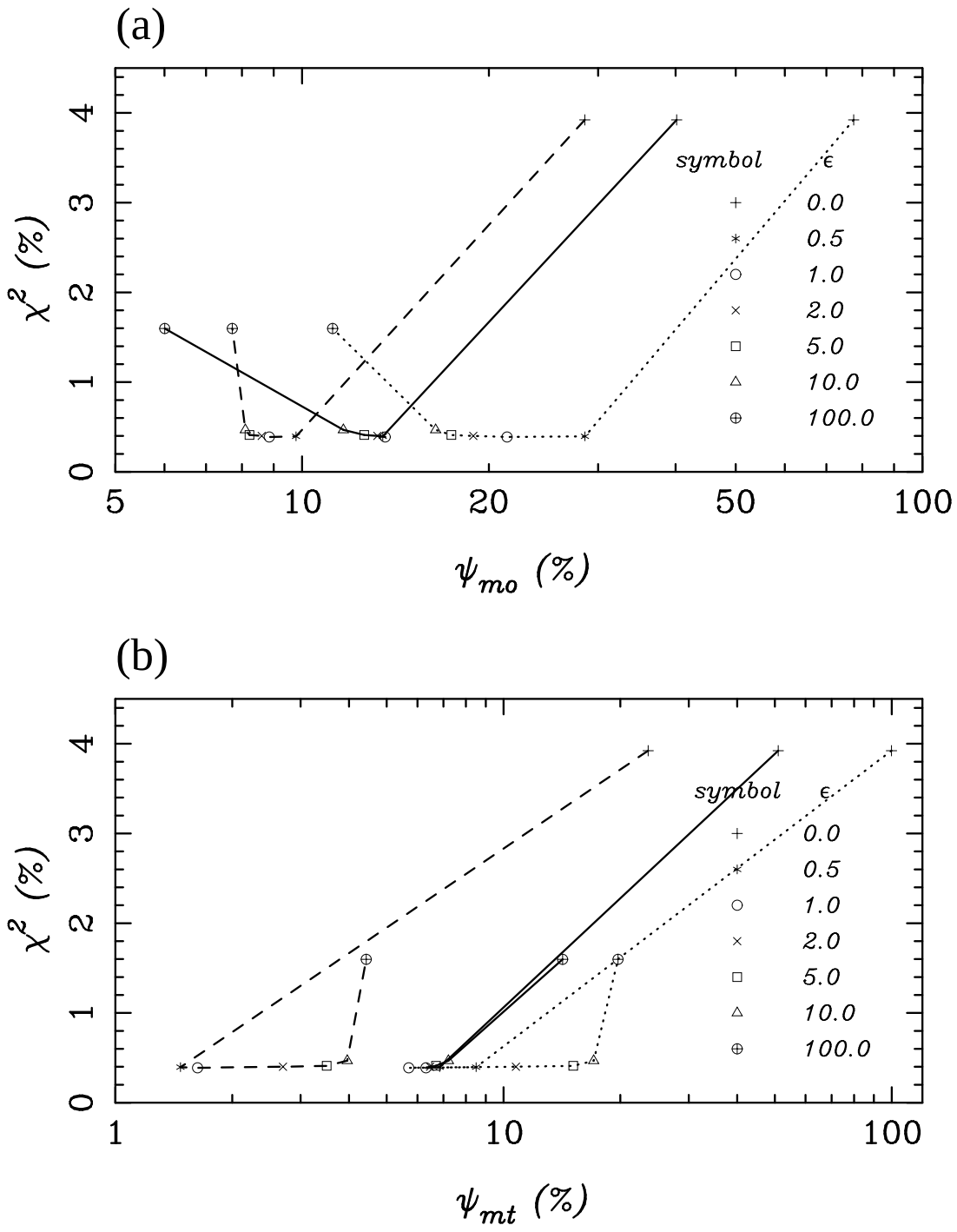

Figure 4.23: (a) χ^2 data misfit (Equation 4.20) versus RMS model perturbation ψ_{mo} (Equation 4.21), and (b) data misfit χ^2 versus model inaccuracy ψ_{mt} (obtained from Equation 4.21 by replacing the initial model $\{m_o^i\}$ with the true model $\{m_t^i\}$) for various values of the damping factor ϵ after four iterations of the inversion using the Model B dataset. The three misfit measures χ^2, ψ_{mo} and ψ_{mt} are plotted as a percentage of their initial values (i.e. at iteration zero). The model perturbation ψ_{mo} (and ψ_{mt}) is determined separately for each parameter type: interface node depth (solid line), layer velocity (dashed line) and layer velocity gradient (dotted line).

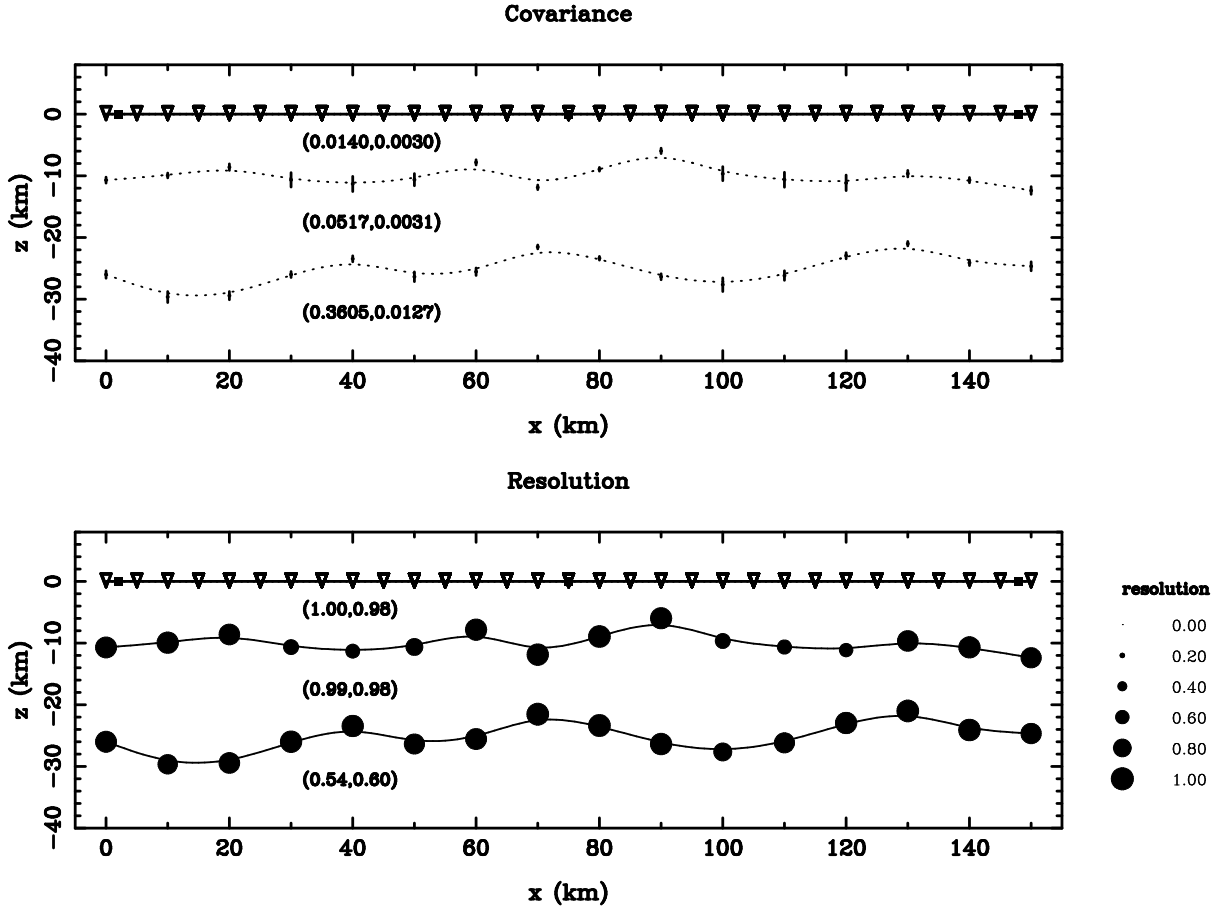

Figure 4.24: Plots of the square root of the diagonal entries of the *a posteriori* covariance matrix $\mathbf{C}_M$ (error bars) and the diagonal entries of the resolution matrix $\mathbf{R}$ (black filled circles) for the (Model B) solution shown in Figure 4.21. Labels in each layer represent the covariance or resolution of velocity and velocity gradient (v_o,k) parameters respectively.

$\epsilon = 100$ produces a solution that is close to the initial model but the data fit is again poor. The range $1 \leq \epsilon \leq 5$ promises the kind of solutions that satisfy the above requirement. Exactly which value to use in this range is hard to justify on the basis of the shape of the curves in this region, but if they all produce similar models, then the exact value used is not important. Figure 4.23b differs from Figure 4.23a in that the abscissa is plotted against percentage RMS perturbation of the solution model relative to the true model. The $\epsilon = 0.5$ solution best satisfies the velocity parameters, although the $\epsilon = 1$ solution is only marginally poorer. However, the $\epsilon = 1$ solution best matches the interface and velocity gradient parameter classes and is therefore the optimum ϵ value of those tested. In the absence of Figure 4.23b (i.e. in a real data situation), then the poorer models with $\epsilon = 2$ or 5 are valid models as far as Figure 4.23a is concerned. However, these models are only slightly perturbed from the $\epsilon = 1$ model in velocity and velocity gradient. These

perturbations are a result of trade-offs between velocity and velocity gradient parameters and do not result in any significant differences between the corresponding layer velocity fields.

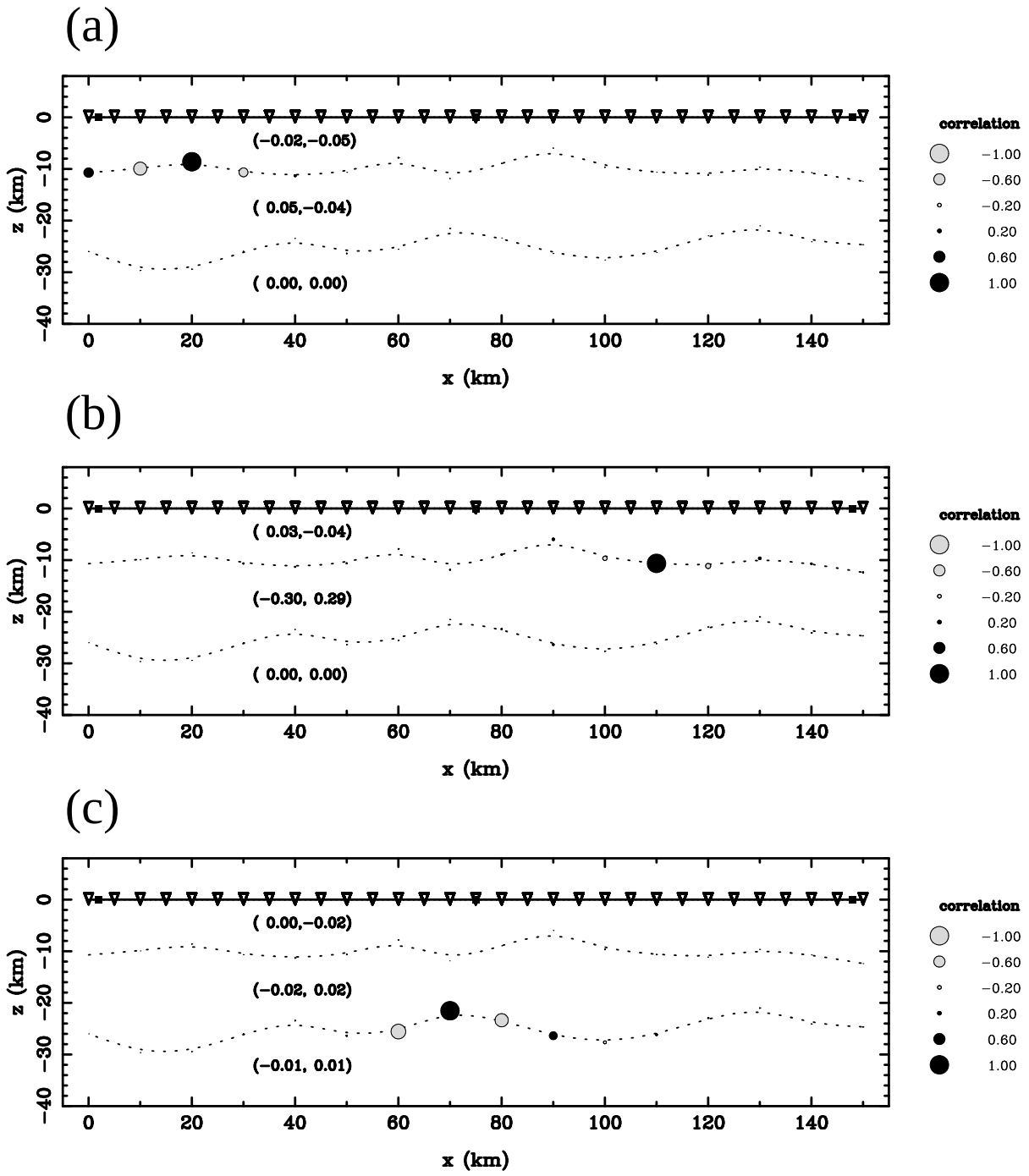

Figure 4.25: Correlation plots for nodes at (a) $x = 20$ km in the top interface, (b) $x = 110$ km in the top interface, and (c) $x = 70$ km in the bottom interface of the Model B inversion shown in Figure 4.21. Correlations with velocity and velocity gradients are shown numerically in brackets: (velocity correlation, velocity gradient correlation).

The great advantage of synthetic tests over real data applications is that the solution model can be compared to the true model. When this is not possible, other means of assessing the accuracy of the reconstruction are required. Here, results from linear theory (see Section 2.4) - namely estimates of *a posteriori* model covariance, resolution and correlation - are used to assess solution quality. Figure 4.24 shows the square roots of the diagonal elements of the *a posteriori* model covariance matrix $\mathbf{C}_M$ and the diagonal elements of the resolution matrix $\mathbf{R}$, calculated at the solution point for the reconstruction shown in Figure 4.21. The square roots of the diagonal elements of the *a posteriori* model covariance matrix can simply be interpreted as the posterior uncertainty associated with each model parameter. Comparison of Figure 4.24 and Figure 4.21 clearly shows that the interface parameters with the largest errors correspond to those parts of the interface that are most poorly recovered. The same holds true for the velocity parameters, with the parameters of the top layer showing the smallest uncertainties (and accurate recovery), and those of the bottom layer showing the largest uncertainties (and slightly poorer recovery). The diagonal elements of the resolution matrix indicate how well each parameter is independently resolved by the dataset. In this case, most of the interface parameters are well resolved (values near 1), and those that are not (values near 0) again correspond to those parts of the solution (Figure 4.21) that are not well recovered. Generally, these indicators of model robustness should be used in a relative rather than absolute sense, since there is a trade-off between resolution and model uncertainty, the problem is non-linear, and the ability of the model to accurately represent the true structure is not accounted for.

Off-diagonal elements of $\mathbf{C}_M$ can be analysed in terms of correlations (see Equation 2.78). Figure 4.25 shows how three interface nodes correlate with the other parameters. The correlation of a parameter with itself is, by definition, 1. The node in the top interface (Figure 4.25a) at $x = 20$ km is anti-correlated with the adjacent nodes in the same interface. In turn, the nodes adjacent but one are positively correlated, although to a much lesser degree. This pattern indicates that the part of the interface surface influenced by the node at $x = 20$ km is well constrained; if the node moves in one direction, the adjacent nodes must move in the opposite direction in order to retain the shape of the interface (recall that the interface structure is defined by bicubic B-splines - see Equation 4.2). Similarly, the node at $x = 70$ km in the bottom interface (Figure 4.25c) describes a well constrained part of the interface. However, the node at $x = 110$ km in the top interface (Figure 4.25b), which is known to be inaccurate, neither correlates nor anti-

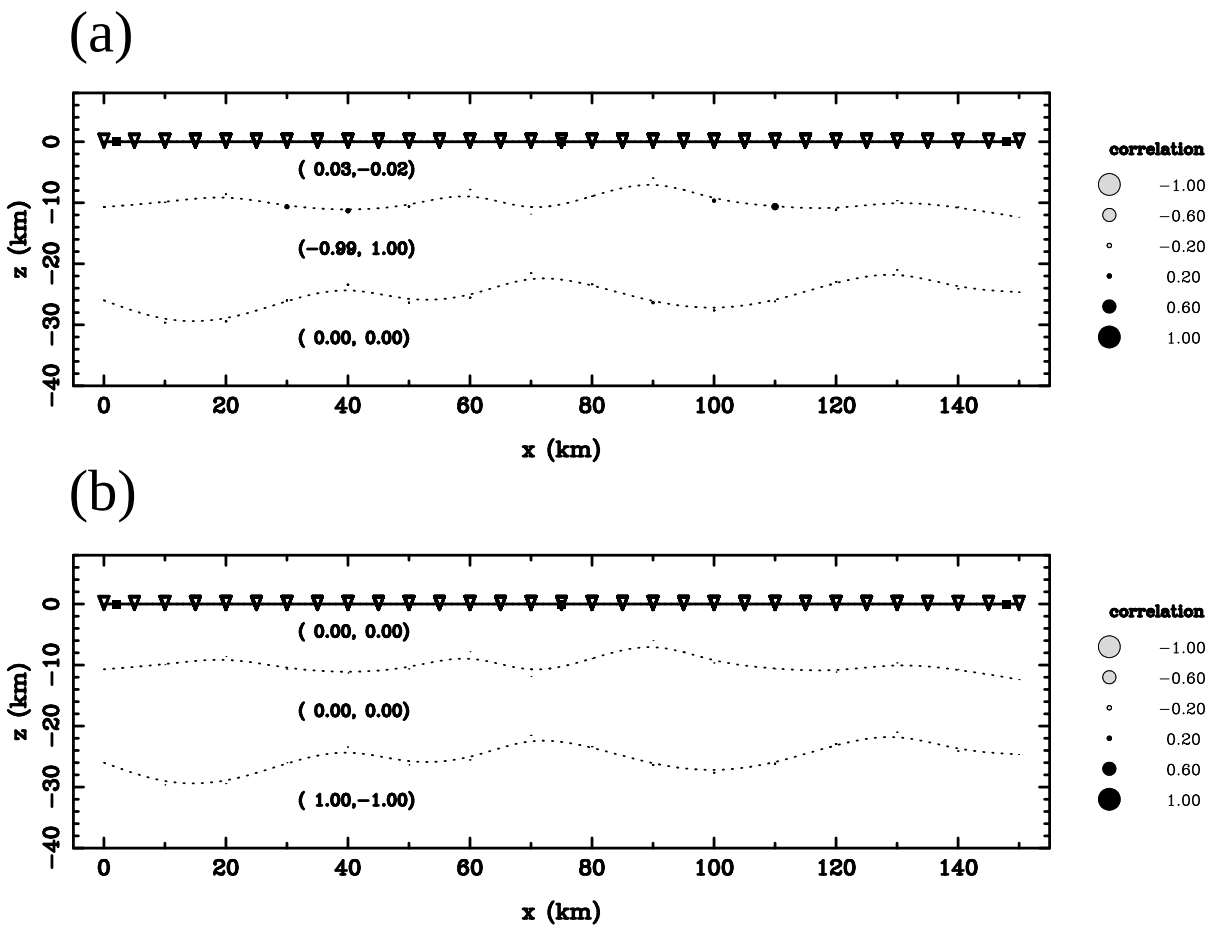

Figure 4.26: Correlation plots for velocity parameters: (a) k in layer 2 and (b) v_0 in layer 3 for the Model B inversion shown in Figure 4.21. Correlations with velocity and velocity gradients are shown numerically in brackets: (velocity correlation, velocity gradient correlation).

correlates significantly with the adjacent nodes. A change in depth of this node does not require any compensatory movement by nearby nodes to satisfy the data, so this part of the interface is not accurately constrained. Interestingly, the velocity v_0 in the middle layer is anti-correlated and the velocity gradient k is positively correlated with the poorly resolved node. This indicates that the data does not adequately resolve the trade-off between the node position and the velocity field of the layer beneath.

Correlations of the velocity parameters can also be examined. Correlation coefficients of the velocity gradient in the middle layer with all the other parameters (Figure 4.26a) shows a strong anti-correlation with the velocity in the same layer. This strong anti-correlation indicates that the velocity field is well resolved as a change in k requires an opposite change in v_o to retain v. Since all other correlations are near zero, there is no trade-off with any other parameter (except to a small degree with the node at $x = 110$

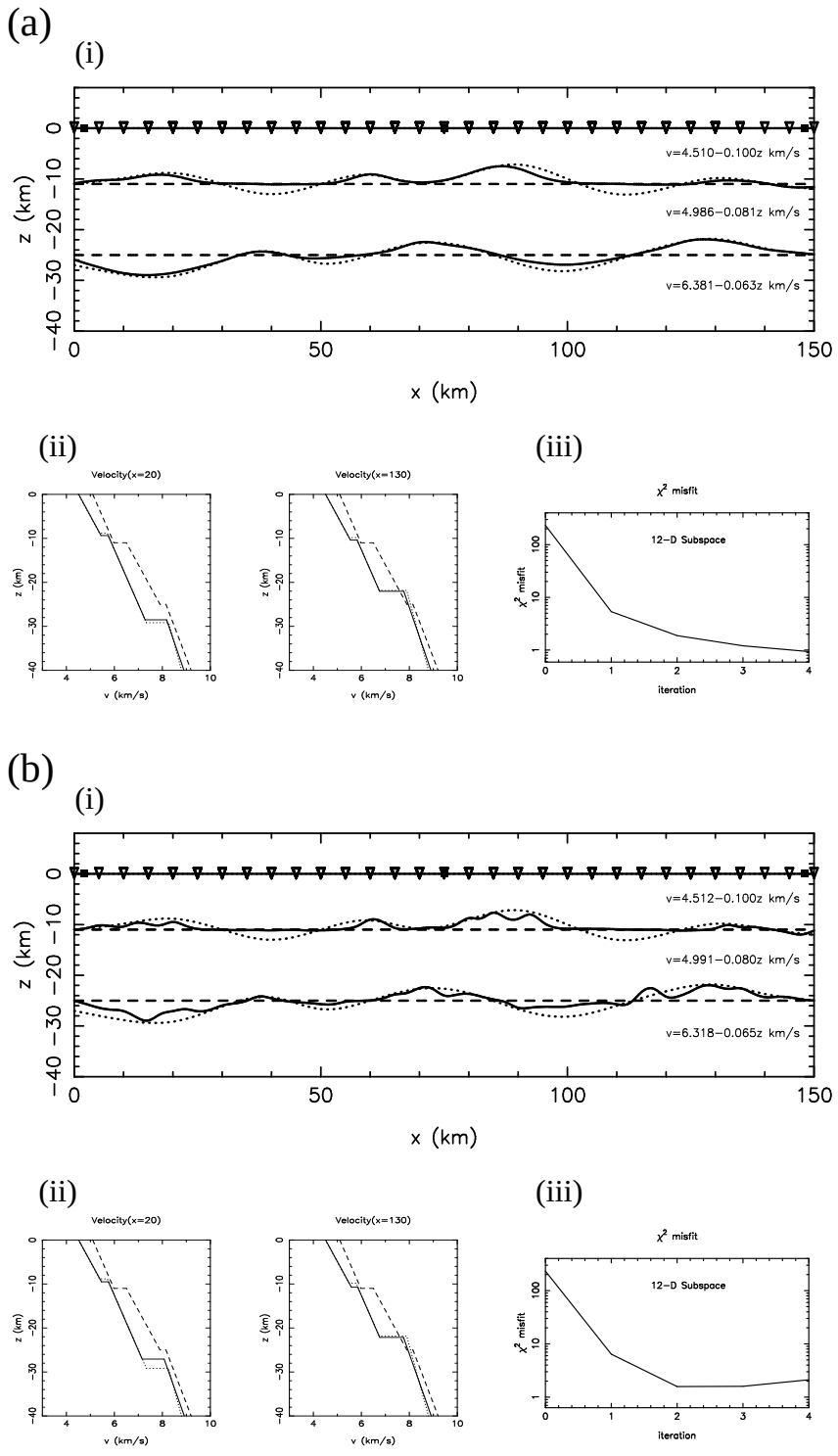

Figure 4.27: Inversion result using model B synthetic data with 70 ms data noise, $\epsilon = 5$ and overparameterised initial models. Initial models, recovered models and true models are denoted by dashed, solid and dotted lines respectively, for a model parameterisation with interface nodes at a uniform 5 km (a) and 2.5 km (b) horizontal spacing. (i) Interface structure, (ii) velocity structure, and (iii) χ^2 misfit function versus iteration.

km in the top layer) so the velocity field is well resolved. A similar scenario occurs for the velocity parameter in the lowest layer (Figure 4.26b).

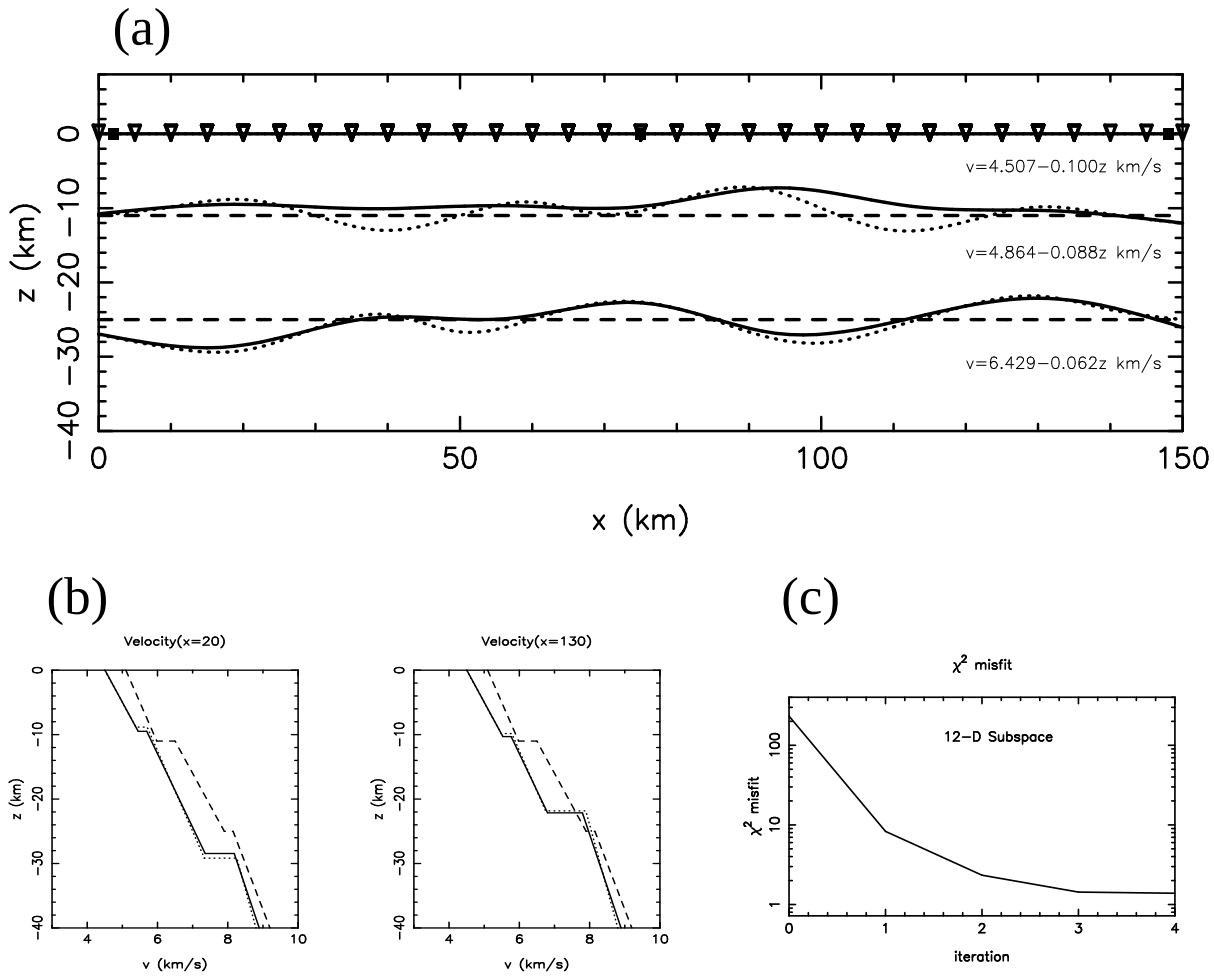

Figure 4.28: Inversion result using the Model B synthetic data with 70 ms data noise, $\epsilon = 1$, and an underparameterised initial model (18.75 km uniform horizontal spacing of interface nodes. (a) Interface structure: initial model shown by dashed lines, recovered model by solid lines and true model by dotted lines. (b) Velocity structure: models denoted as in (a). (c) χ^2 misfit function versus iteration. Solution model achieved after 4 iterations

Another convenience of synthetic tests is that the number and horizontal distribution of parameters is known, so choosing the most appropriate node distribution for a reconstruction is elementary, provided the data is capable of resolution at this level. In real data applications, the optimal model parameterisation uses the minimum number of layers and interface nodes that adequately satisfies the data. Like damping, this is an area where trade-off between model and data considerations govern the solution choice. In the preceding examples, the inversion assumed the same parameterisation as was used to

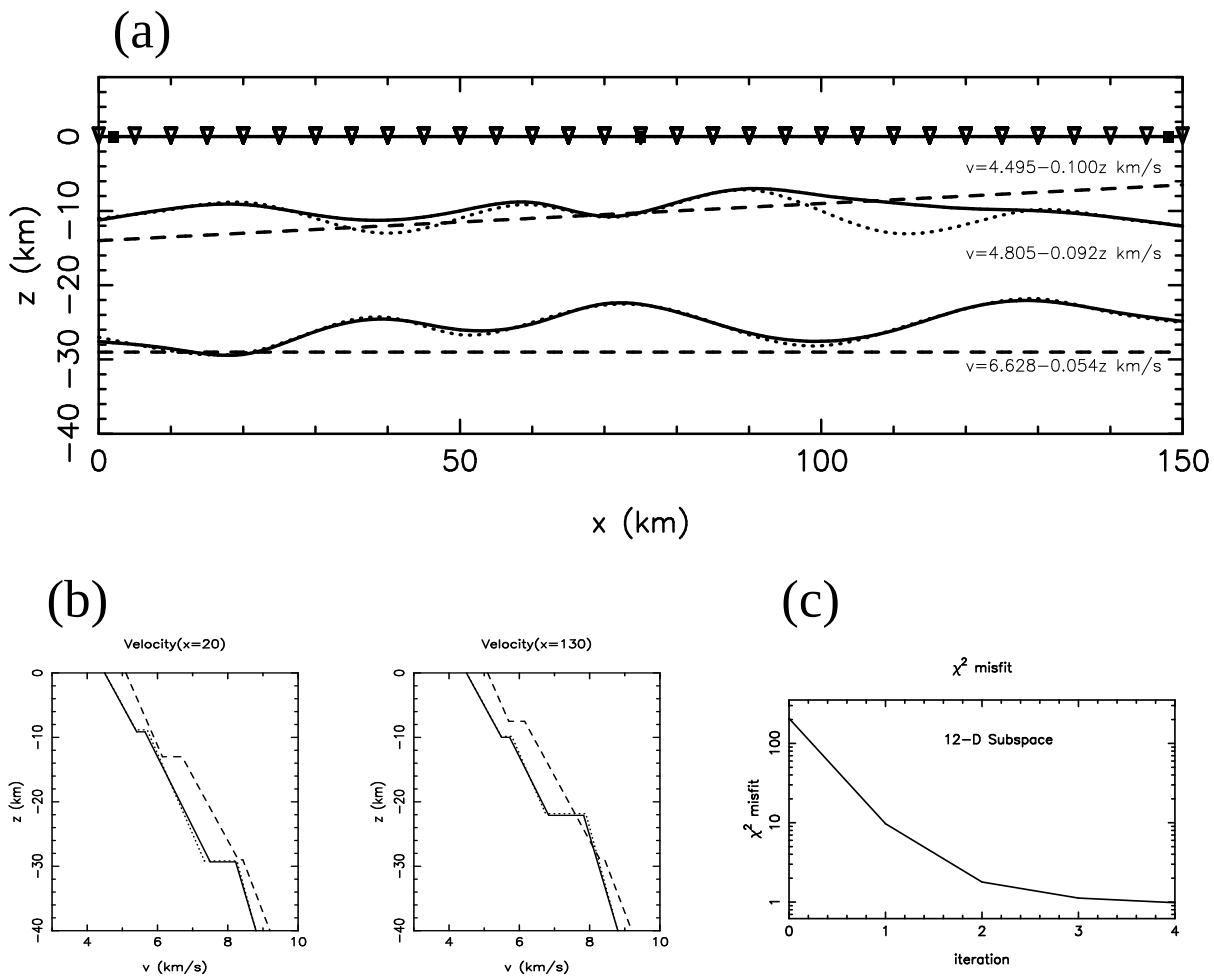

Figure 4.29: Inversion result using the Model B synthetic data with 70 ms data noise, $\epsilon = 1$ and an inaccurate initial model. (a) Interface structure: initial model shown by dashed lines, recovered model by solid lines and true model by dotted lines. (b) Velocity structure: models denoted as in (a). (c) χ^2 misfit function versus iteration. Solution model achieved after 4 iterations

generate the synthetic dataset. Figure 4.27a illustrates the result of inverting the Model B dataset using an interface parameterisation in which the node separation is halved (i.e. each interface is now described by 31 nodes at 5 km spacing). The reconstruction (Figure 4.27a(i)-(ii)) is nearly as accurate as that of Figure 4.21. The χ^2 misfit function again decreases monotonically and drops to just below 1 (Figure 4.27a(iii)). The damping factor was increased to $\epsilon = 5$ in order to achieve monotonic convergence. For smaller ϵ, the solution does not converge. With 5 km node-spacing, the poorly resolved parts of the top interface ($30 \leq x \leq 50$ km and $100 \leq x \leq 120$ km) do not move from their initial positions.

When node spacing is decreased further to a quarter of the original spacing (i.e. each

interface is described by 61 nodes at 2.5 km spacing) the solution shows characteristics typical of overparameterisation (Figure 4.27b). The actual shape of the interfaces are recovered to some degree (Figure 4.27b(i)) and the velocity field is quite accurately determined (Figure 4.27b(ii)), but a short wavelength oscillation is superimposed on the interface structure. This spurious structure is a consequence of the data having insufficient resolving power to constrain these additional high wavenumber components of the solution. The growth of the data misfit function (Figure 4.27b(iii)) after iteration 3 is associated with the development of these spurious high-wavenumber components.

Increasing node spacing to nearly twice the original spacing (i.e. each interface is described by 9 nodes at 18.75 km separation) results in the solution shown in Figure 4.28. Convergence is achieved after four iterations (Figure 4.28c) and the interfaces are approximately reconstructed (Figure 4.28a), although some of the shorter wavelength features are not recovered. As in the previous examples, the layer velocities are quite accurately resolved (Figure 4.28b). The data misfit function behaves monotonically (Figure 4.28c) but it does not decrease to a value of one or below, which indicates that the data is not optimally satisfied. For the inversion of real data, the least number of nodes should be used that results in a solution that adequately satisfies the data.

Setting the initial model interface structure to approximately the horizontal average of the true model interface structure is appropriate here because in a real data application, an initial model could be derived from a 1-D refraction analysis or inversion, a surface wave inversion or a receiver function analysis. It cannot always be assumed, however, that an accurate 1-D model will be available, or, if significant dipping is present, even be desirable. Figure 4.29 shows the result of an inversion in which the interface depths used in the initial model are inaccurately estimated. The bottom initial interface is deeper than the average depth of the true interface and the top initial interface has a 3° positive slope. Despite this, the interface (Figure 4.29a) and velocity (Figure 4.29b) reconstructions are relatively accurate, except for those regions known to be poorly resolved by the data. The χ^2 misfit function (Figure 4.29c) behaves monotonically and indicates that the solution satisfies the data at iteration 4. I showed earlier (see Chapter 3) that teleseismic traveltime residuals do not constrain mean vertical structure, but in the case of wide-angle traveltimes, which are absolute and turn back towards the surface, the initial model estimate need not possess the correct mean vertical structure in order to achieve an accurate reconstruction.

The inversion method described in the previous section is designed to deal with layer

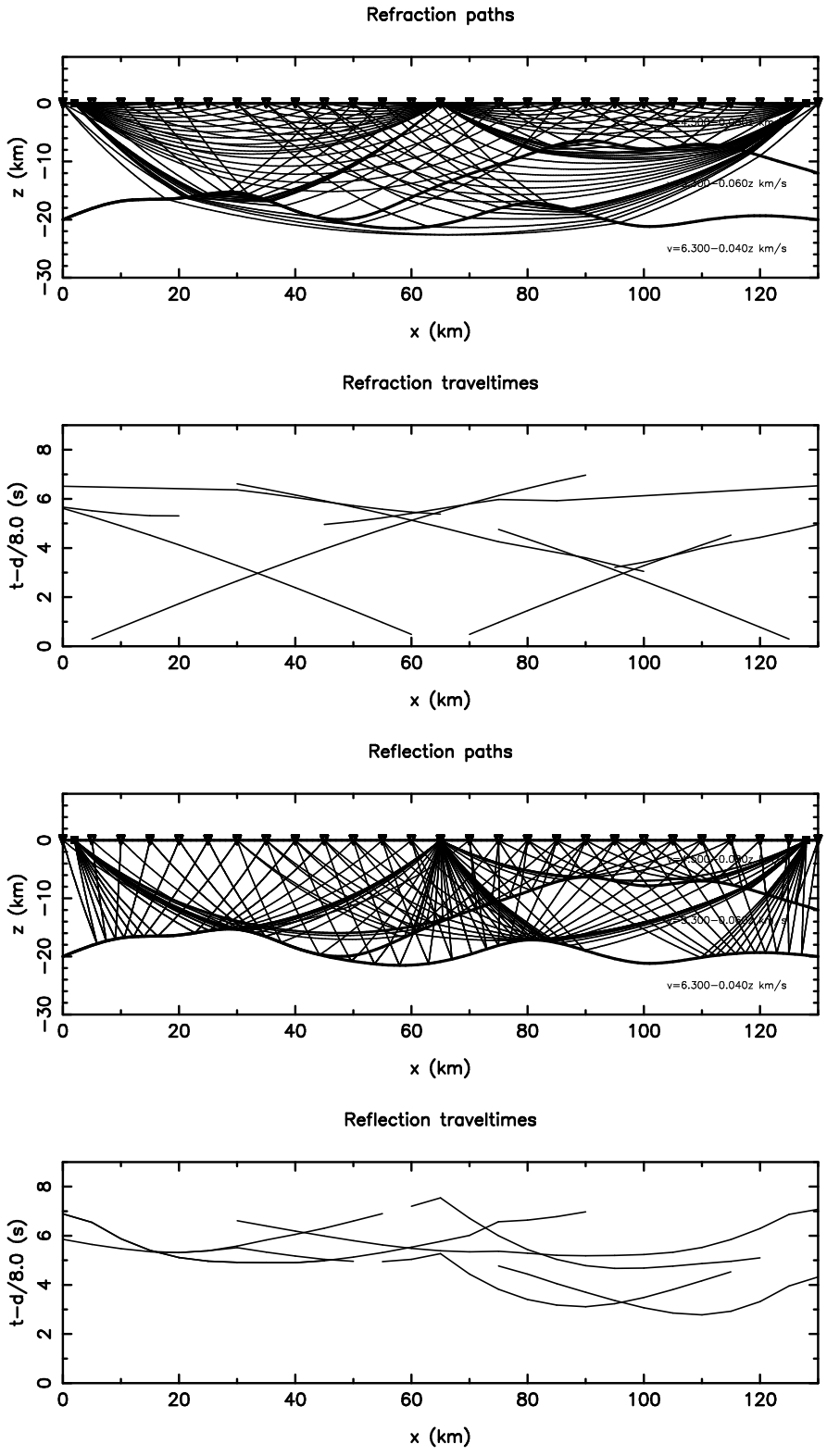

Figure 4.30: Refraction and reflection ray paths through a three-layer model (Model C) in which the middle layer pinches out at about $x = 45$ km. Traveltimes are interpolated to show traveltime curves. Receivers are denoted by ∇ and sources by filled squares.

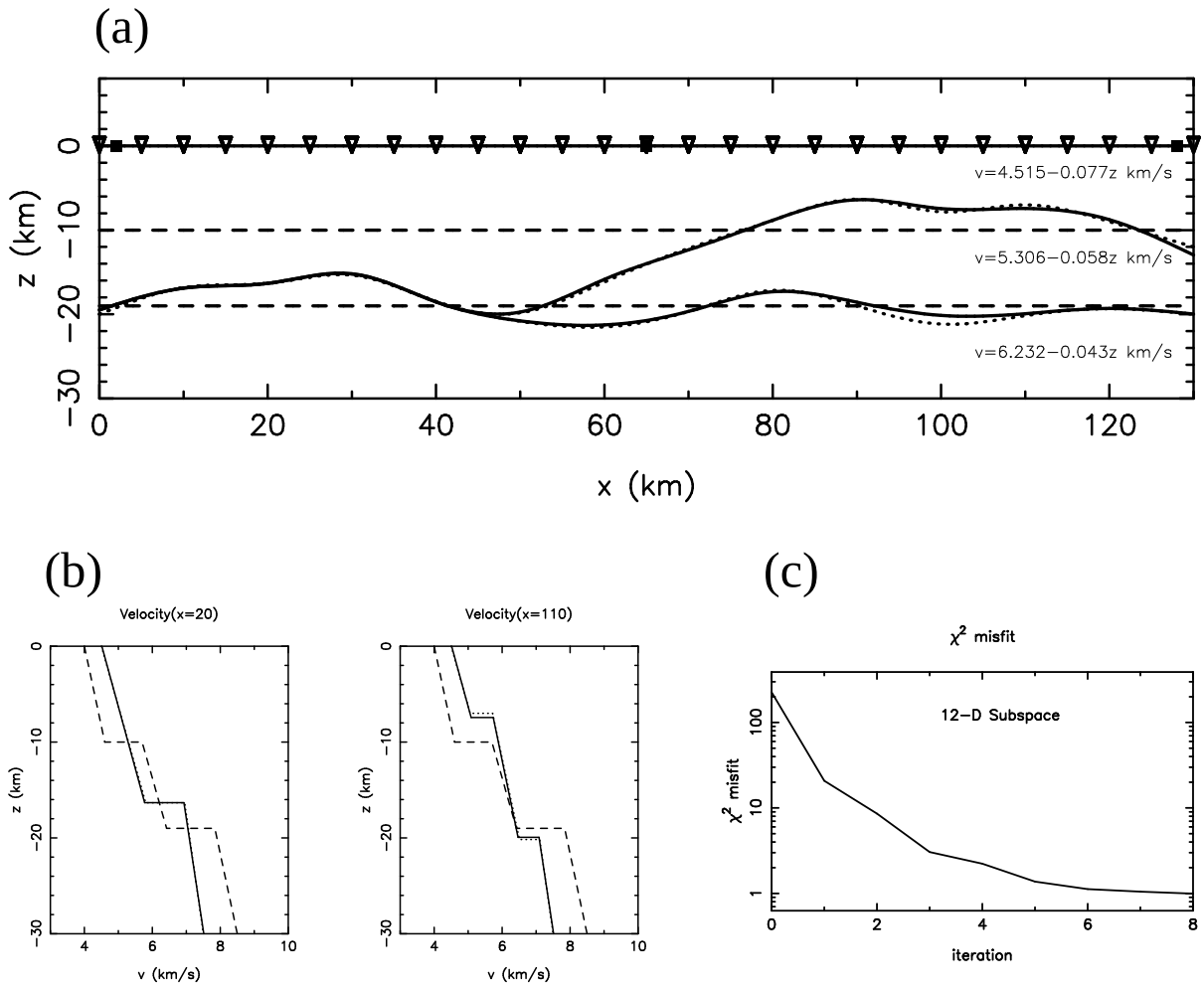

Figure 4.31: Inversion result (after eight iterations) using Model C data with 70 ms data noise and $\epsilon = 2$. (a) Interface structure: initial model shown by dashed lines, recovered model by solid lines and true model by dotted lines. (b) Velocity structure: models denoted as in (a). (c) χ^2 misfit function versus iteration.

pinchouts. This capability is tested here by a final 2-D example. Figure 4.30 shows refracted and reflected rays and their associated traveltimes through a two-interface structure that contains a layer pinchout (Model C). The layer velocities (and layer velocity gradients) are 4.5 (0.08), 5.3 (0.06) and 6.3 (0.04) km/s (s^{-1}) from top to bottom. Three sources and 27 receivers are used in a similar configuration to the previous examples. The traveltimes are contaminated with Gaussian noise of standard deviation 70 ms. Interface node separation is uniform at 10 km and the initial model used for the inversion is 1-D and produces an RMS data misfit of 1.06 s. For the initial model, layer velocities (and velocity gradients) are 4.0 (0.06), 4.9 (0.08) and 6.7 (0.06) km/s (s^{-1}) from top to bottom. The inversion result obtained using a damping value of $\epsilon = 2$ with initial model covariance

estimates of 5 km and 2 km for the top and bottom interfaces respectively and 0.5km/s and 0.02 s^{-1} for the velocity and velocity gradients respectively is shown in Figure 4.31. Both interfaces are accurately reconstructed including the pinched-out region, where the interfaces merge together (Figure 4.31a). The velocity fields are recovered accurately in all layers (Figure 4.31b) and the data misfit function behaves monotonically (Figure 4.31c) as it achieves a reduction to just below $\chi^2 = 1$. Eight iterations of the 12-D subspace method, compared to four in the previous examples, were required to achieve this result, reflecting the inaccuracy of the initial model and the complexity of the structure.

4.3.2 Inversion for 3-D Structure

The 2-D synthetic tests of the previous section have illuminated many characteristics of the inversion method, including its behaviour in the presence of data noise, poor initial model estimates, inhomogeneous data distribution and over/under-parameterisation. However, the method will ultimately be applied to 3-D wide-angle data, so several synthetic tests are now performed to analyse the ability of the method to invert synthetic data for 3-D structure.

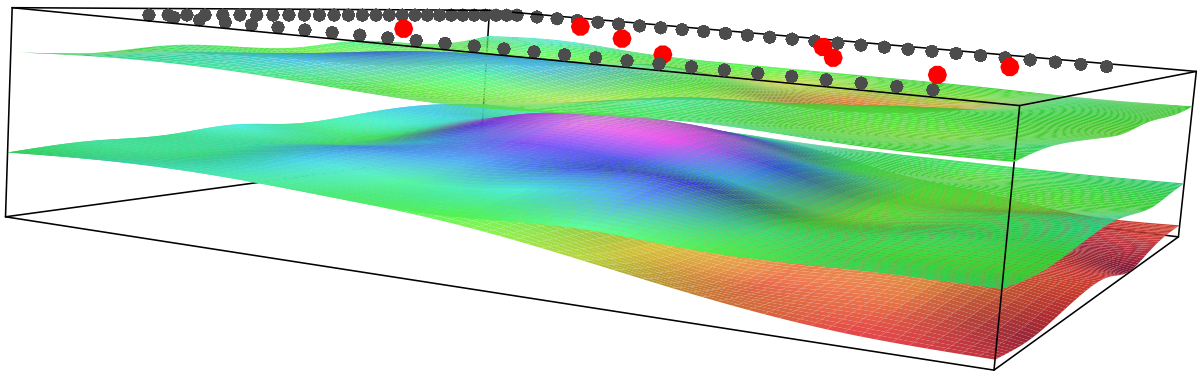

Figure 4.32: Model D used for 3-D synthetic tests. Structure is defined by three interfaces, the lower two of which come together to create a layer pinch-out (LHS of figure). Sources are shown in red and receivers in black. Colour contouring is used to indicate topography. A separate scale is used for the top interface.

The first model considered for the 3-D synthetic tests (Model D) consists of three crustal layers overlying a mantle half-space (Figure 4.32). Significant variations in interface depth are present in the model and the lower crustal interface pinches out against the Moho in a large region. The three interfaces that define the boundaries between upper

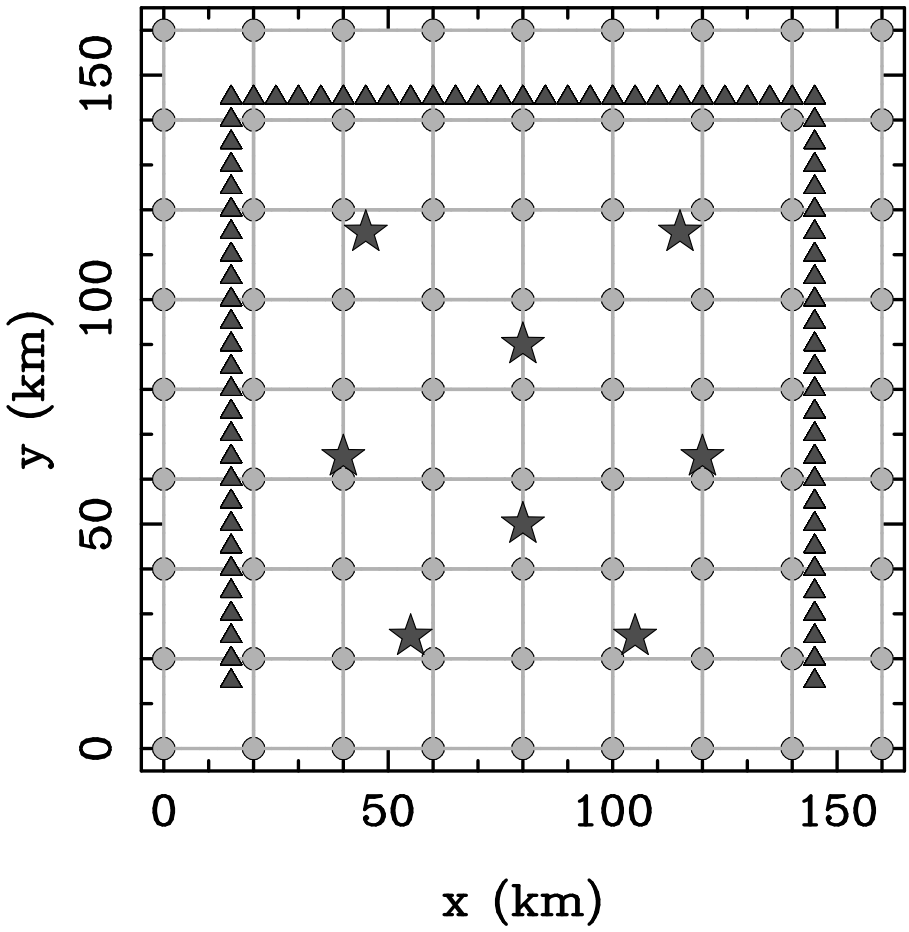

Figure 4.33: Source-receiver array and node distribution for 3-D synthetic test using Model D. Each of the three interfaces has the same node distribution. Nodes are denoted by filled-circles and surface patch boundaries by thin grey lines. Sources are denoted by stars and receivers by triangles.

crust, middle crust, lower crust and mantle are identically parameterised with 9 by 9 vertices (Figure 4.33) spaced evenly in both x and y ($\Delta x = \Delta y = 20$ km) with a horizontal coverage of 160×160 km. Layer velocities (Table 4.1) are representative of continental crust. The entire model is defined by 251 parameters comprised of 81 vertical coordinates for each interface and two velocity parameters for each layer.

The source-receiver geometry used to investigate Model D consists of 79 receivers spaced 5 km apart along three sides of a square, with eight sources lying inside the square (Figure 4.33). The ratio of sources to receivers used here is typical of land-based surveys (e.g. Darbyshire et al., 1998), but the array geometry is perhaps more likely to be encountered in a marine survey (e.g. the TASGO survey- Chudyk et al., 1995), in which case there would be many more sources than receivers. The principle of reciprocity in ray tracing means, however, that the source array could be treated as the receiver array and

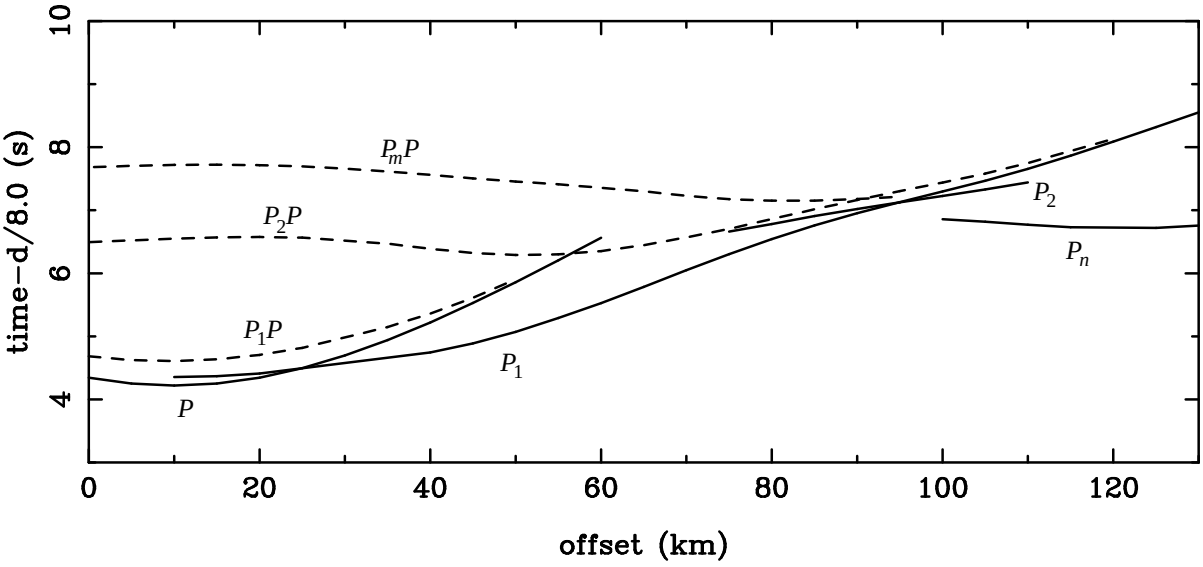

Figure 4.34: Traveltime curves of Model D arrivals from source located at $(x, y) = (55, 25)$ km recorded by receivers that lie along the line $x = 15$ km. Offset is the receiver distance from the start of the line at $(x, y) = (15, 15)$ km, and d is the source-receiver distance. Reflections from the i^{th} interface (P_iP) are denoted by dashed lines, refractions that turn beneath interface i (P_i) by solid lines (P is the direct arrival). Four refraction phases and three reflection phases are evident, indicating the presence of three interfaces.

vice-versa without affecting the inversion result. Computationally, it is more efficient to shoot from a small number of sources to a large number of receivers. The source-receiver array (Figure 4.33) chosen for this test is not optimum for achieving uniform ray coverage and a relatively evenly resolved solution, but instead reflects the kinds of geometries that can be encountered in mixed land and marine type experiments like the TASGO survey.

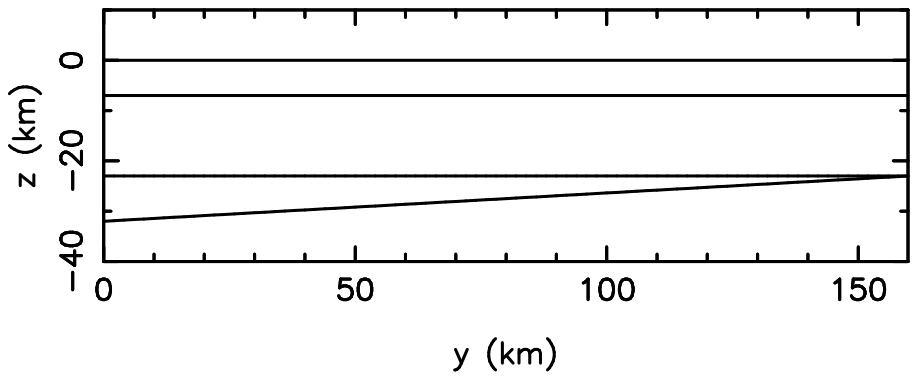

Figure 4.35: Cross-section of the initial model used in the inversion of Model D synthetic data. The structure does not vary with x.

The synthetic dataset was constructed by tracing rays through Model D to determine

paths of up to four refraction phases and three reflection phases for each source-receiver pair. The resulting synthetic dataset consists of the traveltimes of 1917 ray paths (987 refracted and 930 reflected rays). Figure 4.34 shows synthetic traveltime curves from the shot at $(x, y) = (55, 25)$ km recorded by the receivers that lie on the line $x = 15$ km. The four refraction phases correspond to rays that turn in the upper, middle, lower-crustal and mantle layers. The reflection phases are discernible for all three reflectors. The P_2P and P_mP phases merge at an offset of 90 km as a result of the lower-crustal pinch-out. All traveltimes determined by the ray tracing are used in the inversion. With real data, however, the complete offset range of later arrivals determined by ray theory would probably not be picked. To simulate the noise content of real data, Gaussian noise with a standard deviation of 75 ms was added to the synthetic traveltimes.

The initial 3-D model estimate from which the inversion commences has 2-D structure consisting of three planar interfaces. The top two interfaces are horizontal and the depth of the bottom interface varies linearly with distance in the y-direction. A cross-section of the initial model is shown in Figure 4.35 and associated velocity parameters are shown in Table 4.1. Such a starting model could be constructed, for example, from a number of 1-D inversions using separate receiver-source line gathers of the synthetic traveltime dataset.

In executing the synthetic data inversion, the dimension of the subspace inversion scheme was set to 15. Of the 15 basis vectors, seven lie in interface depth parameter space, four lie in velocity parameter space and four lie in velocity gradient parameter space. Since there are only four velocity parameters and four velocity gradient parameters, the basis vectors span the model space of both these parameter classes. In this inversion, a 15-D scheme offered a suitable compromise between the magnitude of the objective function reduction per iteration and the computational effort.

Before commencing the inversion process, the values of the damping parameter ϵ, the data covariance matrix $\mathbf{C}_d$ and the *a priori* model covariance matrix $\mathbf{C}_m$ were specified using a similar approach to that used for the 2-D models in the previous section. The synthetic data was corrupted with Gaussian noise of standard deviation 75 ms, so this value is used in $\mathbf{C}_d : \sigma_d^j = 7.5 \times 10^{-2}$ s, $j = 1, \ldots, N$. In the case of the *a priori* model covariance, the $\{\sigma_m^j\}$ are based on the RMS difference between the true and initial depths of each interface, the true and initial velocities and the true and initial velocity gradients. The values used are 2.0 km for the top interface, 3.0 km for the middle interface, 3.5 km for

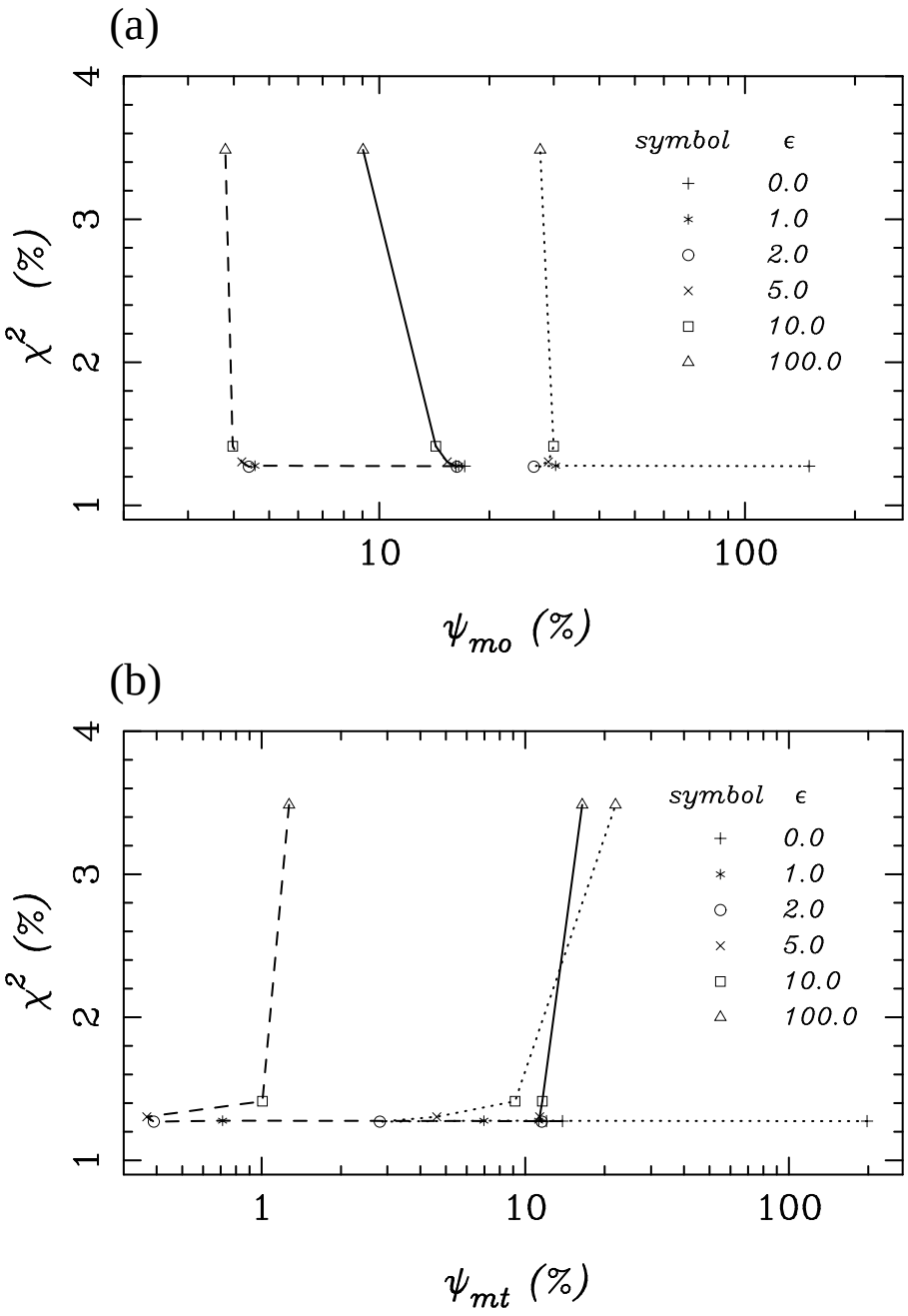

Figure 4.36: (a) χ^2 data misfit (Equation 4.20) versus RMS model perturbation ψ_{mo} (Equation 4.21), and (b) data misfit χ^2 versus model inaccuracy ψ_{mt} (obtained from Equation 4.21 by replacing the initial model $\{m_o^i\}$ with the true model $\{m_t^i\}$) for various values of the damping factor ϵ after seven iterations of the inversion using the Model D dataset. The three misfit measures χ^2, ψ_{mo} and ψ_{mt} are plotted as a percentage of their initial values (i.e. at iteration zero). The model perturbation ψ_{mo} (and ψ_{mt}) is determined separately for each parameter type: interface node depth (solid line), layer velocity (dashed line) and layer velocity gradient (dotted line).

the bottom interface, 0.23 km/s for the velocities and 0.01 s^{-1} for the velocity gradients. To determine the most appropriate value of ϵ, several seven-iteration inversions were

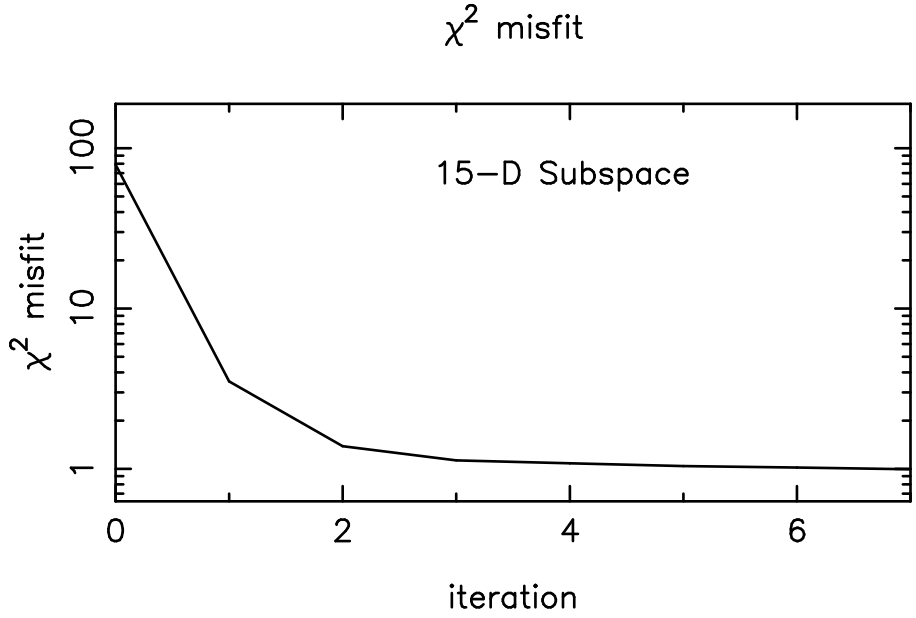

Figure 4.37: χ^2 data misfit versus iteration for the seven iteration inversion using Model D data with $\epsilon = 2.0$ shown in Figure 4.38.

layer	initial model		true model		recovered model		resolution	
	v_0 (kms^{-1})	k (s^{-1})	v_0 (kms^{-1})	k (s^{-1})	v_0 (kms^{-1})	k (s^{-1})	v_0	k
1	4.60	0.060	4.30	0.050	4.31	0.049	1.00	0.97
2	5.00	0.030	5.20	0.040	5.23	0.039	0.99	0.98
3	6.20	0.040	6.00	0.030	6.00	0.030	0.81	0.79
4	7.20	0.030	7.40	0.020	7.41	0.021	0.71	0.72

Table 4.1: Velocity parameter values of initial, true and recovered models for the Model D synthetic test. The corresponding resolution values associated with the recovered model are also given. Layer 1 is the upper crustal (top) layer and layer 4 is the mantle half-space

carried out using values of ϵ between 0 and 100. Figure 4.36a shows the reduction in the data residual χ^2 versus RMS perturbation of the solution model (relative to the initial model) for six different values of ϵ for each parameter class. In the range $1.0 \leq \epsilon \leq 5.0$ the solution is near the minima of the data residual without being highly perturbed from the initial model (Figure 4.36a). It can also be seen (Figure 4.36b) that this range of damping parameters optimises the fit of the solution to the true model. Based on this test, $\epsilon = 2.0$ is chosen as providing the optimal solution, which is described below.

For $\epsilon = 2.0$, the χ^2 data misfit decreases monotonically (Figure 4.37) from an initial value of 69.12 to 1.02 at iteration 7. Correspondingly, the RMS traveltime misfit decreases

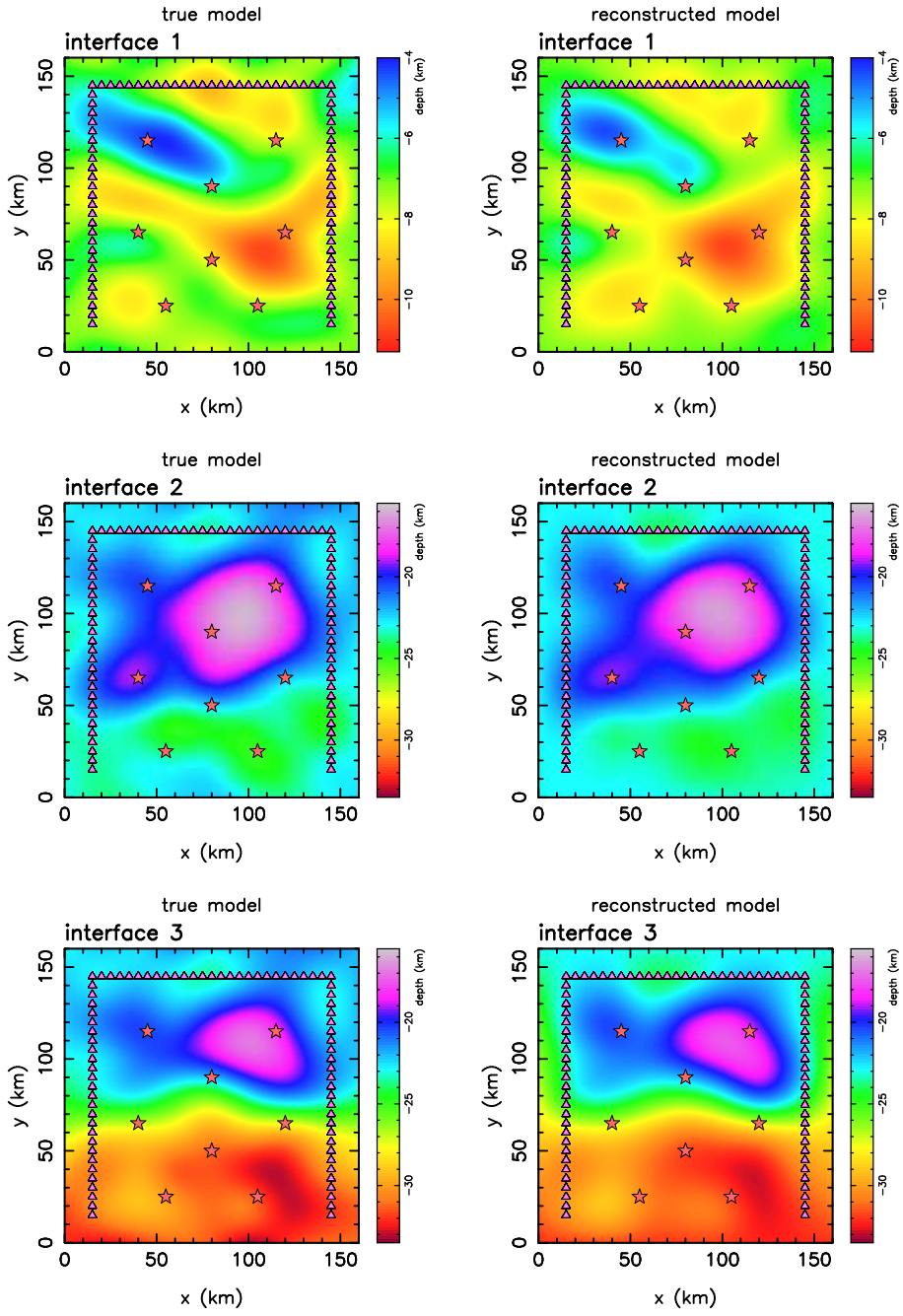

Figure 4.38: Comparisons between true model interface structure (left column) and inverted model interface structure (right column) after seven iterations of the inversion using Model D synthetic data with $\epsilon = 2.0$. The bottom two interfaces (interfaces 2 and 3) are given the same colour scale to help identify the pinched-out regions.

from 667 ms to 75 ms, a value equal to the standard deviation of the noise added to the data. The improvement in χ^2 data misfit between iterations 4 and 7 is very small ($\sim$0.1), and is accompanied by practically negligible changes in the model parameter values. Such behaviour is indicative of a stable inversion. Comparing the interface structure of the true

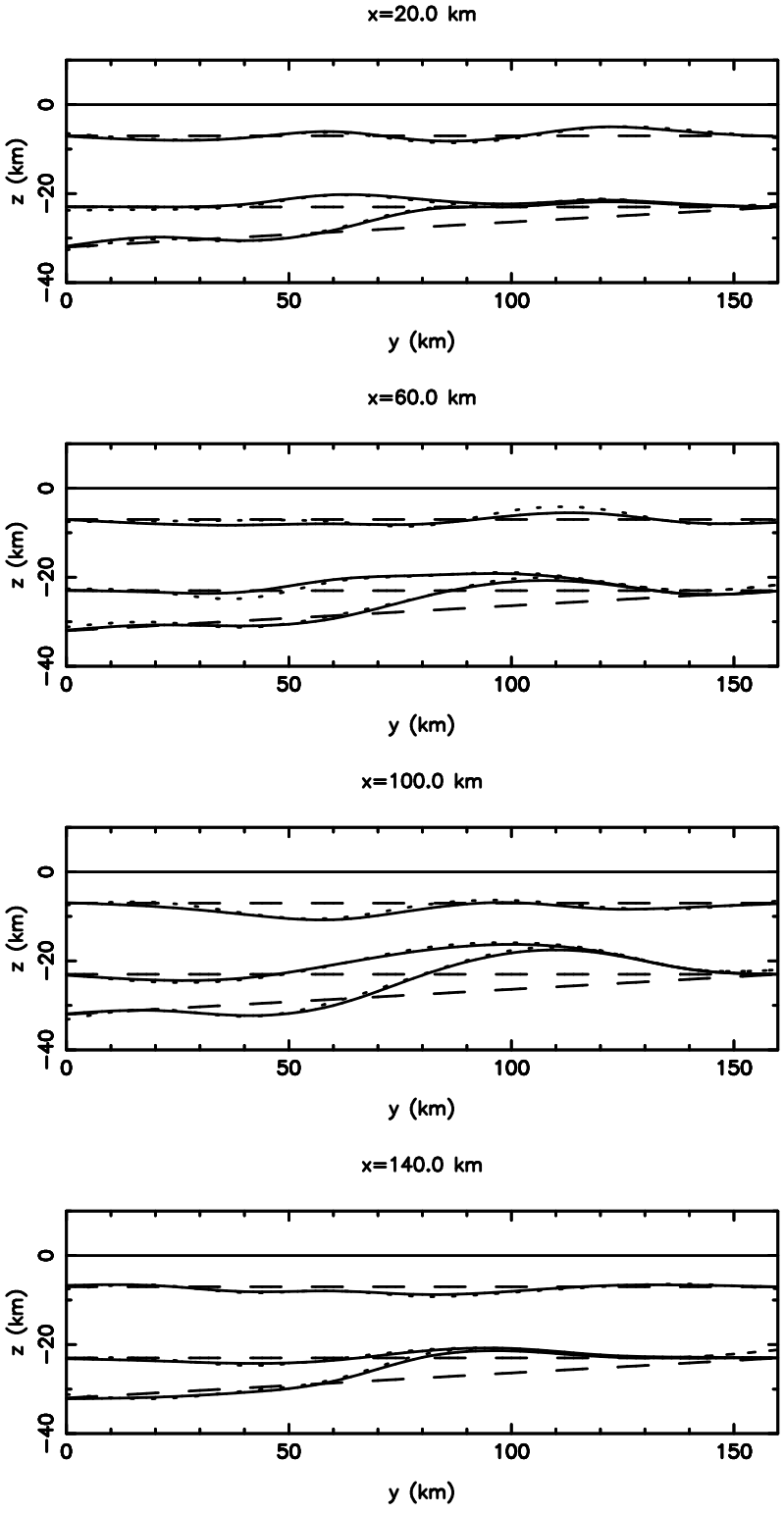

Figure 4.39: Four cross-sections at constant x through the initial model (dashed lines), true model (dotted lines) and reconstructed model (solid lines) obtained by inversion of Model D traveltimes.

model with that of the reconstructed model after seven iterations (Figure 4.38), the basic features of each interface are well recovered. Figure 4.39 shows, in four cross-sections at

constant x, the starting model, the true model and the reconstructed model. It is clear from these sections that even at $(x, y) = (100, 100)$ km, where the difference between the initial model and true model is large, the reconstruction is relatively accurate. Table 4.1 and Figure 4.40 show that the velocity parameters are accurately recovered by the inversion.

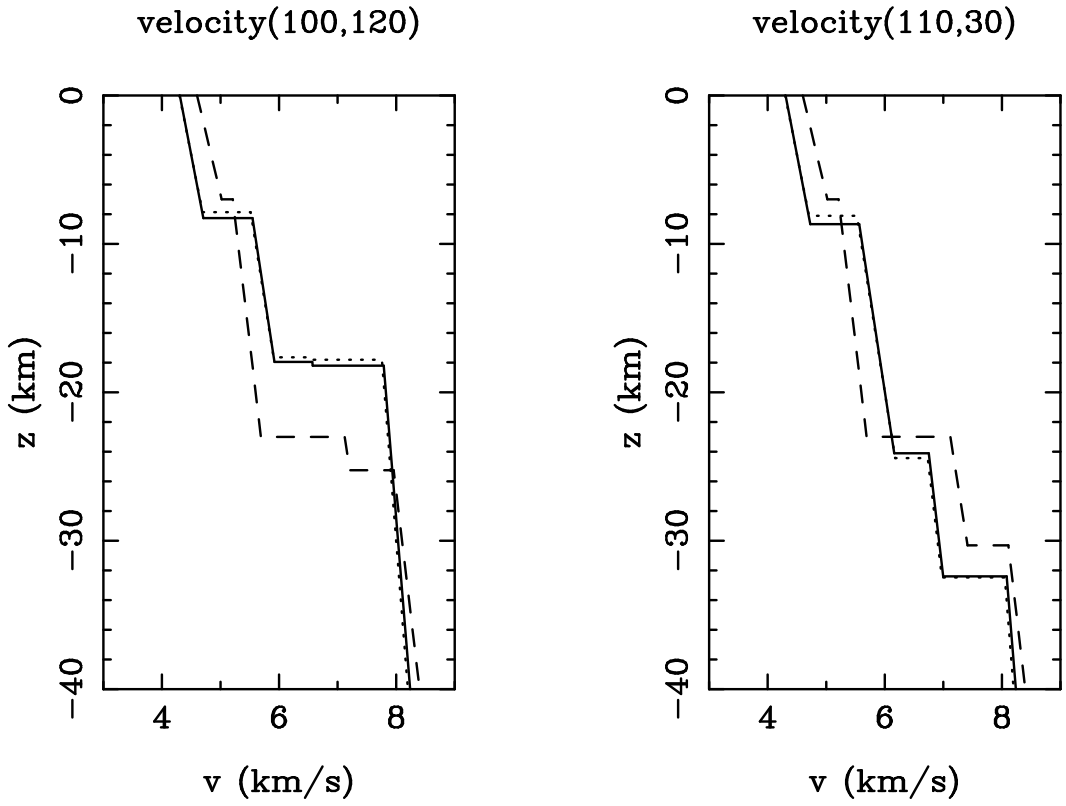

Figure 4.40: Velocity versus depth at two locations in the initial model (dashed lines), true model (dotted lines) and reconstructed model (solid lines). Due to the layer pinchout, the model at $(x, y) = (100, 120)$ km essentially shows a two-interface structure while the model at $(x, y) = (110, 130)$ km shows a three-interface structure.

Estimates of model robustness based on linear theory are obtained in the same way as for the 2-D examples in the previous section. Contour plots are made to show the variation in the square roots of the diagonal elements of the *a posteriori* model covariance matrix $\mathbf{C}_M$ (Figure 4.41a) and the diagonal elements of the resolution matrix $\mathbf{R}$ (Figure 4.41b). Note that the definition of $\mathbf{C}_M$ (see Equation 2.77) means that posterior covariance cannot exceed prior covariance no matter what damping factor is used. Thus, uncertainty in interfaces one, two and three is limited by the prior estimates of 2.0, 3.0 and 3.5 km respectively (Figure 4.41a). The plots of uncertainty (Figure 4.41a) have the same contour

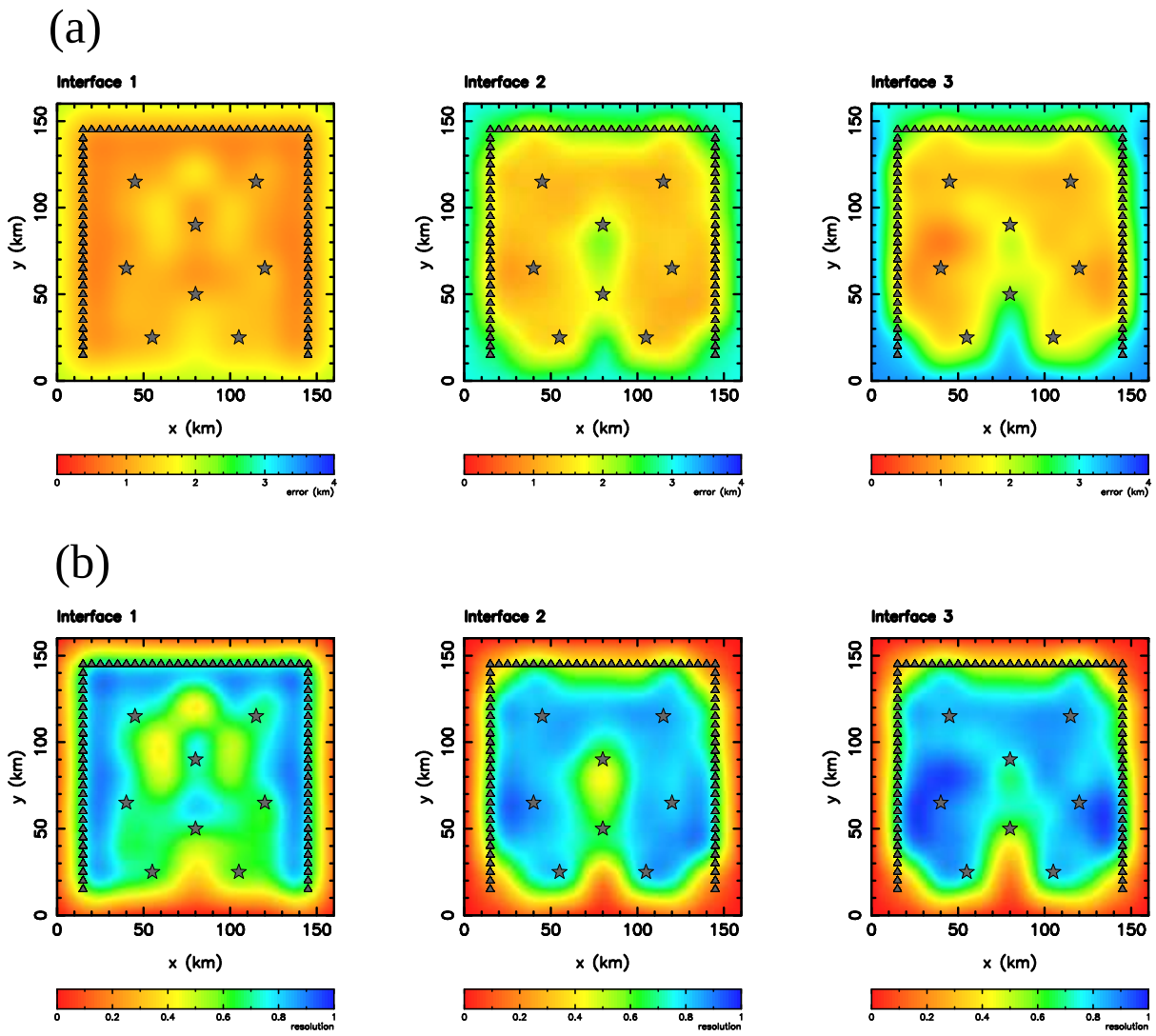

Figure 4.41: Robustness estimates for inversion solution (see Figure 4.38) using Model D synthetic dataset. (a) Square root of diagonal elements of *a posteriori* model covariance, and (b) diagonal elements of resolution matrix.

patterns as the plots of resolution (Figure 4.41b) because $\mathbf{C}_M$ and $\mathbf{R}$ are linearly related (see Equation 2.76); well resolved parameters have a corresponding low uncertainty. This means that these two quantities do not really need to be described separately. The most striking feature of Figure 4.41b is the contrast between the resolution of the parameters that lie outside the square formed by the receivers and those that lie inside. This contrast is expected because the ray paths do not sample structure that lies outside the array. The low resolution values correlate well with those parts of the model that are not accurately reconstructed. For example, (see Figure 4.38), at $(x, y) = (0, 100+)$ km and $(x, y) = (160, 100+)$ km, the inversion has failed to pull the bottom interface upwards to pinchout

the lower crustal layer. The interface parameters that lie directly adjacent to the receiver lines are consistently better resolved for interface 1 than for the two deeper interfaces because the shallow depth of interface 1 results in a concentration of ray-interface hits close to the sources and receivers. Comparison of the interface resolution values with the location of ray-interface hit points (Figure 4.42) shows that good resolution of the interface parameters is closely dependent on the proximity of ray-interface hits - particularly of reflections.

Within the region bounded by the receiver array, the resolution is generally > 0.5 for those parts of the interfaces that are accurately reconstructed. Where the reconstruction is less accurate, e.g. at $(x, y) = (80, 80)$ km in interface 2 (Figure 4.38), a low value for the corresponding resolution matrix entry (0.4 in this case) can usually be observed. The resolution matrix entries for the layer velocities and velocity gradients are shown in Table 4.1. The velocity parameters of the top two layers are well resolved (as expected) because they are quite densely penetrated by rays. The velocity parameters of the third layer are less well resolved, probably because the layer pinchout means that relatively fewer refracted rays turn in this layer.

Correlation diagrams offer an insight into the interdependencies of model parameter resolution. Figure 4.43 shows the correlations of two interface nodes; one that is well resolved (Figure 4.43a) and one that is poorly resolved (Figure 4.43b). The well-resolved parameter has a checkerboard-like pattern of correlations with adjacent parameters in the same interface and only small correlations with nodes in adjacent interfaces. The local checkerboard pattern indicates a well resolved part of the interface because surrounding nodes must be adjusted to satisfy the data if this node is perturbed (c.f. Figure 4.25). The poorly resolved parameter (Figure 4.43b) does not generate such a pattern of correlations, and in fact only one node shows a small anticorrelation. Thus, if the poorly resolved parameter is perturbed, surrounding nodes do not have to be adjusted to satisfy the data.

According to the resolution diagrams (Figure 4.41b, Figure 4.42a), all the parameters that lie beyond the horizontal extent of the source-receiver array are poorly constrained by the data. The interface depths in these peripheral regions are essentially inherited from the initial model. If the initial model is inaccurate in these regions, then significant errors in the reconstruction near the horizontal limits of the model can be expected. Figure 4.44 shows the same cross-sections seen in Figure 4.39 except that a different initial

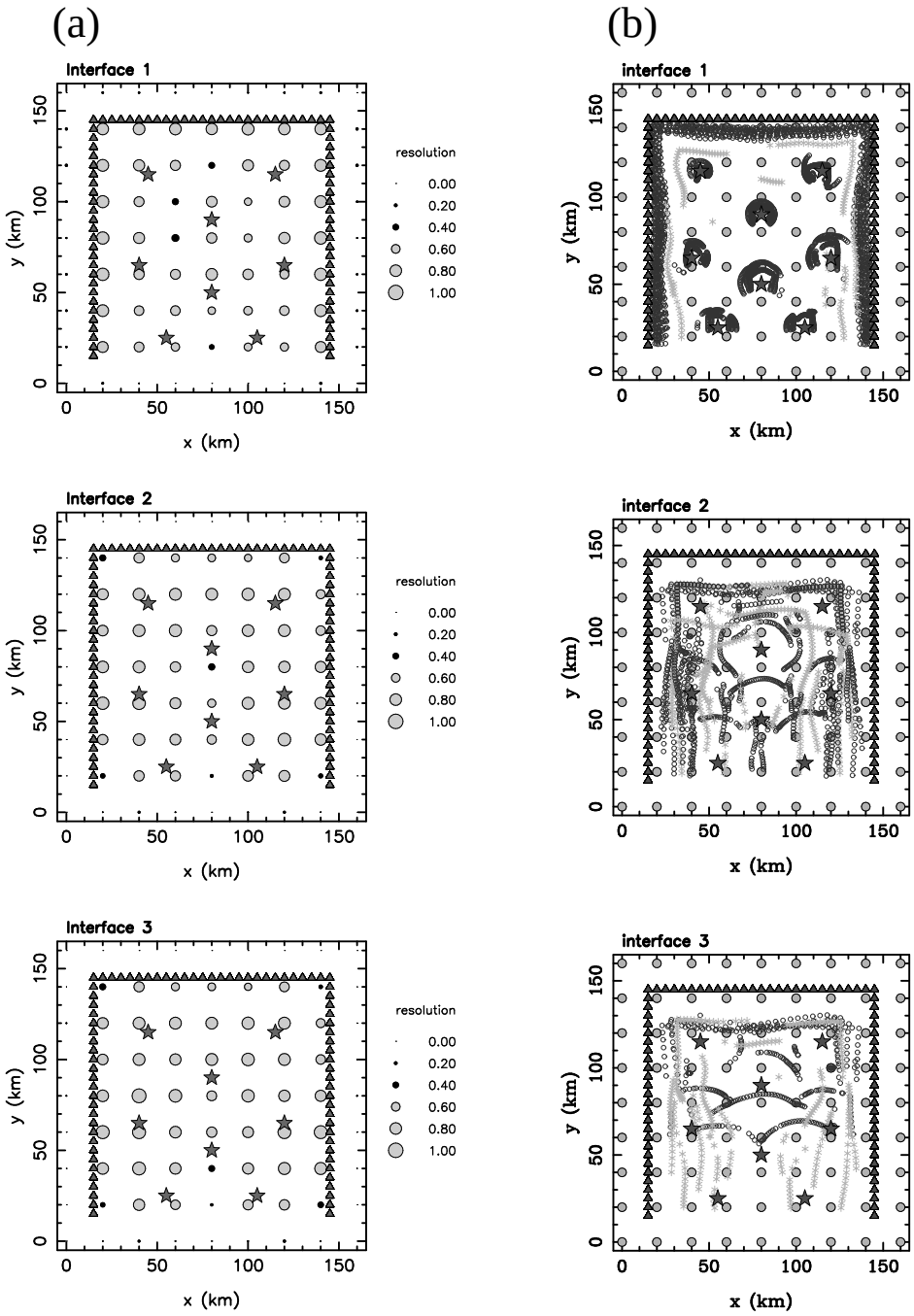

Figure 4.42: Comparison of resolution with ray-interface hits for the reconstruction (Figure 4.38) using Model D dataset. (a) Diagonal elements of resolution matrix. The circles that indicate the size of the resolution are grey-filled for values ≥ 0.5 and black-filled for values < 0.5. (b) Ray-interface hits for synthetic test solution model (Figure 4.38). Interface nodes are denoted by grey-filled circles, sources by stars and receivers by triangles. Rays that transmit through an interface are denoted by black circles and rays that reflect are denoted by grey asterisks.

model estimate was used in the inversion of the same dataset. The bottom interface of the solution model poorly represent the true model near the edges, but the model is

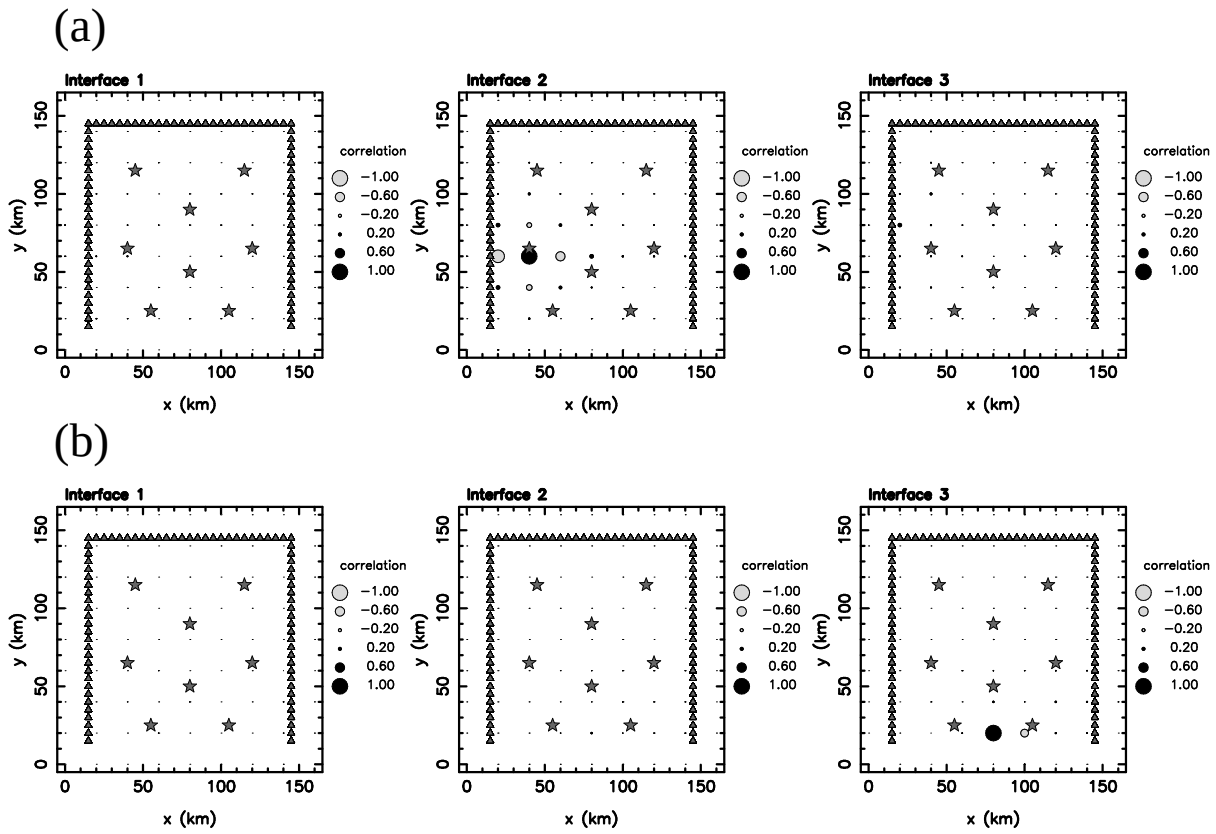

Figure 4.43: Correlation plots for two interface nodes for the inversion solution (using the model D dataset) shown in Figure 4.38. (a) Correlations for node at $(x, y) = (40, 60)$ km in interface 2, and (b) correlations for node at $(x, y) = (80, 20)$ km in interface 3.

reconstructed quite accurately within the bounds of the receiver array.

It is common practice with the diagonal elements of the resolution matrix to assign a cut-off value, below which the associated model parameters are considered to be poorly constrained by the data and hence unreliable. For example, Zelt & Smith (1992) use a value of 0.5, while Lutter & Nowack (1990) use a value of 0.6. Several synthetic inversions with different array geometries and models were carried out, and results suggested that parameters whose diagonal elements of the resolution matrix are ≥ 0.5 are generally well resolved.

Most methods of seismic data inversion use a regular parameterisation to represent structure. Regular parameterisations, such as a rectangular grid of interface nodes, are easy to generate and make the task of ray tracing, in particular the problem of finding ray-interface intersection points, easier than it might otherwise be. The use of an irregular parameterisation, such as that proposed by Sambridge & Gudmundsson (1998) which uses Delauney tetrahedra and Voronoi polyhedra, means that the detail or wavelength

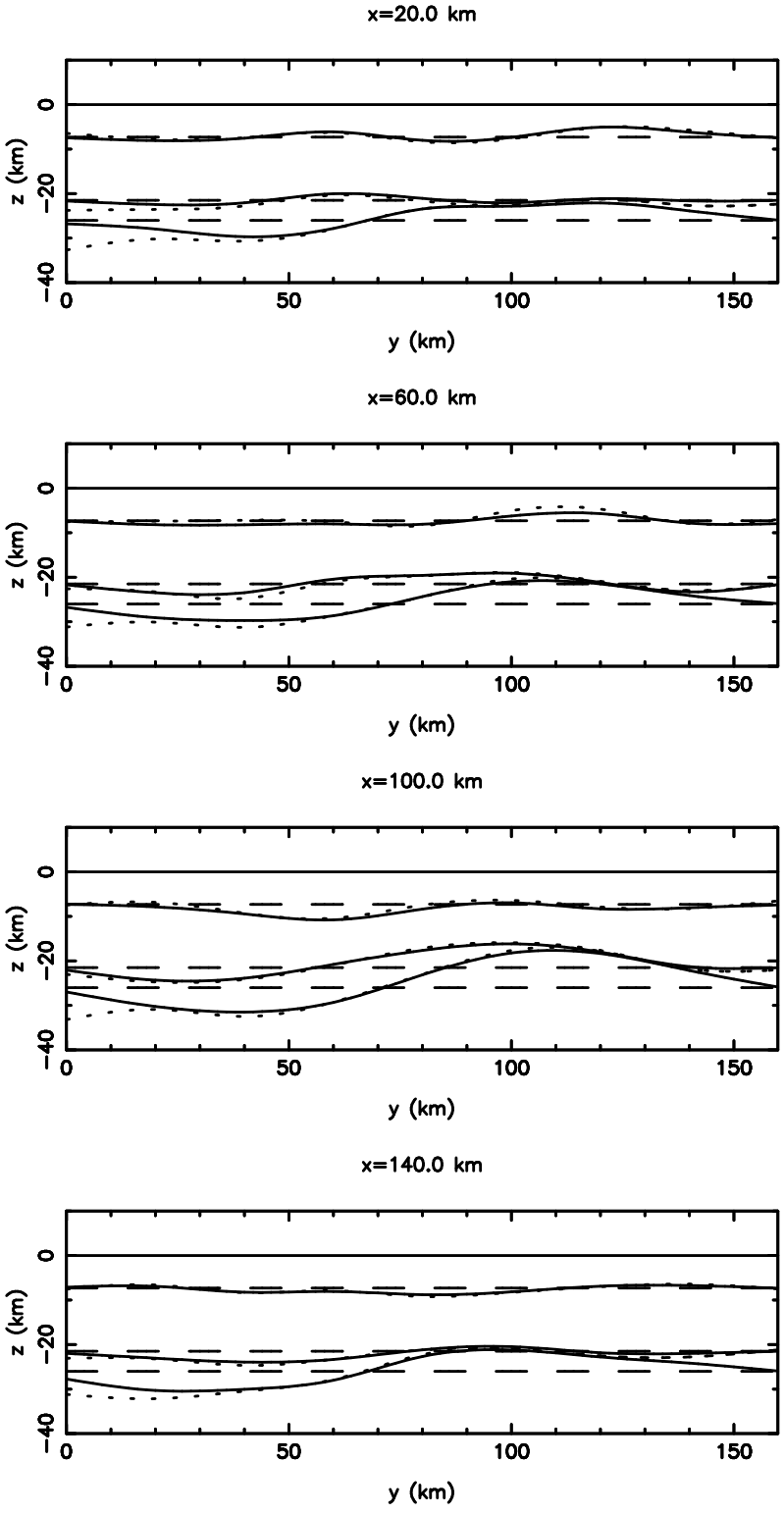

Figure 4.44: Inversion result using the Model D dataset and a starting model with 1-D structure. Four cross-sections at constant x through the initial model (dashed lines), true model (dotted lines) and reconstructed model (solid lines) are shown. c.f. Figure 4.39.

of the solution can be varied to suit the resolving power of the dataset. The method used here also permits variable density parameterisation, for example using large surface patches (widely-spaced nodes) in regions of poor data coverage and small surface patches (closely-spaced nodes) in regions of good data coverage. Potential advantages of decreasing node density in poorly resolved regions include reducing computation time and memory space while producing a solution that adequately satisfies the data with increased model parameter resolution.

To examine the behaviour of inversions using variable node densities, a new synthetic dataset is constructed by finding source-receiver traveltimes for rays through a single interface structure (Model E, Figure 4.45a) defined by 357 nodes on a rectangular grid. The velocity parameter values $(v_o(\mathrm{kms}^{-1}), k(\mathrm{s}^{-1}))$ in the top and bottom interfaces are $(4.2, 0.05)$ and $(5.2, 0.06)$ respectively. The source-receiver array was chosen to produce a very non-uniform ray coverage (Figure 4.45c). The Model E dataset consists of 1074 traveltimes (832 refraction, 242 reflection) corrupted by 45 ms of Gaussian noise. Figure 4.45b shows the result of a four iteration inversion for interface structure only using a 4-D subspace method. Correct layer velocities are assumed in the initial model estimate, which is a horizontal planar interface at 7 km depth described by the same regular horizontal node distribution as Model E. In this inversion, $\epsilon = 1$ and the uncertainty of each interface node is set at 3.0 km (for use in $\mathbf{C}_m$). The inversion result (Figure 4.45b) accurately reconstructs the interface in the region bounded by the central square of receivers. The interface directly inboard/beneath the outer rectangle of receivers is also quite accurately reconstructed, but the region between the two sets of receivers is generally not recovered. Inspection of the ray-interface hit diagram (Figure 4.45c) reveals the cause of this pattern of resolution; reflection and refraction ray-hits are heavily concentrated within the inner ring of receivers and a line of refraction hits traces its way just inboard of the outer receiver array. Also evident are a few reflected rays that make it to the outer array and thus help to constrain the structure to the left and right of the central square of receivers. The plot of the diagonal elements of $\mathbf{R}$ (Figure 4.45d) provides a more rigorous quantification of model resolution, consistent with the ray-hit diagram. The initial data misfit for this inversion is 233 ms and the data misfit after four iterations is 48 ms, an 80% reduction, and close to the noise level of the data.

A second inversion of the Model E dataset, shown in Figure 4.46, uses an irregular distribution of nodes to define the interface (Figure 4.46c) so that the number of unknowns

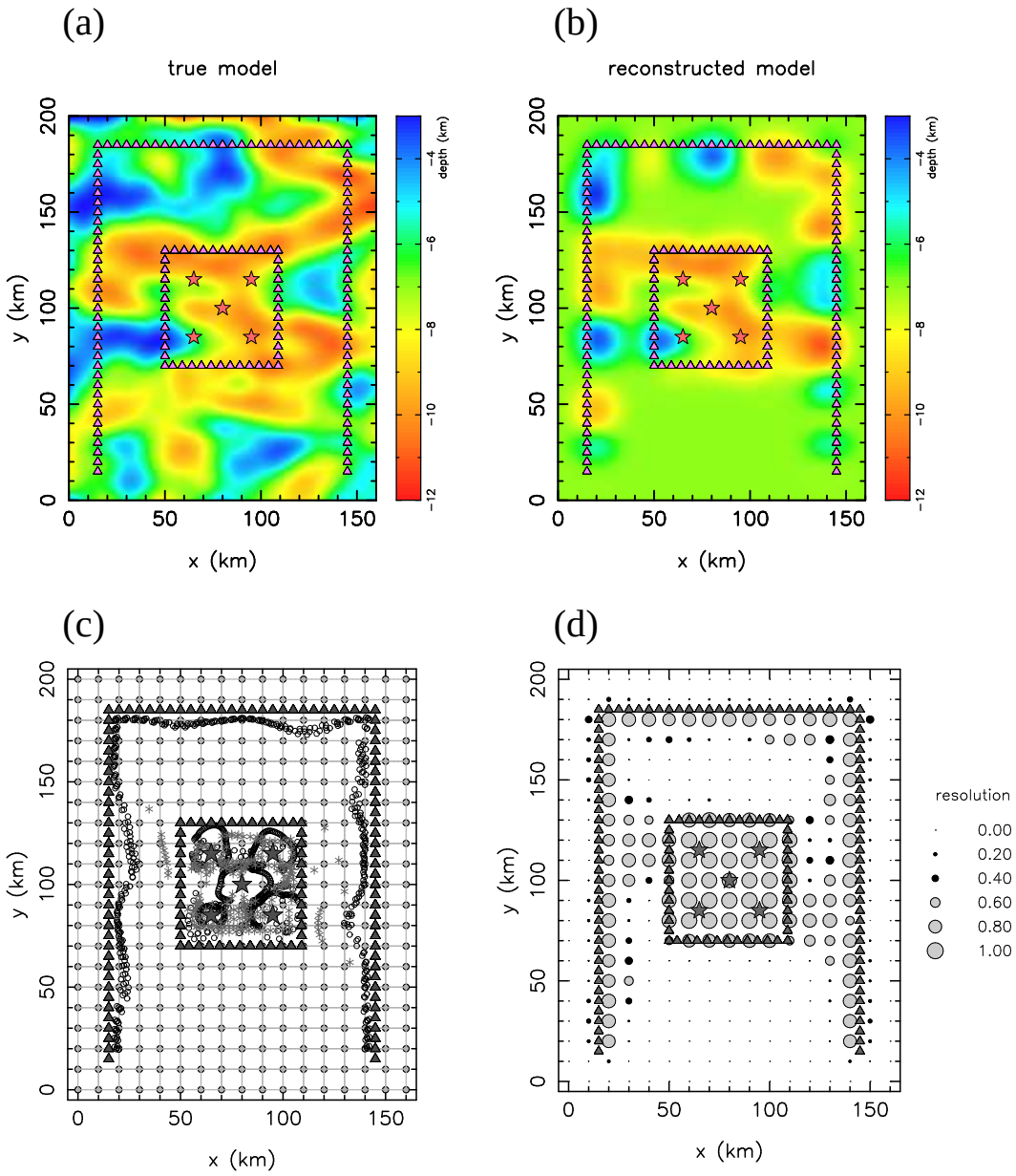

Figure 4.45: Inversion for a single interface using Model E synthetic data and a regular parameterisation with a highly inhomogeneous data distribution. Sources are denoted by stars and receivers by triangles. (a) True interface structure defined by 357 nodes arranged in a regular rectangular array. (b) Reconstructed interface defined by 357 nodes after 4 iterations of a 4-D subspace method. (c) Node distribution of solution model (and true model) and ray-interface hits for the solution model. Surface patch boundaries are shown by thin grey lines. Refraction intersection points are denoted by black circles and reflection points by grey asterisks. (d) Diagonal elements of the resolution matrix determined at iteration 4.

in the inversion is reduced from 357 to 130. Again, $\epsilon = 1$ and all node uncertainties are set to 3.0 km. The node distribution of Figure 4.46c is defined so as to retain nodes that are well resolved (e.g. within the inner square of receivers) and eliminate nodes that are poorly

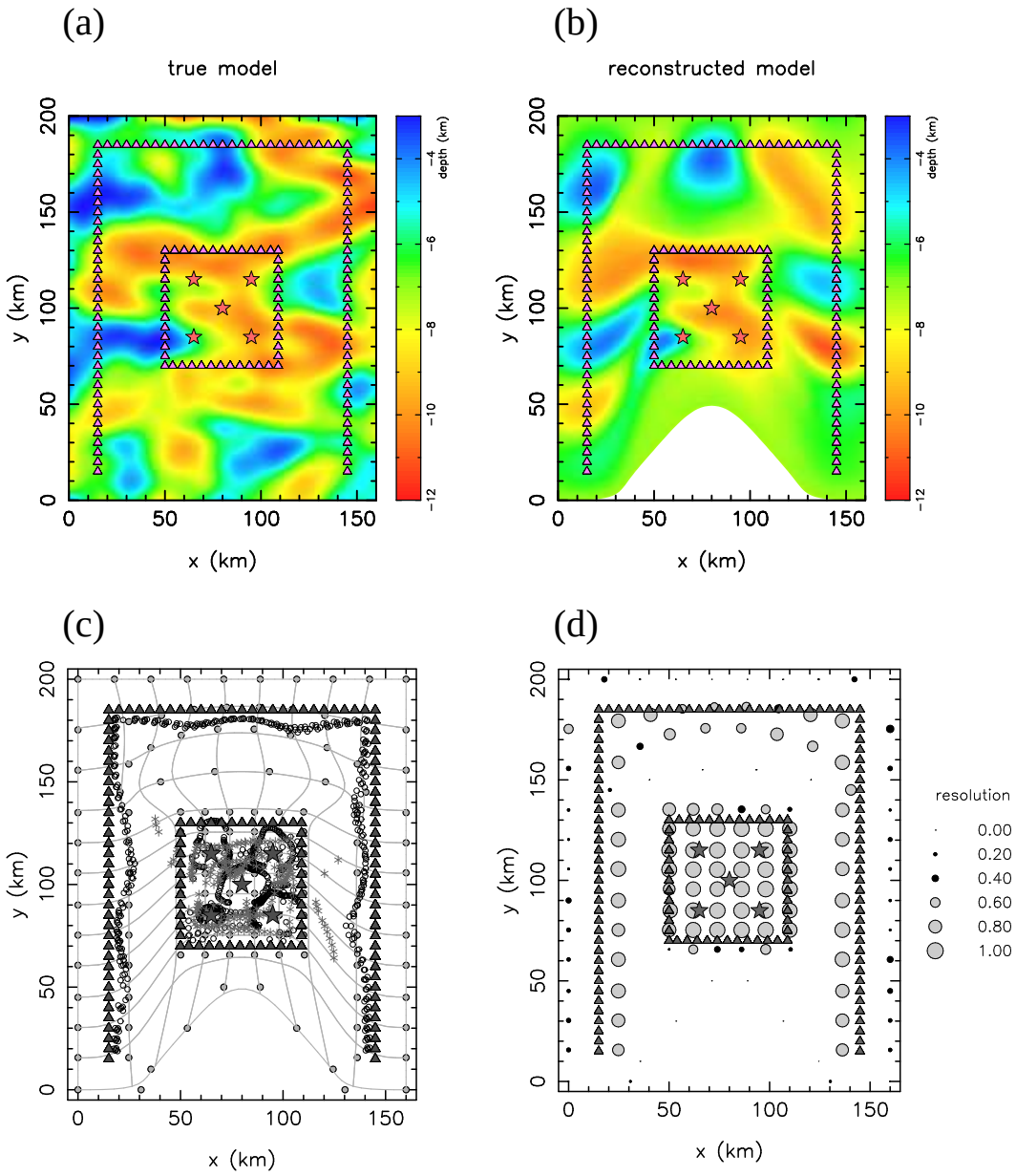

Figure 4.46: Inversion for a single interface using Model E data and an irregular parameterisation with a inhomogeneous data distribution (c.f. Figure 4.45). Receivers are denoted by stars and recorders by triangles. (a) True interface structure defined by 357 nodes. (b) Reconstructed interface defined by 130 nodes after 4 iterations of a 4-D subspace method. Note that the boundary of the reconstructed surface is no longer rectangular. (c) Node distribution and ray-interface hits for the solution model. Surface patch boundaries are shown by thin grey lines. Refraction intersections are denoted by black circles and reflection intersections by grey asterisks. (d) Diagonal elements of the resolution matrix determined at iteration 4.

resolved (i.e. most of the nodes between the outer and inner receiver arrays). Again, the solution after four iterations (Figure 4.46b), accurately reconstructs the interface within the inner receiver array and beneath the outer receiver array. The data misfit for this

inversion is reduced from 233 ms to 56 ms after four iterations, a 76% reduction. While this is slightly worse than that achieved by the inversion with a regular grid, the important point is that only 36% of the nodes used in the regular parameterisation were required by the irregular parameterisation to satisfy the data to nearly the same level.

The apparent desirability of the solution produced using the irregular interface mesh is tainted by two factors. First, although the resolution diagram (Figure 4.46d) shows that significant portions of the interface are well resolved in the regions between the two receiver arrays, e.g. ($20 \leq x \leq 50$ km, $60 \leq y \leq 140$ km), comparison of Figure 4.46a and Figure 4.46b shows that the reconstruction does not seem to be particularly accurate in this region. This occurs because the shape of the surface patches are long and thin so that the minimum permissible wavelength of structure varies significantly with azimuth. An interpretation of the solution must take this into account. Second, the computation time of the irregular-node inversion was approximately the same as the regular-node inversion, even though 64% fewer nodes were used in the former inversion. The relative inefficiency is mainly caused by the complexities involved in finding the ray-interface hit points. However, calculating the resolution matrix was much faster because the dimension of the matrix is equal to the number of unknowns in the inversion. In short, the use of an irregular parameterisation can produce more desirable models (i.e. fewer parameters satisfying the data to the same level), but special care needs to be taken with regard to node distribution and surface patch shape. Any solution interpretation and examination of model resolution should not be done without close attention to these factors.

4.3.3 Subduction Zone Setting

The 3-D synthetic tests of the preceding section were based on relatively simple layered crustal structures. To demonstrate the flexibility and power of the inversion method, I now describe the inversion of a synthetic dataset for a 3-D crustal model that represents a subduction zone setting. Subduction zones occur at convergent plate margins and typically involve oceanic crust subducting beneath continental crust or other oceanic crust. Features associated with a subduction zone, apart from the downgoing slab, often include an ocean trench, accretionary prism, underplating, frontal and back-arc basins, volcanic arcs and even foreland thrust belts such as the Andes (Moores & Twiss, 1995). Lateral variations in structure may be extreme in these regions, making accurate seismic

imaging a challenge.

Much of the current knowledge about the deep structure of subduction zones has been gained from seismology, usually in the form of velocity tomography and/or hypocenter relocation. Local studies using LET (Local Earthquake Tomography) and teleseismic tomography have been employed to image subduction zones (e.g. Zhao et al., 1992; Dorbath & Paul, 1996; Graeber & Asch, 1999). LET studies use events associated with the subducting slab (i.e. the Benioff zone) and a joint inversion for velocity and hypocenter location is usually possible. However, the depth extent of these kinds of analyses is limited by the maximum depth at which earthquakes can occur. Teleseismic tomography can be used to probe deeper into the earth than LET and is capable of imaging strong variations in lateral structure. Regional or global tomography is usually required to examine the structure of the entire subducting slab (van der Hilst et al., 1991, 1997; Widiyantoro & van der Hilst, 1997), but in the following example, I focus on what can be learned about relatively shallow lithospheric structure using a plausible wide-angle experiment.

Wide-angle seismic studies in subduction zones are limited to imaging the uppermost part of the subducting slab because the type of sources commonly used in this situation (airguns) generally cannot probe to depths of more than 40-50 km. However, several wide-angle studies of subduction zones have been carried out (Iwasaki et al., 1990; Zelt, 1996; Ye et al., 1997) in 2-D. The advantage of this type of experiment is that it is possible to constrain both interface depth and velocity variation. Good data coverage and *a priori* information can make it possible to constrain a model defined by many interfaces (e.g. Iwasaki et al. (1990) uses eight interfaces) including perhaps layer pinchouts caused by the dipping lithospheric slab. In 3-D, Zelt et al. (1999), invert wide-angle reflection and refraction data from the central Chilean margin for interface structure and lateral velocity variation. Features of their solution model include the Valparaiso forearc basin, the accretionary wedge and the subducting plate. Three subhorizontal interfaces describe discontinuous velocity structure, but layer pinchouts were not required to satisfy the data.

A 3-D synthetic model (Model F) representing a plausible near-surface subduction zone structure was constructed as shown in Figures 4.48 and 4.49. The source-receiver array used to generate the synthetic dataset is shown in Figure 4.47, along with the horizontal node distribution used to parameterise all six interfaces. Eight on-shore receivers and 259 marine sources at sea level spaced 2 km apart in four lines, consistent with an

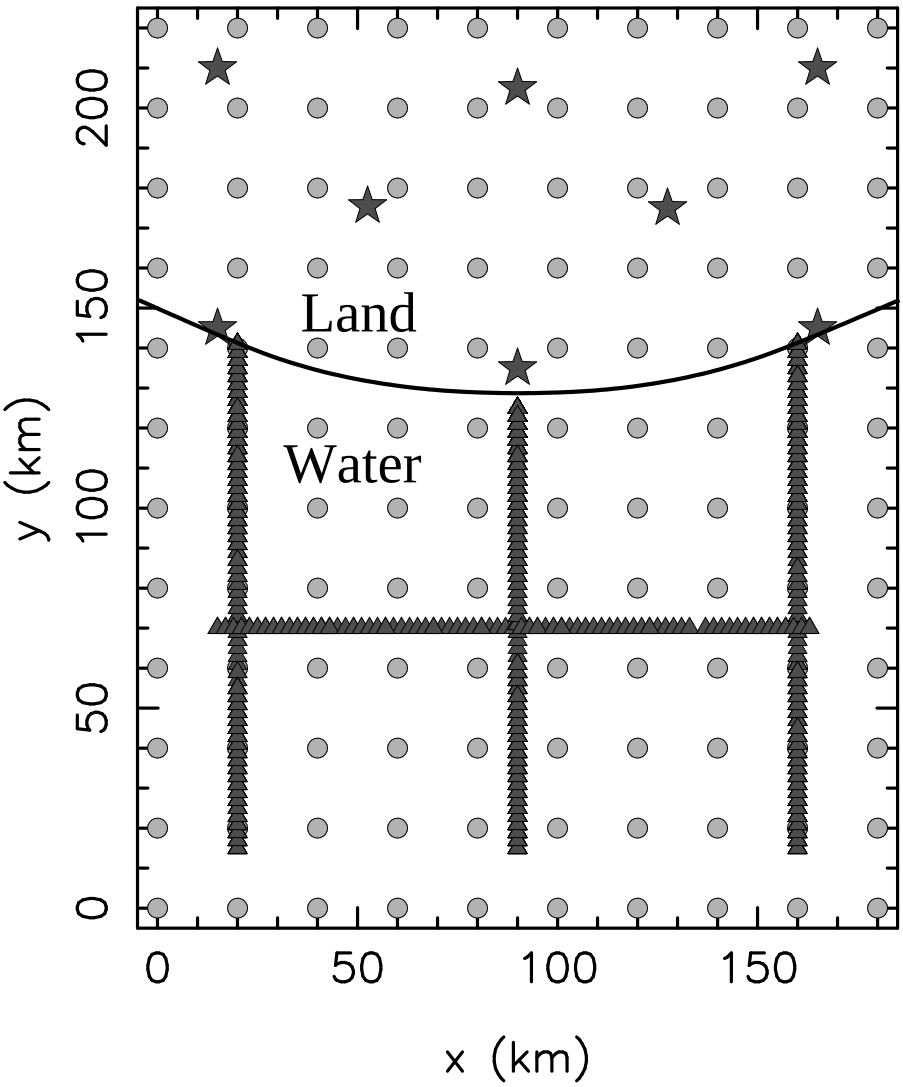

Figure 4.47: Map view of a subduction zone setting with source-receiver array and horizontal node distribution used to describe Model F. Sources are shown by triangles and receivers by stars. The interface node (grey dots) distribution is identical for all interfaces and the coast is shown as a solid line.

experiment in which normal-incidence marine profiling is coupled with several land-based receivers to obtain wide-angle ray trajectories. Although this experiment does not provide homogeneous ray coverage for a 3-D inversion, it illustrates what can be achieved with the deployment of a relatively small number of land recorders in conjunction with a marine experiment whose primary target is normal-incidence reflection profiling. The 3-D subduction structure illustrated in Figure 4.48 consists of six interfaces, each identically parameterised by 120 evenly-spaced nodes ($\Delta x = \Delta y = 20$ km). The entire model is defined by 734 parameters (720 interface, 7 velocity and 7 velocity gradient). Figure 4.49 shows a series of cross-sections through Model F, which is described as follows. Beneath

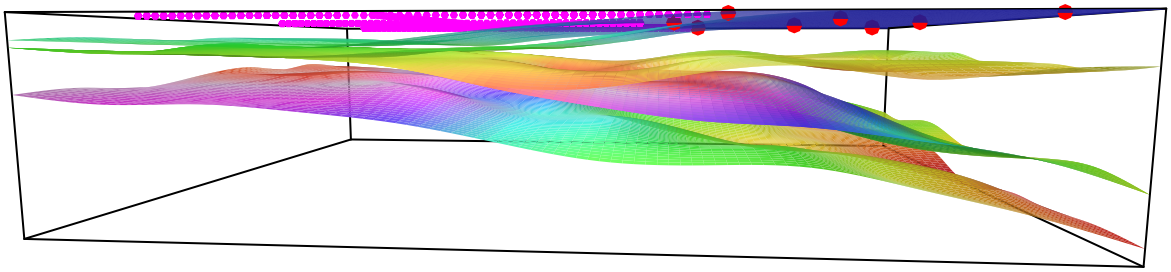

Figure 4.48: Perspective view of 3-D test model F which represents a subduction zone. Structure is defined by six interfaces, all of which bound layers that pinch-out at some point, except for the bottom interface. Sources are shown in pink and receivers in red. Colour contouring is designed to enhance variations in interface topography.

the ocean (light blue), a thin sediment layer (yellow) overlies the oceanic crust (dark blue). The sediment layer pinches out as it reaches sea-level above the overriding continental crust, which consists of an upper crustal layer (green) and a lower crustal layer (amber). A lens of low velocity underplated rocks (grey) is located between the subducted ocean plate and the continental crust and pinches out in all directions. Mantle lithosphere is shown in red in Figure 4.49. The interface and velocity structure of the synthetic model is inspired by the 2-D wide-angle inversion results of Ye et al. (1997) for the Kodiak shelf and the 2-D wide-angle forward modelling results of Iwasaki et al. (1990) for the Ryukyu Island Arc. Ye et al. (1997) constrained a zone of low velocity underplated rock that had a maximum thickness of 20 km.

The Model F synthetic dataset consists of 2053 source-receiver traveltimes (from 1308 refracted and 745 reflected ray paths) which have been corrupted by 70 ms of Gaussian noise. The initial model estimate from which the inversion process commences is essentially 2-D except that the bathymetry is assumed known and is taken from the true model (Model F), and all interfaces have a slight curvature in the x-direction due to the shape of the coastline. The initial model contains the basic features of the subduction zone, including all of the target layers, but the complexity of the true structure is absent. The initial model is consistent with what could be expected from normal incidence reflection interpretation and 2-D wide-angle interpretation along the three parallel shot lines. The square roots of the diagonal entries of $\mathbf{C}_M$ are set at 1.0 km for the second interface and 2.0 km for interfaces 3-6. The uncertainty in velocity and velocity gradient are set at 0.2 km/s and 0.004 s^{-1} respectively.

In inverting the synthetic data, the dimension of the subspace inversion scheme was set

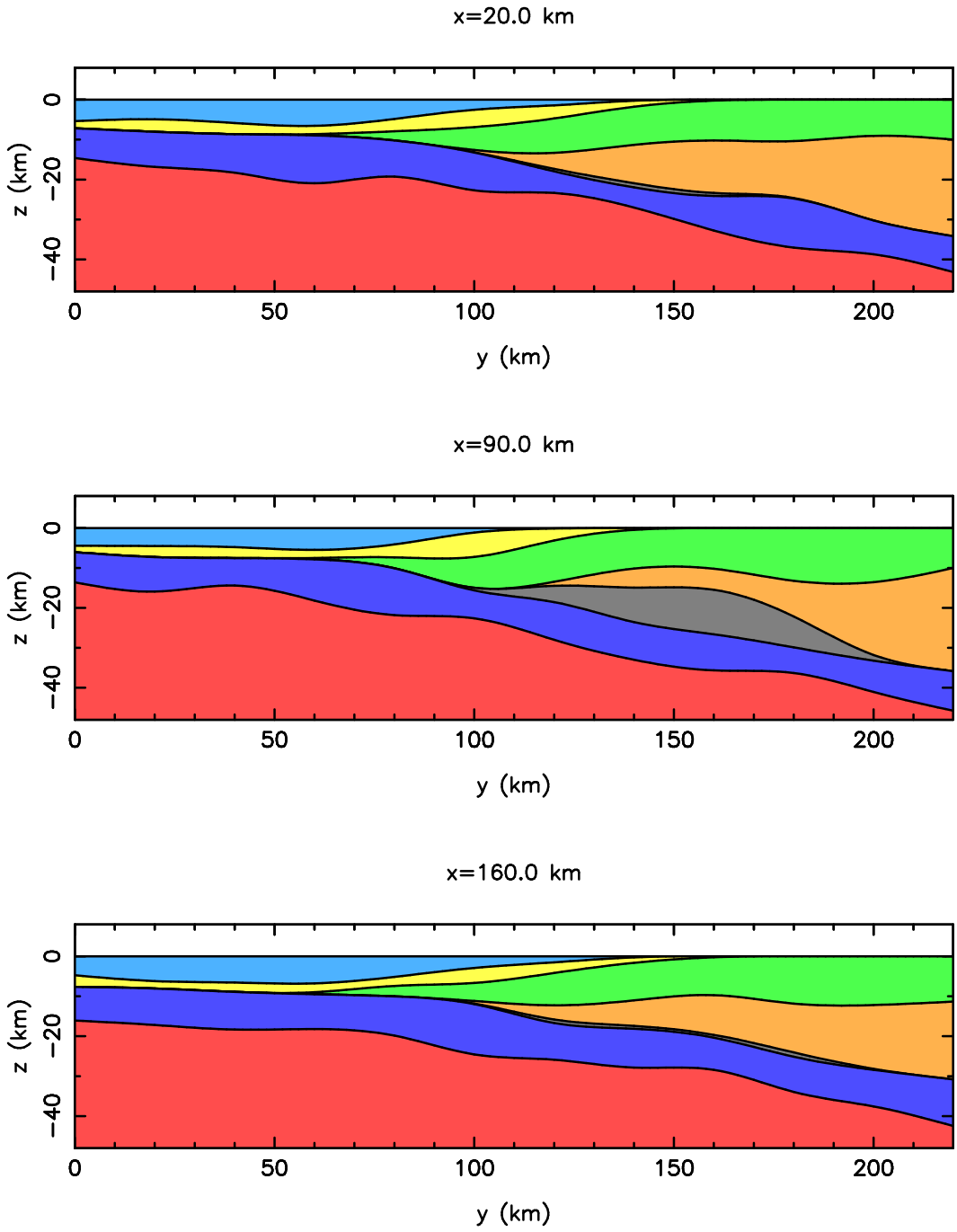

Figure 4.49: Three cross-sections taken at constant x through Model F. The ocean layer is shown in light blue, the sediment layer in yellow, the upper crustal layer in green, the lower crustal layer in amber, the low-velocity zone in grey, the subducting ocean crust in dark blue and the lithospheric mantle in red. Figure 4.48 gives a perspective view of the entire structure.

to 20 and the damping parameter was set to $\epsilon = 1$ using the data fit/model perturbation trade-off criteria established previously. Of the 20 basis vectors, 10 lie in interface depth space, five lie in velocity parameter space and five lie in velocity gradient parameter

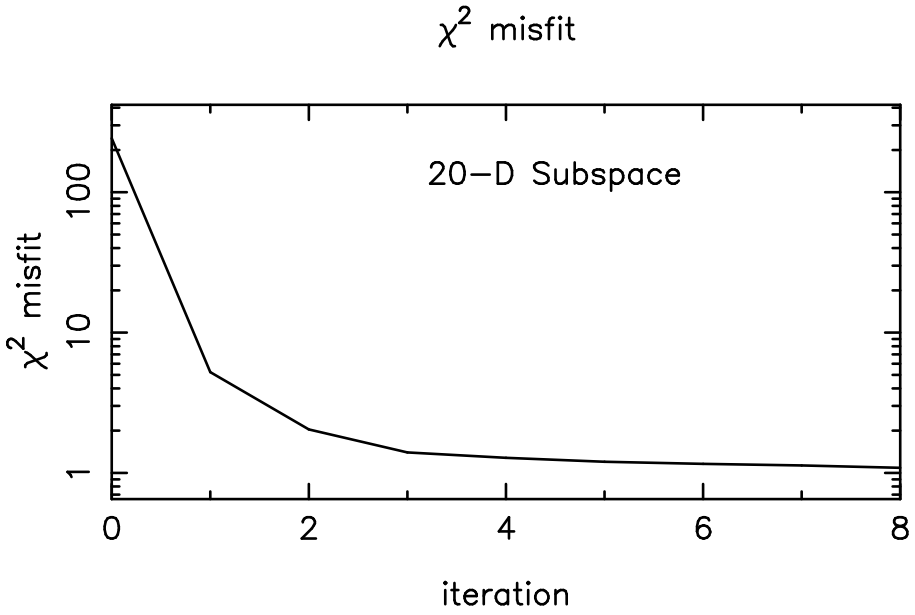

Figure 4.50: χ^2 misfit function versus iteration number for 20-D subspace inversion of Model F dataset with damping parameter $\epsilon = 1.0$.

space. This 20-D scheme offers a suitable compromise between the magnitude of the objective function reduction per iteration and computation time. All model parameters were inverted for except those which describe the sea-floor (assumed known) and the water layer, which has a fixed velocity of 1.5 km/s. The χ^2 misfit function that results from the inversion (Figure 4.50) decreases monotonically from an initial value of 242.5 (1.09 s RMS misfit) to a value of 1.08 (73 ms RMS misfit) at iteration 8, which is similar to the standard deviation of the Gaussian noise added to the data.

Figure 4.51 shows, in three cross-sections of constant x (c.f. Figure 4.49), the starting model, the true model and the reconstructed model at iteration 8. It is clear from these sections that the inversion has produced an accurate solution, particularly for the low-velocity lens, which pinches out at $x \leq 20$ km and $x \geq 160$ km. The mid-crustal interface (interface 3) is also quite accurately reconstructed from its initial near-horizontal position. The three cross-sections shown in Figure 4.51 are taken along the three parallel shot lines, so it might be expected that the reconstruction is most accurate in these regions. Figure 4.52 shows two cross-sections taken at constant y. The cross-section taken along the ocean ($y = 50$ km) shows that the initial model is not very different from the true model in this region, and the reconstruction of the Moho is not particularly good at around $x = 125$ km. However, the cross-section taken along the continental crust ($y = 160$ km) is quite accurately imaged even in regions not collinear with the three parallel shot lines. The

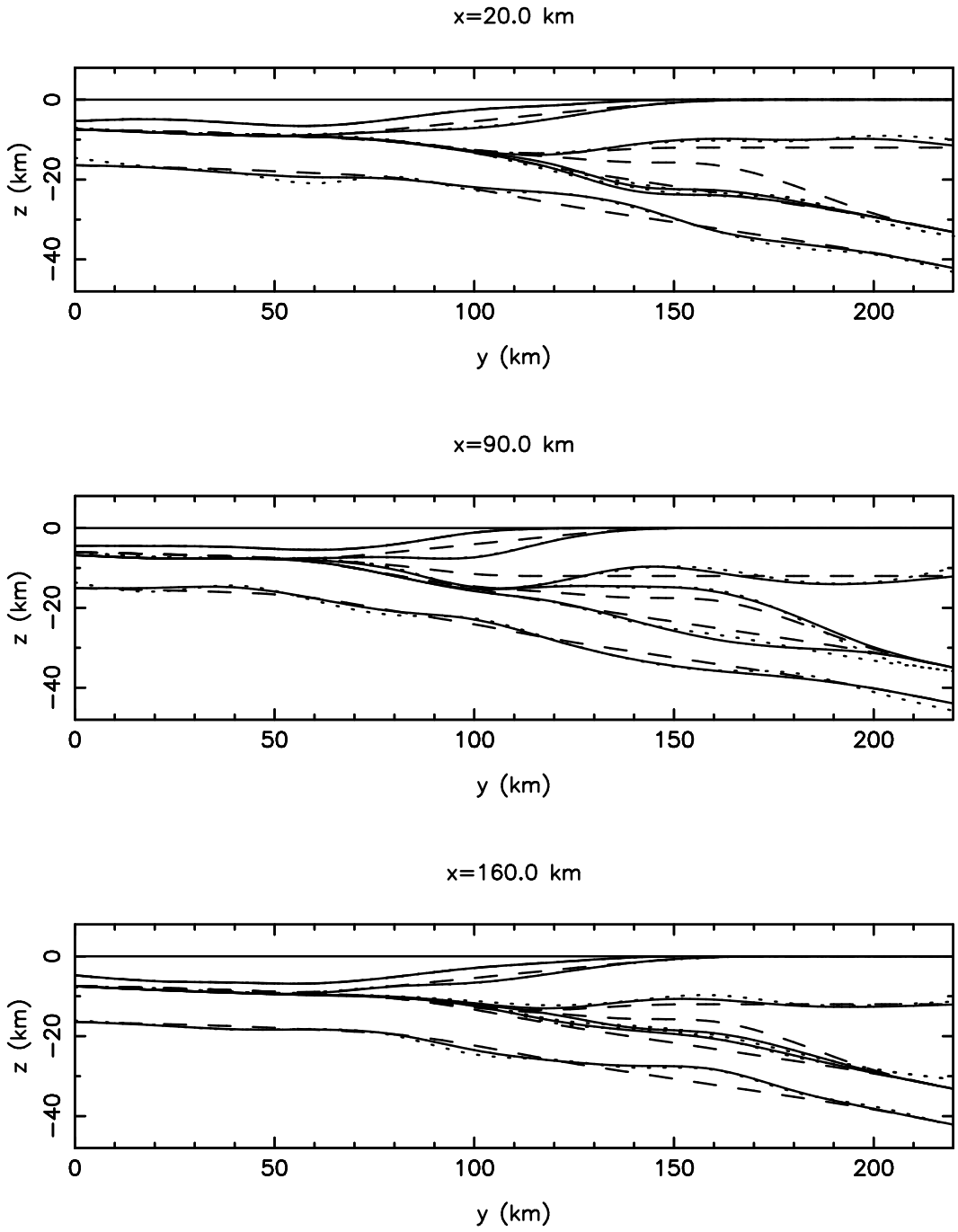

Figure 4.51: Three cross-sections taken at constant x through the true model (dotted lines), initial model (dashed lines) and solution model (solid lines) after eight iterations of the inversion of the Model F dataset.

lenticular nature of the low velocity zone is best seen in this cross-section, and the solution resolves its structure accurately, except at the extreme edges of the model. The accuracy of the velocity reconstruction is shown by the velocity profiles of Figure 4.53. The profile at $(x, y) = (20, 50)$ km shows the oceanic crust with the constant-velocity water layer on

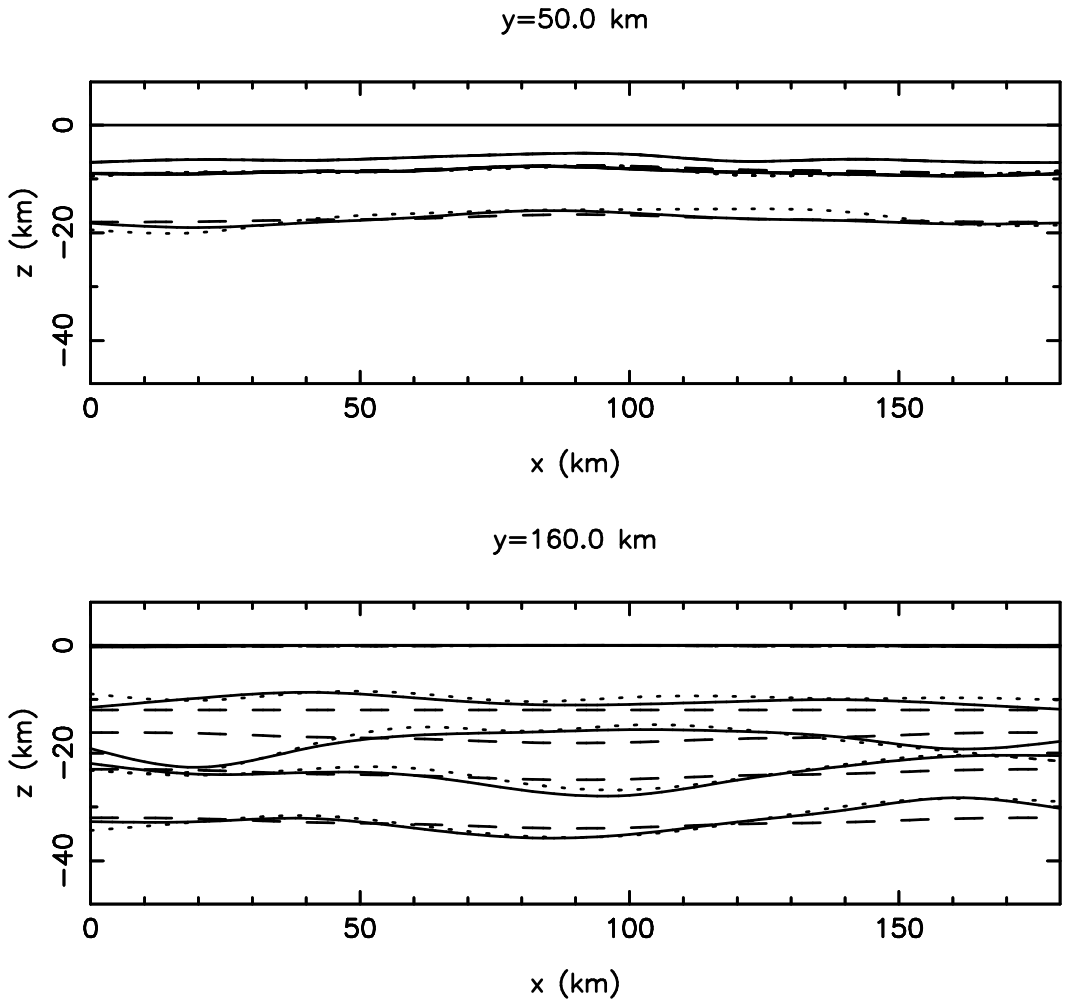

Figure 4.52: Two cross-sections taken at constant y through the true model (dotted lines), initial model (dashed lines) and solution model (solid lines) after eight iterations of the inversion using the Model F dataset.

top - the true, initial and solution models coincide for the ocean layer. The low velocity zone can be seen in the other two sections - $(x, y) = (90, 115)$ and $(x, y) = (180, 180)$ km - and it is clear from this figure that all layer velocities are recovered accurately by the inversion.

Inaccuracies in the reconstruction of the oceanic crust are largely explained by the ray-interface hit diagrams (Figure 4.54). Resolution plots for this experiment are not illustrated, but as established in the previous synthetic tests, good interface resolution is associated with the close proximity of ray-interface hit points, particularly of reflections. Accurately reconstructed parts of the model correlate well with interface nodes that have relatively large (generally ≥ 0.5) resolution values. Interfaces 3-5 are pinched together beneath the ocean layer and consequently have identical ray hits in this region (i.e. directly

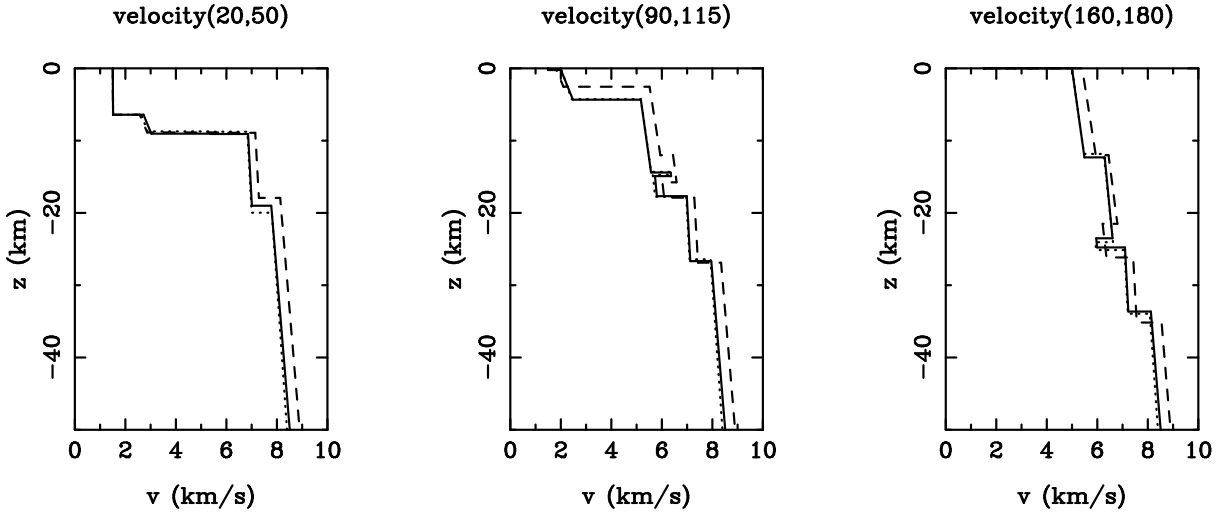

Figure 4.53: Three velocity profiles from the subduction zone taken at (x, y) = (20,50), (90,115) and (160,180) km respectively. The true model (Model F) is denoted by dotted lines, the initial model by dashed lines and the reconstruction by solid lines.

beneath the shot lines). The ray hits in the vicinity of the sources are quite localised in interface 3 but more widely sample the lower interfaces. The ray hits move further away from the receivers with depth; in the case of interface 6, no ray hits are found in the region $y \geq 180$ km. The depth of the Moho (interface 6) beneath the ocean crust means that refracted rays sample a greater part of that interface compared to the shallower interfaces in the same region. Overall, the inversion has been successful in reconstructing the 3-D structure of the subduction zone despite regions of poor ray coverage.

4.4 Summary

In this chapter, a method for the inversion of wide-angle seismic traveltimes for 3-D layered crustal structure has been presented and tested. The method is unique in that both refracted and reflected traveltimes can be inverted simultaneously for multiple interface structure and layer velocity. The description of interfaces using bicubic B-spline surface patches in parametric form means that interfaces are smooth, may be multi-valued with depth, and can be of variable complexity since node spacing may be arbitrary. Defining layer velocity as a linear function of depth means that rays can be traced analytically as circular arc segments, thus simplifying the solution of the initial value problem and allowing for an efficient shooting method of ray tracing. The subspace method allows simultaneous inversion of multiple parameter classes without resorting to arbitrary weight-

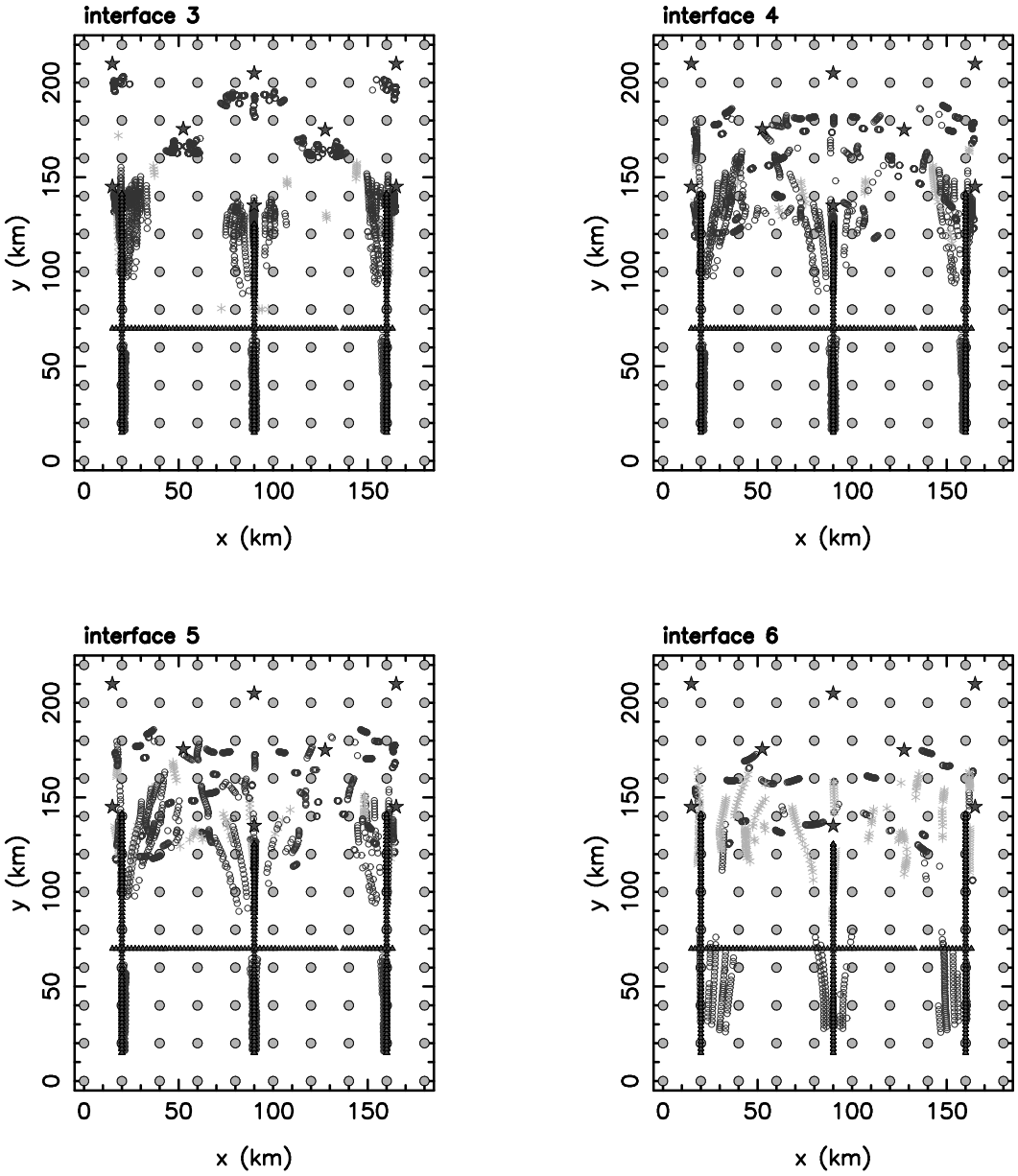

Figure 4.54: Ray-interface hit diagrams for the bottom four interfaces of the Model F traveltime inversion solution. Sources are denoted by triangles and receivers by stars. Refracted ray hits are shown by black circles and reflected ray hits are shown by grey asterisks. Interface nodes are denoted by grey dots. Interface 3 separates the mid and lower crustal layers, interface 4 the lower crustal layer and the low velocity zone, interface 5 marks the top of the subducting slab and interface 6 is the Moho.

ing methods. The synthetic tests that were carried out investigated the characteristics of the inversion method. The 2-D inversions verified the need for adequate ray coverage to properly resolve structure and established the superiority of the subspace method over other gradient methods in the presence of multiple parameter classes. The need for damping in the inversion of noisy data with inhomogeneous coverage was demonstrated

and an appropriate strategy for the determination of the damping factor was developed. It was also shown, in both 2-D and 3-D, that layer pinchouts can be reconstructed by the method, despite the presence of significant data noise. The use of variable-size surface patches was investigated and it was found that, for regions of very inhomogeneous data coverage, non-uniform node-separations can dramatically reduce the number of interface parameters required to satisfy the data compared to a uniform grid of nodes. However, it was also found that particular attention needed to be paid to surface patch shape in such circumstances. Inversions that produced good results were found to be associated with monotonically decreasing χ^2 misfit functions that levelled out at approximately the level of the data noise. Analysis of solution robustness via covariance and resolution matrices and ray-interface hit diagrams was found to be reliable. Application of the method to a synthetic dataset from a hypothetical 3-D subduction zone setting showed that the method is well suited to the interpretation of wide-angle datasets that may be recorded as a secondary objective to a normal-incidence reflection survey - wide-angle data coverage in this situation may be highly variable. The synthetic tests indicate that the wide-angle seismic inversion method is robust and capable of mapping complex 3-D structure defined by many interfaces.

Chapter 5

Crustal Studies of Tasmania

5.1 Tectonic Evolution of Tasmania

The island state of Tasmania lies several hundred kilometres off the southern tip of mainland Australia and has a surface area of approximately 68,000 km^2 and a maximum elevation of 1,600 m above sea level. It is composed of continental crust but is flanked by passive continental margins on all sides except the north, where the Bass Basin connects it to mainland Australia. The continental shelves on the east, west and southern edges of Tasmania are narrow (10-50 km) and the adjacent continental slopes plunge rapidly to depths of 3 km or more over distances of only a few tens of km. Two continental fragments lie adjacent to Tasmania and complicate the transition from continental to oceanic crust. The South Tasman rise has an area of 200,000 km^2 (Exon & Hill, 1997) and lies several hundred kilometres to the south with a maximum elevation of about 800 m below sea level. The East Tasman Plateau has an area of 50,000 km^2 (Exon & Hill, 1997) and lies less than 200 km east of Hobart with a maximum elevation of 2,500 m below sea level. The tectonic evolution of Tasmania is described below, along with the formation of its major structural features, which are shown in Figure 5.1.

Recent SHRIMP zircon dating (Turner et al., 1998) estimate the oldest exposed rocks in Tasmania to be about 1180 million years in age. The samples consisted of schistose metasediment from the Bowry Formation of the Arthur Metamorphic Complex in NW Tasmania. The original deposition of these sediments constitutes the first recognised event in the evolution of Tasmania. Widespread Neoproterozoic successions are evident in all of the current tectonic elements except the Northeast Tasmania Element. These successions

contain characteristic diamacite, dolomite and basaltic units, which suggest that western Tasmania has existed as a single entity since the Precambrian (Brown et al., 1998).

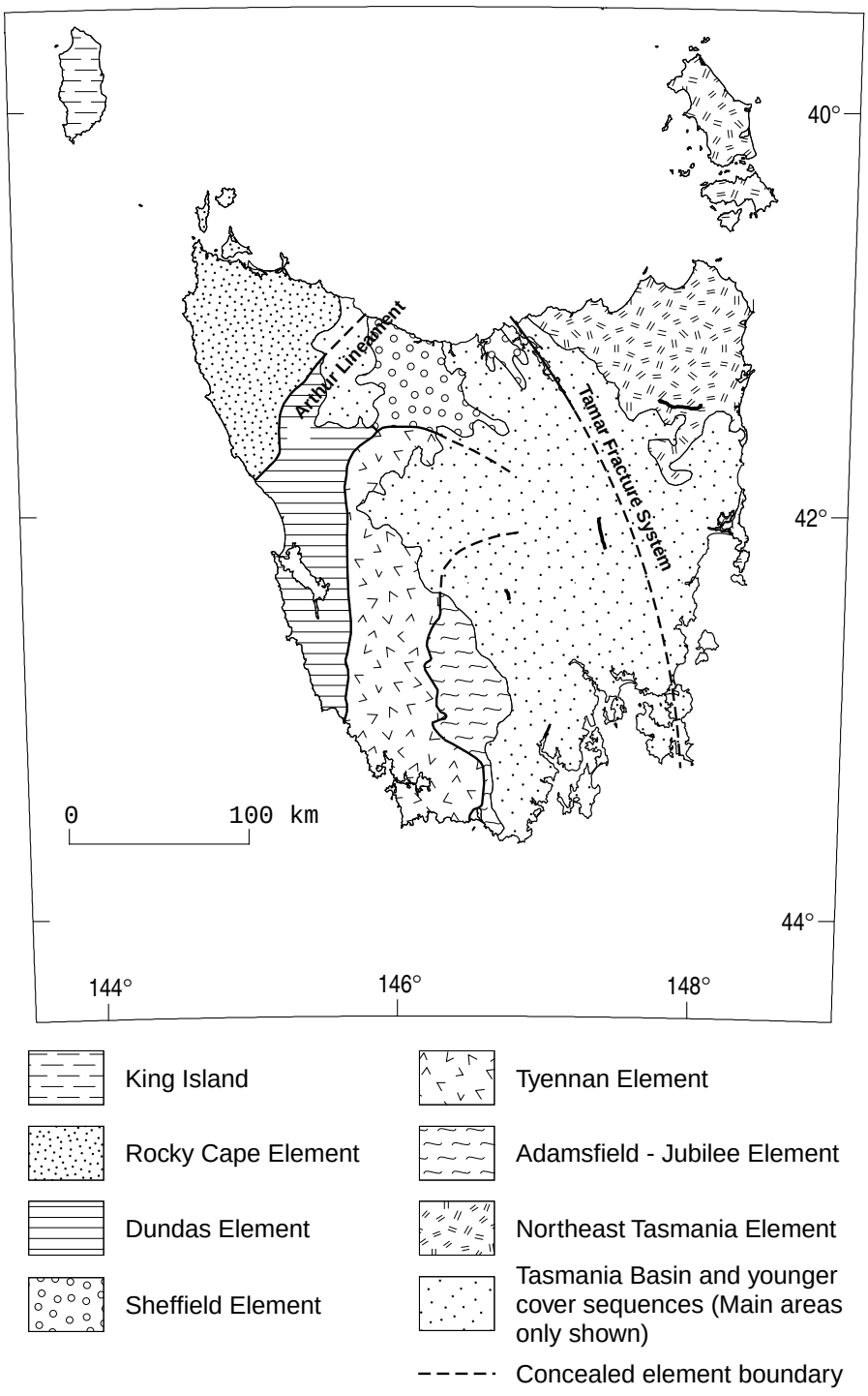

Figure 5.1: Tectonic elements and structural boundaries of Tasmania (after Brown et al., 1998). The Tasmania Basin conceals several of the element boundaries.

The first recorded orogenic event that shaped Tasmania was the Wickham Orogeny (Turner et al., 1998), which occurred between 800-750 Ma. It resulted in regionally varied strain, with prolific granite emplacement on King Island and the deposition of the thick turbidite piles of the Burnie and Oonah formations. However, the Rocky Cape Element in NW Tasmania (Figure 5.1) only experienced relatively gentle folding and faulting during this time and the high-strain metamorphic belt whose surface expression is the Arthur Lineament (Figure 5.1) probably formed after this episode of mountain building (Turner et al., 1998).

The Rocky Cape Element contains the Rocky Cape Group, a 1-3 km thick sequence of shallow marine quartz sandstone and mudstone (Williams, 1989). To the east, it shares a transitional contact with the Arthur Lineament which trends NE and marks the boundary between the Rocky Cape Element and the Dundas Element. The gradual nature of the transition from the Rocky Cape sediments to the pelitic, calcic and mafic schists of the Arthur Lineament suggests that the lineament was composed of the same sedimentary material before deformation. Therefore, the Rocky Cape Group is likely to be of a similar age (Mesoproterozoic) to the Arthur Lineament metasediments dated by (Turner et al., 1998). According to Williams (1989) and Corbett (1994), the Arthur Lineament was formed in the Late Proterozoic and may represent a leading-edge effect of the so-called Penguin Orogeny. However, while retaining the term "Penguin Orogeny" to describe the deformation episode that formed the Arthur Lineament, Turner et al. (1998) put the time of creation of the Arthur Lineament at around 500Ma on the basis of K-Ar ages from the Bowrey Formation. This estimate of the formation age coincides with the earlier phases of the the Tyennan Orogeny.

The Tyennan Orogeny occurred primarily in the Middle to Late Cambrian, which was a period of substantial deformation, expressed by significant metamorphism and the allochthonous emplacement of serpentinitic thrust sheets over much of Tasmania (Elliot et al., 1993; Brown et al., 1998). Crawford & Berry (1992) develop a hypothesis for this period of significant tectonic activity: (i) In the Late Proterozoic, eastern Tasmania is a passive margin with adjacent oceanic lithosphere subducting further eastward beneath an intra-oceanic arc, (ii) in the Middle Cambrian, the intra-oceanic arc collides with the passive margin and overthrusts it as a series of mafic-ultramafic nappes. The collision is followed by a period of platform subsidence and basin formation, and (iii) a brief period of westerly subduction led to the formation of the Mount Read Volcanics in the Dundas Ele-

ment during the mid-upper Cambrian. The postcollisional magmatism is associated with a narrow tensional rift zone caused by extension along the margin. Subsequent rebound backthrusting and erosion exhumed Proterozoic crust which now comprises much of the Tyennan Element. The collision did not produce a significant mountain belt (Münker & Crawford, 2000) as the emplacement of the allochthons produced only limited uplift and deformation. Volcanic-related successions accumulated rapidly in the Dundas, Sheffield and Adamsfield-Jubilee Elements as a result of the mid-upper Cambrian magmatism (Brown et al., 1998).

A number of other plate tectonic models for the Tyennan Orogeny have been considered. Corbett et al. (1972) discuss four different possibilities, which include : (i) Oceanic crust joined to the Tyennan Element subducting to the west beneath the Rocky Cape Element to form the Mt Read Volcanic Arc (Figure 5.2a), (ii) oceanic crust joined to the Rocky Cape Element subducting to the east beneath the Tyennan Element to form the Mt Read Volcanic arc (Figure 5.2b), (iii) the Rocky Cape Element and the Tyennan Element separated by a shallow marginal sea (the Dundas Element) with oceanic crust joined to the Adamsfield-Jubilee Element subducting westerly beneath the Tyennan Element to form the Mt Read Volcanic arc (Figure 5.2c), and (iv) the Rocky Cape Element, Tyennan Element and Jubilee Element separated by troughs, with the Mt Read Volcanics forming as a result of extension-related magmatism (Figure 5.2d). While there is still no strong consensus on the most appropriate tectonic model for the Tyennan Orogeny, allochthonous thrusting is generally thought to have occurred in the late Cambrian (Woodward et al., 1993; Elliot et al., 1993), thus requiring significant compressional deformation. The felsic Mt. Read Volcanic arc is of considerable economic importance as it hosts five major massive sulphide deposits. Undoubtedly, this fact heightens interest in the tectonic mechanisms that resulted in its emplacement.

In the Late Cambrian-Early Ordovician, major fault reactivation and faulting associated with the Delamerian Orogeny occurred in Western Tasmania (Brown et al., 1998). This event is also recorded in the Adelaide Fold Belt, New Zealand and the Transantarctic Mountains (Crawford & Berry, 1992). The Northeast Tasmania Element is often regarded as a separate entity at this time because there is no evidence of the Delamerian Orogeny during the deposition of the Mathinna Group. The Mathinna group overlies much of the Northeast Tasmania Element and consists of slate and interbedded quartzwacke, siltstone and mudstone (Williams, 1989).

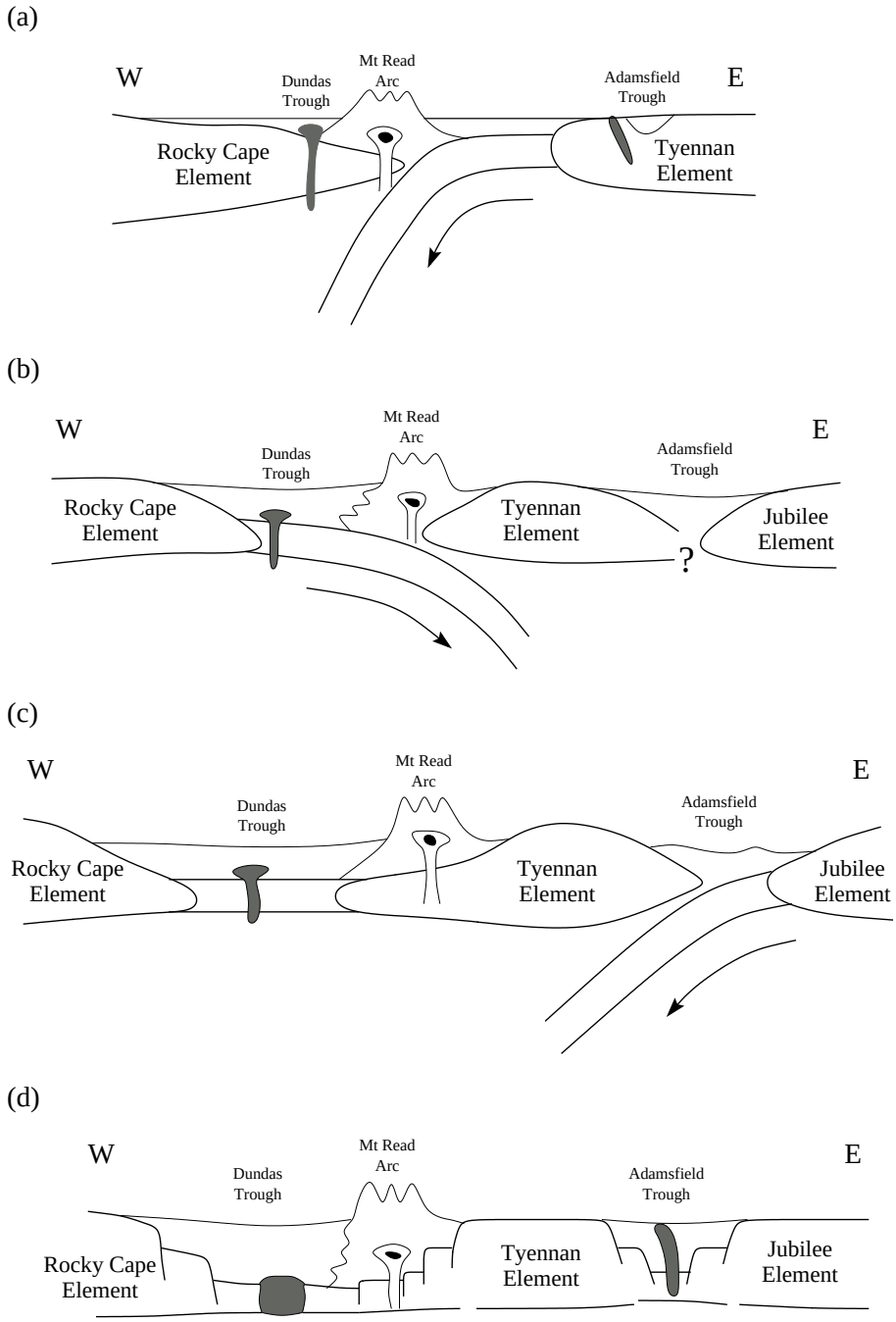

Figure 5.2: Schematic diagrams illustrating some of the possible models for the distribution of Lower Palaeozoic tectonic elements in Tasmania (after Corbett et al., 1972). See text for further explanation.

Comparison of the Eastern and Western Tasmania terranes suggest that the Northeast Tasmania Element was separate from the rest of Tasmania prior to the Silurian/ Late Devonian (Baille & Powell, 1991). The suture between the two terranes is represented by the so-called Tamar Fracture System. The Lower Ordovician and Devonian Mathinna beds to the east of the Tamar Valley are turbidite-quartzwacke sequences, while to the

west, the equivalent successions are carbonate and quartz-rich shelf deposits (Williams, 1989). The contrast in lithology suggests that the Tamar Valley marks the site of a lithospheric scale fracture system brought about by the juxtaposition of two previously separate tectonic elements, for example by subduction (Corbett & Turner, 1989). On the basis of geophysical evidence (magnetic, gravity and conductivity), however, Leaman (1994) argues against the presence of a major fracture system and instead attributes the terrane change to carriage of distal basin elements to the Tamar from the northeast by a complex frontal thrust system.

The effects of the Tabberabberan Orogeny, which occurred in eastern Australia in the Mid-Devonian, can be seen throughout Tasmania. Elliot et al. (1993) correlate this event with westward-directed thrusting of the Early and Mid Palaeozoic strata in the Beaconsfield block over the Badger Head Block (just west of the Tamar valley in northern Tasmania), and the apparent juxtaposition of the East and West Tasmania terranes. Major folding and metamorphism can be observed elsewhere in Tasmania; evidence of north-south shortening at this time can be seen in the western Fossey Mountains, central Tasmania, and east-vergent backthrusting occurred in the Rocky Cape Element (Woodward et al., 1993). Woodward et al. (1993) also suggest that the East Tasmania terrane has been emplaced on the West Tasmanian basement during the orogeny, citing aeromagnetic evidence for the West Tasmania terrane extending all the way to the east coast (some 125 km) beneath the Northeast Tasmania Element. However, no consensus has yet emerged about the significance of the Tamar Fracture System.

Late Devonian to Early Carboniferous times saw the intrusion of both S and I-type granites throughout much of Tasmania. These granitoids are responsible for all the middle-Palaeozoic ore deposits with the exception of the Beaconsfield gold field (Williams, 1989). The granitoids in the east appear to be largely unroofed and slightly older than the only partially unroofed granitoids in the west (Williams, 1989). In both cases, the granite intrusions also appear to define the margins of the continental masses (Leaman, 1989), and emplacement is post-Tabberabberan. There is evidence to suggest that Tasmania was closer to mainland Australia at this time; the Wilsons Promontory granite belongs to the same igneous suite as the East Tasmania granites (Elliot et al., 1991), although the association with the Lachlan Fold Belt granites is unclear. The Tasmanian granitoids also correlate with those found in northeast Victoria Land, Antarctica (Elliot & Gray, 1992), consistent with Tasmania's Palaeozoic location between Antarctica and mainland

Australia within the Gondwana supercontinent.

The Tasmania Basin (Figure 5.1) was initiated in the Late Carboniferous, with principle sedimentary deposits including upper Carboniferous-Permian glacigene and glacimarine deposits and Triassic fluviatile sequences (Williams, 1989) with a total thickness exceeding 1 km. Overlying these successions is an extensive sheet of Jurassic dolerite (Elliot et al., 1991), which has no equivalent in the Lachlan Fold Belt, emplaced at about 174 Ma (Williams, 1989). It covers roughly half the area of Tasmania and much of the southeast continental shelf. The emplacement of the dolerite corresponds to a period of extension in the Jurassic that preceded the breakup of Gondwana (Williams, 1989).

The initiation of seafloor spreading between Australia, Antarctica and New Zealand during the breakup of Gondwana began in the Cretaceous, and represents the last significant tectonic event to effect Tasmania. The onset of drift between Australia and Antarctica did not occur until about 95Ma (Veevers & Eittreim, 1988), and complete separation did not occur until the Oligocene, when Antarctica broke away from the South Tasman Rise (Exon & Crawford, 1997). The Tasman sea between Australia and New Zealand ceased to open at about 57 Ma (Williams, 1989). Within Gondwana, Tasmania is usually placed at the triple junction between Mainland Australia, New Zealand and Antarctica (e.g. Dalziel, 1991). Elliot & Gray (1992) point to the differing style of pre-Jurassic stratigraphy and deformation between Tasmania and mainland Australia and Antarctica and suggest that relative to the mainland, Tasmania lay about 245 km east of its present position in Gondwana. East-west dextral displacement between Tasmania and mainland Australia since the initiation of Gondwana breakup was required to achieve the current configuration.

A number of continental rift basins were created as a result of extension associated with the breakup of Gondwana. The Otway, Sorell, Bass and Gippsland basins were all formed during the Cretaceous, and are filled with fluvial and marine sediments, with intrusive and extrusive basaltic rocks commonly found throughout these successions (Williams, 1989). The hydrocarbon deposits found in these basins were emplaced during the Tertiary. The Sorell Basin formed largely as a result of wrench tectonics within the Southern Rift System between Australia and Antarctica (Hill et al., 1997). Extension between Tasmania and mainland Australia has been estimated at 119 km (Elliot & Gray, 1992) and occurred during early Cretaceous times, resulting in the opening of Bass Strait. However, the Bass Basin remained non-marine until Palaeocene times.

The break-up of Gondwana also formed the South Tasman Rise and the East Tasman Plateau. Recent analysis of satellite-derived gravity data, shipboard bathymetry and magnetic data collected over these regions (Royer & Rollet, 1997) point to the South Tasman Rise being composed of two distinct terranes. The two terranes were welded together in Late Paleocene/Early Eocene times. The Western terrane rifted from North Victoria Land, Antarctica during southerly movement of the Antarctic plate, while the Eastern terrane rifted from Tasmania and the East Tasman Plateau also as a result of this southerly movement. On the basis of seismic , magnetic and gravity profiles, Royer & Rollet (1997) conclude that sea-floor spreading began between the two microcontinental blocks in the Late Cretaceous but ceased not long afterwards.

5.2 Previous Geophysical Work

Geophysics has played an important role in helping to unravel the structural genesis and composition of Tasmania, but it has been used principally in the context of mineral and hydrocarbon exploration. At most, these kinds of studies concentrate on the upper few kilometres of the crust. The emphasis in this thesis is on deep crustal structure, rather than delineation of near-surface features. Consequently, this overview will concentrate on those geophysical studies that have attempted to map crustal scale structure. There have not been many: several refraction profiles, a few gravity and magnetic studies and a small number of heat flow measurements.

The first refraction study that included Tasmania was the Bass Strait Upper Mantle Project (BUMP), carried out in 1966. This project used nine 1-ton bundles of obsolescent depth charges exploded on the sea bed in Bass Strait and recorded the seismic energy at 13 permanent and 42 temporary seismic stations distributed throughout Tasmania, Victoria and southern New South Wales (see Figure 5.3). A single quarry blast at Jindabyne was also used. Underwood (1969) used standard refraction analysis (i.e. linear regression of first-arriving phases and interpretation assuming constant velocity layers separated by horizontal planar interfaces) and Johnson (1973) used delay time analysis (assuming a crustal velocity of 6.0 km/s and a mantle velocity of 8.0 km/s) to determine a crustal structure for SE Australia. This study showed the crustal thickness to be 37 km under the Snowy Mountains, thinning to 25 km under Bass strait (Underwood, 1969) before increasing to 30-35km under central Tasmania (Johnson, 1973). Underwood (1969) also

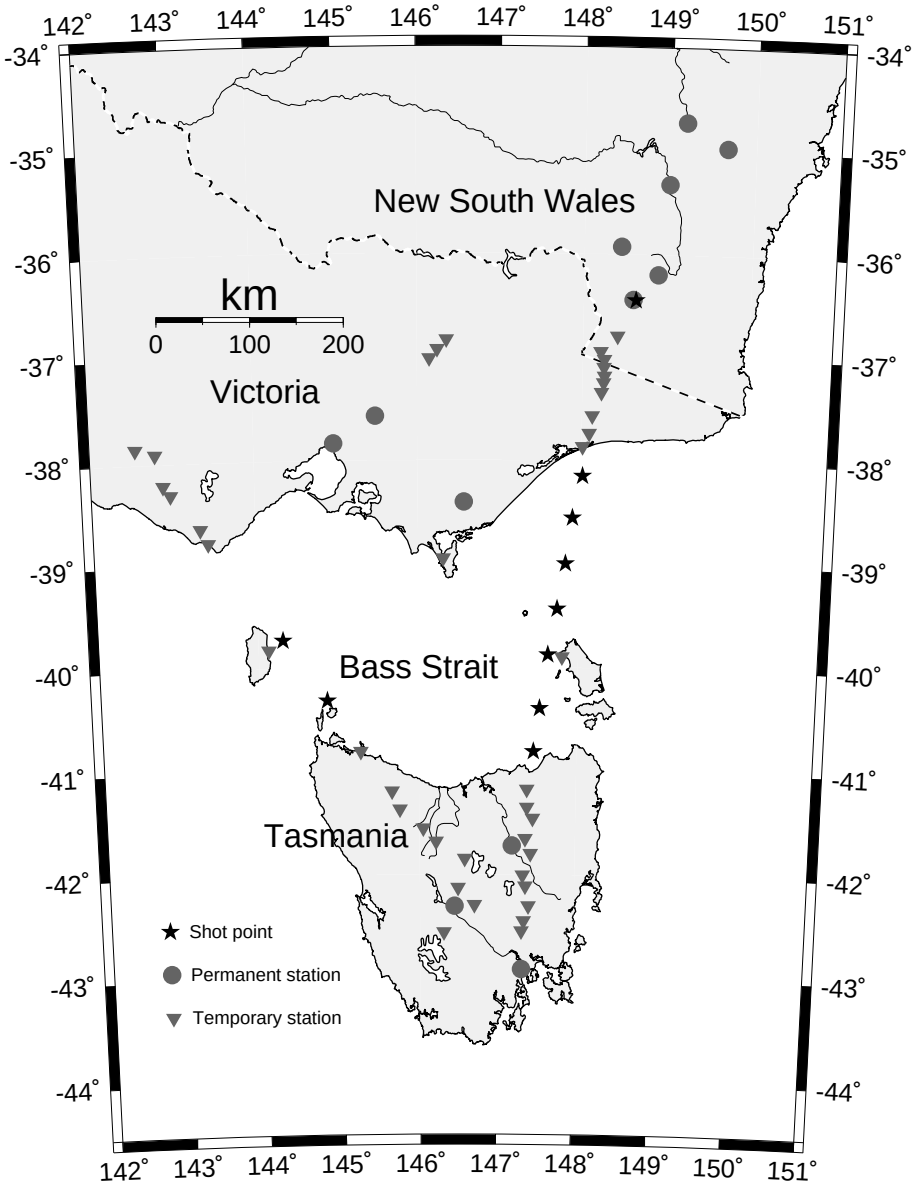

Figure 5.3: Sources and receivers of the BUMP (Bass Strait Upper Mantle Project) refraction survey (after Underwood, 1969).

determined the upper crustal velocity of Tasmania to be 6.0 km/s, the lower crustal velocity to be 7.1 km/s and the P_n velocity (velocity of the mantle immediately below the Moho) to be 7.8 km/s.

Richardson (1980) used a reversed seismic traverse between Savage River and Binalong Bay in Northern Tasmania (see Line A, Figure 5.4) to determine variations in crustal structure. A total of 22 recorders were placed approximately in-line along the 260 km traverse between the eastern and western ends of the island and shots were fired at Binalong Bay and Savage River. Using both refraction and reflection data, Richardson (1980)

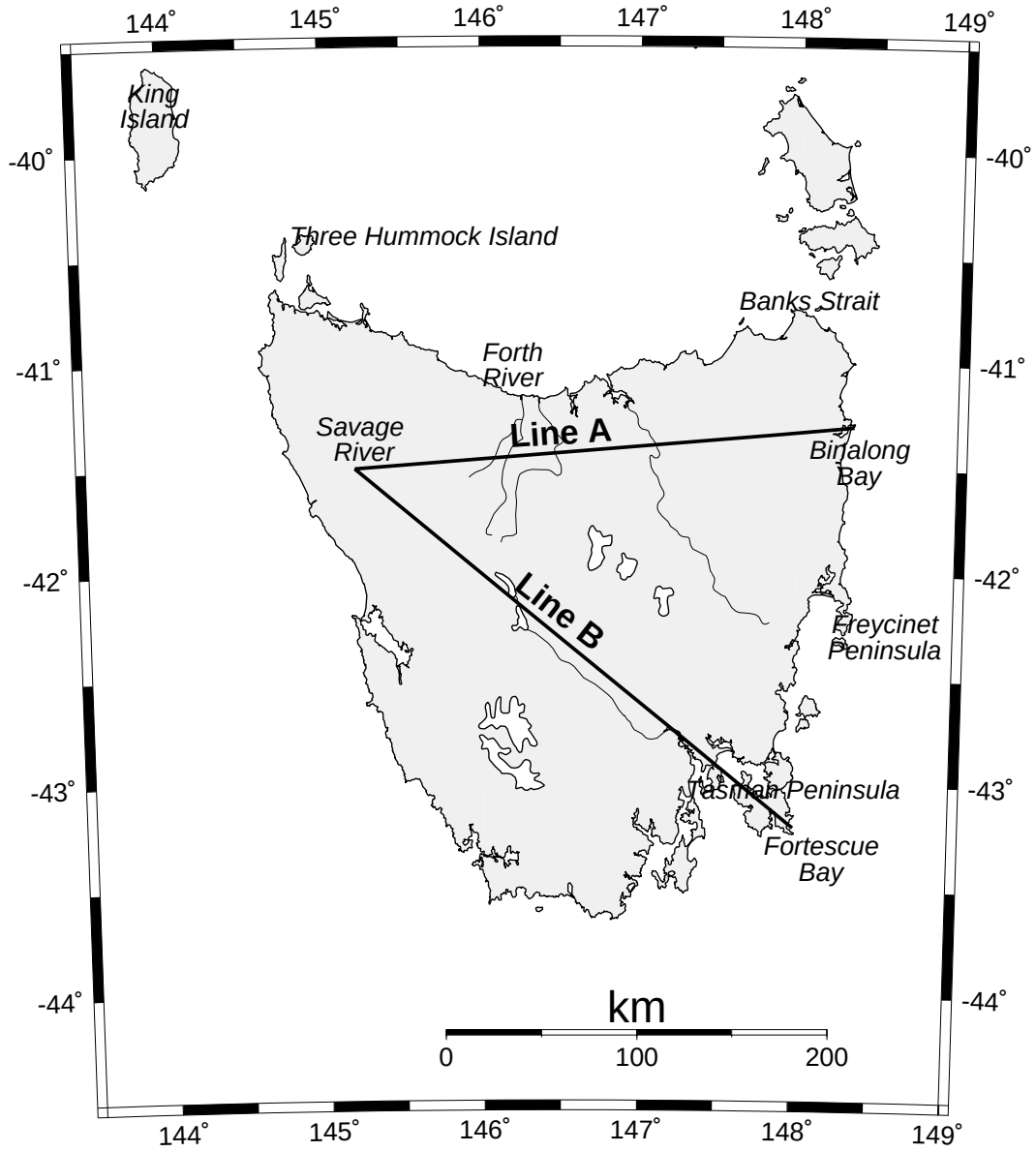

Figure 5.4: Location of two seismic lines from which estimates of crustal structure were made. Line A data was interpreted by Richardson (1980) and Line B data is discussed in Richardson (1989).

interpreted a three-layer crust with an average crustal P-wave velocity of 5.83 km/s and an average P_n velocity of 7.95 km/s. The crustal velocity varies between 5.5 km/s and 6.0 km/s and depths to the upper and middle crustal interfaces are about 8 km and 14 km respectively. The structures of these interfaces are poorly constrained by the data towards the middle of Tasmania due to the source-receiver configuration. The depth of the Moho was found to vary from 22.3 km beneath Binalong Bay, to 27.4 km in the vicinity of the Tamar fracture zone before thinning to 23.4 km near Savage River (see Figure 5.5). The depression of the Moho beneath the Tamar Fracture system was interpreted

by Richardson (1980) to be the expression of a major fault zone between northeast and northwest Tasmania. The velocities of the upper crustal layer have been interpreted as being consistent with granitic and/or metamorphosed Precambrian rocks. Richardson (1980) also picked refraction arrivals consistent with a sub-Moho layer with a bottom interface at about 45 km depth and an average velocity of about 8.0 km/s.

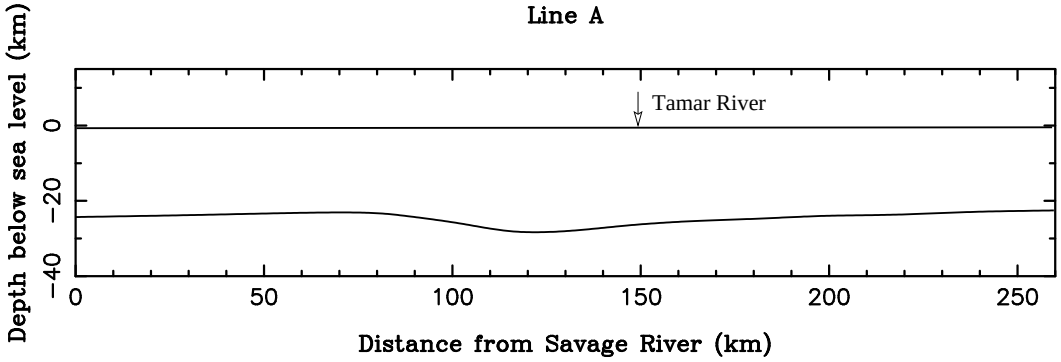

Figure 5.5: Moho depth profile along Line A (see Figure 5.4) after Richardson (1980).

The most recent (prior to TASGO) refraction/wide-angle reflection profile recorded in Tasmania covers a traverse between Savage River and Fortescue Bay (see Line B Figure 5.4). As discussed briefly by Richardson (1989), conventional refraction and reflection methods were used to determine an average crustal velocity of 6.0 km/s and a P_n velocity of 8.0 km/s. Crustal thickness was determined to vary from about 26 km near Savage River to about 34 km under central Tasmania, before thinning to around 27 km near Fortescue Bay (Figure 5.6).

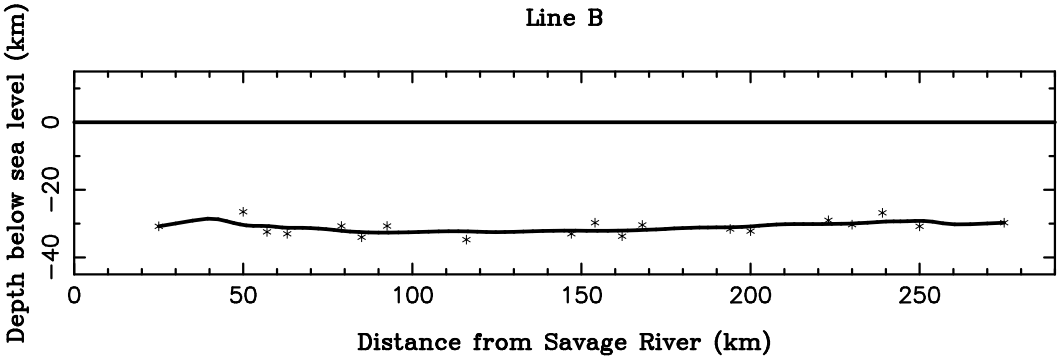

Figure 5.6: Moho depth profile along Line B (see Figure 5.4) plotted from point measurements provided by Richardson (1989). The solid line was calculated using a running average filter applied to the depth points.

The gravity field of Tasmania has been mapped to a high resolution (see Figure 7.39 in Chapter 7 for a recent gravity anomaly map). By 1989, the gravity database included more than 40,000 stations (Leaman & Richardson, 1989). Onshore, the primary contributors to the data base are the University of Tasmania, the Tasmanian Department of Mines, exploration companies and the Australian Geological Survey Organisation (AGSO). The station spacing ranges from 1 to 7 km onshore and from 5 to 15 km offshore, with at least half the island covered at a spacing of 2 km or less (Leaman, 1989). Bouguer anomalies range from about -50 to 100 mGal onshore to 250 mGal offshore (Leaman, 1989). Leaman & Richardson (1989) constructed a crustal model of Tasmania (MANTLE-88) using this gravity data, a study which represented the first attempt to constrain crustal structure using the Tasmanian gravity field. MANTLE-88 is defined in terms of crustal scale masses, including granitic intrusions, basement blocks and Moho structure. The Moho structure of MANTLE-88 is of relatively low resolution but it shows the crust to be about 27.5 km thick under central Tasmania and thinning towards the coast, where the crust is about 23 km thick (see Figure 5.7). In this model, the structure of the Moho is dependent on a number of assumptions (including density inferred from crustal velocities), with relative depth variation based on the longer wavelength components of the gravity field. The absolute depth of the Moho is less meaningful because gravity data alone do not constrain the absolute depth of a density anomaly. Removing the effects of MANTLE-88 from the gravity field leaves a residual gravity map dominated by short wavelength variations, which more directly reflects near-surface structure and is therefore more useful in exploration.

MANTLE-88 also delineates many of the granitic plutons that were intruded during the Devonian. These plutons have roots to depths of 9 to 10 km, with those found in eastern Tasmania being largely unroofed. Also based on the gravity data, two deep early Palaeozoic rift troughs, which exceed 12 km in depth and 25 km in width, have been interpreted in the vicinity of the Mt. Read volcanics (Leaman, 1989). These rifts are largely filled by Cambrian rocks. Gravity surveys have also suggested the presence of Jurassic dolerite feeders within the Tasmania Basin with a concentration of 1 per 100 km^2, falling off to less than 1 per 1000 km^2 outside the basin (Leaman, 1989). Volcanic material with a thickness of 6 to 8 km is interpreted to occur in the Bass Basin.

More recently, Roach et al. (1993) developed a new crustal density model of Tasmania for regional-residual separation. They used the onshore gravity database (TASGRAV)

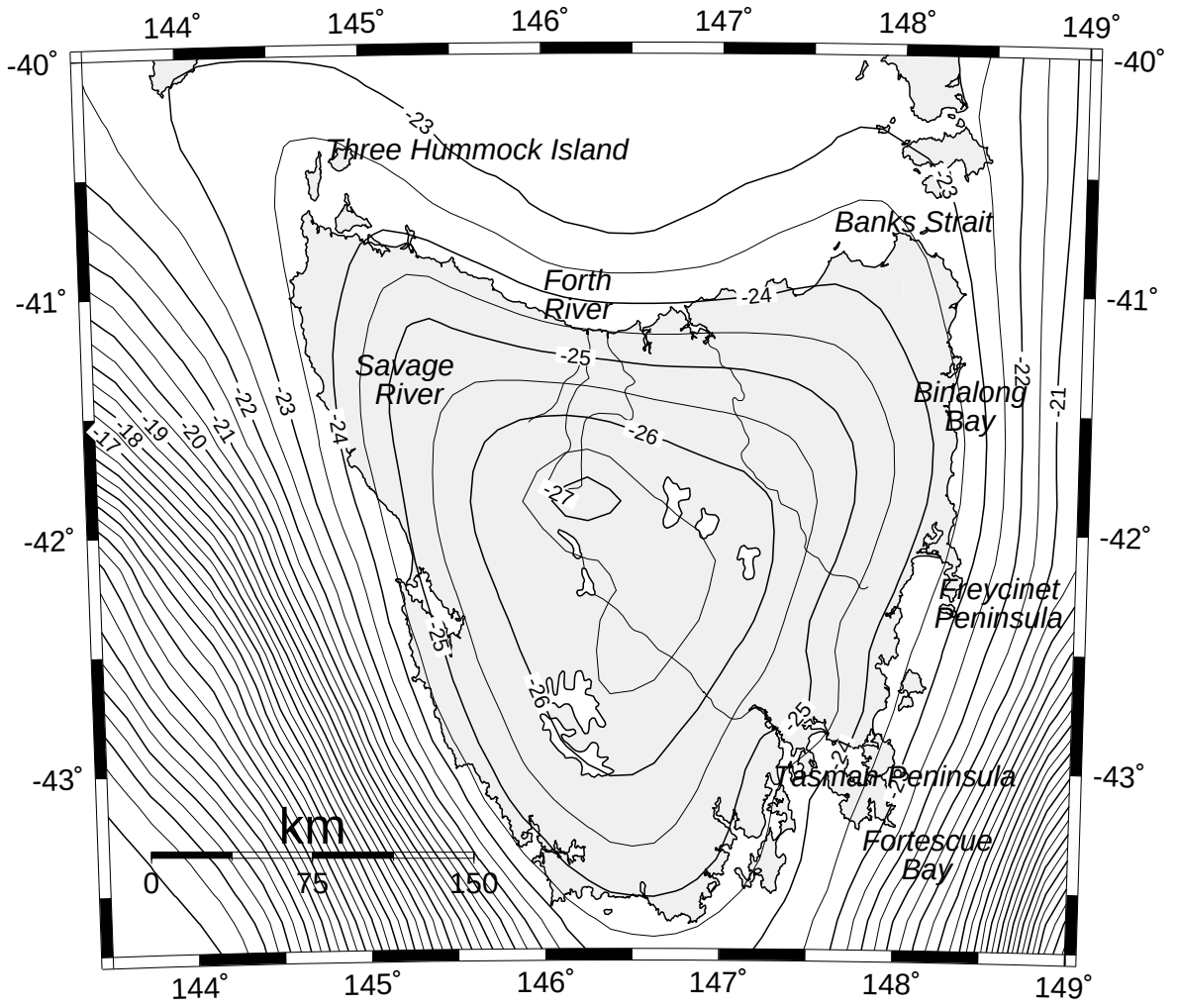

Figure 5.7: Inferred Moho depth below sea-level derived from gravity data for the Mantle-88 model. (after Leaman & Richardson, 1989).

from the Mineral Resources Tasmania, consisting of about 50,000 stations and offshore data from the AGSO (Australian Geological Survey Organisation) database. Starting from the MANTLE-88 model of Leaman & Richardson (1989), but including an improved model for oceanic crust, they applied forward modelling techniques to obtain a revised structure/density model for Tasmania. The new crustal model differs from MANTLE-88 principally in that the crust now has a maximum thickness of 29.5 km beneath central Tasmania.

Aeromagnetic data collected in Tasmania (see Figure 7.40 in Chapter 7 for a recent total magnetic intensity map of Tasmania) are dominated by anomalies generated by young dolerite and basalt cover sequences that cover roughly half of the state (Parkinson & Richardson, 1989). Numerous strong magnetic lineaments, such as the Arthur Lineament, are observed in the data, and are often associated with zones of mineralisation.

The objective of most magnetic surveys in Tasmania has been the location and definition of ore-bearing or coal bearing environments (e.g. Leaman, 1994; Richardson, 1994, 1997), although on a regional scale, the magnetic field has been useful in defining the boundaries and near-surface structure of Tasmania's tectonic elements. Gunn et al. (1997) interpret aeromagnetic, gravity and geological data to produce a map showing the geometric distribution of the main basement units of the state. For this interpretation they used a 1:500,000 scale total magnetic intensity map produced by AGSO and by Tasmania Development and Resources in 1995. The Arthur Lineament is revealed as an extended composite zone of highly magnetic linear units with a NE-SW orientation. The magnetic intensity data indicates that the lineament extends offshore beneath the Bass Basin and to southwest offshore areas, where it is disrupted by granite intrusion and offset by Mesozoic basin extension. The Devonian granitoids, which show up clearly in the gravity data (Leaman & Richardson, 1989), are generally non-magnetic and are not delineated by the aeromagnetic data. Sedimentary basins off the west coast, which include the Sorell Basin and the King-Island Sub-basin are evident as areas of longer wavelength magnetic anomalies due to the increased depth of the magnetic basement.

The surface heat flow of Tasmania is, on average, greater than 80 mW/m^2 (Green, 1989), making it anomalously high compared to mainland Australia. The values range from 57 mW/m^2 to 159 mW/m^2, with the minimum reading probably affected by underground water flow and heat refraction through quartzites, and the maximum reading probably affected by heat production within a nearby alkali granite pluton which is known to host uranium mineralisation (Green, 1989). A relatively recent 1983-1984 survey referred to by Green (1989) obtained heat flow measurements at three locations (western north coast, mid east coast and central Tasmania) to depths of nearly 1 km. The average geothermal gradient measured at these locations was 33°C/km. Linear extrapolation of these gradients would imply extensive melting of the upper mantle beneath Tasmania (Green, 1989). However, it is probable that the geothermal gradient reduces with depth due to the significant contribution of crustal heat production to the observed near-surface gradient.

5.3 TASGO Wide-Angle Seismic Survey

The remainder of this thesis deals with the description, processing and interpretation of a wide-angle seismic dataset recorded as part of the TASGO project. In 1995, AGSO's research vessel *Rig Seismic* circumnavigated Tasmania while firing approximately 36,000 air-gun shots with a nominal shot spacing of 50 m. A network of 38 portable analogue recorders and 6 digital observatory stations distributed throughout Tasmania recorded seismic energy from the air-guns. Figure 5.8 shows the source-receiver configuration of the survey superimposed on an elevation and bathymetry map of Tasmania and the surrounding oceans, and Table 5.1 lists the location and elevation of each station. Marine deep reflection profiles were recorded concurrently with the wide-angle dataset (Barton et al., 1995), but do not form part of this study, except where interpreted sections (e.g. Barton, 1999a) are available for comparison.

5.3.1 Aims of the TASGO Project

The TASGO project was established in 1994 by the Tasmanian Geological Survey in conjunction with AGSO as part of the National Geoscience Mapping Accord (NGMA). The overall goals of TASGO, to be accomplished by a variety of geological and geophysical techniques, as stated by Barton et al. (1995) and Chudyk et al. (1995) are:

- to increase exploration, development and investment in Tasmania
- to increase Tasmania's mineral and petroleum potential
- to develop a tectonic framework for Tasmania's major geologic structures
- to understand the geological controls on Tasmania's geology at depth and how its mineral and petroleum systems fit into this framework.

To achieve these goals, the project utilised aeromagnetic data, marine deep reflection profiles (see Figure 5.8), on-shore deep reflection profiles at three locations (Barton et al., 1995), and wide-angle seismic recordings (see Figure 5.8). In the cruise proposal for the seismic component of TASGO, Hill & Yeates (1995) state that the aims of the normal incidence reflection survey are to:

- establish the crustal architecture and nature of tectonic provinces around the periphery of Tasmania, and investigate the petroleum and mineral resources implications.

Station Number	Site Name	Recorder Type	Station Location		Elevation (m)
			Longitude (°E)	Latitude (°S)	
1	Melaleuca	portable analogue	146.1557	43.4120	38
2	Mt. Wart	portable analogue	145.6447	42.8687	186
3	Stahan	portable analogue	145.4165	42.1507	200
4	Reece Dam	portable analogue	145.0933	41.7423	200
5	Nelson Bay River	portable analogue	144.8187	41.1957	139
6	West Montagu	portable analogue	144.8608	40.7987	37
7	Grassy Road	portable analogue	143.9908	39.9445	86
8	South Weld	portable analogue	146.6965	43.0318	178
9	Lapoinya	portable analogue	145.5497	41.0242	134
10	Forth	portable analogue	146.2768	41.2307	214
11	Kelso	portable analogue	146.7835	41.1098	0
12	Bridport	portable analogue	147.3478	40.9972	14
13	Rushy Lagoon	portable analogue	147.9752	40.8320	38
14	Priory	portable analogue	148.1567	41.2208	170
15	Coles Bay Road	portable analogue	148.2332	41.9565	36
16	Greenhills Road	portable analogue	147.9003	42.3983	50
17	Randor Road	portable analogue	147.8025	43.1572	419
18	Bruny Island	portable analogue	147.2560	43.3735	189
19	Catamaran	portable analogue	146.8535	43.5792	43
20	Guilford	portable analogue	145.6473	41.4098	633
21	Shoulder of Mutton	portable analogue	146.7472	41.4990	213
22	Stone House	portable analogue	147.6857	42.2662	371
23	Gladstone	portable analogue	148.0528	40.9432	68
24	Cracroft	portable analogue	145.6550	42.3593	232
25	Trowutta	portable analogue	145.1230	41.0430	151
26	Ringarooma	portable analogue	147.7443	41.2645	277
27	Mags Road	portable analogue	146.1780	41.7588	854
28	Lake River Road	portable analogue	147.0942	41.9480	606
29	Fosterville	portable analogue	147.4310	41.9640	241
30	Drypoles Road	portable analogue	146.7222	42.6453	365
31	Three Hummock Is.	portable analogue	144.9163	40.4517	74
32	Port Davey	portable analogue	145.9488	43.1728	43
33	Moorlands	portable analogue	147.1903	42.4417	401
34	Badger Head	portable analogue	146.7003	41.1163	36
35	Strathblane	portable analogue	146.9355	43.3560	72
36	Needles	portable analogue	146.4113	42.7558	460
37	Lake Echo	portable analogue	146.6240	42.2813	749
38	Strickland	portable analogue	146.6485	42.3728	521
39	Mount Read	digital observatory	145.5437	41.8463	975
40	Sheffield	digital observatory	146.3075	41.3375	213
41	Tarraleah	digital observatory	146.4500	42.3042	579
42	Savannah	digital observatory	147.1888	41.7208	180
43	Strathgordon	digital observatory	146.0533	42.7508	484
45	Scotts Peak	digital observatory	146.2750	43.0383	425

Table 5.1: Locations and elevations of the 44 seismic recorders used in the TASGO wide-angle survey of Tasmania. See Figure 5.8 for map of positions.

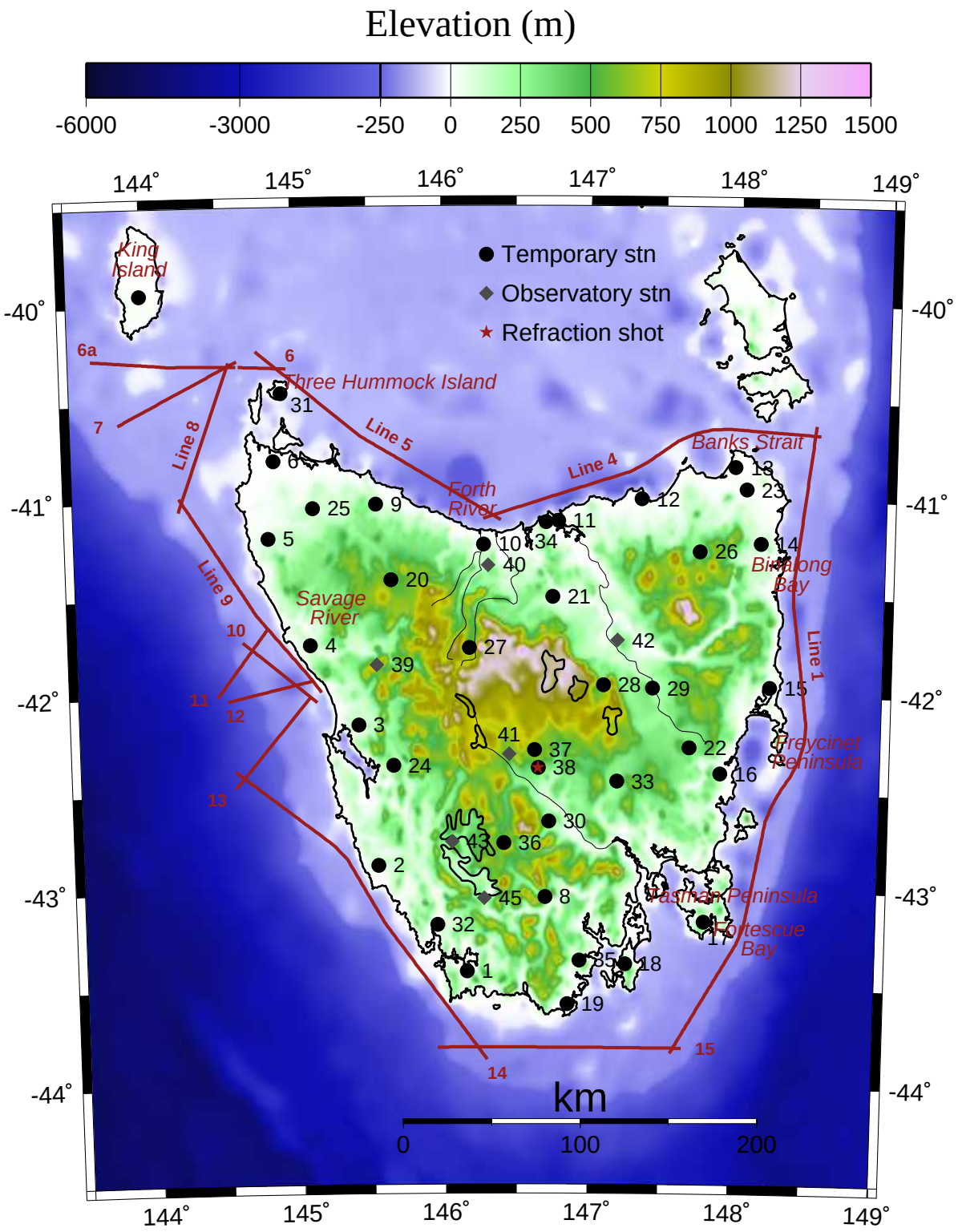

Figure 5.8: Source-receiver configuration of TASGO wide-angle seismic survey. Solid red lines indicate the path taken by *Rig Seismic* during the operation of its airguns. Topography (from USGS EROS Data Center) has 0.5 minute resolution and satellite-derived bathymetry (from NGDC) has 2 minute resolution.

- map the offshore extensions of major Tasmanian crustal structures that have been mapped geologically or geophysically onshore,

while the aim of the wide-angle survey is to:

- map, in 3-D, the principal structural and tectonic elements that make up the Tasmanian craton, and to better understand the evolution of this crustal block.

This thesis contributes to these aims through the development and application of methods for the inversion of refraction and wide-angle reflection traveltimes for 3-D layered crustal structure. The structural models obtained from these inversions will be interpreted in terms of crustal scale geological and tectonic features.

5.3.2 Details of the TASGO Wide-Angle Survey

Detailed descriptions of the recorders, energy sources, station recording times and clock drifts associated with the TASGO wide-angle seismic survey can be found in Chudyk et al. (1995).

The 38 portable analogue recorders used in the survey were developed by AGSO. Powered by 12V external batteries, data are recorded onto magnetic tape. Two basic types of recording systems were used: modified Precision Instruments (PI) 1/2 inch tape decks with 2195 m tapes and modified Akai or Tandberg 1/4 inch tape decks with 548 m tapes. Using a sampling frequency of 62.5 Hz, they were capable of continuous recording for 4 (1/4 inch tapes) or 16 (1/2 inch tapes) days. Each station was equipped with a single vertical component seismometer with a natural frequency of 1.5 Hz. Generally, a gain of 96 dB and bandpass filtering were applied to the signal before it was recorded. The PI recorders used bandpasses of 6-100 Hz while the remaining recorders used bandpasses of 0.01-20 Hz or 0.2-25 Hz. Two additional channels were used to separately record a coded clock signal synchronised to the radio time standard and 10 second pulses from the Omega radio navigation facility at Yarram, Victoria. The analogue recorders were deployed by ground vehicles, helicopters and fixed wing aircraft throughout Tasmania (Figure 5.8). As far as practicable, recorders were positioned to be in line with one or more of the offshore traverses. Pronav GPS receivers were used to estimate seismometer positions to within 100 m of their true positions. All recorders were deployed by 1/3/1995 and collected by 12/4/1995.

Six permanent seismic observatory stations maintained by the University of Tasmania operated during the survey period. The output from the observatory stations was digitised on a PC-based system and stored on hard disk. A sampling frequency of 50 Hz was used for these stations.

Pre-processing of the analogue data involved digitisation and the application of timing corrections. These processes were completed at AGSO using a semi-automated procedure that involved a PDP11 computer linked to a tape playback system with analogue to digital conversion being carried out by Data Translation hardware and library routines. Data from both observatory and analogue stations were reformatted into the standard AGSO refraction seismic format (Drummond & Downie, 1985) so that subsequent processing of the data did not have to discriminate between data of different origin. The complete pre-processing procedures are described in detail by Collins & Semenova (2000).

The principle seismic energy sources for the TASGO wide-angle survey were air-gun shots fired by *Rig Seismic* during its circumnavigation of Tasmania (Figure 5.8). The air-gun array consisted of 20 separate 150 c.i. (2.46 litres) air guns which operated at 1800 psi. Shots were fired 10 m below the surface at 50 m intervals along each traverse. The ship's average speed was 5 knots, so one shot was fired about every 20 seconds. Firing times were obtained using *Rig Seismic's* Data Acquisition System clock which was synchronised with GPS time signals. The route taken by Rig Seismic during the operation of its air-guns (Figure 5.8) was designed to produce reflection sections parallel to the coast. Non-parallel lines (e.g. lines 11 and 12) were included to target particular structures.

In addition to air-gun shots, other known seismic sources that could in principle be used for seismic inversion include explosive shots, quarry blasts and earthquakes. Two explosive shots were fired 20 minutes apart at Strickland in central Tasmania (Figure 5.8) with the aim of providing some reversed coverage to the air-gun shots. The first explosion used 600 kg of charge and the second explosion used 912 kg. Further, at least 22 quarry blasts, ranging in size from 130 kg to 19,360 kg, were performed during the operation of the survey. The on-land shots provide additional reversed coverage from within the receiver array. A number of large earthquakes also occurred during March and early April 1995. According to the IRIS database, 12 had magnitudes greater than 6.0, the largest being a magnitude 8.0 in the Tonga Islands. These events could be used to help constrain crustal structure, but the combination of wide-angle and teleseismic data sources was considered to be beyond the scope of this thesis.

5.3.3 Data Coverage and Quality

The TASGO wide-angle seismic data were generously made available to the author by AGSO, following the pre-processing procedures described above. Only the records associated with air-gun shots were provided. The explosive shots at Strickland were apparently lost in the noise and the quarry blasts were not considered. Several of the larger teleseismic events were also checked, but apparently they could not be detected.

With a total of ∼36,000 air-gun shots and 44 recorders, the number of source-receiver combinations for the TASGO wide-angle dataset is over 1.5 million. However, several problems including poor signal-to-noise ratio and recorder failure resulted in a substantially reduced usable dataset. Table 5.2 summaries all of the data made available by AGSO for the purposes of this project, in terms of station-line combinations and a data quality indicator. The data status is subjectively determined using processed (i.e. stacked, filtered etc.) refraction sections. *Good* data have very clear arrivals (e.g. Figure 5.9a), *fair* data have quite clear arrivals (e.g. Figure 5.9b), *marginal* data have arrivals that barely stand out from the noise (e.g. Figure 5.9c) and *poor* data have no detectable signal (e.g. Figure 5.9d) and are therefore not used. Thus, of the 119 station-line combinations listed in Table 5.2, only 77 result in usable data. This compares to a maximum of 572 station-line combinations if all the recorders recorded signal from all the shot lines. Figure 5.10 shows all 77 station-line combinations for which there are usable data. The eastern part of the state experiences the poorest coverage, but note that Figure 5.10 does not show ray path coverage; in some cases useful data are only obtained from part of the line.

Of the 44 recorders used to collect wide-angle data, 20 did not record any usable data (Figure 5.10) due to station failure or unacceptable signal-to-noise ratios. The resultant dataset is much smaller and coverage is less dense and more heterogeneous than originally anticipated. In may ways, this makes the wide-angle inversion method presented in Chapter 4 an appropriate choice to interpret the data. The method works efficiently when there are relatively few sources and many receivers (or vice versa, as in this case), its parameterisation can be adapted to suit the resolving power of the dataset, and both refraction and reflection arrivals can be used to constrain structure. The use of reflections is important because generally the most prominent arrival on all the refraction sections are reflections from the Moho.

Station	Line	Status	Station	Line	Status	Station	Line	Status
14	1	Good	42	5	Poor	39	10	Marginal
15	1	Poor	43	5	Marginal	43	10	Good
17	1	Good	45	5	Poor	45	10	Poor
18	1	Good	5	6	Marginal	2	11	Poor
22	1	Good	7	6	Good	27	11	Good
30	1	Fair	31	6	Good	32	11	Poor
39	1	Poor	39	6	Poor	39	11	Good
40	1	Poor	40	6	Poor	40	11	Good
42	1	Poor	6	7	Poor	43	11	Good
43	1	Fair	7	7	Good	45	11	Poor
45	1	Marginal	27	7	Marginal	2	12	Poor
10	4	Good	31	7	Good	27	12	Good
11	4	Poor	39	7	Poor	32	12	Poor
13	4	Poor	40	7	Poor	39	12	Fair
17	4	Marginal	43	7	Poor	40	12	Fair
21	4	Fair	5	8	Marginal	43	12	Fair
23	4	Marginal	7	8	Fair	2	13	Fair
27	4	Fair	25	8	Marginal	27	13	Fair
39	4	Fair	27	8	Marginal	32	13	Poor
40	4	Marginal	31	8	Good	39	13	Good
41	4	Poor	39	8	Poor	40	13	Marginal
42	4	Poor	40	8	Poor	41	13	Marginal
43	4	Marginal	43	8	Poor	43	13	Good
45	4	Poor	3	9	Poor	45	13	Marginal
6	5	Poor	4	9	Marginal	2	14	Fair
7	5	Fair	5	9	Marginal	17	14	Poor
10	5	Good	6	9	Poor	30	14	Fair
11	5	Poor	7	9	Poor	32	14	Fair
15	5	Poor	25	9	Poor	39	14	Fair
16	5	Poor	27	9	Good	41	14	Poor
21	5	Marginal	31	9	Good	43	14	Good
22	5	Marginal	32	9	Poor	45	14	Good
25	5	Marginal	39	9	Fair	2	15	Marginal
27	5	Good	40	9	Fair	8	15	Poor
28	5	Marginal	41	9	Marginal	18	15	Good
29	5	Good	43	9	Good	19	15	Poor
31	5	Good	45	9	Poor	30	15	Fair
39	5	Good	2	10	Poor	32	15	Fair
40	5	Good	27	10	Fair	45	15	Fair
41	5	Poor	32	10	Poor			

Table 5.2: Status of available data in terms of station-line combinations. See Figure 5.8 for station-line locations and Figure 5.9 for examples of data quality.

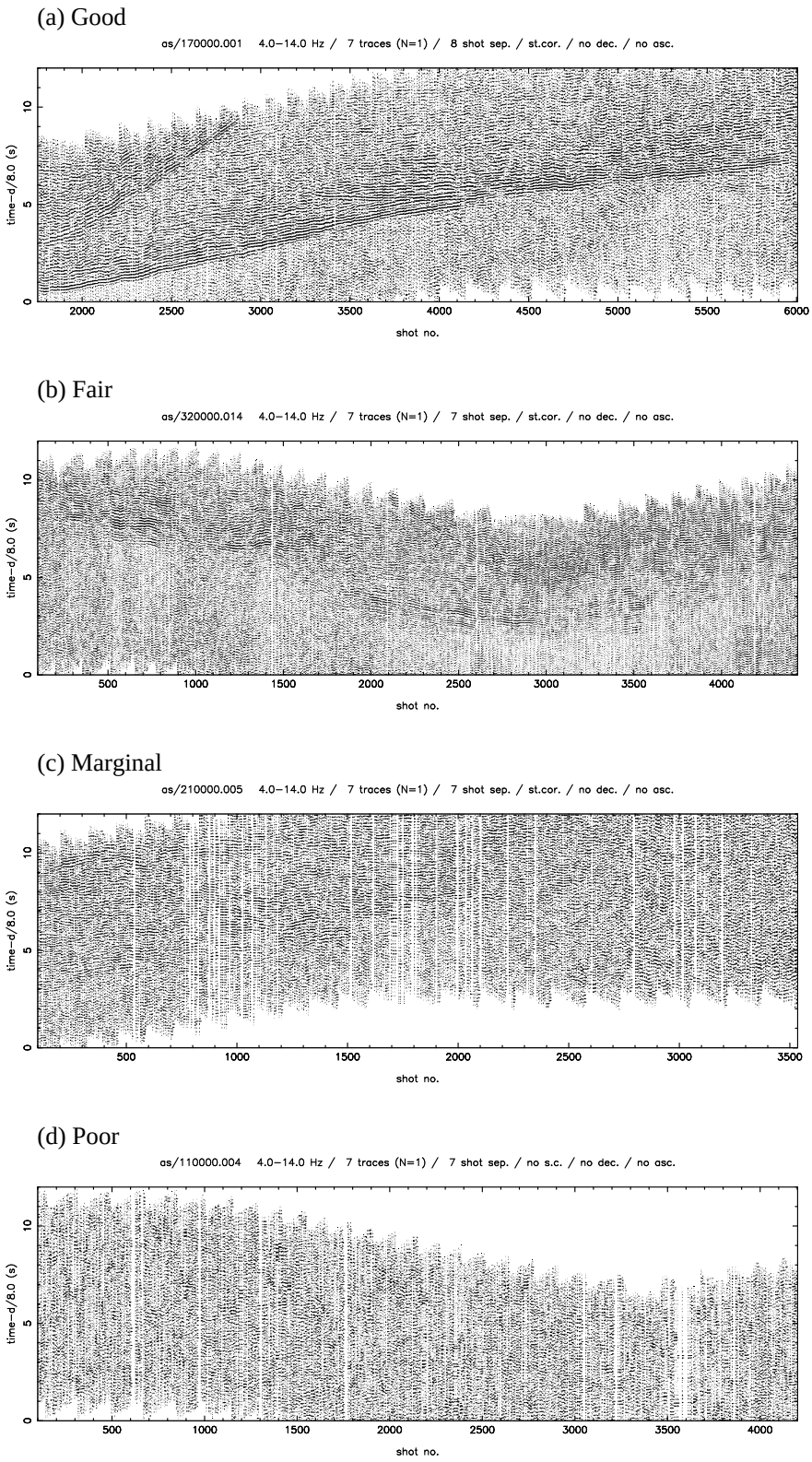

Figure 5.9: Examples of TASGO wide-angle seismic data illustrating the quality criterion used in Table 5.2. The station number *sn* and line number *ln* are indicated for each of these sections by *as/sn0000.ln* where *as* refers to a portable analogue station.

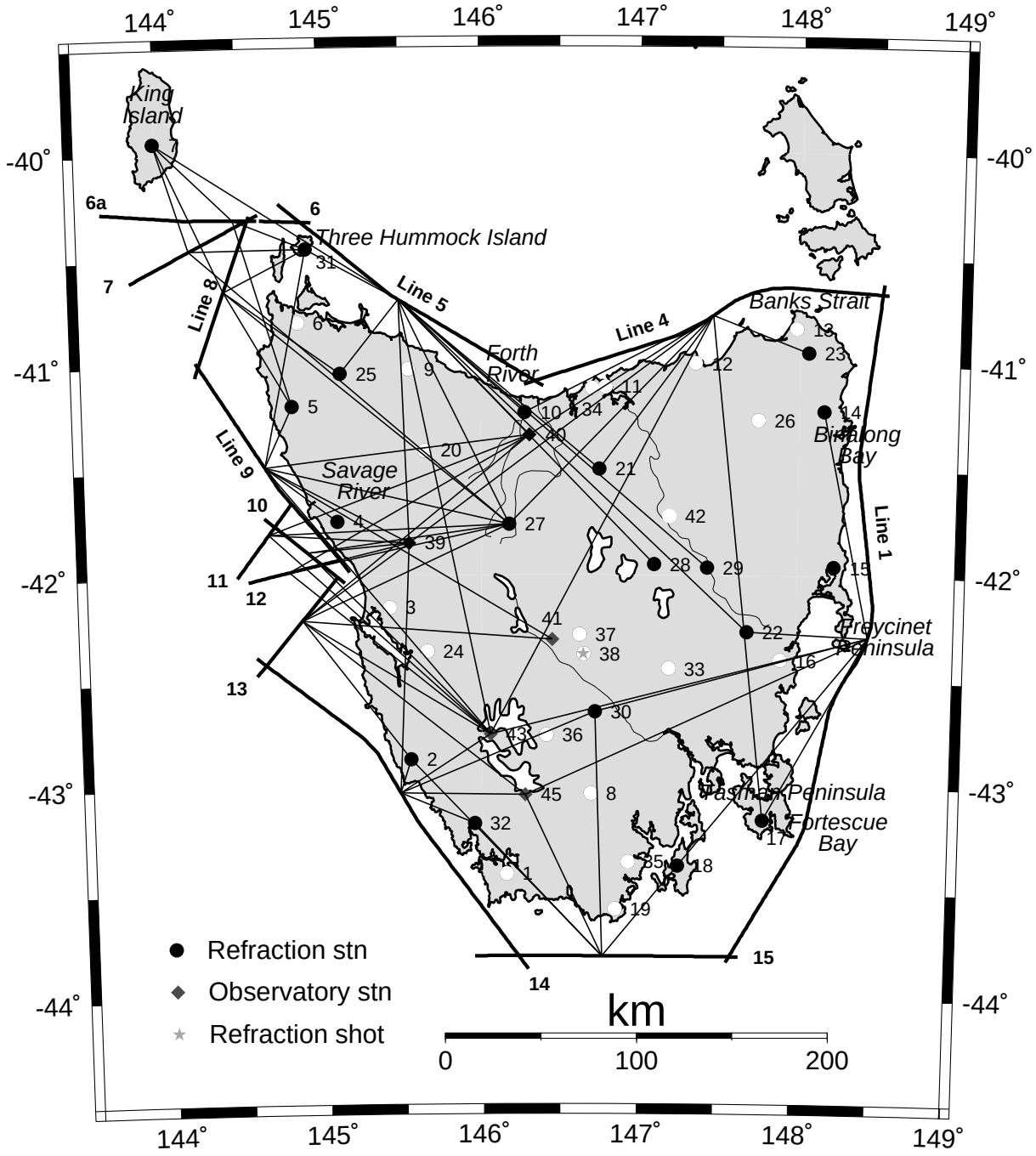

Figure 5.10: Schematic indication of station-line combinations for which data is available. A line is drawn from each station to the middle of each shot line for all station-line combinations with a data quality that is marginal or better (see Table 5.2). Stations denoted by white dots did not record any usable data.

Chapter 6

Processing and Picking of TASGO Data

6.1 Introduction

The inversion of the TASGO wide-angle dataset for seismic structure uses the source-receiver traveltimes of first-arriving refracted phases and later arriving, but generally larger amplitude, reflected phases. The standard record-section display shows traces from adjacent shots to a single receiver on a time versus offset graph (e.g. Figure 6.1). Offset is generally indicated here by shot number (a measure of the distance between shots) rather than the distance between source and receiver since many of the shot lines are broadside to the receivers. On these *refraction profiles*, arriving phases appear as correlated events which vary systematically from trace to trace and may be interpolated to define continuous *traveltime curves*. Identification of these curves makes the picking of the traveltimes of different phases for particular events more straightforward. The ordinate axis of refraction profiles (e.g. Figure 6.1) are usually plotted as reduced time ($t - d/v$ where d is source-receiver offset and v is a nominal reduction velocity), which helps account for the effect of increased traveltime with increased offset. The result is that traveltime curves are "unbunched" and easier to discriminate from one another.

The purpose of the processing step is to improve the signal-to-noise ratio and trace-to-trace coherency of the data to aid the picking process. Methods that are investigated include filtering, stacking, static correction and deconvolution, all of which are discussed in this chapter. That such processing is necessary can be seen in Figure 6.1, which shows raw

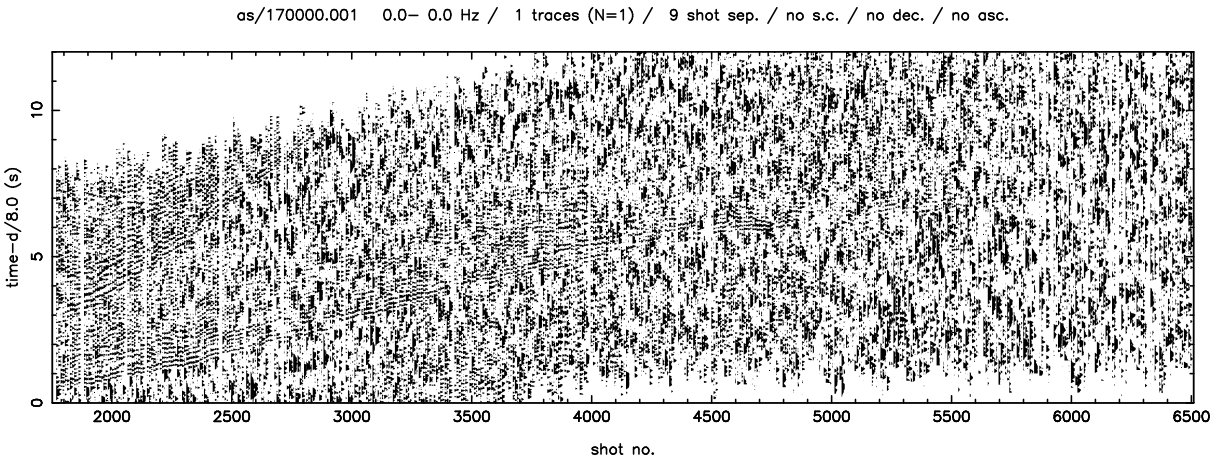

Figure 6.1: Unprocessed data collected at station 17 from line 1 shots displayed with a reduction velocity of 8 km/s.

data recorded at station 17 from line 1 shots; of all the TASGO wide-angle data, this has one of the highest raw signal-to-noise ratios. A vast amount of literature is dedicated to the processing of normal-incidence reflection data. Many of the techniques employed are transferable to refraction data. However, the differences in source-receiver geometry and the ultimate goal of the processing mean that some care is required in applying reflection-based processing techniques to refraction data. While a number of papers (e.g. Purdy, 1982; Klemperer & Luetgert, 1987; Zelt et al., 1987; Chian et al., 1996) have addressed various aspects of refraction processing, every dataset requires separate consideration of the necessary processing steps and parameters.

Picking of the data involves identifying the initial onset of events, associating the event with a phase (e.g. P_n, P_1P), and estimating the arrival time and its uncertainty. Data processing and interactive picking of phases were carried out using software developed during the course of this PhD (see Appendix F).

6.2 Trace Visualisation

The recorded traces represent variations in ground displacement as a result of the passage of seismic waves, and some consideration needs to be given to how these variations are plotted. Telford et al. (1990) describe several approaches for plotting reflection data, including wiggle, variable area, variable density and wiggle superimposed on variable density. Wiggle and variable area displays were both tested here (Figure 6.2), and I found that variable area tended to be more effective for identifying traveltime curves.

Marine wide-angle data is quite dense (shot lines with up to 7,500 shots at 50 m spacing in the case of TASGO), and the wiggle display generally results in a more confusing picture unless only a small portion of the data is visualised.

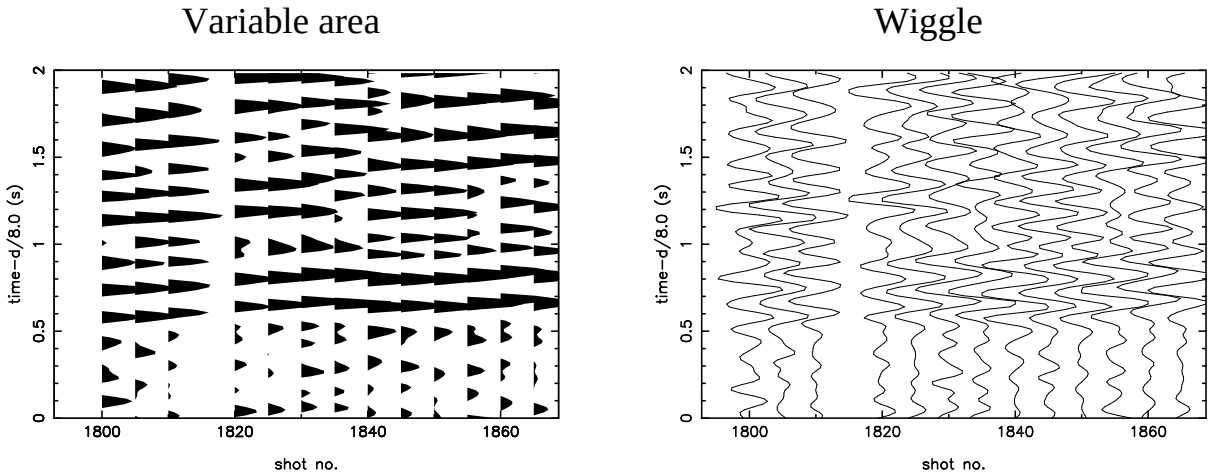

Figure 6.2: Two types of trace visualisation: variable area and wiggle display.

Before display, the width of the trace needs to be scaled in order to maximise the visual impact of coherent arrivals. *Trace normalisation* involves choosing a distance equal to some proportion of the trace separation on the profile, and scaling the maximum amplitude of the trace to this value. Caution is required in this process because: (i) if high amplitude noise spikes occur in the data, the source wavetrain may be scaled to a width that makes it hard to detect, and (ii) if some arrivals (e.g. Moho reflections) are of much greater amplitude than others (e.g. Moho refractions), then the larger amplitude arrival will be visible at the expense of the smaller amplitude arrival. Moho reflections are particularly prominent in much of the TASGO data, and one affect of trace normalisation is that first arrivals may appear to fade out slightly due to the normalisation based on large-amplitude reflections.

The method used here to plot the horizontal position A_{ji} of a normalised trace sample is described by the following equation:

$$A_{ji} = \begin{cases} \dfrac{p\Delta s}{w\sigma_i} a^m_{ji} + s_i & : \quad |a^m_{ji}| < w\sigma_i \\ \dfrac{a^m_{ji}}{|a^m_{ji}|} p\Delta s + s_i & : \quad |a^m_{ji}| \geq w\sigma_i \end{cases} \tag{6.1}$$

where $a^m_{ji} = a_{ji} - \sum_{j=1}^{m} a_{ji}$ is the j^{th} sample of the i^{th} trace (from which the mean has been

removed) of the recorded data. Δs is the trace separation, σ_i is the standard deviation of a_{ji}^m for the i^{th} trace, and m is the total number of samples in a trace; s_i is the offset of the i^{th} trace, and p and w are user-supplied values which control the allowable width of the trace and the level of clipping respectively. Traces with raw amplitudes greater than $w\sigma_i$ are clipped and the maximum amplitude of a normalised trace is therefore $p\Delta s$. This approach makes it possible to improve the visibility of small-amplitude arrivals by reducing the value of w, so that the trace amplitude is effectively magnified but still clipped at $p\Delta s$. High amplitude noise spikes in the data do not detrimentally affect the normalisation procedure using this method. As w increases in size, the clipping level is raised and the amplification is decreased. Most of the data examples shown in this thesis use $p = 1.7$ and $w = 2.1$. Thus, the half-width of traces does not exceed 1.7 times the separation between adjacent traces and amplitudes greater than 2.1 standard deviations are clipped at this limit.

6.3 Filtering

The aim of filtering is to remove unwanted frequency components from the recorded waveform. Filtering is most effective when the frequency of the noise mostly lies outside the band of frequencies occupied by the arriving source signal. Filtering in the frequency domain is accomplished by transforming the time-domain data into the frequency domain, applying a filter function and then transforming back into the time domain. The transformation can be accomplished using the Fourier Transform, which for discrete data can be written:

$$F_j = \frac{1}{m} \sum_{i=0}^{m-1} f_i \exp^{-2\pi ij/m} \tag{6.2}$$

$$f_i = \sum_{j=0}^{m-1} F_j \exp^{2\pi ij/m} \tag{6.3}$$

where m is the number of equally spaced observations of the time series $f(t)$, whose Fourier transform is $F(\omega)$ with frequencies $\omega_j = j/m\Delta t$. To perform a Discrete Fourier Transform on a time series of length m requires $O(m^2)$ calculations, but the number of operations can be decreased by rewriting the Fourier transform as the sum of two transforms of length $m/2$. This process can be used recursively to subdivide the data to transforms of length 1, provided m is a power of 2. The number of computations required to determine

the transform is then of $O(m \log_2 m)$ and the optimised procedure is referred to as the Fast Fourier Transform or FFT. In this application, the FFT code of Press et al. (1992) is used. The length of the digitised TASGO source-receiver traces is generally around 12 s, and with a sampling interval of 16 ms, this corresponds to approximately $m = 750$ samples per trace. Before applying the FFT, a linear ramp function is separately applied to either end of the traces (usually 20-30 samples) to reduce the amplitude to zero in order to obtain a periodic waveform. Failure to do so can result in the appearance of the Gibbs phenomenon (i.e. high frequency artifacts in the frequency spectrum). Traces are padded with zeros to achieve $m = 1024 = 2^{10}$ when the FFT is performed.

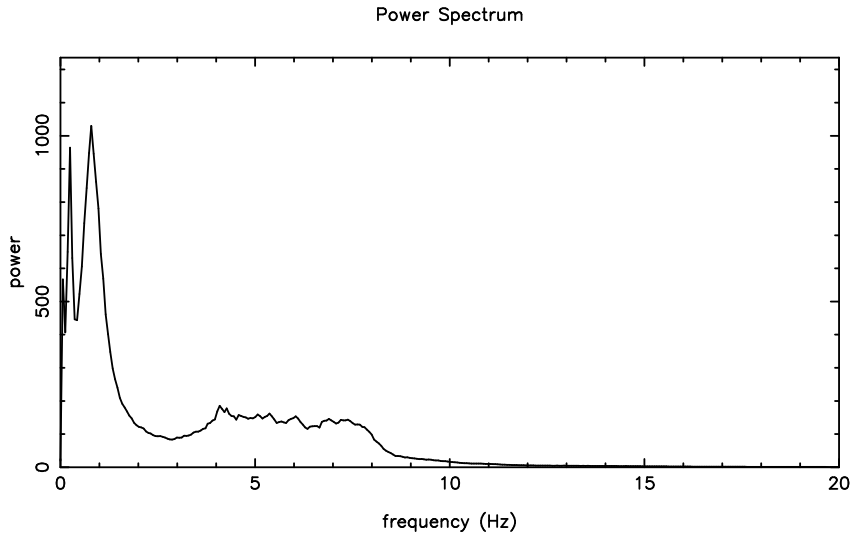

Figure 6.3: Power spectrum of traces collected at station 17 from line 1 shots. The signal falls mainly in the range 4-8 Hz.

Figure 6.3 shows a plot of the power spectrum of the traces in Figure 6.1. The power $|F_j|^2$ at each frequency is determined from the transform series $\{F_j\}$ stacked over all traces. Signal power peaks between 4 and 8 Hz, but the dominant observed frequencies occur below 1 Hz. The latter are due primarily to noise from ocean waves. These noise components may be removed by applying simple bandpass filtering to the data. The frequency domain filter function (Figure 6.4) is based on a simple trapezoid, which passes the signal unchanged in the central range of frequencies and ramps to zero at either end. For the TASGO data, the values chosen for h_1, h_2, h_3 and h_4 are typically 4.0, 5.0, 13.0 and 14.0 Hz respectively. A running average filter is used to smooth the trapezoid so that gradient discontinuities in the filter function do not cause "ringing" to occur at the corner

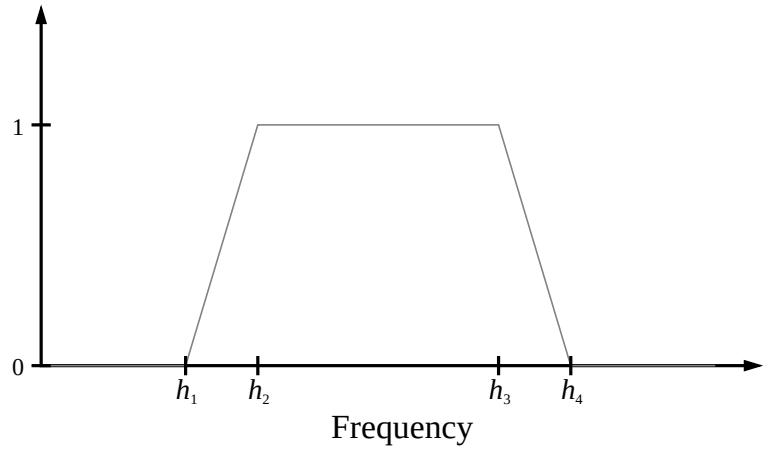

Figure 6.4: Filter function used for bandpass filtering. Corners are smoothed with a running average filter.

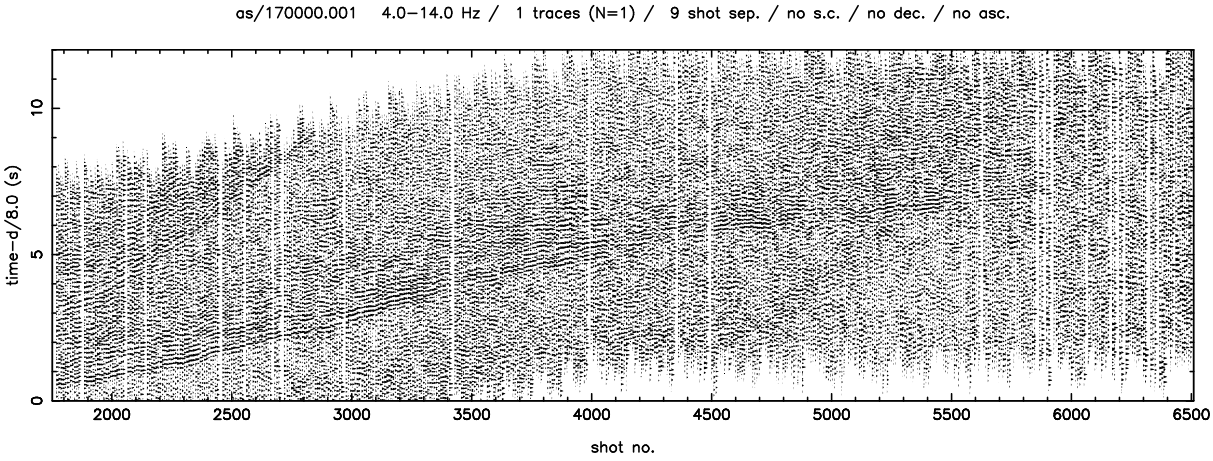

Figure 6.5: The raw data sample of Figure 6.1 with bandpass filtering (4.0-14.0 Hz) applied.

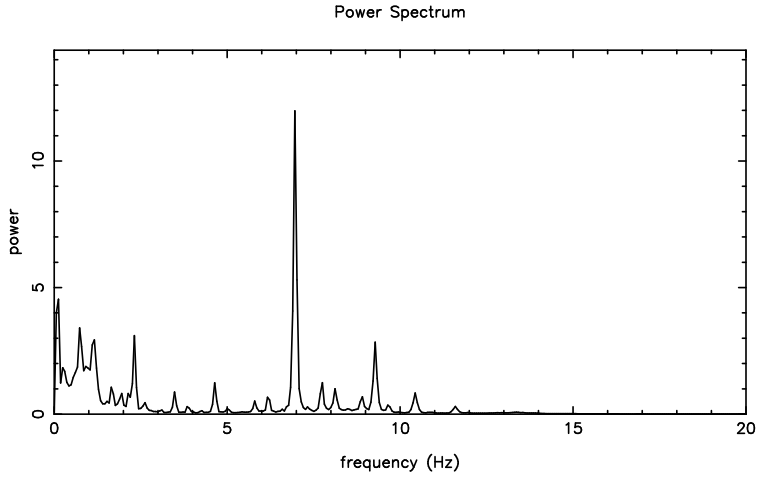

Figure 6.6: Power spectrum of data recorded by station 25 from line 8 shots. The noise spike at 7 Hz was removed by a notch filter.

frequencies. Application of the filter simply requires the filter function to be multiplied with the FFT of the data and then the inverse FFT to be applied. The effect of bandpass filtering on the raw data shown in Figure 6.1 can be seen in Figure 6.5. The signal is now much clearer due mainly to the removal of the low frequency noise.

If noise is present at specific frequencies within the frequency range of the bandpass filter, a notch filter can be used to remove it. Several of the TASGO stations in western Tasmania exhibit 7 Hz noise spikes (Figure 6.6) which are removed using a notch filter, which passes all frequencies unchanged except a narrow band containing the unwanted frequency (6.8-7.2 Hz in this case). The filter is smooth in order to avoid the "ringing" effects alluded to above. The cause of the 7 Hz noise is unknown.

6.4 Stacking

Another method for increasing the signal-to-noise ratio of raw data is stacking. It operates under the dual assumptions that noise is random, and that the component of the recorded waveform due to the source signal is coherent for adjacent shots. Thus, stacking adjacent shots using a suitable stacking velocity will result in the signal being boosted and the noise being reduced. If the phase has an apparent slowness $1/v_s$, each signal in the stack is delayed by $\Delta t = \Delta s/v_s$, where Δs is the change in offset relative to the central signal and v_s is the stacking velocity. The optimal number of traces to stack depends on how much the arriving signal waveform changes from shot to shot. Figure 6.7 shows the filtered data of Figure 6.5 that has subsequently been stacked using either three traces (Figure 6.7a) or seven traces (Figure 6.7b) and a stacking velocity of 8.0 km/s. Both are an improvement on Figure 6.5, although the seven trace stack is superior to the three trace stack. Generally, a seven or nine trace stack was used for picking the data. The stacking velocity of 8 km/s is optimal for phases that display as horizontal events in Figure 6.7, but it also improves the signal-to-noise ratio for other phases.

Chian et al. (1996) refer to the above stacking method as a "simple stack". They develop a two-pass stacking technique for wide-angle airgun shots that generally produces better results than a simple stack. The method is applied to data from a dense in-line array of receivers and shots. They described an example with 400 recorders at a 500 m spacing and shots fired at a 70 m spacing. The traces of each receiver gather are stacked at a 500 m aperture with a stacking velocity of 8 km/s. The stacked traces are then

(a) 3 trace stack

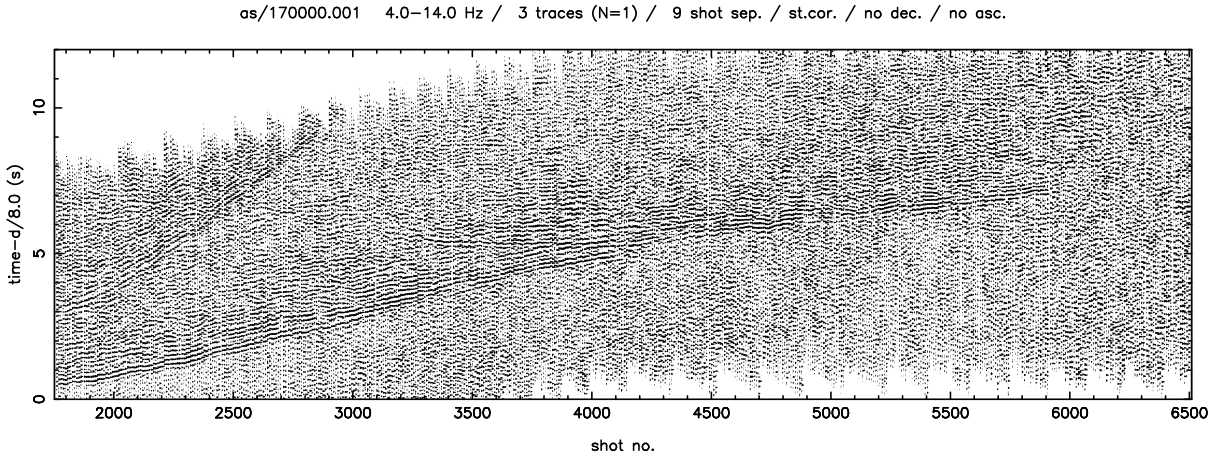

(b) 7 trace stack

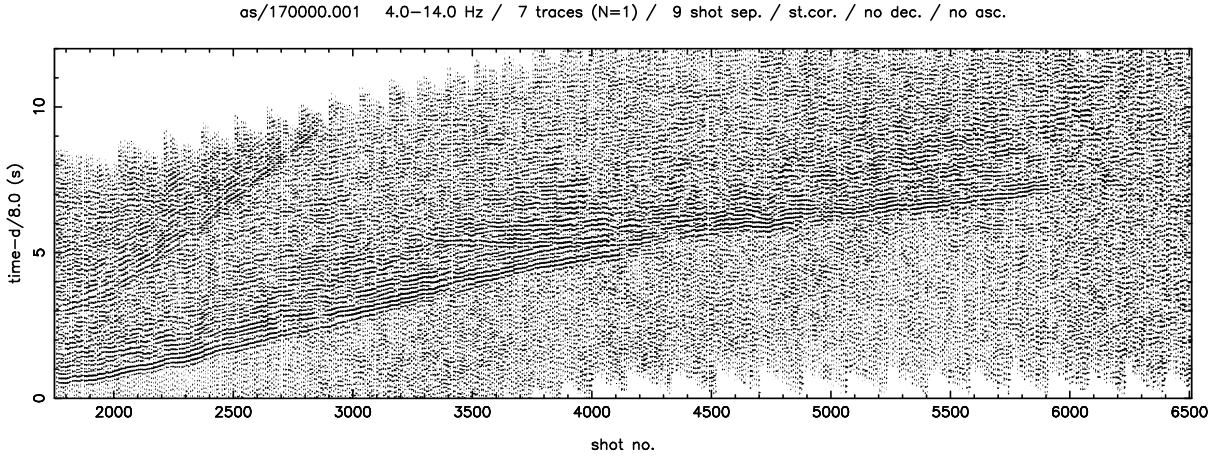

Figure 6.7: Simple (linear) stack of adjacent traces from Figure 6.5 to boost signal-to-noise ratio using a stacking velocity of 8.0 km/s. (a) 3 trace stack, (b) 7 trace stack.

re-ordered in terms of increasing offset and stacked a second time using the same stacking velocity and an aperture of 500 m or less. In some ways, their method can be seen as the wide-angle equivalent to the common-mid-point method for normal incidence reflection data. However, their method is not applicable to the case of the TASGO wide-angle dataset because receivers are too far apart.

In a simple stack, the discrete amplitude components of adjacent traces are added without weighting. Muirhead (1968) introduced the concept of an Nth root stack in the context of trying to eliminate false alarms caused by noise spikes during the automatic detection of seismic events. If $\{A_{ji}\}$ describes a set of n traces ($i = 1, \ldots, n$) of length m

(a) 4th root stack

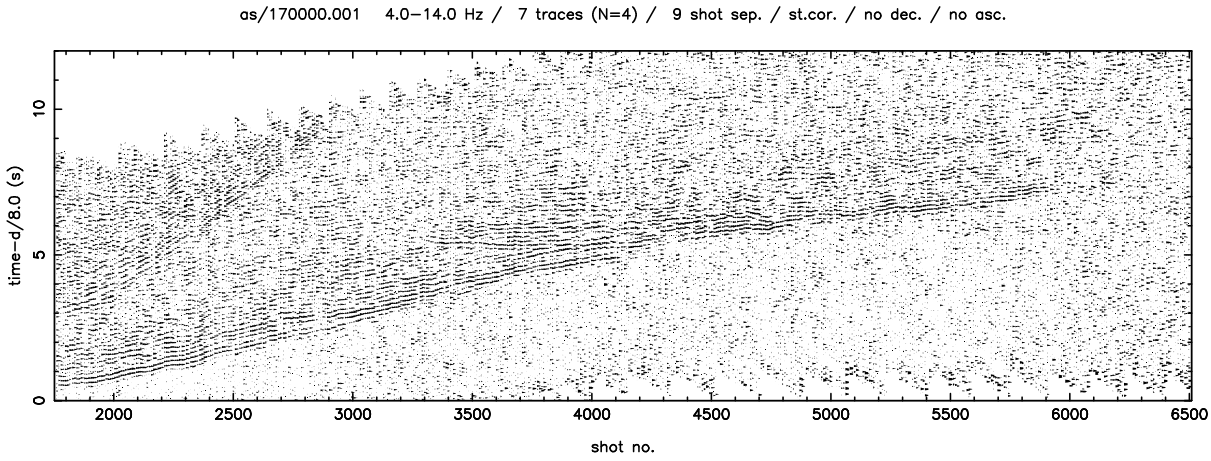

(b) 8th root stack

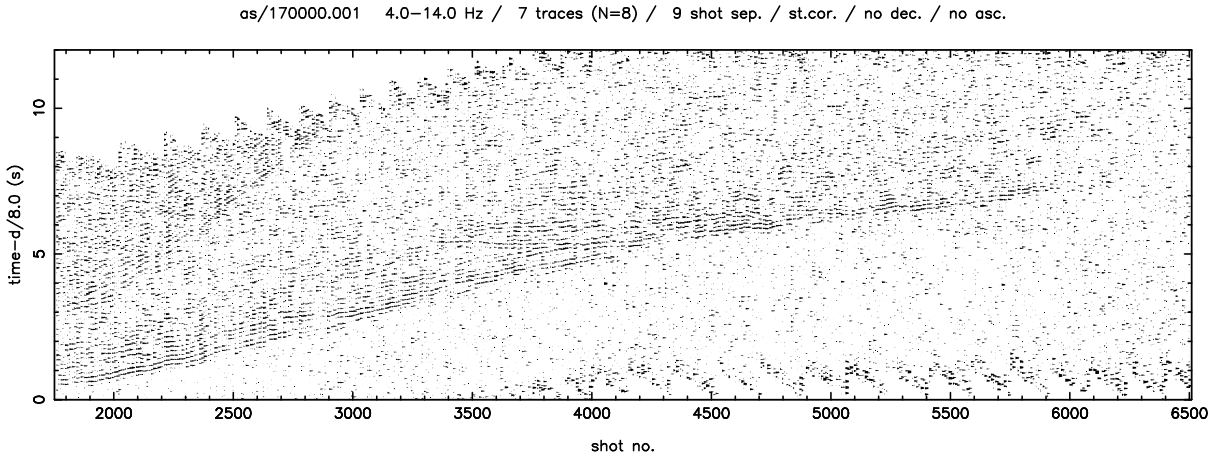

Figure 6.8: Two examples of N the root stack applied to the dataset shown in Figure 6.5. (a) 4th root stack, (b) 8th root stack. The 8th root stack increases the contrast between signal and noise compared to the 4th root stack, but signal distortion results in the traveltime curves being more "patchy".

$(j = 1, \ldots, m)$, then the Nth root stack of these n traces is defined by:

$$R_j = \left[\frac{1}{n} \sum_{i=1}^{n} \sqrt[N]{A_{ji}} \right]^N \tag{6.4}$$

with signs being retained in taking the Nth root and in raising to the Nth power.

If the variance of the noise in a set of n traces with no signal is σ^2, then the variance of the noise in the resulting Nth root stacked trace will be σ^2/n^N (McFadden et al., 1986). In the presence of a coherent signal, the noise reduction is not as dramatic, and as the signal-to-noise ratio increases, the noise reduction approaches that of a linear stack, σ^2/n, which is constant, regardless of the signal-to-noise ratio (McFadden et al., 1986). Hence,

an Nth root stack with $N > 1$ exhibits a dynamic noise reduction that usually results in improved noise suppression compared to the linear stack ($N = 1$). However, the non-linearity will introduce a signal distortion; in the presence of incoherent noise, those parts of a signal wavelet that have low amplitude are more likely to be attenuated relative to the higher amplitude parts of the wavelet. The net effect is a sharpening of the wavelets. This distortion of the signal means that the Nth root stack does not necessarily produce a better outcome than a linear stack. For example, if an infinite number of traces were available to be stacked (i.e. all with the same signal, but random noise added), then a linear stack would reproduce the signal exactly but an Nth root stack would produce a sharpened version of the signal. Increasing N increases the distortion but decreases the noise.

The refraction profiles shown in Figure 6.7 are the result of $N = 1$ stacking (i.e. linear stacking). Using the same data, again with a stack of $n = 7$ traces and a stacking velocity of 8 km/s, Figure 6.8 shows the result of stacking using $N = 4$ (Figure 6.8a) and $N = 8$ (Figure 6.8b). Compared to the linear stack, these stacks show a much greater contrast between those parts of the section that contain noise (e.g. before the first breaks) and those that contain signal. However, signal distortion has an evident effect; the traveltime curves tend to look less continuous for the non-linear stacks than the linear stack, because parts of the curve that have a relatively low signal-to-noise ratio tend to be suppressed relative to those parts of the curve that have higher signal-to-noise ratio. The general conclusion reached about Nth root stacking applied to the TASGO dataset is that it doesn't necessarily produce a better result than the linear stack; rather, its usefulness lies in giving a different perspective to the data with little added computational burden. As a result, all picking was carried out using $N = 1$, with values of $N > 1$ used mainly to help decide which phases to pick

6.5 Static Correction

The success of the stacking process depends largely on the level of coherency between adjacent traces. If the signal waveforms of a set of traces to be stacked are significantly out of phase, they may destructively interfere and produce a poor stack. In marine surveys, undulations in the sea floor can result in significant trace-to-trace time shifts since the velocity contrast between the water and underlying crust is large. A common

way of addressing this problem is to apply a static correction for variable water depth (e.g. Clement et al., 1994). Such corrections are approximate because different phases are affected differently by the sea floor undulations. The most accurate way of dealing with the problem is to include the water layer in the model for inversion, but using a static correction in the processing stage means that the model representation is simplified and stacking can be improved.

The static correction methods applied here use a common datum approach, in which traveltimes are adjusted by subtracting the traveltime in the water layer and adding the traveltime through an equivalent crustal layer, relative to a common datum, which in this case is sea level. If the incidence angle of the ray path in the water layer is small (i.e. the ray is near-vertical), then the corrected time, t_{sc}, is given approximately by:

$$t_{sc} = t_0 - h\left(\frac{1}{v_w} - \frac{1}{v_c}\right) \tag{6.5}$$

where t_0 is the uncorrected traveltime, h is the depth of the water beneath the source, v_w is the velocity of water (1.5 km/s), and v_c is the velocity of the crust beneath the water layer. The velocity v_c can be determined approximately from the gradient of the first refraction phase (usually around 5-6 km/s). If $v_c = 5.0$ km/s for example, the correction that needs to be subtracted from t_0 is 47 ms per 100 m of water traversed.

As the ray paths become less vertical beneath the sources, the accuracy of Equation 6.5 decreases and Snell's law may be used to compute a more accurate approximation. If it is assumed that the sea-floor is locally flat at the point intersected by the ray, that the subsurface is horizontally layered with no lateral velocity variations, and that rays become headwaves with refractor velocity v_n, then the correction is (see Appendix E):

$$t_{sc} = t_t - \frac{h}{v_n}\left[\frac{\sqrt{v_n^2 - v_w^2}}{v_w} - \frac{\sqrt{v_n^2 - v_c^2}}{v_c}\right] \tag{6.6}$$

where h is water depth at the ray-seafloor intersection point. The correction is most accurate for the refraction phase that turns in the layer with velocity v_n, which again can be estimated from the gradient of the appropriate traveltime curve. As $v_n \to \infty$, then Equation 6.6 becomes equivalent to Equation 6.5 for vertical rays.

Water depth was measured at each shot location in the TASGO survey (e.g. Figure 6.9). Since receivers are generally not collinear with the shot lines, these data may be used in a straightforward application of Equation 6.6 if it is assumed that depth variation

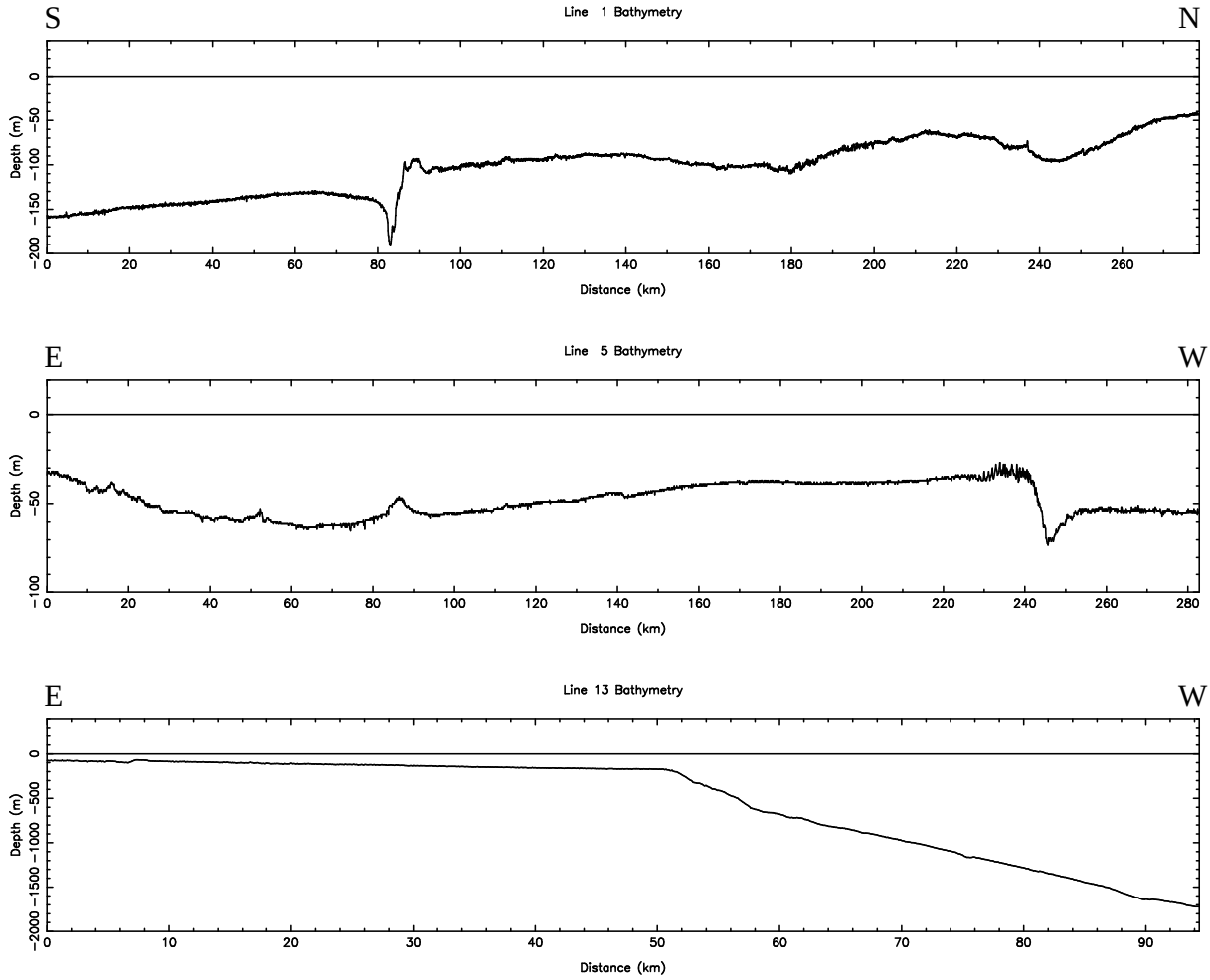

Figure 6.9: Bathymetry along three of the shot lines of the TASGO survey. (a) Line 1, (b) Line 5, (c) Line 13. Refer to Figure 5.8 for line locations.

perpendicular to the shot line is small. The depth of the sea floor doesn't exceed 200 m along most of the profiles (e.g. Figure 6.9) and the undulations in sea floor depth are generally quite smooth. The depths become large only near the oceanward ends of a few lines that traverse part of the continental slope (1.7 km in the case of line 13). The typical variation in depth over the range of nine shots (400 m) is generally not more than 5-10 m on the continental shelf, but may be as great as 40-50 m on the continental slopes.

The assumption of near vertical rays in the ocean beneath the sources is valid because a large positive contrast in velocity going from water to the uppermost crust means that the incidence angle of critically refracted rays is small. For example, if the uppermost crust has a velocity of 5 km/s, the critical angle is 17° and the difference in path length between the vertical ray and the critical ray is only 4.8 m per 100 m depth (if the seafloor is flat), which gives a difference in traveltime of only 3 ms per 100 m. For water 1.5 km

deep, the difference between the two approximations amounts to 72 m and 48 ms. The simple correction Equation 6.5 is therefore adequate in most cases, but because Equation 6.6 accounts for moveout of the ray path and is simple to calculate, it is applied here even though it assumes a horizontally stratified medium. As expected, applying the pre-stack static correction for water depth does not result in any perceptible improvement in the quality of the stacked data, though it produces a small downward shift in the traces where the water is relatively deep.

Purdy (1982) examines several different methods for correcting for the traveltime effects of seafloor topography, including a datum correction method and two water delay correction methods: water column and water path. Although expressed differently, the datum correction given by Purdy (1982) is in fact equivalent (see Appendix E) to Equation 6.6. Water delay methods relocate the shot to the sea floor. The water column method places the shot directly beneath its true position at a depth equal to the depth at which the ray path intersects the sea floor. The direction of the ray is obtained from the ray parameter. The water path method places the shot at the point where the ray intersects the sea floor, and thus requires a horizontal position correction in addition to the time and vertical correction. Purdy (1982) recommends using water path corrections when data is dense and datum corrections when data is sparse with large variations in seafloor topography. Water delay methods were not investigated with the TASGO dataset, even though the shots are closely spaced. Based on the results of the corrections to datum described above, no detectable improvement should be expected if the more accurate water delay methods are applied.

Apart from variations in water depth, other factors such as laterally heterogeneous near surface layers may cause trace-to-trace incoherency. In reflection seismology, automatic static correction (ASC) is usually employed to help align the signal portion of each trace before stacking. ASC uses the cross-correlation function to achieve optimum alignment. The cross-correlation of two traces $\{x_i\}$ and $\{y_i\}$ where $i = 1, \ldots, m$ is defined by:

$$\phi_{xy}(\tau) = \sum_{k=0}^{m-1} x_k y_{k+\tau} \tag{6.7}$$

for $1 - m \leq \tau \leq m - 1$. Thus, the cross-correlation is a measure of the similarity of two traces; one trace is displaced relative to the other, and corresponding values are multiplied and then summed to give the value of the cross-correlation for a particular time shift τ. If n traces of length m are to be stacked, then cross-correlation of the central trace with each

of the other traces will give the time shift Δt_i $(i = 1, \ldots, n)$ that needs to be applied to each trace to give optimum alignment with the central trace (i.e. the time shift for which the cross-correlation is maximised). Stacking may then produce a trace with better signal-to noise ratio than a stack performed without ASC. Here, the autocorrelation function is calculated in the frequency domain (see Press et al., 1992).

In designing an ASC process, two other considerations are important. First, it is possible for the cross-correlation to produce a local maximum when the signals in adjacent traces are displaced by $i\delta t_p$, where i is an integer and δt_p is dominant period of the signal. The dominant frequency in much of the TASGO data is around 7 Hz, which corresponds to a period of about 140 ms. This suggests that it would be sensible to only permit time adjustments less than about 70 ms, or ± 4 sample intervals (each of 16 ms). Second, there is no point in cross-correlating parts of either trace that only contain noise. Specifying a correlation window that only spans regions of signal will result in a more robust ASC. Also, since the central trace to which adjacent traces are time shifted may itself be late or early, it is corrected by an amount equal to the average time shift of the adjacent traces after stacking. Figure 6.10 shows the result of applying ASC to data from line 1 collected at station 17 with a correlation window width of about 1 s spanning the obvious first-arrivals. Essentially, the results appear to be no better than those of Figure 6.7b which, apart from the ASC, is processed in the same way. In fact, there are several regions (e.g. around shot 3300), where the ASC has resulted in poorer stack quality.

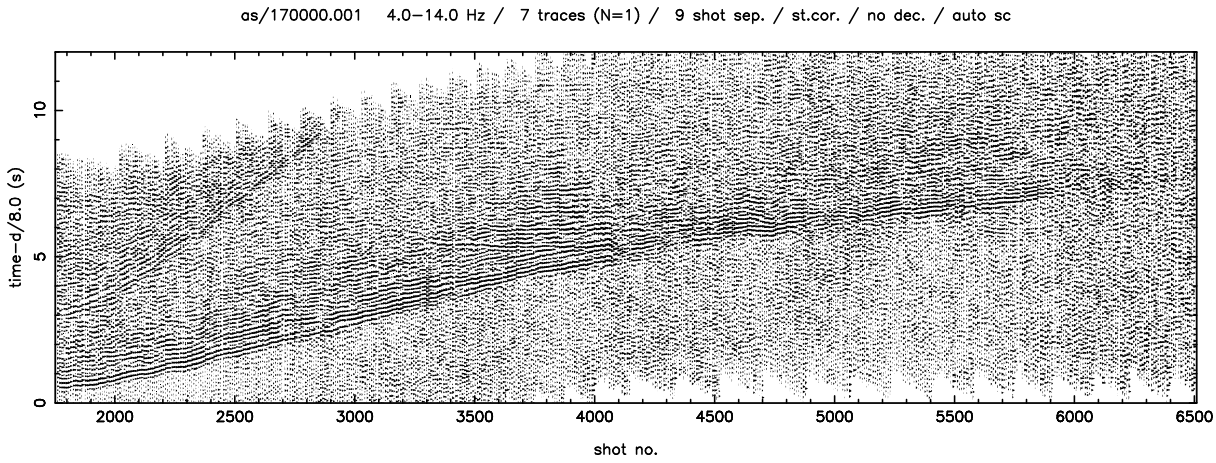

Figure 6.10: Automatic static corrections applied to data collected at station 17 from line 1. Other processing steps as for Figure 6.7b.

When ASC is applied to reflection data (e.g. Hileman et al., 1968; Disher & Naquin,

1970), improvements in arrival time coherency generally occur. Two factors contribute to making ASC a more robust method in normal incidence reflection processing compared to wide-angle processing. First, ASC is more successful if signal waveforms from adjacent traces are similar. Laterally continuous sedimentary beds (e.g. Hileman et al., 1968) will produce reflection sections that conform to this condition. However, even for horizontal beds, the signal wavetrain in a refraction section will vary from trace-to-trace. Second, the multiple-fold shooting geometries encountered in reflection seismic surveys have an inherent redundancy associated with the common midpoint design which is unlikely to be matched in a refraction survey. Application of ASC to the TASGO wide-angle dataset did not result in noticeable improvements, perhaps for the reasons given above. It is worth noting, however, that Zelt et al. (1987) developed a picking method for refraction data that was based on trace cross-correlation, including a Monte Carlo technique to avoid cycle skipping and spectral balancing to boost semblance. It is possible that the application of these techniques here may have resulted in a more successful ASC, but equally it might be inferred from the results of Figures 6.7b and 6.10 that static errors are of negligible magnitude in the TASGO dataset.

6.6 Deconvolution

The ideal seismic refraction profile will only show the impulse response of the earth (i.e. at each station only a single pulse would be observed for each phase type). In reality, this doesn't occur because, apart from random noise, (i) the source wavelet is not a single spike, (ii) in marine surveys, multiple arrivals can result from reflections at the top and bottom of the water layer (reverberation), and (iii) shingling often occurs (Sheriff & Geldart, 1995). Shingling is usually characterised by a series of parallel alignments on the section that follow the onset of head wave arrivals. The effect is due to the lengthening of the refraction wavetrain caused by several different phenomena, including reflection of head waves from parallel reflectors above the refractor, repeated reflections within the refractor and a velocity gradient below the refractor that can lead to multiple reflections of the turning rays. Refraction profiles influenced by one or more of these problems often have their later arrivals obscured by the unwanted portions of the wavetrain from earlier phases. As a result, it can be difficult to accurately identify the onset times of reflection phases.

If the recorded trace is denoted by the time series z_t, the earth's impulse response by e_t and the waveform caused by the combined effects of shingling, marine reverberations and the source wavelet by f_t, then:

$$z_t = e_t * f_t \tag{6.8}$$

where $*$ is the convolution operator. If f_t is known, then *deconvolution* can be used to extract e_t. Deconvolution is most efficiently performed in the frequency domain since convolution in the time domain is equivalent to point-wise multiplication in the frequency domain. The Fourier transform of z_t is divided by the transform of f_t in order to obtain an estimate of the transform of e_t, which is then inverse transformed to get e_t. The main difficulty with deconvolution is to accurately estimate f_t.

A simple estimate of f_t is obtained from an undeconvolved trace in which the first-arriving headwave is clearly identified. The estimate of f_t includes the wavetrain from the headwave until the onset of the next phase (if it can be identified) or until it becomes lost in the noise. Here, this method is referred to as wave-specified deconvolution. Figure 6.11 shows a refraction profile deconvolved in this way. Some of the ringing effects have been removed, although the clarity of later arrivals has not necessarily been improved.

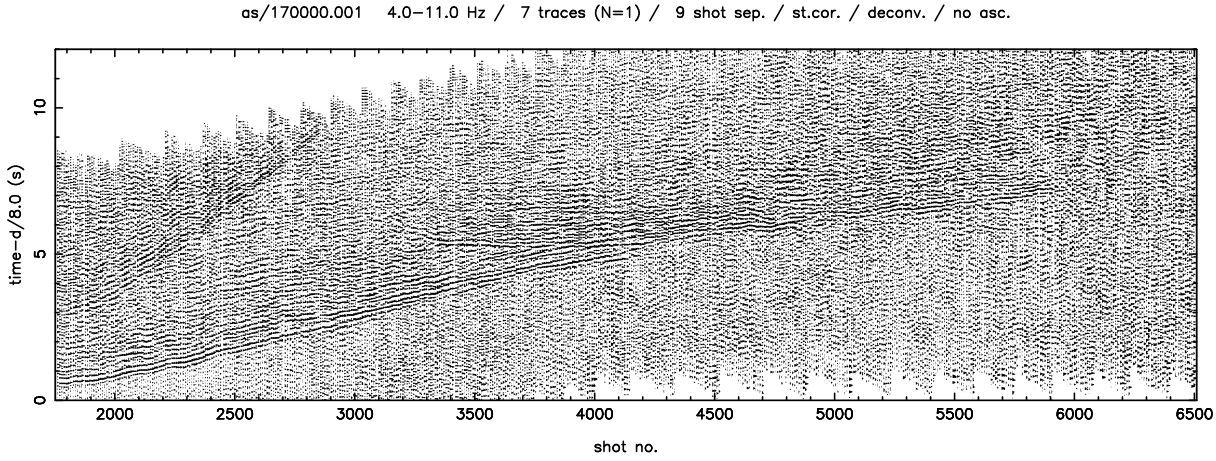

Figure 6.11: Data recorded at station 17 from line 1 with wave-specified deconvolution applied. The waveform used in the deconvolution was obtained from a 350 ms record following the first break at about shot number 2000. Other processing steps as for Figure 6.7b.

Predictive deconvolution (Robinson & Treitel, 1980) is another method for removing reverberation and other effects that can mask later arrivals. The two basic assumptions used in predictive deconvolution theory are: (i) reverberation spike train and source pulse

are minimum delay, and (ii) the earth's impulse response is random and uncorrelated. A minimum delay wavelet has most of its energy concentrated near the beginning. If, for example, reverberations are caused by a water layer acting as a wave guide, then the assumption of minimum delay is justified because the reflection coefficient of the the sea floor will be less than 1. If c is the reflection coefficient of the sea floor (the reflection coefficient of water-air interface is 1), then the z-transform (Robinson & Treitel, 1980) of the reverberation is:

$$C(z) = 1 - cz^n + c^2z^{2n} - c^3z^{3n} + \ldots = \frac{1}{1 + cz^n} \tag{6.9}$$

which shows that energy decreases along the wavelet. The inverse filter can be written as $A(z) = 1 + cz^n$ so that $A(z)C(z) = 1$. The operator $A(z)$ deconvolves the reverberation spike train $C(z)$ to the unit spike at zero delay requiring only the water depth and the reflection coefficient c. In reality, the nature of the reverberations is more complicated, which is why predictive deconvolution based on the recorded data can be more effective.

Predictive deconvolution is a special case of optimum Wiener filtering, which minimises, in the least-squares sense, the difference between the actual and desired output. Consider the simple case of a known input wavelet (x_0, x_1), a desired output (y_0, y_1, y_2) and an inverse filter (a_0, a_1). Convolution of the inverse filter and the input wavelet yields $(a_0x_0, a_1x_0 + a_0x_1, a_1x_1)$. Defining the error E as the sum of the squares of the differences between the actual and desired amplitudes:

$$E = (a_0x_0 - y_0)^2 + (a_1x_0 + a_0x_1 - y_1)^2 + (a_1x_1 - y_2)^2 \tag{6.10}$$

the unknown operator (a_0, a_1) is determined by minimising E. Setting $\partial E/\partial a_0$ and $\partial E/\partial a_1$ to zero gives two equations for the two unknowns:

$$\begin{bmatrix} {x_0}^2 + {x_1}^2 & x_0x_1 \\ x_0x_1 & {x_0}^2 + {x_1}^2 \end{bmatrix} \begin{bmatrix} a_0 \\ a_1 \end{bmatrix} = \begin{bmatrix} x_0y_0 + x_1y_1 \\ x_0y_1 + x_1y_2 \end{bmatrix} \tag{6.11}$$

If r_i represents the autocorrelation of the input wavelet at lag i, then it is evident that the elements of the matrix are simply the entries of the autocorrelation series $r_0 = {x_0}^2 + {x_1}^2$ and $r_1 = x_0x_1$. If the earth's impulse response is truly random, then the autocorrelation of the input wavelet will be identical to the autocorrelation of the recorded seismic trace, which is a convolution of the input wavelet and the earth's impulse response. Thus, the matrix on the LHS of Equation 6.11 can be estimated from the recorded seismic trace.

If the desired output is a time-advanced form of the input wavelet, then the RHS of Equation 6.11 can also be evaluated. For example, if the prediction lag is $\alpha = 1$, where α represents the lag of the input wavelet, then $y_0 = x_1$, $y_1 = 0$ and $y_2 = 0$ and the RHS entries are $x_0y_0 + x_1y_1 = r_1$ and $x_0y_1 + x_1y_2 = 0$. This suggests the general form for Equation 6.11 with a prediction filter of length n and a time lag of length α:

$$\begin{bmatrix} r_0 & r_1 & r_2 & \cdots & r_{n-1} \\ r_1 & r_0 & r_1 & \cdots & r_{n-2} \\ r_2 & r_1 & r_0 & \cdots & r_{n-3} \\ \cdot & \cdot & \cdot & \cdots & \cdot \\ \cdot & \cdot & \cdot & \cdots & \cdot \\ r_{n-1} & r_{n-2} & r_{n-3} & \cdots & r_0 \end{bmatrix} \begin{bmatrix} a_0 \\ a_1 \\ a_2 \\ \cdot \\ \cdot \\ a_{n-1} \end{bmatrix} = \begin{bmatrix} r_\alpha \\ r_{\alpha+1} \\ r_{\alpha+2} \\ \cdot \\ \cdot \\ r_{\alpha+n-1} \end{bmatrix} \tag{6.12}$$

When the desired output is a time-advanced form of the input wavelet ($\alpha > 1$), then the filtering is referred to as predictive deconvolution. Equation 6.12 exhibits a Toeplitz structure and can be solved efficiently by using the method of Levinson (see Robinson & Treitel, 1980) to obtain the prediction operator coefficients $\{a_i\}$, which can be used to construct the prediction error operator:

$$g_t = [1, 0, 0, \ldots, 0, -a_0, -a_1, \ldots, -a_{n-1}] \tag{6.13}$$

where the number of zeros is equal to $\alpha - 1$. The operator g_t can then be convolved with the recorded trace to yield a trace from which reverberations have been removed. In this application, g_t is calculated separately for each trace.

For the case of $\alpha = 1$, it can be shown (e.g. Özdoğan, 1987) that predictive deconvolution is equivalent to spiking deconvolution, where the desired output is a zero-lag spike. To implement predictive deconvolution, the value of several parameters need to be set. These include the length of the prediction filter n, the prediction lag α and the percentage of pre-whitening. Pre-whitening is the addition of white noise to ensure numerical stability in solving the inverse problem (Equation 6.12). Numerical instability can arise if the amplitude spectrum of the input wavelet contains regions that are near zero, because the amplitude spectrum of the prediction operator is approximately equal to the inverse of the amplitude spectrum of the input wavelet (Özdoğan, 1987). Pre-whitening can be accomplished by simply adding a small constant ϵ to the coefficient of the zero lag of the autocorrelation function (i.e. $(1 + \epsilon)r_0$) wherever it appears in the matrix of Equation

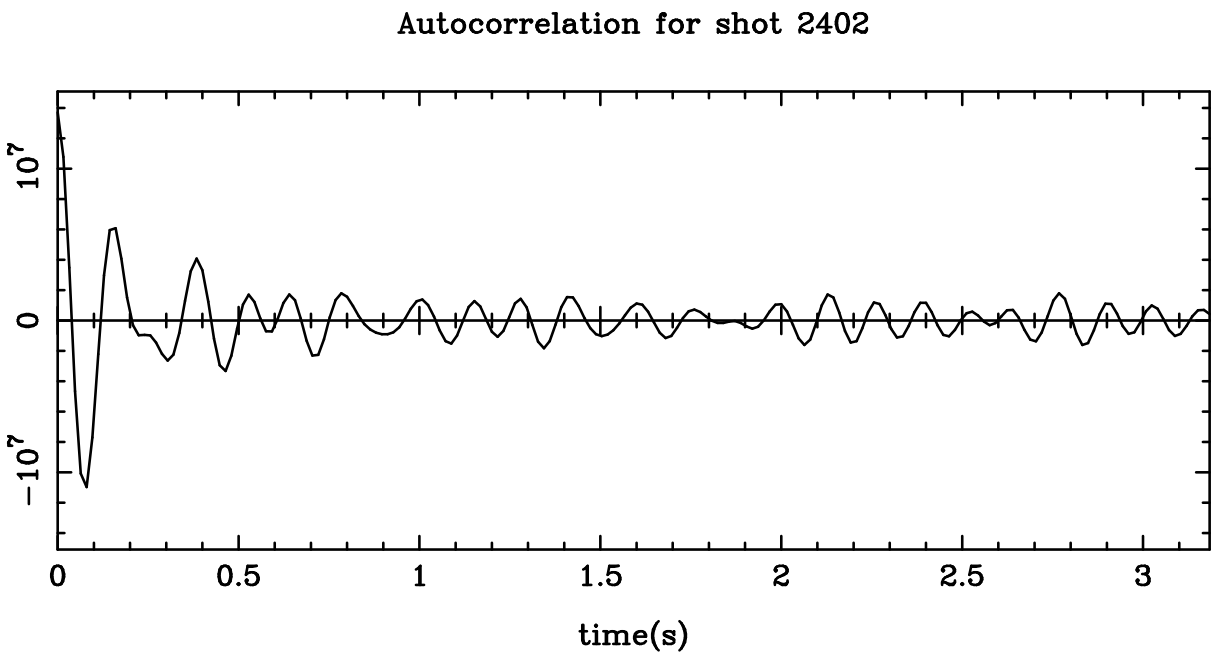

Figure 6.12: Autocorrelation function for shot 2402 from line 1 recorded at station 17. The function decreases in amplitude to "noise" level after about 0.6 s. Hence, the operator length n is chosen to be 38 (16 ms sampling interval).

6.12. A pre-whitening level of 0.5% is used here. The choice of operator length n is generally based on the length of the input wavelet autocorrelation function (Özdoğan, 1987). If the assumption of a random impulse response of the earth filter holds, then the autocorrelation of the input wavelet is approximated by that of the seismic trace. Figure 6.12 shows the autocorrelation function for shot 2402 from line 1 recorded at station 17. The autocorrelation function drops to the background level at about 0.6 s, so an operator length of $n = 38$ is chosen.

Increasing the value of the prediction lag α causes the output from predictive deconvolution to become less spiky, since the output wavelet will be α samples long. Using $\alpha = 1$, which results in spiking deconvolution, can have undesirable effects; in particular, it boosts high-frequency noise (Özdoğan, 1987). In fact, the bandwidth of the output can be controlled to some extent by adjusting the prediction lag. Robinson & Treitel (1980) recommend using, on the basis of empirical studies, a value of α that corresponds to the second zero crossing of the autocorrelation function to suppress short-period reverberations. The autocorrelation of a seismic trace contaminated by short-period reverberations has a distinct waveform near the beginning that gradually dies out, while long period reverberations are characterised by distinct waveforms separated by quiet zones. Inspection

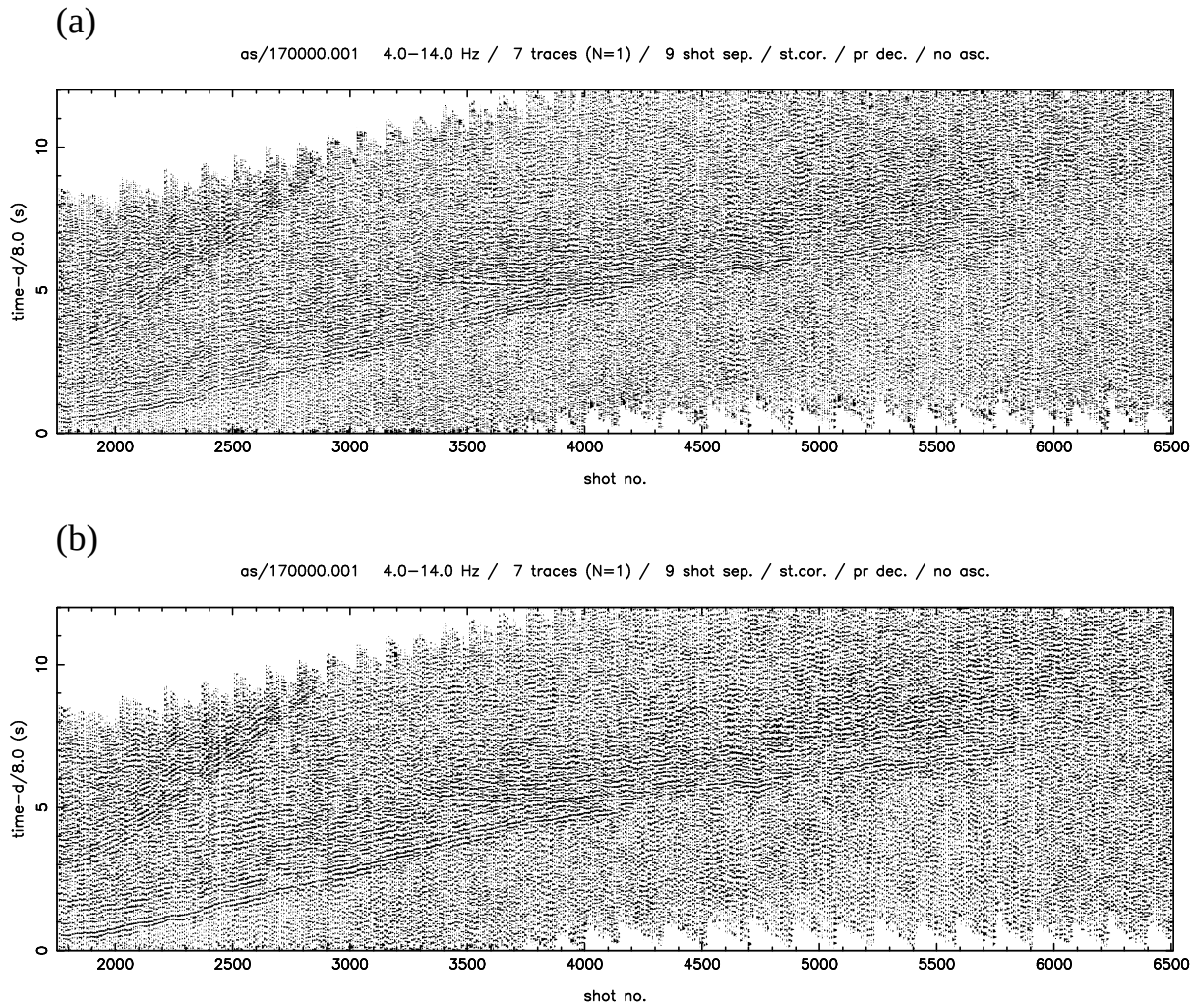

Figure 6.13: Data recorded at station 17 from line 1 with deconvolution applied using n=38 and 0.5% pre-whitening. Other processing steps as for Figure 6.7. (a) Spiking deconvolution ($\alpha = 1$), (b) Predictive deconvolution with a prediction lag equal to the second crossing of the autocorrelation function.

of the autocorrelation function (Figure 6.12) suggests that the former case is more typical of TASGO data. This is to be expected because the water layer below the shot lines is generally quite shallow. Long period reverberations, usually referred to as multiples in reflection seismic sections, can be suppressed by using a suitably large value of n, although to avoid suppression of genuine reflections, it may be better to use a dual approach where predictive deconvolution is used to suppress the multiple (using an α value that is greater than the length of the first part of the autocorrelogram that represents the input wavelet) followed by spiking deconvolution ($\alpha = 1$) to compress the wavelet to a spike (Özdoğan, 1987).

Figure 6.13a shows the result of using spiking deconvolution on data recorded at station

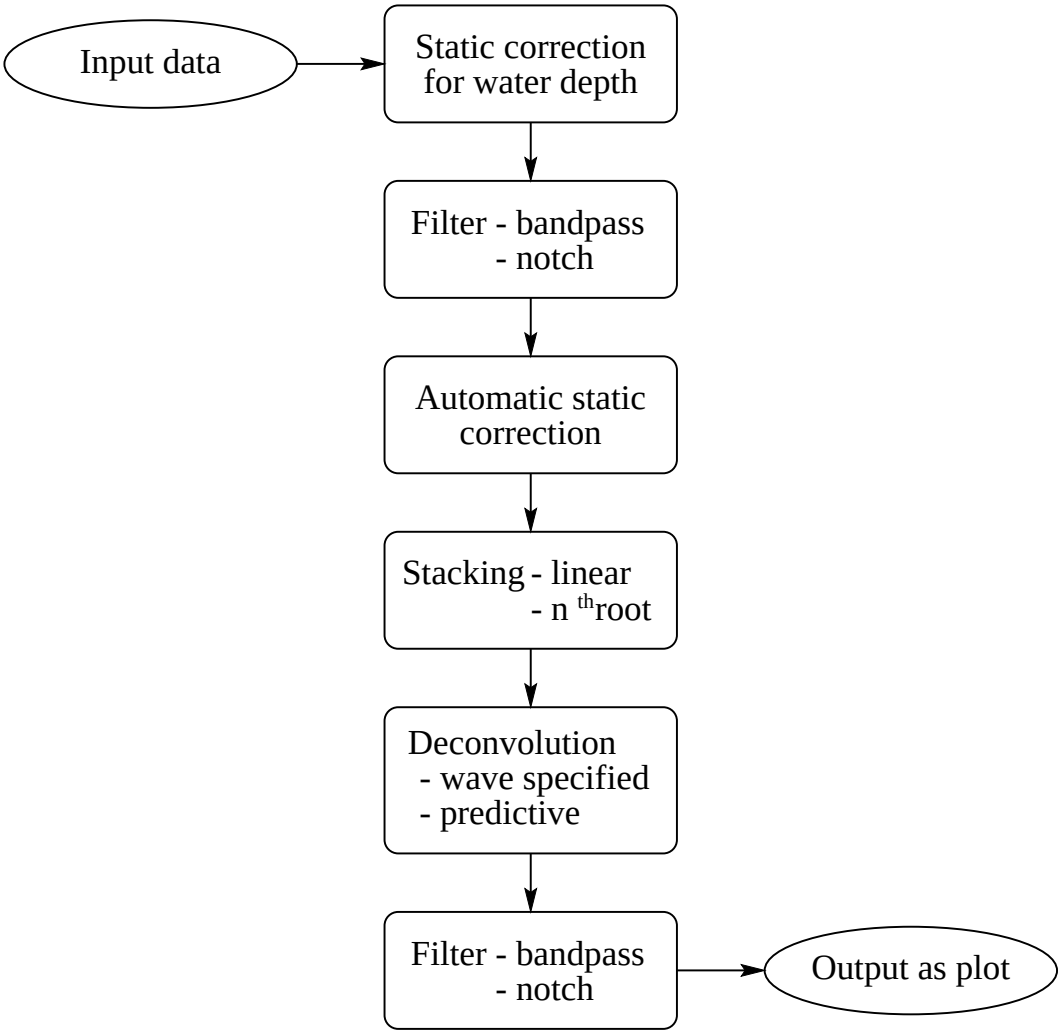

Figure 6.14: Data processing flow chart. Bandpass filtering and stacking were applied to all data that was picked. The other processing steps were not always used. Filtering may be performed before and/or after ASC, stacking and deconvolution.

17 from line 1, while Figure 6.13b shows the same data with predictive deconvolution using a prediction lag equivalent to the second crossing of the autocorrelation function. In both examples, some of the reverberation effect is removed, although the predictive case (Figure 6.13b) seems to produce a less noisy result. In addition, the Moho reflection (P_mP) traveltime curve is easier to identify on both plots, although there appears to be some trade-off in signal-to-noise ratio. Predictive deconvolution (and to a lesser extent wave-specified deconvolution) was mainly used to help discriminate between coherent later arrivals. These arrivals tended to be more prolific in the undeconvolved sections, but once particular phases were identified (e.g. as P_1P, P_mP etc.) with the help of deconvolution, they tended to be easier to pick from the undeconvolved data.

The flowchart of Figure 6.14 shows the possible steps involved in processing the data to produce a refraction section from which the data were picked. Note that band-pass filtering, stacking and static correction for water depth were always used, while the remaining processing steps only proved useful for some of the data.

6.7 Picking of TASGO Data

In forward modelling, it is not always necessary to make actual data picks because synthetic traveltimes can be superimposed on the data profiles, and a direct visual assessment can be made by the user as to whether the "fit" is acceptable (e.g. Recq et al., 1998; Stadtlander et al., 1999). However, robust picking of arrival times is essential for any traveltime inversion algorithm, since these picks are used directly to constrain model structure. The approach used to pick data can depend on the clarity of the wavefield and the types of phases that may be utilised by the inversion method. For example, if the inversion method is designed to invert first-arrivals only, then the task of picking these arrivals is generally straight-forward, as they are represented by the first-motion of the signal wavetrain. However, if later arrivals can also be used, then the task of picking may become more problematic, as these phases are often contaminated by waveforms associated with earlier arrivals. In such situations, it may be useful to develop a preliminary model using only the first arrivals, determine the synthetic traveltimes associated with this model, and then compare these directly with the observed data to see whether the later-arriving synthetic traveltimes correspond approximately with any coherent phases evident in the data (Zelt, 1999).

Phases associated with reflections from a particular interface or refractions that turn in a particular layer are represented by relatively continuous traveltime curves on a refraction section. The identification of these phases in terms of where they turn in the subsurface (e.g. P_1, P_2, P_n for refractions, P_1P, P_mP for reflections) may or may not be possible from examination of the data alone. If the subsurface is layered with significant velocity contrasts across the interfaces, then refraction arrivals will usually exhibit noticeable discontinuities in gradient at cross-over points (i.e. where the traveltime curve from one headwave intersects the headwave from an adjacent interface). These changes in gradient permit subsurface layering to be defined approximately, with subsequent association of refraction arrivals and layers. Reflection arrivals can also be used to help determine the

subsurface layering. Reflections from a particular interface are linked to the refractions from the layer directly beneath because they essentially share a path (and traveltime) at the critical incidence angle.

Zelt (1999) advocates that the first-arrival refraction phases be grouped in a single traveltime curve, and that individual picks be associated with layers of the current model estimate based on the minimisation of source-receiver traveltime. In regions where the velocity variation is relatively continuous with depth, this approach makes sense because a layer-type subdivision based on the traveltime curve would be arbitrary if the cross-over points cannot be identified. Without *a priori* information on the layering of the subsurface, a non-layered model may be preferable in this case unless reflection phases can be identified. If it is possible to associate phases with layers, however, then it is better to incorporate this information in the inversion, because it provides additional constraints on the solution. This latter approach also permits refraction phases to be used even if they are not first-arrivals.

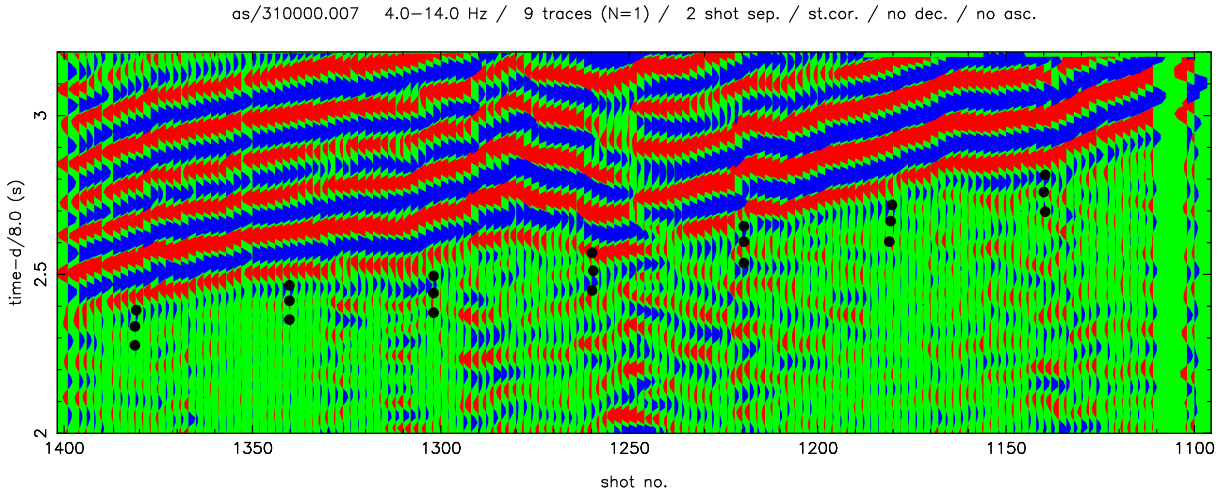

Figure 6.15: Several picks of the P_1 phase recorded at station 31 from line 7 shots. Each cluster of three dots represents the picked arrival time (central dot) and the associated error estimate (half the difference between the upper and lower dot).

When arrival times are picked, it is also necessary to estimate the uncertainty associated with the pick. This is often done through inspection (Zelt, 1999) and considering the frequency content of the signal and the signal-to-noise ratio. First-arrivals will generally be more accurately picked than later arrivals, since they are not overprinted by earlier phases. The clarity and wavelength of arrivals usually decreases with offset, so distant

arrivals will often have a larger pick uncertainty than near-offset arrivals. The size of the traveltime uncertainty is significant in two ways. First, the uncertainties are used in the diagonal elements of the data covariance matrix to weight the relative importance of traveltimes; a traveltime with a large error will have less influence on the objective function than a traveltime with a small error (see Equation 4.15). Second, a model estimate satisfies the data in an absolute sense if the χ^2 misfit function (Equation 4.20), which incorporates the uncertainties in a similar way, is reduced to a value of 1 or below.

The TASGO wide-angle seismic data are picked interactively using the processing and display software described earlier in this chapter. A zoom capability allows picking to be carried out with high precision and trace colouring may be implemented to aid phase identification. The data are picked using a mouse; for each best estimate pick (t_p) of a phase from a particular trace, an estimate of the earliest (t_e) and latest (t_l) possible arrival time of the phase is made. The uncertainty estimate associated with t_p is then defined as half the difference between the latest and earliest pick (i.e. $(t_l - t_e)/2$). The frequency of the signal waveform is generally around 5-8 Hz for much of the TASGO data. Half a cycle therefore has a period of around 60-100 ms. Generally, first-arrivals were picked with a half-cycle error estimate while later arrivals had full-cycle error estimates, with adjustments depending on the amount of noise present and the degree to which later arrivals are obscured by the wavetrains of earlier phases. Figure 6.15 shows a close-up of several picks. The RMS picking error of all the TASGO data used in subsequent interpretation is 134 ms. Where possible, picks are made every 2km (40 shots) along shot lines.

Generally, it was possible to discriminate between the different refraction phases in the TASGO data and associate each refraction pick with a ray that turns within a particular layer. Similarly, each reflection pick is associated with a ray that reflects off a particular interface. Below, four picked refraction sections which are broadly representative of the TASGO data are illustrated and discussed.

Figure 6.16 shows data from line 5 recorded at station 10 both with and without picks superimposed. Note that for clarity, each picked phase is represented by an interpolated traveltime curve and uncertainties are not indicated. The four refraction phases (P, P_1, P_2 and P_n) and three reflection phases (P_1P, P_2P and P_mP) suggest a three-layered crust. The P_n phase is of relatively low amplitude and only just stands out from the noise. Weak P_n phases are characteristic of the TASGO dataset, possible due to a low vertical velocity

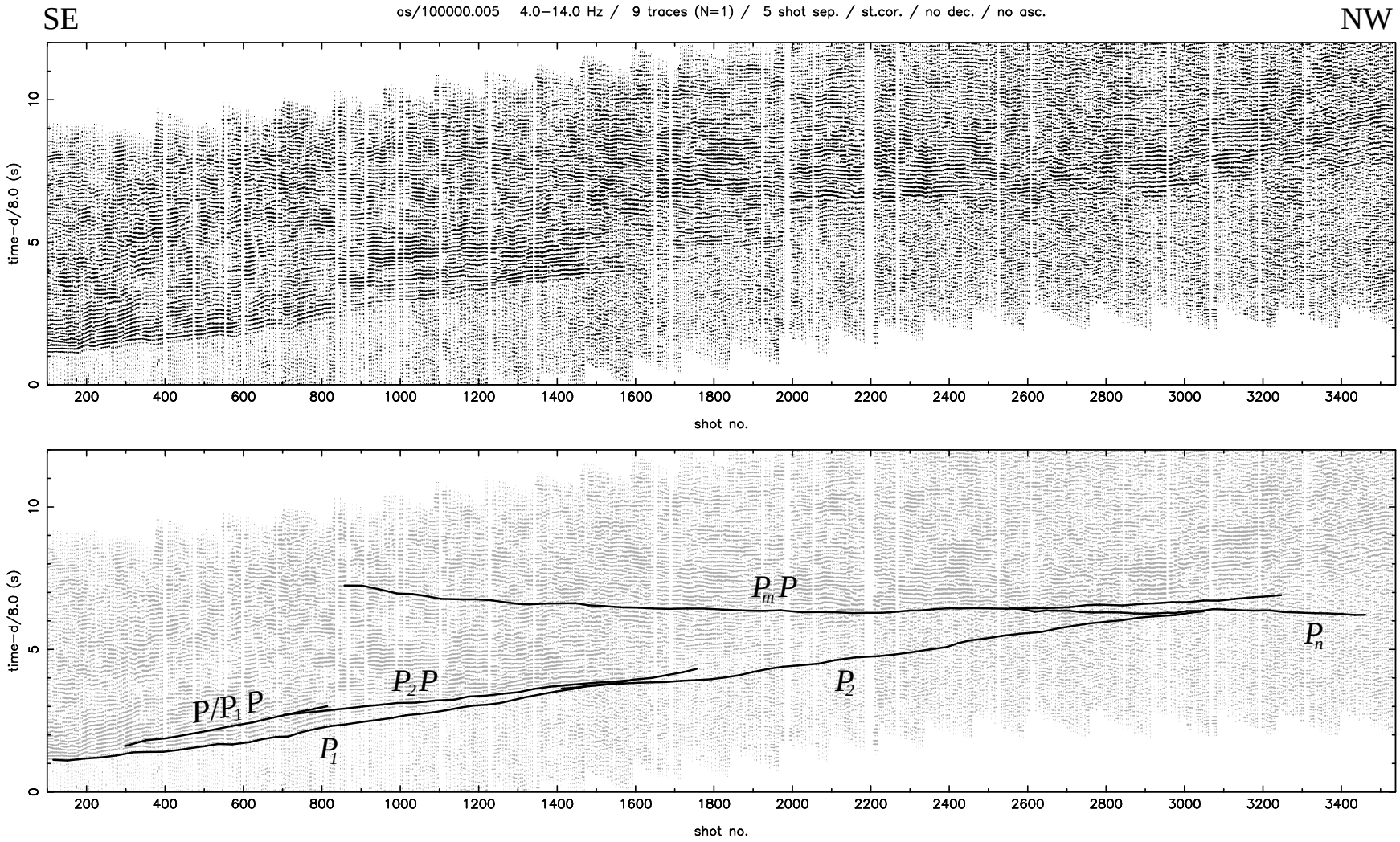

Figure 6.16: Picks for data recorded at station 10 from line 5 shots (see Figure 5.8 for station and line locations). Four refraction phases (P, P_1, P_2, P_n) and three reflection phases (P_1P, P_2P and P_mP) are identified, although the P and P_1P phases are picked as coincident. Shot separation is nominally 50 m so 200 shots will traverse a distance of about 10 km.

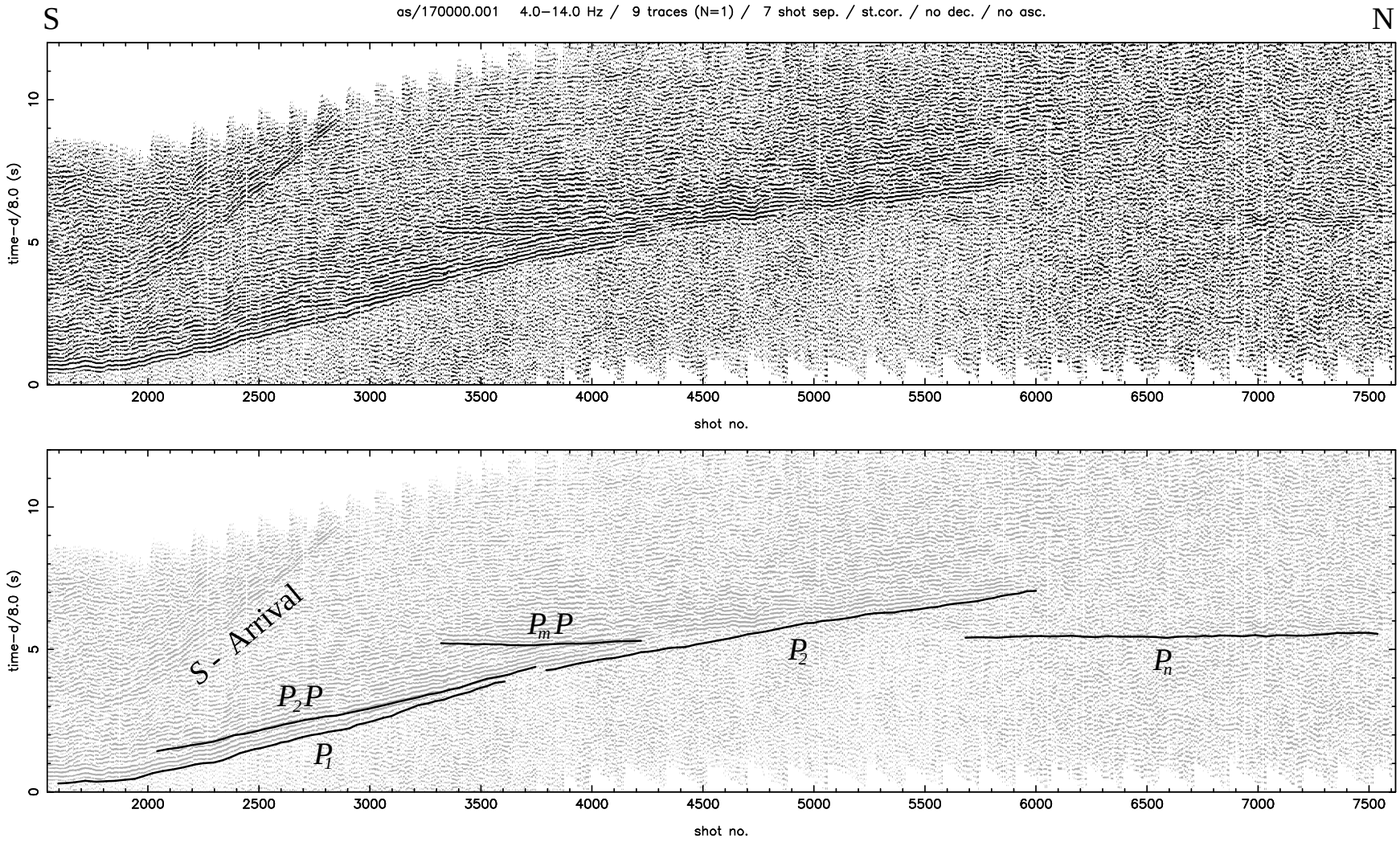

Figure 6.17: Picks for data recorded at station 17 from line 1 shots (see Figure 5.8 for station and line locations). Three refraction phases (P_1, P_2, P_n) and two reflection phases (P_2P and P_mP) are evident in the record. An S-wave arrival is also visible in the data. Shot separation is nominally 50 m so 200 shots will traverse a distance of about 10 km.

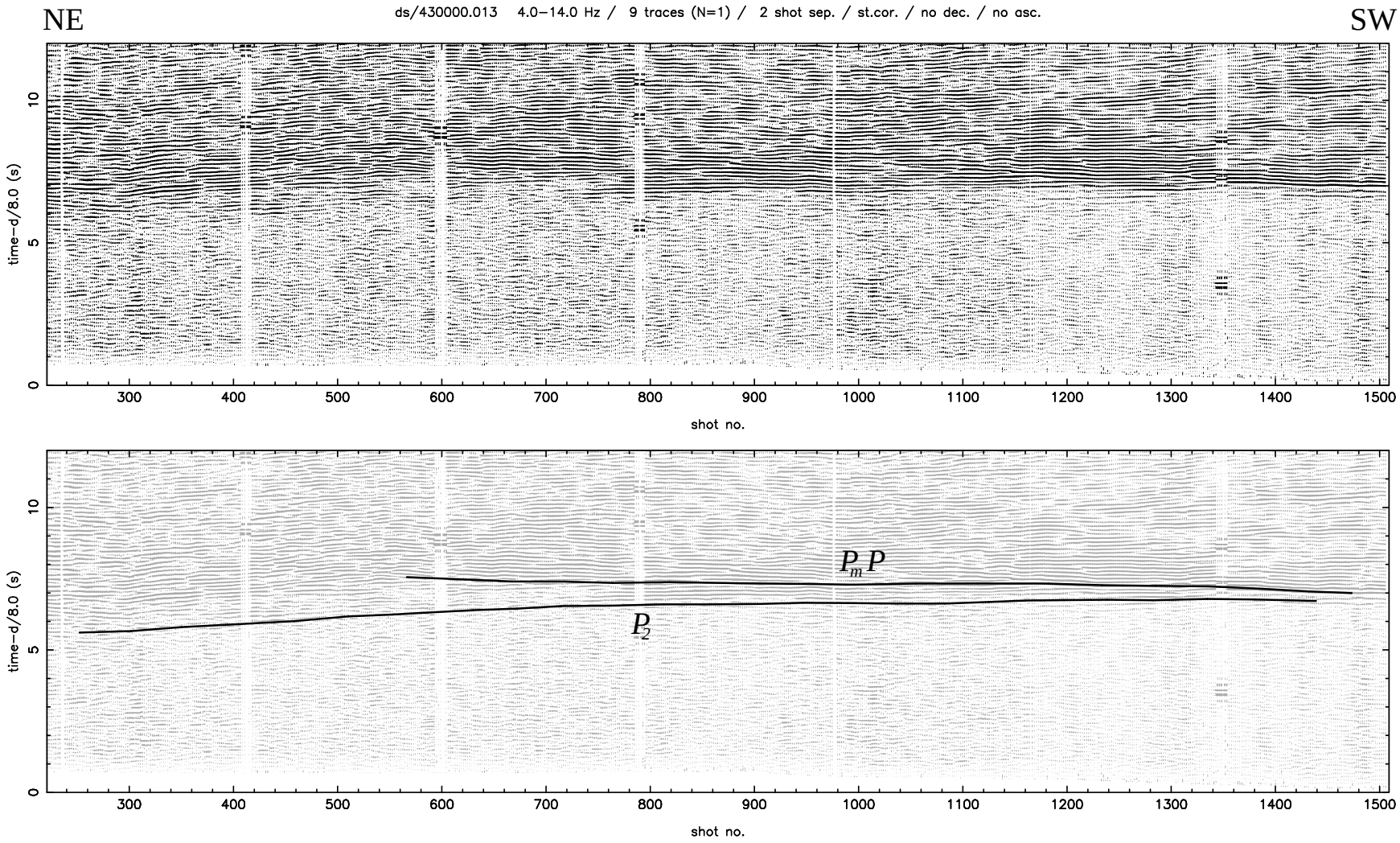

Figure 6.18: Picks for data recorded at station 43 from line 13 shots (see Figure 5.8 for station and line locations). One refraction phase (P_2) and one reflection phase ($P_m P$) is evident in the data. The station is broadside to the shot line in this case. Shot separation is nominally 50 m so 200 shots will traverse a distance of about 10 km.

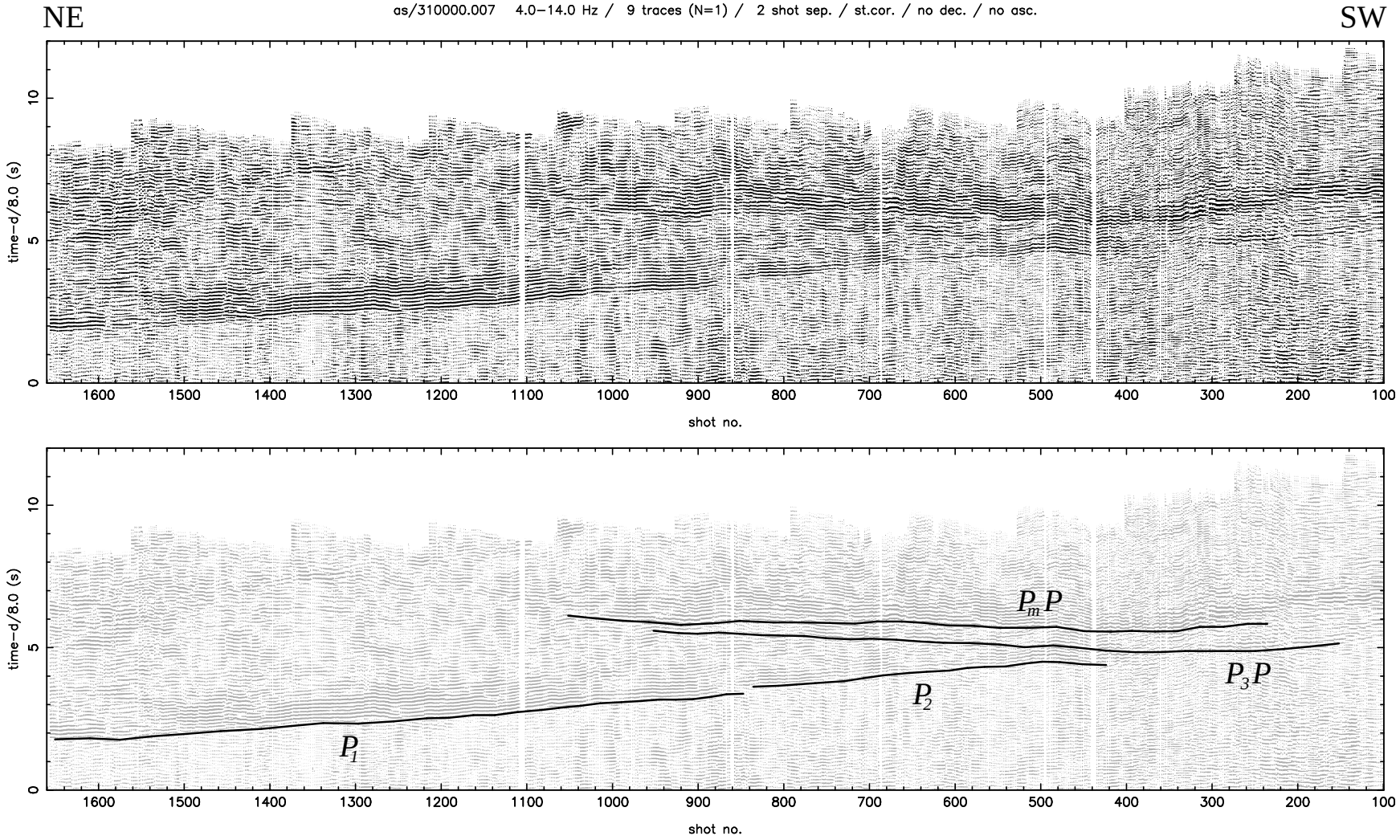

Figure 6.19: Picks for data recorded at station 31 from line 7 shots (see Figure 5.8 for station and line locations). Two refraction phases (P_1, P_2) and two reflection phases (P_3P and P_mP) are evident in the data. The P_3P phase corresponds to a lower crustal reflector that merges with the Moho towards the SE. Shot separation is nominally 50 m so 200 shots will traverse a distance of about 10 km.

gradient in the mantle beneath the Moho, and are not always detectable. The P_mP phase stands out clearly from the noise, however, and is picked over a broad offset range even though it is not a first arrival. These strong Moho reflections are also characteristic of the TASGO data and suggest a significant velocity contrast across the Moho. The direct P phase occurs only as a later arrival since station 10 lies some distance (about 17 km) from the start of line 5 (Figure 5.8). At this offset, the P_1P phase should be nearly coincident with the direct P phase, and it does not seem possible to separate the two phases.

Picks from line 1 shots recorded at station 17 in SE Tasmania are shown in Figure 6.17. In addition to P phases, a later arriving S phase is also clearly evident in the data. However, S-waves are not considered in the inversion of TASGO data. The P_1 and P_2 refraction phases stand out clearly from the noise and can be picked with a high degree of accuracy (<100 ms). The P_n phase is visible to large offset (257 km from station 17) and can be picked for almost 100 km along the shot line. One of the most distinctive features of this refraction section is the clarity of the P_mP phase. It has a relatively short wavetrain and clearly cross-cuts other later arrivals, although it becomes overprinted as it approaches the first-arriving P_2 phase. This feature is consistent with a Moho defined by a large velocity discontinuity. Unlike Figure 6.16, the arrivals picked here suggest a two-layer crust, with no shallow layer. Note, however, that the labelling of phases is consistent with a three-layer crust since subsequent data interpretation indicates that the Tasmanian crust can be described by an upper crust and a lower crust, with an overriding sediment layer that is not present everywhere.

The previous two picked sections (Figures 6.16 and 6.17) are for recorders that are nearly collinear with shot lines. In these examples, it is relatively easy to pick the different phases as traveltime varies principally with offset. When a shot line has a significant broadside component to a receiver, it may be more difficult to discriminate between the different phases. Figure 6.18 shows data (and traveltime picks) recorded at station 43 from line 13 shots. The shot-receiver offset along this 69 km line only varies by 11 km and initial inspection of the unpicked data reveals that the separation of phases observed in Figure 6.16 and Figure 6.17 is much less obvious in this case. In these situations, the synthetic traveltimes generated from a preliminary model can be useful in helping to identify phases. In this case, the P_2 and P_mP phases were picked and then compared to the traveltimes of a 1-D model estimate of Tasmania determined from several nearly in-line profiles. The picked phases are close to the predicted arrivals from the 1-D model

estimate, confirming the identification.

The final example (Figure 6.19) from NW Tasmania shows data recorded at station 31 from line 7 shots. In addition to identifying a P_1, P_2 and P_mP phase, a relatively weak P_3P phase is also identified. This P_3P reflection phase is also evident for the station/line combinations 31/6, 7/5, 7/6 and 7/8, but not for the combinations 10/5, 31/5 or 31/9 (see Figure 5.8 for location). This observation suggests the presence of an additional crustal layer above the mantle between Three-Hummock Island and King Island that pinches out towards the SE. This pinched-out layer can also be identified at the NW end of the normal-incidence reflection section for line 5 (Barton, 1999b). Of all the TASGO wide-angle data that has been picked, this is the only clear evidence of a major lateral variation in crustal structure.

Chapter 7

Inversion of TASGO Data

7.1 Introduction

In this chapter, both refraction and reflection traveltimes picked from the TASGO wide-angle dataset are inverted for layered crustal structure. To obtain a preliminary picture of Tasmania's subsurface structure, I first describe 1-D inversions of data from single receiver/shot line combinations. These inversions were done preferentially for receiver/shot line combinations with a significant offset range between the receiver and the shots and with phases that are relatively easy to identify. As well as providing preliminary results, these 1-D models were also used to construct initial models for inversions that permitted lateral variations in structure.

Following the description of the 1-D inversions, a 2-D inversion is described using data from line 5 collected at stations 7, 10 and 31 (Figure 5.8). This part of the array is unique in having several receivers lying approximately in-line and suitably distributed along the shot line so as to result in a relatively well constrained solution. Furthermore, the predominant surface structure in the region (Green, 1998) is aligned approximately perpendicular to line 5. The 2-D inversion provides insight into the crustal structure along the western part of the north coast of Tasmania and also provides a useful reference for comparison with subsequent 3-D inversion results.

Following the description of the 2-D inversion of line 5 data, the results of the 3-D reconstructions are presented. The inversion for 3-D structure has been divided into two parts. First, data from NW Tasmania are inverted to provide a detailed four-layer crustal model of that region. Most of the usable data recorded by the TASGO wide-angle survey

was from NW Tasmania, so a dedicated study of this region is appropriate. Second, P_mP and P_n data from all receiver/shot line combinations for which arrivals could be picked are inverted for Moho depth beneath all of Tasmania. Reflections from the Moho (P_mP) are by far the most common type of arrival identifiable on the TASGO wide-angle records. This phase type offers strong constraints on Moho depth. Outside NW Tasmania, however, the density of picked crustal phases is insufficient to provide constraints on a more complex crustal model, so the inversion of data from all regions of Tasmania is based on a single-layer variable depth model of the Moho. The validity of the single-layer inversion is then tested by comparing the NW part of the Tasmanian Moho model with the Moho determined for the four-layer crustal model of NW Tasmania. Further tests which include a mid-crustal interface show that this interface is, in general, poorly sampled by the reflected and refracted rays throughout most of Tasmania. However, the test demonstrates how structural variations within the crust could affect the determination of Moho depth.

Following the presentation of the inversion results, the solution models are interpreted in terms of their geological and tectonic implications, and compared with the results of other studies. In particular, comparison is made with interpretations of the normal incidence reflection lines that were collected concurrently with the wide-angle data. The source-receiver distribution of the TASGO wide-angle survey means that only large scale features of the 3-D structure can be delineated and that near-surface structure is generally poorly constrained. Nevertheless, the inversion results presented here greatly advance our knowledge of the deep crustal structure of Tasmania.

7.2 Inversion for 1-D Structure

The construction of 1-D models from large datasets such as the TASGO wide-angle dataset serves a dual purpose. First, it provides preliminary results on the crustal structure of the region of interest. Second, the 1-D models can be used to develop initial model estimates for subsequent inversions that include lateral variations in structure. Here, 1-D models are constructed using data collected at a single receiver from a single shot line. All identifiable reflection and refraction phases are utilised in each inversion and the number of layers used in each case is defined by the phases present. To invert the traveltimes for 1-D structure, the 2-D version of the wide-angle inversion method described in Chapter 4 is

used. The only modification made to the method when used here is that the interfaces are constrained to be horizontal. Thus, the inversion method attempts to satisfy the specific data constraints from a single receiver/shot line combination in terms of a horizontally layered velocity structure. Velocity within a layer is assumed to vary linearly with depth. Negative velocity gradients and low velocity layers are permitted by the method. Offsets are computed precisely from source-receiver distance so non-collinearity of receiver and shot line is irrelevant within the context of the assumed 1-D structure.

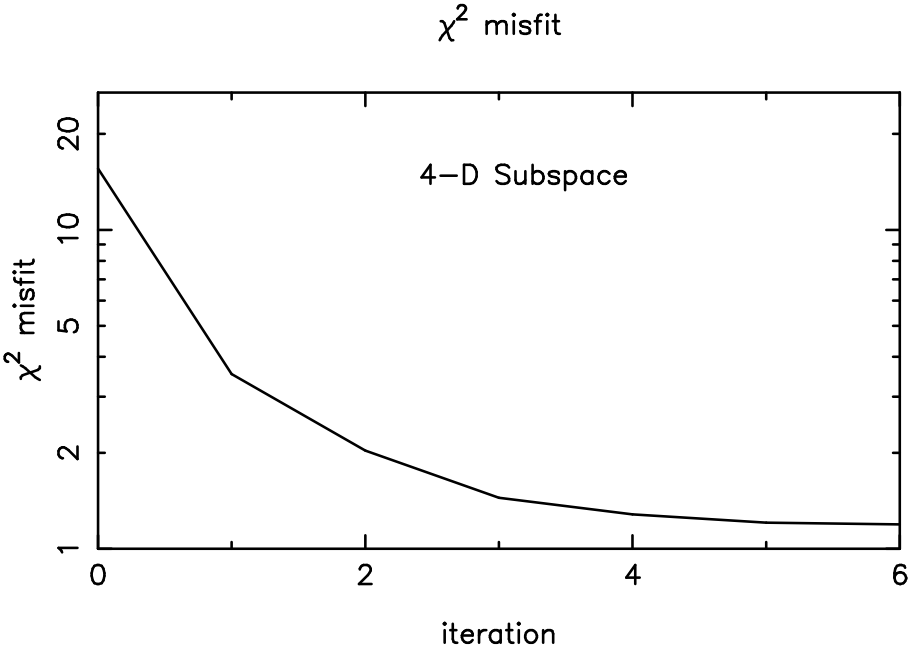

Figure 7.1: χ^2 misfit versus iteration number for the station 10/line 5 inversion for 1-D structure.

The first inversion uses data collected at station 10 from line 5 (Figure 5.8). As shown in Figure 6.16, four refracted and three reflected phases have been picked, indicating three crustal layers. Before proceeding with the inversion, an initial model estimate is required. In the absence of accurate *a priori* information, an approximate 1-D model can be produced using standard 1-D refraction interpretation (e.g. Dobrin & Savit, 1988). Assuming stratified constant velocity layers separated by horizontal interfaces (with velocity increasing monotonically with depth), refracted phases in this medium propagate downwards until they are refracted at the critical angle, whereupon they become head waves before returning to the surface. By approximating each refraction phase with a line of best fit, the unknown velocity and depth parameters are uniquely determined. The velocity within each layer is simply defined by the inverse of the gradient of the straight line

(plotted on a time vs offset graph) that represents the appropriate phase. The interface depths can be determined from shallowest to deepest by successive use of the formula:

$$T_n = \frac{2}{v_n} \sum_{i=1}^{n-1} \frac{h_i}{v_i} \sqrt{v_n^2 - v_i^2} \tag{7.1}$$

where n is the number of refraction phases (so there are $n-1$ layers overlying a half-space), T_n is the intercept time of the n^{th} refraction phase, h_i is the thickness of layer i and v_i is the velocity of layer i. Applying this method to the picked refraction phases of line 5/station 10 data (Figure 6.16) gives a four-layer solution with interface depths of 2 km, 7 km and 30 km and velocities from the top layer to the mantle layer of 5.1 km/s, 5.8 km/s, 6.2 km/s and 8.1 km/s respectively.

This initial model estimate precludes velocity gradients, but velocity gradients were introduced into the initial model using values consistent with continental crust. Starting model parameters for the formal inversion were adjusted manually until a reasonable fit between observed (now including reflection traveltimes) and predicted data was obtained. In this case, the RMS misfit was 0.38 s. No damping was used in the inversion ($\epsilon = 0.0$) because there were no available estimates of *a priori* model covariance, and the relatively few model parameters are well constrained by the data.

Figure 7.1 shows the behaviour of the χ^2 misfit function during the first six iterations of a 4-D subspace inversion (two interface basis vectors, one velocity basis vector and one velocity gradient basis vector). The χ^2 misfit decreases monotonically from an initial value of 15.6 to a final value of 1.2, which corresponds to an RMS data misfit of 0.10 s. The corresponding ray paths and interface positions at the solution point are shown in Figure 7.2; the fit of the model predictions to the observed data is generally accurate for both the refraction and reflection phases. Comparison between the initial and final models (Figure 7.3) shows significant differences in Moho depth (increased to 34 km) and the depth of the mid-crustal interface (increased to 10 km). Perturbing the values of the initial model parameters generally resulted in very similar inversion solutions, suggesting that the model parameters are well constrained by the data.

Another four 1-D inversions obtained for other receiver/shot line combinations from northern Tasmania are shown in Figure 7.4. The initial model used in each case is the same as the initial model used for the station 10/line 5 inversion, except that when the shallow layer cannot be identified in the data, it is excluded from the initial model. As shown in Figure 7.4, the final model in each case is associated with a χ^2 value of order

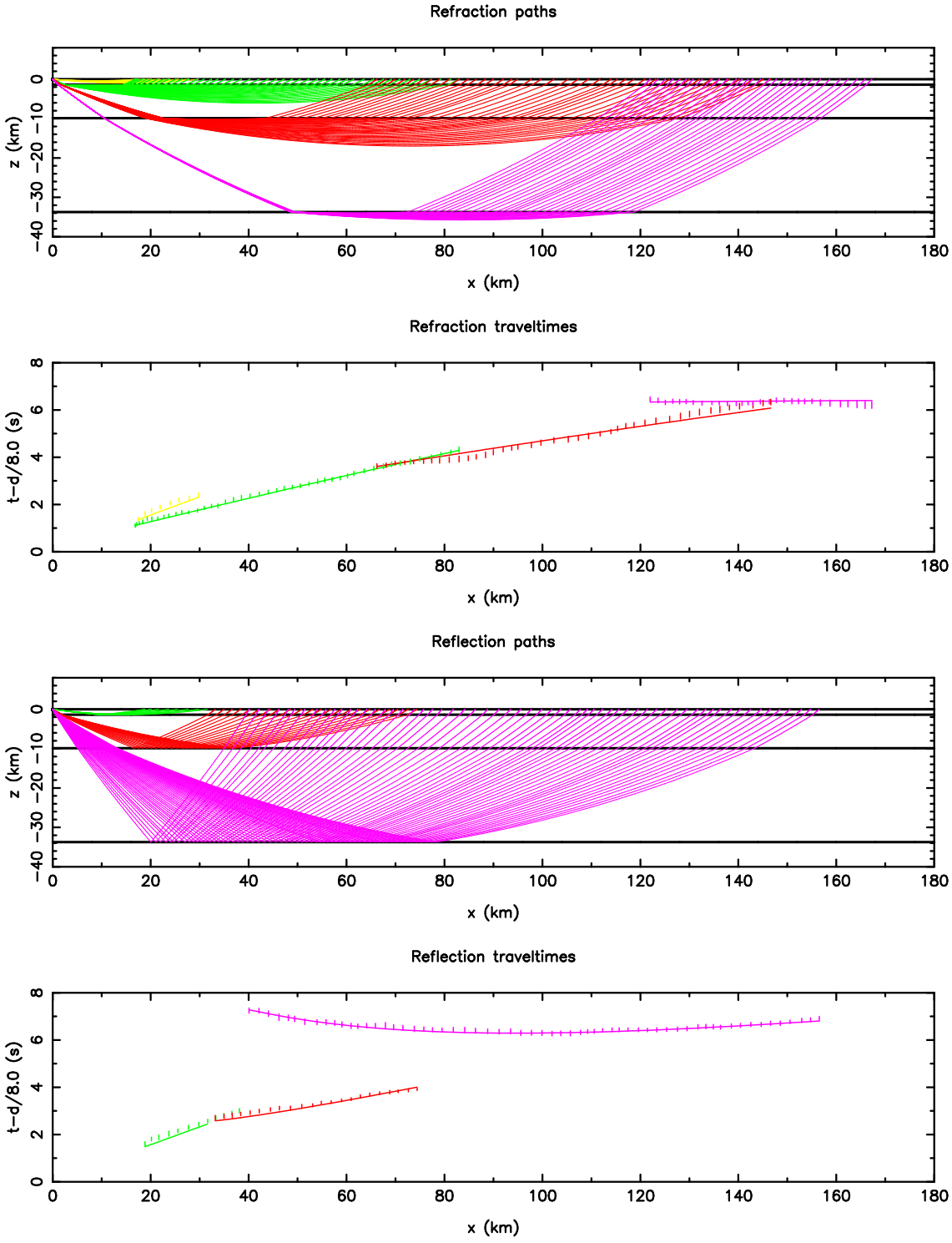

Figure 7.2: Ray paths and traveltimes for the 1-D inversion solution of station 10/line 5 data. Observed traveltimes are denoted by error bars and calculated traveltimes are denoted by solid lines.

2-3. A χ^2 value of 1.0 should not be expected for these inversions because the simple parameterisation used does not permit lateral variations in structure. The model for the station 7/line 5 inversion also includes a lower crustal layer because reflections from the

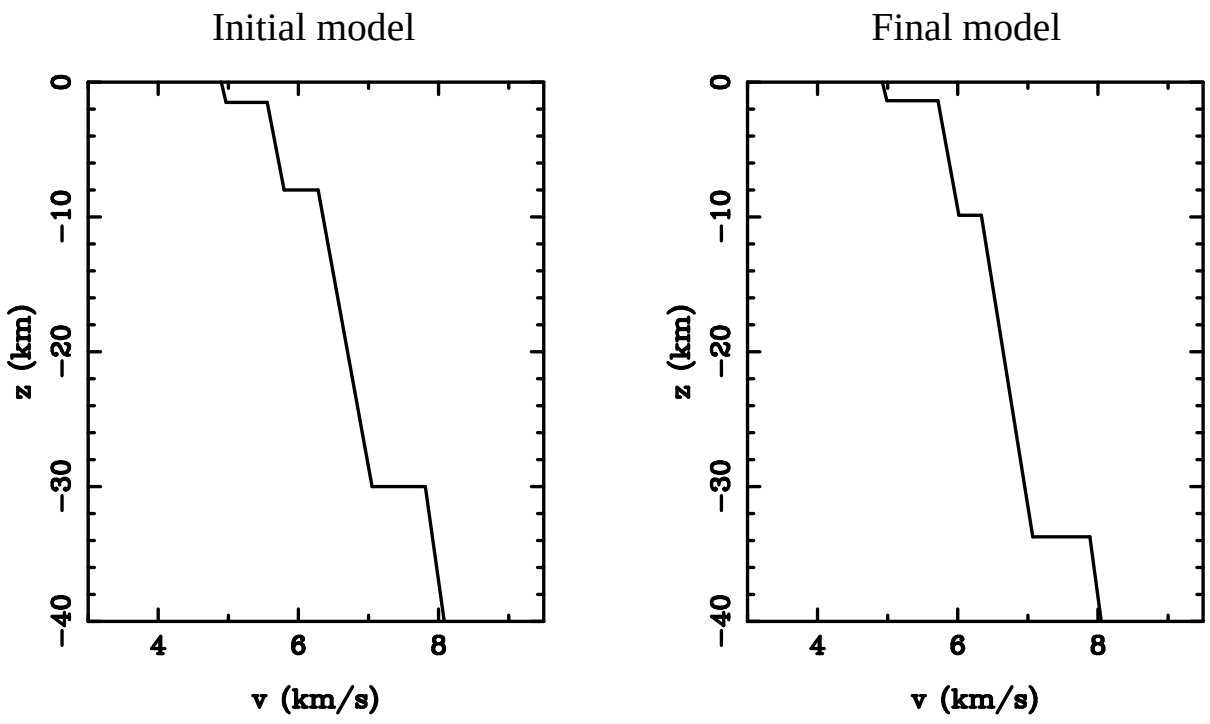

Figure 7.3: Initial and final (after six iterations) model for the station 10/line 5 inversion. The initial and final χ^2 values are denoted by χ^2_i and χ^2_f respectively, and the initial and final RMS traveltime misfits are denoted by T^i_{RMS} and T^f_{RMS}.

layer	v_0 (kms^{-1})	σ_v (kms^{-1})	k (s^{-1})	σ_k (s^{-1})	interface	z (km)	σ_z (km)
1	4.93	0.01	0.045	0.001	1	-1.4	0.1
2	5.50	0.38	0.036	0.004	2	-8.0	1.4
3	6.03	0.29	0.024	0.014	3	-30.1	3.3
4	7.01	0.02	0.027	0.003			

Table 7.1: Velocities, velocity gradients and interface depths for an average three crustal-layer model of Tasmania derived from the nine 1-D inversions shown in Figures 7.3 to 7.5. Standard deviations are also given. Layer 1 is a thin overlying layer and Layer 4 is the mantle half-space. Interface 1 separates the thin overlying layer from the upper crustal layer and interface 3 represents the Moho.

top of this layer were identified in the data. The greatest variation in Moho depth occurs between station 27/line 5 (35 km) and station 10/line 4 (25 km). Station 27 is located near the centre of Tasmania (Figure 5.8) in a region of high topography, so a thicker

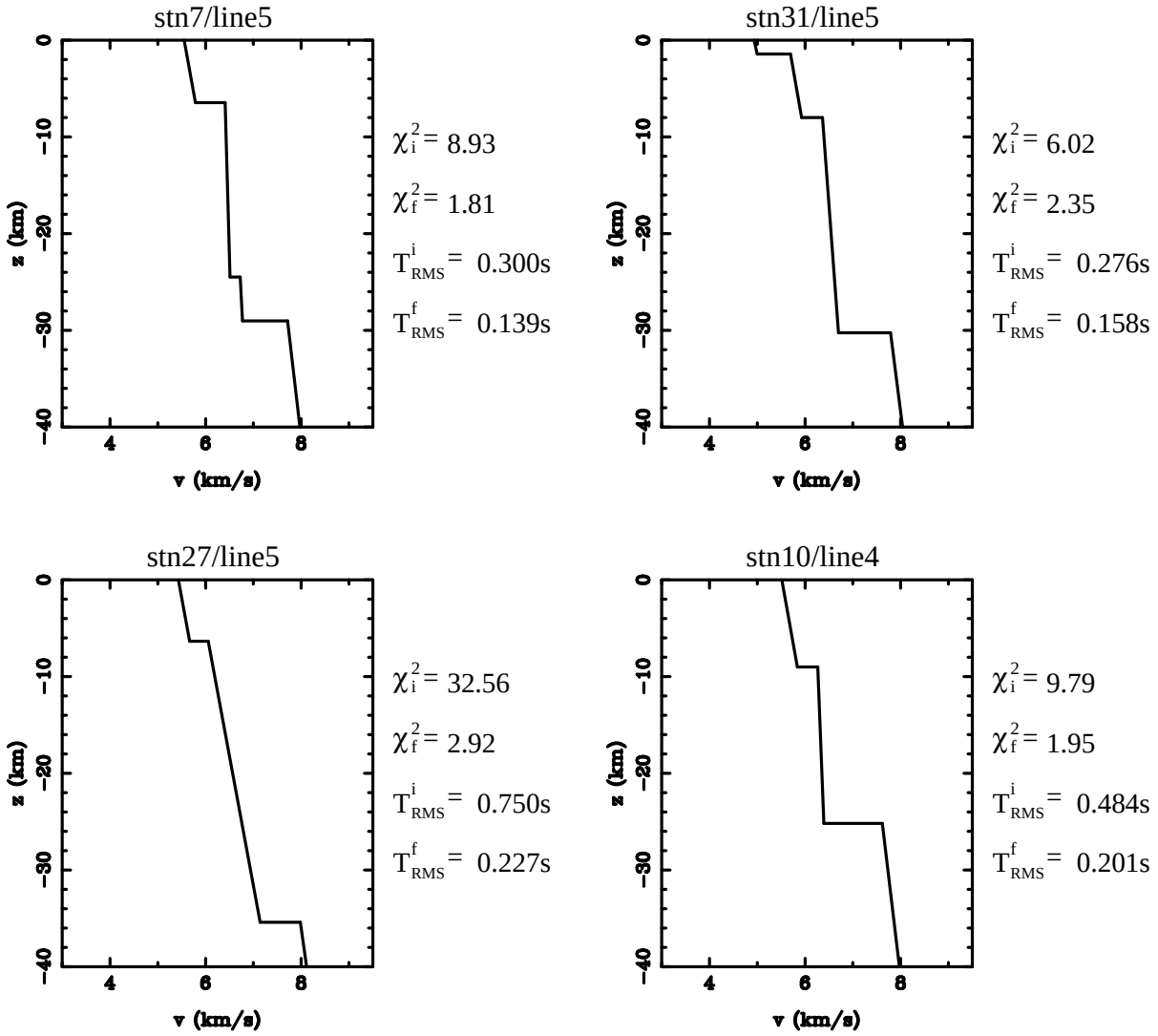

Figure 7.4: 1-D models for northern Tasmania derived by inversion for velocity, velocity gradient and interface depth. The initial model is shown in Figure 7.3. The initial and final χ^2 values are denoted by χ^2_i and χ^2_f respectively, and the initial and final RMS traveltime misfits are denoted by T^i_{RMS} and T^f_{RMS}. See Figure 5.8 for receiver/shot-line locations.

crust is expected. The station 27/line 5 model is also distinguished by a greater velocity gradient in the lower crustal layer compared to the other models.

Four 1-D inversion models for east and west Tasmania were also constructed (Figure 7.5). Phases associated with a thin overlying layer could not be identified in any of the data outside NW Tasmania, so these inversion models include only two crustal layers. The initial model estimate shown in Figure 7.3 was again used for these inversions, but without the thin shallow layer. A χ^2 value of order 1-3 is common to all solutions. As the initial χ^2 values indicate, the initial model is generally a poorer approximation to the recovered structure of these regions than in northern Tasmania. Nevertheless, several

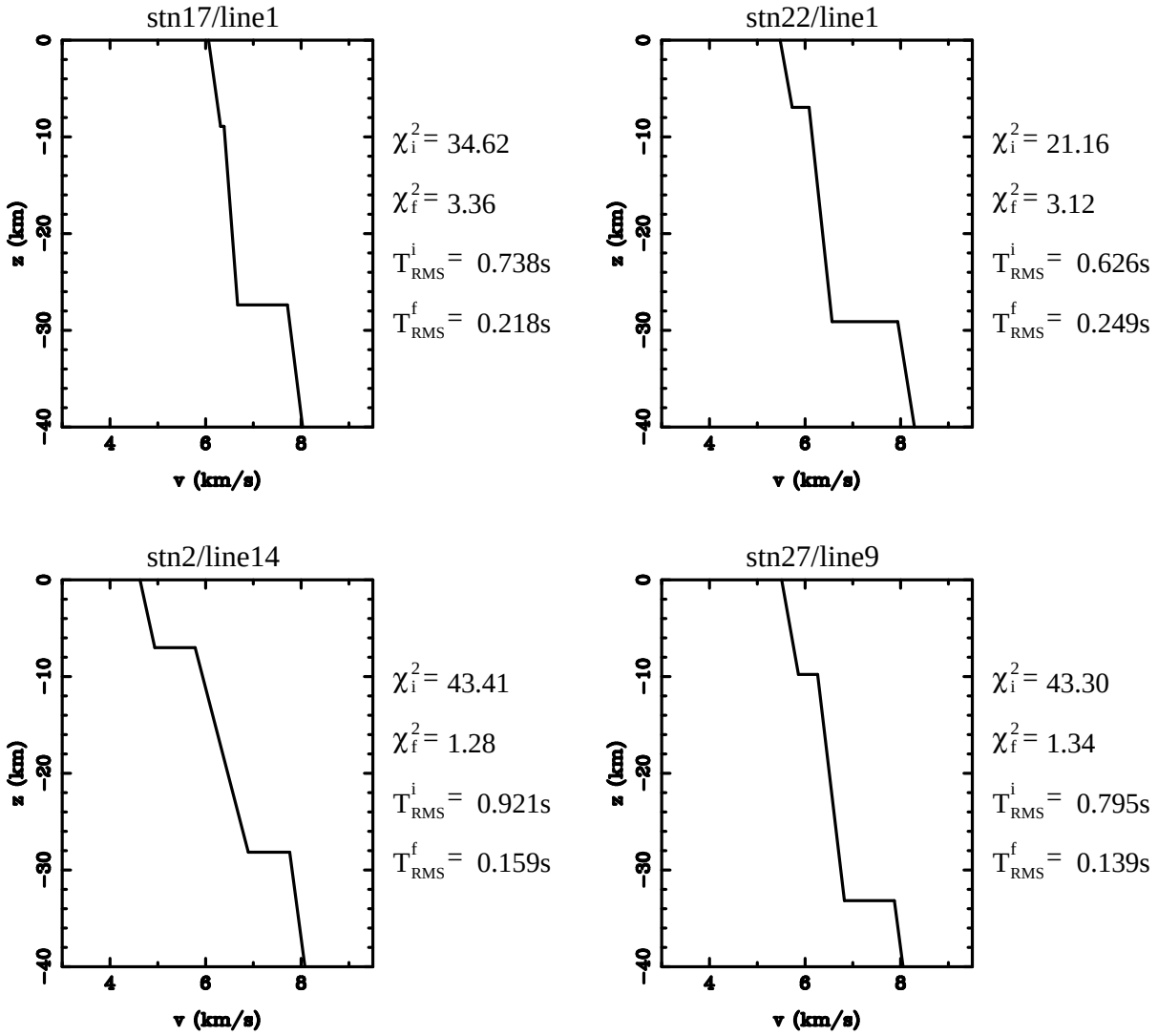

Figure 7.5: 1-D models for east and west Tasmania derived by inversion for velocity, velocity gradient and interface depth. The initial model is shown in Figure 7.3. The initial and final χ^2 values are denoted by χ_i^2 and χ_f^2 respectively, and the initial and final RMS traveltime misfits are denoted by T_{RMS}^i and T_{RMS}^f. See Figure 5.8 for receiver/shot line locations.

other different initial models were tried without finding solution models that fit the data as well. A simple average of all nine 1-D inversion results gives an "average" crustal model of Tasmania (Table 7.1). The top layer (layer 1) is only identified in NW Tasmania and the lower crustal layer identified for station 7/line 5 is not included. According to this result, the average velocity of the Tasmanian crust is 6.3 km/s and the average Moho depth is 30 km. The average P_n velocity is estimated to be 7.8 km/s, although it should be noted that not all station-line combinations have sufficient Moho refractions to constrain this value robustly.

7.3 Inversion for 2-D Structure

In general, the TASGO wide-angle seismic dataset is not conducive to 2-D interpretation because the receivers are generally not collinear with shot lines and shot lines are not necessarily perpendicular to the dominant structural grain. However, line 5 in NW Tasmania has three receivers (7, 10 and 31) that lie almost in-line and are sufficiently distant from each other to provide an adequate angular coverage of ray paths. Construction of a 2-D model as a precursor to a 3-D inversion is a useful exercise because 2-D inversions are generally easier to produce and interpret than their 3-D counterparts. The results of the 2-D inversion also make an interesting comparison with subsequent 3-D inversion results.

A total of 536 traveltimes (247 refractions and 289 reflections) are inverted for the 2-D structure beneath line 5, along the western north coast of Tasmania (Figure 5.8). The refraction and reflection phases picked from the records of the three receivers indicate a three-layer crust in this region, with an additional lower crustal layer in the NW which pinches out towards the SE. Figures 7.3 and 7.4 from the previous section show 1-D models of this region that conform to the above description. The starting model (Figure 7.6) chosen for the 2-D inversion is thus based on the three 1-D models associated with line 5 shots to receivers 7, 10 and 31. Figure 7.6 has essentially 1-D structure except for the lower crustal layer that pinches out near station 31. The depths to the interfaces in Figure 7.6 are set to approximately the average depths of the equivalent interfaces of the three 1-D models. Initial velocity and velocity gradients (see Table 7.2) are similarly chosen. The termination point of the pinchout was estimated by ray tracing through the initial model for a range of termination points; the point which best satisfied the data was used (Figure 7.6).

Although the source-receiver subset used here is considered suitable for 2-D modelling, the shot line is not straight and the three receivers don't coincide with any portion of the line. In such cases, it is necessary to apply a correction if the data are to be treated strictly in 2-D. Here, the method suggested by Zelt (1999) is used. A best fit straight line for the (x, y) locations of the sources and receivers is found, the three receivers are projected perpendicularly onto the best-fit line, and the sources are projected onto the best-fit line in such a way that the correct source-receiver offsets are maintained. A given shot point will therefore have three different projected positions along the best-fit line.

The RMS picking error of all the traveltimes used in the inversion is 103 ms, and the

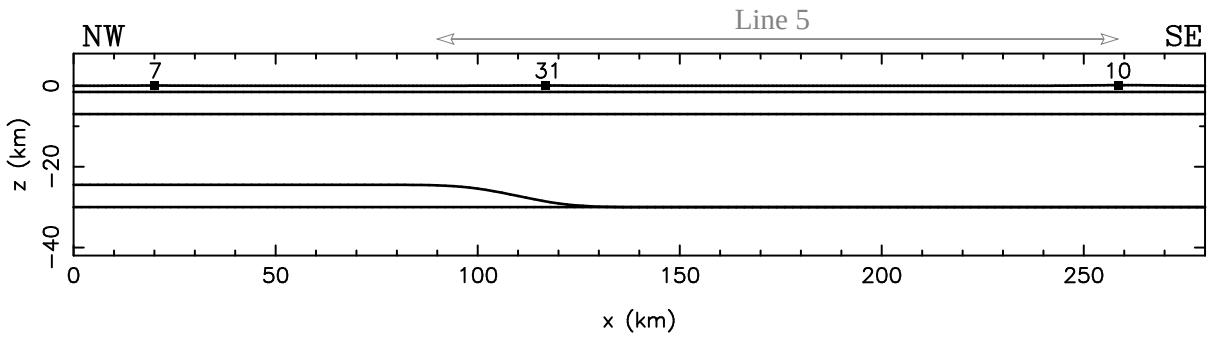

Figure 7.6: Initial model used for the inversion of TASGO data for 2-D structure. Four crustal layers overlying a mantle half-space are defined. Layer 4 pinches out beneath station 31. Velocity parameters are specified in Table 7.2.

individual picking errors are used in the diagonal entries of the data covariance matrix. Interface, velocity and velocity gradient uncertainties for the model covariance matrix were estimated from variations between the three 1-D models. From the top interface to the bottom, uncertainties were estimated at 0.6, 1.5, 1.8 and 1.8 km. Only the station7/line 5 model includes the interface that bounds the top of the pinched out layer, so that interface is assigned the same uncertainty as the Moho. The uncertainties assigned to the velocities and velocity gradients were a uniform 0.4 km/s and 0.003 s^{-1} respectively.

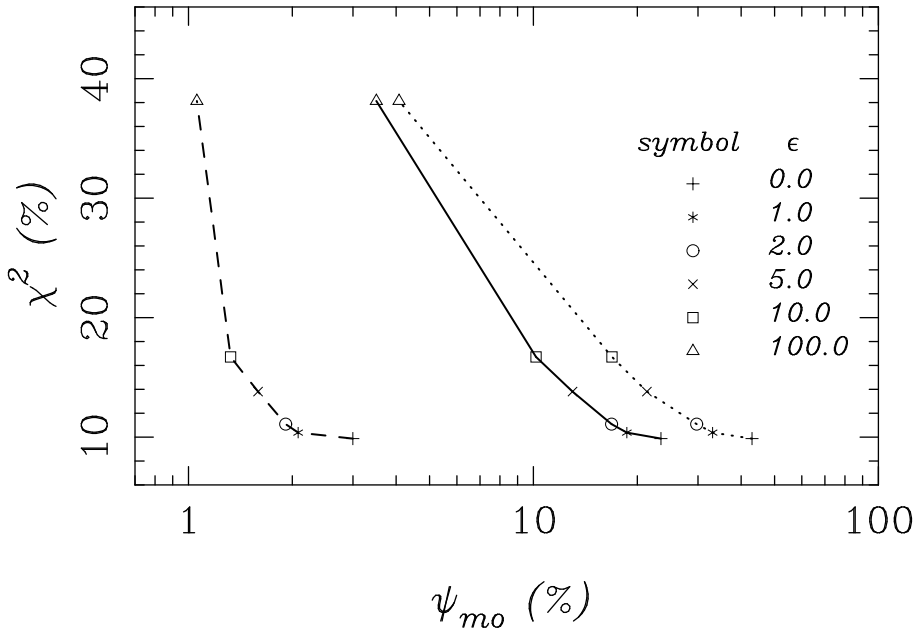

Figure 7.7: Data inversion trade-off curves for various values of the damping factor ϵ after four iterations of the 2-D inversion. The two misfit measures χ^2 and ψ_{mo} (Equation 4.21) are plotted as a percentage of their initial values (i.e. at iteration zero). The model perturbation ψ_{mo} is determined separately for each parameter type: interface node depth (solid line), layer velocity (dashed line) and layer velocity gradient (dotted line).

For the inversion, the initial model (Figure 7.6) is defined by a total of 60 interface and 10 velocity and velocity gradient parameters. Each interface is described by 15 nodes spaced a uniform 20 km apart. Several inversions were run with nodes at different spacing and it was determined that 20 km was the maximum node spacing for which the data could be satisfied. The use of a smaller node spacing would invite spurious structure to be present in the solution.

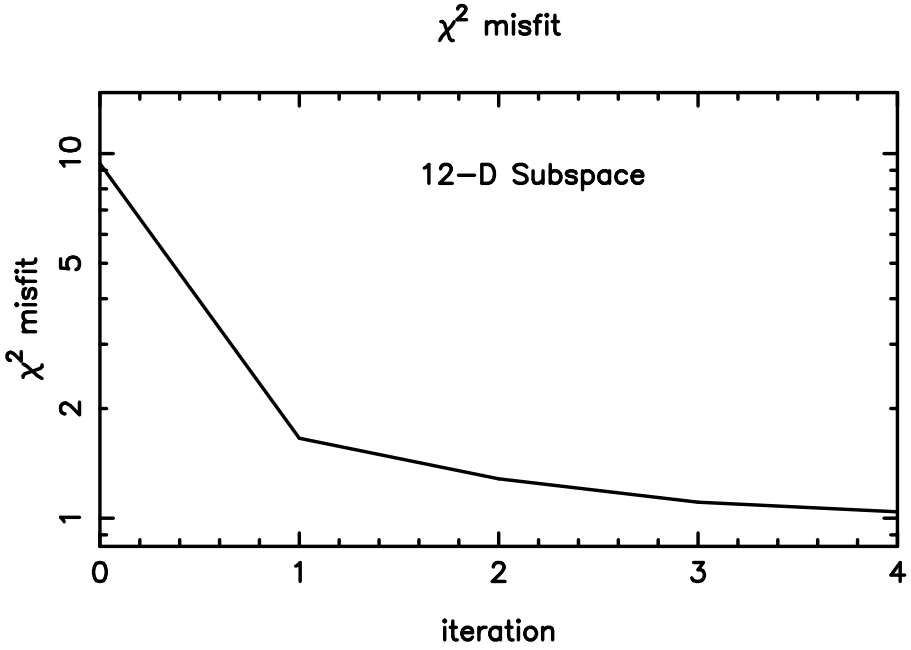

Figure 7.8: χ^2 misfit function versus iteration number for the 2-D inversion of line 5 data using a damping factor of $\epsilon = 2.0$.

Rays are traced through the model with all shot points at sea level ($z = 0$) and all receivers at their measured heights above sea level (86 m, 214 m and 74 m for stations 7, 10 and 31 respectively). The dimension of the subspace used in the inversion was set to 12, six basis vectors in interface depth model space, three basis vectors in velocity (v_0) model space and three basis vectors in velocity gradient (k) model space. This 12-D subspace scheme offers a suitable compromise between the reduction of the χ^2 misfit function per iteration and the computational burden. To choose an appropriate value of the damping factor ϵ, a number of four-iteration inversions were run using different values of ϵ. Figure 7.7 shows a plot of the χ^2 misfit function (as a percentage of its initial value) versus percentage model perturbation for six values of ϵ between 0 and 100. Values of $\epsilon = 1.0$ or 2.0 result in solutions that appear to provide the best compromise between minimising the

layer	initial model		recovered model		resolution	
	v_0 (kms^{-1})	k (s^{-1})	v_0 (kms^{-1})	k (s^{-1})	v_0	k
1	4.90	0.045	4.87	0.045	1.00	0.007
2	5.60	0.035	5.72	0.031	1.00	0.100
3	6.00	0.033	6.22	0.016	1.00	0.720
4	6.50	0.021	6.52	0.012	0.94	0.040
5	7.00	0.030	7.00	0.030	0.94	0.062

Table 7.2: Velocity parameter values of the initial and final 2-D models for the line 5 dataset. The resolution values determined for the recovered model are also given. Layer 1 is the upper crustal (top) layer and layer 5 is the mantle half-space. Note that the actual velocity at a given depth is defined by Equation 4.1. Resolution values ≥ 0.5 indicate that a parameter is reasonably well constrained (see Section 4.3.2).

data misfit (χ^2) and minimising the departure from the initial model (ψ_{mo}). A damping value of $\epsilon = 2.0$ is used for the inversion results described below.

The χ^2 misfit for $\epsilon = 2.0$ (Figure 7.8) exhibits monotonic behaviour and reduces to a value of 1.04 at iteration 4. The corresponding RMS traveltime misfit at iteration 4 is 100 ms; the RMS picking error of the data is 103 ms. Thus, the inversion solution with $\epsilon = 2.0$ adequately satisfies the data. In general, the fit between the observed and predicted traveltime curves (Figure 7.9) is good for both the reflected and refracted phases, although some of the shorter wavelength features of the observed phases are not present in the model traveltime curves. The ray paths through the final model (Figure 7.9) exhibit good angular coverage between stations 31 and 10. In comparison, the region between stations 7 and 31 is quite poorly covered, due to the distance between station 7 and the NW end of line 5. Thus, there are few effective constraints on the depths of interfaces 1 and 2 in this region. A comparison between the final and initial model interface structures is shown in Figure 7.10a. The largest perturbations occur in the three lower interfaces, consistent with the greater *a priori* uncertainty on these interfaces ($\sigma \geq 1.5$ km/s) compared to the top interface ($\sigma = 0.6$ km/s) and the stronger data constraints (indicated by the ray density on Figure 7.9). Velocity versus depth profiles at three locations along the initial and final models are compared in Figure 7.10b. Changes in interface depth and a reduction of the velocity gradient in the lower crustal layer represent the most significant adjustments to the solution model. Initial and final velocity

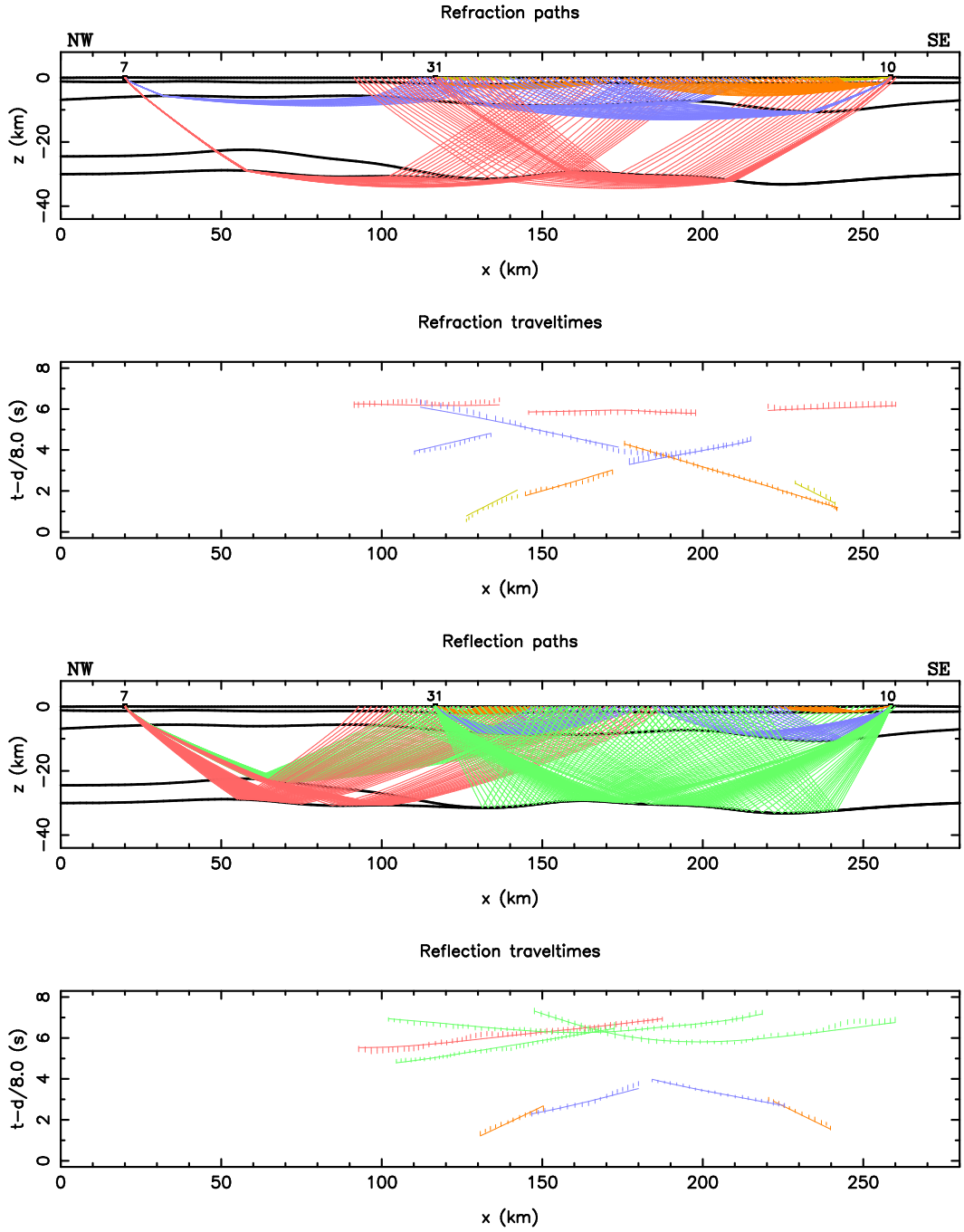

Figure 7.9: Ray paths and traveltimes for the 2-D solution model. Observed traveltimes are denoted by error bars and calculated traveltimes are denoted by solid lines. Rays and traveltime curves are colour coded to help discriminate between the different phase types.

and velocity gradient parameter values are compared in Table 7.2.

Inspection of the diagonal elements of the resolution matrix (Figure 7.11) associated with the Figure 7.10 solution confirms what can be seen in the ray path plot (Figure 7.9). On the whole, the interfaces in the region between stations 10 and 31 are quite well

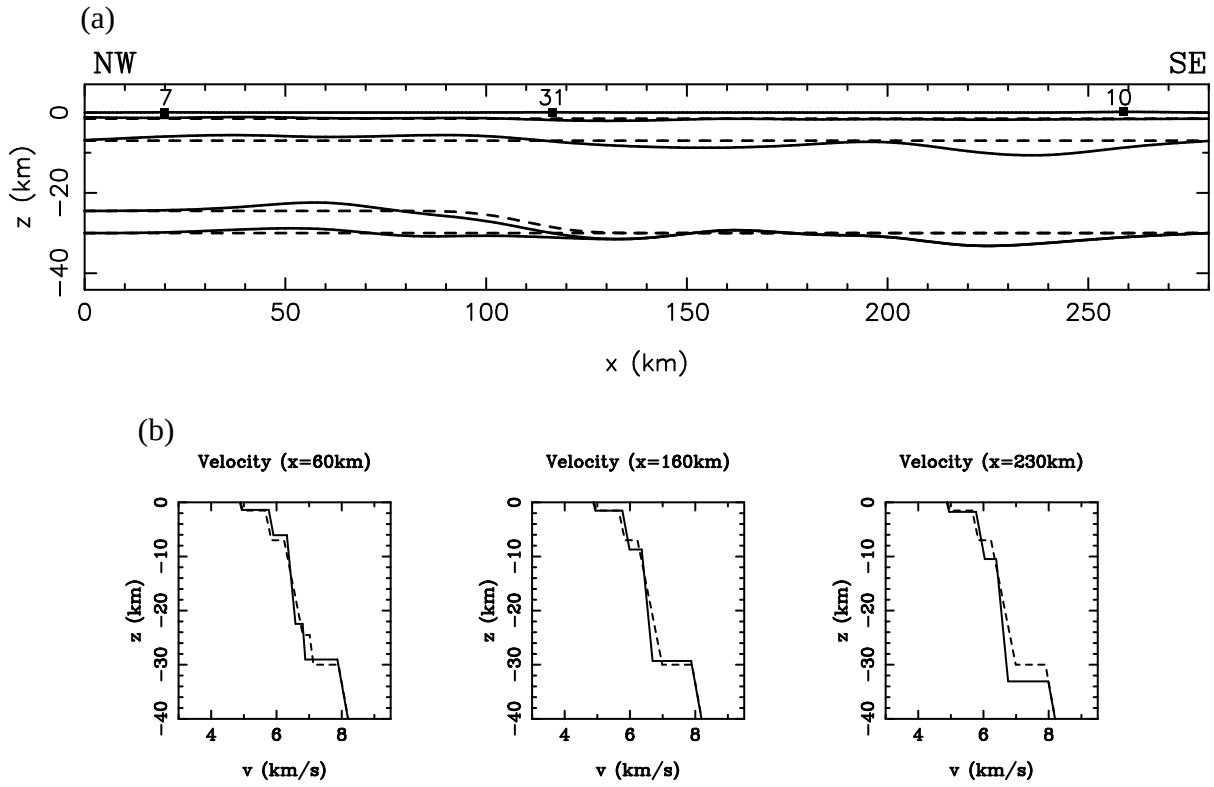

Figure 7.10: Comparison between the initial and final 2-D solution model obtained after four iterations with $\epsilon = 2.0$. The initial model is denoted by dashed lines and the solution model by solid lines. (a) Initial and final model interface structure and (b) velocity versus depth at three locations along the model.

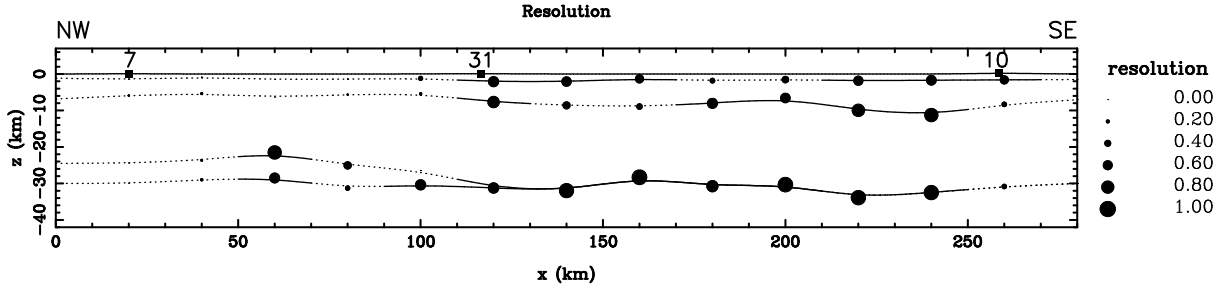

Figure 7.11: Diagonal elements of the resolution matrix for each interface node. Dashed portions of the interfaces have a depth resolution less than 0.5.

resolved, with the exception of the lower two interfaces at $x > 250$ km where there is no ray path coverage. Between stations 7 and 31, resolution is generally poor, except for a limited interval of good resolution near $x = 60$ km where reflected and refracted ray paths to station 7 constrain the lower two interfaces.

The resolution of the velocity parameters, along with initial and final parameter estimates, are given in Table 7.2. All velocity parameters are well constrained according to

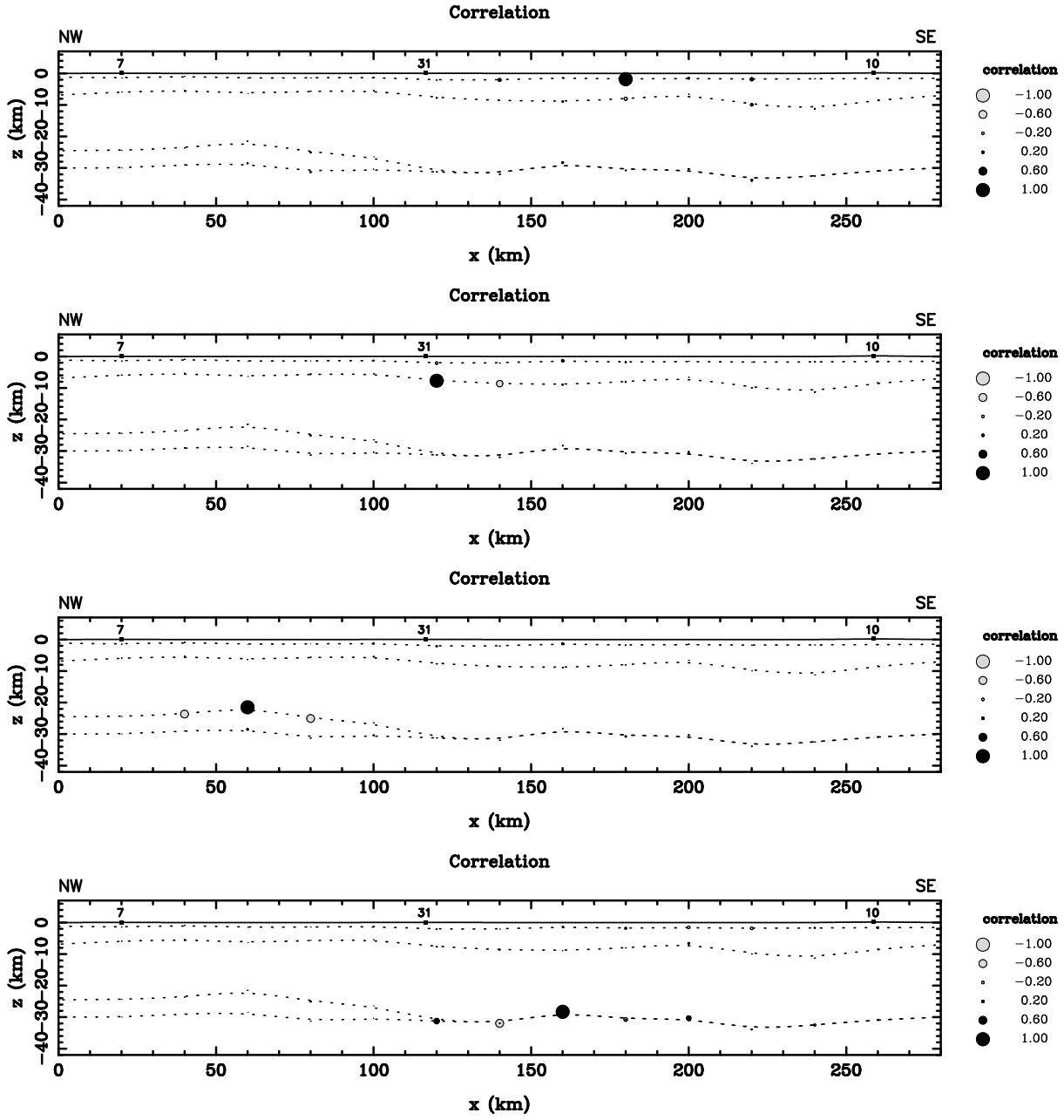

Figure 7.12: Correlation coefficients of four interface nodes for the 2-D inversion solution. The reference node in each case has a correlation value of 1.0.

this criteria, with no resolution value lower than 0.9. In contrast, the velocity gradients are poorly constrained, with the exception of the third layer (the thickest crustal layer) which has a resolution value of 0.72. The top layer is extremely thin, with few turning rays, so it is not surprising that the velocity gradient is poorly constrained. Similarly, the lower crustal layer that pinches out is thin and contains no turning rays. The mantle half space and the second layer are sampled by a number of turning rays, but the traveltimes

of these rays are apparently not sensitive to the velocity gradients. The third layer, which has relatively good velocity gradient resolution, is sampled by many rays and is sufficiently thick to allow the velocity gradient to strongly influence the shape of the traversing ray paths.

Correlation coefficients for four representative interface nodes are shown graphically in Figure 7.12. The reference node in each case has a correlation value of 1.0. The node in the top interface is poorly correlated with adjacent interface nodes, indicating that it may be perturbed without requiring adjacent nodes to move in order to satisfy the data. Therefore, this region of the interface is not well resolved by the data. The node in the second interface at $x = 120$ km is slightly anticorrelated with the node at $x = 140$ km but there is no correlation with the node at $x = 100$ km, which suggests that the interface NW of the $x = 120$ km node is poorly resolved. The nodes examined for the lower two interfaces indicate that interface structure in these regions is well resolved, as adjacent nodes are anticorrelated.

In summary, the basic features of the 2-D model (Figure 7.10) between stations 31 and 10 appear robust. In particular, the upward deflection of the Moho between $150 \leq x \leq 200$ km and the corresponding upward deflection of the overlying interface appear well constrained. The depths of the interfaces above and below the pinched out layer at about $x = 60$ km are also well resolved according to the resolution diagram (Figure 7.11), although the depths on either side are not. The average Moho depth along the profile of Figure 7.11 is 31 km, the average sub-Moho (P_n) velocity is 7.9 km/s, and the average crustal velocity is 6.3 km/s, all of which agree closely with the relevant 1-D model results of the previous section (Figures 7.3 and 7.4).

7.4 Inversion for 3-D Structure

Following the preceding descriptions of inversion for 1-D structure at nine different locations around Tasmania (Section 7.2) and inversion for 2-D structure along the western north coast (Section 7.3), I now describe the use of TASGO wide-angle traveltime data in 3-D layered crustal structure inversions. Due to the relatively sparse distribution of receivers (Figure 5.8) and failure of approximately half of these to record useful wide-angle data (see Table 5.2 and Figure 5.10), ray coverage is generally poor for most of Tasmania except the NW corner. With this in mind, the inversion for 3-D structure has

been divided into two parts. First, the structure of NW Tasmania is determined using a four-layer crustal model in which over 2000 refraction and reflection traveltimes are inverted for interface depth, layer velocity and layer velocity gradient. In a second separate inversion, the Moho structure beneath all of Tasmania is determined using all picked P_n and P_mP arrivals from the TASGO dataset. The low number of crustal phases that can be identified in data collected outside NW Tasmania implies that internal crustal interfaces would be poorly constrained by the data in an inversion for Tasmania-wide crustal structure. The P_mP phases, which are relatively numerous, provide good constraints on Moho depth, although a large region in central Tasmania is poorly covered by Moho reflections. The validity of assuming a laterally homogeneous crust for this inversion is tested by comparing the all-Tasmania Moho model with that of the four-layer NW Tasmania model. Another robustness test is also made by including a mid-crustal interface and associated phases in the all-Tasmania inversion. Although the mid-crustal interface is poorly resolved by the data, the test gives some indication of how sensitive the Moho reconstruction is to lateral variations in internal crustal structure.

When synthetic tests were performed with 3-D structures (see Section 4.3.2), the source-receiver geometry was specified in Cartesian coordinates consistent with the coordinate system used for the model parameterisation. In these 3-D inversions, the source and receiver positions (latitude and longitude) are projected from spherical to Cartesian space for this reason. Pearson (1990) recommends using a conical projection to minimise distortion, compared to other projections, in the latitude range 30° to 60°. Two types of conical projections were considered: Albers equal area with two standard parallels, and Lambert conformal with two standard parallels. An equal area projection preserves the ratio of areas from the earth to the map, while a conformal projection preserves angles. The two standard parallels occur as a result of the projection surface (a cone) being secant to the earth; the latitudinal lines of intersection define the standard parallels. Both types of projections were tested on the source and receiver coordinates and the differences in the mapped positions were so minimal that they had no effect on the inversion solutions. The equal area projection is used in the following results.

Ideally, the inversion should also account for the differences between traveltimes for a spherical earth and those determined by tracing rays through a locally flat earth. According to Zelt (1999), the effects caused by assuming a flat earth are only significant when source-receiver offsets exceed 500 km. Since the greatest source-receiver offset of

picked data (the P_n phase for station 17/line 1) is only 285 km, observed traveltimes are transferred to the Cartesian model without further correction.

7.4.1 Crustal Structure of NW Tasmania

The data subset used to constrain the crustal structure of NW Tasmania consists of traveltimes from eight shot lines (5,6,7,8,9,10,11 and 12) to nine receivers (4,5,7,10,25,27,31,39 and 40). Figure 7.13 shows the array subset. A total of 1054 refraction and 1347 reflection traveltimes have been picked (Table 7.3), with picking errors ranging from 49 ms for a near offset first break to 243 ms for a wide-angle Moho reflection. The RMS picking error of all the traveltimes used in the inversion is 125 ms. As in the inversion for 2-D structure (Figure 7.9), the picked phases indicate a four layer crust overlying a mantle half-space, with the lower-most crustal layer pinching out towards the SE.

The initial model used in the inversion is based on the 1-D models derived for NW Tasmania in Section 7.2. The starting structure is essentially 1-D except for the lower-most crustal layer which pinches out to the SE (see Figure 7.14). The line which defines where the layer pinches out is chosen so that it intersects the pinchout point of the 2-D model and is approximately perpendicular to line 5 (i.e. parallel to the x-axis). This choice is influenced by the principal structural variations mapped in this part of NW Tasmania and it provides an initial model that satisfies the data reasonably well (the RMS traveltime residual is 300 ms). The depths of the four interfaces (Figure 7.14) are 1.5, 7.5, 24.5 and 31 km and the *a priori* estimated uncertainties are 0.6, 1.8, 2.0 and 2.0 km respectively. The initial velocity and velocity gradient for each layer are given in Table 7.4, with uniform uncertainties of 0.3 km/s and 0.002 s^{-1} assumed for the velocities and velocity gradients respectively. Visual comparison of the fit between picked phases and calculated phases for the initial model (Figure 7.15) suggests that the principle features required to explain the data are present, although there is clear room for improvement in the choice of model parameter values.

For the 3-D inversion, an irregular grid of nodes is used to describe the upper two interfaces and a regular grid of nodes is used to describe the lower two interfaces (Figure 7.13). The upper two interfaces are each described by 88 nodes and the bottom two interfaces are each described by 208 nodes. The node density in the upper two interfaces varies with position because the distribution of the sources and receivers means that these

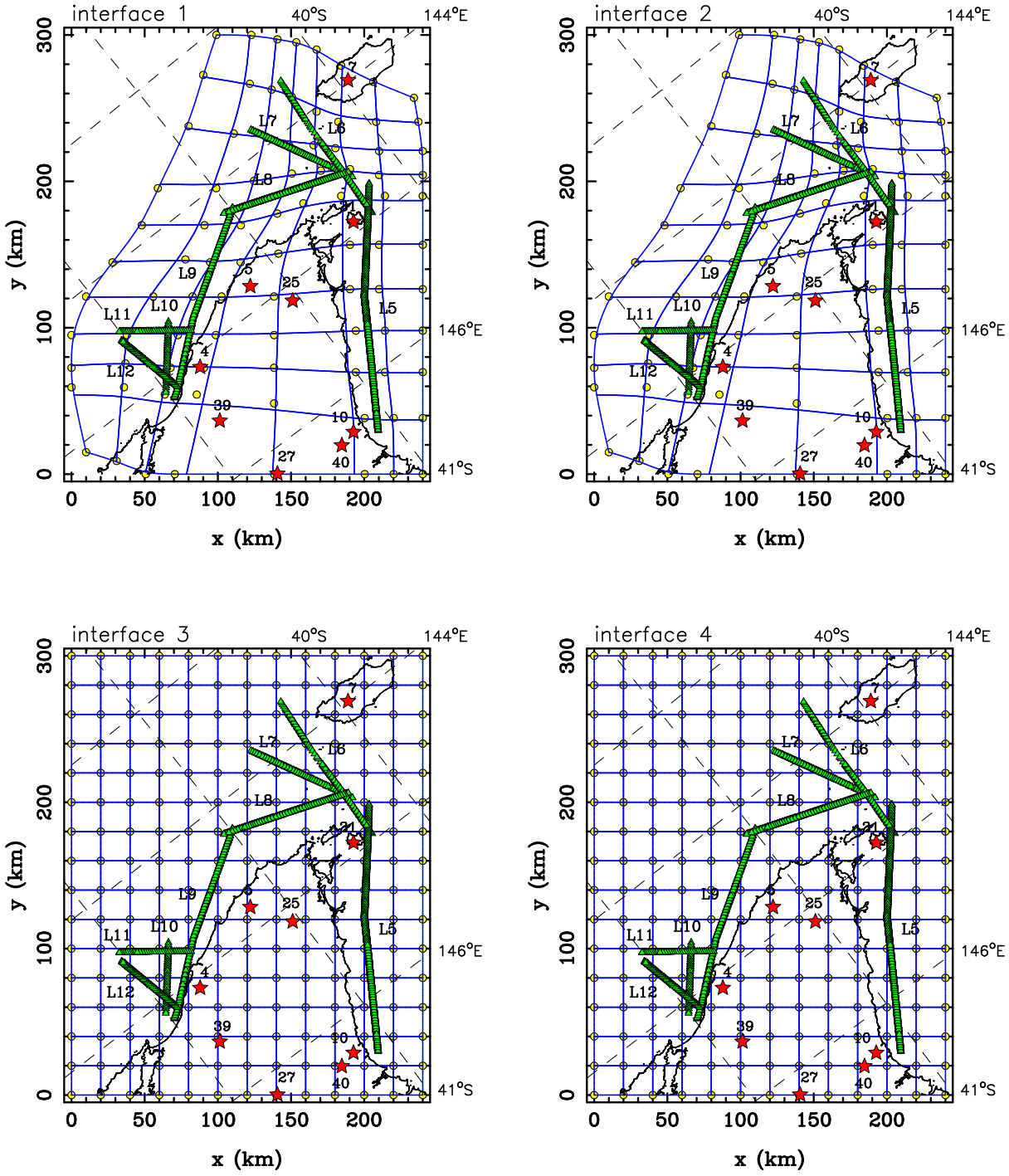

Figure 7.13: Subset of TASGO source-receiver array used to image the crustal structure of NW Tasmania. Receivers are denoted by red stars and picked sources by green triangles. Also shown are the nodes (yellow dots) and associated patch boundaries (blue lines) of the four interfaces that comprise the initial model. Dashed lines indicate lines of constant latitude and longitude.

shallow interfaces (Figure 7.14) have large regions that are not intersected by any rays. Most refracted ray paths penetrate these interfaces in the vicinity of the sources and receivers. Because the receivers are widely separated, the ray paths, although numerous,

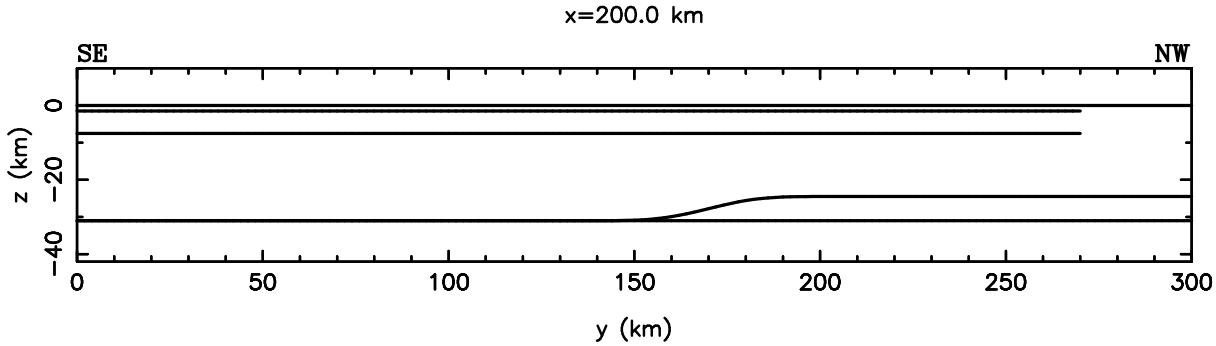

Figure 7.14: Cross-section through initial model used for the 3-D inversion of NW Tasmania data. The structure is invariant with respect to x. The upper two interfaces terminate at the irregular boundaries of the bicubic B-spline mesh (see Figure 7.13).

Station	Line	P	P_1	P_2	P_n	P_1P	P_2P	P_3P	P_mP
4	9	-	-	-	-	-	-	-	25
5	8	-	27	-	-	-	-	-	28
5	9	-	-	-	-	-	19	-	16
7	5	-	-	16	30	-	9	51	59
7	6	-	25	17	-	-	-	23	20
7	8	-	27	12	15	-	9	39	41
10	5	8	45	41	30	12	22	-	61
25	5	-	-	-	-	-	-	-	16
25	8	-	-	-	-	-	-	-	28
27	5	-	-	42	28	-	-	-	63
27	8	-	-	-	36	-	-	-	-
27	9	-	-	38	41	-	-	-	55
27	10	-	-	21	-	-	-	-	55
27	11	-	-	-	10	-	-	-	35
27	12	-	-	25	7	-	-	-	33
31	5	12	17	25	23	12	18	-	54
31	6	12	16	15	-	-	-	24	21
31	7	-	28	18	-	-	-	28	28
31	8	-	26	25	-	-	-	-	28
31	9	-	-	-	33	-	-	-	46
39	5	-	-	23	11	-	-	-	44
39	9	-	21	9	-	-	-	-	38
39	10	-	-	-	-	-	-	-	29
39	11	-	-	16	-	-	11	-	24
39	12	-	15	36	-	-	-	-	18
40	5	27	33	23	18	24	19	-	43
40	9	-	-	-	13	-	-	-	39
40	11	-	-	-	10	-	-	-	26
40	12	-	-	-	20	-	-	-	32

Table 7.3: Number of picks for each phase of each station-line combination used in the inversion for the 3-D structure of NW Tasmania.

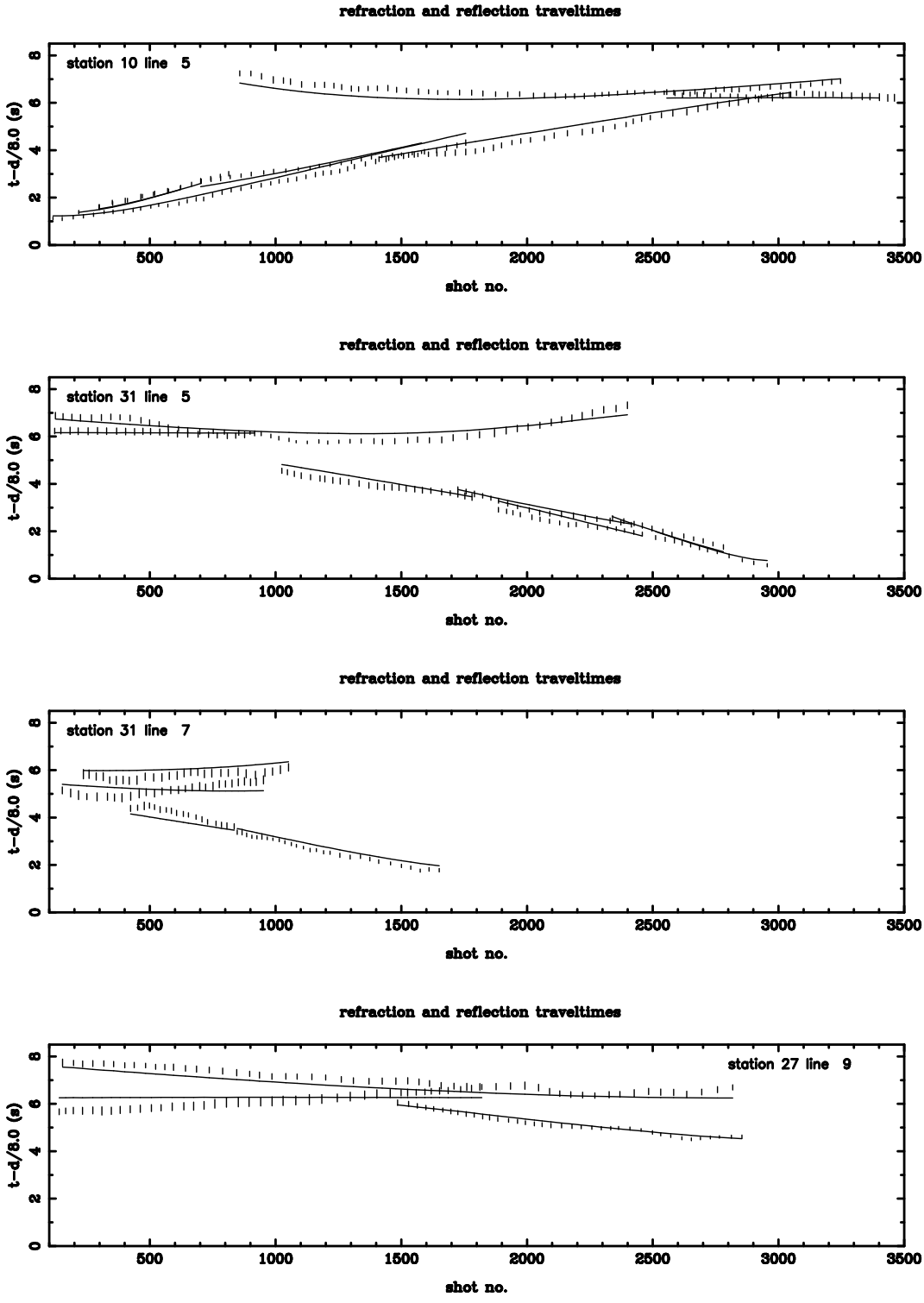

Figure 7.15: Predicted and observed traveltimes for four different station-line combinations in the initial 3-D model of NW Tasmania. Observed traveltimes are indicated by error bars and predicted traveltimes are denoted by continuous lines. Refer Figure 7.13 for station and line locations.

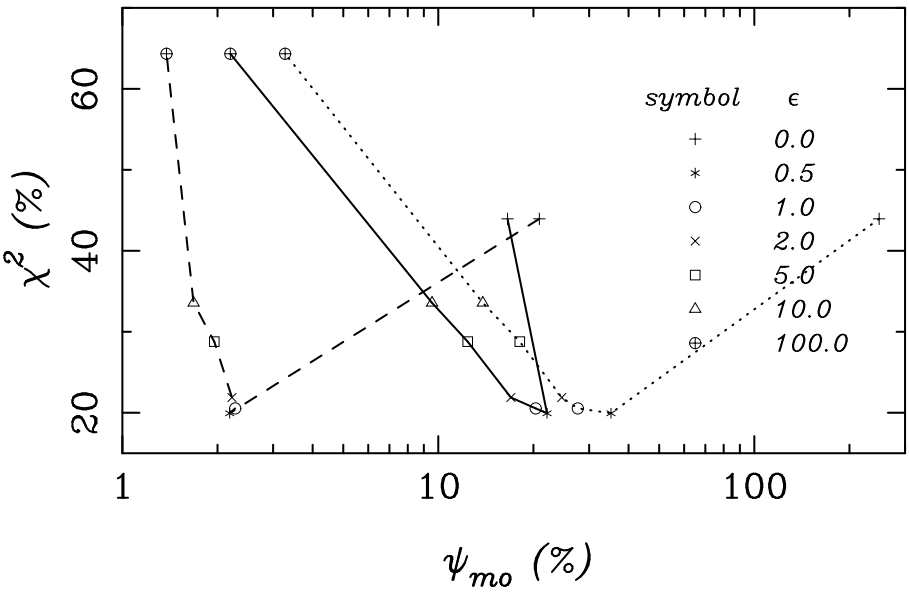

Figure 7.16: Data inversion trade-off curves for various values of the damping factor ϵ after five iterations of the inversion for the 3-D structure of NW Tasmania. The two misfit measures χ^2 and ψ_{mo} (Equation 4.21) are plotted as a percentage of their initial values (i.e. at iteration zero). The model perturbation ψ_{mo} is determined separately for each parameter type: interface node depth (solid line), layer velocity (dashed line) and layer velocity gradient (dotted line).

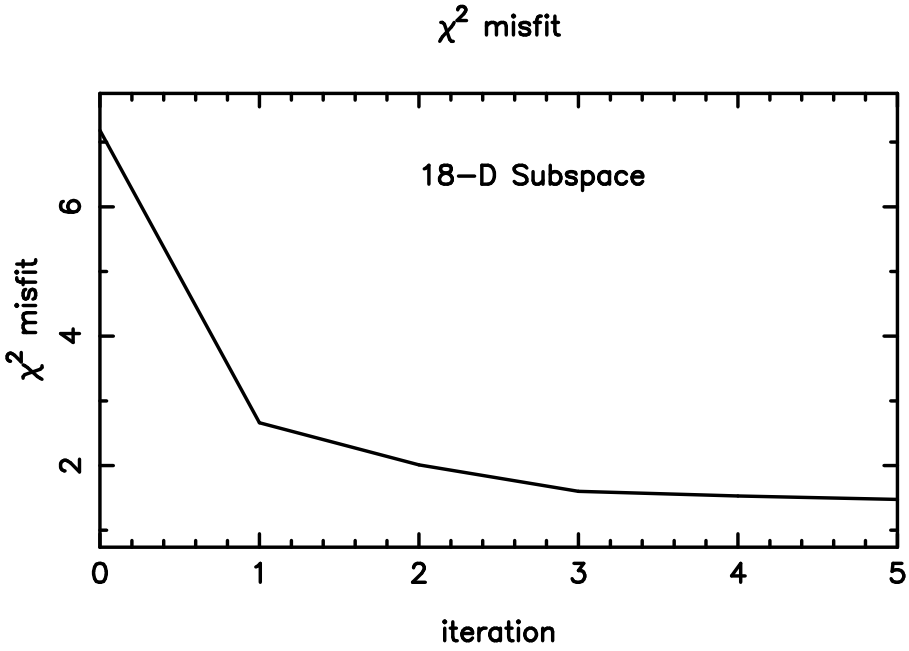

Figure 7.17: χ^2 misfit function versus iteration for five iterations of the inversion for the 3-D structure of NW Tasmania with $\epsilon = 1.0$.

penetrate the upper two interfaces as dense bundles around each receiver and therefore poorly constrain depth. The regions beneath the shot lines are better constrained because

layer	initial model		recovered model		resolution	
	v_0 (kms^{-1})	k (s^{-1})	v_0 (kms^{-1})	k (s^{-1})	v_0	k
1	4.90	0.045	4.95	0.044	1.00	0.002
2	5.50	0.036	5.61	0.029	1.00	0.310
3	5.90	0.033	6.04	0.024	1.00	0.810
4	6.50	0.020	6.46	0.020	0.96	0.036
5	7.00	0.030	7.13	0.032	0.96	0.148

Table 7.4: Velocity parameter values of initial and final 3-D models of NW Tasmania. The resolution values associated with the recovered model are also given. Layer 1 is the upper crustal (top) layer and layer 5 is the mantle half-space. Note that the actual velocity at a given depth is defined by Equation 4.1.

the picked shot points are closely spaced along the lines. Thus, the grid of nodes in the upper two interfaces (Figure 7.13) has been deformed to provide a denser coverage of surface patches beneath the shot lines and a less dense coverage elsewhere. All 2401 refraction and reflection traveltimes are simultaneously inverted for all 602 interface, velocity and velocity gradient parameters.

Ray tracing through the model is performed with all shot points at sea level ($z = 0$) and all receivers at their measured heights above sea level; station 39 has the greatest elevation at 975 m (see Table 5.1). In the inversion, the dimension of the subspace was set to 18. 10 basis vectors lie in interface depth model space, four basis vectors lie in layer velocity model space and four basis vectors lie in layer velocity gradient model space, resulting in a scheme which offers a suitable compromise between the magnitude of the objective function reduction per iteration and the computational effort. Inversions were run for values of the damping parameter ϵ in the range $0 \leq \epsilon \leq 100$. On the basis of the trade-off between data residual and model perturbation (Figure 7.16), $\epsilon = 1$ was chosen as providing the optimum choice in terms of minimising χ^2 and ψ_{mo}. The plot of χ^2 misfit versus iteration number for $\epsilon = 1.0$ (Figure 7.17) follows a monotonically decreasing path that levels out at a value of 1.48, which corresponds to an RMS traveltime misfit of 145 ms.

In Figure 7.18, the observed traveltime curves are compared with the predictions of the solution model; the fit is much improved relative to the corresponding plots for the initial model traveltimes (see Figure 7.15). The RMS picking error is 125 ms, so evidently

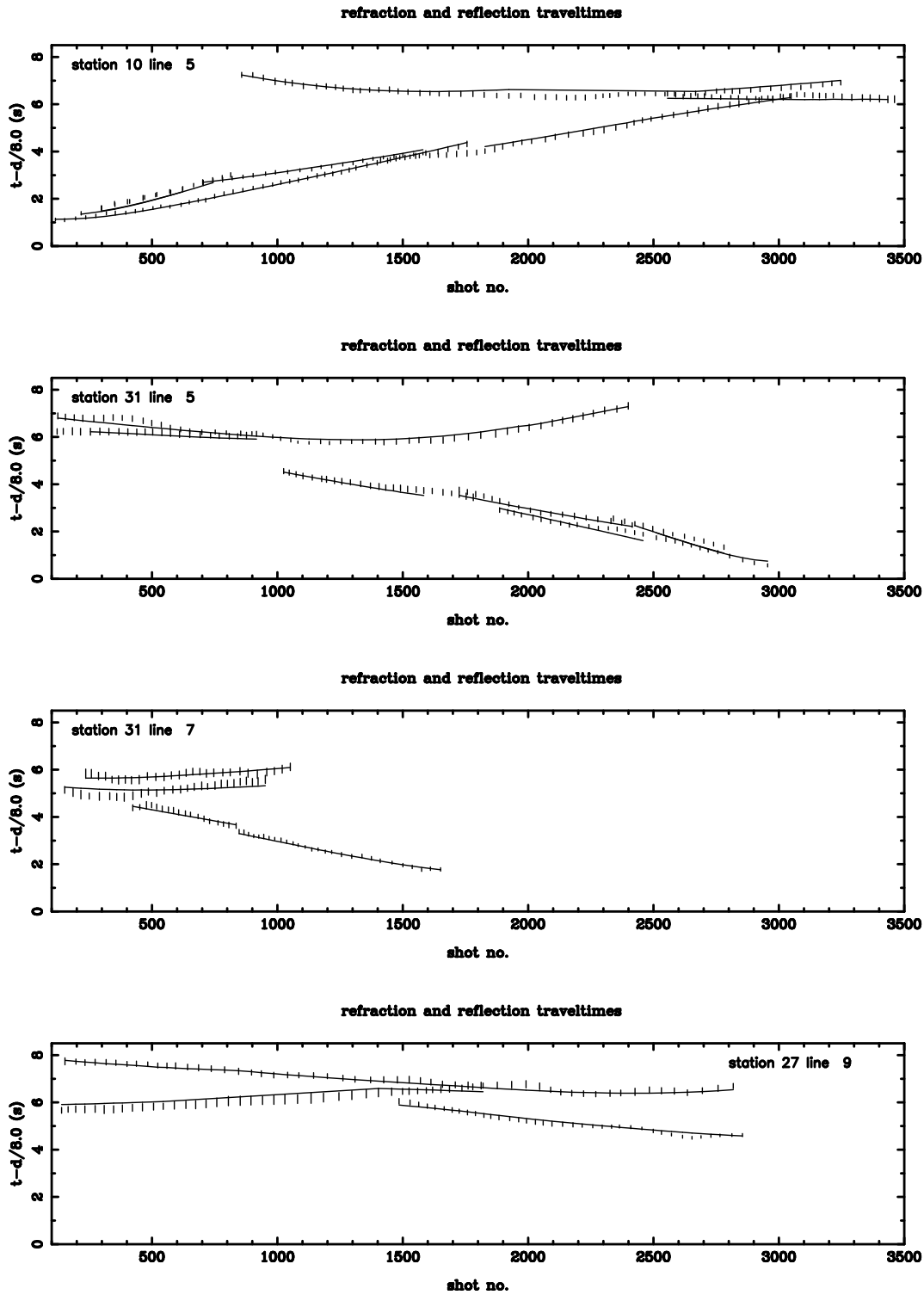

Figure 7.18: Observed and predicted traveltimes for the 3-D solution model for four different station-line combinations in NW Tasmania. Observed traveltimes are indicated by error bars and predicted traveltimes are denoted by continuous lines. c.f. Figure 7.15.

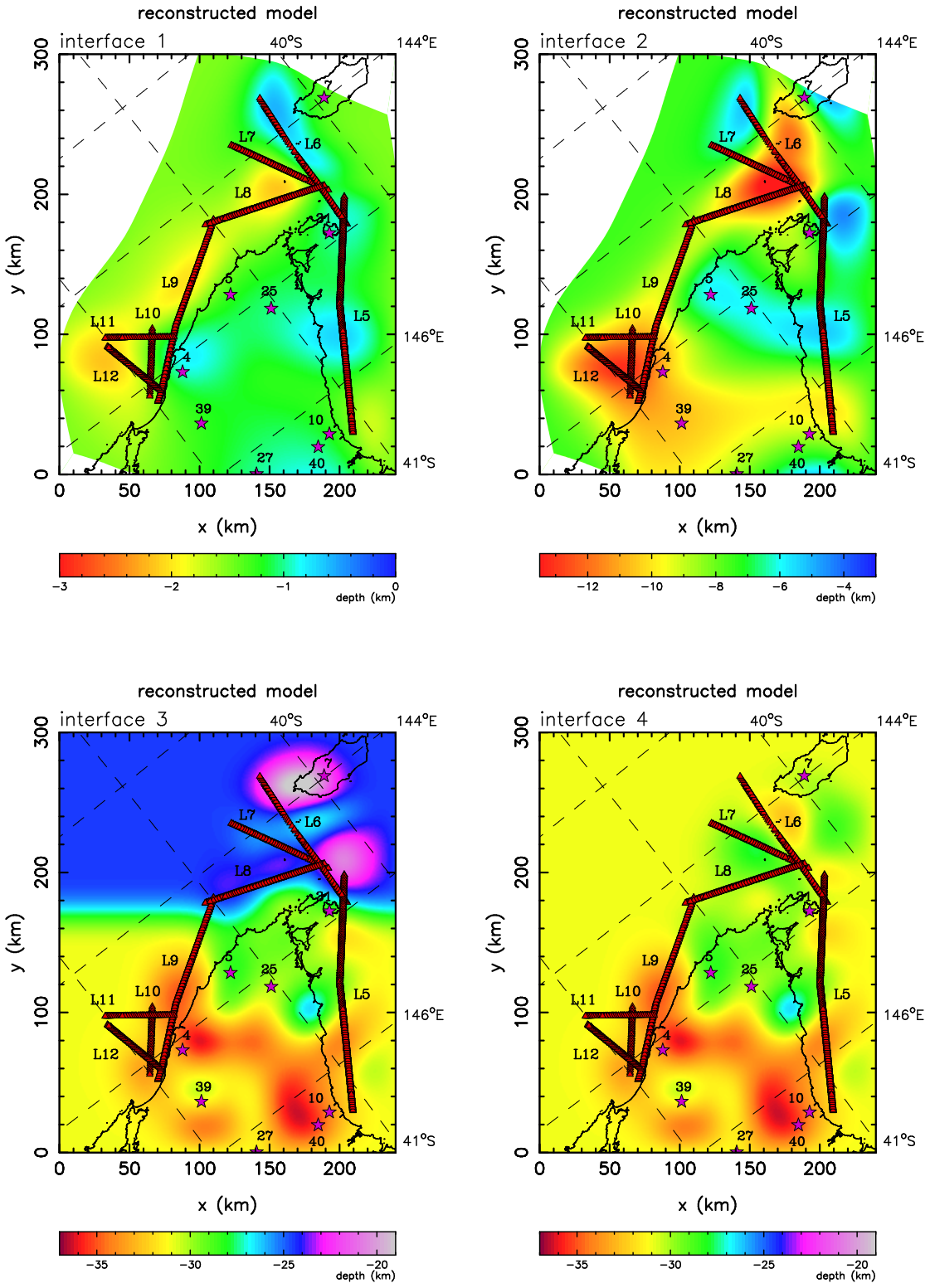

Figure 7.19: Solution model interface structure for NW Tasmania obtained after five iterations with $\epsilon = 1$. The top two interfaces are non-rectangular due to their description by an irregular mesh of interface nodes (see Figure 7.13). Picked shot points are denoted by red triangles and receivers by pink stars. Lines of latitude and longitude are indicated by dashed lines.

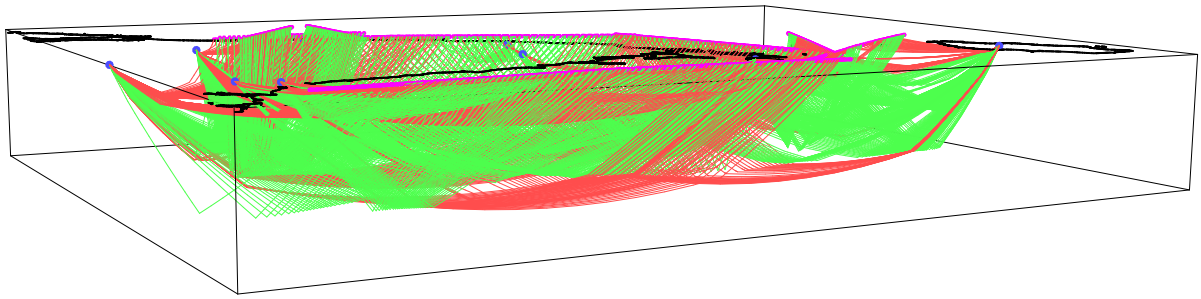

Figure 7.20: Perspective view of ray paths through the solution model of NW Tasmania. Refracted rays are shown in red and reflected rays in green. Shots are denoted by pink dots and receivers by blue dots. The attached CD contains an MPEG movie of these ray paths (Appendix F). Refer Figure 7.19 for interface geometry.

the solution model doesn't fully satisfy the data, but the misfit is relatively small and can be explained largely by shorter wavelength variations in the observed traveltime curves not being matched by the predicted traveltimes. The short wavelength variations may be due to heterogeneous near-surface structure that cannot be represented within this model parameterisation. If lateral variations in velocity of a similar length scale to the interface variations were permitted, then the data may well be better satisfied, but it is doubtful whether there is sufficient ray coverage to robustly constrain a model that contains many more parameters.

The solution model interface structure after five iterations with $\epsilon = 1.0$ is shown in Figure 7.19, and a projection of all the ray paths through the solution model is shown in Figure 7.20 (see also the MPEG movie on the enclosed CD, whose contents are described in Appendix F). The contour diagrams of Figure 7.19 clearly show the departures from the initially flat (except for the pinchout) interface structure that are introduced as the inversion process attempts to find a model that better fits the data. Regions poorly constrained by the data, such as ($x \leq 100, y \geq 100$) km on the bottom two interfaces (interfaces 3 and 4), tend not to deviate from their prior values. Consideration is now given to ray coverage and estimates of model parameter resolution.

Ray-interface intersection points for the solution model are shown in Figure 7.21 and the diagonal elements of the resolution matrix (determined at the solution point) for the interface nodes are shown in Figure 7.22. The ray-interface hit diagram (Figure 7.21) clearly shows why regions outside the array are not constrained by the data. Figure 7.22 affirms this by quantifying the formal resolution estimates. Figure 7.21 also shows that the vast majority of ray-interface hits for interface 1 occur almost directly beneath

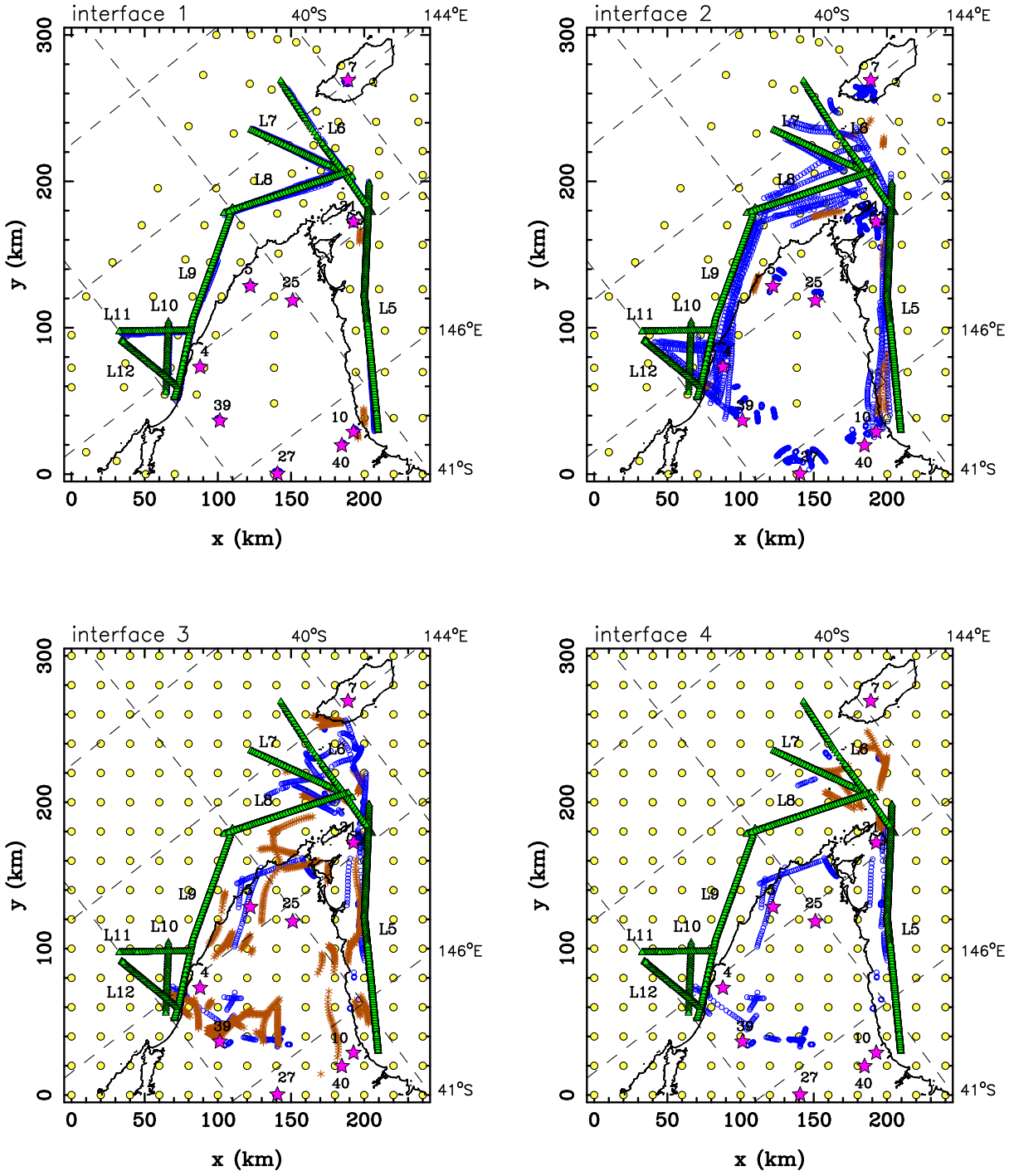

Figure 7.21: Ray-interface hit points for the solution model shown in Figure 7.19. Transmitted ray hit points are denoted by blue circles and reflected ray hit points by brown asterisks. Interface nodes are denoted by yellow dots, receivers by pink stars and picked shot points by green triangles. Interface 4 has no reflection points indicated for about $y \leq 180$ km where it coincides with interface 3.

the receivers and shot lines (in many cases, the hit point symbols are obscured by the source symbols), a consequence of the shallowness of the interface. Correspondingly, the resolution plot (Figure 7.22) shows that interface 1 is poorly resolved by the data, with

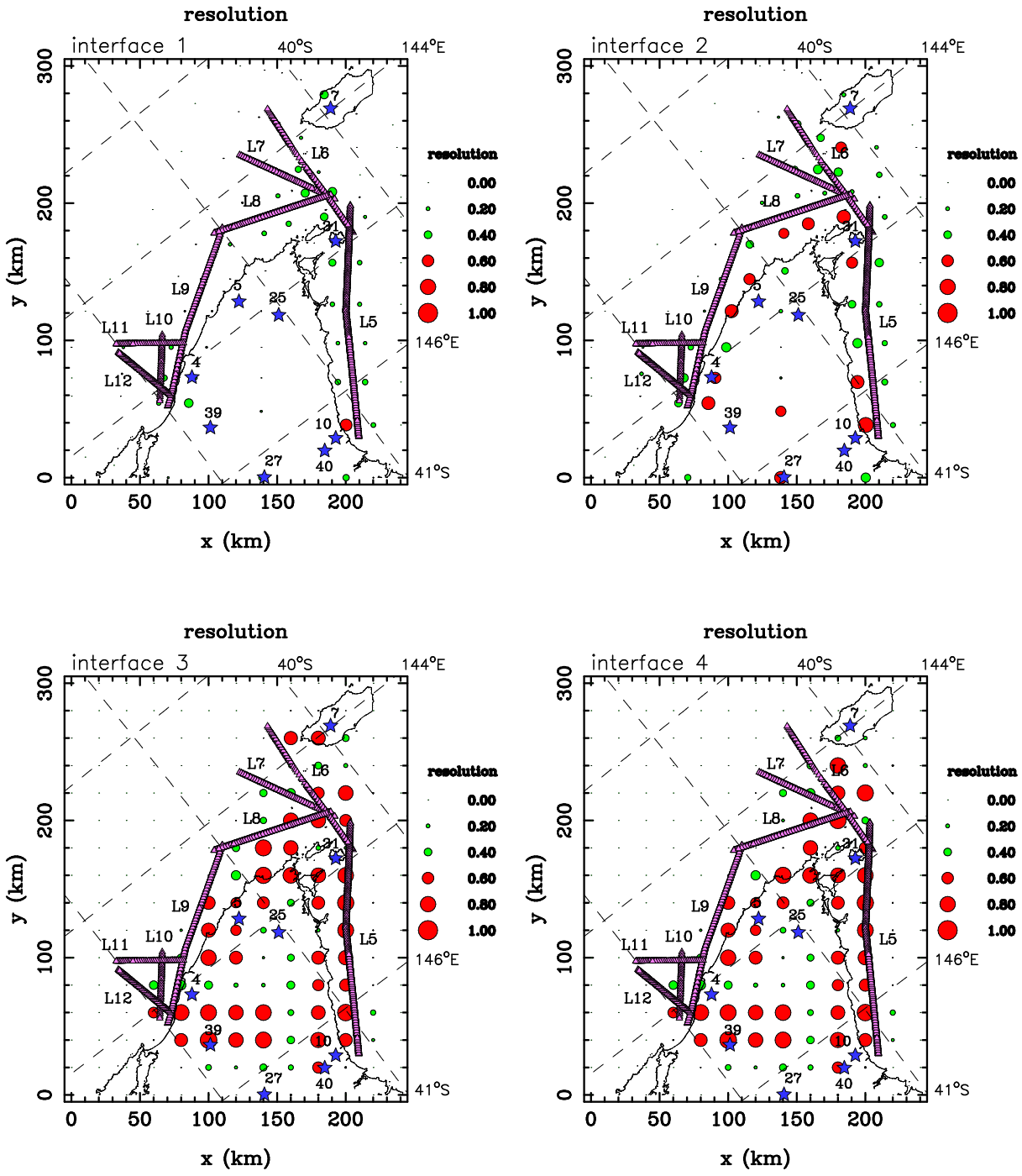

Figure 7.22: Diagonal elements of the resolution matrix for interface node depth. Resolution is calculated at the solution point. Nodes with a resolution less than 0.5 are green, while nodes with a resolution ≥ 0.5 are red. Picked shot points are indicated by pink triangles and receivers are denoted by blue stars. Lines of constant latitude and longitude are dashed.

only one parameter meeting the "well resolved" criterion of ≥ 0.5 due to the presence of reflections. Although it is poorly resolved, inclusion of interface 1 in the inversion does not effect the traveltimes of deeper phases enough to have a significant effect on the

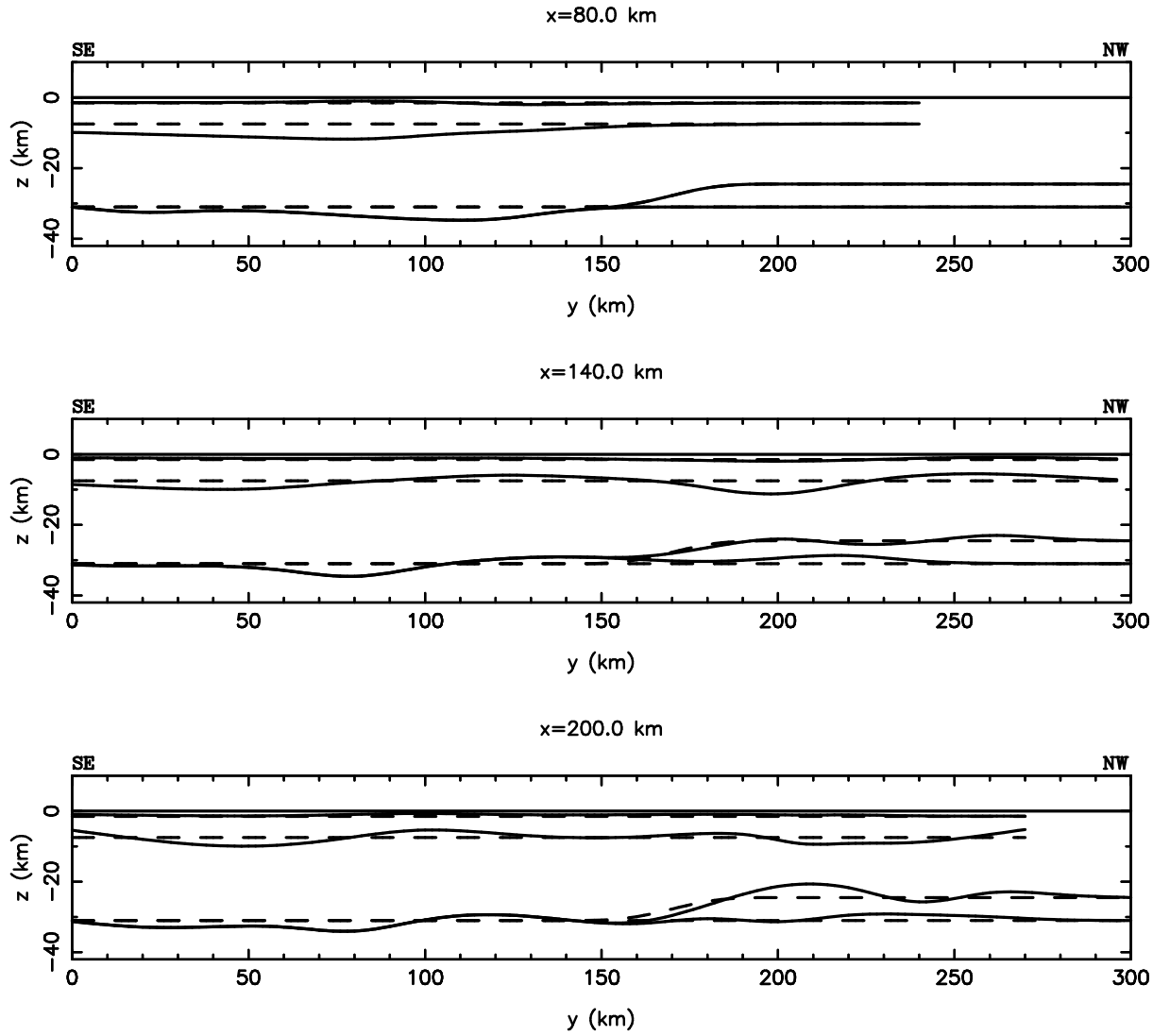

Figure 7.23: Slices at constant x through the initial (dashed lines) and solution (solid lines) model as shown in map view in Figure 7.19. Note that the upper two interfaces have a different horizontal extent than the lower two interfaces.

geometry of deeper structures, mainly because the deflections of interface 1 are of a very small amplitude (Figure 7.23). This assertion was verified by running the inversion with the upper interface nodes forced to remain at their initial depth.

Interface 2 is better resolved than interface 1 (Figure 7.22), a result consistent with the ray-interface hit diagram (Figure 7.21) which shows the paths intersecting along a broader region and a greater number of reflections. However, this interface is also predominantly constrained by transmitted rather than reflected rays and the angular coverage is poor in that the area covered by the hit points is only a relatively narrow band inboard of the shot line. Thus, the resolution is reasonable in the vicinity of the shot lines but poor

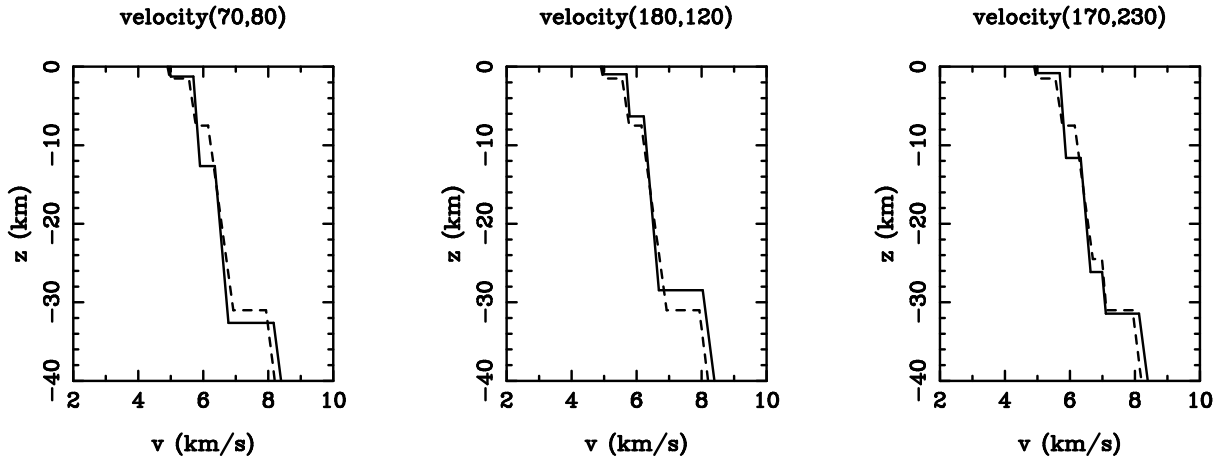

Figure 7.24: Vertical velocity variation at three points through the initial (dashed lines) and solution (solid lines) models of NW Tasmania. The (x, y) coordinates of each profile (in the plot title) indicate the location on Figure 7.19.

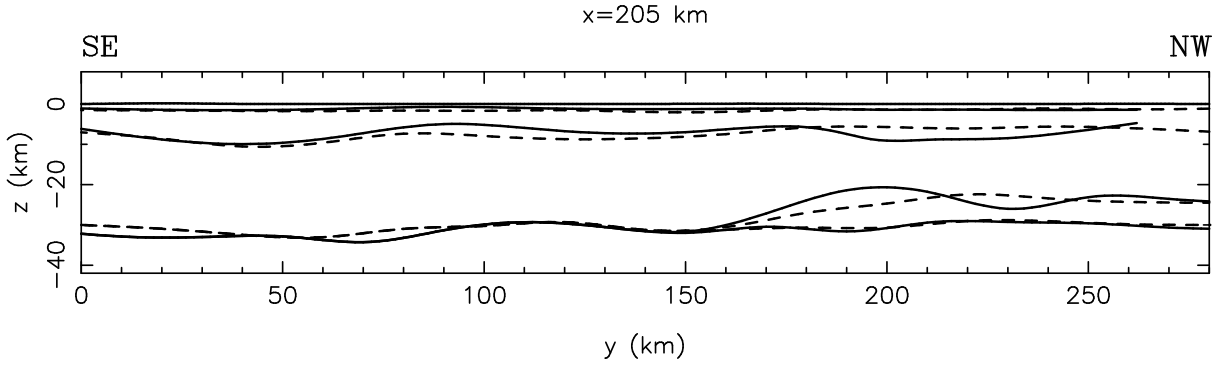

Figure 7.25: Comparison between the 2-D model (dashed lines) of the western north coast of Tasmania (Figure 7.10) and a slice through the 3-D model (solid lines) of NW Tasmania along approximately the same line. Horizontal coordinates are consistent with the 3-D model (Figure 7.19).

elsewhere. The lower two interfaces are generally well resolved within the array, although it should be noted that they coincide for approximately $y \leq 200$ km where layer 4 pinches out and therefore represent the same layer boundary in this region. The poorest interface resolution within the array occurs in the central region around $(x, y) = (150, 100)$ km. The distribution of good resolution values at this depth can be attributed to the relative profusion and good angular coverage of P_mP phases.

A comparison between the initial and final layer velocity structure is given by the three velocity versus depth profiles in Figure 7.24. The most noticeable changes in the layer velocities (Table 7.4) of the solution model compared to the initial model are the decrease in the velocity gradient of the lower crustal layer (layer 3) and the increase in velocity below the Moho. The resolution of the velocity parameters (Table 7.4) indicates

that all of the layer velocities are well resolved, but all of the velocity gradients are poorly resolved except for the velocity gradient of layer 3. The average crustal velocity of the solution model is 6.3 km/s, the average mantle velocity beneath the Moho is 8.1 km/s and the average depth of the Moho is 31 km. These values agree quite closely with the 2-D model solution (Section 7.3) and the relevant 1-D model solutions (Section 7.2), although the average P_n velocity of 8.1 km/s is 0.2 km/s greater than for the 2-D inversion solution.

Figure 7.25 compares the interface structure of the 2-D inversion solution (Figure 7.10) with the same slice through the 3-D inversion solution (Figure 7.19). The Moho structure of the 3-D model is quite similar to that of the 2-D model, but the interface that forms the upper boundary of the pinched out layer is as much as 5 km shallower near $y = 190$ km. Similarly, the interface that separates the upper crust from the lower crust is fairly similar for $y \leq 180$ km but not for $y > 180$ km. The reason for the poor misfit above $y = 180$ km is that the data poorly resolves the model in this region for the 2-D inversion (Figure 7.11), and only partially resolves it in the 3-D case (Figure 7.22); the 3-D solution has additional constraints from shot lines 6 and 8. Other factors such as the assumption of 2-D structure and the projection of the sources and receivers onto a straight line for the 2-D inversion (Figure 7.10) may contribute to the differences between these two solutions, but the close correlation between regions of the two models that are well resolved suggests that the differences arise only in those parts of the model that are not adequately constrained by the data.

7.4.2 Moho Structure of Tasmania

As shown by Table 7.3, a significant portion of picks from NW Tasmania are of reflected rays from the Moho (P_mP phases). Data from the remainder of Tasmania also have Moho reflections as the predominant observable phase type. As the next step in constructing a crustal structure model for all of Tasmania, I now describe a 3-D inversion in which all picked P_mP and P_n phases from the TASGO dataset are used to constrain a two-layer model. The crust is represented as a single layer in this inversion and is described by two velocity parameters (velocity v_o and velocity gradient k) and a Moho of variable depth. I later test the validity of this assumption by comparing the Moho structure of the Tasmanian Moho model with the Moho structure of the five layer (including the mantle half space) NW Tasmania solution model described above. While crustal phases

are observed outside NW Tasmania, coverage is very poor and the inclusion of crustal interfaces will result in a poorly constrained solution, as demonstrated below.

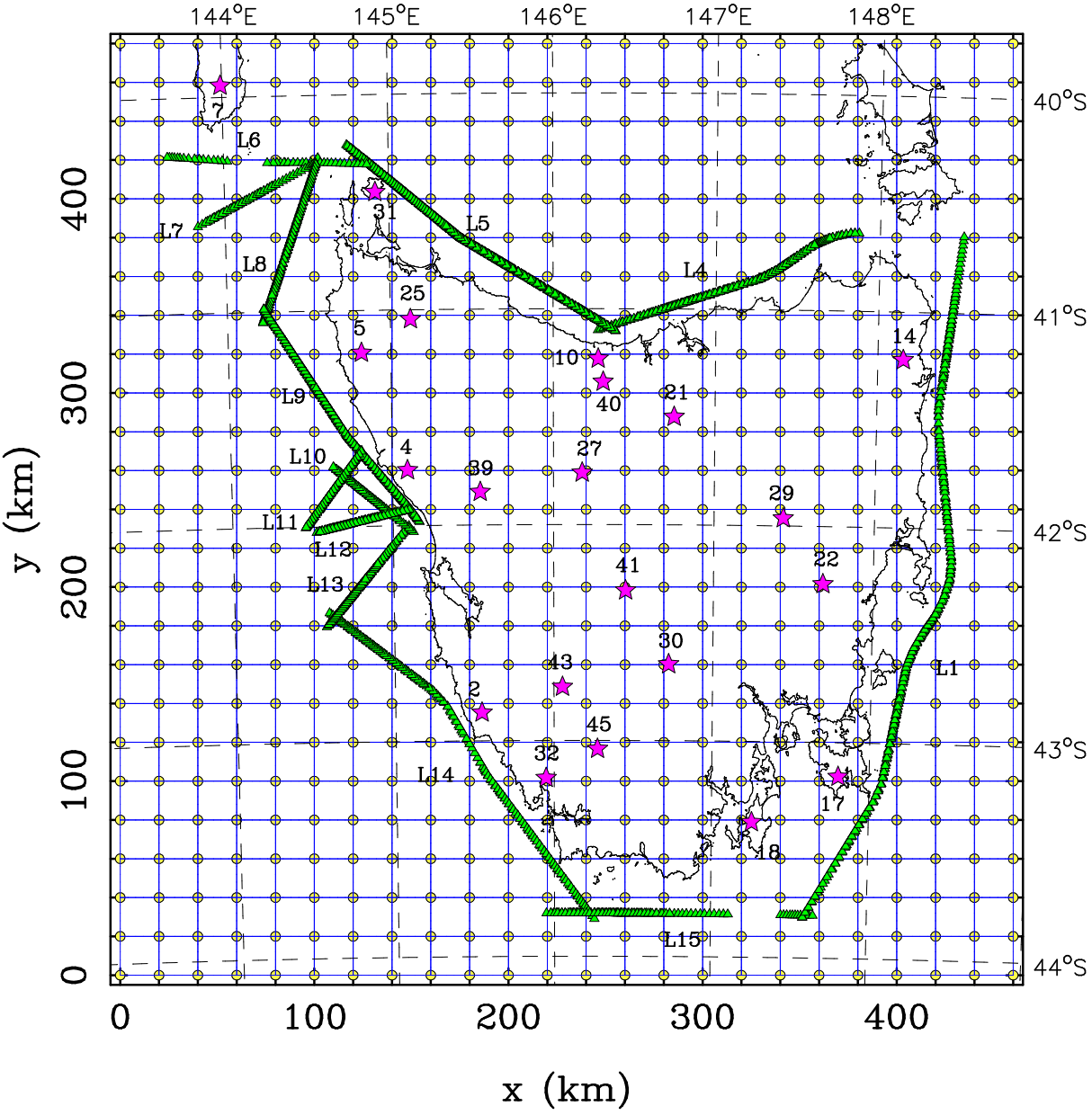

Figure 7.26: Source-receiver array used in the inversion for the Moho structure of Tasmania. Pink stars denote receivers and green triangles denote picked shot points. Gaps in the shot lines (e.g. the eastern end of line 4) occur because no traveltimes could be picked for these shots. Also shown are the grid of nodes (yellow dots) and associated patch boundaries (blue lines) used to describe interface structure. Dashed lines represent lines of constant latitude and longitude.

In the inversion for Moho structure, P_mP and P_n traveltimes from 13 shot lines to 21 receivers (Figure 7.26) are employed. Data from the remaining receivers either do not

layer	initial model		recovered model		resolution	
	v_0 (kms^{-1})	k (s^{-1})	v_0 (kms^{-1})	k (s^{-1})	v_0	k
1	5.70	0.033	6.10	0.009	0.99	0.32
2	7.00	0.030	7.17	0.028	0.96	0.29

Table 7.5: Velocity parameter values of the initial and final 3-D model of the Tasmanian Moho. The resolution values associated with the recovered model are also given. Layer 1 is the crustal layer and layer 2 is the mantle half-space. Note that the actual velocity at a given depth is defined by Equation 4.1.

exist due to recorder failure or timing problems, or were unable to be picked due to poor signal-to-noise ratio. A total of 2590 traveltimes, consisting of 2148 P_mP arrivals and 442 P_n arrivals, are used in the inversion. The RMS picking error of these traveltimes is 143 ms, somewhat greater than the 125 ms RMS picking error of the set of traveltimes used in the inversion for the crustal structure of NW Tasmania. This increase is expected because: (i) the source-receiver offsets are larger, (ii) the P_mP phase does not occur as a first arrival, and (iii) the P_n phase has a relatively small amplitude at large offset.

A model with 1-D structure, based on the results of the set of 1-D inversions (see Section 7.2), is used as a starting model for this 3-D inversion. The Moho depth of the starting model is 30 km, and the crust and mantle velocity parameters are specified in Table 7.5; the average velocity of the crust in the initial model is 6.2 km/s and the P_n velocity is 7.9 km/s. The *a priori* uncertainties associated with interface depth, velocity and velocity gradient are estimated as 3 km, 0.3 km/s and 0.002 s^{-1} respectively. To describe interface structure, a rectangular grid of 600 nodes spaced 20 km apart in both x and y is used (Figure 7.26). Although many of the grid nodes lie outside the array (Figure 7.26), a regular grid was simplest to implement, and the computational cost of additional unconstrained nodes was not significant. A comparison between observed traveltimes and traveltimes predicted for the initial model for 10 station/line combinations is given in Figure 7.27. In all cases, except station 43/line 13, significant adjustments to the model are required before model traveltimes match observed traveltimes. The P_mP phase recorded at station 17 from line 1 is the most poorly matched of the 10 examples; all model traveltimes are over one second greater than the observed traveltimes in this case. The RMS traveltime residual associated with the initial model is 371 ms.

Similar to the NW crustal inversion (Section 7.4.1), ray tracing through the model is

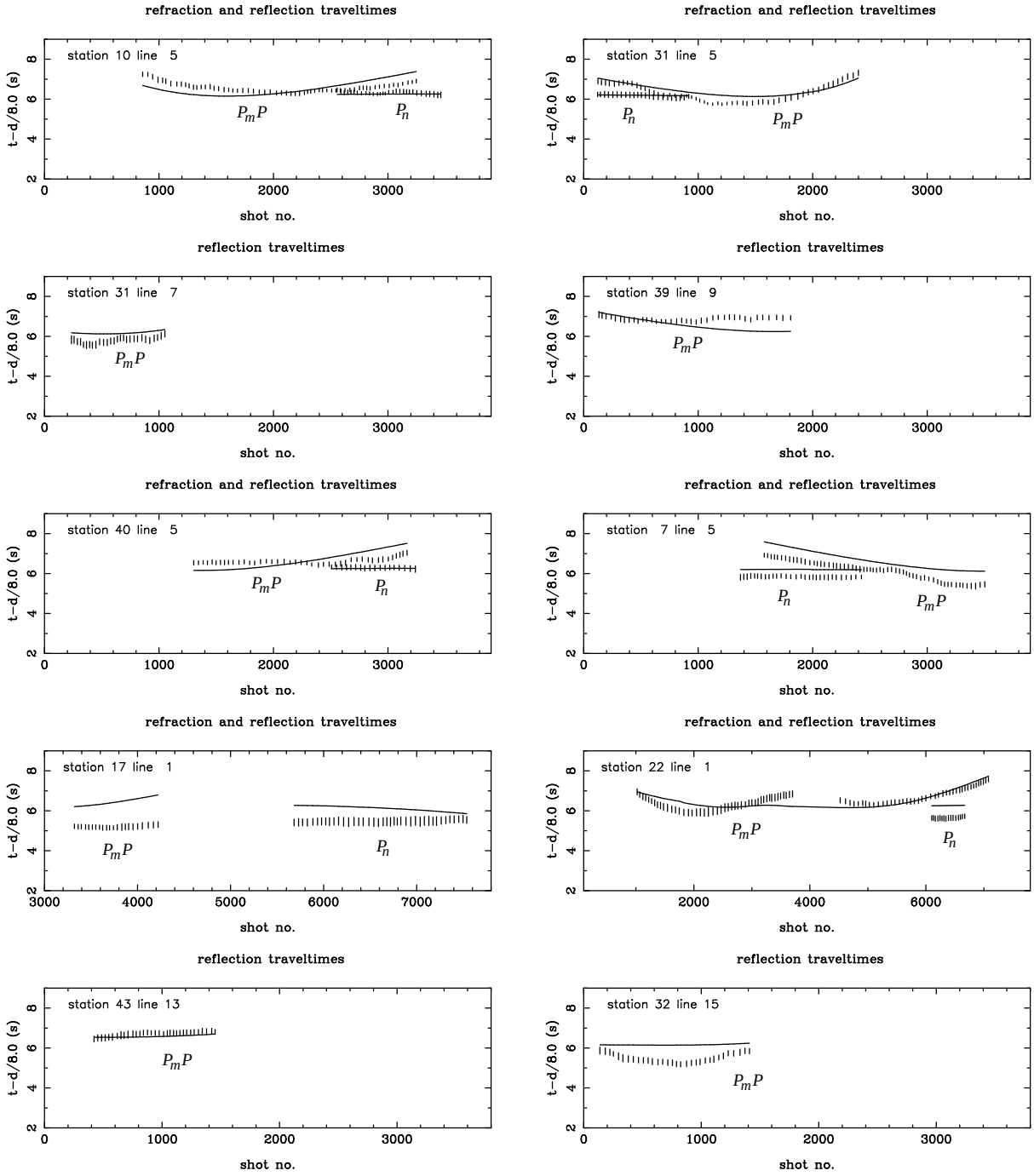

Figure 7.27: Comparison between observed traveltimes (error bars) and initial model predictions (solid lines) for 10 representative station-line combinations used in the inversion for Tasmanian Moho structure.

performed with all shot points at sea level ($z = 0$) and all receivers at their measured heights above sea level. Of the 21 stations used, station 39 has the greatest elevation at 975 m (see Table 5.1). In this inversion, the dimension of the subspace was set to 14. Of these, ten basis vectors lie in interface depth parameter space, two span velocity

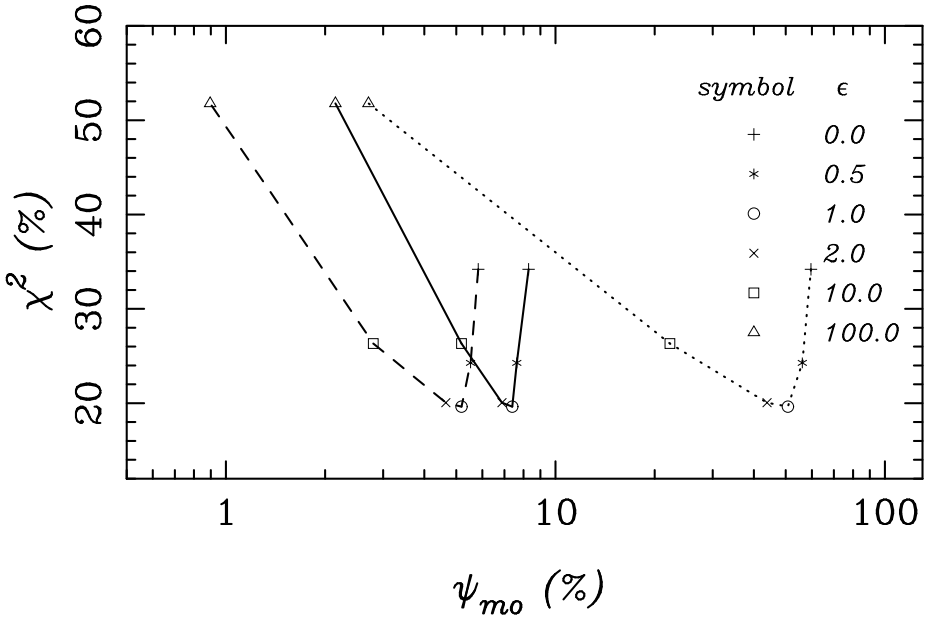

Figure 7.28: Data inversion trade-off curves for various values of the damping factor ϵ after four iterations of the inversion for the Moho structure of Tasmania. The two misfit measures χ^2 and ψ_{mo} (Equation 4.21) are plotted as a percentage of their initial values (i.e. at iteration zero). The model perturbation ψ_{mo} is determined separately for each parameter type: interface node depth (solid line), layer velocity (dashed line) and layer velocity gradient (dotted line).

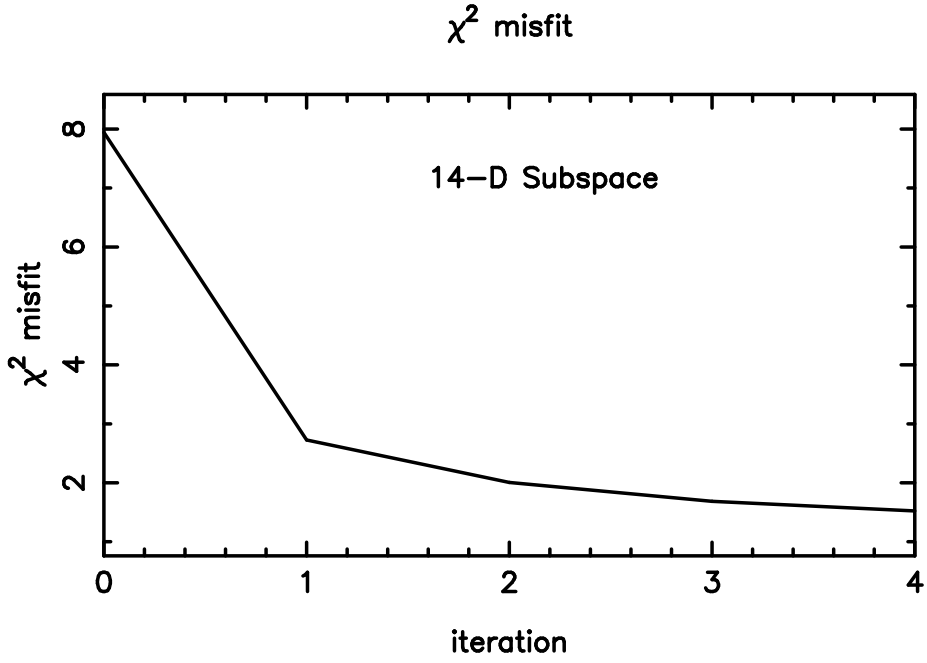

Figure 7.29: χ^2 misfit versus iteration number for the inversion (using $\epsilon = 1.0$) of P_n and P_mP traveltimes for the Moho structure of Tasmania.

parameter space and two span velocity gradient parameter space, resulting in an acceptable compromise between rate of convergence and computational effort. The value of the

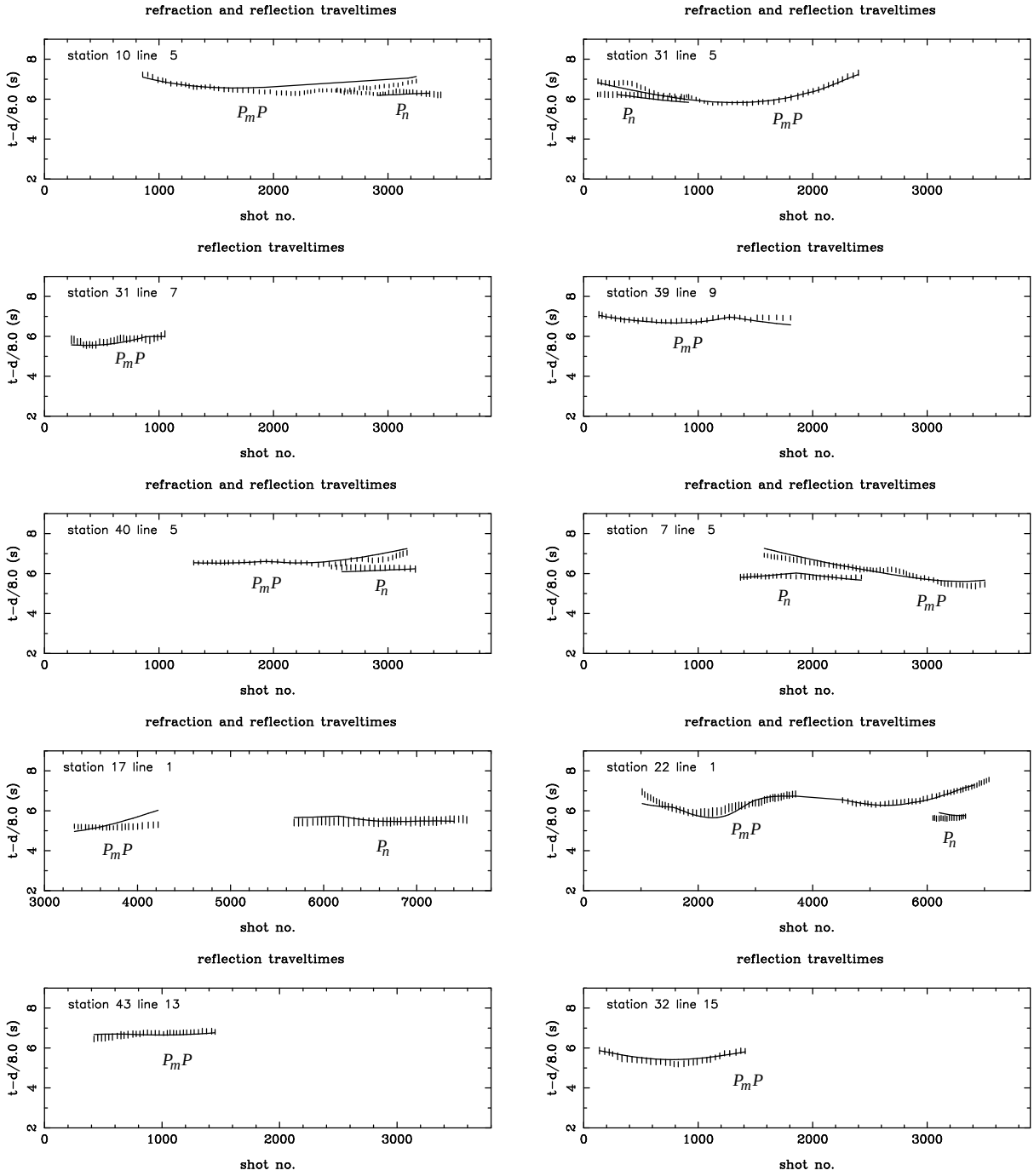

Figure 7.30: Comparison between observed traveltimes (error bars) and solution model predictions (solid lines) for 10 representative station-line combinations used in the inversion for the Moho structure of Tasmania.

damping parameter was set to $\epsilon = 1.0$ on the basis of the trade-off curves shown in Figure 7.28; this value of ϵ provides the optimum choice in terms of minimising χ^2 and ψ_{mo}. The plot of χ^2 data misfit versus iteration (Figure 7.29) for $\epsilon = 1.0$ decreases monotonically from its initial value of $\chi^2 = 7.94$ to $\chi^2 = 1.52$ after four iterations. Subsequent iterations

resulted in only superficial changes to the χ^2 value. The RMS traveltime residual of the solution model after four iterations is 176 ms, which represents a 53 % decrease in RMS residual relative to the initial model. The improved fit is evident in the comparison of Figure 7.30, which shows observed traveltimes and solution model predictions, with the corresponding graphs that show observed traveltimes and initial model predictions (Figure 7.27). The reflection phase for station 17/ line 1 data is still not well matched by the solution model predictions, but the fit is improved relative to that of the initial model. Although most of the picked arrivals shown in Figure 7.30 are quite accurately matched by this relatively simple single interface model, those arrivals for which significant misfit is observed may well indicate lateral variation of structure within the crust. These misfits are few, however, and a more complex crustal model is hard to justify purely on this basis.

Figure 7.31 shows the Moho structure of the solution model after four iterations with $\epsilon = 1.0$. Ray-interface hit and resolution diagrams are provided in Figure 7.32 and Figure 7.33 respectively. There is a close correlation between the ray-interface hit diagram and the resolution plot. Resolution is best in NW Tasmania where the concentration of ray hits is greatest. A zone of poor resolution extends from central Tasmania to the NE (Figure 7.33), which explains why the solution model (Figure 7.31) does not vary from the initial model in these regions. Similarly, outside the array, the resolution rapidly drops to zero and correspondingly, the Moho depth assumes its initial value. Using a resolution criterion of 0.5 (i.e. structure associated with a resolution greater than 0.5 is well constrained), most of NW Tasmania is well resolved except for a small patch beneath station 25. The remainder of Tasmania is not very well resolved, except for limited regions along the SW and southern coasts and at two regions along the east coast. Figure 7.34 shows four cross-sections at constant x through the final and initial models. Flat portions of the Moho that overlie the initial model are usually not well resolved by the data. The average depth of the Moho beneath the Tasmanian crust as predicted by the resolved portion of the Moho-only crustal model is about 31 km. The posterior uncertainty in Moho depth estimated by C_M varies between 1.0 and 1.4 km in well resolved regions of the solution model; this is substantially reduced from the *a priori* estimate of 3 km. However, as cautioned by both Zelt & Smith (1992) and Wang & Braile (1996), these uncertainty estimates are best considered in a relative rather than absolute sense. The sensitivity of the average depth of the Moho to its initial depth estimate was tested by

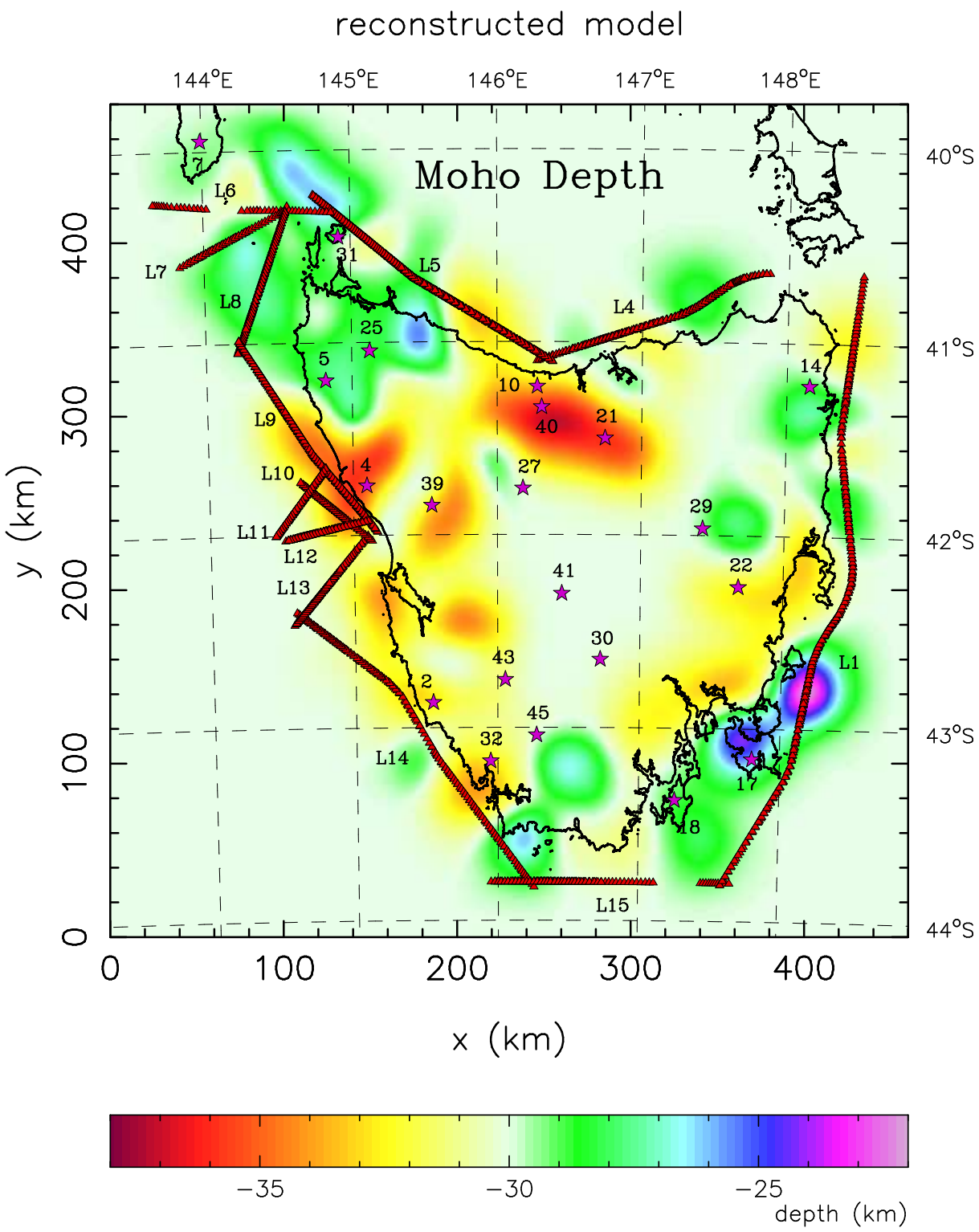

Figure 7.31: Moho depth of the solution model derived by inversion of all picked P_n and P_mP phases. Pink stars indicate receivers and red triangles indicate picked shot points. Regions where there is no data coverage tend to be unperturbed from the initial Moho depth of 30 km. Dashed lines indicate lines of constant latitude and longitude.

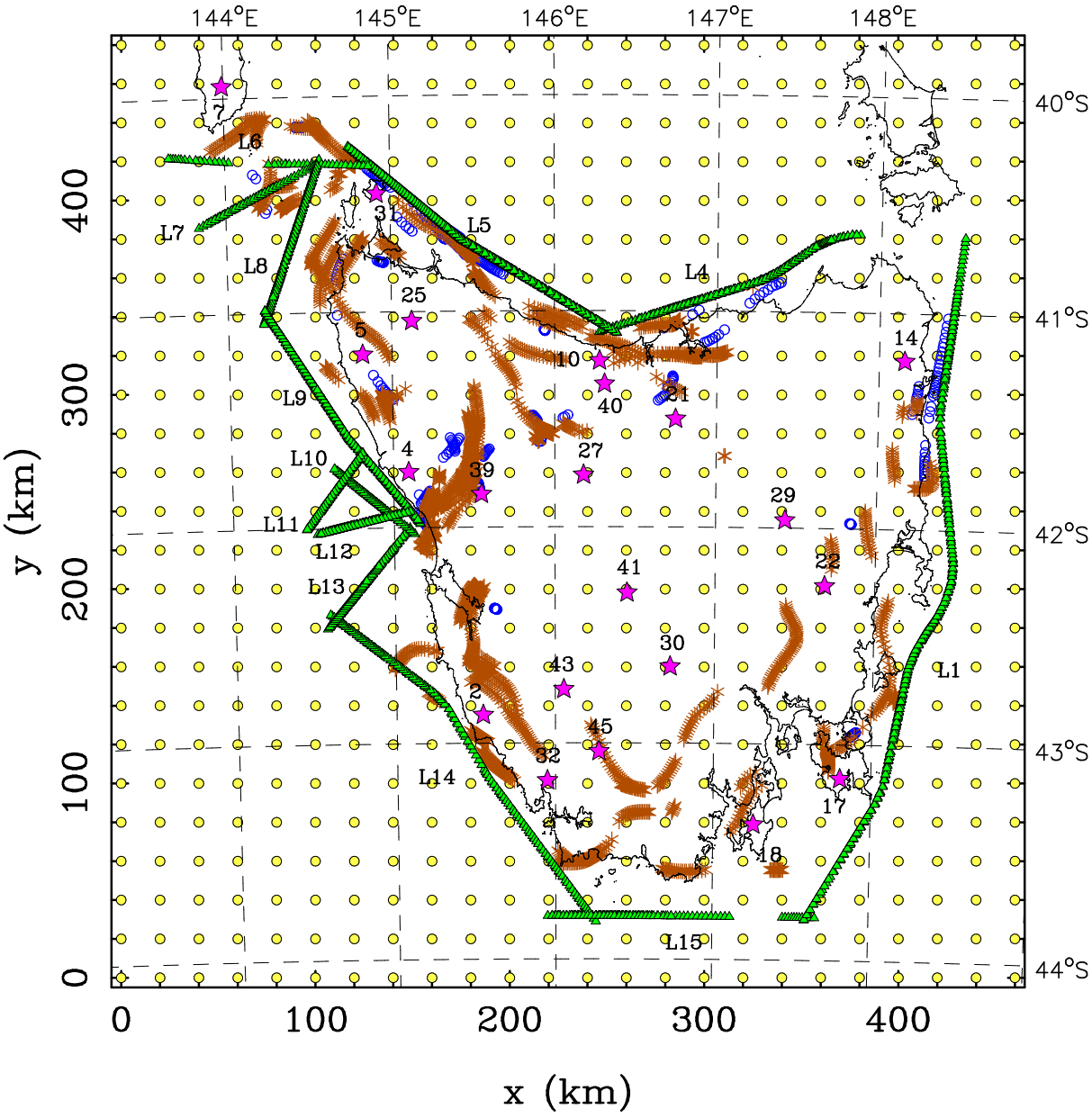

Figure 7.32: Ray-interface hit points for the solution model shown in Figure 7.31. Transmitted ray hit points are denoted by blue circles and reflected ray hit points by brown asterisks. Interface nodes are denoted by yellow dots, receivers by pink stars and picked shot points by green triangles.

using initial models with Moho depths of 29 km and 31 km. In both cases, the average depth in well resolved regions of the solution was 31 km, suggesting that this value is robust.

The crust and mantle velocity parameters of the solution model are shown in Table 7.5 along with their resolution values. In keeping with results from the NW Tasmania inversion (Table 7.4), the velocity parameters are well resolved and the velocity gradient parameters are poorly resolved. It is not particularly surprising that the velocity gradient

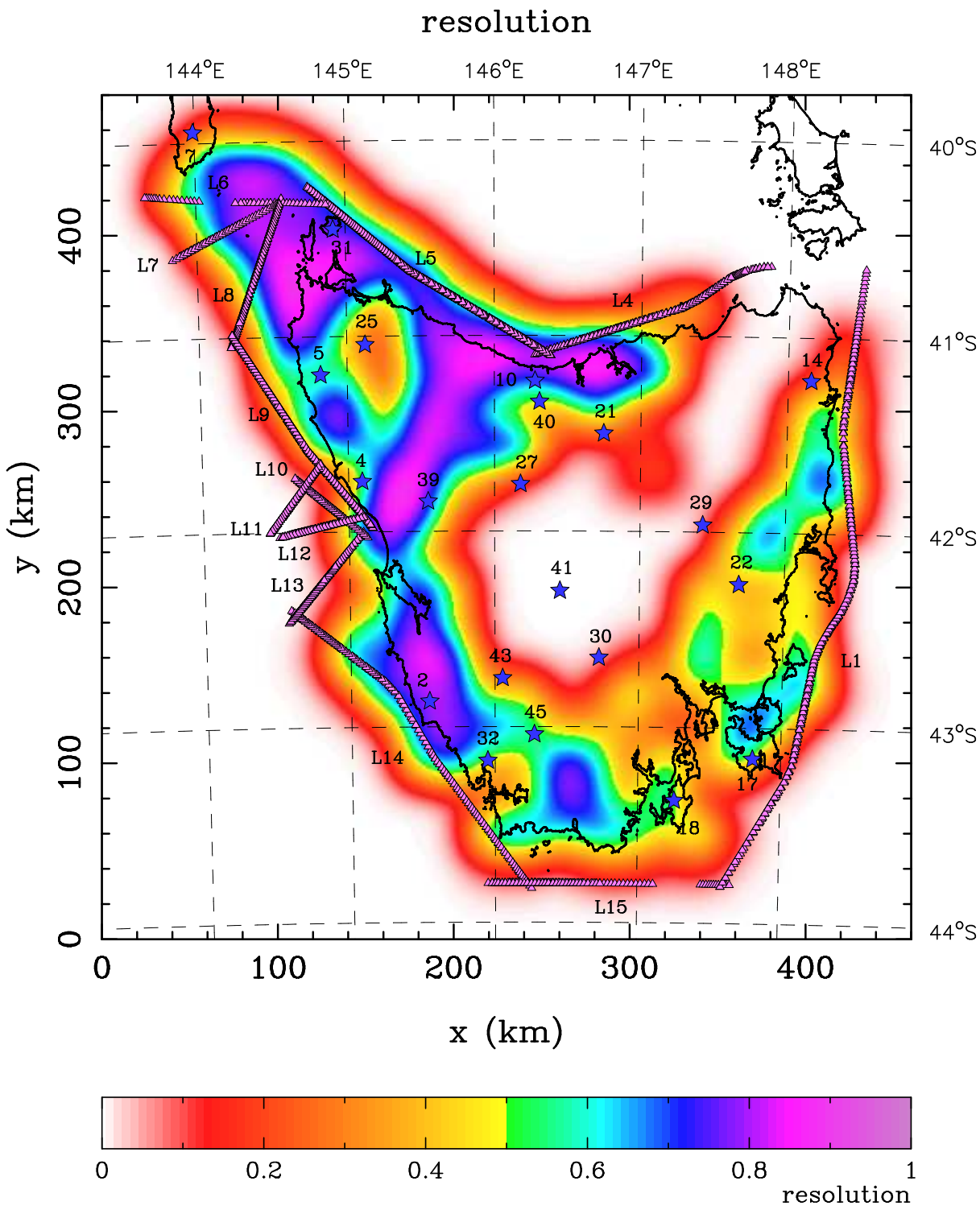

Figure 7.33: Contours of the diagonal elements of the resolution matrix for Moho depth parameters of the Figure 7.31 model. The discontinuity in the colour scale at 0.5 is introduced to highlight regions of good resolution (i.e. ≥ 0.5). Blue stars indicate receivers and pink triangles indicate picked shot points.

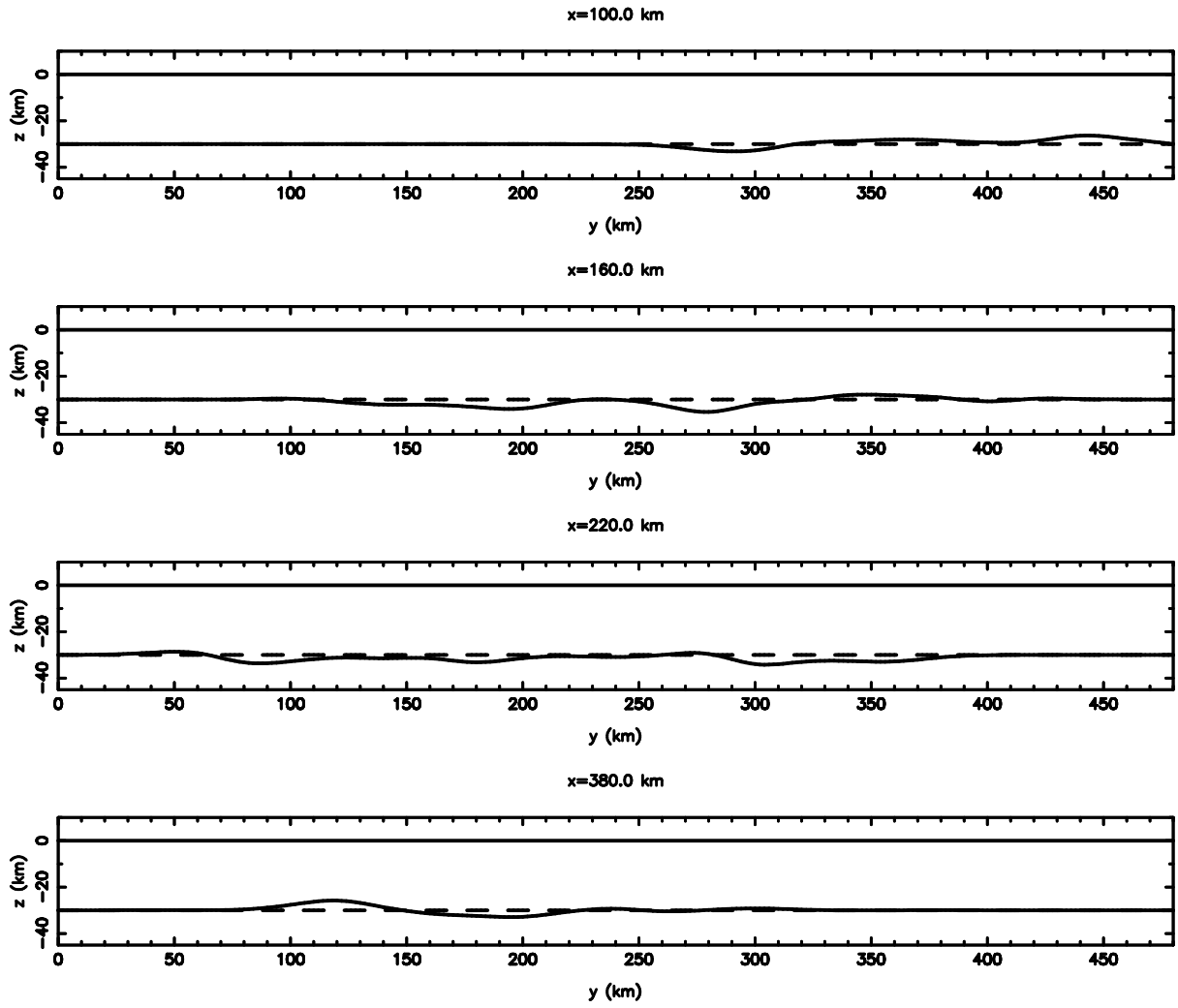

Figure 7.34: Four cross-sections at constant x through the initial (dashed line) and solution (solid line) model. Refer Figure 7.31 for line locations.

of the crust is poorly resolved since no refracting rays are included that turn in this layer. The average crustal velocity of 6.24 km/s and average P_n velocity of 8.0 km/s are, however, consistent with previous inversion results described above. Velocity versus depth profiles at six places through the model are shown in Figure 7.35. The relatively low crustal velocity gradient of 0.0094 s^{-1} is not a well constrained component of the solution, but the average crustal velocity appears to be robust.

The above discussion considers the robustness of the solution from the point of view of how well the parameters of a particular model are constrained by the data. However, model accuracy is also influenced by the assumptions made in the representation of structure. In this case, the crust is defined as a single layer whose velocity is described by only two parameters. Lateral variations in velocity within the crust may result in an inaccu-

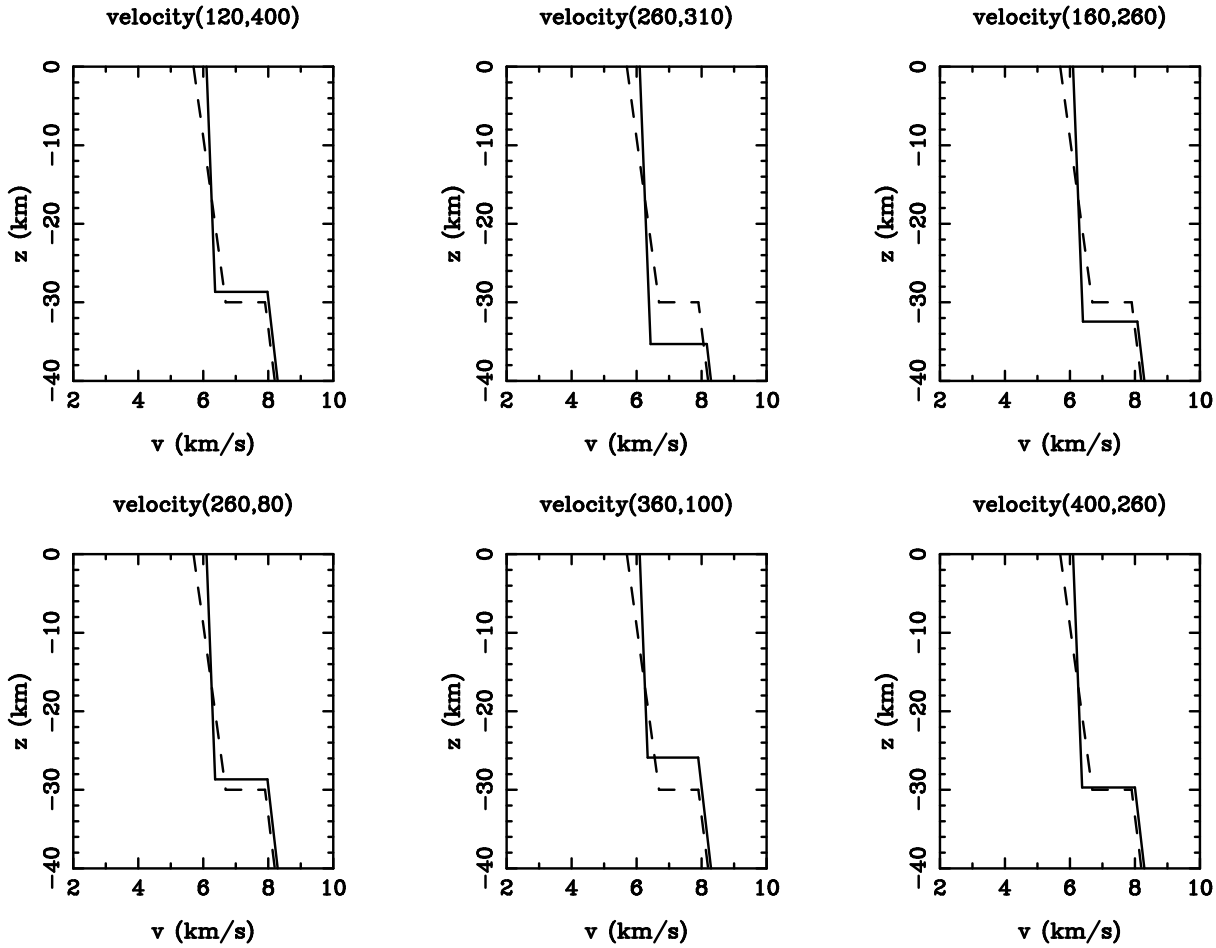

Figure 7.35: Six velocity versus depth profiles through the initial (dashed line) and final (solid line) models of Tasmanian Moho structure. Refer Figure 7.31 for profile locations given by the title of each plot in (x, y) coordinates.

rate image of the true Moho, even in regions that are shown as well resolved in Figure 7.33. A comparison of the Tasmanian Moho model (Figure 7.31) with the Moho structure (interface 4) of the NW Tasmania model (Figure 7.19) shows a very close resemblance despite the much simpler crustal structure assumed in the all-Tasmania Moho inversion. The main feature of the Moho in this region, apparent in both solution models, is a decrease in crustal thickness from about 33-36 km in the SE to 26-29 km in the NW. The zone of thickened crust in the vicinity of stations 10 and 40 in Figure 7.31 is also present in Figure 7.19, although it does not extend as far eastward in the latter case, presumably because data from station 21 were not included in the inversion for NW Tasmania crustal structure.

At shorter wavelengths, the two patterns of Moho depth variations are also similar, with minor exceptions such as the Moho beneath the NW end of Line 5, which is shown to

be 26-27 km deep in Figure 7.31 but about 30-32 km deep in Figure 7.19. This difference can be attributed to the lower crustal layer that pinches out in Figure 7.19. Laterally, this is a zone of high velocity (see Figure 7.24), and is locally thick beneath the end of line 5. Therefore, rays that penetrate this region travel more quickly, which suggests why the Moho-only model (Figure 7.31) exhibits a relatively shallower Moho in this region. Another minor difference occurs near the relatively shallow almost linear feature between stations 4 and 39 (Figure 7.31) in the Moho-only model. While this local shallowing of the Moho west of station 39 also appears in the NW Tasmania inversion solution, it appears 2 km deeper and is truncated to the west by a local depression in the Moho near the southern end of line 9. This difference may be due in part to the omission of data from line 13 in the NW Tasmania inversion. Overall, however, the comparison between the Moho structure of the two models shows that inverting only phases from the Moho and ignoring lateral variations in crustal structure seems to result in a relatively accurate Moho map.

Assuming a laterally invariant crust when inverting P_mP and P_n phases for Moho structure is apparently valid in NW Tasmania, but the validity of this approach for the rest of Tasmania can also be tested. To do so, an inversion was performed using all the picked data except phases associated with the sediment layer (layer 1) and the lower crustal layer that pinches out (layer 4) in NW Tasmania (Figure 7.19). Most of the data from outside NW Tasmania suggest a two layer crust, so the phases associated with these crustal layers along with all the P_n and P_mP phases used above to constrain the Moho model are utilised. The total number of traveltimes used in this inversion is 4746, of which 2243 are refractions and 2503 are reflections. The initial model has 1-D structure and consists of two crustal layers overlying a mantle half space. The depth to the Moho was set to 30 km and the depth of the mid-crustal interface was set to 8.5 km. Each interface is defined by 600 interface nodes spaced a uniform 20 km apart in both x and y dimensions (as in Figure 7.26). A total of 1206 interface and velocity parameters were therefore constrained by the inversion of the 4746 traveltimes.

Using a 16-D subspace inversion and a damping value of $\epsilon = 1.0$, the RMS misfit function was reduced from an initial value of 462 ms (χ^2=13.5) to a final value of 216 ms (χ^2=2.7) after four iterations. In this case, the data fit indicated by χ^2 is significantly poorer than that of the Moho-only solution model (for which $\chi^2 = 1.5$), but the Moho depth distribution (Figure 7.36a) is very similar to that of Figure 7.31. The resolution of

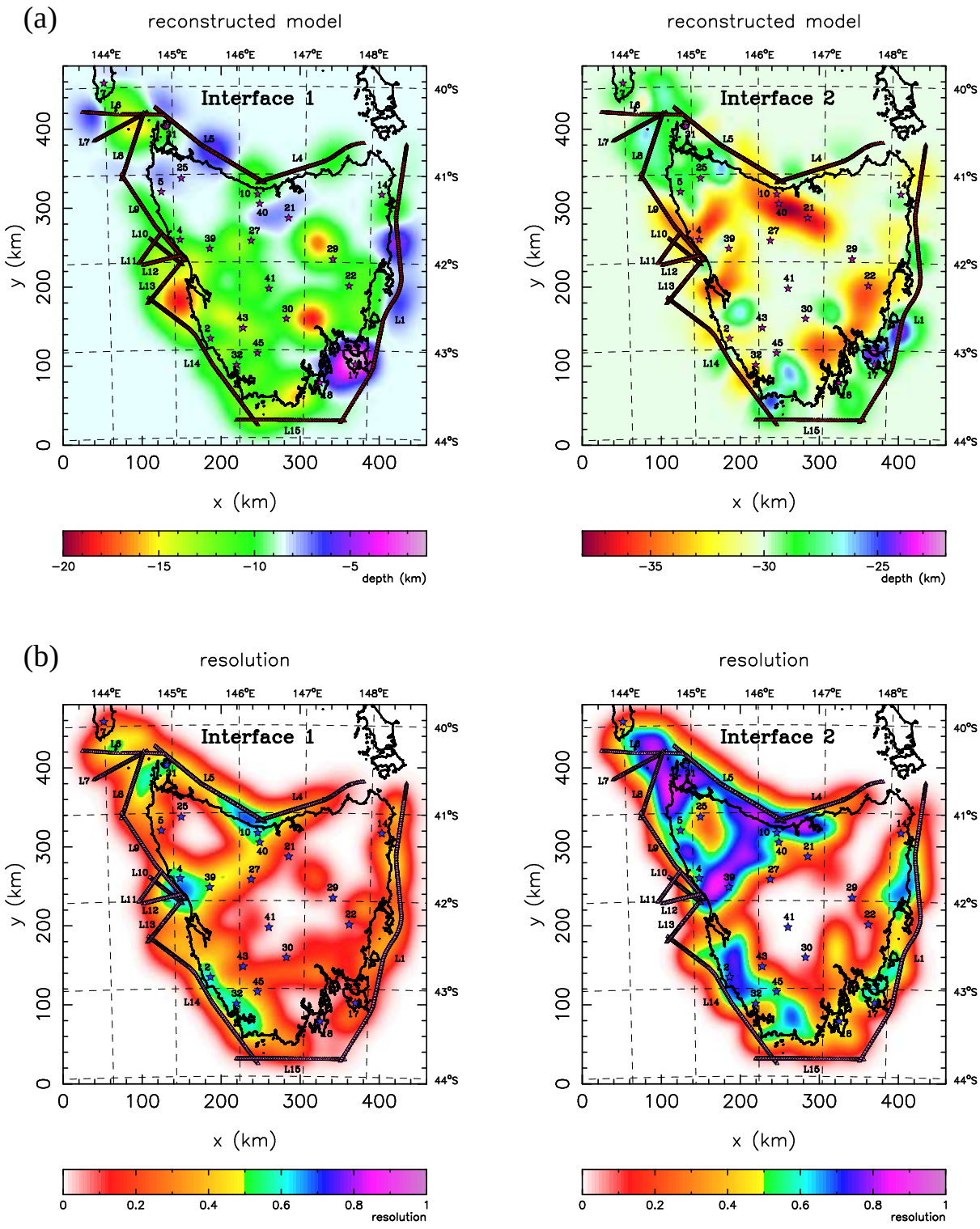

Figure 7.36: Results of the inversion using a two-layer representation of Tasmania's crust. (a) Interface depth variations of the mid-crustal interface (interface 1) and the Moho (interface 2) (c.f. Figure 7.31). (b) Contoured resolution values for each of the interfaces shown in (a) (c.f. Figure 7.33). Stars indicate receivers and triangles indicate picked shot points in both cases.

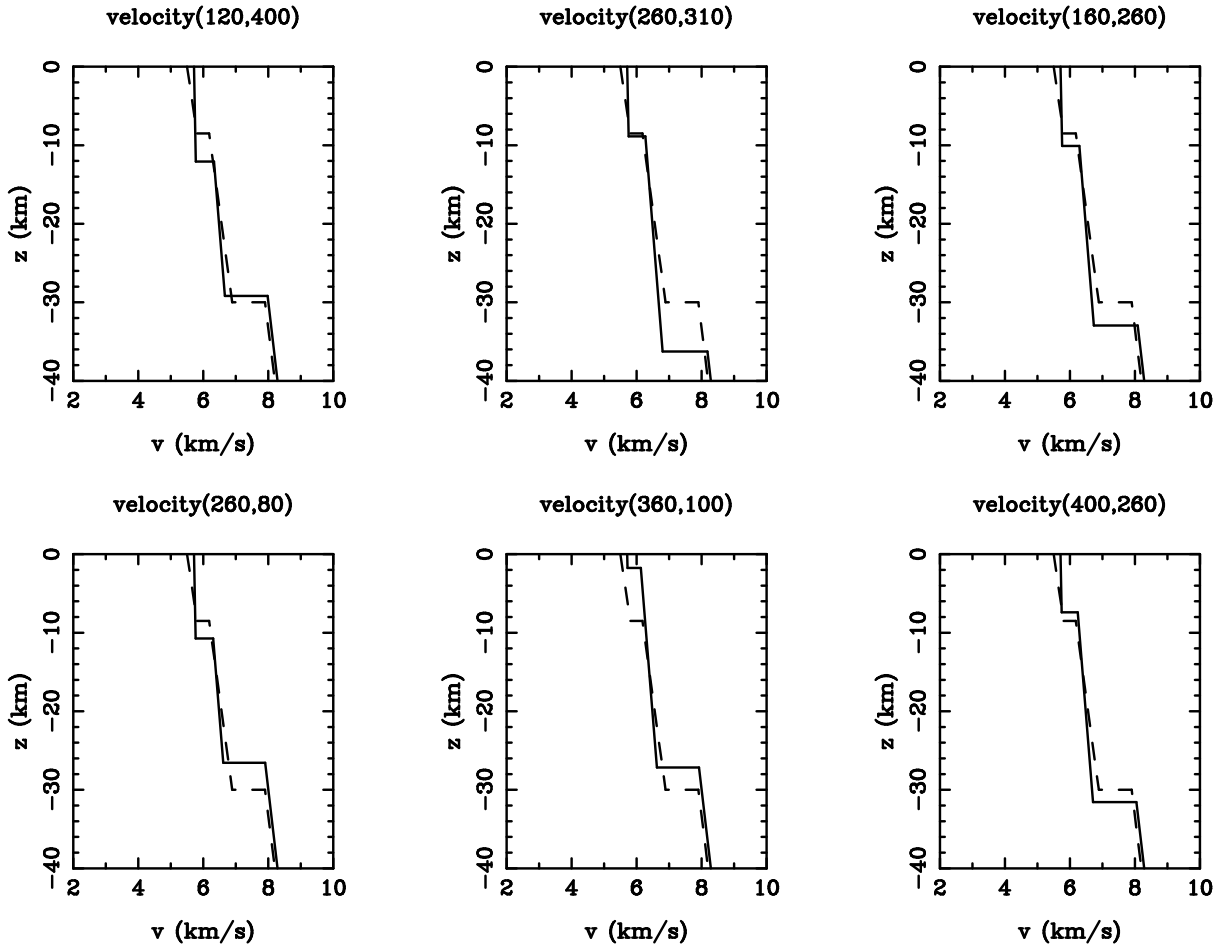

Figure 7.37: Six velocity versus depth profiles through the initial (dashed line) and solution (solid line) models from the inversion for the two-layered crustal structure of Tasmania. These profiles correspond in position to those of Figure 7.35 for the Moho-only model.

interface 1 in the two-interface inversion is generally poor (Figure 7.36b), but the large fluctuations in depth of this interface do not seem to cause major differences in the Moho structure compared to the single-interface inversion solution (Figure 7.31), even though the velocity contrast across interface 1 is significant (Figure 7.37). One discrepancy is the thinner crust (about 26 km) just NW of station 43 (Figure 7.36a); in (Figure 7.31), the corresponding depth is about 30 km. A similar mismatch occurs just east of station 30, but the interfaces in both inversion solutions are not well resolved by the data in this region. Elsewhere, the relative locations of local maxima and minima are generally well matched.

The reason for the relatively poor data misfit of the two-interface inversion is mainly due to mismatches between the shallow (P_1) phases. In particular, for station 17/line 1 (Figure 6.17) the traveltime of the P_1 phase for shot 2100 is about 4.45 s (0.82 s

reduced time) for a source-receiver offset of 29 km. The traveltime of the P_1 phase for station 10/line 5 data (Figure 6.16) at shot 395, which also occurs at an offset of about 29 km, is about 5.38 s (1.75 s reduced time), which is nearly 1 s greater. Hence, the near-surface crustal velocity in the vicinity of station 17 is perhaps 20% greater than the near surface crustal velocity in the vicinity of station 10, though part of the difference might be accounted for by the relatively low velocity sediment layer that is present in NW Tasmania. Although the two-interface model requires that interface 1, in the vicinity of station 17, be perturbed to shallow depths (Figure 7.36a) in order to satisfy the P_2P phase, the Moho in this region is very similar to the Moho in Figure 7.31. Regional differences in upper crustal velocity are also suggested by the 1-D inversion results (see Section 7.2). Describing the upper crust by a single layer with no lateral velocity variation is therefore not sufficient if the solution model is to reconcile P_1 phases from these different regions. Ideally, the model should allow lateral velocity variations to account for these regional differences. In principal, lateral velocity variation could be incorporated here by introducing an extra interface that pinches out against the surface and the mid-crustal reflector so that the upper crust is divided laterally into two velocity regions. However, shallow interfaces are very poorly constrained in inversions based on the TASGO dataset, except in isolated regions close to shot lines. Because the Moho structure derived from both one-layer and two-layer crustal models appears to be relatively insensitive to shallow regional velocity variation (represented in the two layer model by the depth variations of a mid-crustal interface), there is little to be gained by constructing a more elaborate model of the shallow structure unless a dataset with denser coverage is available.

7.5 Comparison with Results from Other Deep Crustal Studies of Tasmania

I now turn to a comparison of the solution models generated from the inversion of TASGO wide-angle seismic traveltimes with results from other deep crustal studies. In particular, the comparisons with independent interpretations of the normal incidence reflection data that were collected concurrently with the TASGO wide-angle data, and with a recent gravity map of Tasmania, are significant. Prior to the TASGO survey, most knowledge of the deep crustal structure of Tasmania came from gravity surveys (Leaman, 1989) and

from two seismic refraction profiles (Richardson, 1989). An important outcome of this thesis is whether or not the crustal models of Tasmania determined from the TASGO wide-angle dataset are consistent with results from these earlier studies, which have been used in interpretations of various aspects of Tasmania's tectonic environment and geological history (e.g. Leaman, 1994).

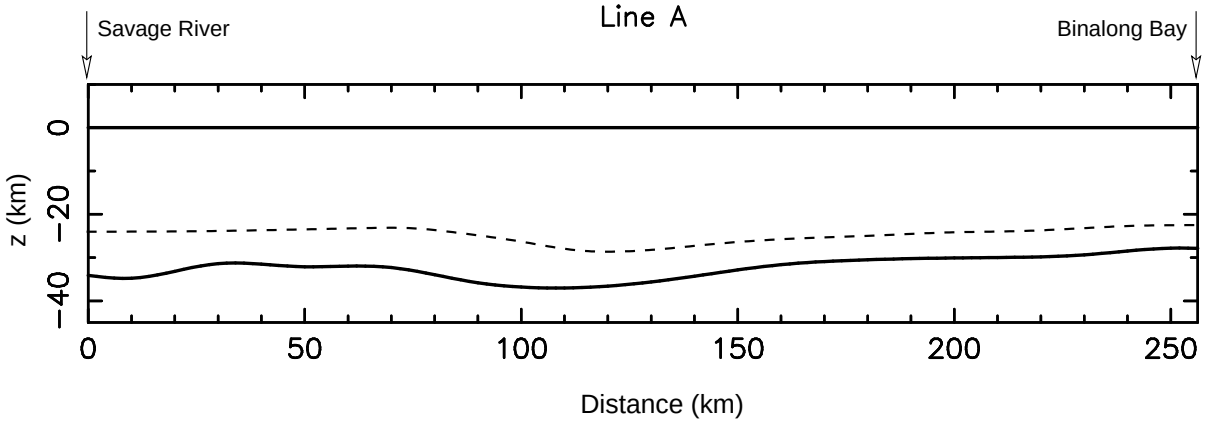

Figure 7.38: Comparison between Moho depth derived by Richardson (1980) (dashed line) along line A (see Figure 5.4 for location) and Moho depth obtained by inversion (Figure 7.31) of all picked P_n and P_mP phases from the TASGO dataset (solid line).

One key result of the present study is that, in regions where the Moho depth beneath Tasmania is well resolved, the average depth is about 31 km (Figure 7.31). The actual average may be greater than this value because the unresolved part of the Moho beneath central Tasmania, where topography is relatively high (see Figure 5.8), is not included. This value contrasts significantly with previous results. Using gravity data, Leaman (1989) estimated the maximum crustal thickness to be 27.5 km under central Tasmania, thinning towards the coastline by up to 5 km (see Mantle-88 model, Figure 5.7). Leaman's model has an average crustal thickness of less than 26 km, significantly less than that derived here by the inversion of TASGO wide-angle data. The crustal model produced by Roach et al. (1993) is constrained by more gravity data than Mantle-88 and exhibits a similar distribution of crustal thickness, with a maximum of 29.5 km and a minimum of 25 km. Although Roach et al. (1993) estimate increased crustal thickness compared to Mantle-88, they still indicate an average thickness well below that given by the TASGO wide-angle results presented in this chapter. However, gravity data provide poor constraints on absolute crustal thickness, so these gravity-based models are best seen as indicating

relative rather than absolute depths.

Apart from the difference in mean depth, the relative variation in the gravity derived map of crustal thickness (Figure 5.7) also does not correlate very closely with the Moho depth variations (Figure 7.31) derived from the TASGO data. However, comparison is not very straight forward since the Mantle-88 model is described by very long wavelength features and does not allow the kind of detail observed in the TASGO Moho model. In addition, a large region of the Moho beneath central Tasmania is not resolved by the TASGO data (Figure 7.33) and therefore is unperturbed from its initial value (Figure 7.31). The Mantle-88 model shows a thickened crust in central Tasmania that thins towards the coast, with contour lines approximately parallel to the coast line. The Moho shallows rapidly from the coast to the deep ocean. In eastern Tasmania, the TASGO Moho model (Figure 7.31) bears some resemblance to the Mantle-88 Moho in that the crust tends to thin towards the ocean; this is especially evident near the southern end of line 1, where onshore the Moho is around 32 km deep, and just offshore the Moho thins to around 23 km. Along the west coast, between stations 4 and 32, the TASGO model of the Moho does not suggest a shallowing of the Moho from onshore to offshore. However, northward along the coast from station 4 sees a marked shallowing of the Moho from around 35 km to about 26 km north of Three Hummock Island. While a similar shallowing occurs in the Mantle-88 gravity model, it is much more gradual.

The refraction profile across northern Tasmania analysed by Richardson (1980) reveals a three-layer crust with an average crustal velocity of 5.86 km/s and an average P_n velocity of 7.95 km/s. The depth of the Moho varies from 23 km in the west, to 27 km in the vicinity of the Tamar fracture system before thinning to 22 km near the east coast (Figure 5.5). Taking the same slice along the TASGO Moho model allows a comparison to be made (Figure 7.38), which shows a clear difference in the absolute depth of the Moho as determined from these two different datasets. The Richardson (1980) Moho varies between 22 and 27 km in depth while the TASGO Moho varies between just over 28 km to nearly 37 km in depth. This discrepancy may be partially explained by the difference in average crustal velocity: 5.86 km/s for the Richardson model and 6.24 km/s for the TASGO Moho model. At a depth of 30 km, a difference in average velocity of this magnitude will result in a depth perturbation of about 1.8 km for a vertically reflected ray, 2.3 km for a reflected ray inclined at 45° and 3.3 km for a reflected ray inclined at 60° to the vertical. The difference between the TASGO and Richardson (1980) models

thus cannot be fully explained by a trade-off between crustal velocity and thickness. The reason for the difference remains unclear, although the density of ray paths is much greater, and the accuracy of picked arrivals possibly more reliable for the TASGO dataset. For the 1-D, 2-D and 3-D inversions of the TASGO wide-angle data, the average crustal velocity is invariably estimated at between 6.2 and 6.3 km/s; this value appears to be well constrained.

Despite the difference in average depth, the relative variations in interface depth are quite similar for the two models. The TASGO model shows the Moho at about 34 km depth at Savage River (distance 0 km in Figure 7.38) before thinning to around 30 km depth at distance 30 km. It then plunges to a depth of nearly 37 km at distance 110 km before thinning to less than 30 km at Binalong Bay. The Richardson model exhibits the same behaviour except for the local thickening near Savage River. The amplitude of the variations are also smaller, perhaps due to Richardson's assumption of 2-D structure and the method used to construct the model, which involved inverting for 1-D structure locally along the line. Generally, this method can be expected to have the effect of averaging structure along the line. The other feature of the Richardson (1980) model is that the upper crustal layer, whose base is at 8 km depth beneath Savage River, pinches out beneath the Tamar River. The TASGO crustal models also show the bottom of the upper crust to be at about 8 km depth, with thinning near the Tamar river, although the mid-crustal interface is not well resolved in this region (Figure 7.36).

Comparison between the Moho depth estimates of the Line B wide-angle experiment (Figure 5.6), described by Richardson (1989), and the TASGO Moho model are less meaningful because Line B runs through central Tasmania, much of which is poorly resolved in the latter model. However, near either end of the line (Savage River and Fortescue Bay), where the TASGO Moho model is well resolved, the Moho depths are in approximate agreement, although the localised zone of thin crust seen beneath the Tasman Peninsula in Figure 7.31 is not evident in Figure 5.6. Apart from the above studies and the even earlier BUMP survey (see Section 5.2) which estimated a crustal thickness of 30-35 km beneath central Tasmania, there has not been any other major study on the deep crustal structure of Tasmania outside the TASGO survey. Recently, Clitheroe et al. (2000) measured the crustal thickness of Australia using receiver function analysis of crustal P to S conversions recorded at 65 locations throughout Australia. Only one recorder was located in Tasmania, on the SE coast corresponding to the point $(x, y) = (330, 125)$ km on

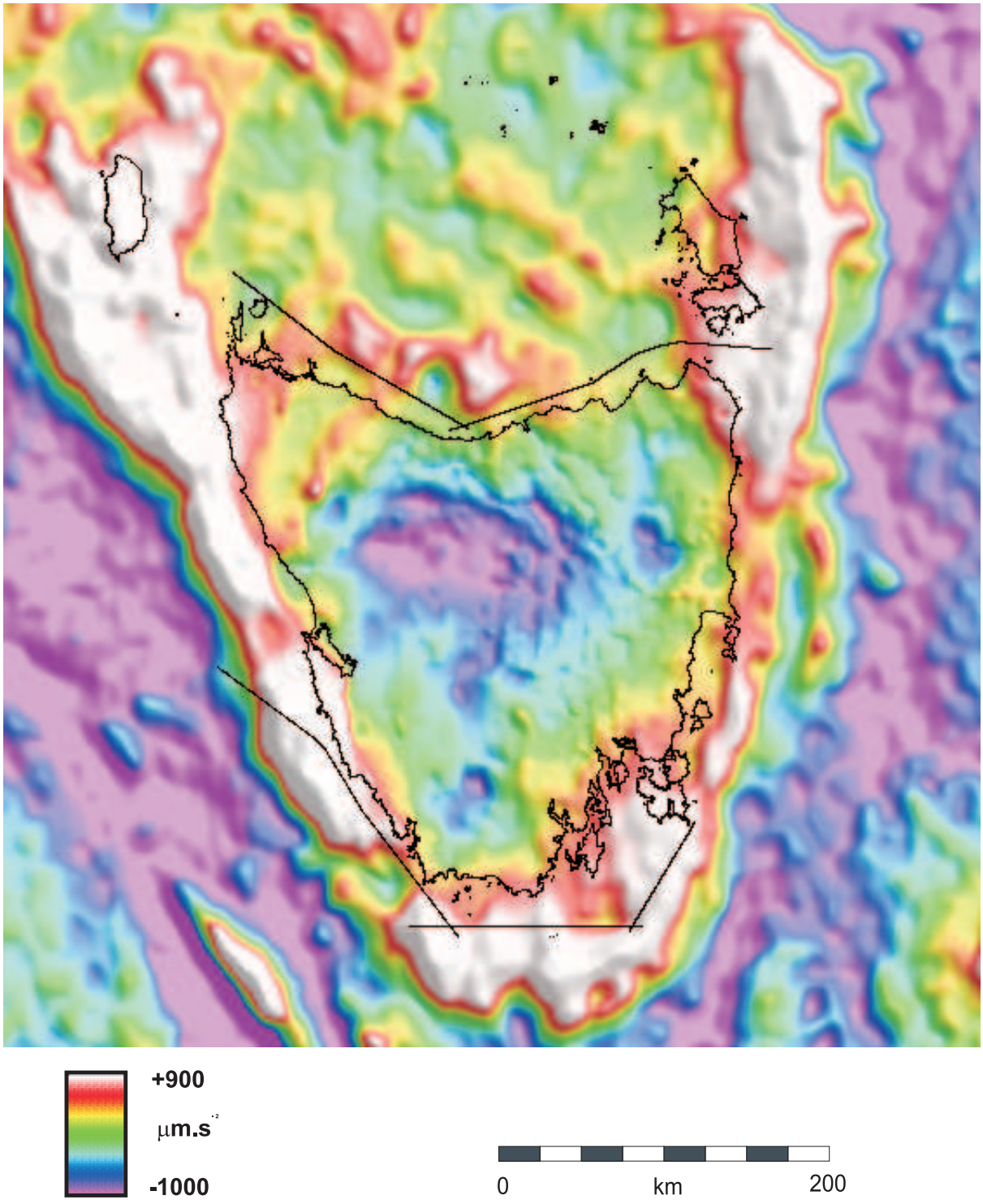

Figure 7.39: Gravity map of the Tasmanian region (from Murray et al., 1997) showing Bouguer anomalies onshore and free-air anomalies offshore.

the TASGO Moho map (Figure 7.31). Clitheroe et al. (2000) measured a crustal thickness of 32 km at this point, which agrees accurately with the estimate from the TASGO Moho map (also 32 km), although resolution is not particularly good in this region.

As pointed out above, gravity data poorly constrain absolute crustal thickness, but can provide insight into lateral variations in structure. Figure 7.39 shows a residual gravity map of Tasmania and the surrounding region constructed from recent AGSO data (Murray et al., 1997). The principal onshore feature of this map is a large Bouguer gravity low in central Tasmania, which gradually decreases towards the shoreline. The gravity low is associated with the high topography in central Tasmania as expected if isostasy implies a local depression of the Moho and hence thicker crust. Alternatively, the high topography could be balanced by a region of less dense though not necessarily thicker crust, which would also produce a negative Bouguer anomaly. The former interpretation is more likely given the results of the TASGO wide-angle survey and the previous studies cited above. Another interesting feature of the gravity map is NW Tasmania, which exhibits significant positive anomalies, and in particular, a NE-SW trending gravity high. This feature correlates well with the surface expression of the Arthur Lineament (see Figure 5.1). The relatively rapid transition from strong negative gravity anomalies in central Tasmania to positive anomalies seen in NW Tasmania (Figure 7.39) is well correlated with the rapid thinning of the crust found in the TASGO Moho map (Figure 7.31) and in the NW Tasmania model (Figure 7.19). The region of thinned crust in NW Tasmania corresponds closely with the region of relatively positive Bouguer gravity northwest of the Arthur Lineament. The strong gravity gradient across the continental margin with associated bands of strong positive and negative anomalies are a characteristic continental margin signature, attributed to the large decrease in crustal thickness from continent to ocean.

On a smaller scale, the relatively narrow band of high gravity anomaly seen in the vicinity of the Arthur Lineament does not correspond to any Moho feature seen in Figure 7.19 or Figure 7.31. However, the length scale of the gravity lineament is smaller than that which would be easily resolved by the interface parameterisation. Alternatively, the gravity high may be caused by near-surface density variations. Comparison with the NW Tasmania model (Figure 7.23) shows an upward deflection of interface 2 at $y = 100$ km for the slice $x = 200$ km that is well resolved and correlates with the gravity lineament. Other comparisons worthy of note are the relatively deep Moho beneath stations 10 and 40 (not all resolved according to Figure 7.33) which corresponds to a decrease in gravity, and the gravity high in the vicinity of the Tasman Peninsula (station 17), which sits above thinned crust. However, the region of locally shallow crust that lies just SE of station 45 (Figure

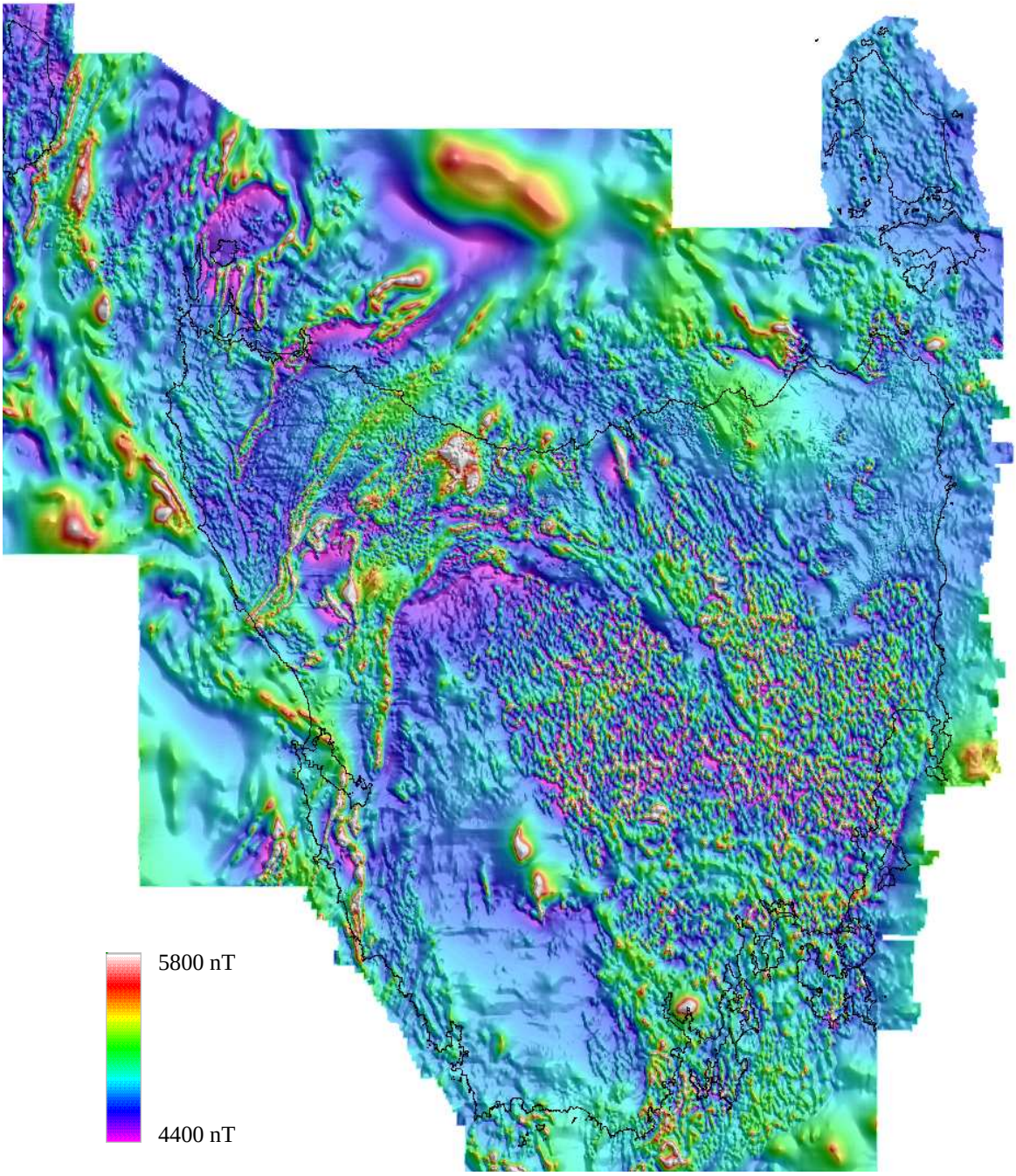

Figure 7.40: Total magnetic intensity map of the Tasmanian region (from Mackey et al., 1995).

7.31) corresponds to a gravity low and is thus not consistent with the general negative correlation between gravity and crustal thickness. Offshore, relating crustal structure to free-air gravity is more difficult because the water layer is much less dense than the crust beneath, so the variations in gravity principally reflect the sea floor bathymetry rather than lateral variations in crustal structure. Thus, regions of high topography beneath the

sea floor, such as the East Tasman Rise (near SE corner of Figure 7.39), appear as gravity highs, and regions of low topography, such as the deep ocean, appear as gravity lows.

Comparison between the TASGO wide-angle traveltime inversion results and Tasmania's magnetic field can also be made. Figure 7.40 shows a total magnetic intensity map of Tasmania produced by Mackey et al. (1995) from aeromagnetic data. As noted in Chapter 5, the magnetic response throughout much of Tasmania is dominated by young dolerite and basalt cover sequences. However, in the NW of the state, strong magnetic lineaments are evident. In particular, the Arthur Lineament is revealed as a NE-SW trending zone of highly magnetic linear units. This magnetic lineament correlates well with the band of high gravity anomaly (Figure 7.39) discussed previously, and lies above the region of rapidly thinning Moho from SE to NW (see Figures 7.19 and 7.31). Further SE, an arcuate band of high magnetic intensity corresponds to the calc-alkaline rocks of the Mount Read Volcanics (Gunn:1997). Again, there does not appear to be any Moho feature in Figures 7.19 or 7.31 that can be directly related to this magnetic response, but the basic trend of the Volcanic belt is from a northerly (further south) to an easterly orientation (further north), a trend that is represented to some degree by the Moho deflections seen in Figure 7.31. The Moho deflections in the vicinity of stations 4 and 39 have a roughly NE-SW orientation while the Moho depression beneath stations 10, 40 and 21 has an approximately easterly orientation.

Normal incidence reflection data collected concurrently with the wide-angle data, although not utilised in the inversions presented in this chapter, have been independently interpreted and therefore make an interesting comparison with the wide-angle traveltime inversion results. Barton (1999a,b) processed the reflection data from Lines 4 and 5 and interpreted the results with the aid of satellite-derived gravity and regional aeromagnetic data. The Moho on these lines was interpreted by Barton as the region where strong reflection events are observed at the base of the reflective lower crust. Although depths are not accurately constrained by the deep reflection processing methods used by Barton (1999a,b), the line 5 interpretation (Figure 7.41) indicates an $\sim$30 km deep Moho which thins to $\sim$27 km before thickening again to $\sim$31 km in the SE. A crustal detachment feature above the Moho, consistent with the layer pinchout evident in the NW Tasmania model (figures 7.19 and 7.23), has also been interpreted by Barton (1999a,b) beneath the NW end of line 5. The undulation of the Moho interpreted from the normal incidence reflection data correlates well with the undulations of the NW Tasmania model presented

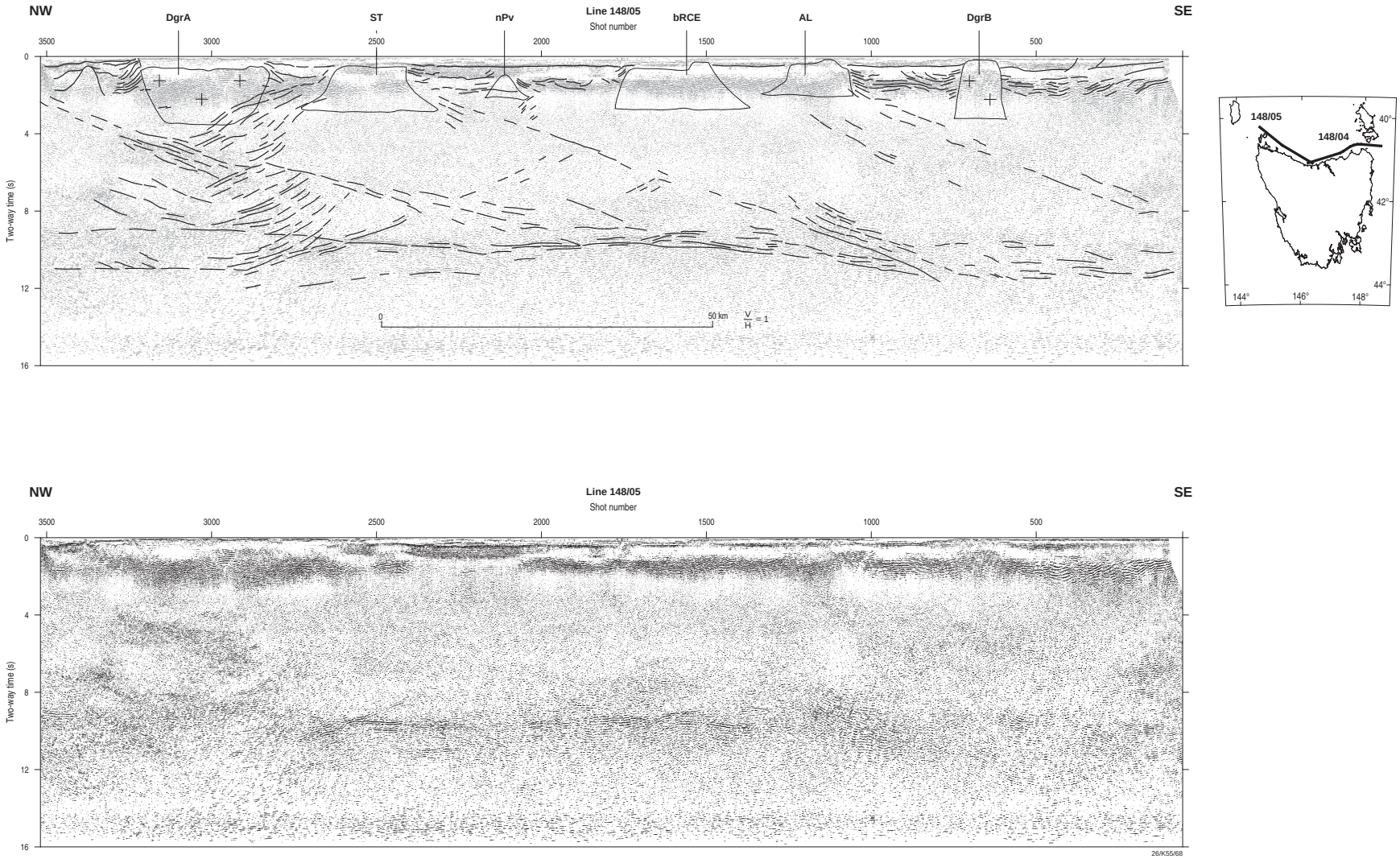

Figure 7.41: Interpreted (top) and uninterpreted (bottom) reflection profile along shot line 5 (from Barton, 1999a).

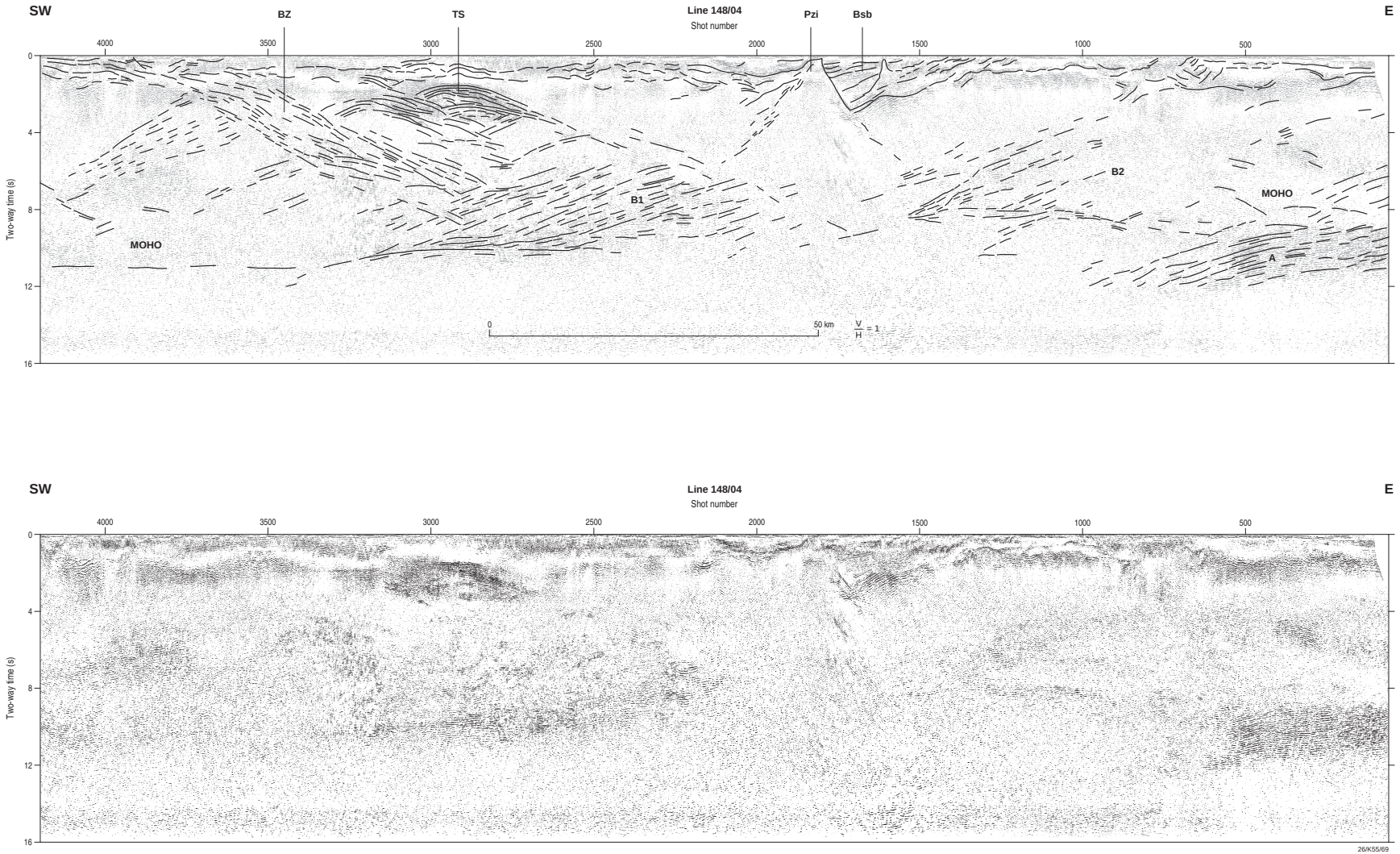

Figure 7.42: Interpreted (top) and uninterpreted (bottom) reflection profile along shot line 4 (from Barton, 1999a).

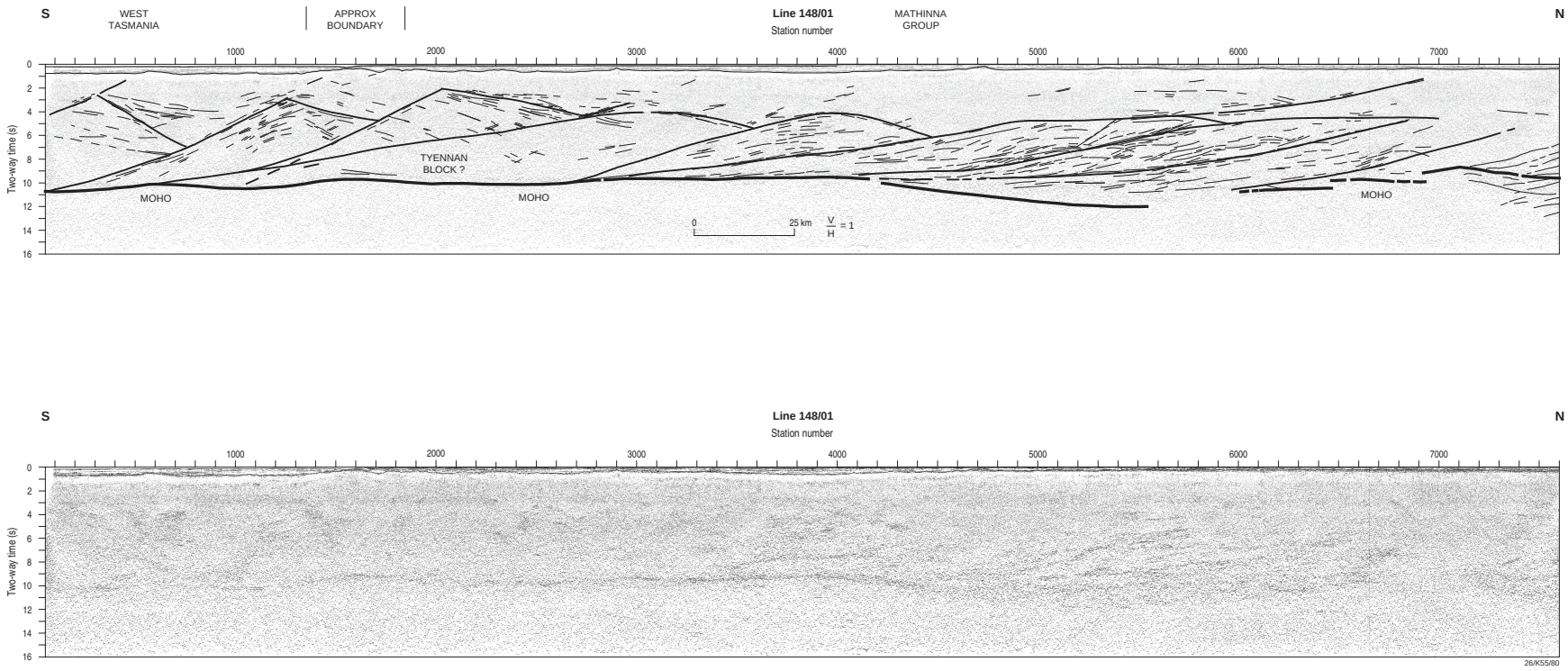

Figure 7.43: Interpreted (top) and uninterpreted (bottom) reflection profile along shot line 1 (from Drummond et al., 2000).

here (slice $x = 200$ km of Figure 7.23). The mid-crust beneath line 5 is generally unreflective except near the NW end of the line (Figure 7.41). The base of the upper crust is defined by the base of a number of bodies, including the Devonian Three Hummock Island granite associated with gravity lows, and Neoproterozoic volcanics associated with gravity highs. The reflectivity signature of upper crust below 4 s Two-Way Time (TWT), which equates to ∼10 km depth, and the base of this zone is therefore consistent with the depth of interface 2 in the NW Tasmania inversion model.

Much of the region beneath line 4 is not well resolved by the wide-angle data (Figure 7.33). The normal incidence reflection interpretation (Figure 7.42) beneath this line shows an ∼30 km thick crust at the SW end of the line gradually thinning to ∼24 km at the NE end. This trend is roughly consistent with the wide-angle results but the lack of resolution in the 3-D inversion makes the comparison less meaningful. The mid-crust is much more reflective beneath line 4 than line 5 and the package of reflectors near the SW end of the line (BZ in Figure 7.42) has been interpreted (Barton, 1999b) as the boundary between eastern and western Tasmania terranes.

Line 1 normal incidence reflections (Figure 7.43) have been interpreted by Drummond et al. (2000). A clear feature of this data is a relatively thin, high amplitude reflection packet at a TWT of around 10 s that is nearly laterally continuous along the line. These reflections have been interpreted to represent the Moho at an average depth of around 30 km. From south to north, the Moho begins at ∼31 km depth and shallows to ∼26 km beneath shot 4000, before descending to nearly 34 km at the northern end of the line. Again, much of the Moho structure beneath Line 1 is poorly resolved by the wide angle data (Figure 7.33) but the average depth appears consistent with the Figure 7.43 interpretation. The shallowest part of the wide-angle Moho model (Figure 7.31) occurs beneath line 1 near shot 3000. The depth of 23 km inferred from the 3-D inversion solution is somewhat shallower than that interpreted from the reflection data (∼26.5 km). The interpreted tilted crustal blocks that lie above the Moho (Figure 7.43) may be the result of Late Neoproterozoic extension of continental crust followed by NE-SW shortening (Drummond et al., 2000).

The Moho depths suggested by the three reflection lines considered here are clearly consistent with the wide-angle models presented in this chapter in that they indicate a generally deeper Moho and hence thicker crust than was inferred by earlier interpretations.

7.6 Geological and Tectonic Implications

Several well constrained features of the models produced in this chapter by the inversion of wide-angle traveltimes for the layered crustal structure of Tasmania are now considered in terms of their geological and tectonic implications. Most of the reliable information that can be obtained from the inversion solutions pertains to the depth of the contact between the crust and lithospheric mantle, as shown in Figure 7.31. Lateral variations in upper crustal structure have been estimated in NW Tasmania by using both 2-D (Figure 7.10) and 3-D (Figure 7.19) inversions, but resolution is limited. The inversions for 1-D structure also provide information on lateral variations in crustal structure from region to region, although they assume locally invariant horizontal structure.

The Rocky Cape Element, located in NW Tasmania (Figure 5.1), is bounded to the SE by the Arthur Lineament, which separates it from the Dundas Element. The northern part of the Arthur Lineament is masked by material deposited during the formation of the Tasmania Basin in the Carboniferous (Williams, 1989). There is a strong correlation between the transition from the Rocky Cape Element to the Dundas Element and the steep gradient in crustal thickness seen in both the Moho-only model of Tasmania (Figure 7.31) and the multi-layered crustal model of NW Tasmania (Figure 7.19). That the crust of the Rocky Cape Element is considerably thinner than the crust of the elements that lie to the SE gives credence to its classification as a crustal-scale element (e.g. Corbett et al., 1972; Brown et al., 1998), and suggests that the metamorphic band of rocks comprising the Arthur Lineament may extend to the deep crust.

One of the distinguishing surface characteristics of the Rocky Cape element is the Rocky Cape Group, a sequence of shallow marine quartz sandstones and mudstones. Its thickness probably doesn't exceed 2-3 km (Williams, 1989), which agrees with the estimated thickness of layer 1 in the NW Tasmania model (Figure 7.19), although this layer is generally poorly constrained by the wide-angle data. Deposition of the Rocky Cape Group occurred in the Mesoproterozoic and is not seen in other regions of Tasmania. During the Tyennan Orogeny in the middle and late Cambrian, substantial E-W shortening was experienced throughout much of Tasmania, expressed by the allochthonous emplacement of thrust sheets (Elliot et al., 1993) and significant metamorphism. However, the Rocky Cape Element behaved as a resistant cratonic block during the early Tyennan Orogeny (Turner et al., 1998) and was not substantially thickened; the NW limit of the orogeny

is identified with the Arthur Lineament, which was composed of the same sedimentary material as the Rocky Cape Group before deformation (Williams, 1989). The reduced orogenic activity in the Rocky Cape Element compared to regions in the SE during the Early Cambrian may help explain the present-day crustal thickness contrast. Other factors, such as Cretaceous extension related to the break-up of Gondwana, may also have contributed to the relatively thin crust of the Rocky Cape Element. The Bass and Sorell Basins, which were formed during this period, lie offshore of the Element to the north and west.

Upper crustal features in NW Tasmania, as described by interface 2 of Figure 7.19, are also indicative of structure aligned with the Arthur Lineament. However, it should be noted that good resolution (Figure 7.22) is limited to regions close to the shot lines, so the variation in depth of interface 2 from ∼10 km SE of the Arthur Lineament to ∼5 km to the NW is not robustly constrained below station 25. Inspection of a cross-section of the NW Tasmania model beneath line 5 ($x = 200$ km, Figure 7.23), shows the upward deflection of the Moho (around $y = 100$ km) that has been interpreted as the transition to the thinner crust of the Rocky Cape Element. The deflection in the mid-crustal interface closely matches the Moho deflection but is offset to the SE. The offset may indicate a north-westerly dipping deep crustal structure associated with the Arthur Lineament. Figure 7.31 suggests that the steep gradient in interface depth extends offshore to the NE, but is more ambiguous to the SW, an observation that is consistent with the recent interpretation of magnetic intensity data by Gunn et al. (1997), which clearly shows that the Arthur Lineament extends offshore beneath the Bass Basin in the NE, but is less clear offshore beneath the Sorell Basin in the SW (see Figure 7.40).

The lower crustal layer that pinches out in NW Tasmania (Figure 7.19) is correlated with a region of enhanced reflectivity in the normal incidence reflection sections of line 5 (Figure 7.41). The upper surface of this feature was interpreted by Barton (1999a) as a crustal detachment caused by thrusting. It is only resolved in a relatively small region of the model, but as shown by Figures 7.19 and 7.23, its upper surface exhibits significant variations in depth. The velocity of this laterally discontinuous layer is greater than that of the contiguous lower crustal layer (Figure 7.24). One possibility (admittedly controversial) is that it consists of remnants of underplated oceanic crust emplaced by westerly subduction beneath the Rocky Cape Element during the formation of the Mt. Read Volcanics in the Lower Palaeozoic (Corbett et al., 1972).

According to the Moho inversion model (Figure 7.31) a significant downwarp of the Moho occurs in central northern Tasmania (beneath station 40). The depression reaches a maximum depth of 37 km, but is not resolved everywhere by the data according to Figure 7.33. The cross-section across northern Tasmania (Figure 7.38) discussed earlier features this depression and shows how well it correlates, in terms of relative depth variation, with the 2-D wide-angle model produced by Richardson (1980). Richardson (1980) interprets this asymmetric depression to be the result of a major N-S striking thrust fault between northeast and northwest Tasmania, with up to 4 km of downward movement on the eastern side of the fault zone accompanied by drag-folding on the western side. The Tamar Fracture System lies to the east of this major fault zone. Based on the surface geology of the Badger Head region, which lies just west of the Tamar River in Northern Tasmania and hence above the Moho depression determined by the inversion of the seismic traveltimes, Elliot et al. (1993) conclude that westward directed thrusting of Early and Mid Palaeozoic strata of the Beaconsfield Block over the Badger Head Block occurred during the juxtaposition of the East and West Tasmania Terranes in the Mid-Devonian, synchronous with the Tabberabberan Orogeny which occurred in eastern Australia. The crustal shortening that occurred in the Badger Head region as a result of this event has been estimated at 20% (Elliot et al., 1993). The Moho downwarp observed in central northern Tasmania (Figure 7.31) is consistent with this tectonic model.

The Moho beneath the Tamar Valley, which lies at the northern end of the Tamar Fracture System (Figure 5.1), is well resolved by the wide-angle data (Figure 7.33) and is distinguished by an upward deflection aligned in the direction of the Tamar Fracture System. While the shallowing of the Moho here could signify a boundary between two terranes, data coverage was not sufficient to resolve much of the region beneath the Tamar Fracture System. In fact, most of the Tasmanian Moho to the east of the Tamar Fracture system is poorly resolved by the wide-angle data, so whether the crust at depth is any different in east Tasmania compared to west Tasmania cannot be determined from the 3-D inversion results.

During the breakup of Gondwana, seafloor spreading between Australia, Antarctica and New Zealand was initiated in the Cretaceous. Spreading in the Tasman sea began in the Late Cretaceous and ceased at about 57 Ma (Williams, 1989). The extinct spreading ridge in the Tasman sea is clearly observable in satellite-derived gravity data (Royer & Rollet, 1997) and is aligned approximately parallel to Tasmania's east coast. While

extension between Australia and Antarctica began in the Late Jurassic, seafloor spreading wasn't initiated in the Great Australian Bight until the Late Cretaceous (Royer & Rollet, 1997). The position of Tasmania at the SE tip of Australia and the orientation of the spreading ridge implies that Tasmania's western margin was formed as a result of strike-slip motion along the Tasman Fracture Zone, which lies just west of Tasmania. Severe wrench deformation is the principle feature in this region (Royer & Rollet, 1997), contrasting with the extensional deformation associated with the stretching between eastern Tasmania, the East Tasman Plateau and the Lord Howe Rise that occurred prior to sea floor spreading in the Tasman sea. The Moho model (Figure 7.31) is well resolved along the western coast of Tasmania and the crust is generally quite thick south of the Rocky Cape Element. The thickest crust occurs below lines 9 and 10 with Moho depths of around 35 km. Crust of this thickness close to the continental slope is more consistent with a margin that has been formed by wrench tectonics as opposed to extension. The east coast, although generally not well resolved in the 3-D inversion, tends to thin towards the continental slope, especially in the vicinity of the Tasman Peninsula in the SE (around station 17). This thinning is more consistent with a margin formed by extension-related rifting.

Immediately SE of station 45, Figure 7.31 indicates a shallowing of the Moho to a depth of about 26 km, which represents an upward deflection of 5-6 km from the surrounding Moho. This feature could be related to the widespread emplacement of granites in Tasmania during the Devonian. Using magnetic and geological maps, Gunn et al. (1997) identify a large-scale granitic intrusion in this area.

7.7 Summary

In this chapter, a new method for the inversion of wide-angle traveltimes for 3-D layered crustal structure has been applied to the TASGO wide-angle dataset obtained using recorders distributed across Tasmania and shot lines around the island. Crustal models constrained by the data are described by smooth, laterally continuous interfaces that separate layers with velocity that varies linearly with depth. Layer pinchouts can be formed by merging adjacent interfaces. Before carrying out inversions for 3-D structure, data from a number of station-line combinations throughout Tasmania were separately inverted for 1-D structure. These models were used to help build initial models for subsequent inver-

sions in 2-D and 3-D. They were also useful in providing preliminary indications of lateral variations in crustal structure. These results showed that Tasmania could be approximated by a two-layer crust with an average velocity of 6.3 km/s overlying a Moho with an average depth of 30 km and an associated P_n velocity of 7.8 km/s. Moho depths in the 1-D inversion solutions vary from 25 km to 35 km. In the lower crustal layer, velocities don't vary significantly from region to region, but in the upper crust, some variation does occur. In particular, the upper crust in the vicinity of the Tasman Peninsula is just over 6.0 km/s and beneath the southern west coast, it is less than 5.0 km/s. Elsewhere, it is about 5.6 km/s. A 2-D inversion model along the western north coast is constructed using data from one shot line recorded at three receivers. The 2-D model consists of four crustal layers overlying a mantle half space, with one of the crustal layers pinching out to the SE. With most of the useful data concentrated in NW Tasmania, a 3-D inversion model of this region is constructed using 2401 refraction and reflection traveltimes. The upper crustal layers are generally poorly resolved due mainly to the source-receiver configuration, but the solution is similar to the 2-D inversion solution (along the western north coast) and the Moho is generally well resolved. All picked P_mP and P_n traveltimes from the TASGO dataset are then inverted for the structure of the Moho beneath all of Tasmania assuming a laterally homogeneous crust. The Moho structure of the solution model closely matches the Moho of the four-layer NW Tasmania model, and an additional inversion which includes a mid-crustal interface and related phases suggests that the Moho elsewhere in Tasmania is accurately reconstructed under the assumption of lateral homogeneity within the crust. The 3-D inversion models indicate that the average crustal velocity of the Tasmanian crust is 6.2 km/s, the average Moho depth (where resolved) is about 31 km and the average P_n velocity is about 8.0 km/s. The average depth of the crust is a significant result of this study because previous studies have estimated the crust to be substantially thinner. The 3-D inversion results include several interesting features; in NW Tasmania, the Rocky Cape Element is shown to be composed of thinner crust than the tectonic elements to the SE. The transition zone from thick to thinner crust lies nearly beneath the Arthur Lineament, a band of metamorphosed marine sediments, which marks the SE termination of the Rocky Cape Group on the surface. A crustal thickness of nearly 37 km occurs to the west of the Tamar Fracture System in central northern Tasmania, and is consistent with crustal shortening caused by the juxtaposition of the East and West Tasmania Terranes during the Tabberabberan Orogeny. The different formation mecha-

nisms of the east and west Tasmania margins are also reflected in the contrasting crustal thickness variations across these margins; on the west coast wrench faulting associated with the separation of western Tasmania from Antarctica, and on the east coast extension prior to the opening of the Tasman Sea.

Chapter 8

Conclusions

In this study, tomographic inversion methods have been formulated and used to map crustal structure by inversion of seismic P-wave traveltimes. Two data types, teleseismic and wide-angle, are separately considered. Teleseismic arrivals from distant earthquakes recorded by a local receiver array can be used to map structure beneath the array. In doing so, it is assumed that heterogeneities in the earth which lie outside the region of interest do not significantly affect relative arrival times, and that source time uncertainty can be accounted for by subtracting the mean traveltime residual for each source from each reading. Ray paths from distant events tend to propagate through the crust beneath the receivers at relatively steep angles. Wide-angle seismic surveys, on the other hand, use surface sources and receivers offset so that refraction and wide-angle reflection phases with significant horizontal path components are recorded. Generally, such surveys are of crustal scale, so that most detectable arrivals do not penetrate below the upper lithospheric mantle. This is especially the case in marine surveys that use airguns as sources. Due to the differences in relative source-receiver location and hence ray path geometry, teleseismic and wide-angle data do not contain identical information about crustal structure. However, similar methods can be employed to extract this structural information. Here, I have shown that both these classes of data may be successfully used to constrain crustal structure described in terms of layers in which velocity is laterally invariant, but are bounded by interfaces of arbitrary geometry. Using teleseismic data, a 2-D inversion method is tested and applied to data collected in central Australia. A new method that inverts wide-angle reflection and refraction traveltimes for 3-D structure is then developed, tested with synthetic data, and applied to the TASGO dataset collected

in Tasmania in 1995.

Methods that invert teleseismic traveltime residuals for crust and upper mantle structure conventionally use models parameterised in terms of a variable velocity distribution (e.g. Aki et al., 1977; Humphreys & Clayton, 1990). In Chapter 3, the 2-D method of Rawlinson (1996b) was used to assess the ability of teleseismic data to resolve interface structure. The method was then applied to a dataset consisting of teleseismic traveltime anomalies recorded by an in-line array of seismometers across the northern margin of the Musgrave Block, central Australia. In this method, layer boundaries are assumed laterally continuous and are described by a set of nodes interpolated by cubic spline curves. Within a layer, the velocity is assumed constant. A shooting method is used to determine the first-arrival traveltimes of rays from a planar wavefront incident on the crust from below to a set of receivers on the surface. A conjugate gradient method is used to solve the inverse problem, which requires the minimisation of a least-squares type objective function based on the difference between model and observed traveltime residuals. For this inversion, interface node depths are varied, but layer velocities, which are assumed known *a priori*, are held constant. Synthetic tests using a two-layer crust overlying a mantle half-space demonstrate that teleseismic data can accurately constrain the lateral variations of multiple interfaces, but only poorly constrain vertical structure (see Figure 3.5a). The number of interfaces must be chosen *a priori* since single-component teleseismic data do not provide obvious indicators of layer boundaries, such as the reflections or discontinuities in the first-arrival traveltime curve that are observed in wide-angle data. Mode conversions may occur, but the detection of such phases requires three-component data.

In obtaining a crustal structure solution for central Australia, I used data from five source regions that lie almost in-plane with a receiver line of 26 recorders. The initial model used for the inversion was based on information derived from nearby deep crustal reflection data, and consisted of three crustal layers overlying a mantle half-space. The geometry of the layer boundaries were varied simultaneously in the inversion process in order to satisfy the data. The inversion solution (Figure 3.10) exhibits large interface deflections that are relatively well resolved by the data, as demonstrated by the synthetic tests of Figure 3.11. One of the interesting outcomes of this study is that teleseismic traveltime residuals can be used to constrain very heterogeneous lateral structure, represented by variations in interface geometry, using exclusively first-breaks, which may be

identified from seismograms relatively easily and accurately.

In the teleseismic inversion, I have assumed that layer velocities are constant, with lateral variation of structure represented by the deflection of layer interfaces. Including, for example, a vertical velocity gradient would probably not improve the solution because teleseismic traveltimes poorly resolve vertical structure. However, teleseismic data are sensitive to lateral variations of velocity within a layer. Permitting lateral variations in layer velocity would likely result in a new spectrum of solutions that satisfy the data. It is unlikely, though, that near vertical ray paths can resolve the trade-off between interface depth and velocity variation. Inverting for interface structure only can be considered preferable in this case, because the assumptions concerning allowable structure are clearly defined, and fewer parameters are required to satisfy the data. At the other end of the model spectrum, the data may well be adequately fit by models described only in terms of variable velocity distribution. A comparison of these two end member representations is shown in Figure 3.12, where the Musgrave Line teleseismic dataset has been independently inverted for variable velocity distribution (Figure 3.12b) and interface geometry (Figure 3.12c). The two models show many similarities in terms of lateral structure, whether expressed by deflection of an interface or by continuous velocity variation.

In Chapter 4, I describe and test a new method for the inversion of refraction and wide-angle reflection traveltimes for 3-D layered crustal structure. Crustal structure is represented by layers in which velocity varies linearly with depth, separated by smooth interfaces defined by a bicubic B-spline parameterisation. Lateral variations in structure are therefore represented by variations in interface depth only. Unlike teleseismic studies, the absolute source-receiver traveltime is inverted as opposed to the relative traveltime residual, so vertical variations in structure can be constrained. With adequate data coverage, it is possible to invert refraction and reflection traveltimes for both interface depth and velocity variation within a layer and obtain a robust solution. More generally, as has been demonstrated by a number of authors (e.g. Zelt & Smith, 1992; Wang & Braile, 1996; Zelt, 1999), using both refraction and reflection traveltimes in an inversion can help to resolve the trade-off between interface depth and velocity variation.

The assumption of laterally invariant velocity within a layer means that a class of geologically realistic models cannot be explored by the inversion method. However, the method permits adjacent interface surfaces to merge so that layer pinchouts may be represented, thereby allowing another range of structures to be investigated (e.g. the

subduction zone example in Section 4.3.3). In principle, this feature can also be employed to represent gross lateral variations of velocity within a layer by the inclusion of additional internal interfaces which subdivide the layer. In practice, the method is sufficient if it can adequately satisfy the data with a geologically plausible structure. The TASGO wide-angle dataset, to which the method is applied, generally exhibits sparse ray coverage, so the potential is low for obtaining well constrained models described by lateral variations in both interface depth and layer velocity.

Assuming that velocity within a layer varies linearly with depth permits refracting rays to turn back towards the surface and better represents, compared to constant velocity layers, the true vertical variation of velocity in the crust. It also means that ray paths within layers consist of circular arc segments which can be described analytically. This drastically reduces computation time compared to a velocity field (e.g. one described by cubic splines) that requires numerical approximation of ray trajectories. If layers depart significantly from horizontal stratification, implied velocities may vary significantly with depth along an interface. This may not be desirable. However, if the velocity gradient is small, which they tend to be, then this should not be a concern.

An additional flexibility of the parameterisation described here is that interface nodes need not be fixed on a regular grid; the distribution of nodes may therefore be chosen to suit the resolving power of the dataset. Tests using a non-uniform grid of interface nodes are described in Chapter 4, and the inversion of TASGO data (Chapter 7) for the 3-D structure of NW Tasmania uses an irregular node distribution to describe the upper two interfaces. The principal benefit is that fewer parameters can be used to satisfy a dataset, although interpretation of the results must be done with a knowledge of the node distribution.

In contrast to many 3-D wide-angle inversion methods, in which traveltime determination (the forward step of the inverse problem) is based on the finite-difference solution of the eikonal equation (e.g. Hole, 1992; Riahi et al., 1997; Zelt & Barton, 1998), I have used a shooting method of ray tracing. The initial value problem, of propagating a ray from a source to the target receiver plane, is rapidly solved since ray paths consist of a set of piecewise circular arc segments. Ray-interface hit points are determined using a generalised Newton method and Snell's law is used to find the new direction of the ray path after interaction with the interface. The correct two-point ray path is found by shooting a spread of rays from the source to the receiver array and progressively targeting receivers

with increasingly concentrated groups of rays, before iteratively locating the initial trajectory parameters of the correct ray path by assuming a locally linearised dependence of the ray emergence point on the initial projection angles. The C_2 nature of the bicubic B-spline surfaces is important to this assumption. The shooting method works most efficiently for arrays described by many receivers and few sources or vice versa (e.g. marine surveys), as the principle of reciprocity in ray tracing applies. The shooting method may find multiple paths (if they exist) of the same phase for a source-receiver pair, in which case the first-arrival is used. If a model is composed of p layers, the first-arrivals of up to p refraction and $p-1$ reflection phases can be found. This ray tracing scheme is an efficient method for the determination of traveltime with the layered, constant velocity gradient parameterisation used here. The effectiveness of the ray tracing technique is demonstrated in Chapters 4 and 7.

The aim of the inversion procedure is to minimise the misfit between observed and calculated traveltimes by adjusting the values of the model parameters (interface depth nodes, layer velocity and layer velocity gradient) subject to regularisation constraints. To formalise the minimisation problem, a least-squares type objective function is constructed (Equation 4.15) consisting of a data misfit term and a model misfit term. A damping factor (ϵ) is used to govern the trade-off between data fit and how near the solution model is to the initial model. The teleseismic inversions (Chapter 3) worked well with zero damping. Although damping is generally included in order to prevent the formation of spurious structure in unconstrained parts of the model, the lack of a damping term in these inversions did not appear necessary because the solution models obtained were generally well constrained by the data alone. Including damping requires an estimate of the relative uncertainties of model parameters. For teleseismic inversions, these uncertainties, together with the model parameters of the initial model estimate, are typically obtained from *a priori* information about the structure. Inversions using wide-angle data, on the other hand, are less reliant on *a priori* information. The number of interfaces to use in the inversion model can be derived from the data alone. As demonstrated in Chapter 7, creating a number of 1-D models from particular source-receiver combinations is a reliable way of finding an initial model. Uncertainty estimates for velocities and layer depths may be based on the variability of these 1-D models. These uncertainties are used to define the *a priori* model covariance matrix used in the model term of the objective function.

The teleseismic inversion method devised by Rawlinson (1996b) uses a conjugate gra-

dient method to minimise the objective function. The method works well in this case, where the inversion only constrains a single parameter class, interface depth. However, in the case of the 3-D wide-angle inversion method, the inversion constrains three parameter classes (interface depth, velocity and velocity gradient) simultaneously. A strong dependence on scaling and poor convergence may be observed when gradient methods like steepest descent or conjugate gradients are applied to problems with different parameter classes. These problems were demonstrated using 2-D inversion in Section 4.3.1, where I showed, using both steepest descents and conjugate gradients, that the inversion attempts to satisfy the data by preferentially perturbing velocity gradient, since a perturbation in velocity gradient will produce a greater change to the objective function than will a similar perturbation to interface depth or velocity. To bypass such problems, a subspace inversion method was employed to minimise the objective function. The subspace inversion method works by restricting the minimisation of the quadratic approximation of the objective function to an n-dimensional subspace of the model space defined by the span of n basis vectors. The basis vectors are chosen so that each vector lies in the model space of only one parameter class. Thus, the minimisation of the objective function in the direction specified by a particular basis vector will not have a dependence on the relative scaling of the different parameter classes. The 2-D synthetic tests (Section 4.3.1) clearly establish the subspace method as superior to both steepest descent and conjugate gradients for single parameter class inversions and, especially, for inversions involving multiple parameter classes.

The 2-D and 3-D synthetic tests carried out in Chapter 4 illustrate a number of characteristics of the method and its application to data. The 2-D inversions demonstrate the need for damping when parts of the interface structure are poorly constrained by ray paths; setting the damping parameter ϵ to zero can result in unrealistic interface and velocity perturbations and hence a poor solution. A procedure was established for determining the optimum value of ϵ. Varying ϵ modifies the final solution of the inversion because it alters the trade-off between satisfying the data and satisfying the initial model. The optimum value of ϵ occurs for the solution that minimises the data misfit and at the same time minimises unnecessary structure as defined by deviation from the initial model. Graphs of data misfit versus model misfit typically show a trade-off curve from which the optimum value can be chosen near the elbow of the curve. Estimates of *a posteriori* model covariance, resolution and correlations derived from linear theory were also made,

and tests showed that they are a reliable indicator of solution quality. The diagonal elements of the resolution matrix may be interpreted as indicators of how well particular parameters are constrained by data. Generally, parameters whose resolution value were ≥ 0.5 were found to be well resolved. Synthetic tests were also performed with over and under parameterised initial models. Overparameterised initial models (i.e. models whose interfaces are described by more nodes than are required to represent the synthetic structure) tend to produce spurious short wavelength structure but can still map the long wavelength structure reasonable accurately. In these solutions, the data is not necessarily better fit and the inversion may become unstable. Using underparameterised models (i.e. models whose interfaces are described by fewer nodes than are required to represent the synthetic structure) result in solutions that only include features with wavelengths equal to or greater than the node separation. The inversion tends to be stable in this case, with the data misfit decreasing monotonically, although the quality of the data fit is degraded by the inability of the solution to include the shorter wavelength components of the structure.

Synthetic tests using structures containing layer pinchouts were carried out in both 2-D and 3-D (Section 4.3). In both cases, pinchouts could be well resolved even if the initial model estimates were defined with 1-D structure. In one case (Figure 4.33), the 3-D inversion used a source-receiver configuration that resulted in a relatively inhomogeneous coverage of rays, especially near the surface, but nonetheless a satisfactory solution was obtained. Use of an irregular mesh of nodes to represent interface structure was also examined in 3-D. A single interface structure was used together with a source-receiver configuration that resulted in large areas of the interface not being intersected by rays. It was demonstrated that in such cases, an irregular parameterisation (Figure 4.46) can result in more desirable models (fewer parameters required to fit the data to the same level), but the node distribution and surface patch shape must be taken into account when the solution is interpreted.

A final synthetic test (Section 4.3.3) applied the inversion method to a synthetic model representing a 3-D subduction zone setting. The source-receiver array simulated a marine survey, with eight land based receivers and four marine shot lines. The subduction zone was described by six crustal layers overlying a mantle half-space, with three of the crustal layers pinching out. A total of 734 interface and velocity parameters describe the synthetic model and 2053 traveltimes were used in the inversion. The initial model used in this case

contained essentially 2-D structure, and the accuracy of the inversion solution showed that the method could feasibly be used in regions of complex structure not well approximated by laterally continuous layers.

Compared to other published methods for inverting 3-D wide-angle seismic data, the scheme developed in this study perhaps holds more in common with many published 2-D inversion methods in the way that structure is represented. In 2-D wide-angle analysis, crustal structure is commonly represented by a series of layers of variable thickness. Interface structure and layer velocity are normally allowed to vary in an attempt to satisfy the data. For example, Stadtlander et al. (1999) derive a crustal and upper mantle structure beneath the southern Ural Mountains, representing upper, middle and lower crustal layers in addition to an upper mantle half-space. They also divide the upper crust into a large number of laterally discontinuous layers. Kodaira et al. (1998) use wide-angle traveltimes to constrain a crustal model consisting of no fewer than eight layers, four of which are laterally discontinuous, beneath the Jan Mayan microcontinent. They invert for both interface geometry and layer velocity structure. Others who have used similar approaches to constrain 2-D multi-layered crustal structure include Kanasewich et al. (1994), Darbyshire et al. (1998), Navin et al. (1998) and Vogt et al. (1998). In 3-D most authors avoid the kind of structural detail that is included in such 2-D models. For example, it is common practice to invert the traveltimes of only the first-arrivals of a 3-D dataset for continuous velocity structure (e.g. Hole, 1992; Zelt & Barton, 1998), or invert for the structure of a single interface using first arrivals (e.g. Hole, 1992) or reflected phases (e.g. Riahi et al., 1997). The wide-angle inversion method presented in Chapter 4 allows multiple interfaces and discontinuous layers to be used, which is similar to the 2-D methods mentioned above. The main difference is that lateral variations in velocity are not incorporated. However, 3-D datasets commonly have poorer ray coverage than 2-D datasets, so the potential for resolving the trade-off between lateral velocity variation and interface depth is lower.

The wide-angle inversion method was applied to data collected in Tasmania in 1995 as part of the TASGO project, as described in Chapter 7. The source-receiver array consisted of approximately 36,000 shots at a 50 m spacing around Tasmania, recorded at a network of 44 analogue and digital recorders distributed throughout the island. Of the 44 stations, only 24 recorded data with a detectable signal. Ultimately, data from only 21 recorders were utilised, because for the other three recorders, it was not possible to identify the onset of arrivals with acceptable accuracy. The production of a robust 3-D

model of Tasmania based on this data was challenging because coverage is quite variable (most usable data was collected in NW Tasmania), with near-surface structure generally poorly sampled by ray paths, but deep crustal structure generally well sampled except in central Tasmania.

The data were picked using an interactive picking program developed during the course of this project. The program processes and visualises the data and records the interactive picks to file (see Chapter 6). Error estimates for each pick are also made during this process. Picked data are assigned to specific reflection or refraction phase prior to the inversion. Incorrect assignment may result in that portion of the data being poorly satisfied, but such "mispicks" are generally easily identified and reassigned. Knowing which traveltime is associated with which phase is *a priori* information as far as the inversion is concerned, so if it is possible to identify this in the data, then it should be used to help constrain the solution.

A preliminary picture of Tasmania's subsurface structure was obtained by inverting data from particular receiver-source line combinations for 1-D structure (Section 7.2). These results suggest that variations in Moho depth are significant (Figures 7.3 to 7.5) and that the crust can be approximated by a relatively thin (∼8 km) upper-crustal layer overlying a much thicker (∼22 km) lower crustal layer. In the NW, the seismic signature of the Rocky Cape Group, an overlying sedimentary sequence, was also interpreted in the data and a laterally discontinuous lower crustal layer was identified. The preliminary 1-D models provided the *a priori* information for the subsequent inversions that permitted lateral variations in crustal structure. Hence, the inversion results did not depend on *a priori* information from other studies. The crustal structure in this case is entirely defined by traveltime information from the TASGO dataset in contrast to the teleseismic inversion, which required an assumed mean vertical velocity structure, against which the traveltime residuals constrain the lateral variation.

Although the TASGO wide-angle dataset is not very conducive to 2-D interpretation, an approximate 2-D inversion model along the western north coast of Tasmania was constructed using data collected at three stations from a single shot line (Section 7.3). The source and receiver positions were projected onto a straight line that was roughly perpendicular to the strike of major surface features. Four layers are used to represent the crust, which overlies a mantle half-space. One of the crustal layers pinches out against the Moho. The solution model satisfies the data in the sense that the χ^2 parameter is

reduced to near 1, the level attributed to noise. The solution reveals significant lateral structure in NW Tasmania (Figure 7.10).

The 3-D interpretation of the wide-angle data (Section 7.4) is done in two stages because most of the data is concentrated in NW Tasmania. Relatively few crustal phases could be identified outside this region. The initial model used to describe the NW region is consistent with the initial model used in the 2-D inversion, and therefore consists of four crustal layers, one of which pinches out, overlying a mantle half-space. The upper two interfaces use an irregular mesh of interface nodes in an attempt to efficiently accommodate the very inhomogeneous ray path distribution near the surface. The second stage of the 3-D inversion attempts to recover the structure of the Moho beneath the entirety of Tasmania. All available P_n and P_mP phases are inverted for the Moho structure assuming a laterally invariant crustal layer. The principle assumption of this inversion is that the Moho phases are relatively unaffected by lateral variations in the velocity structure of the crust. This assumption was tested by repeating the inversion including a mid-crustal interface and all related phases. The two-interface inversion revealed a very similar Moho structure to the single-interface inversion, despite large depth fluctuations in the mid-crustal interface, which was generally poorly resolved by the data. The interface structure in the NW of the Moho-only inversion model of Tasmania is also very similar to the Moho of the four crustal layer NW Tasmania model.

The inversion models suggest that Tasmania has an average crustal velocity of 6.2 km/s, an average P_n velocity of 8.0 km/s and an average Moho depth (in resolved regions) of approximately 31 km. The latter result is very significant because previous studies have estimated the crust to be significantly thinner, in particular Richardson (1980) estimated the crust to vary in thickness between 22 and 27 km in northern Tasmania, and Leaman (1989) estimated the crust to be 27.5 km thick in central Tasmania, thinning by up to 5 km towards the coast.

Geological and tectonic implications of the TASGO inversion results were discussed in Section 7.6. The Rocky Cape Element in NW Tasmania is composed of relatively thin crust, with the transition to thicker crust in the SE occurring principally beneath the Arthur Lineament, a band of metamorphosed marine sediments. Just west of the Tamar Fracture zone, the crust is nearly 37 km thick, a result consistent with tectonic models that suggest crustal shortening in this region due to the juxtaposition of the East and West Tasmania Terranes during the Tabberabberan Orogeny. The inversion models

also suggest that the crust is generally thicker beneath the west coast of Tasmania than beneath the east coast, reflecting the geological history of a transform margin in the west and an extensional margin in the east, both of which formed during the breakup of Gondwana in the Cretaceous.

The work presented in this study involves the application of tomographic inversion techniques to seismic traveltimes in order to constrain layered crustal structure. The significant outcomes of the project are summarised below.

1. Teleseismic traveltime residuals can be successfully used to constrain significant variations in lateral structure described by variations in the geometry of interfaces that bound sub-horizontal layers.

2. Inverting teleseismic traveltime residuals for interface structure is a viable alternative to inverting for continuous velocity distribution.

3. Wide-angle data potentially offers more constraints than teleseismic data, and can be used to construct well constrained preliminary models described by only a few parameters. These models can be used to construct initial models for subsequent inversions involving many more parameters.

4. A new method for the inversion of wide-angle refraction and reflection traveltimes for 3-D layered crustal structure has been developed, tested and successfully applied. The method simultaneously inverts all traveltimes for all model parameters (interface depth, velocity and vertical velocity gradient) and permits an arbitrary number of interfaces to be used. Adjacent interfaces may merge together to form layer pinchouts, allowing complex tectonic environments such as subduction zones to be represented. No other 3-D wide-angle inversion method currently has this capability.

5. The inversion of TASGO data reveals much new information on Tasmania's deep crustal structure. The crust is shown to be thicker than previously thought, and the Rocky Cape Element is composed of much thinner crust than the other tectonic elements, with the Arthur Lineament on the surface lying above the transition from thinner to thicker crust.

Possible future work on the 3-D wide-angle inversion method should be directed towards allowing for lateral variations in velocity within individual layers. This capability would

permit additional flexibility in representing geological structures. However, it has been demonstrated in this study that models without this flexibility can satisfy real wide-angle datasets with plausible structures. Further development of the teleseismic inversion method could also include lateral variations of velocity within a layer. However, it is unlikely that teleseismic traveltime data alone could resolve the trade-off between interface depth and velocity variation. Ultimately, the methods developed here could be adapted without significant modification to facilitate a joint inversion of teleseismic and wide-angle data for crustal structure. One of the limitations of the TASGO dataset is that ray coverage is poor in central Tasmania, which is why the inversion solutions tend to be well resolved only in regions near the coast. If teleseismic data were available from the 44 recorders of the TASGO array, they would offer few constraints on crustal structure due to the large station separation. However, if a good angular coverage of teleseismic data were recorded by a more closely spaced array of stations in central Tasmania, and there is adequate overlap with the TASGO wide-angle dataset, then a joint inversion of the two datasets is likely to result in an improved model of Tasmania's crustal structure.

References

Abers, G. A., 1994. Three-dimensional inversion of regional P and S arrival times in the East Aleutians and sources of subduction zone gravity highs, *J. Geophys. Res.*, **99**, 4395–4412.

Achauer, U., 1994. New ideas on the Kenya rift based on the inversion of the combined dataset of the 1985 and 1989/90 seismic tomography experiments, *Tectonophysics*, **236**, 305–329.

Aki, K. & Lee, W. H. K., 1976. Determination of the three-dimensional velocity anomalies under a seismic array using first P arrival times from local earthquakes 1. A homogeneous intial model, *J. Geophys. Res.*, **81**, 4381–4399.

Aki, K. & Richards, P. G., 1980. *Quantitative seismology: theory and methods*, W. H. Freeman, San Francisco.

Aki, K., Christoffersson, A., & Husebye, E. S., 1977. Determination of the three-dimensional seismic structure of the lithosphere, *J. Geophys. Res.*, **82**, 277–296.

Ammon, C. J., Randall, G. E., & Zandt, G., 1990. On the nonuniqueness of receiver function inversions, *J. Geophys. Res.*, **95**, 15,303–15,318.

Ankeny, L. A., Braile, L. W., & Olsen, K. H., 1986. Upper crustal structure beneath the Jemez Mountains volcanic field, New Mexico, determined by three-dimensional simultaneous inversion of seismic refraction and earthquake data, *J. Geophys. Res.*, **91**, 6188–6198.

Baille, P. W. & Powell, C. M., 1991. Tectonic affinity of the Lachlan Fold Belt in Tasmania, in *Tectonics and mineralization of the Lachlan Fold Belt*, vol. 29, p. 2, Geological Society of Australia.

Baker, G. E., Minster, J. B., Zandt, G., & Gurrola, H., 1996. Constraints on crustal structure and complex Moho topography beneath Piñon Flat, California, from teleseismic receiver functions, *Bull. Seism. Soc. Am.*, **86**, 1830–1844.

Barsky, B. A., 1982. End conditions and boundary conditions for uniform B-spline curve and surface representations, *Computers in Industry*, **3**, 17–29.

Bartels, R. H., Beatty, J. C., & Barsky, B. A., 1987. *An introduction to splines for use in computer graphics and geometric modelling*, Morgan Kaufmann, Los Altos.

Barton, T. J., 1999. *Crustal structure of Northern Tasmania, Australia*, Msc thesis, Monash University.

Barton, T. J., 1999. Crustal structure of northern Tasmania based upon a deep seismic transect, in *Last conference of the millenium*, vol. 53, pp. 3–4, Geological Society of Australia.

Barton, T. J., Johnstone, D. W., & Richardson, R. G., 1995. "TASGO" seismic survey 1995: Operational report, Record 1995/72, Australian Geological Survey Organisation.

Benz, H. M. & Smith, R. B., 1984. Simultaneous inversion for lateral velocity variations and hypocenters in the Yellowstone region using earthquake and refraction data, *J. Geophys. Res.*, **89**, 1208–1220.

Benz, H. M., Zandt, G., & Oppenheimer, D. H., 1992. Lithospheric structure of northern California from teleseismic images of the upper mantle, *J. Geophys. Res.*, **97**, 4791–4807.

Bishop, T. P., Bube, K. P., Cutler, R. T., Langan, R. T., Love, P. L., Resnick, J. R., Shuey, R. T., Spindler, D. A., & Wyld, H. W., 1985. Tomographic determination of velocity and depth in laterally varying media, *Geophysics*, **50**, 903–923.

Blundell, C. A., 1993. *Resolution analysis of seismic P-wave velocity estimates using reflection tomographic inversion*, Ph.D. thesis, Monash University.

Bosch, M., 1997. P wave velocity tomography of the Venezuelan region from local arrival times, *J. Geophys. Res.*, **102**, 5455–5472.

Boschetti, F., Dentith, M. K., & List, R. D., 1996. Inversion of seismic refraction data using genetic algorithms, *Geophysics*, **61**, 1715–1727.

Bowman, R. & Kennett, B. L. N., 1993. The velocity structure of the Australian shield from seismic traveltimes, *Bull. Seism. Soc. Am.*, **83**, 25–37.

Bregman, N. D., Bailey, R. C., & Chapmans, C. H., 1989. Crosshole seismic tomography, *Geophysics*, **54**, 200–215.

Brown, A. V., Seymour, D. B., Calver, C. R., Green, G. R., & Yeates, A. N., 1998. Overview of Tasmania's tectonic framework, geological history and mineralisation, in *Mineral systems and the crust-upper mantle of southeast Australia*, Record 1998/2, pp. 13–24, Australian Geological Survey Organisation.

Cao, S. & Greenhalgh, S., 1994. Finite-difference solution of the eikonal equation using an efficient, first-arrival, wavefront tracking scheme, *Geophysics*, **59**, 632–643.

Cara, M. & Lévêque, J. J., 1987. Waveform inversion using secondary observables, *Geophys. Res. Lett.*, **14**, 1046–1049.

Carrion, P., Costa, J., Pinheiro, J. E. F., & Schoenberg, M., 1992. Cross-borehole tomography in anisotropic media, *Geophysics*, **57**, 1194–1198.

Carroll, S. & Beresford, G., 1996. Combining reflection tomography with layer replacement for velocity analysis of near-surface reefs, *Geophysics*, **61**, 561–569.

Cassell, B. R., 1982. A method for calculating synthetic seismograms in laterally varying media, *Geophys. J. Royal Astr. Soc.*, **69**, 339–354.

Červený, V., 1987. Ray tracing algorithms in three-dimensional laterally varying layered structures, in *Seismic tomography: With applications in global seismology and exploration geophysics*, edited by G. Nolet, pp. 99–133, D. Reidel, Dordrecht.

Červený, V. & Firbas, P., 1984. Numerical modelling and inversion of travel times of seismic body waves in inhomogeneous anisotropic media, *Geophys. J. Royal Astr. Soc.*, **76**, 41–51.

Červený, V. & Pšenčik, I., 1983. Gaussian beams and paraxial ray approximation in three-dimensional elastic inhomogeneous media, *J. Geophys.*, **53**, 1–15.

Červený, V., Klimeš, L., & Pšenčik, I., 1984. Paraxial ray approximations in the computation of seismic wavefields in inhomogeneous media, *Geophys. J. Royal Astr. Soc.*, **79**, 89–104.

Chapman, C. H. & Drummond, R., 1982. Body-wave seismograms in inhomogeneous media using Maslov asymptotic theory, *Bull. Seism. Soc. Am.*, **72**, S277–S317.

Chávea-Pérez, S., Louie, J. N., & Pullammanappallil, S. K., 1998. Seismic depth imaging of normal faulting in the southern Death valley basin, *Geophysics*, **63**, 223–230.

Cheng, N. & House, L., 1996. Minimum traveltime calculations in 3-D graph theory, *Geophysics*, **61**, 1895–1898.

Chian, D., Hall, J., & Marillier, F., 1996. Lithospheric wide-angle seismic profiles using stacked airgun shots, *Geophys. Res. Lett.*, **23**, 2077–2080.

Chiarabba, C., Amoto, A., & Meghraoui, M., 1997. Tomographic images of the El Asnam fault zone, *J. Geophys. Res.*, **102**, 24,485–24,498.

Chiu, S. K. L., Kanasewich, E. R., & Phadke, S., 1986. Three-dimensional determination of structure and velocity by seismic tomography, *Geophysics*, **51**, 1559–1571.

Chudyk, E. C., Bracewell, R., & Collins, C. D. N., 1995. Operational report for the 1995 seismic refraction, wide-angle reflection and tomography survey of Tasmania, Record 1995/74, Australian Geological Survey Organisation.

Clayton, R. W. Comer, R. P., 1983. A tomographic analysis of mantle heterogeneities from body wave travel times, *Eos., Trans. AGU*, **64**, 776.

Clayton, R. W. & McMechan, G. A., 1981. Inversion of refraction data by wave field continuation, *Geophysics*, **46**, 860–868.

Clement, W. P., Carbonell, R., & Smithson, S. B., 1994. Shear-wave splitting in the lower crust beneath the Archean crust of southwest Greenland, *Tectonophysics*, **232**, 195–210.

Clitheroe, G., Gudmundsson, O., & Kennett, B. L. N., 2000. The crustal thickness of Australia, *J. Geophys. Res.*, **105**, 13,697–13,713.

Collins, C. D. N., 1988. Seismic velocities in the crust and upper mantle of Australia, Bull. 277, Bur. Min. Resour., Aust.

Collins, C. D. N. & Semenova, T. O., 2000. Seismic tomography of Tasmania: data processing report, Record 2000/14, Australian Geological Survey Organisation.

Corbett, K., 1994. Stratigraphic mapping, Tyennan connection, Cambrian orogenies, the Arthur Lineament, and the tectonic context of the Mount Read Volcanics, in *Abstracts*, vol. 39, pp. 35–37, Geological Society of Australia.

Corbett, K. D. & Turner, N. J., 1989. Early Palaeozoic deformation and tectonics, in *Geology and Mineral Resources of Tasmania*, edited by C. F. Burrett & E. L. Martin, vol. 15 of **Special Publication**, pp. 154–181, Geological Society of Australia.

Corbett, K. D., Banks, M. R., & Jago, J. B., 1972. Plate tectonics and the Lower Palaeozoic of Tasmania, *Nature Physical Science*, **240**, 9–11.

Cotton, F. & Avouc, J. P., 1994. Crustal and upper-mantle structure under the Tien Shan from surface-wave dispersion, *Phys. Earth Planet. Inter.*, **84**, 95–109.

Crawford, A. J. & Berry, R. F., 1992. Tectonic implications of Late Proterozoic-Early Palaeozoic igneous rock associations in western Tasmania, *Tectonophysics*, **214**, 37–56.

Dalziel, W. D., 1991. Pacific margins of Laurentia and East Antarctica-Australia as a conjugate rift pair: Evidence and implications for an Eocambrian supercontinent, *Geology*, **19**, 598–601.

Darbyshire, F. A., Bjarnason, I. J., White, R. S., & Flórenz, O. G., 1998. Crustal structure above the Iceland mantle plume, imaged by the ICEMELT refraction profile, *Geophys. J. Int.*, **135**, 1131–1149.

Davis, P. M., 1991. Continental rift structures and dynamics with reference to teleseismic studies of the Rio Grande and East African rifts, *Tectonophysics*, **197**, 309–325.

Davison, C., 1978. *The founders of seismology*, Arno Press, New York.

Debayle, E., 1999. *SV*-wave azimuthal anisotropy in the Australian upper mantle: preliminary results from automated Rayleigh waveform inversion, *Geophys. J. Int.*, **137**, 747–754.

Dijkstra, E. W., 1959. A note on two problems in connection with graphs, *Numer. Math.*, **1**, 269–271.

Disher, D. A. & Naquin, P. J., 1970. Statistical automatic statics analysis, *Geophysics*, **35**, 574–585.

Dobrin, M. B. & Savit, C. H., 1988. *Introduction to geophysical prospecting*, McGraw-Hill Book Co., New York.

Dorbath, C. & Paul, A., 1996. Tomography of the Andean crust and mantle at 20°S: First results of the Lithoscope experiment, *Phys. Earth Planet. Inter.*, **97**, 133–144.

Drijkoningen, G. G. & White, R. S., 1995. Seismic velocity structure of oceanic crust by inversion using genetic algorithms, *Geophys. J. Int.*, **123**, 653–664.

Drummond, B. J. & Downie, D. N., 1985. BMR regional seismic refraction data - disc and magnetic tape file structures and data formats, Record 1985/5, Australian Geological Survey Organisation.

Drummond, B. J., Barton, T. J., Korsch, R. J., Rawlinson, N., Yeates, A. N., Collins, C. D. N., & Brown, A. V., 2000. Evidence for crustal extension and inversion in eastern Tasmania, Australia, during the Neoproterozoic and Early Palaeozoic, *Tectonophysics*, **329**, 1–21.

Dueker, K., Humphreys, E., & Biasi, G., 1993. Teleseismic imaging of the western United States upper mantle structure using the simultaneous iterative reconstruction technique, in *Seismic tomography: theory and practice*, edited by H. M. Iyer & K. Hirahara, pp. 265–298, Chapman & Hall, London.

Dziewonski, A. M. & Woodhouse, J. H., 1987. Global images of the earth's interior, *Science*, **236**, 37–48.

Dziewonski, A. M., Hager, B. H., & O'Connell, R. J., 1977. Large-scale heterogeneities in the lower mantle, *J. Geophys. Res.*, **82**, 239–255.

Dziewonski, A. M., Chou, T. A., & Woodhouse, J. H., 1981. Determination of earthquake source parameters from waveform data for studies of global and regional seismicity, *J. Geophys. Res.*, **86**, 2825–2852.

Eberhart-Phillips, D., 1990. Three-dimensional P and S velocity structure in the Coalinga Region, California, *J. Geophys. Res.*, **95**, 15,343–15,363.

Eberhart-Phillips, D. & Michael, A. J., 1993. Three-dimensional velocity structure, seismicity, and fault structure in the Parkfield Region, central California, *J. Geophys. Res.*, **98**, 15,737–15,758.

Elliot, C. G. & Gray, D. R., 1992. Correllations between Tasmania and the Tasman-Transantarctic orogen: Evidence for easterly derivation of Tasmania relative to mainland Australia, *Geology*, **20**, 621–624.

Elliot, C. G., Gray, D. R., & Woodward, N. B., 1991. Relating Tasmania to the Lachlan Fold Belt, in *Tectonics and mineralization of the Lachlan Fold Belt*, vol. 29, p. 15, Geological Society of Australia.

Elliot, C. G., Woodward, N. B., & Gray, D. R., 1993. Complex regional fault history of the Badger Head region, northern Tasmania, *Australian Journal of Earth Sciences*, **40**, 155–168.

Evans, J. R., 1982. Compressional wave velocity structure of the upper 350 km under the Eastern Snake River Plain near Rexburg, Idaho, *J. Geophys. Res.*, **87**, 2654–2670.

Exon, N. & Crawford, A. J., 1997. West Tasmanian margin and offshore plateaus: geology, tectonic and climatic history, and resource potential, *Australian Journal of Earth Sciences*, **44**, 539–541.

Exon, N. & Hill, P., 1997. The continental margin off west Tasmania, and Tasmania's marginal plateaus, *AGSO Research Newsletter*, **27**, 4–8.

Faria, E. L. & Stoffa, P. L., 1994. Traveltime computation in transversely isotropic media, *Geophysics*, **59**, 272–281.

Farra, V. & Madariaga, R., 1988. Non-linear reflection tomography, *Geophys. J.*, **95**, 135–147.

Fehler, M. & Pearson, C., 1984. Cross-hole seismic surveys: Applications for studying subsurface fracture systems at a hot dry rock geothermal site, *Geophysics*, **49**, 37–45.

Fischer, R. & Lees, J. M., 1993. Shortest path ray tracing with sparse graphs, *Geophysics*, **58**, 987–996.

Fletcher, R. & Reeves, C. M., 1964. Function minimization by conjugate gradients, *Comput. J.*, **7**, 149–154.

Gjøystdal, H., Reinhardsen, J. E., & Ursin, B., 1984. Traveltime and wavefront curvature calculations in three-dimensional inhomogeneous layered media with curved interfaces, *Geophysics*, **49**, 1466–1494.

Glahn, A. & Granet, M., 1993. Southern Rhine Graben: Small-wavelength tomographic study and implications for the dynamic evolution of the graben, *Geophys. J. Int.*, **113**, 399–418.

Goleby, B. R., Wright, C., Collins, C. D. N., & Kennett, B. L. N., 1988. Seismic reflection and refraction profiling across the Arunta Block and the Ngalia and Amadeus Basins, *Australian Journal of Earth Sciences*, **35**, 275–294.

Goulty, N. R., 1993. Controlled-source tomography for mining and engineering applications, in *Seismic tomography: theory and practice*, edited by H. M. Iyer & K. Hirahara, pp. 797–813, Chapman & Hall, London.

Grad, M., Shiobara, H., Janik, T., Guterch, A., & Shimamura, H., 1997. Crustal model of the Bransfield Rift, West Antarctica, from detailed OBS refraction experiments, *Geophys. J. Int.*, **130**, 506–518.

Graeber, F. M. & Asch, G., 1999. Three-dimensional models of P wave velocity and P-to-S velocity ratio in the southern central Andes by simultaneous inversion of local earthquake data, *J. Geophys. Res.*, **104**, 20,237–20,256.

Graeber, F. M., Houseman, G. A., & Greenhalgh, S. A., 2002. Regional teleseismic tomography of the western Lachlan Orogen and the Newer Volcanic Province, southeast Australia, *Geophys. J. Int.*, **149**, 249–266.

Granet, M. & Trampert, J., 1989. Large-scale P-velocity structures in the Euro-Mediterranean area, *Geophys. J. Int.*, **99**, 583–594.

Green, D. C., 1989. Heat flow and heat production in Tasmania, in *Geology and Mineral Resources of Tasmania*, edited by C. F. Burrett & E. L. Martin, vol. 15 of **Special Publication**, pp. 461–463, Geological Society of Australia.

Green, G. R., 1998. The mineral systems of Tasmania, in *Mineral Systems and the Crust-upper Mantle of Southeast Australia*, edited by D. M. Finlayson & L. E. A. Jones, vol. 2 of **AGSO Record**, pp. 88–92, Australian Geological Survey Organisation.

Greenhalgh, S. A., Tapley, D., & Singh, R., 1989. Crustal heterogeneity in South Australia, earthquake evidence, *Geophys. J.*, **96**, 85–99.

Greenhalgh, S. A., von der Borch, C. C., & Tapley, D., 1989. Explosion seismic determination of crustal structure beneath the Adelaide Geosyncline, South Australia, *Phys. Earth Planet. Inter.*, **58**, 323–343.

Greenhalgh, S. A., Sugiharto, S., Wright, C., & Goleby, B. R., 1990. Tomographic reconstruction of upper crustal velocity variations in the Arunta Block, central Australia, *Tectonophysics*, **173**, 63–72.

Gubbins, D., 1992. *Seismology and plate tectonics*, Cambridge University Press, Cambridge.

Guiziou, J. L., Mallet, J. L., & Madariaga, R., 1996. 3-D seismic reflection tomography on top of the GOCAD depth modeler, *Geophysics*, **61**, 1499–1510.

Gunn, P. J., Mackey, T. E., Yeates, A. N., Richardson, R. G., Seymour, D. B., McClenaghan, M. P., Calver, C. R., & Roach, M. J., 1997. The basement elements of Tasmania, *Exploration Geophysics*, **28**, 225–231.

Hasegawa, A., Umino, N., & Takagi, A., 1978. Double-planed deep seismic zone and upper-mantle structure in the northeastern Japan arc, *Geophys. J. Royal Astr. Soc.*, **54**, 281–296.

Haslinger, F., Kissling, E., Ansorge, J., Hatzfeld, D., Papadimitriou, E., Karakostas, V., Makropoulos, K., Kahle, H. G., & Peter, Y., 1999. 3D crustal structure from local earthquake tomography around the Gulf of Arta (Ionian region, NW Greece), *Tectonophysics*, **304**, 201–218.

Hearn, T. M., 1996. Anisotropic *Pn* tomography in the western United States, *J. Geophys. Res.*, **101**, 8403–8414.

Herrin, E., Tucker, W., Taggart, J., Gordon, D. W., & Lobdell, J. L., 1968. Estimation of surface focus *P* travel times, *Bull. Seism. Soc. Am.*, **58**, 1273–1291.

Hestenes, M. & Stiefel, E., 1952. Methods of conjugate gradients for solving linear systems, *Nat. Bur. Stand. J. Res.*, **49**, 409–436.

Hildebrand, J. A., Dorman, L. M., Hammer, P. T. C., Schreiner, A. E., & Cornuelle, B. D., 1989. Seismic tomography of Jasper Seamount, *Geophys. Res. Lett.*, **16**, 1355–1358.

Hileman, J. A., Embree, P., & Pflueger, J. C., 1968. Automated static corrections, *Geophysical Prospecting*, **16**, 326–358.

Hill, P. J. & Yeates, A. N., 1995. Circum-Tasmania and South Tasman Rise: Cruise proposal for deep crustal seismic data acquisition, Record 1995/13, Australian Geological Survey Organisation.

Hill, P. J., Meixner, A. J., Moore, A. G., & Exon, N. F., 1997. Structure and development of the west Tasmanian offshore sedimentary basins: results of recent marine and aeromagnetic surveys, *Australian Journal of Earth Sciences*, **44**, 579–596.

Hole, J. A., 1992. Nonlinear high-resolution three-dimensional travel-time tomography, *J. Geophys. Res.*, **97**, 6553–6562.

Hole, J. A. & Zelt, B. C., 1995. 3-D finite-difference reflection travel times, *Geophys. J. Int.*, **121**, 427–434.

Hole, J. A., Clowes, R. M., & Ellis, R. M., 1992. Interface inversion using broadside seismic refraction data and three-dimensional traveltime calculations, *J. Geophys. Res.*, **97**, 3417–3429.

Humphreys, E. & Clayton, R. W., 1988. Adaption of back projection tomography to seismic travel time problems, *J. Geophys. Res.*, **93**, 1073–1085.

Humphreys, E. D. & Clayton, R. W., 1990. Tomographic image of the Southern California Mantle, *J. Geophys. Res.*, **95**, 19,725–19,746.

Humphreys, E. D. & Dueker, K. G., 1994. Western U.S. upper mantle structure, *J. Geophys. Res.*, **99**, 9615–9634.

Inoue, H., Fukao, Y., Tanabe, K., & Ogata, Y., 1990. Whole mantle *P*-wave travel time tomography, *Phys. Earth Planet. Inter.*, **59**, 294–328.

Ivansson, S., 1987. Crosshole transmission tomography, in *Seismic tomography: With applications in global seismology and exploration geophysics*, edited by G. Nolet, pp. 159–188, D. Reidel, Dordrecht.

Iwasaki, T., Hirata, N., Kanazawa, T., Melles, J., Suyehiro, K., Urabe, T., Möller, L., Makris, J., & Shimamura, H., 1990. Crustal and upper mantle structure in the Ryukyu Island Arc deduced from deep seismic sounding, *Geophys. J. Int.*, **102**, 631–651.

Johnson, B. D., 1973. A time term analysis of the data obtained during the Bass Strait upper mantle project (Operation BUMP), *Bull. Aust. Soc. Explor. Geophys.*, **4**, 15–20.

Jones, C. H. & Phinney, R. A., 1998. Seismic structure of the lithosphere from teleseismic converted arrivals observed at small arrays in the southern Sierra Nevada and vicinity, California, *J. Geophys. Res.*, **103**, 10,065–10,090.

Julian, B. R. & Gubbins, D., 1977. Three-dimensional seismic ray tracing, *J. Geophys.*, **43**, 95–113.

Kanao, M., 1997. Variations in the crustal structure of the Lützow-Holm Bay region, East Antarctica using shear wave velocity, *Tectonophysics*, **270**, 43–72.

Kanasewich, E., Burianyk, M. J. A., Ellis, R. M., Clowes, R. M., White, D. J., Lôté, T., Forsyth, D. A., Luetgert, J. A., & Spence, G. D., 1994. Crustal velocity structure of the Omineca Belt, southwestern Canadian Cordillera, *J. Geophys. Res.*, **99**, 2653–2670.

Kanasewich, E. R. & Chiu, S. K. L., 1985. Least-squares inversion of spatial seismic refraction data, *Bull. Seism. Soc. Am.*, **75**, 865–880.

Kao, H. & Rau, R. J., 1999. Detailed structures of the subducted Philippine Sea plate beneath northeast Taiwan: A new type of double seismic zone, *J. Geophys. Res.*, **104**, 1015–1033.

Kawakatsu, H., 1985. Double seismic zone in Tonga, *Nature*, **316**, 53–55.

Kennett, B. L. N., 1998. *Seismic wave propagation and seismic tomography*, Research School of Earth Sciences, Institute of Advanced Studies, The Australian National University, Canberra.

Kennett, B. L. N. & Engdahl, E. R., 1991. Traveltimes for global earthquake location and phase identification, *Geophys. J. Int.*, **105**, 429–465.

Kennett, B. L. N., Sambridge, M. S., & Williamson, P. R., 1988. Subspace methods for large scale inverse problems involving multiple parameter classes, *Geophys. J.*, **94**, 237–247.

Kirkpatrick, S., Gelatt, Jr, C. D., & Vecchi, M. P., 1983. Optimization by simulated annealing, *Science*, **220**, 671–680.

Klemperer, S. L. & Luetgert, J. H., 1987. A comparison of reflection and refraction processing and interpretation methods applied to conventional refraction data from coastal Maine, *Bull. Seism. Soc. Am.*, **77**, 614–630.

Klimeš, L. & Kvasnička, M., 1994. 3-D network ray tracing, *Geophys. J. Int.*, **116**, 726–738.

Kodaira, S., Mjelde, R., Gunnarsson, K., Shiobara, H., & Shimamura, H., 1998. Structure of the Jan Mayen microcontinent amd implications for its evolution, *Geophys. J. Int.*, **132**, 383–400.

Kohler, M. D., 1997. Three-dimensional velocity structure and resolution of the core-mantle boundary region from whole-mantle inversions of body waves, *Phys. Earth Planet. Inter.*, **101**, 85–104.

Kohler, M. D. & Davis, P. M., 1997. Crustal thickness variations in southern California from Los Angeles Region Seismic Experiment passive phase teleseismic travel times, *Bull. Seism. Soc. Am.*, **87**, 1330–1344.

Kosloff, D., Sherwood, J., Koren, Z., Machet, E., & Falkovitz, Y., 1996. Velocity and interface depth determination by tomography of depth migrated gathers, *Geophysics*, **61**, 1511–1523.

Lambaré, G., Lucio, P. S., & Hanyga, A., 1996. Two-dimensional multivalued traveltime and amplitude maps by uniform sampling of a ray field, *Geophys. J. Int.*, **125**, 584–598.

Lambeck, K., 1983. Structure and evolution of the intracratonic basins of central Australia, *Geophys. J. Royal Astr. Soc.*, **74**, 843–886.

Lambeck, K. & Burgess, G., 1992. Deep crustal structure of the Musgrave Block, central Australia: results from teleseismic traveltime anomalies, *Australian Journal of Earth Sciences*, **39**, 1–19.

Lambeck, K. & Penney, C., 1984. Teleseismic travel time anomalies and crustal structure in central Australia, *Phys. Earth Planet. Inter.*, **34**, 46–56.

Lambeck, K., Burgess, G., & Shaw, R. D., 1988. Teleseismic travel-time anomalies and deep crustal structure in central Australia, *Geophys. J.*, **94**, 105–124.

Langan, R. T., Lerche, I., & Cutler, R. T., 1985. Tracing of rays through heterogeneous media: An accurate and efficient procedure, *Geophysics*, **50**, 1456–1465.

Langston, C. A., 1989. Scattering of teleseismic body waves under Pasadena, California, *J. Geophys. Res.*, **94**, 1935–1951.

Leaman, D. & Richardson, R. G., 1989. Production of a residual gravity field map for Tasmania and some implications, *Exploration Geophysics*, **20**, 181–184.

Leaman, D. E., 1989. The gravity field, in *Geology and Mineral Resources of Tasmania*, edited by C. F. Burrett & E. L. Martin, vol. 15 of **Special Publication**, pp. 451–455, Geological Society of Australia.

Leaman, D. E., 1994. The Tamar Fracture System in Tasmania: Does it exist?, *Australian Journal of Earth Sciences*, **41**, 73–74.

Lee, W. H. K. & Pereyra, V., 1993. Mathematical introduction to seismic tomography, in *Seismic tomography: theory and practice*, edited by H. M. Iyer & K. Hirahara, pp. 9–22, Chapman & Hall, London.

Lévêque, J. J. & Masson, F., 1999. From ACH tomographic models to absolute velocity models, *Geophys. J. Int.*, **137**, 621–629.

Lévêque, J. J., Rivern, L., & Wittlinger, G., 1993. On the use of the checker-board test to assess the resolution of tomographic inversions, *Geophys. J. Int.*, **115**, 313–318.

Lévêque, J. J., Debayle, E., & Maupin, V., 1999. Anisotropy in the Indian Ocean upper mantle from Rayleigh- and Love-waveform inversion, *Geophys. J. Int.*, **133**, 529–540.

Li, X. D. & Romanowicz, B., 1996. Global mantle shear velocity model developed using nonlinear asymptotic coupling theory, *J. Geophys. Res.*, **101**, 22,245–22,272.

Lindsay, J. f. & Korsch, R. J., 1991. The evolution of the Amadeus Basin, central Australia, in *Geological and Geophysical Studies in the Amadeus Basin, Central Australia*, edited by R. J. Korsch & J. M. Kennard, pp. 7–32, AGPS, Canberra.

Luca, G. D., Filippi, L., Caccamo, D., Neri, G., & Scarpa, R., 1997. Crustal structure and seismicity of southern Tyrrhenian basin, *Phys. Earth Planet. Inter.*, **103**, 117–133.

Lutter, W. J. & Nowack, R. L., 1990. Inversion for crustal structure using reflections from the PASSCAL Ouachita experiment, *J. Geophys. Res.*, **95**, 4633–4646.

Lutter, W. J., Nowack, R. L., & Braile, L., 1990. Seismic imaging of upper crustal structure using travel times from the PASSCAL Ouachita experiment, *J. Geophys. Res.*, **95**, 4621–4631.

Lutter, W. J., Catchings, R. D., & Jarchow, C. M., 1994. An image of the Columbia Plateau from inversion of high-resolution seismic data, *Geophysics*, **59**, 1278–1289.

Mackey, T. E., Milligan, P. R., & Richardson, R. G., 1995. Total magnetic intensity map of Tasmania, 1:500 000, Tech. rep., Australian Geological Survey Organisation.

McCann, D. M., Baria, R., Jackson, P. D., & Green, A. S. P., 1986. Application of cross-hole seismic measurements in site investigation surveys, *Geophysics*, **51**, 914–929.

McCaughey, M. & Singh, S. C., 1997. Simultaneous velocity and interface tomography of normal-incidence and wide-aperture seismic traveltime data, *Geophys. J. Int.*, **131**, 87–99.

McFadden, P. L., Drummond, B. J., & Kravis, S., 1986. The nth-root stack: Theory, applications, and examples, *Geophysics*, **51**, 1879–1892.

McMechan, G. A., 1983. Seismic tomography in boreholes, *Geophys. J. Royal Astr. Soc.*, **74**, 601–612.

McMechan, G. A., Clayton, R. W., & Mooney, W. D., 1982. Application of wave field continuation to the inversion of refraction data, *J. Geophys. Res.*, **87**, 927–935.

McQueen, H. W. S. & Lambeck, K., 1996. Determination of crustal structure in central Australia by inversion of traveltime residuals, *Geophys. J. Int.*, **126**, 645–662.

Montagner, J. P. & Jobert, N., 1988. Vectorial tomography - II. Application to the Indian Ocean, *Geophys. J. Royal Astr. Soc.*, **94**, 309–344.

Montagner, J. P. & Tanimoto, T., 1991. Global upper mantle tomography of seismic velocities and anisotropies, *J. Geophys. Res.*, **96**, 20,337–20,351.

Moores, E. M. & Twiss, R. J., 1995. *Tectonics*, W. H. Freeman and Company, New York.

Morelli, A., 1993. Teleseismic tomography: core-mantle boundary, in *Seismic tomography: theory and practice*, edited by H. M. Iyer & K. Hirahara, pp. 163–189, Chapman & Hall, London.

Morozov, I. B., Smithson, S. B., Hollister, L. S., & Diebold, J. B., 1998. Wide-angle seismic imaging across accreted terranes, southeastern Alaska and western British Columbia, *Tectonophysics*, **299**, 281–296.

Moser, T. J., 1991. Shortest path calculation of seismic rays, *Geophysics*, **56**, 59–67.

Mota, L., 1954. Determination of dips and depths of geological layers by the seismic refraction method, *Geophysics*, **19**, 242–254.

Muirhead, K. J., 1968. Eliminating false alarms when detecting seismic events automatically, *Nature*, **217**, 533–534.

Münker, C. & Crawford, A. J., 2000. Cambrian arc evolution along the SE Gondwana active margin: A synthesis from Tasmania-New Zealand-Australia -Antarctica correlations, *Tectonics*, **19**, 415–432.

Murray, A. S., Morse, M. P., Milligan, P. R., & Mackey, T. E., 1997. Gravity anomaly map of the Australian region (second ed.), 1:500 000, Tech. rep., Australian Geological Survey Organisation.

Nakanishi, I., 1993. Surface wave tomography: velocity and Q, in *Seismic tomography: theory and practice*, edited by H. M. Iyer & K. Hirahara, pp. 92–132, Chapman & Hall, London.

Nakanishi, I. & Yamaguchi, K., 1986. A numerical experiment on nonlinear image reconstruction from first-arrival times for two-dimensional island arc structure, *J. Phys. Earth*, **34**, 195–201.

Navin, D. A., Peirce, C., & Sinha, M. C., 1998. The RAMESSES experiment -II. Evidence for accumulated melt beneath a slow spreading ridge from wide-angle refraction and multichannel reflection seismic profiles, *Geophys. J. Int.*, **135**, 746–772.

Neele, F., VanDecar, J., & Snieder, R., 1993. The use of P wave amplitude data in a joint inversion with travel times for upper mantle velocity structure, *J. Geophys. Res.*, **98**, 12,033–12,054.

Nielsen, L., Thybo, H., & Solodilov, L., 1999. Seismic tomographic inversion of Russian PNE data along profile Kraton, *Geophys. Res. Lett.*, **26**, 3413–3416.

Nolet, G., 1985. Solving or resolving inadequate and noisy tomographic systems, *J. Comp. Phys.*, **61**, 463–482.

Nolet, G., 1987. Waveform tomography, in *Seismic tomography: With applications in global seismology and exploration geophysics*, edited by G. Nolet, pp. 301–322, D. Reidel, Dordrecht.

Nolet, G. & Moser, T. J., 1993. Teleseismic delay times in a 3-D Earth and a new look at the S discrepency, *Geophys. J. Int.*, **114**, 185–195.

Nowack, R. L. & Lyslo, J. A., 1989. Fréchet derivatives for curved interfaces in the ray approximation, *Geophys. J.*, **97**, 497–509.

Oncescu, M. C., Burlacu, V., Anghel, M., & Smalbergher, V., 1984. Three-dimensional P-wave velocity image under the Carpathian Arc, *Tectonophysics*, **106**, 305–319.

Owens, T. J., Zandt, G., & Taylor, S. R., 1984. Seismic evidence for an ancient rift beneath the Cumberland Plateau, Tennessee: A detailed analysis of broadband teleseismic P waveforms, *J. Geophys. Res.*, **89**, 7783–7795.

Özdoğan, Y., 1987. *Seismic data processing*, Society of Exploration Geophysicists, Tulsa.

Papazachos, C. & Nolet, G., 1997. *P* and *S* deep velocity structure of the Hellenic area obtained by robust nonlinear inversion of travel times, *J. Geophys. Res.*, **102**, 8349–8367.

Parkinson, W. D. & Richardson, R. G., 1989. The magnetic field, in *Geology and Mineral Resources of Tasmania*, edited by C. F. Burrett & E. L. Martin, vol. 15 of **Special Publication**, pp. 455–458, Geological Society of Australia.

Parsons, T. & Zoback, M. L., 1997. Three-dimensional upper crustal velocity structure beneath San Francisco Peninsula, California, *J. Geophys. Res.*, **102**, 5473–5490.

Parsons, T., McCarthy, J., Kohler, W. M., Ammon, C. J., Benz, H. M., Hole, J. A., & Criley, E. E., 1996. Crustal structure of the Colorada Plateau, Arizona: Application of new long-offset seismic data analysis techniques, *J. Geophys. Res.*, **101**, 11,173–11,194.

Pearson, F., 1990. *Map projections: theory and applications*, CRC Press, Boca Raton.

Pereyra, V., Lee, W. H. K., & Keller, H. B., 1980. Solving two-point seismic-ray tracing problems in a heterogeneous medium, *Bull. Seism. Soc. Am.*, **70**, 79–99.

Plumb, K. A., 1979. The tectonic evolution of Australia, *Earth Sci. Rev.*, **14**, 205–249.

Podvin, P. & Lecomte, I., 1991. Finite difference computation of traveltimes in very contrasted velocity models: a massively parallel approach and its associated tools, *Geophys. J. Int.*, **105**, 271–284.

Pratt, R. G. & Goulty, N. R., 1991. Combining wave-equation imaging with traveltime tomography to form high-resolution images from crosshole data, *Geophysics*, **56**, 208–224.

Pratt, R. G., McGaughey, W. J., & Chapman, C. H., 1993. Anisotropic velocity tomography: A case study in a near-surface rock mass, *Geophysics*, **58**, 1748–1763.

Pratt, R. G., Song, Z. M., Williamson, P., & Warner, M., 1996. Two-dimensional velocity models from wide-angle seismic data by wavefield inversion, *Geophys. J. Int.*, **124**, 323–340.

Press, W. H., Tuekolsky, S. A., Vetterling, W. T., & Flannery, B. P., 1992. *Numerical Recipes in FORTRAN*, Cambridge University Press, Cambridge.

Priestley, K., Cipar, J., Egorkin, A., & Pavlenkova, N., 1994. Upper-mantle velocity structure beneath the Siberian platform, *Geophys. J. Int.*, **118**, 369–378.

Prothero, W. A., Taylor, W. J., & Eickemeyer, J. A., 1988. A fast, two-point, three-dimensional raytracing algorithm using a simple step search method, *Bull. Seism. Soc. Am.*, **78**, 1190–1198.

Purdy, G. M., 1982. The correction for the travel time effects of seafloor topography in the interpretation of marine seismic data, *J. Geophys. Res.*, **87**, 8389–8396.

Qin, F., Luo, Y., Olsen, K. B., Cai, W., & Schuster, G. T., 1992. Finite-difference solution of the eikonal equation along expanding wavefronts, *Geophysics*, **57**, 478–487.

Quintanar, L., Yamamoto, J., & Jiménez, Z., 1999. Source mechanism of two 1994 intermediate-depth-focus earthquakes in Guerrero, Mexico, *Bull. Seism. Soc. Am.*, **89**, 1004–1018.

Rawlinson, N., 1996. Methods and codes used in seismic tomography, Record 1996/21, Australian Geological Survey Organisation.

Rawlinson, N., 1996. *Tomographic inversion for subsurface velocity structure using teleseismic traveltimes*, Hons. thesis, Monash University.

Rawlinson, N., 2000. *Inversion of Seismic Data for Layered Crustal Structure*, Ph.D. thesis, Monash University.

Rawlinson, N. & Houseman, G. A., 1998. Inversion for interface structure using teleseismic traveltime residuals, *Geophys. J. Int.*, **133**, 756–772.

Recq, M., Goslin, J., Charvis, P., & Operto, S., 1998. Small-scale crustal variability within an intraplate structure: The Crozet Bank (southern Indian Ocean), *Geophys. J. Int.*, **134**, 145–156.

Riahi, M. A. & Juhlin, C., 1994. 3-D interpretation of reflected arrival times by finite-difference techniques, *Geophysics*, **59**, 844–849.

Riahi, M. A. & Lund, C. E., 1994. Two-dimensional modelling and interpretation of seismic wide-angle data from the western Gulf of Bothnia, *Tectonophysics*, **239**, 149–164.

Riahi, M. A., Lund, C. E., & Pederson, L. B., 1997. Three-dimensional image of the Moho undulations beneath the Gulf of Bothnia using wide-angle seismic data, *Geophys. J. Int.*, **129**, 461–471.

Richardson, R. G., 1980. *Crustal Structure*, Ph.D. thesis, University of Tasmania.

Richardson, R. G., 1989. Crustal structure, in *Geology and Mineral Resources of Tasmania*, edited by C. F. Burrett & E. L. Martin, vol. 15 of **Special Publication**, pp. 465–467, Geological Society of Australia.

Richardson, R. G., 1994. New geophysical data for northeastern Tasmania, in *Abstracts*, vol. 39, pp. 65–68, Geological Society of Australia.

Richardson, R. G., 1997. Government-sponsored geophysics in Tasmania, *Exploration Geophysics*, **28**, 119–122.

Ritsema, J., Nyblade, A. A., Owens, T. J., Langston, C. A., & VanDecar, J. C., 1998. Upper mantle seismic velocity structure beneath Tanzania, east Africa: Implications for the stability of cratonic lithosphere, *J. Geophys. Res.*, **103**, 21,201–21,213.

Ritzwoller, M. H. & Levshin, A. L., 1998. Eurasian surface wave tomography: Group velocities, *J. Geophys. Res.*, **103**, 4839–4878.

Roach, M. J., Leaman, D. E., & Richardson, R. G., 1993. A comparison of regional-residual separation techniques for gravity surveys, *Exploration Geophysics*, **24**, 779–784.

Robinson, E. A. & Treitel, S., 1980. *Geophysical signal analysis*, Englewood Cliffs, New Jersey.

Romanowicz, B., 1995. A global tomographic model of shear attenuation in the upper mantle, *J. Geophys. Res.*, **100**, 12,375–12,394.

Royer, J.-Y. & Rollet, N., 1997. Plate-tectonic setting of the Tasmanian region, *Australian Journal of Earth Sciences*, **44**, 543–560.

Ryberg, T., Wenzel, F., Mechie, J., Egorkin, A., Fuchs, K., & Solodilov, L., 1996. Two-dimensional velocity structure beneath northern Eurasia derived from the super long-range seismic profile Quartz, *Bull. Seism. Soc. Am.*, **86**, 857–867.

Saltzer, R. L. & Humphreys, E. D., 1997. Upper mantle P wave velocity structure of the eastern Snake River Plain and its relationship to geodynamic models of the region, *J. Geophys. Res.*, **102**, 11,829–11,841.

Sambridge, M. & Gudmundsson, O., 1998. Tomographic systems of equations with irregular cells, *J. Geophys. Res.*, **103**, 773–781.

Sambridge, M. S., 1990. Non-linear arrival time inversion: Constraining velocity anomalies by seeking smooth models in 3-D, *Geophys. J. Int.*, **102**, 653–677.

Sambridge, M. S. & Drijkoningen, G., 1992. Genetic algorithms in seismic waveform inversion, *Geophys. J. Int.*, **109**, 323–342.

Sambridge, M. S. & Kennett, B. L. N., 1990. Boundary value ray tracing in a heterogeneous medium: A simple and versatile algorithm, *Geophys. J. Int.*, **101**, 157–168.

Sato, T., Kosuga, M., & Tanaka, K., 1996. Tomographic inversion for P wave velocity structure beneath the northeastern Japan arc using local and teleseismic data, *J. Geophys. Res.*, **101**, 17,597–17,615.

Scales, J. A., 1987. Tomographic inversion via the conjugate gradient method, *Geophysics*, **52**, 179–185.

Seber, D., Barazangi, M., Tadili, B. A., Ramdani, M., Ibenbrahim, A., & Sari, D. B., 1996. Three-dimensional upper mantle structure beneath the intraplate Atlas and interplate Rif mountains of Morocco, *J. Geophys. Res.*, **101**, 3125–3138.

Sethian, J. A. & Popovici, A. M., 1999. 3-D traveltime computation using the fast marching method, *Geophysics*, **64**, 516–523.

Shalev, E., 1993. Cubic B-slines: Strategies of translating a simple structure to B-spline parameterization, *Bull. Seism. Soc. Am.*, **83**, 1617–1627.

Sheehan, A. F., Abers, G. A., Jones, C. H., & Lerner-Lam, A. L., 1995. Crustal thickness variations across the Colorado Rocky Mountains from teleseismic receiver functions, *J. Geophys. Res.*, **100**, 20,391–20,404.

Sheriff, R. E. & Geldart, L. P., 1995. *Exploration seismology*, Cambridge University Press, Cambridge.

Sjögren, B., 1984. *Shallow refraction seismics*, Chapman and Hall, London.

Snieder, R., 1993. Global inversions using normal modes and long-period surface waves, in *Seismic tomography: theory and practice*, edited by H. M. Iyer & K. Hirahara, pp. 23–63, Chapman & Hall, London.

Spakman, W., 1991. Delay-time tomography of the upper mantle below Europe, the Mediterranean and Asia Minor, *Geophys. J. Int.*, **107**, 309–332.

Stadtlander, R., Mechie, J., & Schulze, A., 1999. Deep structure of the southern Ural mountains as derived from wide-angle seismic data, *Geophys. J. Int.*, **137**, 501–515.

Staples, R. K., White, R. S., Brandsdóttir, Menke, W., Maguire, P. K. H., & McBride, J. H., 1997. Färoe-Iceland Ridge experiment 1. Crustal structure of northeastern Iceland, *J. Geophys. Res.*, **102**, 7849–7866.

Steck, L. K., Thurber, C. H., Fehler, M., Lutter, W. J., Roberts, P. M., Baldridge, W. S., Stafford, D. G., & Sessions, R., 1998. Crust and upper mantle P wave velocity structure beneath Valles caldera, New Mexico: Results from the Jemez teleseismic tomography experiment, *J. Geophys. Res.*, **103**, 24,301–24,320.

Stern, T. A. & McBride, J. H., 1998. Seismic exploration of continental strike-slip zones, *Tectonophysics*, **286**, 63–78.

Stoffa, P. L., Buhl, P., Diebold, J. B., & Wenzel, F., 1981. Direct mapping of seismic data to the domain of intercept time and ray parameter - A plane-wave decomposition, *Geophysics*, **46**, 255–267.

Su, W.-J. & Dziewonski, A. M., 1997. Simultaneous inversion for 3-D variations in shear and bulk velocity in the mantle, *Phys. Earth Planet. Inter.*, **100**, 135–156.

Tarantola, A., 1987. *Inverse problem theory*, Elsevier, Amsterdam.

Telford, W. M., Geldart, L. P., Sheriff, R. E., & Keys, D. A., 1976. *Applied Geophysics*, Cambridge University Press, Cambridge.

Telford, W. M., Geldart, L. P., & Sheriff, R. E., 1990. *Applied Geophysics*, Cambridge University Press, Cambridge.

Thomson, C. J. & Gubbins, D., 1982. Three-dimensional lithospheric modelling at NORSAR: linearity of the method and amplitude variations from the anomalies, *Geophys. J. Royal Astr. Soc.*, **71**, 1–36.

Thurber, C. H., 1983. Earthquake locations and three-dimensional crustal structure in the Coyote Lake area, central California, *J. Geophys. Res.*, **88**, 8226–8236.

Thurber, C. H., 1993. Local earthquake tomography: Velocities and V_p/V_s - theory, in *Seismic tomography: theory and practice*, edited by H. M. Iyer & K. Hirahara, pp. 563–583, Chapman & Hall, London.

Trampert, J. & Woodhouse, J. H., 1995. Global phase velocity maps of Love and Rayleigh waves between 40 and 150 seconds, *Geophys. J. Int.*, **122**, 675–690.

Turner, N. J., Black, L. P., & Kamperman, M., 1998. Dating of Neoproterozoic and Cambrian orogenies in Tasmania, *Australian Journal of Earth Sciences*, **45**, 789–806.

Um, J. & Thurber, C., 1987. A fast algorithm for two-point seismic ray tracing, *Bull. Seism. Soc. Am.*, **77**, 972–986.

Underwood, R., 1969. A seismic refraction study of the crust and upper mantle in the vicinity of Bass Strait, *Aust. J. Phys.*, **22**, 573–587.

van der Hilst, R., Engdahl, R., Spakman, W., & Nolet, G., 1991. Tomographic imaging of subducted lithosphere below northwest Pacific island arcs, *Nature*, **353**, 37–43.

van der Hilst, R. D., Widiyantoro, S., & Engdahl, E. R., 1997. Evidence for deep mantle circulation from global tomography, *Nature*, **386**, 578–584.

van Trier, J. & Symes, W. W., 1991. Upwind finite-difference calculation of traveltimes, *Geophysics*, **56**, 812–821.

VanDecar, J. C. & Snieder, R., 1994. Obtaining smooth solutions to large, linear, inverse problems, *Geophysics*, **59**, 818–829.

VanDecar, J. C., James, D. E., & Assumpção, M., 1995. Seismic evidence for a fossil mantle plume beneath South America and implications for plate driving forces, *Nature*, **378**, 25–31.

Veevers, J. J. & Eittreim, S. L., 1988. Reconstruction of Antarctica and Australia at breakup (95 ± 5ma) and before rifting (160 ma), *Australian Journal of Earth Sciences*, **35**, 355–362.

Vidale, J. E., 1988. Finite-difference calculations of traveltimes, *Bull. Seism. Soc. Am.*, **78**, 2062–2076.

Vidale, J. E., 1990. Finite-difference calculations of traveltimes in three dimensions, *Geophysics*, **55**, 521–526.

Vinje, V., Iversen, E., & Gjøystdal, H., 1993. Traveltime and amplitude estimation using wavefront construction, *Geophysics*, **58**, 1157–1166.

Vogt, U., Makris, J., O'Reilly, B., Hausser, F., Readman, P. W., Jacob, A. W. B., & Shannon, P. M., 1998. The Hatton Basin and continental margin: Crustal structure from wide-angle seismic and gravity data, *J. Geophys. Res.*, **103**, 12,545–12,566.

Walck, M. C., 1988. Three-dimensional V_p/V_s variations for the Coso region, California, *J. Geophys. Res.*, **93**, 2047–2052.

Walck, M. C. & Clayton, R. W., 1987. P wave velocity variations in the Coso region, California, derived from local earthquake travel times, *J. Geophys. Res.*, **92**, 393–405.

Wang, B. & Braile, L. W., 1996. Simultaneous inversion of reflection and refraction seismic data and application to field data from the northern Rio Grande rift, *Geophys. J. Int.*, **125**, 443–458.

Wang, Y. & Houseman, G. A., 1994. Inversion of reflection seismic amplitude data for interface geometry, *Geophys. J. Int.*, **117**, 92–110.

Wang, Y. & Houseman, G. A., 1995. Tomographic inversion of reflection seismic amplitude data for velocity variation, *Geophys. J. Int.*, **123**, 355–372.

Wang, Y. & Houseman, G. A., 1997. Point source $\tau - p$ transform: A review and comparison of computational methods, *Geophysics*, **62**, 325–334.

Wang, Y. & Pratt, R. G., 1997. Sensitivities of seismic traveltimes and amplitudes in reflection tomography, *Geophys. J. Int.*, **131**, 618–642.

Wang, Z., Tromp, J., & Ekström, G., 1998. Global and regional surface-wave inversions: A spherical-spline parameterization, *Geophys. Res. Lett.*, **25**, 207–210.

Weiland, C. M., Steck, L. K., Dawson, P. B., & Korneev, V. A., 1995. Nonlinear teleseismic tomography at Long Valley caldera, using three-dimensional minimum travel time ray tracing, *J. Geophys. Res.*, **100**, 20,379–20,390.

Wells, A. T., Forman, D. J., Ranford, L. C., & Cook, P. J., 1970. Geology of the Amadeus Basin, central Australia, *Bull. Bur. Miner. Resour. Geol. Geophys.*, **100**.

White, D. J., 1989. Two-dimensional seismic refraction tomography, *Geophys. J.*, **97**, 223–245.

Widiyantoro, S. & van der Hilst, R., 1997. Mantle structure beneath Indonesia inferred from high-resolution tomographic imaging, *Geophys. J. Int.*, **130**, 167–182.

Wiggins, S. M., Dorman, L. M., Cornuelle, B. D., & Hildebrand, J. A., 1996. Hess deep rift valley structure from seismic tomography, *J. Geophys. Res.*, **101**, 22,335–22,353.

Williams, E., 1989. Summary and synthesis, in *Geology and Mineral Resources of Tasmania*, edited by C. F. Burrett & E. L. Martin, vol. 15 of **Special Publication**, pp. 468–499, Geological Society of Australia.

Williamson, P. R., 1990. Tomographic inversion in reflection seismology, *Geophys. J. Int.*, **100**, 255–274.

Wong, J., Hurley, P., & F., W. G., 1983. Crosshole seismology and seismic imaging in crystalline rocks, *Geophys. Res. Lett.*, **10**, 686–689.

Woodward, N. B., Gray, D. R., & Elliott, C. G., 1993. Repeated Palaeozoic thrusting and allochthoneity of Precambrian basement, northern Tasmania, *Australian Journal of Earth Sciences*, **40**, 297–311.

Ye, S., Flueh, E. R., Klaeschen, D., & von Huene, R., 1997. Crustal structure along the EDGE transect beneath the Kodiak shelf off Alaska derived from OBH seismic refraction data, *Geophys. J. Int.*, **130**, 283–302.

Yilmaz, O., 1987. *Seismic data processing*, Society of Exploration Geophysicists, Tulsa.

Young, J. A., 1989. Diffraction tomography applied to crosshole and VSP seismic data, *Exploration Geophysics*, **20**, 169–173.

Zelt, B. C., Ellis, R. M., Clowes, R. M., & Hole, J. A., 1996. Inversion of three-dimensional wide-angle seimic data from the southwestern Canadia Cordillera, *J. Geophys. Res.*, **286**, 209–221.

Zelt, C. A., 1996. Seismic velocity structure of the central Chilean margin near the subducting Juan Fernández ridge: effective inversion of traveltime data across complex, laterally varying structure, in *Abstracts*, 7th Int. Symp., Deep Seismic Profiling of the Continents, Asilomar, CA.

Zelt, C. A., 1998. Lateral velocity resolution from three-dimensional seismic refraction data, *Geophys. J. Int.*, **135**, 1101–1112.

Zelt, C. A., 1999. Modelling strategies and model assessment for wide-angle seismic traveltime data, *Geophys. J. Int.*, **139**, 183–204.

Zelt, C. A. & Barton, P. J., 1998. Three-dimensional seismic refraction tomography: A comparison of two methods applied to data from the Faeroe Basin, *J. Geophys. Res.*, **103**, 7187–7210.

Zelt, C. A. & Smith, R. B., 1992. Seismic traveltime inversion for 2-D crustal velocity structure, *Geophys. J. Int.*, **108**, 16–34.

Zelt, C. A. & Zelt, B. C., 1998. Study of out-of-plane effects in the inversion of refraction/wide-angle reflection traveltimes, *Tectonophysics*, **286**, 209–221.

Zelt, C. A., Drew, J. J., Yedlin, M. J., & Ellis, R. M., 1987. Picking noisy refraction data using semblance supplemented by a Monte Carlo procedure and spectral balancing, *Bull. Seism. Soc. Am.*, **77**, 942–957.

Zelt, C. A., Hojka, A. M., Flueh, E. R., & McIntosh, K. D., 1999. 3D simultaneous seismic refraction and reflection tomography of wide-angle data from the central Chilean margin, *Geophys. Res. Lett.*, **26**, 2577–2580.

Zhang, J. & Toksöz, M. N., 1998. Nonlinear refraction traveltime tomography, *Geophysics*, **63**, 1726–1737.

Zhang, Y. S. & Lay, T., 1996. Global surface wave phase velocity variations, *J. Geophys. Res.*, **101**, 8415–8436.

Zhao, D., Hasegawa, A., & Horiuchi, S., 1992. Tomographic imaging of P and S wave velocity structure beneath Northeastern Japan, *J. Geophys. Res.*, **97**, 19,909–19,928.

Zhao, D., Hasegawa, A., & Kanamori, H., 1994. Deep structure of Japan subduction zone as derived from local, regional, and teleseismic events, *J. Geophys. Res.*, **99**, 22,313–22,329.

Zhao, D., Kanamori, H., & Humphreys, E., 1996. Simultaneous inversion of local and teleseismic data for the crust and mantle structure of southern California, *Phys. Earth Planet. Inter.*, **93**, 191–214.

Zhao, Z., Kubota, R., Fumio, S., & Iizuka, S., 1997. Crustal structure in the southern Kanto-Tokai region derived from tomographic method for seismic explosion survey, *J. Geophys. Res.*, **45**, 433–453.

Zhou, B., Sinadinovski, C., & Greenhalgh, S. A., 1992. Non-linear inversion travel-time tomography: imaging high-contrast inhomogeneities, *Exploration Geophysics*, **23**, 459–464.

Zhu, H. & Ebel, J. E., 1994. Tomographic inversion for the seismic velocity structure beneath northern New England using seismic refraction data, *J. Geophys. Res.*, **99**, 15,331–15,357.

Zielhuis, A. & van der Hilst, R. D., 1996. Upper-mantle shear velocity beneath eastern Australia from inversion of waveforms from SKIPPY portable arrays, *Geophys. J. Int.*, **127**, 1–16.

Appendix A

Linearisation

The traveltime of a ray in a continuous velocity medium $v(\mathbf{x})$ is:

$$t = \int_{L(v)} \frac{1}{v(\mathbf{x})} \mathrm{d}l \tag{A.1}$$

where L is the ray path and $v(\mathbf{x})$ is the velocity field. Equation A.1 is non-linear since the integration path depends on the velocity. If $v(\mathbf{x}) = v_0(\mathbf{x}) + \delta v(\mathbf{x})$ where $v_0(\mathbf{x})$ is a reference velocity field and $\delta v(\mathbf{x})$ is a perturbation, and $L(v) = L_0(v) + \delta L(v)$ where $L_0(v)$ is the known path in $v_0(\mathbf{x})$, then using a Taylor series expansion:

$$t(v, L) = t(v_0, L_0) + \frac{\partial t}{\partial v}\bigg)_{v_0} \delta v + \frac{\partial t}{\partial L}\bigg)_{v_0} \delta L + O(\delta v^2, \delta v \delta L, \delta L^2) \tag{A.2}$$

Since $L = L(v)$, $\delta L = (\partial L/\partial v)\delta v$ to first order, so Equation A.2 may be written:

$$t(v, L) = t(v_0, L_0) + \frac{\partial t}{\partial v}\bigg)_{v_0} \delta v + \frac{\partial t}{\partial L}\bigg)_{v_0} \frac{\partial L}{\partial v}\bigg)_{v_0} \delta v + O(\delta v^2) \tag{A.3}$$

Fermat's Principle states that the traveltime for a ray path is stationary (i.e. $\partial t/\partial L)_{v_0} = 0$), so Equation A.3 becomes:

$$t(v, L) = t(v_0, L_0) + \frac{\partial t}{\partial v}\bigg)_{v_0} \delta v + O(\delta v^2) \tag{A.4}$$

and discarding terms of $O(\delta v^2)$ gives:

$$\delta t = \frac{\partial t}{\partial v}\bigg)_{v_0} \delta v \tag{A.5}$$

where $\delta t = t(v, L) - t(v_0, L_0)$. Thus, a perturbation of the traveltime expression in Equation A.1 can be written:

$$\delta t = \int_{L_0} \delta \left(\frac{1}{v_0}\right) \mathrm{d}l + O(\delta v^2) = -\int_{L_0} \frac{\delta v}{v_0^2} \mathrm{d}l + O(\delta v^2) \tag{A.6}$$

An alternative way of obtaining Equation A.6 is to consider the expansion:

$$t(v, L_0) = t(v_0, L_0) + \frac{\partial t}{\partial v}\bigg)_{v_0} \delta v + O(\delta v^2) \tag{A.7}$$

which is the same as Equation A.2 except that the ray path is not perturbed. Rearranging Equation A.7 for the partial derivative term gives:

$$\frac{\partial t}{\partial v}\bigg)_{v_0} = \frac{t(v, L_0) - t(v_0, L_0)}{\delta v} + O(\delta v) \tag{A.8}$$

which can be written in terms of δt and δv using Equation A.5:

$$\delta t = t(v, L_0) - t(v_0, L_0) + O(\delta v^2) \tag{A.9}$$

Now substitute in Equation A.1 for the time terms $t(v, L_0)$ and $t(v_0, L_0)$:

$$\delta t = \int_{L_0} \frac{1}{v_0 + \delta v} \mathrm{d}l - \int_{L_0} \frac{1}{v_0} \mathrm{d}l + O(\delta v^2) \tag{A.10}$$

which can be written:

$$\delta t = -\int_{L_0} \frac{\delta v}{v_0^2 + v_0 \delta v} \mathrm{d}l + O(\delta v^2) \tag{A.11}$$

and since the integrand can be expanded as:

$$\frac{\delta v}{v_0^2 + v_0 \delta v} = \frac{\delta v}{v_0^2} - \frac{\delta v^2}{v_0^3} + \frac{\delta v^3}{v_0^4} - \ldots \tag{A.12}$$

the compact form of Equation A.11 is:

$$\delta t = -\int_{L_0} \frac{\delta v}{v_0^2} \mathrm{d}l + O(\delta v^2) \tag{A.13}$$

The implication of Equation A.13 is that if the velocity along the path is perturbed, then the corresponding traveltime perturbation calculated along the original path will be accurate to first order.

Appendix B

Ray Tracing Equations

The purpose of this appendix is to use the calculus of variations to derive the ray tracing equations (Equation 4.5) and associated traveltime equation (Equation 4.6) for a medium in which the velocity varies linearly with depth. The traveltime integral in such a medium between two points L_1 and L_2 is given by:

$$t = \int_{L_1}^{L_2} \frac{1}{v} \mathrm{d}l \tag{B.1}$$

where notation is consistent with that used in Section 4.2.2 and $v = v_0 - kz$. Since the ray path must lie in a vertical plane, let w be the horizontal coordinate that lies in this plane. Thus, $\mathrm{d}l = \sqrt{1 + z'^2}\mathrm{d}w$ (with $z' = \mathrm{d}z/\mathrm{d}w$) and Equation B.1 can be written as:

$$t = \int_{W_1}^{W_2} \frac{\sqrt{1 + z'^2}}{v} \mathrm{d}w \tag{B.2}$$

Equation B.2 is extremized using the Euler-Lagrange equation:

$$\frac{\partial f}{\partial z} - \frac{\mathrm{d}}{\mathrm{d}w}\left(\frac{\partial f}{\partial z'}\right) = 0 \tag{B.3}$$

where in this case $f = \sqrt{1 + z'^2}/v$. The solution of Equation B.3 thus describes a true ray path as Fermat's principle is satisfied. Since f doesn't explicitly depend on w, Equation B.3 simplifies to:

$$f - z'\frac{\partial f}{\partial z'} = C \tag{B.4}$$

where C is a constant. Substituting f into Equation B.4 gives:

$$\frac{\sqrt{1 + z'^2}}{v} - \frac{z'^2}{v\sqrt{1 + z'^2}} = C \tag{B.5}$$

The constant C is preserved along the ray path and is usually referred to as p, the ray parameter. Equation B.5 reduces to:

$$\frac{1}{v\sqrt{1+z'^2}} = p \tag{B.6}$$

and re-arranging for $\mathrm{d}w/\mathrm{d}z = 1/z'$ gives:

$$\frac{\mathrm{d}w}{\mathrm{d}z} = \pm\frac{vp}{\sqrt{1-p^2v^2}} \tag{B.7}$$

Using a vector notation to describe the path means that we can ignore the $\pm$ sign in Equation B.7, which merely indicates that the ray can go in the negative or positive w direction. Let $\mathbf{s} = [g, c]$ be a unit tangent vector to the path at any point so that $\mathrm{d}z/\mathrm{d}w = c/g$. Substitution of this expression into Equation B.6 results in:

$$p = \frac{1}{v\sqrt{1+c^2/g^2}} = \frac{g}{v} \tag{B.8}$$

Solving for w in Equation B.7 with reference to an origin point (w_o, z_o):

$$w = \int_{z_o}^{z} \frac{vp}{\sqrt{1-p^2v^2}}\mathrm{d}z + w_o \tag{B.9}$$

Let $g = pv$ be the substitution variable in Equation B.9 so that:

$$\begin{aligned} w &= -\frac{1}{pk}\int_{g_o}^{g} \frac{g}{\sqrt{1-g^2}}\mathrm{d}g + w_o \\ &= \frac{1}{pk}\left[\sqrt{1-g^2}\right]_{g_o}^{g} + w_o \\ &= \frac{1}{pk}(c - c_o) + w_o \end{aligned} \tag{B.10}$$

For the vertical coordinate, $v = v_0 - kz = v(z_o) - k(z - z_o)$ so:

$$\begin{aligned} z &= \frac{1}{k}[v(z_o) - v] + z_o \\ &= \frac{1}{pk}(g_o - g) + z_o \\ &= \frac{v(z_o)}{g_o k}\left[\sqrt{1-c_o^2} - \sqrt{1-c^2}\right] + z_o \\ &= \frac{v(z_o)}{k}\left[1 - \sqrt{\frac{1-c^2}{1-c_o^2}}\right] + z_o \end{aligned} \tag{B.11}$$

For a ray path through the 3-D model, the horizontal ray direction w is dependent on (x, y). Thus, let $\mathbf{s} = [a, b, c]$ be the unit tangent vector to the ray path, where $a^2 + b^2 = g^2$

so that $x = aw/g$ and $y = bw/g$. Transforming Equation B.10 into parametric equations for x and y gives:

$$\left.\begin{aligned} x &= \frac{a_o v(z_o)}{(1-c_o^2)k}[c - c_o] + x_o \\ y &= \frac{b_o v(z_o)}{(1-c_o^2)k}[c - c_o] + y_o \end{aligned}\right\} \tag{B.12}$$

Equations B.11 and B.12 are equivalent to Equation 4.5.

To determine traveltime, $v = \mathrm{d}l/\mathrm{d}t$ where $dl = \sqrt{1 + z'^2}$, so:

$$\frac{\mathrm{d}t}{\mathrm{d}z} = \frac{1}{v}\sqrt{\left(\frac{\mathrm{d}w}{\mathrm{d}z}\right)^2 + 1} \tag{B.13}$$

Substituting in Equation B.7 gives:

$$\frac{\mathrm{d}t}{\mathrm{d}z} = \frac{1}{v\sqrt{1 - p^2v^2}} \tag{B.14}$$

which can be integrated for t:

$$t = \int_{z_o}^{z} \frac{1}{v\sqrt{1 - p^2v^2}}\mathrm{d}z + t_o \tag{B.15}$$

Using $g = pv$ (see Equation B.8) as the substitution variable we get:

$$\begin{aligned} t &= \frac{1}{k}\int_{g_o}^{g} \frac{-1}{g\sqrt{1-g^2}}\mathrm{d}g + t_o \\ &= \frac{1}{k}\left[\ln\left(\frac{1+\sqrt{1-g^2}}{g}\right)\right]_{g_o}^{g} + t_o \\ &= \frac{1}{k}\ln\left[\frac{g_o}{g}\left(\frac{1+c}{1+c_o}\right)\right] + t_o \end{aligned} \tag{B.16}$$

which can be written:

$$t = \frac{1}{2k}\ln\left[\left(\frac{1+c}{1-c}\right)\left(\frac{1-c_o}{1+c_o}\right)\right] + t_o \tag{B.17}$$

Equation B.17 is thus identical to Equation 4.6.

Appendix C

Fréchet Derivatives

Fréchet Derivatives for Velocity and Velocity Gradient

Fréchet derivatives for velocity parameters are usually derived by assuming that a velocity perturbation doesn't cause a perturbation of the ray path, resulting in first order accurate expressions according to Fermat's principle (see Section 2.3.2). Here, analytic expressions for the Fréchet derivatives are derived (for the velocity parameters v_o and k in Section 4.2.1) assuming only that the endpoints of ray segments are fixed. Where this assumption is valid, exact analytic expressions for the Fréchet derivatives are obtained (e.g. for rays that don't interact with any interface). Where interfaces are involved, the resulting expressions provide accurate approximations. The basic problem, to find the derivatives $\partial t/\partial v_0$ and $\partial t/\partial k$ for a ray between two points in a layer, can be considered in 2-D since all ray path segments must lie in a vertical plane.

Consider a ray path segment that originates at (x_o, z_o) and ends at (x_e, z_e) with the x-axis defined such that $x_e > x_o$. The ray path between the two points is given parametrically by (see Appendix B):

$$x_e = \frac{v(z_o)}{k}\left[\frac{(c_e - c_o)}{\sqrt{1 - {c_o}^2}}\right] + x_o \tag{C.1}$$

$$z_e = \frac{v(z_o)}{k}\left[1 - \sqrt{\frac{1 - {c_e}^2}{1 - {c_o}^2}}\right] + z_o \tag{C.2}$$

and the traveltime is:

$$t = \frac{1}{2k}\ln\left[\left(\frac{1 + c_e}{1 - c_e}\right)\left(\frac{1 - c_o}{1 + c_o}\right)\right] \tag{C.3}$$

where c_o and c_e are the vertical components of the unit tangent vector to the ray segment at (x_o, z_o) and (x_e, z_e) respectively. The partial derivative of traveltime with respect to the velocity parameter v_0 is:

$$\frac{\partial t}{\partial v_0} = \frac{\partial t}{\partial c_o}\frac{\partial c_o}{\partial v_0} + \frac{\partial t}{\partial c_e}\frac{\partial c_e}{\partial v_0} \tag{C.4}$$

$\partial t/\partial c_o$ and $\partial t/\partial c_e$ are easily calculated from Equation C.3 as:

$$\frac{\partial t}{\partial c_o} = \frac{1}{k({c_o}^2 - 1)} \qquad \frac{\partial t}{\partial c_e} = \frac{1}{k(1 - {c_e}^2)} \tag{C.5}$$

To obtain $\partial c_o/\partial v_0$ and $\partial c_e/\partial v_0$, rearrange Equation C.1 and Equation C.2 to get, respectively:

$$c_e = c_o + r\sqrt{1 - {c_o}^2} \qquad 1 - {c_e}^2 = s^2(1 - {c_o}^2) \tag{C.6}$$

where $r = k(x_e - x_o)/(v_0 - kz_o)$ and $s = 1 - k(z_e - z_o)/(v_0 - kz_o)$. Implicit differentiation of each expression in Equation C.6 with respect to v_0 and solving the resulting system of two linear equations for the two unknowns $\partial c_o/\partial v_0$ and $\partial c_e/\partial v_0$ yields:

$$\frac{\partial c_o}{\partial v_0} = \frac{k(1 - {c_o}^2)[c_e(x_o - x_e) - s(z_o - z_e)\sqrt{1 - {c_o}^2}]}{v(z_o)^2[rc_ec_o + (c_os^2 - c_e)\sqrt{1 - {c_o}^2}]} \tag{C.7}$$

$$\frac{\partial c_e}{\partial v_0} = \frac{sk(1 - {c_o}^2)[c_os(x_o - x_e) + (z_o - z_e)(rc_o - \sqrt{1 - {c_o}^2})]}{v(z_o)^2[rc_ec_o + (c_os^2 - c_e)\sqrt{1 - {c_o}^2}]} \tag{C.8}$$

The partial derivative of traveltime with respect to the velocity gradient parameter k is:

$$\frac{\partial t}{\partial k} = \frac{\partial t}{\partial c_o}\frac{\partial c_o}{\partial k} + \frac{\partial t}{\partial c_e}\frac{\partial c_e}{\partial k} - \frac{1}{2k^2}\ln\left[\left(\frac{1 + c_e}{1 - c_e}\right)\left(\frac{1 - c_o}{1 + c_o}\right)\right] \tag{C.9}$$

where the third term on the RHS is included since k appears explicitly in Equation C.3. The partial derivatives $\partial c_o/\partial k$ and $\partial c_e/\partial k$ can be determined using the approach employed to calculate $\partial c_o/\partial v_0$ and $\partial c_e/\partial v_0$ above which gives:

$$\frac{\partial c_o}{\partial k} = \frac{v_o(1 - {c_o}^2)[c_e(x_e - x_o) + s(z_o - z_e)\sqrt{1 - {c_o}^2}]}{v(z_o)^2[rc_ec_o + (c_os^2 - c_e)\sqrt{1 - {c_o}^2}]} \tag{C.10}$$

$$\frac{\partial c_e}{\partial k} = \frac{sv_o(1 - {c_o}^2)[c_os(x_e - x_o) + (z_e - z_o)(rc_o - \sqrt{1 - {c_o}^2})]}{v(z_o)^2[rc_ec_o + (c_os^2 - c_e)\sqrt{1 - {c_o}^2}]} \tag{C.11}$$

Fréchet Derivatives for Interface Depth

The shape of a single surface patch depends on 16 vertices, so a single ray-interface intersection will contribute 16 partial derivatives of the form $[\partial t/\partial {z_v}^{k,l}]$ where $k, l =$

$1, \ldots, 4$ and z_v refers to the z-coordinate of an interface vertex. Exact analytic expressions for these Fréchet derivatives are out of the question, but relatively simple analytic formulae that are accurate to first order can be obtained. The basic approach for doing this has been outlined in Section 2.3.2. Hence, only the component of the solution that is relevant to a uniform B-spline parameterisation will be derived.

The perturbation in traveltime caused by the perturbation of an interface node is calculated to first order accuracy in Section 2.3.2 as (c.f. Equation 2.69):

$$\frac{\partial t}{\partial {z_v}^{k,l}} \approx \left[\frac{\mathbf{w}_j \cdot \mathbf{w}_n}{v_j} - \frac{\mathbf{w}_{j+1} \cdot \mathbf{w}_n}{v_{j+1}} \right] [\mathbf{w}_n \cdot \mathbf{w}_z] \frac{\partial z_{int}}{\partial {z_v}^{k,l}} \tag{C.12}$$

where z_{int} is the z-coordinate of the intersection point and the vector notation is defined in Section 2.3.2. The part of Equation C.12 that is specific to B-splines is $\partial z_{int}/\partial {z_v}^{k,l}$, and given the form of Equation 4.2 is simple to calculate:

$$\frac{\partial z_{int}}{\partial {z_v}^{k,l}} = b_k(u_{int}) b_l(v_{int}) \tag{C.13}$$

where (u_{int}, v_{int}) is the point of intersection in (u, v) coordinates. When phantom vertices are involved in the description of the surface patch that is intersected, then it is necessary to adjust the expression for $\partial z_{int}/\partial {z_v}^{k,l}$ since the phantom vertices are derived in terms of pre-existing vertices (see Equation 4.4). For example, if a ray intersects the corner surface patch adjacent to the $(i = 1, j = 1)^{th}$ node, the rate of change in depth of the intersection point with respect to a change in the depth of the corner node is given by:

$$\frac{\partial z_{int}}{\partial {z_v}^{1,1}} = b_0(u_{int}) b_0(v_{int}) + 4 b_{-1}(u_{int}) b_{-1}(v_{int}) + 2 b_{-1}(u_{int}) b_0(v_{int}) + 2 b_0(u_{int}) b_{-1}(v_{int}) \tag{C.14}$$

All three classes of Fréchet derivative calculation defined in this appendix have been tested by comparison with finite difference approximations obtained by shooting rays through a model, perturbing a model parameter and re-shooting the rays. Several of these tests were performed and good agreement between the analytic and numerical solutions occurred in all cases.

Appendix D

Description of Inversion Program

This appendix provides a brief synopsis of the 3-D wide-angle seismic inversion software used in this thesis. The method on which it is based is described in detail in Section 4.2. There are three component programs that make up the software: *trace3d*, which determines traveltimes and Fréchet derivatives, *invers* which inverts the traveltimes for model parameter values and *tomo* which calls both *trace3d* and *invers* to solve the nonlinear inverse problem. Each of these programs are described below.

tomo

tomo is a short program of 118 lines written in C. Its purpose is simply to sequentially call the ray tracing program *trace3d* and the inversion program *invers* until a specified number of iterations are achieved. It also deals with the book-keeping associated with two interacting but independent programs. *tomo* is designed to allow the iterative process to resume from where it last left off or from the beginning. A flow chart of tomo is shown in Figure D.1.

trace3d

trace3d is a FORTRAN77 program 4822 lines in length. It implements the ray tracing method described in Section 4.2.2. Briefly, it is designed to find first-arrival source-receiver ray paths and traveltimes of specified phases through 3-D layered structures in which velocity varies linearly with depth and interfaces are described by mosaics of

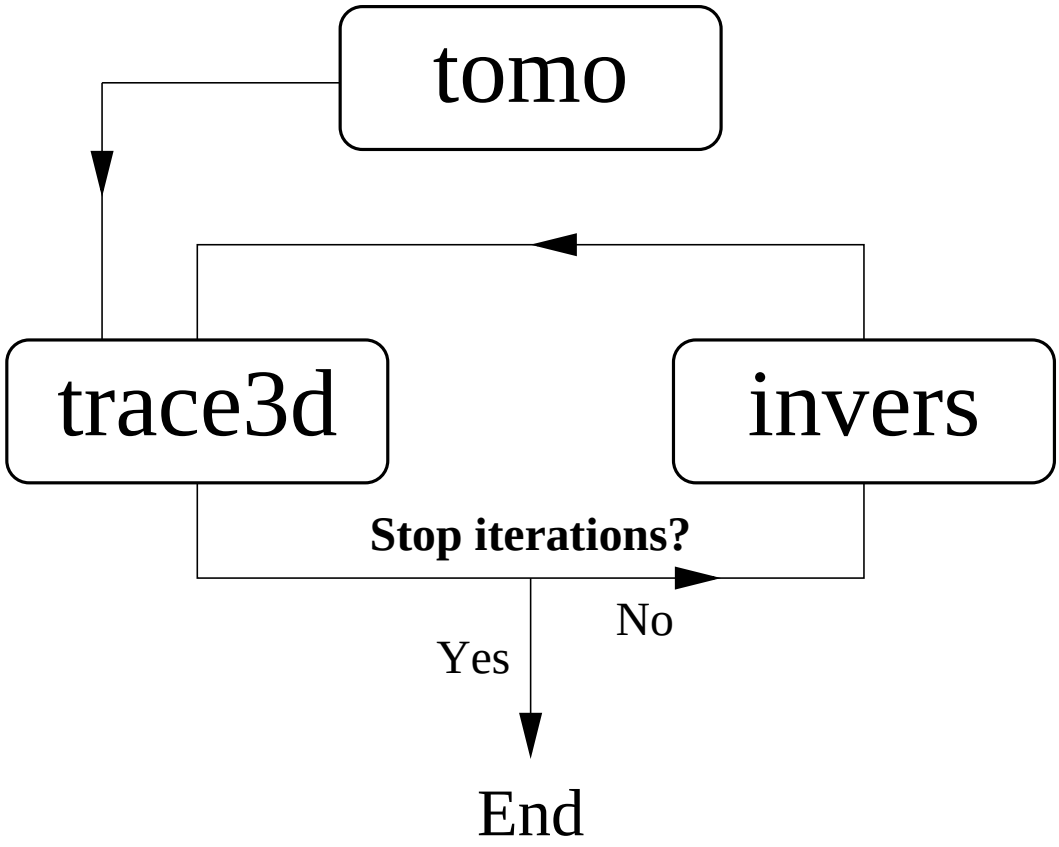

Figure D.1: Flow chart for the program *tomo* which solves the non-linear inverse problem.

bicubic B-spline surface patches in parametric form. While the initial value problem can find multiples, the shooting scheme is not designed to find two-point multiples. Multi-valued interfaces and layer pinchouts can be handled by *trace3d* and arbitrarily shaped surface patches are permitted. Phases are identified by the interface they reflect from in the case of reflections and by the deepest layer sampled in the case of refractions. The Fréchet derivatives derived in Appendix C are also calculated by *trace3d*. A flow chart of the program is shown in Figure D.2, and the functions of the subroutines and data files are described below.

Input files There are five input files:

- **inputp.dat:** Contains information like the number of rays in the initial and refined shoots (in both inclination and azimuth), whether to find refractions, reflections or both, patch dicing for initial guess (i.e. number of triangles to approximate patch), accuracy of ray-interface intersection point and tolerance for ray-receiver distance.

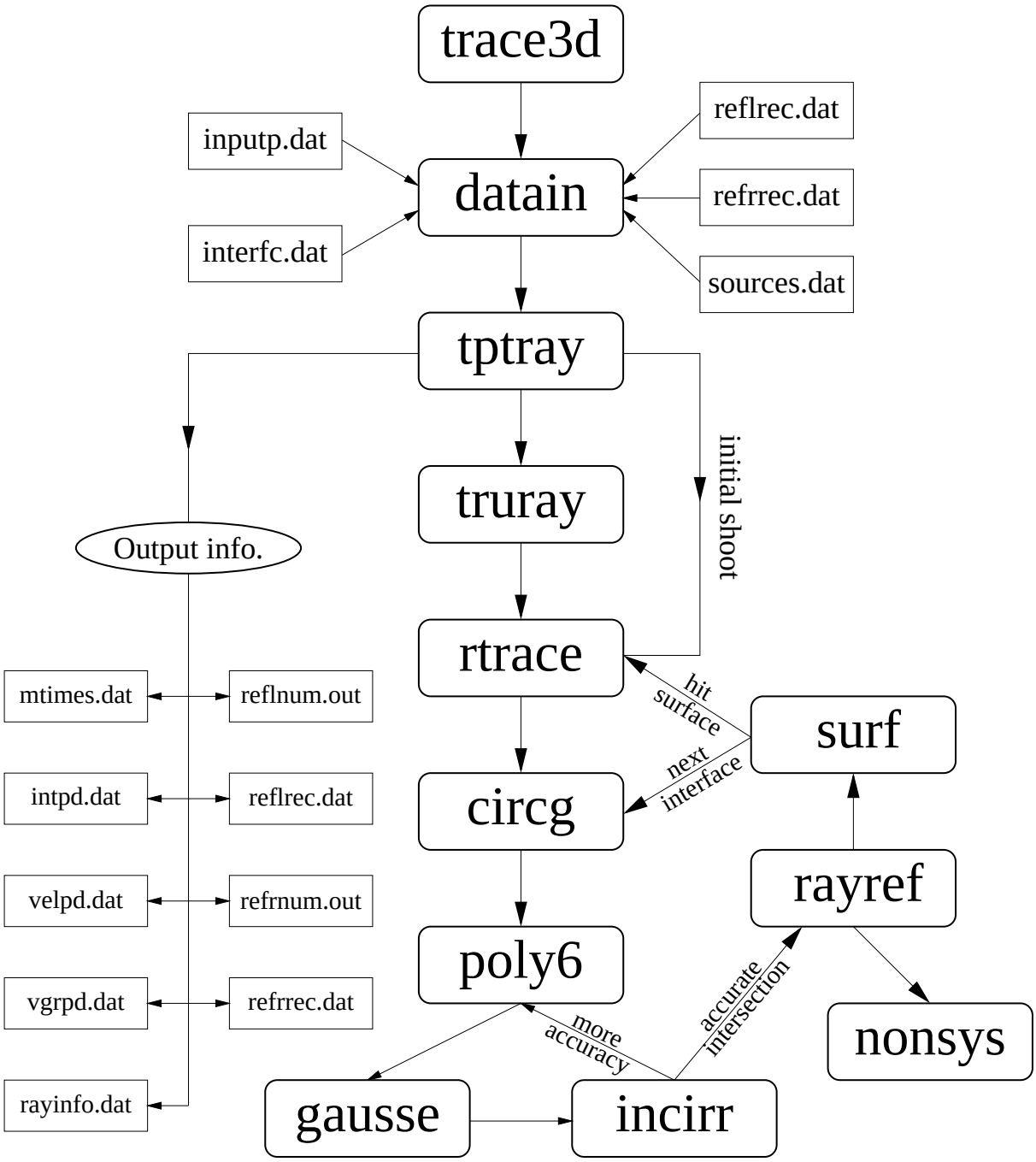

Figure D.2: Flow chart for the program *trace3d* which solves the 2-point ray tracing problem for 3-D layered structures and evaluates Fréchet derivatives.

- **interfc.dat:** coordinates of interface vertices and the values of the velocity and velocity gradient for each layer.
- **sources.dat:** Coordinates of sources and inclination and azimuth range for initial shoot from each source.
- **refrrec.dat:** Coordinates of each receiver to be hit by a refracting ray of a

specified phase.

- **reflrec.dat:** Coordinates of each receiver to be hit by a reflecting ray of a specified phase.

Subroutines There are 11 subroutines. Note that the subroutines *circg* and *poly6* may be replaced by *strtg* and *poly3* when the ray path is straight (e.g. constant velocity medium). In practice, this rarely occurs, so for simplicity the flow chart (Figure D.2) does not list them.

- **datain:** Reads the input files listed above.
- **tptray:** Finds all the required source-receiver ray paths and traveltimes. *tptray* shoots out fans of rays (via multiple calls of *rtrace*) and then calls *truray* to find a 2-point ray. If more than one path of the same phase is found between a source and receiver, *tptray* retains the ray with minimum traveltime. *tptray* also writes ray path, traveltime and Fréchet derivative information to the output files.
- **truray:** Given three rays near a receiver, this subroutine uses a Newton-type method to locate a 2-point ray path.
- **rtrace:** Solves the initial value problem for a single ray path. When requested, it also calculates the Fréchet derivatives for interface node depth, layer velocity and layer velocity gradient. It calls the subroutines *circg*, *poly6*, *rayref* and *surf*.
- **circg:** Finds the point of intersection between a circular ray path and a triangular plate approximation to the B-spline interface. The value determined is used as an initial guess in subroutine *poly6*.
- **poly6:** Accurately finds the point of intersection between a circular ray path and a bicubic B-spline surface patch using a generalised Newton method. Calls *gausse* and *incirr*.
- **gausse:** Gaussian elimination with partial pivoting subroutine used to solve 3×3 system of linear equations.
- **incirr:** Determines the accuracy of the ray-interface intersection point. Used in conjunction with tolerance criterion.

- **rayref:** Finds new direction of ray after intersection with interface (i.e. refracts or reflects the ray path). Calls *nonsys*.
- **nonsys:** Solves a system of three equations, one of which is non-linear, in order to find the new propagation direction of the ray path.
- **surf:** Calculates the point of intersection between a ray path and a receiver plane.

Output files There are nine output files, which save information on traveltimes, ray geometry, Fréchet derivatives and ray tracing problems.

- **mtimes.dat:** All required source-receiver traveltimes.
- **intpd.dat:** Interface Fréchet derivatives.
- **velpd.dat:** Layer velocity Fréchet derivatives.
- **vgrpd.dat:** Layer velocity gradient Fréchet derivatives.
- **reflnum.out:** Number of reflection rays for each source and phase successfully found.
- **reflrec.dat:** Reflection ray path geometry.
- **refrnum.out:** Number of refraction rays for each source and phase successfully found.
- **refrrec.dat:** Refraction ray path geometry.
- **rayinfo.dat:** Logs problems/features of the ray tracing, including ray failures caused by ray-interface or two-point shooting errors. Also records the number of ray multipaths found.

invers

invers is a FORTRAN77 program 1142 lines in length that is designed to update the model estimate defined by interface and velocity parameters. It performs a single inversion iteration of the subspace method or the conjugate gradient method (see Section 4.2.3). A flow chart for the program is given in Figure D.3 and the input files, subroutines, and output files are described below.

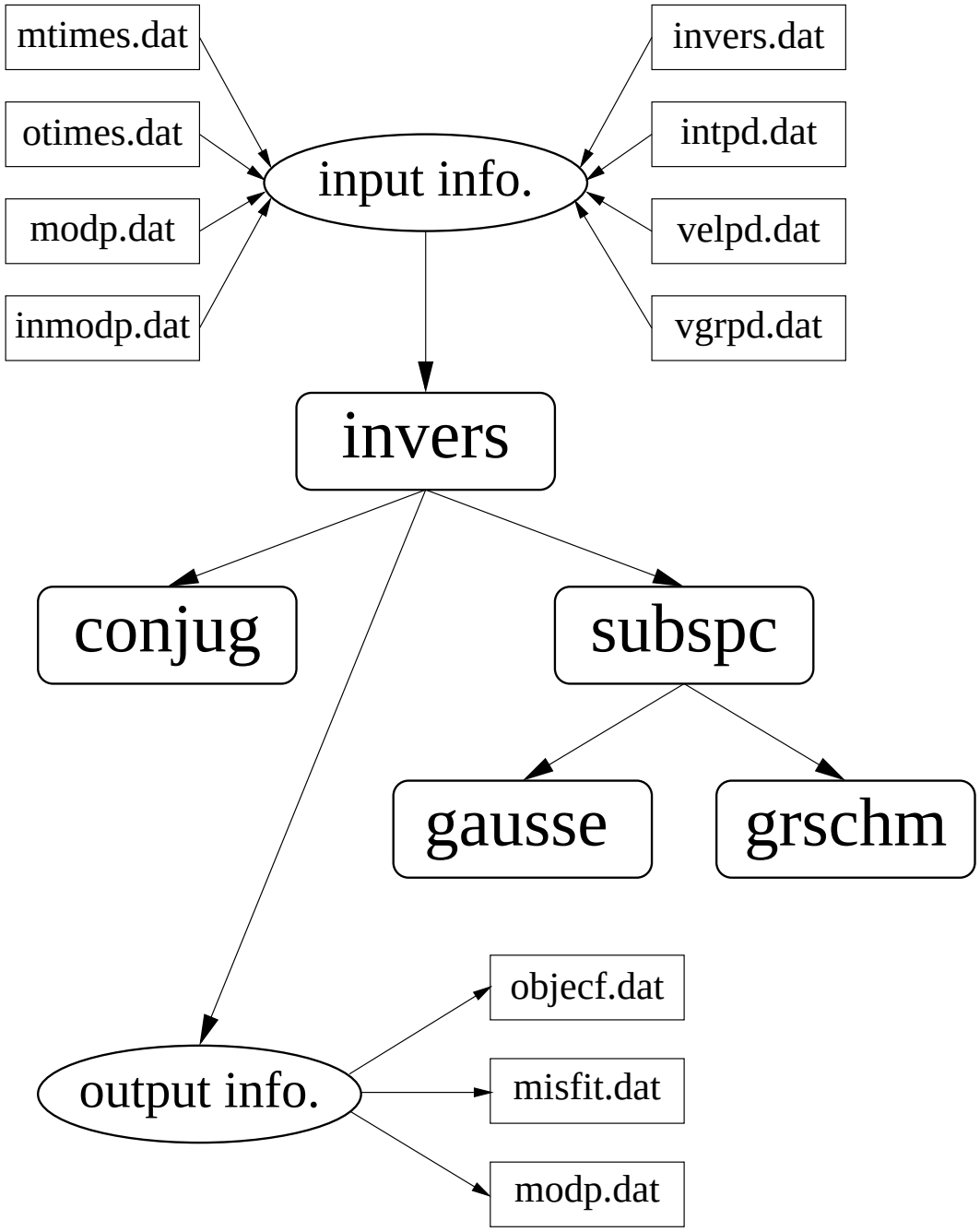

Figure D.3: Flow chart for the program *invers* which inverts traveltimes for interface and depth-dependent velocity structure.

Input files There are eight input files, some of which are the same as the output files of *trace3d*.

- **invers.dat:** Contains input options including flags to select the the type of inversion method (e.g. subspace inversion), the subspace dimension, the value of the damping factor, whether to invert reflections, refractions or both etc.

- **modp.dat:** Interface node coordinates, layer velocities and layer velocity gradients from previous iteration.
- **inmodp.dat:** Interface node coordinates, layer velocities and layer velocity gradients for initial estimate model plus diagonal elements of *a priori* model covariance matrix.
- **mtimes.dat:** Model source-receiver traveltimes for current model as determined by *trace3d*.
- **otimes.dat:** Observed source-receiver traveltimes plus diagonal elements of *a priori* data covariance matrix.
- **intpd.dat:** Interface Fréchet derivatives.
- **velpd.dat:** Layer velocity Fréchet derivatives.
- **vgrpd.dat:** Layer velocity gradient Fréchet derivatives.

Subroutines There are five program subroutines.

- **invert:** Inputs the above files and outputs the results. *invert* also tests to see whether interfaces overlap (i.e. whether layer pinch-outs are present).
- **conjug:** Uses the conjugate gradient method to obtain a new model estimate.
- **subspc:** Uses the generalised subspace inversion method to obtain a new model estimate. Calls *grschm* and *gausse*. Can also be used as a steepest descent algorithm.
- **gausse:** Gaussian elimination with partial pivoting is implemented to solve a system of $n \times n$ linear equations where n is the subspace dimension.
- **grmschm:** Given a set of vectors $\{\mathbf{a}^j\}$, this subroutine uses Gram-Schmidt orthogonalisation to produce an orthonormal set that spans the same space.

Output files There are three output files. Two additional files (grobjf.dat and sdmod.dat) are used merely to store gradient information for future iterations and are not described.

- **objecf.dat:** Contains the value of the objective function at each iteration.
- **misfit.dat:** Contains the value of the model misfit function at each iteration.

- **modp.dat:** Interface node coordinates, layer velocities and layer velocity gradients from current iteration.

Appendix E

Static Correction for Water Depth

This appendix derives an expression for the static correction for water depth. The static correction involves substitution of the water layer with an equivalent thickness crustal layer so that the traveltime effects of the water layer can be ignored in subsequent modelling. The seafloor is assumed to be locally flat at the point of ray intersection, the subsurface is assumed to be laterally invariant, and the ray path is assumed to be that of a horizontally propagating head wave. Figure E.1 illustrates these assumptions and the meanings of the variables used in the following derivation.

If t_{sc} is the static-corrected arrival time and t_0 is the uncorrected arrival time, then the relationship between these two values is defined by:

$$t_{sc} = t_0 - (t_{SE} + t_{ED} - t_{BC}) \tag{E.1}$$

where the other terms refer to the traveltimes between the points marked on Figure E.1. These traveltimes are defined by:

$$\left.\begin{aligned} t_{SE} &= \frac{h_1}{v_1 \cos\theta_1} \\ t_{ED} &= \frac{h_2}{v_2 \cos\theta_2} \\ t_{BC} &= \frac{1}{v_n}(h_1 \tan\theta_1 + h_2 \tan\theta_2) \end{aligned}\right\} \tag{E.2}$$

and since:

$$\left.\begin{aligned} \cos\theta_1 &= \frac{\sqrt{{v_n}^2 - {v_1}^2}}{v_n} \quad \cos\theta_2 = \frac{\sqrt{{v_n}^2 - {v_2}^2}}{v_n} \\ \tan\theta_1 &= \frac{v_1}{\sqrt{{v_n}^2 - {v_1}^2}} \quad \tan\theta_2 = \frac{v_2}{\sqrt{{v_n}^2 - {v_2}^2}} \end{aligned}\right\} \tag{E.3}$$

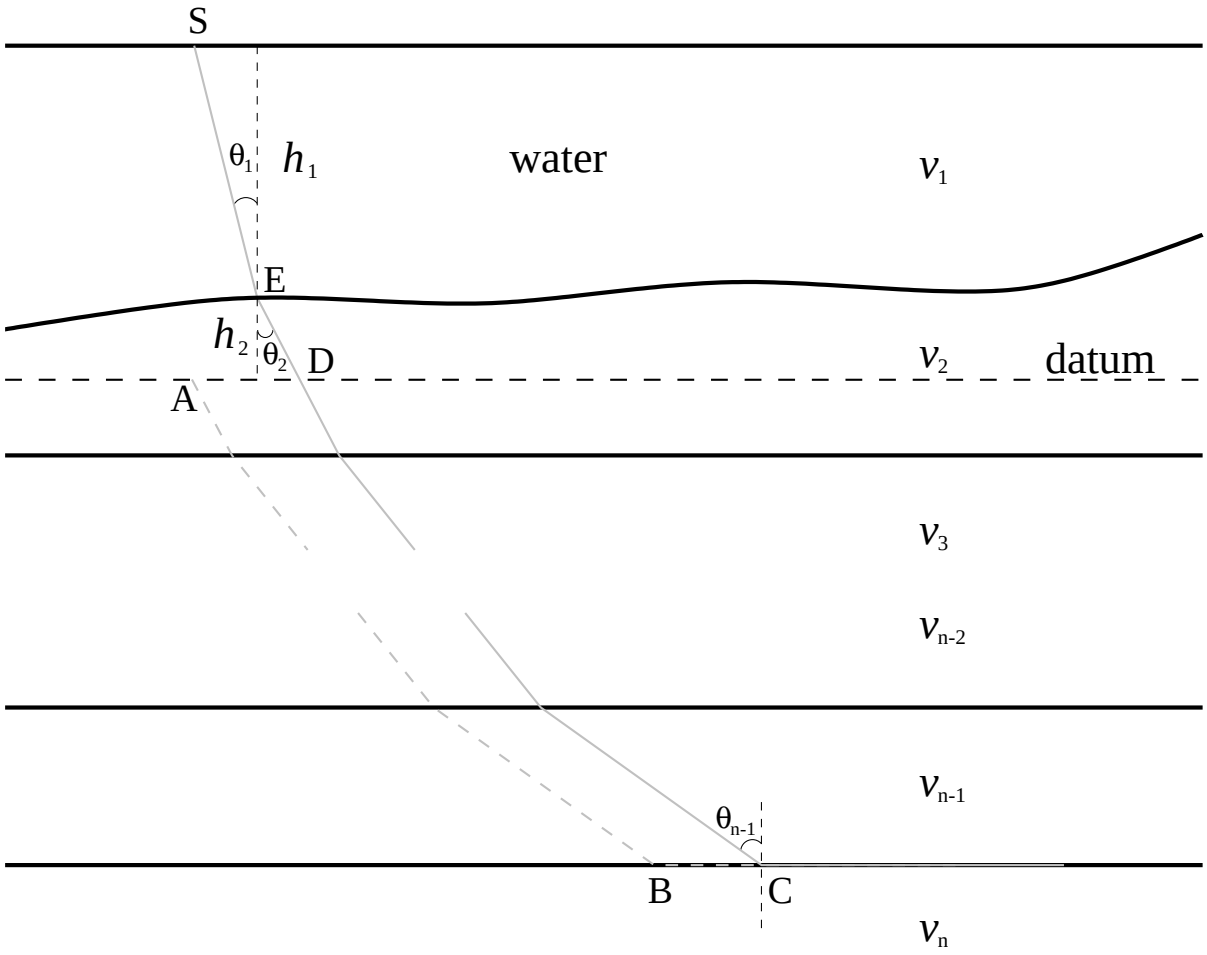

Figure E.1: Static correction for water depth. The shot point S is vertically relocated to point A on the datum plane.

then substitution of Equation E.3 into Equation E.2, followed by substitution of Equation E.2 into Equation E.1 yields:

$$t_{sc} = t_0 - \frac{v_n h_1}{v_1\sqrt{{v_n}^2 - {v_1}^2}} - \frac{v_n h_2}{v_2\sqrt{{v_n}^2 - {v_2}^2}} + \frac{1}{v_n}\left(\frac{h_1 v_1}{\sqrt{{v_n}^2 - {v_1}^2}} + \frac{h_2 v_2}{\sqrt{{v_n}^2 - {v_2}^2}}\right) \tag{E.4}$$

which can be simplified to:

$$t_{sc} = t_0 - \frac{1}{v_n}\left(\frac{h_1\sqrt{{v_n}^2 - {v_1}^2}}{v_1} + \frac{h_2\sqrt{{v_n}^2 - {v_2}^2}}{v_2}\right) \tag{E.5}$$

The correction therefore requires values of v_1, v_2, v_n, h_1 and h_2. v_1 is just P-wave velocity in sea water, v_2 is the velocity of the uppermost crust, which can be estimated from near-offset first-arrivals, and v_n can be determined from the gradient of the first-arrival curve in question. The sea-floor topography is assumed known, which gives h_1, and since the datum depth is specified *a priori*, h_2 can also be found.

If the datum is chosen to be the sea surface, then $h_2 = -h_1 = h$ and the correction becomes:

$$t_{sc} = t_0 - \frac{h}{v_n}\left(\frac{\sqrt{{v_n}^2 - {v_1}^2}}{v_1} + \frac{\sqrt{{v_n}^2 - {v_2}^2}}{v_2}\right) \tag{E.6}$$

as used in Equation 6.6, with $v_w = v_1$ and $v_2 = v_c$. Purdy (1982), in his investigation of methods for correcting traveltimes for seafloor topography, gives the following datum correction formula:

$$t_{sc} = t_t - h\left[\frac{\sqrt{1 - v_w^2 p^2}}{v_w} - \frac{\sqrt{1 - v_c^2 p^2}}{v_c}\right] \tag{E.7}$$

where p is the ray parameter, which can be estimated from the gradient of the time vs. offset traveltime curves. Since $p = (\sin i)/v = 1/v_n$, where i is the inclination angle of the ray with the vertical, Equation E.7 is actually equivalent to Equation E.6.

Appendix F

Contents of Enclosed CD

Attached to the back cover of this thesis is a CD containing an animation, all of the digitised TASGO data, and a number of computer programs developed during the course of my PhD work. These programs are used in the thesis to invert traveltime data for layered crustal structure and visualise the results. This appendix briefly describes the contents of the CD. The README.TXT file located in the root directory of the CD also contains similar information.

MPEG Movie

The file *tasman.mpg* is an MPEG movie file which shows the structure of the four-layer NW Tasmania model (Figure 7.19) and the ray paths used to constrain it (Figure 7.20). The movie contains approximately 720 frames and was generated using the free graphics package Geomview. The model is rotated, translated and scaled using TCL script. Note that the model and ray paths shown are for a slightly earlier version of the solution; in particular, interfaces 1 and 2 have a rectangular shape in the older version. However, the model structure and ray paths are essentially the same. *tasman.mpg* resides in the root directory of the CD.

Programs

Seven subdirectories containing computer programs and example input files can also be found in the root directory of the CD. All programs are provided as source code and

need to be compiled into executable form before use. The contents of each of these subdirectories are described as follows:

1. Tasdata

dataplot.f Program for processing, visualising and picking TASGO data.

dataplot.dat Required input file for dataplot.f which may use the following files: statc.dat, waven17.1, win17.1, label.txt, opicks.dat.

dataplot.pdf Instructions for using *dataplot*.

port.tar.gz All digitised data from the portable analogue recorders.

observ.tar.gz All data from digital observatory stations.

The program *dataplot* can be used to view all of the TASGO wide-angle data that was digitised and made available by AGSO. In addition, *dataplot* allows the picked data used in this thesis (see directories Example1 and Example2 below) to be superimposed on the the observed data for comparison.

2. Wideainv

tomo.c Program for tomographic inversion of wide-angle seismic traveltimes for 3-D layered crustal structure.

modpot.f Housekeeping program for *tomo*.

trace3d.f Program for determining source-receiver traveltimes of refracted and reflected ray paths through a 3-D layered crustal structure (uses header file trace3d.h).

invers.f Program that updates the model estimate using the subspace inversion method (or steepest descents or conjugate gradients). Uses a header file called invers.h.

resolve.f Program for determining *a posteriori* model covariance and resolution.

coords.f This program is not strictly part of the inversion routine but it is a necessary interface when real data is used. It organises picked files into the correct format for input into *tomo* and projects lat/long coordinates into Cartesian space using one of two conic projections: Albers equal area or Lambert conformal.

tomo.pdf Instructions for using the tomographic inversion routine.

These programs can be tested on the example files provided (see directories Example1-Example3).

3. Graphics

This subdirectory contains programs used for generating many of the figures contained in this thesis. All programs listed below (except plot3d.f) require the PGPLOT subroutine libraries in order to function. These libraries may be obtained freely over the WWW at: http://www.astro.caltech.esu/∼tjp/pgplot.

cont.f Draws colour contours of interface structure defined by bicubic B-splines in parametric form. Works even if interface spacing is irregular.

misfit.f Plots χ^2 misfit or RMS misfit versus iteration number from *tomo* output.

objecf.f Plots magnitude of objective function versus iteration number from *tomo* output.

plot3d.f Program which converts output from *trace3d* (ray paths, interfaces, sources, receivers, coastline) into OOGL format suitable for visualisation using the free graphics software Geomview, which is available from the WWW at: http://www.geom.umn.edu/software/download.

rvis3d.f Plots linearised estimates of *a posteriori* covariance, resolution and correlation. Values are represented using contouring or dots of various sizes.

slice1d.f Plots velocity versus depth profiles of 3-D model determined by inversion of wide-angle traveltimes at specified points along the model.

slice2d.f Displays 2-D slices of the 3-D model determined by inversion of wide-angle traveltimes.

tim.f Plots observed and model traveltime curves including pick uncertainties if required.

vmodg.f Plots horizontal shape of surface patch boundaries, horizontal node positions and ray-interface hit points.

graphics.pdf Instructions for using graphics programs.

4. Example1

This directory contains all the files necessary for performing the first synthetic 3-D inversion example described in Section 4.3.2.

5. Example2

This directory contains all the files necessary (including all picks from interactive use of *dataplot*) for carrying out the inversion of TASGO wide-angle traveltimes for the four-layered crustal structure of NW Tasmania (see Section 7.4.1).

6. Example3

This directory contains all the files necessary (including all picks from interactive use of *dataplot*) for carrying out the inversion of all picked P_mP and P_n phases from the TASGO dataset for the Moho structure of Tasmania (see Section 7.4.2).

7. Teleseis

This directory contains the inversion package of Rawlinson (1996b) which was used in Chapter 3 to determine 2-D layered crustal structure in Central Australia from teleseismic traveltime residuals. Instructions for using the package are provided.